THE MINISTRY OF SCIENCE AND HIGHER EDUCATION OF THE RUSSIAN FEDERATION

ST. PETERSBURG STATE POLYTECHNICAL UNIVERSITY

JOURNAL

Physics and Mathematics

VOLUME 15, No.3.1, 2022

Peter the Great St. Petersburg
Polytechnic University
2022

ST. PETERSBURG STATE POLYTECHNICAL UNIVERSITY JOURNAL.
PHYSICS AND MATHEMATICS

The journal is included in the List of leading peer-reviewed scientific journals and other editions to publish major findings of theses for the research degrees of Doctor of Sciences and Candidate of Sciences.

The publications are presented in the VINITI RAS Abstract Journal and Ulrich's Periodical Directory International Database.

The journal is published since 2008 as part of the periodical edition 'Nauchno-tekhnicheskie vedomosti SPb-GPU'.

The journal is registered with the Federal Service for Supervision in the Sphere of Telecom, Information Technologies and Mass Communications (ROSKOMNADZOR). Certificate ПИ № ФС77-52144 issued December 11, 2012.

The journal is distributed through the CIS countries catalogue, the «Press of Russia» joint catalogue and the «Press by subscription» Internet catalogue. The subscription index is 71823.

The journal is in the **Web of Science** (Emerging Sources Citation Index), **Scopus,** the **Russian Science Citation Index** (RSCI) and the **Directory of Open Access Journals** (DOAJ) databases.

Address: 195251 Politekhnicheskaya St. 29, St. Petersburg, Russia.

Phone: (812) 294-22-85.

http://ntv.spbstu.ru/physics

MESSAGE FROM THE EDITORIAL BOARD

St. Petersburg State Polytechnical University Journal: Physics and Mathematics starts a series of special issues collecting the proceedings of international conferences in physics and mathematics.

Since its inception in 2008 as part of, the journal has been published 4 times a year. This year marks our 15th anniversary. The journal has upheld the high standards of research excellence, with all manuscripts subjected to stringent peer review procedures. Our reviewers are world-class scientists, many of them leading their own research teams. Our papers are indexed by both Russian (RSCI) and international databases such as Scopus and Web of Science. The Editorial Board welcomes manuscripts combining approaches from different fields of physical and mathematical sciences: thus, the journal provides a unique platform for exchange and dissemination of new knowledge. The Editorial Board comprises renowned scientists from major research institutions around the world.

The journal has previously published selected papers from international conference proceedings. Opening a series of conference proceedings, this issue exclusively contains the reports presented at the Sixth Asian School-Conference on Physics and Technology of Nanostructured Materials (ASCO-Nanomat 2022). The Editorial Board believes that publishing materials from international conferences facilitates the exchange of scientific information, advancing the present state of physical knowledge. Furthermore, all researchers, especially young scientists, are given an opportunity to publish their best reports at international conferences, with further indexing in international databases.

Preserving the best traditions of Russian university journals, we are open to new ideas, striving to address the international scientific community. The Editorial Board hopes that additional conference issues will give us an opportunity to expand our readership around the world.

Professor Vadim Ivanov,
Editor-in-Chief

PREFACE

The Sixth Asian School-Conference on Physics and Technology of Nanostructured Materials (ASCO-Nanomat 2022) has been held under the auspices of the Institute of Automation and Control Processes of the Far Eastern Branch of Russian Academy of Sciences and Far Eastern Federal University, in Vladivostok on April, 25–29, 2022. ASCO-NANOMAT 2022 was intended as a forum for senior and young scientists and technologists from Asian and European universities, academic institutes and industrial enterprises where they can present their latest findings and develop new synergies in the field of Physics and Technology of Nanostructured Materials and related subjects.

Vladivostok is a Russian city in the Far Eastern region, geographically close to Asian countries: China, Japan, Korea, India, Taiwan, Australia and others. Therefore, the primary goal of this School-Conference is to stimulate multidisciplinary contacts and cooperation between scientists from Asia and Europe. Russia acts here as a bridge connecting two parts of the world. The second goal is to give young scientists an opportunity to deliver their presentations in an international conference, with awards for the best oral or poster report to motivate them.

The conference was held in hybrid format, both on-site and online. The live sessions were held at the FEFU campus, attended by 56 participants from Vladivostok and 35 from other cities, including foreign students. The rest of the contributors from Russia and from abroad participated in an online format due to coronovirus restrictions. The School-Conference has been deemed a success achieving all of its goal. Due to a large number of reports, the conference was simultaneously held in two halls. Overall, 9 plenary, 17 invited, 59 oral and 125 poster reports have been presented (on-site and online) by the participants, including renowned professors, young scientists and post-graduate students from 13 Asian and European countries, including Russian Federation. The ASCO-Nanomat 2022 is a multidisciplinary school-conference, which has been held for the sixth time, and had six scientific sections:

- Physics of nanostructures and interfaces, self-organization processes, two-dimensional materials
- Physics of semiconducting nanostructures and heterostructures, including silicide, Group-IV alloy materials, A3B5 and A2B6 heterostructures: experiment, calculations and technology
- Ferromagnetic and ferroelectric materials, including nanomaterials, a spintronics
- Nanostructured coverages, nanocomposites, functional hybrid materials: formation, structure and properties
- Laser nanofabrication, all-dielectric materials, nanomaterials: fundamentals and applications

Photonic and electronic devices: integrated circuits, solar cells, nanophotonics, biophotonics
Abstracts of all reports were published electronically by Dalnauka publishing house.

At the end of the conference, 8 young scientists (under 35 years old) were awarded prizes for the best oral and poster presentations. After the conference, the on-site participants visited an open-air zoo 60 km from Vladivostok.

The Publishing Committee and International Program Committee have selected 43 unpublished articles, which were recommended for publication in *St. Petersburg Polytechnic University Journal: Physics and Mathematics* as selected Proceedings.

We, the International Program Committee, are very pleased to publish selected articles of ASCO-NANOMAT 2022 for scientists, researchers and students with interest in the physics and technology of nanostructured materials.

We would like to take this opportunity to thank all authors, plenary and invited lectors, the Organizing Committee and International Program Committee members for their contributions to the conference.

Professor Nikolay G. Galkin,
Chairman of ASCO-Nanomat 2022,
Vladivostok, Institute of Automation
and Control Processes FEB RAS
(galkin@iacp.dvo.ru)

Contents

Condensed matter physics

Simulation of physical processes

Atom physics and physics of clusters and nanostructures

Physical electronics

Physical materials technology

CONDENSED MATTER PHYSICS

Conference materials
UDC 538.9 + 535.3
DOI: https://doi.org/10.18721/JPM.153.101

Formation, structure, and optical properties of single-phase CaSi and $CaSi_2$ films on Si substrates

N. G. Galkin [1, 2] ✉, K. N. Galkin [1], O. V. Kropachev [1], I. M. Chernev [1],
S. A. Dotsenko [1], D. L. Goroshko [1, 2], E. Yu. Subbotin [1], A. Yu. Alekseev [3], D. B. Migas [3]

[1] Institute of Automation and Control Processes FEB RAS, Vladivostok, Russia;
[2] Far Eastern Federal University, Vladivostok, Russia;
[3] Belarusian State University of Informatics and Radioelectronics, Minsk, Belarus

✉ galkin@iacp.dvo.ru

Abstract: In this paper, we report on optimizing the conditions for subsequently growing single-phase films of calcium monosilicide (CaSi) and calcium disilicide ($CaSi_2$) on single-crystal silicon by reactive deposition epitaxy (RDE) and molecular beam epitaxy (MBE). The temperature range for the growth of CaSi films (400–500 °C) was determined, as well as the temperature range (600–680 °C) for the growth of $CaSi_2$ films on silicon with three orientations: (111), (100) and (110). The minimum temperatures for the epitaxial growth of CaSi films by the RDE method and $CaSi_2$ films by the MBE method were determined, amounting to, respectively, T = 475 °C and T = 640 °C. An increase in the ratio of Ca to Si deposition rates to 26 made it possible to grow a large-block $CaSi_2$ epitaxial film with the hR6 structure by the MBE method at T = 680 °C. Raman spectra and reflection spectra from single-phase epitaxial CaSi and $CaSi_2$ films on silicon were recorded and identified for the first time. The correspondence between the experimental reflection spectra and the theoretically calculated reflection spectra in terms of amplitude and peak positions at photon energies of 0.1–6.5 eV has been established. Single-phase CaSi and $CaSi_2$ films retain transparency in the photon energy range 0.4–1.2 eV.

Keywords: CaSi films, $CaSi_2$ films, silicon, single-phase growth, optical functions, energy band structure, ab initio calculations

Funding: The study was supported by a Russian Foundation for Basic Research grant no. 20-52-00001-Bel_a.

Citation: Galkin N.G., Galkin K.N., Kropachev O.V., Chernev I.M., Dotsenko S.A., Goroshko D.L., Subbotin E.Yu., Alekseev A.Yu., Migas D.B., Formation, structure, and optical properties of single-phase CaSi and $CaSi_2$ films on Si substrates. St. Petersburg State Polytechnical University Journal. Physics and Mathematics. 15 (3.1) (2022) 9–15. DOI: https://doi.org/10.18721/JPM.153.101

Материалы конференции
УДК 538.9 + 535.3
DOI: https://doi.org/10.18721/JPM.153.101

Формирование, структура и оптические свойства однофазных пленок CaSi И $CaSi_2$ на Si подложках

Н. Г. Галкин [1,2] ✉, К. Н. Галкин [1], О. В. Кропачев [1], И. М. Чернев [1],
С. А. Доценко [1], Д. Л. Горошко [1,2], Е. Ю. Субботин [1], А. Ю. Алексеев [3], Д. Б. Мигас [3]

[1] Институт автоматики и процессов управления ДВО РАН, г. Владивосток, Россия;
[2] Дальневосточный федеральный университет, Владивосток, Россия;
[3] Белорусский государственный университет информатики и радиоэлектроники, г. Минск, Беларусь

✉ galkin@iacp.dvo.ru

Аннотация. В работе оптимизированы условия и выращены однофазные пленки моносилицида кальция (CaSi) и дисилицида кальция ($CaSi_2$) на монокристаллическом кремнии с тремя ориентациями: (111), (100) и (110). Определена минимальная температура эпитаксиального роста пленок CaSi методом РДЭ: T = 475 °C и пленок $CaSi_2$ методом МЛЭ: T = 640 °C, выращена крупноблочная эпитаксиальная пленка $CaSi_2$ со структурой hR6. Впервые зарегистрированы и идентифицированы спектры КР и спектры отражения от однофазных эпитаксиальных пленок CaSi и $CaSi_2$ на кремнии. Установлено соответствие между экспериментальными спектрами отражения и теоретически рассчитанными спектрами отражения при энергиях фотонов 0,1 − 6,5 эВ. Однофазные пленки CaSi и $CaSi_2$ сохраняют прозрачность в диапазоне энергий фотонов 0,4−1,2 эВ.

Ключевые слова: пленки CaSi и $CaSi_2$, кремний, однофазный рост, оптические функции, зонная структура, первопринципные расчеты

Финансирование: Работа выполнена при поддержке гранта РФФИ № 20-52-00001-Бел_а.

Ссылка при цитировании: Галкин Н. Г., Галкин К. Н., Кропачев О. В., Чернев И. М., Доценко С. А., Горошко Д. Л., Субботин Е. Ю., Алексеев А. Ю., Мигас Д. Б., Формирование, структура и оптические свойства однофазных пленок CaSi И $CaSi_2$ на Si подложках // Научно-технические ведомости СПбГПУ. Физико-математические науки. 2022. Т. 15. № 3.1. С. 9−15. DOI: https://doi.org/10.18721/ JPM.153.101

Introduction

Calcium silicides are environmentally friendly materials, taking a special place among alkaline earth metal silicides. This is primarily due to a wide range of properties of calcium silicides from semiconducting [1] to semimetallic [2]. This shows promise for their widespread use in various fields of technology and electronics. However, growing single-phase films of semimetallic monosilicide (CaSi) and calcium disilicide ($CaSi_2$) on silicon and studying their optical properties are challenging tasks due to the presence of at least 6 silicides of different compositions in the Ca-Si system [3] and the lack of methods for separating the preferred orientation during growth silicon silicides.

The purpose of this work is to grow single-phase CaSi and $CaSi_2$ epitaxial films on silicon with different orientations and to determine the features of their band structure and optical properties by experimental and theoretical methods.

Experimental

The growth of CaSi and $CaSi_2$ films was carried out in an ultra-high vacuum (UHV) chamber of the OMICRON Compact setup (2×10^{-11} Torr) equipped with a LEED analytic equipment and different sources of Si and metals (Mg, Ca) [4]. The deposition of Ca (RDE method) or Ca and Si (MBE method) was carried out on an atomically clean Si(111)-7x7 surface in two temperature ranges: 400−500 °C and 600−680 °C. The deposition rates of Si and Ca were calibrated using a quartz thickness gauge. Data on growth regimes and structures of grown Ca silicide films are presented in Table 1.

Experimental equipment for optical and Raman spectroscopy and conditions for recording transmission (T) and reflection (R) spectra are described in [4]. The crystal structure of the grown films was studied by X-ray diffraction (XRD) using the equipment presented in [5]. The analysis of the optical characteristics of the grown films was carried out in the framework of a two-layer model [6]. Methods for the first-principle calculation of the band structure of CaSi and $CaSi_2$ in bulk form and the form of films are presented in [7].

Table 1

Growth regimes and structures of CaSi and CaSi2 films on silicon substrates

Sample	Substrate	Growth method	V_{Ca}/V_{Si}	Substrate temperature, °C	Film thickness, nm	XRD data
C440	Si(111)	MBE	8.7	500	40	CaSi(010)‖Si(111) CaSi(100)‖-Si(111)
V688	Si(111)	RDE	–	400	100	CaSi (010)/Si(111)
V691	Si(111)	RDE	–	475	90	CaSi (100)/Si(111)
C317	Si(001)	MBE	26	680	400	hR6-$CaSi_2$[100]‖Si[10] hR6-$CaSi_2$(01)‖Si(002)
C446	Si(001)	MBE	29.3	640	120	hR6-$CaSi_2$(01)‖Si(111), hR6-$CaSi_2$(012)‖Si(111)
V694	Si(111)	RDE	–	625	80	hR6-$CaSi_2$(001)/Si(111) hR3-$CaSi_2$(001)/Si(111)
V699	Si(110)	RDE	–	600	140	hR3-$CaSi_2$(001)/Si(110)

Results and Discussion

Studies of the morphology and structure of films formed by the RDE method at temperatures of 400–475 °C showed that there is a temperature limit (475 °C) when CaSi grains crystallize in the form of rectangular nanocrystals with dimensions 30–50 nm wide and 200–300 nm long. Application of the MBE method for film growth at a temperature of 500°C made it possible to form a single-phase CaSi film (Fig. 1,*a*), which also consisted of ordered rectangular nanocrystals (Fig. 1,*a*, inset). The formation of $CaSi_2$ films was detected during Ca RDE method in the temperature range of 600–625 °C on two types of substrates: Si(111) (V694, Table 1) and Si(110) (V699, Table 1). Regardless of the substrate orientation, the growth of grains with the hR3-$CaSi_2$(001)/Si(111) epitaxial orientation was observed. However, in the case of growth on a Si(111) substrate at a temperature of 625°C, the appearance of a polymorphic $CaSi_2$ phase with the hR6-$CaSi_2$(001)/Si(111) epitaxial orientation was also observed. During the growth of $CaSi_2$ films, the orientation of the formed grains depended on the substrate temperature and the ratio of calcium to silicon deposition rates. An increase in the ratio of the Ca to Si deposition rate to 26 at a temperature of 680°C led to the formation by MBE method of a thick (400 nm) large-block $CaSi_2$ film (sample C317) with epitaxial relationships: hR6-$CaSi_2$[100]‖Si[1 $\bar{1}$ 0] and hR6-$CaSi_2$(01 $\bar{1}$)‖Si(002) (Table 1). With a decrease in the substrate temperature and an approximate preservation of the ratio of rates, the formation of epitaxial grains with two epitaxial orientations was observed: hR6-$CaSi_2$(01)‖Si(111) and hR6-$CaSi_2$(012)‖Si(111) (Fig. 1, *b*).

After the samples were unloaded from the growth chambers, the transmission and reflection spectra were recorded in the photon energy range from 0.05 eV to 6.5 eV. The main features for

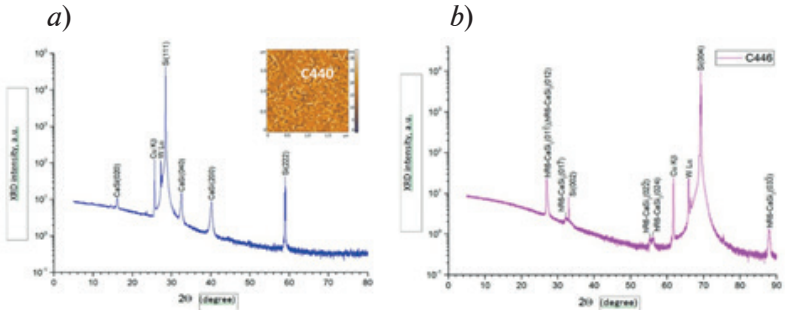

Fig. 1. XRD spectra for a single-phase CaSi film grown by MBE at T = 500 °C (*a*) and a single-phase CaSi2 film (MBE, T = 640 °C, sample C446) (*b*)
The inset in (*a*) shows the AFM image of the CaSi film (sample C440)

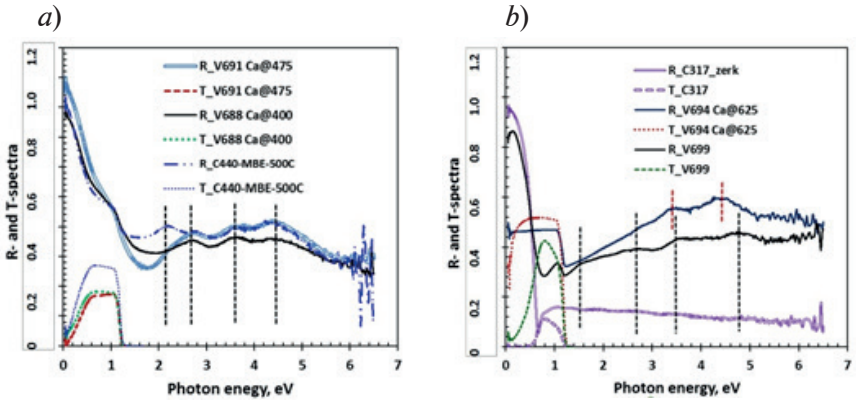

Fig. 2. Reflectance and transmittance spectra for CaSi (*a*) (samples V688, V691, C440) and $CaSi_2$ (*b*) (samples V694, V699, C317) films on Si substrates

the CaSi and $CaSi_2$ films were the partial transparency of both films in the photon energy range of 0.2–1.1 eV and the plasma minimum in reflection, which was previously observed for $CaSi_2$ films [8] with semimetallic properties. The transparency of $CaSi_2$ films (Fig. 2, *b*) is slightly higher than the transparency of CaSi (Fig. 2, *a*).

Registration of Raman spectra showed that single-phase CaSi and $CaSi_2$ films have several individual peaks, which are in good agreement with the data of theoretical calculations [8] and preliminary experimental studies for nanocrystalline and non-single-phase films [9, 10]. Therefore, Raman spectroscopy data can be used to identify the elemental composition and its single-phase nature.

Comparison with the data of theoretical reflection spectra for three planes of a single crystal of CaSi (Fig. 4, *a*) and $CaSi_2$ (Fig. 4, *b*) shows good agreement in the position of the plasma minimum for both silicides, which is associated with the contribution of two types of carriers, according to the calculations performed in this work. The reflection spectra also agree in magnitude and position of the main peaks in the photon energy range of 1.5–6.5 eV, which corresponds to the main interband transitions in CaSi and $CaSi_2$ single crystals.

Calculations of the optical functions of CaSi films from the reflection and transmission spectra (Fig. 2, *a*) within the two-layer model [6], taking into account multiple reflection and absorption, made it possible to obtain the spectral dependences of the refractive index and extinction coefficient (Fig. 5, *a*), absorption coefficient spectra (Fig. 5, *b*) and optical conductivity spectrum (Fig. 5, *c*) for CaSi films on silicon in the photon energy range of 0.1–1.2 eV. CaSi films in both samples (V691 and V688) have an almost constant absorption coefficient $(4–5)\cdot10^4$ cm^{-1} at energies of 0.4–1.2 eV and increasing absorption on free carriers at energies less than 0.4 eV, which is consistent with the plasma minimum in the reflection spectrum (Fig. 2, *a*). An increase in the concentration of free carriers correlates with an increase in optical conductivity (Fig. 5, *c*).

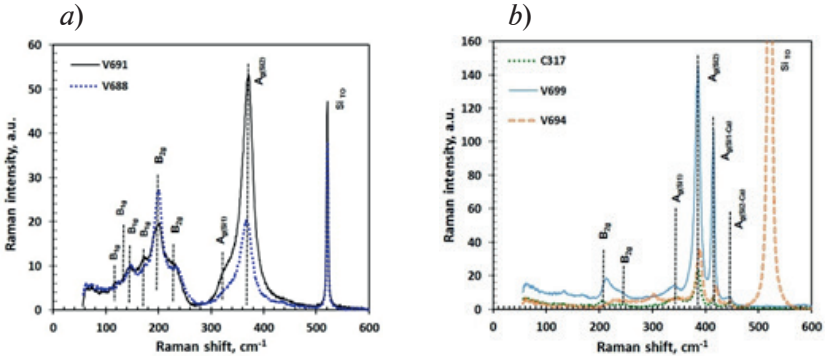

Fig. 3. Raman spectra for CaSi (*a*) (samples V688, V691, C440) and $CaSi_2$ (*b*) (samples V694, V699, C317) films on Si substrates

Calculations of the optical functions of $CaSi_2$ films from the reflection and transmission spectra (Fig. 2, *a*) within the two-layer model, taking into account multiple reflection and absorption, made it possible to obtain the spectral dependences of the refractive index and extinction coefficient (Fig. 6, *a*), absorption coefficient spectra (Fig. 6, *b*) and optical conductivity spectrum (Fig. 6, *c*) for $CaSi_2$ films on silicon in the photon energy range of 0.1–1.2 eV. $CaSi_2$ film in the sample V699 has a slightly variable absorption coefficient $(3–4)\cdot10^4$ cm^{-1} at energies of 0.1–1.2 eV. The film in the V694 sample has a small thickness and may not be continuous, so the calculations showed underestimated values of the absorption coefficient (Fig. 6, *c*). The increase in optical conductivity in the sample V699 (Fig. 6, *c*) is also associated with plasma reflection on free carriers of two signs, typical for semimetals [2, 5].

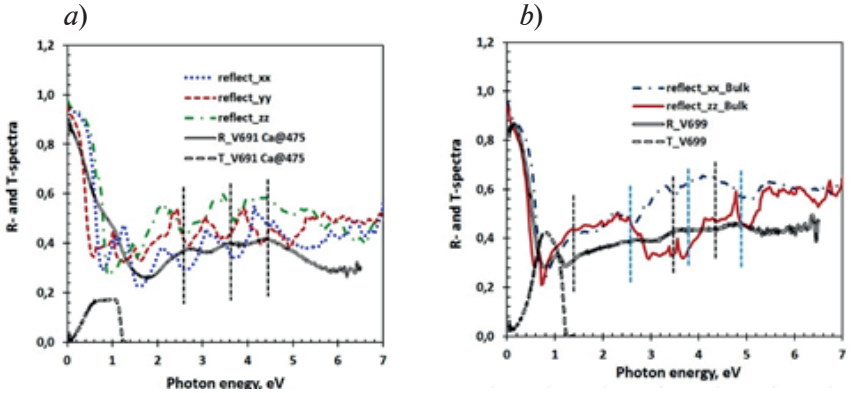

Fig. 4. Comparison of the theoretical (*xx*, *yy*, *zz* correspond to polarizations) and experimental reflection and transmission spectra of CaSi (*a*) (samples V688, V691, C440) and $CaSi_2$ (*b*) (samples V694, V699, C317) films on Si substrates

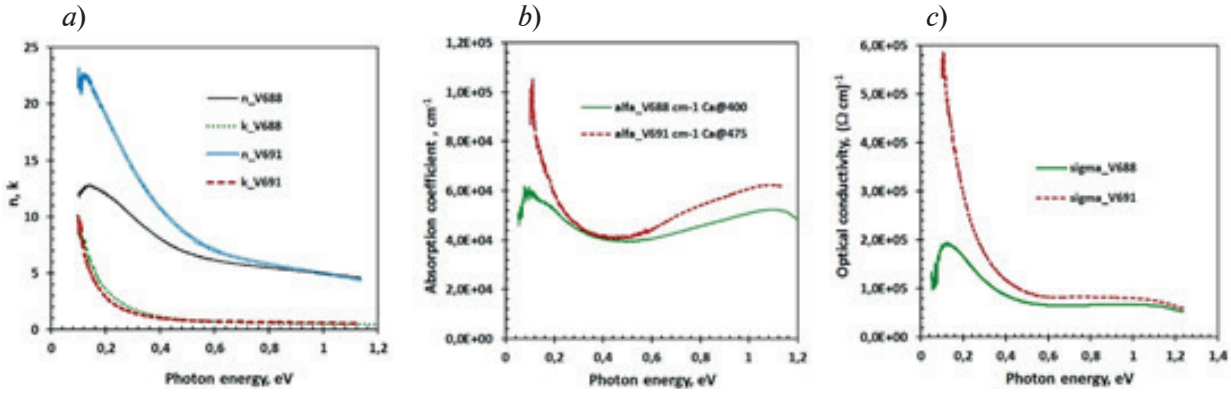

Fig. 5. Spectra for refractive index n and extinction coefficient *k* (*a*), absorption coefficient (*b*) and optical conductivity (*c*) for CaSi films on Si(111) substrates (samples V688 and V691)

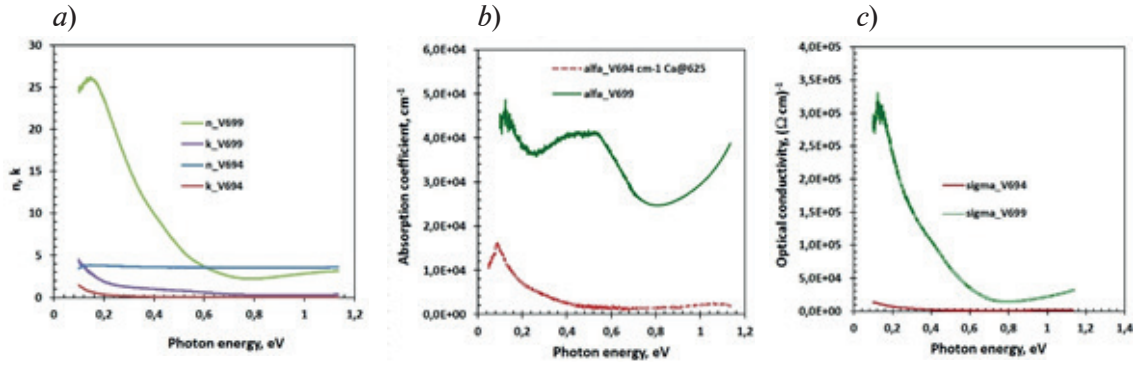

Fig. 6. Spectra for refractive index n and extinction coefficient *k* (*a*), absorption coefficient (*b*) and optical conductivity (*c*) for $CaSi_2$ films on Si(111) substrates (samples V694 and V699)

Conclusion

Methods for growing single-phase films of calcium monosilicide and disilicide on single-crystal silicon in the temperature range 400–680 °C are analyzed. It has been established that a CaSi film with grains without faceting is formed under RDE at a temperature of 400 °C. The faceting of CaSi grains was found at T = 475 oC. Single-phase growth of the CaSi film with epitaxial grain orientation was observed during MBE growth at T = 500 °C. The formation of epitaxial $CaSi_2$ on Si with (111), (100), and (110) orientations was detected in the temperature range 600–680 °C by RDE and MBE methods. During the growth by the RDE method, the formation of two isomorphic phases was observed hR3-$CaSi_2$ and hR6-$CaSi_2$. At the same time, during MBE growth the increase in the ratio of Ca to Si deposition rates up to 26 makes it possible to increase the substrate temperature to 680 °C and grow a large-block epitaxial film with hR6-$CaSi_2$ modification. Raman spectra and reflection spectra from single-phase CaSi and $CaSi_2$ films were recorded and identified, and their correspondence in amplitude and peak positions at 0.1–6.5 eV with the theoretically calculated reflection spectra, as well as with the available theoretical data on Raman spectra, was established. Calculations of the optical functions of single-phase CaSi and $CaSi_2$ films, including the spectra of the absorption coefficient and optical conductivity, showed the retention of high transparency and high conductivity in the energy range of 0.4–1.2 eV and the determining effect of absorption on free carriers on the loss of transparency at energies below 0.4 eV.

REFERENCES

1. **Lebegue S.,** Calculated quasiparticle and optical properties of orthorhombic and cubic Ca_2Si, Phys. Rev. B. 72 (2005) 085103.

2. **Affronte M., Laborde O., Olsece G. L., Palenzona A.,** Low temperature properties of calcium mono- and disilicides, Journal of Alloys and Compounds. 274 (1998) 68.

3. **Manfrinetti P., Fornasini M.L., Palenzona A.,** The phase diagram of the Ca-Si system, Intermetallics. 8 (2000) 223.

4. **Galkin N.G., Galkin K.N., Dotsenko S.A., Pyachin S.A., Astapov I.A.,** Ca_2Si(100) epitaxial films on the Si(111) substrate: template growth, structural and optical properties, Materials Science in Semiconductor Processing. 113 (2020) 105036.

5. **Shevlyagin A.V., Galkin N.G., Galkin K.N., Subbotin E.Y., Il'yaschenko V.M., Gerasimenko A.V., Tkachenko I.A.,** Semimetal hR6-$CaSi_2$ thin film: A transparent contact for Si optoelectronics, J. Alloys and Compounds. 910 (2022) 164893.

6. **Galkin N.G., Maslov A.M., Konchenko A.V.,** Optical and photospectral properties of $CrSi_2$ A-type epitaxial layers on Si(111), Thin Solid Films. 311 (1997) 230.

7. **Blaha, P., Schwarz, K., Madsen, G.K.H., Kvasnicka, D. and Luitz, J.,** WIEN2k, an Augmented Plane Wave. Karlheinz Schwarz, Techn. Universitдt Wien, Austria. 2001.

8. **Li X.D., Li K., Wei C.H., Han W.D., Zhou N.G.,** Structural, electronic, elastic, and thermodynamic properties of CaSi, Ca_2Si and $CaSi_2$ phases from first-principal calculations, Physica B: Condenced Matter. 538 (2018) 54.

9. **Galkin N.G., Dotsenko S.A., Galkin K.N., Migas D.B.,** Conducting $CaSi_2$ transparent in infrared. J. Alloys and Compounds. 770 (2019) 710.

10. **Galkin N.G., Galkin K.N., Tupkalo A.V., Fogarassy Z., Pécz B.,** A low temperature growth of Ca silicides on Si(100) and Si(111) substrates: formation, structure, optical properties and energy band structure parameters, J. Alloys and Compounds, 813 (2020) 152101.

THE AUTHORS

GALKIN Nikolay G.
galkin@iacp.dvo.ru
ORCID: 0000-0003-4127-2988

GALKIN Konstantin N.
galkinkn@iacp.dvo.ru
ORCID: 0000-0001-5386-1013

KROPACHEV Oleg V.
chernobez@gmail.com
ORCID: 0000-0003-4300-0070

CHERNEV Igor M.
igor_chernev7@mail.ru
ORCID: 0000-0002-8726-9832

DOTSENKO Sergei A.
docenko@iacp.dvo.ru
ORCID: 0000-0002-0052-7465

GOROSHKO Dmitrii L.
goroshko@iacp.dvo.ru
ORCID: 0000-0002-1250-3372

SUBBOTIN Evgenii Yu.
jons712@mail.ru
ORCID: 0000-0001-9531-3867

ALEKSEEV Aleksey Yu.
lucky.alexey94@gmail.com
ORCID: 0000-0001-5102-6647

MIGAS Dmitry B.
migas@bsuir.by
ORCID: 0000-0003-3004-7996

Received 04.05.2022. Approved after reviewing 05.07.2022. Accepted 05.07.2022.

Conference materials
UDC УДК 538.958
DOI: https://doi.org/10.18721/JPM.153.102

Electronic structure and optical properties of Ca_2Si films grown on silicon different oriented substrates and calculated from first principles

K. N. Galkin [1]✉, O. V. Kropachev [1], A. M. Maslov [1], I. M. Chernev [1],
E. Yu. Subbotin [1], N. G. Galkin [1], A. Yu. Alekseev [2], D. B. Migas [2]

[1] Institute of Automation and Control Processes FEB RAS, Vladivostok, Russia;
[2] Belarusian State University of Informatics and Radioelectronics, Minsk, Belarus

✉ galkinkn@iacp.dvo.ru

Abstract. The work considered the growth, optical properties and emerging interband transitions in Ca_2Si films grown on silicon substrates with (111), (001), and (110) orientations at two temperatures (250 °C and 300 °C) using the sacrificial-template method. The optimum temperature for MBE single-phase growth of Ca_2Si is 250 °C. Calculations of optical functions from the transmission and reflection spectra were carried out within the framework of a two-layer model and by the Kramers–Kronig method. It is shown that the main peaks in the experimental reflection spectra and the optical conductivity calculated according to Kramers–Kronig are in good agreement with each other. Comparison of *ab initio* calculations of the energy band structure and optical properties of a Ca_2Si single crystal and two-dimensional Ca_2Si layers with experimental data in the region of high-energy transitions showed good coincidence.

Keywords: Ca_2Si films, silicon, growth method, optical functions, energy band structure, *ab initio* calculations

Funding: This work was financially supported by a Russian Foundation for Basic Research/ Belarusian Republican Foundation for Fundamental Research grant no. 20-52-00001_Bel_a.

Citation: Galkin K. N., Kropachev O. V., Maslov A. M., Chernev I. M., Subbotin E. Yu., Galkin N. G., Alekseev A. Yu., Migas D. B. Electronic structure and optical properties of Ca_2Si films grown on silicon different oriented substrates and calculated from first principles. St. Petersburg State Polytechnical University Journal. Physics and Mathematics. 15 (3.1) (2022) 16–21. DOI: https://doi.org/10.18721/JPM.153.102

Материалы конференции
УДК УДК 538.958
DOI: https://doi.org/10.18721/JPM.153.102

Электронная структура и оптические свойства пленок Ca_2Si, выращенных кремниевых подложках с различной ориентацией и рассчитанных из первых принципов

К. Н. Галкин [1]✉, О. В. Кропачев [1], А. М. Маслов [1], И. М. Чернев [1], Е. Ю. Субботин [1],
Н. Г. Галкин [1], А. Ю. Алексеев [2], Д. Б. Мигас [2]

[1] Институт автоматики и процессов управления ДВО РАН, г. Владивосток, Россия
[2] Белорусский государственный университет информатики и радиоэлектроники, г. Минск, Беларусь

✉ galkinkn@iacp.dvo.ru

Аннотация. В работе исследованы рост, оптические свойства и возникающие межзонные переходы в пленках Ca_2Si, выращенных на кремниевых подложках с ориентациями (111), (001) и (110) при двух температурах (250°C и 300°C) с использованием метода расходуемого шаблона. Показано, что основные пики в экспериментальных спектрах отражения и оптической проводимости, рассчитанной по Крамерсу-Кронигу, хорошо согласуются друг с другом. Сравнение первопринципных расчетов зонной энергетической структуры и оптических свойств монокристалла Ca_2Si и двумерных слоев Ca_2Si с экспериментальными данными в области высокоэнергетических переходов показало хорошее совпадение.

Ключевые слова: пленки Ca_2Si, кремний, метод выращивания, оптические функции, зонная структура, первопринципные расчеты

Финансирование: Работа выполнена при финансовой поддержке гранта РФФИ - БРФФИ № 20-52-00001_Бел_а.

Ссылка при цитировании: Галкин К. Н., Кропачев О. В., Маслов А. М., Чернев И. М., Субботин Е. Ю., Галкин Н. Г., Алексеев А. Ю., Мигас Д. Б., Электронная структура и оптические свойства пленок Ca_2Si, выращенных кремниевых подложках с различной ориентацией и рассчитанных из первых принципов // Научно-технические ведомости СПбГПУ. Физико-математические науки. 2022. Т. 15. № 3.1 С. 16–21. DOI: https://doi.org/10.18721/ JPM.153.102

Introduction

At least six silicides are formed in the calcium-silicon system [1], including calcium semi-silicide (Ca_2Si), which has semiconductor properties [2]. Since calcium silicides are formed from environmentally friendly and widely distributed elements in the Earth's crust [3], they are of considerable interest for silicon electronics and optoelectronics. Ca_2Si, the most well-known and obtained in the form of films, has been mainly studied on silicon with the (111) orientation [4], while studies of its structure and optical properties on other surfaces (Si(100) and Si(110)) have not yet been carried out.

The goal of this work is to investigate experimentally and theoretically the parameters of the energy band structure and optical functions for Ca_2Si epitaxial films on silicon substrates with different orientations.

Experimental

Ca_2Si films were grown in an ultrahigh vacuum (UHV) chamber of an OMICRON Compact setup with a base vacuum of $2 \cdot 10^{-11}$ Torr, equipped with a LEED and AES/EELS analyzer, a block of molecular beam sources of silicon (Si), magnesium (Mg), and calcium (Ca) by carrying out the deposition of Mg, Ca and Si on the Si(111), Si(001) and Si(110) substrates. The deposition rates (Ca, Mg, and Si) were calibrated using a quartz thickness sensor. Sources of Ca, Mg, and Si and film growth techniques are described in [4].

The reflection spectra (R-spectra) and transmission spectra (T-spectra) of the grown samples were recorded within one day after unloading at room temperature in the photon energy range of 0.05–6.5 eV on a Hitachi U-3010 spectrophotometer with an integrating sphere and Fourier spectrometer Bruker Vertex 80 v. The optical functions were calculated in the transparency region from the T- and R-spectra in the frame of the two-layer model [5] as well as from the integral Kramers–Kronig relations over the entire range of photon energies.

Calculations of the electronic band structure and optical functions of Ca_2Si were also performed using the method of self-consistent full-potential linearized augmented plane waves (FLAPW) in its scalar-relativistic version using the WIEN2k package [6].

Results and Discussion

The morphology of the grown films was studied by AFM. Most of them for samples C423 and C424 on Si(111), C419 on Si(100) and C422 on Si(110) substrates consist of nanograins with sizes of 50–150 nm. Only the film in sample C425 consists of rectangular grains 200–400 nm in size, what it says about their epitaxial ordering.

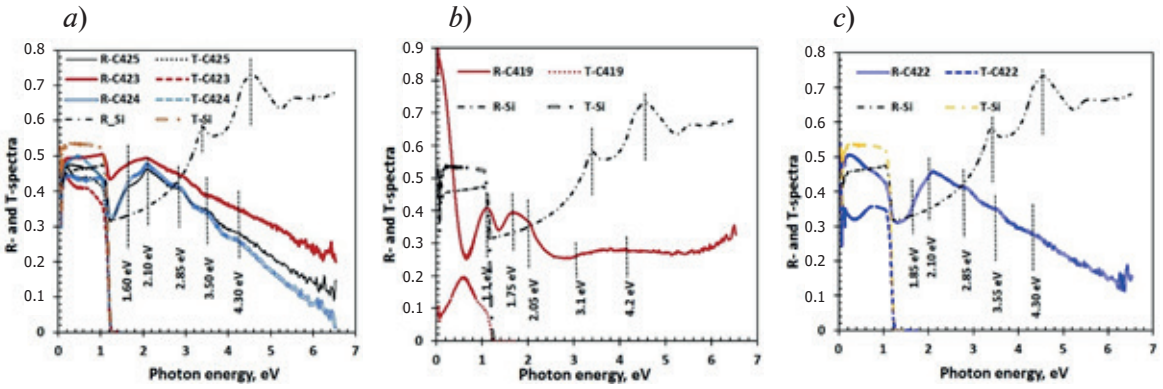

Fig. 1. Reflection and transmission spectra of Ca_2Si films on Si(111) (samples C423, C424, C425) (*a*), Si(001) (sample C419) (*b*) and Si(110) (sample C422) (*c*) substrates

The main features for the selected samples with Ca_2Si films were transparency in the photon energy range of 0.05–1.2 eV. The shape of the reflection spectra (Fig. 1) and the position of the peaks at energies from 1.3 eV to 4.5 eV for Ca_2Si films not covered by silicon are retained also taking into account Ca_2Si films on silicon [4].

Furthermore, absorption coefficient spectra were calculated (Fig. 2, *a*). It can be seen that a high level of the absorption coefficient $(1.0–1.5)\cdot10^4$ cm^{-1} is maintained from 1.0 eV to 0.4 eV, which corresponds to a high density of states in the Ca_2Si band gap. Fundamental absorption of light begins at photon energies above 1.0 eV, which is confirmed by the spectra of the squared absorption coefficient versus photon energy (Fig. 2, *b*). Extrapolation of the linear portions of this dependence for the grown films gives a certain spread in the values of the direct interband transition from 1.02 eV to 1.09 eV, which are close to the values of $E_{1d} = 1.095 \pm 0.15$ eV [4]. The maximum value of the direct interband transition was obtained for a film with a minimum thickness and grown at a temperature of 250 °C.

Comparison with the data of ab initio theoretical calculations of the absorption coefficient spectra (Fig. 3 left panel) and reflection spectra (Fig. 3, right panel) for three light polarizations in $Ca_2Si(100)$ thin films shows a good agreement in terms of peaks in Ca_2Si, which corresponds to the main interband transitions in Ca_2Si single crystals [7] and experimental spectra (Fig. 1).

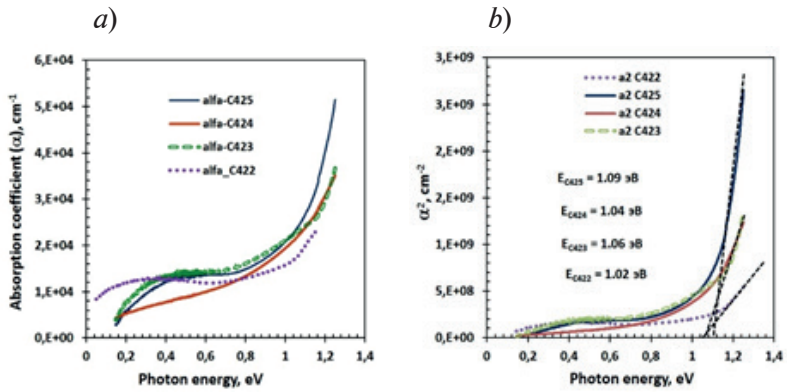

Fig. 2. Spectra for absorption coefficient (*a*) and square of absorption coefficient versus photon energy (*b*) for Ca_2Si films on Si(111) (samples C423, C424, C425) and Si(110) (sample C422) substrates

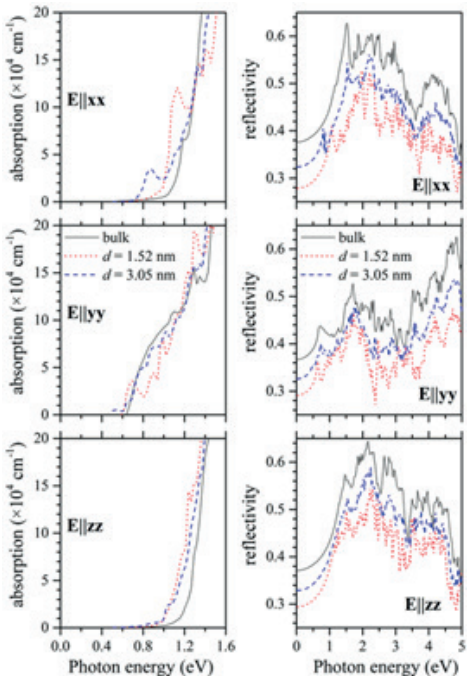

Fig. 3. Dependence of optical absorption (left panel) and reflection (right panel) coefficients on the energy of photons for thin $Ca_2Si(100)$ films in comparison with bulk Ca_2Si material

The absorption edge, according to the calculation data, is at an energy of about 0.72–0.82 eV (Fig. 3, left panel), depending on the polarization of the incident radiation (*xx*, *yy*, *zz*). The strongest interband transition begins at energy of about 1.2 eV. The latter value is in good agreement with the experimental data (E_g = 1.095 eV) [4].

Calculations from the reflection spectra by the Kramers–Kronig method showed the presence in Ca_2Si films on silicon of strong absorption at energies higher than 1.5–2.0 eV, depending on the presence of an additional phase, for example, CaSi (sample C419) (Fig. 4, *a*). This absorption is associated with direct interband transitions occurring with a strong oscillator far enough from the fundamental absorption edge in Ca_2Si (0.88 eV). Calculation of the optical absorption value showed that it starts at energies above 1.5 eV with a peak above 2.1 eV (Fig. 4, *b*) regardless of the crystalline quality of the films and the presence of the calcium monosilicide phase.

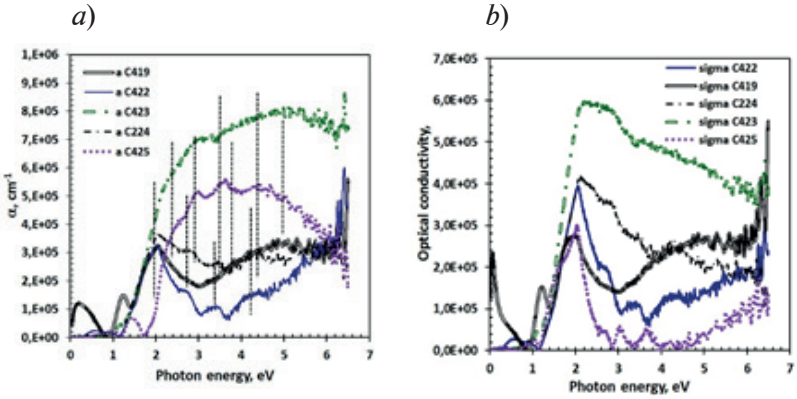

Fig. 4. Spectra for absorption coefficient (*a*) and optical conductivity (*b*) for Ca_2Si films on Si(111), Si(001) and Si(110) substrates in samples C419, C422, C423, C424 and C425

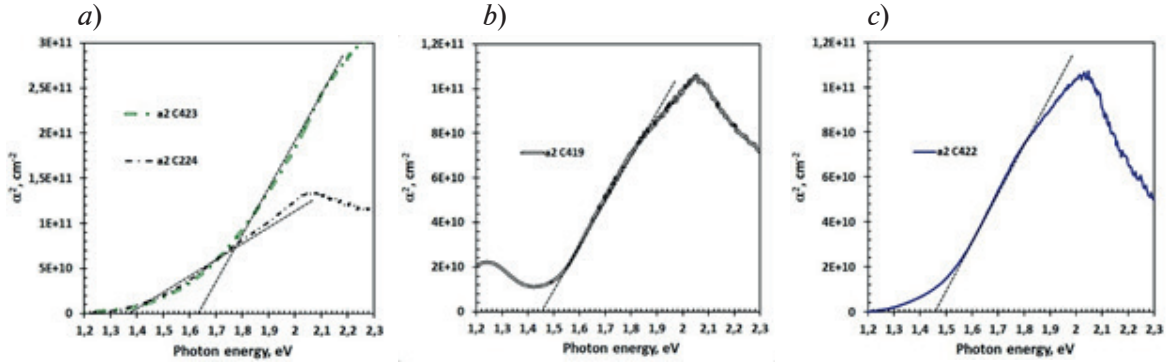

Fig. 5. Spectral dependences of the square of the absorption coefficient versus photon energy for Ca_2Si films on Si(111) (*a*), Si(001) (*b*) and Si(110) (*c*) substrates in samples C423, C424, C419 and C422

The values of interband transitions were determined by the standard procedure for straightening the dependence of the square of the absorption coefficient on the photon energy [9] (Fig. 5). For Ca_2Si films on a Si(111) substrate (samples C423 and C424), two direct interband transitions with energies of 1.37 eV and 1.64 eV were determined (Fig. 5, *a*). For the sample C419 on the Si(001) substrate, which contains the main Ca_2Si phase and an additional CaSi phase, one direct interband transition with an energy of 1.46 eV is observed (Fig. 5, *b*). The same value is observed for the Ca_2Si film on the Si(110) substrate (Fig. 5,*c*, sample C422). For grains of Ca_2Si in the sample C425 the main interband transition is observed at 1.98 eV, and the first one is observed at about 1.27 eV.

Using the rules of integral sums [8] for samples with Ca_2Si films on silicon substrates with (111), (001) and (110) orientations, effective values of the number of electrons per unit cell (n_{eff}) (Fig. 6, *a*) and effective permittivity (ε_{eff}) (Fig. 6, *b*) were calculated. The value of n_{eff} begins to increase at energies above 1.6 eV, which corresponds to the calculated reflectance spectra (Fig. 4). The initial contribution to the effective permittivity (ε_{eff}) (Fig. 6, *b*) is also made by interband transitions with energies from 0.4 eV to 1.4 eV, which is associated with their low oscillator strength according to the theoretical data [7]. This contribution increases with increasing density of states and transition probabilities at energies above 1.6 eV.

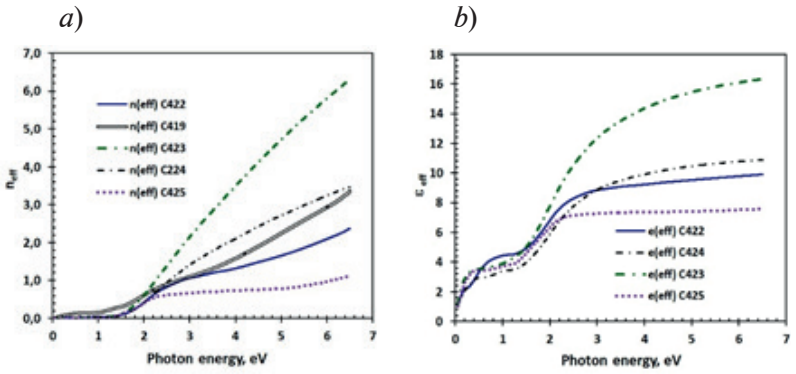

Fig. 6. Spectral dependences of the effective values of the number of electrons per unit cell (n_{eff}) (Fig. 4, *a*) and effective permittivity (e_{eff}) versus photon energy for Ca_2Si films on the Si(111) (*a*), Si(001) (*b*) and Si(110) (*c*) substrates in samples C423, C424, C419 and C422

Conclusion

An analysis of the structure, phase composition, optical and phonon properties of films grown by MBE on silicon surfaces with (111), (100), and (110) orientations showed that the optimum temperature for single-phase formation of Ca_2Si is 250 °C. An increase in the substrate temperature to 300 °C during growth on a template leads to an increase in the contribution of the CaSi phase and blocking the growth of Ca_2Si, regardless of the ratio of the rates of Ca and Si deposition. From Kramers–Kronig calculations it was shown that the main peaks in the optical conductivity spectrum with energies of 1.60, 2.0, 2.67, 3.25 and 4.05 eV repeat the peaks in the reflection spectrum. The absorption coefficient spectrum shows a major increase above 1.6 eV, which corresponds to the contribution from high-energy interband transitions in the Ca_2Si film. The contribution of transitions with lower energies is poorly reproduced due to the contradictions between the idealized two-layer model with a sharp boundary and a film with a developed surface and interface. A comparison of ab initio calculations of the band energy structure and optical properties for a bulk Ca_2Si and 2D Ca_2Si layers with experimental data in the region of high-energy transitions showed good agreement between the main maxima in the theoretical and experimental reflection spectra.

REFERENCES

1. **Manfrinetti P., Fornasini M.L., Palenzona A.,** The phase diagram of the Ca-Si system Intermetallics. 8 (2000) 223.

2. **Lebegue S.,** Calculated quasiparticle and optical properties of orthorhombic and cubic Ca_2Si, Phys. Rev. B. 72 (2005) 085103.

3. **Clarke F.W.,** The relative abundance of the chemical elements, Phil. Soc. Washington Bull. 11 (1889) 135.

4. **Galkin N.G., Galkin K.N., Dotsenko S.A., Pyachin S.A., Astapov I.A.,** Ca_2Si(100) epitaxial films on the Si(111) substrate: template growth, structural and optical properties, Mat. Sci. in Sem. Proc. 113 (2020) 105036.

5. **Galkin N.G., Maslov A.M., Konchenko A.V.,** Optical and photospectral properties of $CrSi_2$ A-type epitaxial layers on Si(111), Thin Solid Films. 311 (1997) 230–238.

6. **Blaha P., Schwarz, K., Madsen, G.K.H., Kvasnicka, D. and Luitz, J.,** WIEN2k, an Augmented Plane Wave + Local Orbitals Program for Calculating Crystal Properties. Karlheinz Schwarz, Techn. Universitдt Wien, Austria. 2001.

7. **Migas D.B., Miglio L., Shaposhnikov V.L., Borisenko V.E.,** Comparative study of structural, electronic and optical properties of Ca_2Si, Ca_2Ge, Ca_2Sn and Ca_2Pb, Physical Review B. 67 (2003) 205203.

8. **Pankov J.I.,** Optical Processes in Semiconductors, 2nd Revised ed. edition, Dover Books on Physics, New York, 2010.

THE AUTHORS

GALKIN Konstantin N.
galkinkn@iacp.dvo.ru
ORCID: 0000-0001-5386-1013

SUBBOTIN Evgenii Yu.
jons712@mail.ru
ORCID: 0000-0001-9531-3867

KROPACHEV Oleg V.
chernobez@gmail.com
ORCID: 0000-0003-4300-0070

GALKIN Nikolay G.
galkin@iacp.dvo.ru
ORCID: 0000-0003-4127-2988

MASLOV Andrei M.
maslov@iacp.dvo.ru
ORCID: 0000-0002-8656-3167

ALEKSEEV Aleksey Yu.
lucky.alexey94@gmail.com
ORCID: 0000-0001-5102-6647

CHERNEV Igor M.
igor_chernev7@mail.ru
ORCID: 0000-0002-8726-9832

MIGAS Dmitry B.
migas@bsuir.by
ORCID: 0000-0003-3004-7996

Received 12.05.2022. Approved after reviewing 29.06.2022. Accepted 05.07.2022.

Conference materials
UDC 538.9
DOI: https://doi.org/10.18721/JPM.153.103

Properties of solid solution $(Cd_{0.69}Zn_{0.31})_3As_2$

V. S. Zakhvalinskii [1] ✉, A. V. Borisenko [1], T. B. Nikulicheva [1], A. V. Kochura [2], Aung Zaw Htet [2], E. A. Pilyuk [1]

[1] Belgorod National Research University, Belgorod, Russia;
[2] Southwest State University, Kursk, Russia
✉ v_zaxval@mail.ru

Abstract: The modified Bridgeman method was used to obtain single crystals of $(Cd_{0,69}Zn_{0.31})_3As_2$. It has been established that the studied sample crystallizes in space group P42/nmc with lattice parameters a = 8.78 Å, b = 12.42 Å. We have investigated the electrical conductivity in the temperature range from 10 to 300 K and in a magnetic field of 1 T, and determined the temperature dependences of the concentration and mobility of charge carriers. We have established that hopping conduction with a variable length of the Mott-type hop takes place in the temperature range from 10 to 33 K, and determined its micro parameters.

Keywords: single crystals, solid solution, hopping conductivity

Citation: Zakhvalinskii V. S., Borisenko A. V., Nikulicheva T. B., Kochura A. V., Htet Aung Zaw, Pilyuk E. A. Properties of solid solution $(Cd_{0.69}Zn_{0,31})_3As_2$. St. Petersburg State Polytechnical University Journal. Physics and Mathematics. 15 (3.1) (2022) 22–26. DOI: https://doi.org/10.18721/JPM. 153.103

Материалы конференции
УДК 538.9
DOI: https://doi.org/10.18721/JPM.153.103

Свойства твердого раствора $(Cd_{0,69}Zn_{0,31})_3As_2$

В. С. Захвалинский [1] ✉, А. В. Борисенко [1], Т. Б. Никуличева [1], А. В. Кочура [2], А. З. Хтет [2], Е. А. Пилюк [1]

[1] Белгородский государственный национальный исследовательский университет, г. Белгород, Россия;
[2] Юго-Западный государственный университет, г. Курск, Россия
✉ v_zaxval@mail.ru

Аннотация. Модифицированный метод Бриджмена был использован для получения монокристаллов $(Cd_{0,69}Zn_{0,31})_3As_2$. Установлено, что исследуемый образец кристаллизуется в пространственной группе P42/nmc с параметрами решетки a = 8,78 Å, b = 12,42 Å. Была исследована электропроводность в диапазоне температур от 10 до 300 К и в магнитном поле 1 Тл, а также определены температурные зависимости концентрации и подвижности носителей заряда. Установлено, что в диапазоне температур от 10 до 33 К имеет место прыжковая проводимость с переменной длиной прыжка типа Мотта, и определены ее микропараметры.

Ключевые слова: монокристалл, твердый раствор, прыжковая проводимость

Ссылка при цитировании: Захвалинский В. С., Борисенко А. В., Никуличева Т. Б., Кочура А. В., Хтет А. З., Пилюк Е. А., Свойства твердого раствора $(Cd_{0,69}Zn_{0,31})_3As_2$ // Научно-технические ведомости СПбГПУ. Физико-математические науки. 2022. Т. 15. № 3.1. С. 22–26. DOI: https://doi.org/10.18721/ JPM.153.103

Introduction

The narrow-gap semiconductor cadmium arsenide (Cd_3As_2) with an inverted structure of energy bands and the highest carrier mobility among semiconductors and semimetals (largely exceeding 10^4 $cm^2/(V·s)$ at room temperature) is distinguished by its chemical stability, low toxicity, and good manufacturability [1,2]. Cd_3As_2 is believed to manifest an inverted band structure due to the spin-orbital coupling (SOC) [3]. The 3D Dirac cones of Cd_3As_2 have been observed in angle-resolved photoemission spectroscopy (ARPES) [2,4,5]. A phase transition from a Dirac semimetal to a semiconductor with an increase in the Zn content was experimentally observed in single crystals of solid solutions $(Cd_{1-x}Zn_x)_3As_2$ at low temperatures [6]. In this study, we report single crystal $(Cd_{0.69}Zn_{0.31})_3As_2$ close to the composition of the concentration phase transition.

Materials and Methods

A modified Bridgman method was used to obtain $(Cd_{0.69}Zn_{0.31})_3As_2$ single crystals. Stoichiometric amounts of Cd_3As_2 and Zn_3As_2 binary compounds were placed in a graphitized and evacuated quartz ampoule. The CZA melt was slowly cooled from the melting temperature of 838 °C at a rate of 5 °C/h in the furnace temperature gradient.

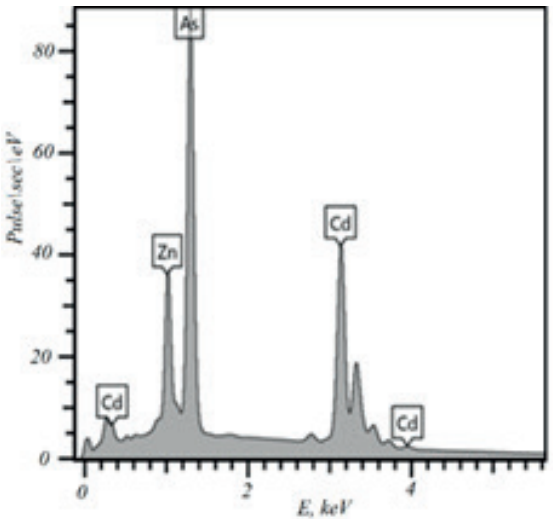

Fig. 1. EDX spectrum from the surface of $(Cd_{0.69}Zn_{0.31})_3As_2$ corresponding to the composition

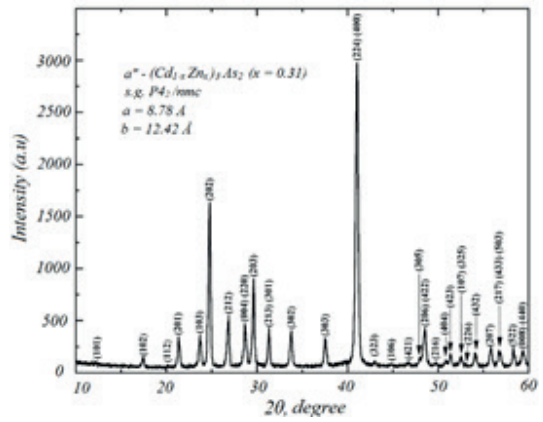

Fig. 2. Powder diffraction pattern of the $(Cd_{0.69}Zn_{0.31})_3As_2$ sample

The composition of the samples and their homogeneity were controlled by powder X-ray diffraction and energy dispersive X-ray spectroscopy (EDX). X-ray phase analysis (XPA) of the sample was performed using a GBC EMMA X-ray diffractometer (Cu Kα radiation, λ = 1.5401 Å) at room temperature. It has been established that the studied sample crystallizes in space group $P4_2/nmc$ with lattice parameters a = 8.78 Å, b = 12.42 Å [7]. To study the composition and distribution of elements on the surface, we used a JSM-6610LV (Jeol) scanning electron microscope (SEM) with an X-Max^N (Oxford Instruments) energy dispersive X-ray spectroscopy (EDX) attachment.

Fig. 1 shows the EDX spectrum from the surface of the $(Cd_{0.69}Zn_{0.31})_3As_2$ sample. Fig. 2 shows the powder diffraction pattern of the $(Cd_{0.69}Zn_{0.31})_3As_2$ sample.

Samples for the study of electrical conductivity by the six-probe method were parallelepipeds with the dimensions of 1.35×0.67×0.50 mm. The temperature dependence of electrical conductivity was studied in the temperature range from 10 to 300 K, and the Hall effect in a magnetic field of 1 T.

The results of the study of the temperature dependence of the resistivity of a solid solution single crystal $(Cd_{0.69}Zn_{0.31})_3As_2$ are shown in Fig. 3. The inset to Fig. 3 highlights the section corresponding to the variable range of the hopping conductivity according to Mott.

Results and discussions

As the temperature decreases from 320 K, the resistivity decreases from $2 \cdot 10^{-3}$ Ω·cm to a minimum of $5 \cdot 10^{-4}$ Ω·cm at 30 K, and then gradually increases. This behavior is typical of the Anderson transition [8]. The study of the Hall Effect in a magnetic field of 1 T made it possible to calculate the Hall coefficient R_H, the concentration and mobility of charge carriers. At a temperature of 10 K, the concentration of charge carriers was equal to $2.81 \cdot 10^{17}$ cm^{-3}, decreasing with increasing temperature to 30 K corresponding to the metal-insulator transition.

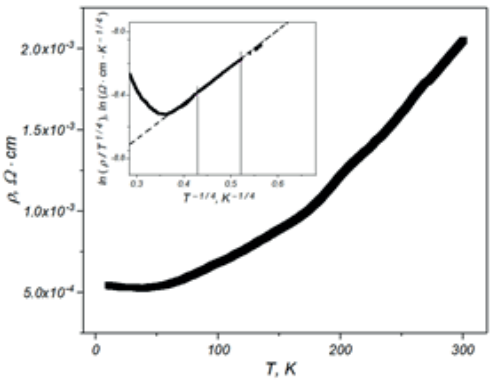

Fig. 3. Temperature dependence for resistivity of $(Cd_{0.69}Zn_{0.31})_3As_2$ solid solution single crystal. The temperature range of 10–33 K in the inset to Fig. 3 corresponds to the Mott variable range hopping conductivity

Above 30 K, an activation increase in the concentration of charge carriers was observed, which is typical for impurity semiconductors up to a value of $3.05 \cdot 10^{17}$ cm^{-3}. The mobility of charge carriers μ exhibits behavior characteristic of semiconductors, increasing with decreasing temperature. The value of mobility is maximum at the metal-dielectric transition point at a temperature of 30 K and is $4.51 \cdot 10^4$ cm^2·V^{-1}·s^{-1}. A further decrease in temperature leads to a decrease in mobility to $4.16 \cdot 10^4$ cm^2·V^{-1}·s^{-1} at a temperature of 10 K. The mechanisms of charge carrier scattering were evaluated.

At low temperatures, in the temperature range from 10 to 30 K, scattering by ionized impurity atoms and mobility $\mu \sim T^{3/2}$ prevail. In the temperature range from 30 to 300 K, scattering by thermal vibrations of the crystal lattice, $\mu \sim T^{-3/2}$, predominates (Fig. 4).

The inset to Fig. 3 shows a linear section of the temperature dependence of resistivity in the temperature range from 10 to 33 K, corresponding to the mechanism of hopping conduction by the states of the impurity band. Hopping conductivity is described by the universal equation (1) [8–10]:

$$\rho(T) = DT^m \exp\left[\left(T_0 / T\right)^p\right], \quad (1)$$

where D is a constant coefficient, T_0 is the characteristic temperature, and the parameters m and p depend on the mechanism of hopping conduction.

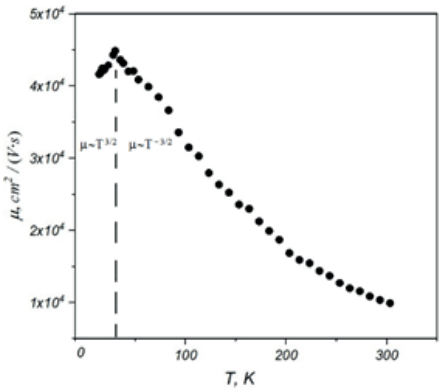

Fig. 4. Temperature dependence of mobility of $(Cd_{0.69}Zn_{0.31})_3As_2$ solid solution single crystal

We have determined the values of the parameters $m = 1/4$ and $p = 1/4$, which indicates the predominance of the mechanism of hopping conduction with a variable range hop according to Mott. When calculating the microparameters, the following obtained values of the coefficients were used: the characteristic temperature of the hopping conductivity $T_0 = 28.60$ K; hopping conduction onset temperature $T_V = 28.44$ K; coefficient $D = 8.488 \cdot 10^{-5}$ Ω·cm·K$^{-1/4.}$ For hopping conduction with a variable hop length, the following values of microparameters were obtained: Coulomb gap width in the density of localized states $\Delta = 0.43$ meV; acceptor zone width $W = 2.45$ meV; the value of the density of localized states outside the parabolic gap $g = 2.93 \cdot 10^{17}$ cm^{-3}·meV^{-1}; charge carrier localization radius $a = 307$ Å.

Conclusions

Single crystals of $(Cd_{0.69}Zn_{0.31})_3As_2$ solid solutions were obtained by the modified Bridgman method. Sample composition and element distribution was controlled using JSM -6610LV (Jeol) scanning electron microscope (SEM) with an X-Max^N (Oxford Instruments) energy dispersive X-ray spectroscopy (EDX) attachment.

It has been established that the studied sample crystallizes in space group $P4_2/nmc$ with lattice parameters $a = 8.78$ Å, $b = 12.42$ Å. We have investigated the electrical conductivity in the temperature range from 10 to 300 K and in a magnetic field of 1 T, and determined the temperature dependences of the concentration and mobility of charge carriers. It has been established that in the temperature range from 10 to 33 K, hopping conduction with a variable range of the Mott-type hop takes place, and its micro parameters have been determined: Coulomb gap width in the density of localized states $\Delta = 0.43$ meV, acceptor zone width $W = 2.45$ meV; charge carrier localization radius $a = 307$ Å. The obtained values do not contradict the literature data, which confirms the conclusion about the type of hopping conductivity.

REFERENCES

1. **Jeon S., Zhou B. B., Gyenis A., Feldman B. E., Kimchi I., Potter A. C., Gibson Q. D., Cava R. J., Vishwanath A., Yazdani A.,** Landau Quantization and Quasiparticle Interference in the Three-Dimensional Dirac Semimetal Cd_3As_2, Nature Materials. 13 (9) (2014) 851–856.

2. **Neupane M., Xu S.-Y., Sankar R., Alidoust N., Bian G., Liu C., Belopolski I., Chang T.-R., Jeng H.-T., Lin H., Bansil A., Chou F., Hasan M. Z.,** Observation of a three-dimensional topological Dirac semimetal phase in high-mobility Cd_3As_2, Nature Commun. 5 (2014) 3786.

3. **Aubin M. J., Caron L. G. & Jay-Gerin J. P.,** Band structure of cadmium arsenide at room temperature, Phys. Rev. B. 15 (1977) 3872–3878.

4. **Liu Z. K., et al,** A stable three-dimensional topological Dirac semimetal Cd_3As_2, Nat. Mater. 13 (2014) 677–681.

5. **Borisenko S., et al,** Experimental realization of a three-dimensional Dirac semimetal, Phys. Rev. Lett. 113 (2014) 027603.

6. **Hong Lu, Xiao Zhang, Yi Bian, Shuang Jia,** Topological Phase Transition in Single Crystals of $(Cd_{1-x}Zn_x)_3As_2$, Scientific Reports. 7 (2017) 3148.

7. **Arushanov E.K.,** Crystal growth and characterization of II3V2 compounds, Prog. Cryst. Growth Charact. 3 (1981) 211–255.

8. **Mott N. F.,** Metal–Insulator Transitions, London: Taylor and Francis, 1990.

9. **Mott N.F. and Davies Ye.A.,** Electron Processes in Non-Crystalline Materials / N.F. Mott. Oxford: Clarendon, 1979.

10. **Shklovskii B.I., Efros A.L.,** Electronic Propertie of Doped Semiconductors / B.I. Shklovskii. Berlin: Springer-Verlag, 1984.

11. **Amarnath R., Bhargavi K. S., Kubakaddi S. S.,** Thermoelectric transport properties in 3D Dirac semimetal Cd_3As_2. Journal of Physics Condensed Matter, 32 (22) (2020): 22570412.

12. **Armitage N.P., Mele E.J., Vishwanath A.,** Weyl and Dirac Semimetals in Three-Dimensional Solids, Rev. Mod. Phys. 90 (2018): 015001.

13. **Chorsi H. T., et al,** Widely Tunable Optical and Thermal Properties of Dirac Semimetal Cd_3As_2, Advanced Optical Materials. 8 (8) (2020) 120302 6.

14. **Crassee I., et al,** 3D Dirac semimetal Cd_3As_2: A review of material properties, Physical Review Materials. 2 (12) (2018) 120302 15.

THE AUTHORS

ZAKHVALINSKII Vasilii S.
v_zaxval@mail.ru
ORCID: 0000-0001-7055-8243

KOCHURA Alexey V.
akochura@mail.ru
ORCID: 0000-0002-7941-8404

BORISENKO Alexander V.
borisenko02.94@mail.ru
ORCID: 0000-0002-2539−3096

HTET Aung Zaw
zawh0898@gmail.com
ORCID: 0000-0003−3771−3082

NIKULICHEVA Tatyana B.
nikulicheva@bsu.edu.ru
ORCID: 0000-0001-6661−3959

PILYUK Evgeniy A.
pilyuk@yandex.ru
ORCID: 0000-0003−4979-5724

Received 14.05.2022. Approved after reviewing 15.07.2022. Accepted 16.07.2022.

Conference materials
UDC 539.216:535.346
DOI: https://doi.org/10.18721/JPM.153.104

Peculiar properties of surface plasmon-polaritons excitation in metal-dielectric structures based on opals

A. V. Cvetkov [1], S. D. Khanin [2], Yu. A. Kumzerov [1, 3], N. I. Puchkov [1],
V. G. Solovyev [1, 2] ✉, A. I. Vanin [1], M.V. Yanikov [1]

[1] Pskov State University, Pskov, Russia;
[2] S. M. Budienny Military Telecommunications Academy, Saint Petersburg, Russia;
[3] Ioffe Physico-Technical Institute RAS, Saint Petersburg, Russia
✉ solovyev_v55@mail.ru

Abstract. The paper reports on the study of optical phenomena peculiarities in metal-dielectric nanocomposite materials based on opal matrices caused by the excitation and propagation of surface plasmon-polaritons along the metal-dielectric interface. It is shown that two types of surface plasmon polaritons ('bright' and 'dark') can occur in the studied structures, which manifests itself in the established anomalies of light transmission and absorption.

Keywords: surface plasmon-polaritons, metal-dielectric structures, opals, optical properties

Funding: This work was partially supported by the German Academic Exchange Service (DAAD) and by the Russian Foundation for Basic Research (RFBR), project no. 20-32-90003.

Citation: Cvetkov A. V., Khanin S. D., Kumzerov Yu. A., Puchkov N. I., Solovyev V. G., Vanin A. I., Yanikov M. V., Peculiar properties of surface plasmon-polaritons excitation in metal-dielectric structures based on opals St. Petersburg State Polytechnical University Journal. Physics and Mathematics. 15 (3.1) (2022) 27–31. DOI: https://doi.org/10.18721/JPM. 153.104

Материалы конференции
УДК 539.216:535.346
DOI: https://doi.org/10.18721/JPM.153.104

Особенности возбуждения поверхностных плазмон-поляритонов в металлодиэлектрических структурах на основе опалов

А. В. Цветков [1], С. Д. Ханин [2], Ю. А. Кумзеров [1, 3], Н. И. Пучков [1],
В. Г. Соловьев [1, 2] ✉, А. И. Ванин [1], М. В. Яников [1]

[1] Псковский государственный университет, Псков, Россия;
[2] Военная академия связи им. С. М. Буденного, Санкт-Петербург, Россия;
[3] Физико-технический институт им. А. Ф. Иоффе РАН, Санкт-Петербург, Россия
✉ solovyev_v55@mail.ru

Аннотация. Представлены результаты исследования особенностей оптических явлений в металлодиэлектрических нанокомпозитных материалах на основе опаловых матриц, обусловленных возбуждением и распространением поверхностных плазмон-поляритонов вдоль границы раздела металл-диэлектрик. Показано, что в изученных структурах могут возникать два типа поверхностных плазмон-поляритонов («светлые» и «темные»), что проявляется в установленных аномалиях пропускания и поглощения света.

Ключевые слова: поверхностные плазмон-поляритоны, металлодиэлектрические структуры, опалы, оптические свойства

Финансирование: Работа частично поддержана Германской службой академических обменов (DAAD) и Российским фондом фундаментальных исследований в рамках проекта № 20-32-90003.

Ссылка при цитировании: Цветков А. В., Ханин С. Д., Кумзеров Ю. А., Пучков Н. И., Соловьёв В. Г., Ванин А. И., Яников М. В., Особенности возбуждения поверхностных плазмон-поляритонов в металлодиэлектрических структурах на основе опалов // Научно-технические ведомости СПбГПУ. Физико-математические науки. 2022. Т. 15. № 3.1. С. 27–31. DOI: https://doi.org/10.18721/ JPM.153.104

Introduction

Surface plasmon-polaritons (SPPs) propagating at tangential directions along metal-dielectric interfaces [1] allows expanding functionality of photonic crystals [2] that control the flows of electromagnetic (EM) radiation [3–5].

One of the most common techniques for SPP excitation using phase-matching to SPP can be achieved by grating coupling:

$$\beta = k_x + 2\pi l/a, \quad (1)$$

where β and $k_x = k\sin\theta$ are tangential projections of wave vectors of SPP and incident photon, respectively, θ is the angle of light incidence, a is the period of grating, l is an integer. Thus, the peculiarity of SPP excitation by this method is that the metal-dielectric interfaces must be profiled. This can be achieved by covering the surface of opal globule [6] monolayer with a thin metal (usually silver) layer which retains the shape and spatial periodicity of the interface between the opal globules and this layer. To clarify these requirements, optical properties of two metal-dielectric opal-based structures were studied in this paper. Assuming that the optical resonator plays the main role in the studied phenomena, we used the first structure with a profiled optical resonator (Fig. 1, *a*) and the second one (control sample) with a flat resonator (Fig. 1, *b*).

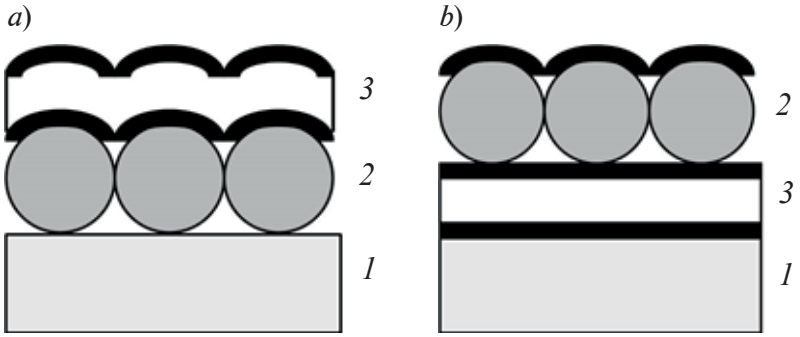

Fig. 1. Schematics of the metal-dielectric opal-based hybrid plasmon-photonic structures: glass substrate *1*, monolayer (ML) *2* of opal globules, $Ag/SiO_2/Ag$ resonator *3*
hybrid plasmon-photonic crystal $Ag/SiO_2/Ag/ML/Ag$ (*a*), hybrid plasmon-photonic crystal $Ag/ML/Ag/SiO_2/Ag$ (*b*)

Materials and Methods

Samples of hybrid plasmon-photonic crystals [7, 8] were fabricated by sequential deposition of metal (Ag) and dielectric (SiO_2) film coatings of a given thickness on a grating that was a monolayer (ML) of opal globules made of polymethyl methacrylate by magnetron sputtering on an ATC Orion Series Sputtering System.

Cross-sectional images of the samples (Fig. 2, 3) were obtained after processing them with a ZEISS FIB-SEM GEMINI scanning electron microscope (SEM). It should be noted that focused ion beam treatment (FIB-technology) probably enhances defect concentration in the $Ag/ML/Ag/SiO_2/Ag$ sample as compared with the $Ag/SiO_2/Ag/ML/Ag$ sample which has higher mechanical strength due to a rather thick SiO_2 layer deposited on the opal globes.

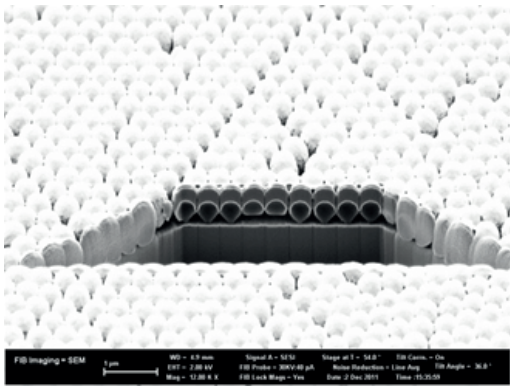

Fig. 2. SEM image of the sample of hybrid plasmon-photonic crystal Ag/SiO_2/Ag/ML/Ag

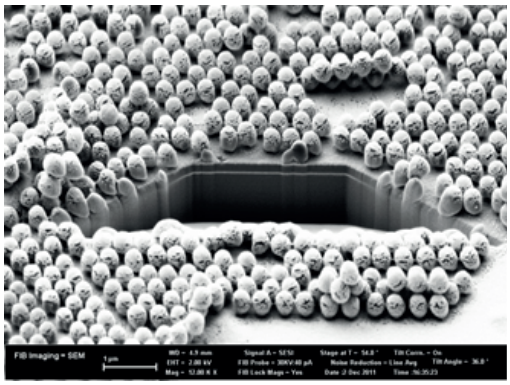

Fig. 3. SEM image of the sample of hybrid plasmon-photonic crystal Ag/ML/Ag/SiO_2/Ag

The transmission and reflectance spectra of *s*- and *p*-polarized light by layered thin-film heterostructures (when the vector of the electric field of the EM wave is perpendicular or parallel to the plane of incidence, respectively) were studied with angular resolution using an experimental setup based on the OceanOptics QE65000 spectrometer.

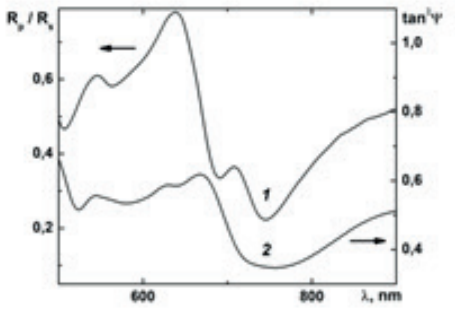

Fig. 4. Optical spectra of hybrid plasmon-photonic crystal Ag/ML/Ag/SiO_2/Ag obtained from the ratio of its reflectance coefficients R_p/R_s (*1*) and from the ellipscometric parameter Ψ (*2*). Angle of light incidence θ = 50°

At large angles θ, Bragg reflectance spectroscopy was successfully complemented with spectral ellipsometry due to the main ellipsometric equation [9, 10]:

$$\tan\Psi \cdot e^{i\Delta} = r_p / r_s, \qquad (2)$$

where r_p and r_s are the amplitude reflectance coefficients for two types of light polarisation, Ψ and Δ are the ellipsometric parameters. In this work, ellipsometric measurements were carried out with the Ellipse-1891 spectral ellipsometer. As can be seen from Fig. 4, experimental results obtained by both optical methods are similar.

Results and Discussion

Both types of hybrid plasmon-photonic crystals under study (Figs. 1, 2 and 3) can be considered to be metal-dielectric optical systems consisting of two optical elements (monolayer of opal globules and resonator with transmission coefficients T_1 and T_2, respectively), series-connected and located one after another. In the absence of interaction between these 'passive' optical elements one can calculate the total transmission coefficient T of this system from the relation $T = T_1 \cdot T_2$, hence, the ratio $r = T/(T_1 \cdot T_2) = 1$. Experiment confirms this assumption [11] only for the control sample, the hybrid plasmon-photonic crystal Ag/ML/Ag/SiO_2/Ag with a flat resonator (Fig. 3), but not for the Ag/SiO_2/Ag/ML/Ag system (Fig. 2), where the outer surface of a thin layer covering the opal globules retained the shape and spatial periodicity characteristic of the interface between the opal-like film and this layer. In this case, excitation of surface plasmon-polaritons of various types at the interfaces profiled metal layer–monolayer of opal globules takes place. Consequently, the ratio r demonstrates a pronounced spectral dependence with the maxima at about 489 and 584 nm and the minima at 392 and 760 nm (Fig. 5, curve *3*).

We attributed these maxima to an extraordinary transmission (EOT) and the minima to an extraordinary absorption (EOA) associated with the excitation of 'bright' and 'dark' surface plasmon-polaritons, respectively [7, 8]. It should be noted that EOT maxima which can be seen in transmission spectrum of a hybrid plasmon-photonic crystal Ag/SiO_2/Ag/ML/Ag (Fig. 5, curve *1*)

correspond to the minima in its reflectance spectrum (Fig. 5, curve *2*). At the same time, we emphasize that the spectral positions of EOA (Fig. 5, curve *3*) correlate with the minima in the reflectance spectrum of the resonator (interference filter itself) $Ag/SiO_2/Ag$ (Fig. 5, curve *4*).

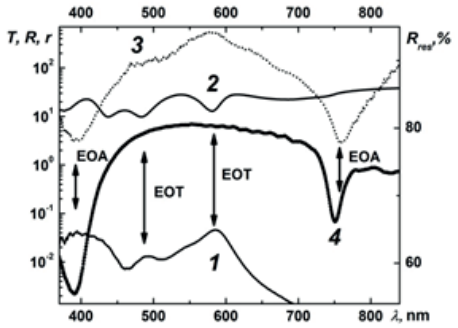

Fig. 5. Transmission ($T(\lambda)$, curve *1*) and reflectance ($R(\lambda)$, curve *2*) spectra of the hybrid plasmon-photonic crystal $Ag/SiO_2/Ag/ML/Ag$ in comparison with the ratio $r(\lambda)= T/(T_1 \cdot T_2)$ (curve *3*) and reflectance spectrum of resonator (interference filter) $Ag/SiO_2/Ag$ ($R_{res}(\lambda)$), curve *4*).
Angle of light incidence $\theta = 50°$

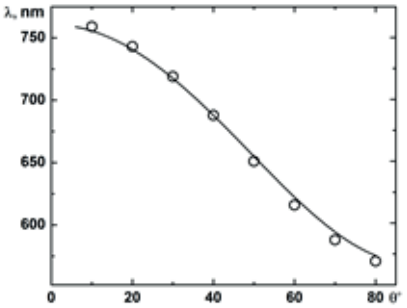

Fig. 6. Angular dispersion of the long wavelength EOA position and that of the corresponding minimum in the reflectance spectrum of resonator $Ag/SiO_2/Ag$ (circles). Solid line shows the angular dependence of the resonator transmission peak ($\lambda = 2d\sqrt{n^2 - \sin^2\theta}$, $d \approx 250$ nm, $n \approx 1.5$)

We observed this correlation for all the light incidence angles θ [7], as can be seen from Fig. 6 where the angular dispersion of the long wavelength EOA position and that of the corresponding minimum in the reflectance spectrum of resonator $Ag/SiO_2/Ag$ (circles) are demonstrated. The solid line shows angular dependence of the resonator transmission peak according to the well-known equation

$$\lambda = 2d\sqrt{n^2 - \sin^2\theta}, \quad (2)$$

where $d \approx 250$ nm is the dielectric layer thickness, $n \approx 1.5$ is its refractive index.

Conclusion

Excitation of surface plasmon-polaritons (SPPs) in opal-based hybrid plasmon-photonic crystals with a complex architecture is possible when the phase synchronism condition is met.

Two types of surface plasmon-polaritons may be excited in such metal-dielectric structures: these are 'bright' SPP, responsible for extraordinary transmission (EOT), and 'dark' SPP causing extraordinary absorption (EOA).

Acknowledgments

The authors are grateful to U. Peschel and D. Ploss for assistance in conducting experiments.

REFERENCES

1. **Maier S. A.,** Plasmonics: Fundamentals and Applications, Springer, New York, 2007.

2. **Romanov S. G., Korovin A., Regensburger A., Peschel U.,** Hybrid colloidal plasmonic-photonic crystals, Advanced Materials. 23 (2011) 2515–2533.

3. **Joannopoulos J. D., Meade R. D., and Winn J. N.,** Photonic Crystals: Molding the Flow of Light, Princeton University Press, Princeton, 2008.

4. Photonic crystals: Advances in design, fabrication, and characterization, Editors K. Busch, S. Lцlkes, R. B. Wehrspohn, H. Föll, Wiley-VCH, 2004.

5. Optical Properties of Photonic Structures: Interplay of Order and Disorder, Editors M. F. Limonov, R. V. De La Rue, CRC Press, 2012.

6. **Balakirev V. G., Bogomolov V. N., Zhuravlev V. V., Kumzerov Yu. A., Petranovskii V. P., Romanov S. G., and Samoilovich L. A.,** Three-dimensional superlattices in opal matrices, Crystallography Reports. 38 (1993) 348–353.

7. **Vanin A. I., Kumzerov Yu. A., Romanov S. G., Solovyev V. G., Khanin S. D., Cvetkov A. V., Yanikov M. V.,** Transmission and conversion of electromagnetic radiation by photonic crystal metal-dielectric systems based on opals, Optics and Spectroscopy. 128 (2020) 2022–2027.

8. **Vanin A. I., Lukin A. E., Romanov S. G., Solovyev V. G., Khanin S. D., Yanikov M. V.,** Optical properties of metal-dielectric structures based on photon-crystal opal matrices, Physics of the Solid State. 60 (2018) 774–777.

9. **Alexeeva N., Cema G., Lukin A., Pan'kova S., Romanov S., Solovyev V., Veisman V., Yanikov M.,** Experimental investigation of self-assembled opal structures by atomic force microscopy, spectroscopic ellipsometry and reflectometry, Journal of Self-Assembly and Molecular Electronics. 1 (2013) 209–222.

10. **Shvets V. A., Spesivtsev E. V., Rykhlitskii S. V., Mikhailov N. N.,** Ellipsometry as a high-precision technique for subnanometer-resolved monitoring of thin-film structures. Nanotechnologies in Russia, 4 (2009) 201–214.

11. **Khanin S. D., Vanin A. I., Kumzerov Yu. A., Solovyev V. G., Cvetkov A. V., Yanikov M. V.,** Peculiar properties of electromagnetic radiation propagation in photonic crystalline metal-dielectric systems based on opals, Radio communication technology. 4 (2021) 89–99.

THE AUTHORS

CVETKOV Alexander V.
aleksandr23031994@gmail.com
ORCID: 0000-0001-8340-9896

KHANIN Samuil D.
sd_khanin@mail.ru
ORCID: 0000-0002-8316-0362

KUMZEROV Yurii A.
yu.kumzerov@mail.ioffe.ru
ORCID: 0000-0002-4661-2702

SOLOVYEV Vladimir G.
solovyev_v55@mail.ru
ORCID: 0000-0002-8452-6928

PUCHKOV Nikolai I.
muxanin@mail.ru
ORCID: 0000-0002-0494-3132

VANIN Alexander I.
a.ivanin@mail.ru
ORCID: 0000-0002-6722-4848

YANIKOV Mikhail V.
losthighway@mail.ru
ORCID: 0000-0002-0116-2787

Received 19.05.2022. Approved after reviewing 04.07.2022. Accepted 04.07.2022.

Conference materials
UDC 538.971:535.215.6
DOI: https://doi.org/10.18721/JPM.153.105

Giant lateral photovoltaic effect in the TiO_2/SiO_2/p-Si heterostructure

T. A. Pisarenko [1, 3] ✉, V. V. Korobtsov [1], A. A. Dimitriev [1, 3], V. V. Balashev [1, 3],
V. V. Zheleznov [2], A. A. Yakovlev [1]

[1] Institute of Automation and Control Processes FEB RAS, Vladivostok, Russia;
[2] Institute of Chemistry FEB RAS, Vladivostok, Russia;
[3] Far Eastern Federal University, Vladivostok, Russia
✉ tata_dvo@iacp.dvo.ru

Abstract: In this work, we study the lateral photovoltaic effect in the TiO_2/SiO_2/p-Si structure. It was found the giant lateral photoeffect occurs in the TiO2/SiO2/p-Si heterostructure due to the high built-in barrier formation at the SiO_2/p-Si interface. The maximum LPE sensitivity ~600 mV/mm is observed in the $TiO_2/SiO_2/p$-Si structure under the TiO_2 film deposition for 45 min. However, the LPE nonlinearity in this structure is too large for practical applications. A decrease of the nonlinearity is achieved by the TiO2 film thickness control. The structure fabricated by the TiO_2 film deposition for 50 min has the LPE sensitivity and LPE nonlinearity are 477 mV/mm and 9%, respectively, which are more suitable for optoelectronic devise. The reason for the significant values of the rise time and fall time at pulsed illumination is the impedance behaviors of the $TiO_2/SiO_2/p$-Si structure in the near-contact region.

Keywords: lateral photovoltaic effect, heterostructure, silicon, titanium dioxide, interface, built-in barrier

Funding: This study was supported by State Task of the Ministry of Science and Higher Education of the Russian Federation, Physics of low-dimensional structures and semiconductor nanomaterials (project no. 0657-2020-0005).

Citation: Pisarenko T. A., Korobtsov V. V., Dimitriev A. A., Balashev V. V., Zheleznov V. V., Yakovlev A. A., Giant lateral photovoltaic effect in the TiO_2/SiO_2/p-Si heterostructure. St. Petersburg State Polytechnical University Journal. St. Petersburg State Polytechnical University Journal. Physics and Mathematics. 15 (3.1) (2022) 32–37. DOI: https://doi.org/10.18721/JPM.153.105

Материалы конференции
УДК 538.971:535.215.6
DOI: https://doi.org/10.18721/JPM.153.105

Гигантский латеральный фотовольтаический эффект в гетероструктуре $TiO_2/SiO_2/p$-Si

Т. А. Писаренко [1,3] ✉, В. В. Коробцов [1], А. А. Димитриев [1,3], В. В. Балашев [1,3],
В. В. Железнов [2], А. А. Яковлев [1]

[1] Институт автоматики и процессов управления ДВО РАН, г. Владивосток, Россия;
[2] Институт химии ДВО РАН, г. Владивосток, Россия;
[3] Дальневосточный федеральный университет, Владивосток, Россия
✉ tata_dvo@iacp.dvo.ru

Аннотация. В данной работе проведено исследование латерального фотовольтаического эффекта в структуре $TiO_2/SiO_2/p$-Si. Установлено, что гигантский латеральный

фотоэффект наблюдался в гетероструктуре $TiO_2/SiO_2/p$-Si вследствие формирования в ней на границе раздела SiO_2/p-Si высокого встроенного барьера. Максимальная чувствительность ЛФЭ ~600 мВ/мм наблюдается в структуре $TiO_2/SiO_2/p$-Si при толщине пленки TiO_2, осажденной в течение 45 мин. Однако, нелинейность ЛФЭ в этой структуре слишком велика для практических применений. Уменьшение нелинейности достигается регулированием толщины пленки TiO_2. Обнаружено, что характеристиками пригодными для оптоэлектронных устройств обладает структура, полученная при осаждении пленки TiO_2 в течение 50 мин, в которой чувствительность и нелинейность ЛФЭ составляют 477 мВ/мм и 9%, соответственно. Причиной значительных величин времени нарастания и спада при импульсном освещении являются импедансные характеристики структуры $TiO_2/SiO_2/p$-Si в области контактов.

Ключевые слова: латеральный фотовольтаический эффект, гетероструктура, кремний, диоксид титана, граница раздела, встроенный барьер

Финансирование: Работа выполнена в рамках Государственного задания Минобрнауки России «Физика низкоразмерных структур и полупроводниковых наноматериалов» (проект № 0657-2020-0005).

Ссылка при цитировании: Писаренко Т. А., Коробцов В. В., Димитриев А. А., Балашев В. В., Железнов В. В., Яковлев А. А. Гигантский латеральный фотовольтаический эффект в гетероструктуре $TiO_2/SiO_2/p$-Si // Научно-технические ведомости СПбГПУ. Физико-математические науки. Научно-технические ведомости СПбГПУ. Физико-математические науки. 2022. Т. 15. № 3.1. С. 32–37. DOI: https://doi.org/10.18721/JPM.153.105

Introduction

Recently, the lateral photoelectric effect (LPE), which is a characteristic feature of semiconductor structures, has been identified as an indispensable and effective method for studying the properties of nanomaterials and nanostructures due to the unique mechanism of operation [1]. It is known [2, 3] that LPE occurs when a laser beam nonuniformly irradiates the surface of a *pn*-junction or heterojunction; as a result, a large number of electron-hole pairs are excited and then separated by this *pn*-junction in the illuminated region by means of the built-in field. Thus, an electric potential difference is created by the carrier concentration gradient between the illuminated and unilluminated regions, which leads to lateral diffusion of non-equilibrium photocarriers from the illuminated region to the contacts. Interest in this effect is due to the linear dependence of the lateral photovoltage on the laser spot position between the electrodes, which makes it possible to convert light signals into electrical signals, which can be used as components of photovoltaic systems in various areas of optoelectronics, for example, in position-sensitive detectors (PSD) [2, 4–6]. The main operating characteristics of these optoelectronic devices are the LPE sensitivity and LPE nonlinearity [4, 5], as well as the response times under pulsed illumination [7, 8]. Innovations in the LPE scientific research field are precisely aimed at improving these characteristics.

It is known [1, 5, 6, 8–11] that LPE sensitivity is determined by several critical factors, such as the distance between the electrodes, the power and wavelength of the light source, the choice of a material for the top layer and substrate, and the thickness of the top layer of hybrid structures. The development of nanotechnologies has offered a new direction in LPE research, attracting attention to hybrid structures such as metal-oxide-semiconductor (MOS) structures [1, 5, 12] and heterostructures [1, 13, 14]. In these cases, one of the ways to increase the LPE sensitivity is to choose a material for the top layer with high resistivity and high work function. The high work function provides a significant band bending at the interface (structures with an inversion layer are preferred [15]), and the low specific conductivity shifts the optimal film thickness to the range that guarantees the formation of a homogeneous built-in barrier at the interface [16].

Previously, we studied the $Fe/SiO_2/n$-Si [9] and $Fe_3O_4/SiO_2/n$-Si [10] structures in which LPE was observed, and an increase of the top layer resistivity led both to an increase of the LPE

sensitivity by a factor of 4.7 and to a decrease of non-linearity from 6 to 5%. In both cases, there was a dependence of the LPE parameters on the top layer thickness. In this work, we chose low-conductivity TiO_2 films as the top layer satisfying the above properties [17].

Materials and Methods

TiO_2 films doped by manganese were formed on the oxidized silicon surface by the sol-gel method [17]. The film thickness dependence on the deposition time (in the selected time range) closes to linear [18]. To measure the photovoltage, aluminum contacts (2×1) mm were deposited on the film surface o with a distance of 2 mm between them. Illumination was carried out by a He-Ne laser with $\lambda = 633$ nm and a radiation power incident on the sample surface of 0.3 mW. The dependences of the photovoltage $U(x)$ and $U(t)$ were measured using a Keitly-2000 multimeter and an AKIP-4115/5A digital oscilloscope, respectively.

Results and Discussion

The band diagrams presented in Fig. 1 were plotted for the $TiO_2/SiO_2/Si$ structure. For energy calculations, we used the values of the band gap and work function for titanium dioxide, 3.1 eV and 5.87 eV, respectively [19, 20]. It follows from the analysis of these diagrams that in the $TiO_2/SiO_2/Si$ heterostructure a large built-in potential $\varphi_i = 0.62$ eV is formed at the SiO_2/p-Si interface, while $\varphi_i = 0.16$ eV at the SiO_2/n-Si interface. It is the small value of the built-in barrier in the $TiO_2/SiO_2/n$-Si structure that is the reason for the absence of the photovoltaic effect in it.

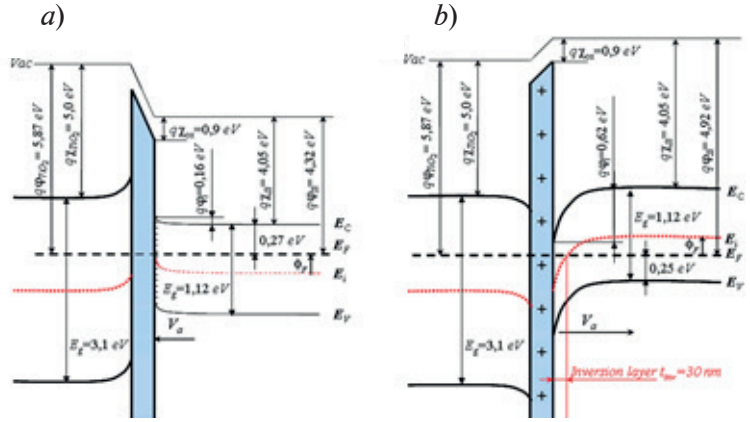

Fig. 1. Energy band diagrams of the heterostructure: $TiO_2/SiO_2/p$-Si (*a*); $TiO_2/SiO_2/n$-Si (*b*)

Fig. 2,*a* shows the dependences of the lateral photovoltage on the laser spot position at different top layer thickness for the $TiO_2/SiO_2/p$-Si structure. As can be seen in Fig. 2, *a*, there is a non-linear dependence of the lateral photovoltage on the film thickness (deposition time). Fig. 2, *b* shows the thickness dependences of the LPE sensitivity and LPE nonlinearity. It can see from Fig. 2, *b* that the LPE sensitivity dependence on the thickness is extreme, as for the structures studied earlier [1, 5, 9, 10], and the LPE nonlinearity dependence decreases exponentially with an increase of the top layer thickness. As can be seen from Fig. 2, *b*, the maximum sensitivity is achieved at the thickness of the titanium dioxide film obtained for 45 min and reaches 605 mV/mm. Unfortunately, the LPE nonlinearity at such a film thickness is 21%, which exceeds the applicability threshold, which is 15% for PSDs [4]. Based on the requirements for the performance characteristics of PSD [4], in this case, the optimal thickness should be a sample obtained for 50 min, having the sensitivity 477 mV/mm and the nonlinearity 9%.

The change in the thickness dependence of the LPE sensitivity is usually explained as follows. In the range of small thicknesses, a decrease in the LPE sensitivity is concerned with a film discontinuity and, accordingly, a decrease of the built-in barrier height [16, 21]. With an increase of the built-in potential, the number of excess photocarriers increases, and diffusion scattering decreases which results in an increase of the lateral photovoltage [16]. The LPE maximum is reached when the film becomes continuous and the height of the built-in barrier becomes homogeneous [9, 10, 21]. The decrease of the LPE sensitivity after passing the maximum is

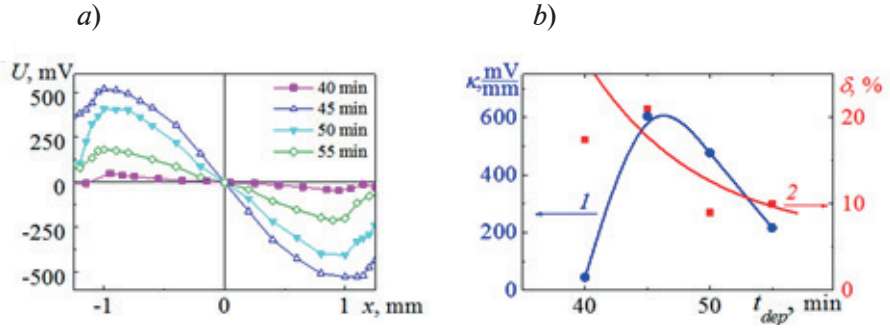

Fig. 2. LPE dependences for the $TiO_2/SiO_2/p$-Si heterostructure: lateral photovoltage dependence on the light spot position (*a*); TiO_2 thickness dependences (*b*), where *1* corresponds to LPE sensitivity and *2* to LPE nonlinearity

due to the shorting of the measuring electrodes because of a decrease of the film resistance with an increase of its thickness. However, in the $TiO_2/SiO_2/p$-Si structure, the resistance of a titanium oxide film is orders of magnitude higher than the resistance of transition metal films [3, 5, 6]; therefore, a decrease in LPE sensitivity with an increase of the TiO_2 film thickness, in our opinion, is due not to a decrease of its resistance, but rather to voltage losses at the contacts because of high film resistance in the transverse direction.

The high value of the LPE nonlinearity in the $TiO_2/SiO_2/p$-Si heterostructure, in our opinion, is due to the strong morphological roughness of the film, which may reach 30–50% of the film thickness [17, 22]. It was shown in Ref. [22] that the roughness in TiO_2 films deposited on a glass substrate reaches ~90 nm at a grain size of ~150 nm.

The time dependences of LPV at a pulsed illumination were also investigated. In this work, the rise time is defined as the time required to increase the photovoltage from 10% to 90% of the peak photovoltage (Umax), and the fall time is defined as the time required to reduce the photovoltage from 90% to 10% Umax. As can be seen from Fig. 3, *a*, the photovoltage signal in the $TiO_2/SiO_2/p$-Si heterostructure with a change of the top film thickness is characterized by both different pulse amplitude and different shape. The amplitude of the photoresponse signal varies proportionally to the change of LPE sensitivity, although it is ~3 times less. The change of the signal shape is related to the difference in the rates of excitation and quenching of photoconductivity in the $TiO_2/SiO_2/p$-Si heterostructure at different thicknesses of the titanium dioxide film. The dependences of the rise time and fall time on the TiO_2 film thickness are shown in Fig. 3, *b*.

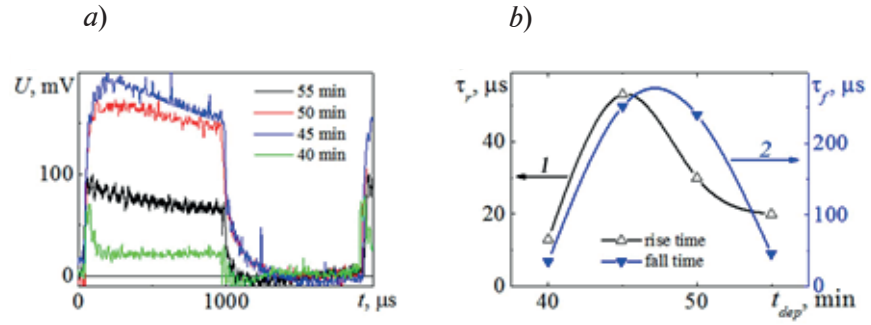

Fig. 3. Transient LPE characteristics of the $TiO_2/SiO_2/p$-Si heterostructure: time dependences of the lateral photovoltage (*a*); thickness dependences (*b*) of rise time (*1*) and fall time (*2*)

In the case of an open measurement scheme in the $TiO_2/SiO_2/p$-Si heterostructure at the optimal film thickness, the rise time is 30 μs and the fall time is 240 μs. It is easy to see that from the point of view of the transient LPE, this structure is also optimal.

Large value of time parameters in the $TiO_2/SiO_2/p$-Si heterostructure, in comparison with the previously studied structures [9, 23, 24], can be explained based on the equivalent circuit, Fig. 4. The equivalent circuit for the $TiO_2/SiO_2/p$-Si heterostructure at 300 K contains the following elements (Fig. 4): C_{pn} and R_{pn} are the capacitance and resistance in the separation region of non-equilibrium photocarriers at the SiO_2/p-Si interface, characterizing the process of

photocarrier generation, R_{inv} and R_{film} are the lateral resistances of the inversion layer and TiO_2 film, characterizing the lateral diffusion of photocarriers, as well as capacitances and resistances arising in the heterostructure near the contact region in transverse direction: C_{ss}, C_{dep}, C_{ox}, C_{TiO_2} are, respectively, the capacitances of surface states, space charge region, silicon oxide layer, TiO_2 film and R_{ss}, R_{dep}, R_{TiO_2} are the resistances of surface states, depletion layer, TiO_2 film. The substrate parameters of R_{sub}, Z_{SC} are not considered in our case since these play a role only for measuring LPE from the substrate side.

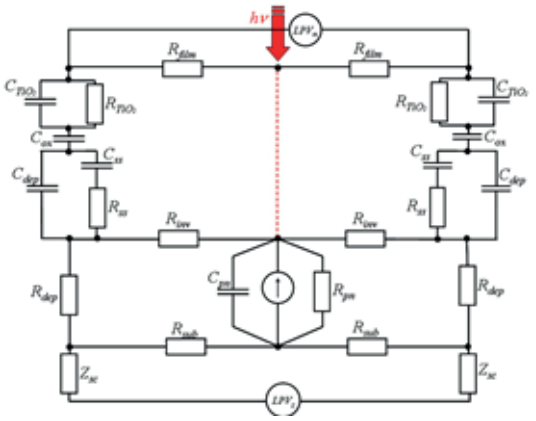

Fig. 4. Equivalent circuit of lateral photoconductivity at pulsed illumination

Since the top layer in the $TiO_2/SiO_2/p$-Si heterostructure is a semi-insulator, current transfer through it does not occur, and this conduction channel is shunted by the inversion layer and the transverse conductivity in the near-contact region. Moreover, as can be seen from Fig. 4, in contrast to conventional MOS structures, in this case, in the transverse direction considering film impedance characteristics a complementary RC-filter for the TiO_2 film is added to the RC-filter of the SiO_2/p-Si interface, which slows down the photoresponse. The decrease of the signal amplitude $U(t)$, from the standpoint of the equivalent circuit, can also be explained by the reactance losses in the transverse direction of the structure in the contact region.

Conclusion

In our opinion, the presented results conclusively prove that the giant lateral photoconductivity in the $TiO_2/SiO_2/p$-Si heterostructure, in which the semi-insulator is used as the top layer, occurs along the inversion layer and near-contact regions, bypassing the top film because of its high resistance. Meanwhile the titanium dioxide film serves only to generate the built-in potential at the SiO_2/p-Si interface.

The LPE characteristics obtained during the study of the $TiO_2/SiO_2/p$-Si heterostructure make it possible to consider this structure as a promising candidate for optoelectronics.

REFERENCES

1. **Qiao S., Liang B., Liu J., et al.,** Lateral photovoltaic effect based on novel materials and external modulations, Journal of Physics D: Applied Physics. 54 (15) (2021) 153003–153031.

2. **Wallmark J. T.,** A new semiconductor photocell using lateral photoeffect, In: Proceedings of the IRE. 45 (4) (1957) 474–483.

3. **Lucovsky G.,** Photoeffects in nonuniformly irradiated *p-n* junctions, Journal of Applied Physics. 31 (6) (1960) 1088–1095.

4. **Henry J., Livingstone J.,** Improved position sensitive detectors using high resistivity substrates, Journal of Physics D: Applied Physics. 41 (2008) 165106–165113.

5. **Yu C., Wang H.,** Large lateral photovoltaic effect in metal-(oxide-) semiconductor structures, Sensors. 10 (11) (2010) 10155–10180.

6. **Chi L., Zhu P., Wang H., et al.,** A high sensitivity position-sensitive detector based on Au-SiO_2-Si structure, Journal of Optics. 13 (2011) 015601–015605.

7. **Cascales J. P., Martinez I., Diaz D., et al.,** Transient lateral photovoltaic effect in patterned metal-oxide semiconductor films, Applied Physics Letters. 104 (23) (2014) 231118–231122.

8. **Wang X., Song B., Huo M., et al.,** Fast and sensitive lateral photovoltaic effects in Fe_3O_4/Si Schottky junction, RSC Advances. 5 (2015) 65048–65051.

9. **Pisarenko T. A., Balashev V. V., Korobtsov V. V., et al.,** The lateral photovoltaic effect in the Fe/SiO_2/Si structure with different silicon conductivity type, Defect and Diffusion Forum. 386 (2018) 137–142.

10. **Pisarenko T. A., Balashev V. V., Vikulov V. A., et al.,** A comparative study of the lateral

photovoltaic effect in $Fe_3O_4/SiO_2/n$-Si and $Fe_3O_4/SiO_2/p$-Si structures, Physics of the Solid State. 60 (7) (2018) 1316–1322.

11. **Nguyen H., Foisal A. R. M., Nguyen T., et al.,** Effects of photogenerated-hole diffusion on 3C-SiC/Si heterostructure optoelectronic position-sensitive detector, Journal of Physics D: Applied Physics. 54 (26) (2021) 2651.

12. **Shikama T., Niu H., Takai M.,** Lateral photovoltaic effect in the weakly inverted and in the depleted MOS interface layers, Japanese journal of applied physics. 33 (10) (1984) 1314–1319.

13. **Zhang Y., Zhang Y., Yao T., et al.,** Ultrahigh position sensitivity and fast optical relaxation time of lateral photovoltaic effect in Sb_2Se_3/p-Si junctions, Optics Express. 26 (26) (2018) 34214–34223.

14. **Cong R., Qiao S., Liu J., et al.,** Ultrahigh, ultrafast, and self-powered visible-near-infrared optical position sensitive detector based on a CVD-prepared vertically standing few-layer MoS_2/Si heterojunction, Advanced Science. 5 (2) (2018) 1700502.

15. **Konorov P. P., Tarantov Yu. A.,** The surface lateral photovoltaic effect in germanium, The aspects of solid state electronics, Scientific papers of the State university of Leningrad. 370 (17) (1974) 114–120.

16. **Rahmatallahpur S., Yegane M.,** Effect of nanopatches on electrical behavior of Ni/*n*-type Si Schottky diode, Physica B: Condensed Matter. 406 (8) (2011) 1351–1356.

17. **Opra D. P., Gnedenkov S. V., Sinebryukhov S. L., et al.,** Doping of titania with manganese for improving cycling and rate performances in lithium-ion batteries, Chemical Physics. 538 (2020) 110864.

18. **Sonawane R. S., Hegde S. G., Dongare M. K.,** Preparation of titanium (IV) oxide thin film photocatalyst by sol-gel dip coating, Materials chemistry and physics. 77 (3) (2003) 744–750.

19. **Kiejna A., Pabisiak T., Gao S.W.,** The energetics and structure of rutile TiO_2 (110), Journal of Physics: Condensed Matter. 18 (17) (2006) 4207.

20. **Xiong G., Shao R., Droubay T. C., et al.,** Photoemission electron microscopy of TiO_2 anatase films embedded with rutile nanocrystals, Advanced Functional Materials. 17 (13) (2007) 2133–2138.

21. **Huang X., Mei C., Hu J., et al.,** Potential superiority of *p*-type silicon based metal-oxide-semiconductor structures over *n*-type for lateral photovoltaic effects, IEEE Electron Device Letters. 37 (2016) 1018–1021.

22. **Lias J., Shahadan S. A., Rahim M. S. A., et al.,** Influences of deposition time on TiO_2 thin films properties prepared by CVD technique, Jurnal Teknologi. 78 (10–3) (2016) 1–7.

23. **Pisarenko T. A., Korobtsov V. V., Balashev V. V., Dimitriev A. A.,** The influence of temperature on the lateral photovoltaic effect in the $Fe_3O_4/SiO_2/n$-Si structure, Solid State Phenomena. 312 (2020) 92–97.

24. **Pisarenko T. A., Korobtsov V. V., Balashev V. V., et al.,** The features of the lateral photovoltaic effect in the $Fe_3O_4/SiO_2/n$-Si structure depending on silicon substrate orientation, Solid State Phenomena. 312 (2020) 98–104.

THE AUTHORS

PISARENKO Tatiana A.
tata_dvo@iacp.dvo.ru
ORCID: 0000-0002-7977-7474

BALASHEV Vyacheslav V.
balashev@dvo.ru
ORCID: 0000-0003-1094-7444

KOROBTSOV Vladimir V.
korobtsov.vv50@mail.ru
ORCID: 0000-0001-6795-4069

ZHELEZNOV Veniamin V.
zhvv53@mail.ru
ORCID: 0000-0001-6795-4069

DIMITRIEV Artem A.
corrupter@mail.ru
ORCID: 0000-0001-5378-605X

YAKOVLEV Aleksey A.
yakovlev@iacp.dvo.ru
ORCID: 0000-0003-4821-3091

Received 19.05.2022. Approved after reviewing 25.06.2022. Accepted 26.06.2022.

Conference materials
UDC 537.622.4, 537.9, 54.057
DOI: https://doi.org/10.18721/JPM.153.106

Effect of Co substitution on the microstructure and magnetic properties of Nd-($Fe_{1-x}Co_x$)-B particles synthesized by a modified Pechini-type chemical method

V. Yu Samardak [1], S. A. Azon [1], A. Yu Samardak [1], E. K. Papynov [1], A. S. Samardak [1], A. V. Ognev [1] ✉

[1] Far Eastern Federal University, Vladivostok, Russia

✉ ognev.av@dvfu.ru

Abstract: Magnetic Nd-(Fe, Co)-B powders prepared by a modified Pechini-type chemical method are investigated. The effect of 0–100 at.% Co concentration on magnetic properties is shown. The structure and morphology of the powders are studied by electron microscopy. The average particle size is determined by electron microscopy. The internal structure of the nanoparticle agglomerates was explored by transmission electron microscopy. The $Nd_2Fe_{14}B$ phase was determined by spot electron diffraction. The dependence of saturation magnetization and coercive force of $NdFe_{1-x}Co_xB$ powders on the cobalt content is investigated and discussed. An increasing coercive force is observed as a result of the increase in Co content. It is shown that the absence of phase purity leads to a decrease in the coercive force in comparison with the Nd-based hard magnetic obtained by metallurgical methods.

Keywords: NdFeCoB magnets, powders, Pechini method, microstructure, elemental analysis, magnetic properties

Funding: The study was supported by the Russian Science Foundation (project 19-72-20071). A. S. Samardak thanks Ministry of Science and Higher Education of the Russian Federation for providing funding as part of State Assignment (project no. 0657-2020-0013) to cover analysis of the surface morphology. A. Yu. Samardak thanks the Government of the Russian Federation for providing funding for project no. 075-15-2021-607 to cover measurement and analysis of magnetic properties.

Citation: Samardak V. Yu, Azon S. A., Samardak A. Yu, Papynov E. K., Samardak A. S., Ognev A. V., Effect of Co substitution on the microstructure and magnetic properties of Nd-($Fe_{1-x}Co_x$)-B particles synthesized by a modified Pechini-type chemical method. St. Petersburg State Polytechnical University Journal. Physics and Mathematics. 15 (3.1) (2022) 38–43. DOI: https://doi.org/10.18721/JPM.153.106

Материалы конференции
УДК 537.622.4, 537.9, 54.057
DOI: https://doi.org/10.18721/JPM.153.106

Влияние Co на микроструктуру и магнитные свойства частиц Nd-($Fe_{1-x}Co_x$)-B, синтезированных модифицированным методом Печини

В. Ю. Самардак [1], С. А. Азон [1], А. Ю. Самардак [1], Е. К. Папынов [1], А. С. Самардак [1], А. В. Огнев [1] ✉

[1] Дальневосточный Федеральный Университет, г. Владивосток, Россия

✉ ognev.av@dvfu.ru

Аннотация. Исследованы порошки Nd-(Fe,Co)-B, синтезированные модифицированным методом Печини. Показано влияние на магнитные свойства и структуру изменение концентрации Co от 0 до 100 ат. %. Методами электронной

микроскопии изучены структура и морфология порошков. По данным сканирующей электронной микроскопии определен средний размер частиц. Методом просвечивающей электронной микроскопии установлена внутренняя структура агломератов наночастиц. С помощью локальной дифракция обнаружена фаза $Nd_2Fe_{14}B$. С помощью вибромагнетометрии при комнатной температуре получены зависимости намагниченности насыщения и коэрцитивной силы порошков $NdFe_{1-x}Co_xB$ от содержания кобальта. Установлено возрастание коэрцитивной силы за счет увеличения содержания Co. Показано, что отсутствие фазовой чистоты приводит к понижению коэрцитивной силы в сравнении с магнитожесткими материалами на основе Nd, полученными металлургическим методами.

Ключевые слова: NdFeCoB, порошковые материалы, метод Печини, микроструктура, элементный анализ, магнитные свойства

Финансирование: Исследование выполнено при поддержке Российского научного фонда (проект 19−72-20071). Самардак А.С. благодарит Минобрнауки России за поддержку по государственному заданию (проект № 0657−2020-0013) в части анализа морфологии поверхности. Самардак А.Ю. благодарит Правительство Российской Федерации за государственную поддержку по проекту № 075-15-2021-607 в части измерения и анализа магнитных свойств.

Ссылка при цитировании: Самардак В. Ю., Азон С. А., Самардак А. Ю., Папынов Е. К., Самардак А. С. Влияние Co на микроструктуру и магнитные свойства частиц Nd-($Fe_{1-x}Co_x$)-B, синтезированных модифицированным методом Печини // Научно-технические ведомости СПбГПУ. Физико-математические науки. 2022. Т. 15. № 3.1. С. 38−43. DOI: https://doi.org/10.18721/JPM.153.106

Introduction

Hard magnetic materials based on $Nd_2Fe_{14}B$ are widely used in automotive transport, generators, micromotors, and microelectronics [1−3]. This is due to their unique technical characteristics, and first, the maximum energy product $(BH)_{max}$ among all permanent magnets [4]. The most promising are composite magnetic materials in which there are two phases: a magnetically hard phase (for example, $Nd_2Fe_{14}B$), including a magnetically soft phase [5]. To form such compounds, we used Nd-based powders made of nanocrystalline alloys with subsequent grinding (top-down approach) or chemical synthesis (bottom-up approach).

At the top-down approach during the ball milling process, it is possible to introduce additives (Tb, DyCo, Cu + DyCo, Al + DyCo, Cu) using mechanosynthesis, which increase the energy product, reduce the degradation of magnetic parameters during sintering [6−8]. These methods also have disadvantages associated with the heterogeneity of the compounds, caused by a wide spread in particle size, segregation of impurities, for example, carbon, oxidation during the manufacturing process, and the high cost of initial pure raw materials.

Bottom-up approaches are based on the synthesis of magnetic powders by chemical methods, which makes it possible to more precisely control the size and structures of particles from nano- to micro-sizes. Different methods are used, for example, sol-gel Pechini [9,10], sol-gel auto combustion [11], and the microwave technique [12]. The powders of magnetic nanomaterials obtained by chemical synthesis are potentially applicable in biomedicine [13] and to solve environmental problems (waste treatment) [14].

In this paper, we present the results of a study of the structure and magnetic properties of $Nd_2(Fe_{1-x},Co_x)_{14}B$ powders with a change in Co concentration from 0 to 100%, obtained by the modified Pechini method. It is shown that the addition of Co leads to the formation of the Fe-Co alloy and increases the coercive force.

Materials and Methods

The synthesis of oxidized Nd-($Fe_{1-x}Co_x$)-B powders was carried out according to the procedure

described in [15]. The reduction of the mixture of oxides was carried out by mixing this powder with calcium hydride CaH_2 (weight ratio 1:1.5) in an argon atmosphere and pressing the resulting mixture into a tablet and subsequent calcination in vacuum (pressure 10^{-3}–10^{-4} Torr) at 800 °C according to the following stepwise heating scheme. The product obtained after heat treatment is subjected to washing from impurities of metallic calcium and its oxide in an aqueous solution of ammonium chloride (NH_4Cl).

The structure and morphology of the powders were studied using a Tecnai G^2 30 transmission electron microscope (TEM) and a Quanta 200 Pegasus scanning electron microscope (SEM).

Magnetic parameters (hysteresis loops, temperature dependences of magnetization) were measured on a Lakeshore 7400 vibromagnetometer.

Results and Discussion

Fig. 1 and 2 show electron microscopic images and elemental microanalysis data of nanopowders with Co content: 0, 30, 60, and 100%. The powder particles in the sample without Co have an asymmetric shape; additionally, 15 μm in size and larger agglomerates are formed. Agglomerates have a loose structure with particles of various sizes and types. The average size of the powders is 870 nm. According to the local elemental analysis, Ca, Cl, O and Si were in the samples, which may have remained due to the powder preparation method (Fig. 2, *a*).

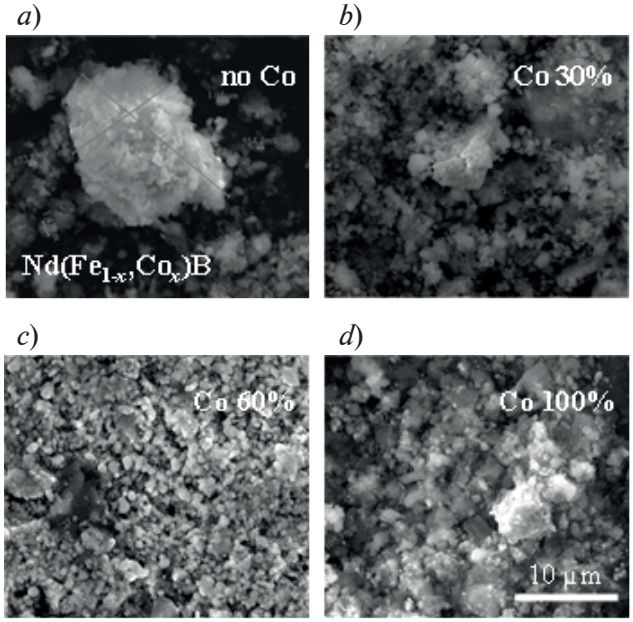

Fig. 1. SEM images of $NdFe_{1-x}Co_xB$ particles without Co (*a*) and the declared percentage of cobalt: 30 (*b*), 60 (*c*), 100% (*d*)

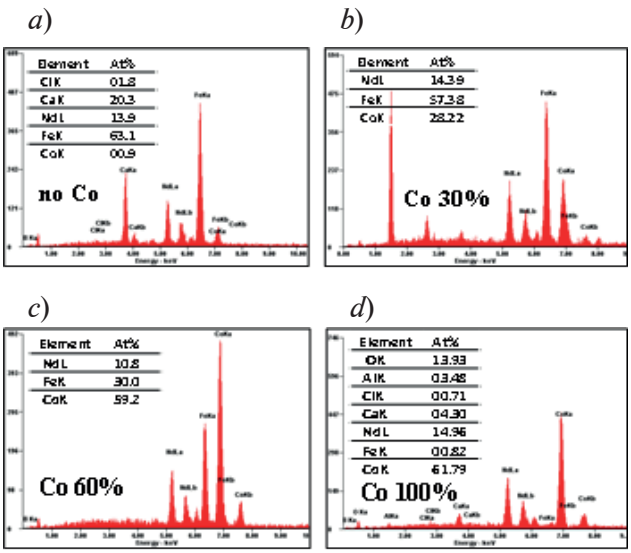

Fig. 2. EDX analysis of $NdFe_{1-x}Co_xB$ particles without Co (*a*) and declared percentage of cobalt: 30 (*b*), 60 (*c*), 100% (*d*)

Fig. 1, *b* shows the SEM image of a sample with 30% Co. The average size of the powders is 690 nm. According to the initial elemental analysis, the composition approaches the expected composition (Fig.2, *b*). For samples with 60% Co, images against the background of agglomerates show mainly 'smooth' particles that do not have sharp protrusions. It can be seen that the particles are fairly close in size. The average particle size is about 550 nm. According to the data of local elemental analysis, the samples predominantly contain the elements Nd, Fe and Co equal to 10.8, 30.0, and 59.2 at%, respectively, without taking into account the content of contaminating elements Ca, Cl and O (Fig. 2, *c*).

In a sample with 100% Co, that is, without iron, particles with clear boundaries and surface relief are observed (Fig. 1, *c*). There are agglomerates and individual particles of different sizes. The average size of the powders is about 620 nm. According to the data of local elemental analysis, Ca, Cl, and O are present in the samples (Fig. 2, *d*). The local content of Co in an individual particle is 61.8 to 78.7 at.%.

Thus, the SEM method showed that the powders contain both individual particles, mostly irregular in shape, and agglomerates. The most uniform in size structure of the powder in the sample with 60% Co. According to the data from local elemental analysis, all of the studied samples contain Ca, Cl, O, and Si, which may have remained due to the powder preparation method. In general, the content of Nd, Fe, and Co in individual particles corresponds to the declared ones.

a) *b*)

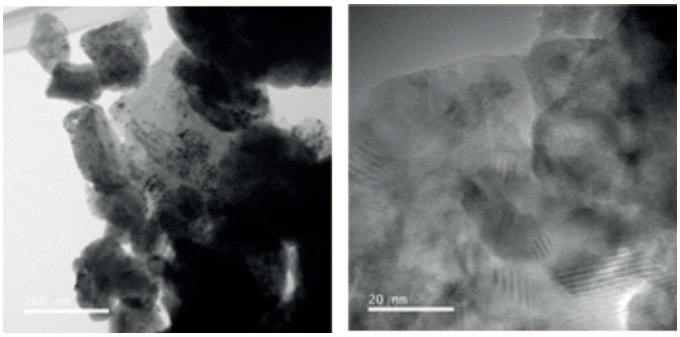

c)

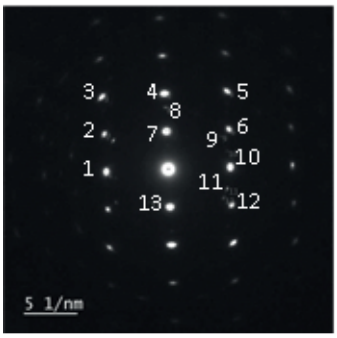

№	d-Spacing (nm)	$Nd_2Fe_{14}B$
1	0,1716	511(334)
2	0,147	416
3	0,1087	448
4	0,1409	515
5	0,1095	448
6	0,1473	416
7	0,2817	222
8	0,1734	510(325)
9	0,1731	510(325)
10	0,18	216
11	0,1727	510(325)
12	0,1721	510(325)
13	0,2775	222

Fig. 3. TEM images of NdFeB particles (without cobalt): bright-field image (*a*), direct resolution of the microstructure (*b*); as well as microelectron diffraction pattern of the NdFeB nanopowder microstructure and its interpretation (*c*)

A TEM study showed (Fig. 3) that the powders contain both individual particles of mostly irregular shapes and agglomerates. In this case, the particle sizes range from 25 to 1500 nm. Some large particles contain smaller particles of the order of (5–20) nm. The nanoparticles in NdFeB samples without Co were identified as the $Nd_2Fe_{14}B$ phase (a = 0.88 nm, c = 1.22 nm), see Fig. 3, *c*.

Fig. 4 shows the magnetic hysteresis loops measured on a vibromagnetometer at room temperature. The maximum value of the specific magnetization σ_{17}, measured in a magnetizing field of 17 kOe, reaches a value of approximately 125 G cm^3/g and the coercive force H_c = 260 Oe of the corresponding powder. Although the cobalt sublattice in the $Nd_2Co_{14}B$ compound has an easy-plane anisotropy, an increase in the coercive force is observed with increasing Co concentration (see the inset in Fig. 5), but the H_c values are not typical for magnetically hard materials (usually several kOe and higher).

Fig. 5 shows the dependence of the maximum specific magnetization σ_{17} and the coercive force H_c of the

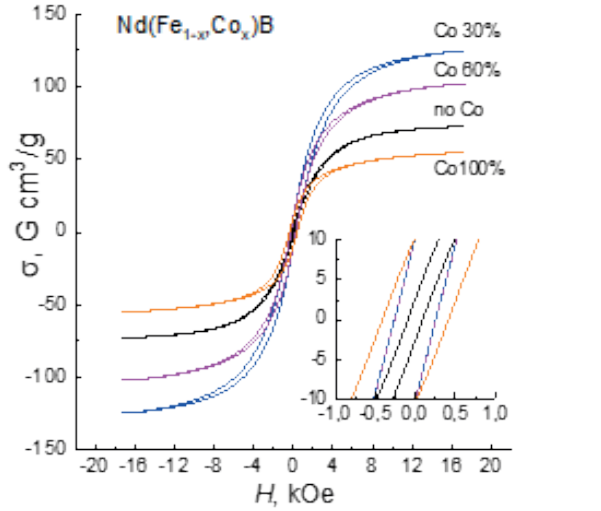

Fig. 4. Magnetic hysteresis loops of $NdFe_{1-x}Co_xB$ powders, depending on Co concentration: 0, 30, 60, and 100. The inset shows enlarged fragments of hysteresis loops

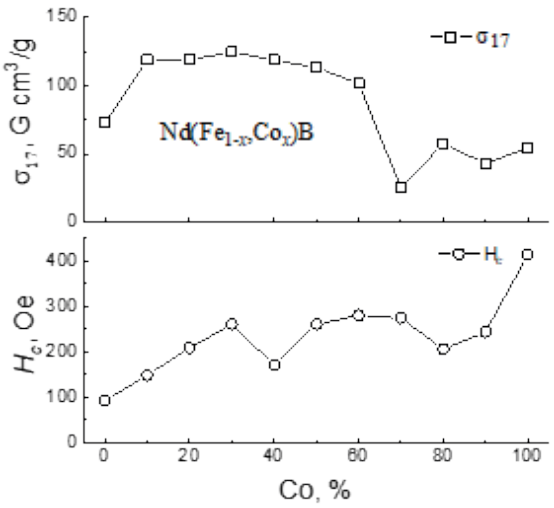

Fig. 5. Dependence of saturation magnetization σ17 and coercive force Hc of $NdFe_{1-x}Co_xB$ powders on cobalt content

$NdFe_{1-x}Co_xB$ powders on the content of cobalt, which replaces iron. After the addition of Co, there is a sharp increase in the magnetization, which decreases with the substitution of iron. The value of H_c increases from 10 to almost 415 Oe with increasing Co concentration.

Thus, $NdFe_{1-x}Co_xB$ powders were obtained, in which nanoparticles of a predominantly magnetically soft phase are formed. It follows from the TEM results that the indicated method can form particles with a magnetically hard $Nd_2Fe_{14}B$ phase. It is theoretically predicted that the maximum values of NS and energy product can be achieved in nanocomposite materials consisting of soft and hard phases [16]. It is likely that the presence of impurities in the samples reduces the purity of the phases, leading to a deterioration in the magnetic properties. A wide spread of particle sizes and their shapes leads to the fact that the magnetization reversal process occurs with the help of different mechanisms (magnetization rotation or domain wall motion). Furthermore, the magnitude of the coercive force in agglomerates of nanoparticles can decrease as a result of magnetostatic interaction. These features appear as a smooth hysteresis loop.

Conclusion

The $NdFe_{1-x}Co_xB$ powders were obtained by chemical synthesis using the modified Pechini method. A series of samples with Co concentrations from 0 to 100% was obtained and studied. The resulting material consists of both individual particles, mostly irregular in shape, and agglomerates (up to 15 μm). The average particle size according to electron microscopy varies from 550 to 870 nm. In this case, particles smaller than 100 nm in size can also be encountered. According to the data from local elemental analysis, all of the studied samples contain Ca, Cl, O, and Si, which may have remained due to the powder preparation method. The content of Nd, Fe, and Co in the particles corresponds to the declared ones. The magnetic properties of powders are typical for soft magnetic materials. An increase in the Co content leads to an increase in the coercive force up to 415 Oe. Probably, such magnetic properties are due to the low phase purity and a wide range of particle sizes.

REFERENCES

1. **Coey J. M. D.,** Magnetic materials, Alloys Compd. 326 (2001) 2–6.

2. **Matsuura Y.,** Recent development of Nd–Fe–B sintered magnets and their applications, J. Magn. Magn. Mater. 303 (2006) 344–347.

3. **Cui J., Kramer M., Zhou L., Liu F., Gabay A., Hadjipanayis G., Balasubramanian B., Sellmyer D.,** Current progress and future challenges in rare-earth-free permanent magnets, Acta Mater. 158 (2018) 118–137.

4. **Coey J.M.D.,** Magnetism and Magnetic Materials, Cambridge University Press, Cambridge, 2010.

5. **Skomski R., Coey J. M. D.,** Giant energy product in nanostructured two-phase magnets, Phys. Rev. B 48 (1993) 15812.

6. **Samardžija, Z., McGuiness, P., Soderžnik, M., Kobe, S., Sagawa, M.,** Microstructural and compositional characterization of terbium-doped Nd-Fe-B sintered magnets. Mater. Charact. 67 (2012) 27–33.

7. **Lee M. W., Bae K. H., Lee S. R., Kim H. J., Jang T. S.,** Microstructure and magnetic properties of NdFeB sintered magnets difusion-treated with Cu/Al mixed Dyco alloy-powder archives of metallurgy and materials 62(2) (2017) 1263–1266.

8. **Samardak V. Yu., Kharitonov V. N., Belov A. A., Shichalin O. O., Papynov E. K., Protasov A. V., Stashkova L. A., Kuranova N. N., Pushin V. G., Samardak A. S., Ognev A. V.,** Structure, Composition and Magnetic Properties of Nd-(Fe,Co)-B Hard Magnetic Copper-Doped Powders. J Supercond Nov Magn 35 (2022) 1703–1708.

9. **Deheri P. K., Swaminathan V., Bhame S. D., Liu Z., Ramanujan R. V.,** Sol-gel based chemical synthesis of $Nd_2Fe_{14}B$ hard magnetic nanoparticles, Chem. Mater. 22 (24) (2010) 6509–6517.

10. **Ahmadpour G., Samardak A. Yu., Korochentsev V. V., Osmushko I. S., Samardak V. Yu., Komissarov A. A., Shtarev D. S., Samardak A. S., Ognev A. V., Nasirpouri F.,** Microstructure, composition and magnetic properties of Nd-$(Fe_{1-x}Co_x)$B oxide magnetic particles synthesized by Pechini-type chemical method, Advanced Powder Technology, 32, 11 (2021) 3964-3979.

11. **Ma H. X., Kim C. W., Kim D. S., Jeong J. H., Kim I. H., Kang Y. S.,** Preparation of Nd-Fe-B

by nitrate-citrate auto-combustion followed by the reduction-diffusion process, Nanoscale. 7 (17) (2015) 8016–8022.

12. **Tan X., Parmar H., Chaudhary V., Zhong Y., Ramanujan R. V.,** Synthesis and reaction mechanism of high (BH)max exchange coupled $Nd_2(Fe,Co)_{14}B$/a-Fe nanoparticles by a novel one-pot microwave technique, New J. Chem. 42 (23) (2018) 19214–19223.

13. **Nethi S. K., Bollu V. S., Patra C. R.,** Rare Earth-Based Nanoparticles: Biomedical Applications, Pharmacological and Toxicological Significance. In: Shukla, A. (eds) Nanoparticles and their Biomedical Applications. Springer, Singapore. (2020).

14. **Papynov E. K., Dran'kov A. N., Tkachenko I. A., Buravlev I. Y., Mayorov V. Y., Merkulov E. B., Fedorets A. N., Ognev A. V., Samardak A. S., Drenin A. S., Tananaev I. G.,** Synthesis and Sorption Characteristics of Magnetic Materials Based on Cobalt Oxides and Their Reduced Forms, Russian Journal of Inorganic Chemistry, 65 (6) (2020) 820–828.

15. **Fischer, R., Leineweber, T., Kronmüller, H.,** Fundamental magnetization processes in nanoscaled composite permanent magnets, Phys. Rev. B: Condens. Matter Mater. Phys. 57 (1998) 10723.

THE AUTHORS

SAMARDAK Vadim Yu.
Samardak_vy@dvfu.ru
ORCID: 0000-0002-1919-113X

PAPYNOV Evgeniy K.
papynov.ek@dvfu.ru
ORCID: 0000-0002-1185-7718

AZON Semen A.
azon.sa@dvfu.ru
ORCID: 0000-0003-3129-1499

SAMARDAK Alexandder S.
samardak.as@dvfu.ru
ORCID: 0000-0001-5917-4361

SAMARDAK Alexey Yu.
samardak.aiu@dvfu.ru
ORCID: 0000-0002-0795-374X

OGNEV Alexey V.
ognev.av@dvfu.ru
ORCID: 0000-0002-1619-3666

Received 21.05.2022. Approved after reviewing 01.07.2022. Accepted 05.08.2022.

Conference materials
UDC 538.9
DOI: https://doi.org/10.18721/JPM.153.107

Phase transitions on trimer lattices of magnetic dipoles

V. S Strongin [1]✉, I. N. Nalivaiko [1] , M. A. Chesnokov [1]

[1] Far Eastern Federal University, Vladivostok, Russia

✉ strongin.vs@dvfu.ru

Abstract: The heat capacity in a trimerized triangular lattice was studied using the GPU-optimized Metropolis algorithm. The presence of phase transitions is discovered, the reasons for their disappearance at certain lattice parameters are explained, and frustration estimates are made for systems with different lattice parameters.

Keywords: spin ice, phase transition, Monte Carlo methods

Funding: The study was supported by Grant of the President of the Russian Federation for support of leading scientific schools of the Russian Federation (НШ-2559.2022.1.2).

Citation: Strongin V. S, Nalivaiko I. N., Chesnokov M. A. Phase transitions on trimer lattices of magnetic dipoles. St. Petersburg State Polytechnical University Journal. Physics and Mathematics. 15 (3.1) (2022) 44–47. DOI: https://doi.org/10.18721/JPM.153.107

Материалы конференции
УДК 538.9
DOI: https://doi.org/10.18721/JPM.153.107

Фазовые переходы на тример решетках магнитных диполей

В. С. Стронгин [1] ✉, И. Н. Наливайко [1], М. А. Чесноков [1]

[1] Дальневосточный Федеральный Университет, г. Владивосток, Россия

✉ strongin.vs@dvfu.ru

Аннотация. При помощи GPU оптимизированного алгоритма Метрополиса исследованы теплоемкость в тримеризованной треугольной решетке. Обнаружено наличие фазовых переходов, объяснены причины их исчезновения при определённых параметрах решетки, сделаны оценки фрустрации систем с различными параметрами решетки.

Ключевые слова: спиновый лёд, фазовый переход, методы Монте-Карло

Финансирование: Грант Президента Российской Федерации для государственной поддержки ведущих научных школ Российской Федерации (НШ-2559.2022.1.2).

Ссылка при цитировании: Стронгин В.С., Наливайко И.Н., Чесноков М.А. Фазовые переходы на тример решетках магнитных диполей // Научно-технические ведомости СПбГПУ. Физико-математические науки. 2022. Т. 15. № 3.1. С. 44–47. DOI: https://doi.org/10.18721/ JPM.153.107

Introduction

Artificial spin ices are nanomagnetic systems consisting of monodomain Ising-type nanomagnets that are lithographically defined onto two- and three-dimensional lattices [1, 2]. A distinctive feature of spin ice is a special lattice geometry, which makes any state of the system of magnetic moments energetically tense, and the artificial spin ice has non-zero entropy even at absolute zero [3]. Because of this property, such system can form phases, unusual for ordinary magnetic substances. However, studies in this area are facing computational problems, such as slow dynamics at low temperatures and exponential growth of computational time. For example, for the long-range action model, the complete enumeration algorithm cannot compute systems larger than $N = 40$ particles. Therefore, the probabilistic Monte Carlo methods, although affected by the problem of critical slowing down, are still among the most important for the study of spin ices.

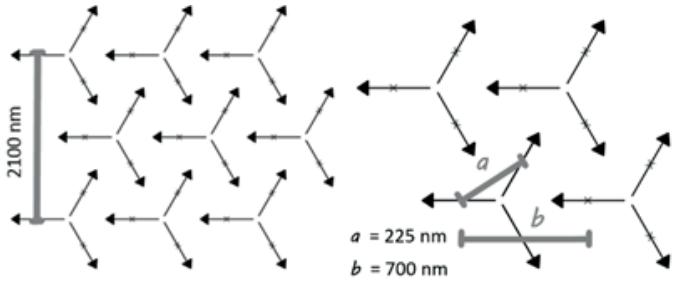

Fig 1. Trimerized triangular lattice with lattice parameters a and b

Trimerized triangular spin ice consists of repeating triplets (trimers) of particles arranged relative to each other at an angle of 60 degrees (Fig. 1) [4].

In this paper, we investigate the heat capacity [5] of a trimerized triangular point dipole spin ice, modeled by GPU-accelerated parallel Metropolis algorithm. The dependence of the heat capacity maximum on the lattice parameter b, as well as on the number of particles was investigated.

Model and computational methods

Energy of dipole-dipole interaction calculated by the formula:

$$E_{ij} = \frac{(\vec{m}_i \vec{m}_j)}{\left|\vec{r}_{ij}\right|^3} - 3\frac{(\vec{m}_i \vec{r}_{ij})(\vec{m}_j \vec{r}_{ij})}{\left|\vec{r}_{ij}\right|^5}, \quad (1)$$

where i, j are the numbers of the interacting dipoles, r is the vector between the centers of the magnetic moments of the interacting dipoles, m is the value of the magnetic moment vector.

To study the properties of the system, we used the GPU-accelerated parallel Metropolis algorithm. The essence of the algorithm was to simultaneously independently simulate many systems at different temperatures. The calculations were performed on the NVIDIA A100 GPU, which allows to simultaneously simulate the system at 6912 temperatures. The probability of adopting a new configuration was calculated by the formula:

$$P\left(E_i \to E_j\right) = \min\left(\exp\left[\frac{\Delta E_{ij}}{k_B T}\right], 1\right). \quad (2)$$

After the new configuration is accepted, thermodynamics averages are recalculated. In this case we recalculate an average energy:

$$\left\langle E \right\rangle = \frac{\sum_i^N E_i}{N}. \quad (3)$$

Next, we can obtain the heat capacity by the formula:

$$C = \frac{\left\langle E^2 \right\rangle - \left\langle E \right\rangle^2}{NT^2}. \quad (4)$$

Therefore, the value of the heat capacity is calculated per particle and there is no direct dependence of the heat capacity on the number of particles.

Results and discussion

Graphs of the heat capacity per particle as a function of temperature were plotted for 1200 particles with different lattice parameters b (Fig. 1,*a*). Fig. 2, b shows some of them. It is easy to see that the graph for $b = 560$ shows a sharp increase in the region of a certain critical temperature. The heat capacity at $b = 600$ exhibits somewhat different behavior. There is no sharp increase at a certain critical temperature.

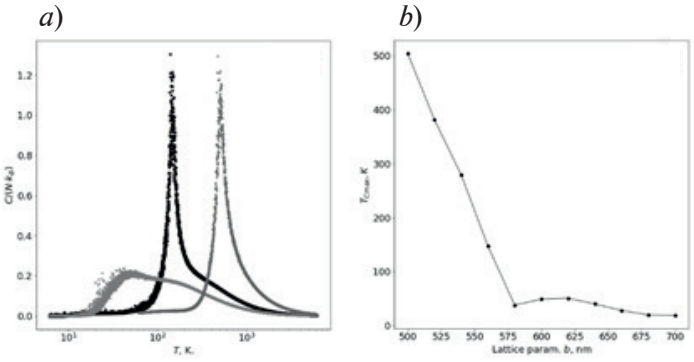

Fig 2. Heat capacity for $b = 600$, 560, 500 respectively (from left to right) (*a*); dependence of the maximum heat capacity on the lattice parameter (*b*).

Fig. 2, b shows the dependence of the maximum heat capacity on the lattice parameter b.

The flatness of the graph can be explained by the strong frustration of the systems having the parameter $b \approx 580$. For the initial study of frustrations in the system, we investigated low energy states (Fig. 3). The low energy states of closed vortexes and frustrated states of trimers having only two states are typical for parameter $b \leq 560$. The frustrated vortexes and low energy states of trimers for the parameter $b \geq 600$ are characteristic, and they have six possible states each.

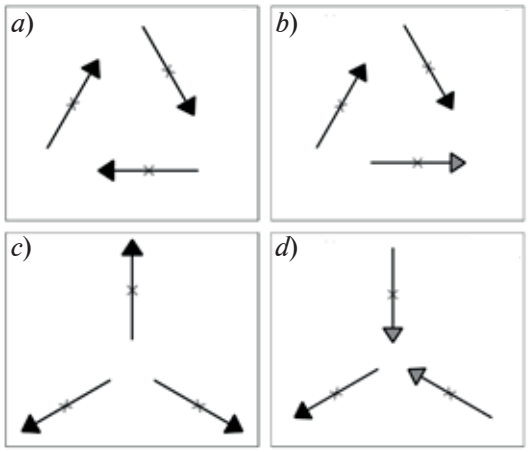

Fig. 3. Typical vortex configuration for low energy configuration for $b \leq 560$ and $b \geq 600$ (*a*, *b*) respectively; typical trimer configuration for $b \leq 560$ and $b \geq 600$ respectively (*c*, *d*).

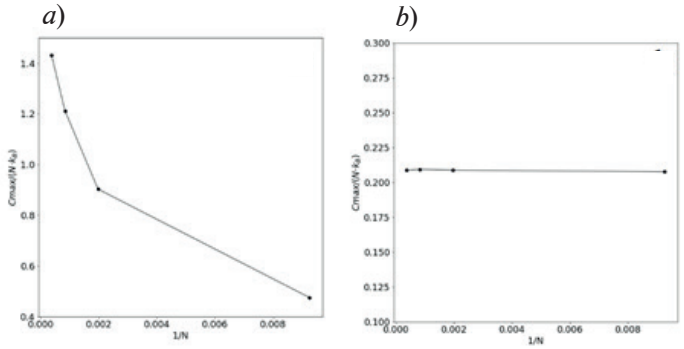

Fig. 4. The presence of a phase transition at $b = 560$ (*a*); absence at $b = 600$ (*b*).

Fig. 4 shows the dependence of the height of the heat capacity peak on the number of particles in the system. An increase in peak height indicates a phase transition. Systems with lattice parameters $b \leq 560$ exhibit a phase transition and systems with do not.

Systems with lattice parameters $560 < b < 600$ is extrimely frustrated and have very complex energy relief and cannot be investigate with the Metropolis method. We are planing to use Wang-Landay and parallel tempering methods in the future to overcome critical slowdown.

Conclusion

Phase transitions in trimerized triangular lattice were investigated, the causes of disappearance are explained, and estimates of the frustration of systems with different lattice parameters are made.

Additional studies are required by methods capable of overcoming the critical slowing down to determine the specific value of the lattice parameter and to investigate the nature of the disappearance of the phase transition.

REFERENCES

1. **Wang R. F. et al.,** Artificial 'spin ice'in a geometrically frustrated lattice of nanoscale ferromagnetic islands, Nature. 439 (7074) (2006) 303–306.

2. **Qi Y., Brintlinger T., Cumings J.,** Direct observation of the ice rule in an artificial kagome spin ice, Physical Review B. 77 (9) (2008) 094418.

3. **Farhan A. et al.,** Exploring hyper-cubic energy landscapes in thermally active finite artificial spin-ice systems, Nature Physics. 9 (6) (2013) 375–382.

4. **Hofhuis K. et al.,** Geometrical frustration and competing orders in the dipolar trimerized triangular lattice, Physical Review B. 104 (1) (2021) 014409.

5. **Shevchenko Yu. A.,** Thermodynamic properties of frustrated spin system FEFU, Vladivostok, PhD thesis (in Russian), 2017.

THE AUTHORS

STRONGIN Vladislav S.
strongin.vs@dvfu.ru
ORCID: 0000-0002-8420-9893

NALIVAIKO Igor N.
nalivaiko.in@students.dvfu.ru
ORCID: 0000-0003-4433-2990

CHESNOKOV Mikhail A.
chesnokov.ma@students.dvfu.ru
ORCID: 0000-0003-1173-8775

Received 22.05.2022. Approved after reviewing 27.07.2022. Accepted 27.07.2022.

Conference materials
UDC 546.824-31:539.211
DOI: https://doi.org/10.18721/JPM.153.108

Estimation of local and long-range ordering of the structure of TiO_2 nanotubes

S. A. Schegoleva [1] ✉, P. L. Titov [1], N. B. Kondrikov [1]

[1] Far Eastern Federal University, Vladivostok, Russia

✉ sveta170@bk.ru

Abstract: We present a study of the scanning electron microscopy images of the TiO_2 nanotube array. The initial and modified samples were examined before and after annealing. It has been found that the annealing of the modified and unmodified samples results in different degrees of the local ordering. The nanotubular coverings were modified by Pt nanoparticles formed by the H_2PtCl_6 solutions infiltration for change of their electro- and photo-catalytic properties estimated by measuring the photoelectric currents. The influence of the morphology and ordering degree of the nanotubular coverings on the manifestation of their functional properties has been studied. A two-dimensional Fourier transform was applied for obtaining information on the occurrence of periodicities in the ordering of nanotubes. Correlation analysis was performed to find out the invisible regularities and periodicities in the structure of the nanotube arrays. The analysis of the photoactivity of the samples was also carried out.

Keywords: nanotubes, titanium dioxide, ordered structure

Citation: Schegoleva S. A., Titov P. L., Kondrikov N. B., Estimation of local and long-range ordering of the structure of TiO_2 nanotubes. St. Petersburg State Polytechnical University Journal. Physics and Mathematics. 15 (3.1) (2022) 48–53. DOI: https://doi.org/10.18721/JPM.153.108

Материалы конференции
УДК 546.824-31:539.211
DOI: https://doi.org/10.18721/JPM.153.108

Оценка локального и дальнего упорядочения массива нанотрубок диоксида титана

С. А. Щеголева [1] ✉, П. Л. Титов [1], Н. Б. Кондриков [1]

[1] Дальневосточный Федеральный Университет, г. Владивосток, Россия

✉ sveta170@bk.ru

Аннотация. В работе проведено исследование изображений сканирующей электронной микроскопии массива нанотрубок диоксида титана. Изучались исходные и модифицированные образцы до и после отжига. Обнаружено, что отжиг образцов приводит к различным степеням локального упорядочения. Исследовано влияние морфологии и степени упорядочения нанотубулярных покрытий на проявление их функциональных свойств.

Ключевые слова: нанотрубки, диоксид титана, упорядоченная структура

Ссылка при цитировании: Щеголева С. А., Титов П. Л., Кондриков Н. Б. Оценка локального и дальнего упорядочения массива нанотрубок диоксида титана // Научно-технические ведомости СПбГПУ. Физико-математические науки. 2022. Т. 15. № 3.1. С. 48–53. DOI: https://doi.org/10.18721/ JPM.153.108

Introduction

Nanostructured and microstructured materials, whose principally new physical properties result from the developed surface and quantum-size effects, constitute the group of promising objects for advanced materials science. In the last decade, adsorption, optical, electrical, catalytic, and photocatalytic properties of TiO_2 have attracted a special interest of researchers [1–3]. Self-organization of titanium dioxide can be attained by its anodization in acids (for instance, sulfuric or phosphoric), most often, in fluorine-containing electrolytes, since dissolution proceeds there through formation of fluoride complexes. Anodic oxidation of titanium in a fluorine-containing electrolyte enables one to obtain nanostructured coatings consisting of TiO_2 nanotubes, whose parameters can be controlled varying the oxidation conditions [4–9].

Materials and Methods

Anodic oxidation of titanium was performed in a two-electrode electrochemical cell using a B5-49 direct current source. Pt served as an auxiliary electrode, the Ti plate was a working electrode. To obtain the nanotubular structure of titanium anodes, an aqueous solution of $NH_4F{\cdot}HF$ with addition of Na_2SO_4 and complexing agents was used. Thereafter, for the sake of properties modification, the obtained Ti/TiO_2(nano) systems were held in an aqueous solution of H_2PtCl_6 of the concentration $3{\cdot}10^{-2}$ mol·l^{-1} for 1 h, dried, and annealed in a muffle furnace at 500 °C for 4 h (Table 1). The surface structure was investigated on a Hitachi S-5500 scanning electron microscope (SEM) (Hitachi, Japan).

Table 1

Modification Condition

Sample	H_2PtCl_6 concentration, M	Anneal time, h
No. 1	–	–
No. 2	–	4
No. 3	$3{\cdot}10^{-2}$	–
No. 4	$3{\cdot}10^{-2}$	4

The photocurrent generated by the sample under the action of the UV radiation was measured to determine the photoactivity of titanium dioxide. The measurements were carried out using the DUV-35W Labino UV xenon lamp with the spectrum within the range of 315–400 nm with the peak at 365 nm. The current was recorded using the AUTOLAB POSTAT-302N potentiostat with PC-controlled data acquisition.

Results and Discussion

Nanotubes with well-defined boundaries of a regular form are observed in the SEM-image of Sample 1 (Fig. 1, *a*, *b*).

A sufficiently great number of boundaries approximates the shape of convex polygons with well-defined directions of sides. The average diameter of nanotubes is approximately 100 nm. Some defects of the surface can be also seen in the sample. Considering the local configurations of nanotubes, it can be observed that they are sufficiently similar in nature to the ‘plate’ structure. Because the boundaries of nanotubes often have marked sides, the nanotubes ‘contact’ each other along these sides. Therefore, different types of local ordering arise. Sometimes, one can also observe the near correct configurations in the shape of square, rectangle and, less frequently, hexagon.

Fig. 1, *c*, *d* show that the boundaries of nanotubes become blurred and widen after annealing. Although the structure deteriorates and becomes generally more uneven, the short-range local order in the relative positioning of nanotubes is preserved. The same stable configurations in the shape of square, rectangle and hexagon can be seen (Fig. 1, *c*).

Let us consider the SEM-image of Sample 3 modified by Pt (Fig. 1, *e*, *f*). A large quantity of platinum nanoparticles can be observed; their size mainly is in the order of 10 nm but can also reach 30 nm. We used the X-ray photoelectron spectroscopy method to confirm that Pt nanoparticles on the surface of nanotubes correspond to the non-oxidized and oxidized states.

The nanotubes, in contrast to Sample 1, have no individual boundaries. Neighboring nanotubes are separated by common and, at the same time, sufficiently wide boundaries (walls), whose thickness can reach 20–50 nm. The inner diameters of nanotubes are commensurate with the wall thickness and predominantly equal 50–60 nm. It can be said that the structure of the nanotube array is completely stochastically uniform, including only rare 'pieces' of regular local configurations of nanotubes.

After annealing, the common structure of the nanotube array acquires a sharpness (Fig. 1, *e*). The boundaries of nanotubes become essentially thinner and, in this case, the inner diameter of nanotubes increases automatically. The image is more contrasted compared to Sample 3, which

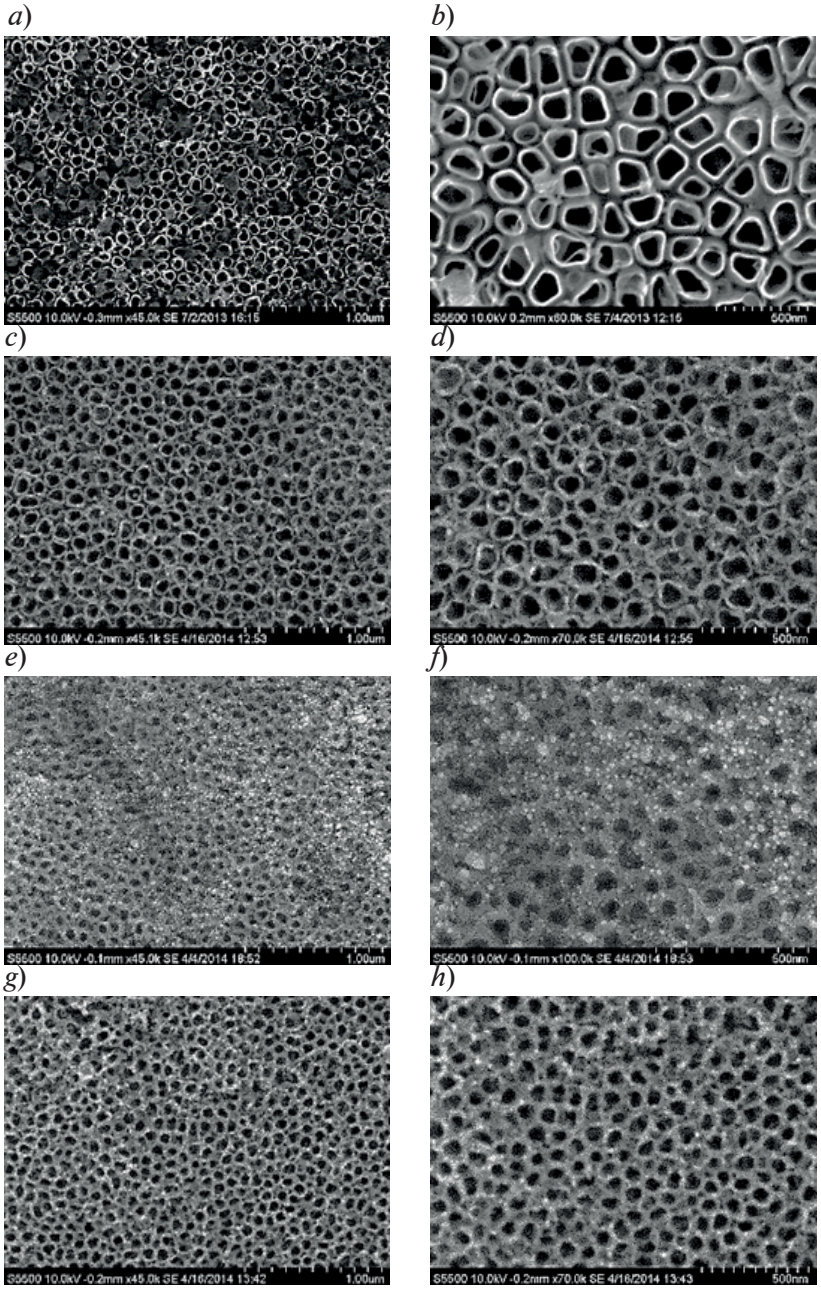

Fig. 1. SEM images of electrode surface: Sample 1 (*a*, *b*); Sample 2 (*c*, *d*); Sample 3 (*e*, *f*); Sample 4 (*g*, *h*).

is to say that the nanotubes become deeper or open. The observed quantity of the platinum nanoparticles decreases essentially compared to Sample 3.

Because the walls of nanotubes become thinner after annealing, this suggests local ordering. Considering the fact that the average diameter of nanotubes changes weakly and the sections of nanotubes are tightly packed on the image plane, the hexagon should be the predominant configuration. The character of the Fourier spectrum may provide evidence to confirm this circumstance.

The two-dimensional Fourier transform [10] allows to reveal the periodicities and regularities in the structure of the object observed in the process of visual analysis. Fig. 2 shows the respective two-dimensional spectra for the SEM-images of the samples considered.

Contrary to expectations, the SEM-images are characterized by roughly the same topology differing only in detail. In all images, the halo responsible for the short-range ordering is present. Such halo is characteristic of the 'amorphous' order where the structural elements have the order only within the limits of the first coordination sphere.

The halo for Sample 1 is poorly expressed in spite of the sharp edges of nanotubes in the SEM-image. There is no pronounced periodicity in all directions, which stipulates the weak intensity of the halo. The presence of the low-frequency region in the spectrum can be identified with the defects of nanotubes structure within the SEM-image. Judging from Sample 1, we can draw the preliminary conclusion that the Fourier spectrum in this case does not reflect the well-defined boundaries of separate nanotubes.

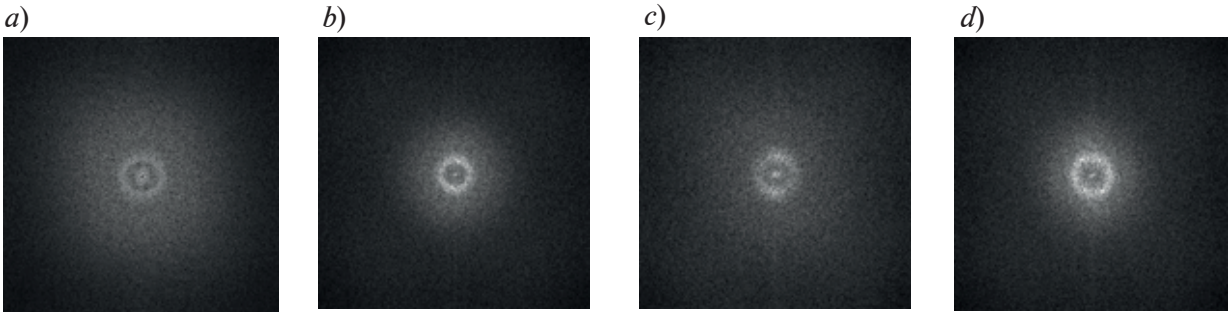

Fig. 2. Fourier spectra of SEM-images: Sample 1 (*a*); Sample 2 (*b*); Sample 3 (*c*); Sample 4 (*d*).

In Spectrum 2, the halo is shown brighter than in Spectrum 1. Such change is due to the fact that the boundaries of nanotubes 'become blurred' under annealing, at the same time the hollows of nanotubes take on a more identical shape. Such 'averaging' of nanotube configurations leads to the fact that the structure within the SEM-image becomes more uniform and isotropic. The uniformity of the structure elements (in the absence of well-defined local configurations) results in the pronounced halo. The low-frequency components in Spectrum 2 (as well as in Spectra 3, 4) are practically non-existent which shows a decrease in the number of defects in the structure of the array of nanotubes.

Modifying the sample with platinum worsens visually the structure of the array of nanotubes. The existence of halo in Spectrum 3 can be related to the fact that the nanoparticles Pt do not cover the nanotubes but lie predominantly at their boundaries. Thereby, the structure is for the most part preserved.

The SEM-image of Sample 4 is similar enough to the image of Sample 2 and differs only in the fact that the boundaries of nanotubes form a solid continuous 'grid'. In the present case, even more significant 'averaging' is observed which touches on the boundaries of nanotubes also. The halo in Spectrum 4 begins to acquire a hexagonal shape with the intensity maxima in its corners. This spectrum coincides with the expectable one.

Next, we turn to correlation analysis which allows to additionally find out the hidden regularities and periodicities in the structure of the nanotube arrays. We use the one-dimensional autocorrelation function (ACF) under the vertical direction of the SEM-image [11].

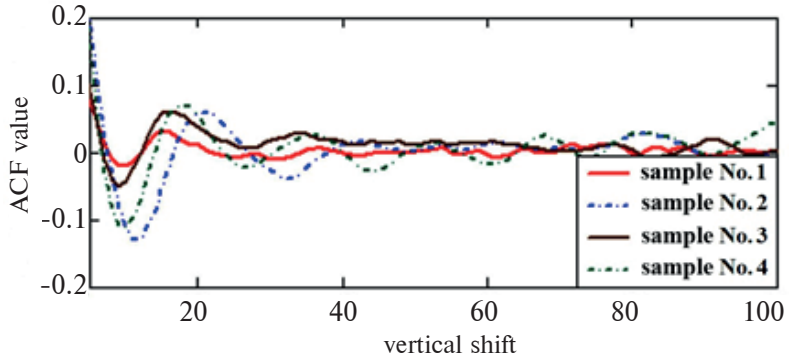

Fig. 3. Fragments of ACF for the SEM-images

It has been established that ACFs do not have overly large differences (Fig. 3). At the same time, the value of the range of the first side maximum allows to obtain the additional information about the ordering. The relative range of the first side maximum for ACFs *1*, *2*, *3* and *4* was 5.3%, 18.8%, 11.2% and 18.2% respectively. Over the first 1–2 periods, ACFs *1* and *3* as well as ACFs *2* and *4* are similar to one another. As seen from Fig. 3 (as well as from presented quantitative evaluations), ACFs *1* and *3* fall within the group of less structured ones. ACFs *2* and *4*, which are characterized by a practically similar value of the first side maximum, are more pronounced. In this case, the same as for analysis of the Fourier spectra, the 'averaging' of the nanotube structure under annealing influences the ACF ordering.

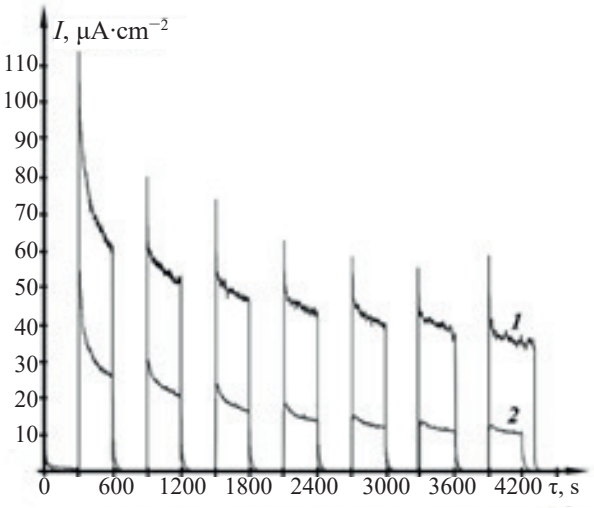

Fig. 4. Impulses of photoinduced current for TiO_2 nanotubes: Sample 4 (*1*); Sample 1 (*2*).

The photoactivity of nanotubular covers of titanium dioxide was also examined. Fig. 4 shows that the sample modified with platinum and exposed additionally to heat treatment has the characteristic values of photocurrents which are 2–3 times as large compared with the non-modified sample.

We can argue that the values of the detected photocurrent change over time from 60–110 mA·cm^{-2} (the first UV-irradiation) to 40–60 mA·cm^{-2} (the final UV-irradiation) for the modified sample. The photocurrent density of the non-modified sample also demonstrates a tendency to reduction with increase of the UV-exposition time, in this case, the values change from 26–54 mA·cm^{-2} to 10–12 mA·cm^{-2}.

Conclusion

In this paper, we have carried out analysis of the ordering indicators of the nanotube arrays both as an independent objective and in connection with the functional properties. The titanium dioxide nanotubes obtained using the aqueous solution of NH_4F·HF with added Na_2SO_4 and complexing agents (Sample 1) have a sufficiently well-defined structure, sections appearing to be shaped as roundish convex polygons as well as boundaries individual for each nanotube. Visually, the local order can be characterized as the most pronounced. Moreover, Sample 1 does not exhibit meaningful ordering at the level of the Fourier-spectra and ACF due to defects of structure.

Modification with Pt (Sample 3) results in changing the character of the nanotube structure and 'coarseness', 'adhesion' of the boundaries of nanotubes with disturbance of geometry as well as appearance of large number of the platinum nanoparticles predominantly at the boundaries of nanotubes. Visually, the given sample is the least ordered.

Annealing of these samples leads to different results. For the unmodified sample, the shape of the nanotube sections became less delineated (Sample 1 → Sample 2). The SEM-image became 'blurred' and local ordering was less pronounced. Conversely, the annealing of the modified sample

(Sample 3 → Sample 4) has resulted in thinning of nanotube boundaries and manifestation of this structure because it has no well-defied structure in the initial state. Therefore, the short-range order of Sample 4 was best manifested in the local configurations of nanotubes, even though not so sharply as in Sample 2. Visually, Samples 2 and 4 are similar enough. According to the Fourier-spectra shapes and behavior of ACFs, they demonstrate homogeneity of the structure and pronounced periodicity.

Morphology of TiO_2 covers was analyzed to determine the elemental composition at different points. It has been established that the elemental composition of covers at different points (inwardly, at the boundary of nanotubes) differs by the ratio of Ti:O with micro-impurities of other elements. Analysis of photoactivity of the samples was also carried out. It has been established that the samples modified with Pt under the UV-irradiation demonstrate the photocurrent values which are 2–3 times higher than non-modified ones.

REFERENCES

1. **Zimina T. M., Luchinin V. V.,** Microsystems for express analysis, Journal of Analytical Chemistry. 66 (12) (2011) 1136–1158.

2. **Moshnikov V. A., Gracheva I., Lenshin A. S., Spivak Y. M., Anchkov M. G., Kuznetsov V. V., Olchowik J. M.,** Porous silicon with embedded metal oxides for gas sensing applications, Journal of Non-Crystalline Solids. 358 (3) (2012) 590–595.

3. **Ferre-Borrull J., Macias G., Pallares J., Marsal L. F.,** Nanostructural Engineering of Nanoporous Anodic Alumina for Biosensing Applications, Materials. 7 (7) (2014) 5225–5253.

4. **Lee K., Mazare A., Schmuki P.,** One-Dimensional Titanium Dioxide Nanomaterials: Nanotubes, Chemical Reviews. 114 (2014) 9385–9454.

5. **Kondrikov N. B., Titov P. L., Schegoleva S. A., Khorin M. A.,** Influence of formation conditions on the level of arrays ordering of anodic titanium oxide nanotubes, Physics Procedia 86 (2017) 37–43.

6. **Titov P. L., Schegoleva S. A., Kondrikov N. B.,** Ordering characteristics of titanium dioxide nanotubes in anodic coatings, Key Engineering Materials. 806KEM (2019) 39–44.

7. **Macak J. M., Tsuchiya H., Ghikov A., Yasuda K., Hahn R., Bauer S., Schmuki P.,** TiO_2 nanotubes: Self-organized electrochemical formation, properties and applications, Current Opinion in Solid State and Materials Science. 11 (2007) 3–18.

8. **Lozovaya O.V., Tarasevich M.R., Bogdanovskaya V.A., Kasatkina I.V., Shcherbakov A.I.,** Electrochemical Synthesis, Investigation and Modification of TiO_2 Nanotubes, Fizikokhimiya poverkhnosti i zashchita materialov. 47 (1) (2011) 45–50.

9. **Fang D., Luo Z., Huang K., Lagoudas D. C.,** Effect of heat treatment on morphology, crystalline structure and photocatalysis properties of TiO_2 nanotubes on Ti substrate and freestanding membrane, Applied Surface Sience 257 (15) (2011) 6451–6461.

10. **Priestley M. B.,** Spectral analysis and time series, Academic Press, New York, 1982.

11. **Dunn P. F.,** Measurement and Data Analysis for Engineering and Science, McGraw-Hill, New York, 2005.

THE AUTHORS

SCHEGOLEVA Svetlana A.
sveta170@bk.ru
ORCID: 0000-0002-0318-8067

KONDRIKOV Nikolay B.
kondrikov.nb@dvfu.ru
ORCID: 0000-0002-0002-8842

TITOV Pavel L.
titov.pl@dvfu.ru
ORCID: 0000-0002-3408-5757

Received 22.05.2022. Approved after reviewing 19.07.2022. Accepted 01.08.2022.

Conference materials
UDC 538.955
DOI: https://doi.org/10.18721/JPM.153.109

Magnetic anisotropy and Dzyaloshinskii–Moriya interaction of Pd/Co/Ta thin films

M. A. Kuznetsova [1], G. S. Suslin [1], A. F. Shishelov [1], D. O. Yushchenko [1],
O. E. Ayanitov [1], E. V. Tarasov [1], A. G. Kozlov [1] ✉

[1] Far Eastern Federal University, Vladivostok, Russia

✉ kozlov.ag@dvfu.ru

Abstract: In this work, we experimentally studied the structure and magnetic properties of epitaxially grown ultrathin Pd/Co/Ta films. We have studied the effect of Ta on the structural and magnetic properties of Pd/Co epitaxial films. The deposition of a Ta layer on an epitaxial Co layer leads to a decrease in the saturation magnetization of the film due to strong magnetic disordering and the formation of a dead magnetic layer with a thickness of about 0.5 nm. Perpendicular magnetic anisotropy is observed for Co layer thicknesses less than 1.3 nm. The volume and surface components of magnetic anisotropy are determined. Additionally, the Dzyaloshinskii–Moriya interaction (DMI) is observed in epitaxial films with perpendicular magnetic anisotropy, with a DMI field value of about 30 mT.

Keywords: epitaxial thin films, perpendicular magnetic anisotropy, Dzyaloshinskii-Moriya interaction

Funding: This research was supported by the grant of the Government of the Russian Federation for state support of scientific research conducted under supervision of leading scientists in Russian institutions of higher education, scientific foundations, and state research centers of the Russian Federation (Project Proposal no. 075-15-2021-607 *Ferrimagnetic spinorbitronic*).

Citation: Kuznetsova M. A., Suslin G. S., Shishelov A. F., Yushchenko D. O., Ayanitov O. E., Tarasov E. V., Kozlov A. G., Magnetic anisotropy and Dzyaloshinskii–Moriya interaction of Pd/Co/Ta thin films. St. Petersburg State Polytechnical University Journal. Physics and Mathematics. 15 (3.1) (2022) 54–58. DOI: https://doi.org/10.18721/JPM.153.109

Материалы конференции
УДК 538.955
DOI: https://doi.org/10.18721/JPM.153.109

Магнитная анизотропия и взаимодействие Дзялошинского-Мории в тонких пленках Pd/Co/Ta

М. А. Кузнецова [1], Г. С. Суслин [1], А. Ф. Шишелов [1], Д. О. Ющенко [1]
О. Е. Аянитов [1], Е. В. Тарасов [1], А. Г. Козлов [1] ✉

[1] Дальневосточный Федеральный Университет, г. Владивосток, Россия

✉ kozlov.ag@dvfu.ru

Аннотация. В данной работе экспериментально исследовались структура и магнитные свойства ультратонких пленок Pd/Co/Ta выращенных эпитаксиально. Мы исследовали влияние Ta на структурные и магнитные свойства эпитаксиальных пленок Pd/Co. Осаждение пленки Ta на эпитаксиальный слой Co приводит к понижению намагниченности насыщения пленки за счет сильного магнитного разупорядочения и формирования магнитомертвого слоя, толщиной около 0,5 нм. При толщине слоя Co меньше 1,3 нм наблюдается перпендикулярная магнитная анизотропия. Определены вклады объемной и поверхностной анизотропии. Также в эпитаксиальных пленках с перпендикулярной магнитной анизотропией наблюдается взаимодействие Дзялошинского-Мории (ВДМ) с величиной поля ВДМ примерно 30 мТл.

Ключевые слова: тонкие эпитаксиальные пленки, магнитная анизотропия, взаимодействие Дзялошинского-Мории

Финансирование: Работа выполнена при поддержке гранта Правительства Российской Федерации для государственной поддержки научных исследований проводимых под руководством ведущих ученых в российских институтах высшего образования, научных организациях и государственных исследовательских центрах (программа Мегагрантов, проект №. 075-15-2021-607 "Ферримагнитная спинорбитроника").

Ссылка при цитировании: Кузнецова М. А., Суслин Г. С., Шишелов А. Ф., Ющенко Д. О., Аянитов О. Е., Тарасов Е. В., Козлов А. Г., Магнитная анизотропия и взаимодействие Дзялошинского-Мории в тонких пленках Pd/Co/Ta // Научно-технические ведомости СПбГПУ. Физико-математические науки. 2022. Т. 15. № 3.1. С. 54–58. DOI: https://doi.org/10.18721/ JPM.153.109

Introduction

As advances are made in spintronics, there is an ongoing search for new nanostructured materials with potential applications in controllable magnetic processes for creating skyrmionium racetrack memory, logic devices etc. Trilayer magnetic structures comprising heavy metal (1)/ferromagnet/heavy metal (2) are very promising for developing spintronics devices. Ultrathin epitaxial magnetic films (~1 nm) have exhibited anisotropy properties, which lead to a series of interface effects: enhanced perpendicular magnetic anisotropy (PMA), interfacial Dzyaloshinskii–Moriya interaction (DMI), spin-Hall effect etc. These effects are used for forming, stabilizing and controlling spin textures. The goal of this paper is to study the prospects of using thin epitaxial films with a Ta layer to create structures with a high DMI. This metal is currently the most interesting, because it is effective in experiments with other magnetic effects. For example, multilayer structures with tantalum have shown large values of the spin-orbit torque effect, as well as the ability to produce high-density skyrmion lattices [1].

Materials and Methods

The epitaxial films were deposited by molecular beam epitaxy in an ultrahigh vacuum chamber with a base pressure of 3Ч10-11 Torr, (Omicron Nanotechnology). We used intrinsic undoped Si(111) substrates with the resistivity of 20–40 $k\Omega\times$cm with a Cu (2.1 nm) buffer layer. Before deposition, the substrates were flash-heated by direct current at 1200 °C a few times and slowly cooled down to room temperature. Cu, Pd and Co films were deposited by effusion cells, and deposition rates were controlled by quartz crystal microbalance and were 1 nm/min for Cu, 0.3 nm/min for Pd, and 0.1 nm/min Co, respectively. Deposition rates measured by quartz crystal microbalance were calibrated using reflection high-energy electron diffraction (RHEED, STAIB Instruments) based on intensity oscillations of specular beam reflection measured during layer deposition. The Cu 2.1 nm buffer layer prevents the intermixing of Pd with Si and protects from formation of amorphous silicide. A value of 2 nm Pd thickness was chosen because the lattice parameter reaches the bulk value, while the roughness parameter is small for the selected thickness [2]; moreover, we varied the thickness of the Co layer from 0.75 nm for inducing strong PMA for deposition on Pd [3, 4] to 4.5 nm. The temperature of the substrate was about 75 °C during Cu deposition and increased up to 110 °C for Pd and Co deposition. Ta (2 nm) layers were deposited by the electron-beam evaporation technique. Finally, films were covered with a Pd (3 nm) protection layer to prevent oxidation of the structure. Magnetization reversal processes and the effective PMA energy were estimated by hysteresis loops, measured by a vibrating-sample magnetometer (VSM, LakeShore 7410). Domain structure images were observed with a magnetooptical Kerr-effect microscope (Evico Magnetics) equipped with an in-plane electromagnet and custom-made out-of-plane electromagnet coil. Investigation of the DMI was performed using the observation of domain walls (DWs) displacement in a combination of IP and OP magnetic fields. The value of the internal Dzyaloshinskii–Moriya interaction field (HDMI) was determined by the minimum in the domain wall velocity dependencies on in-plane magnetic fields [5].

Results and Discussion

Crystalline structure of Si(111)//Cu(2.1)/Pd(2)/Co(d_{Co})/Ta(2)/Pd(3) films was studied *in situ* via RHEED. Detailed investigation of the growth processes of epitaxial Pd and Co was presented in our previous works [2, 4]. A RHEED image of the epitaxial fcc Co (1 nm) layer is presented in Fig. 1, *a*. The mismatch between the lattice parameters of Co (0.354 nm) and Ta (0.331 nm) is insignificant, amounting to about 6.6%. However, due to the difference in crystal symmetry (fcc Co vs bcc Ta), as well as the fact that Ta has a very high melting point (3017 °C), it exhibits a tendency toward amorphous growth, which is accompanied by the disappearance of diffraction stripes and an increase in the background level on the RHEED pattern, as shown in Fig. 1, *b*. Despite the strong disordering of the Ta layer, further deposition of the fcc Pd layer occurs in the (111) direction with the predetermined predominant crystallographic direction retained. This makes it possible to obtain multilayer films with the preservation of the epitaxial orientation.

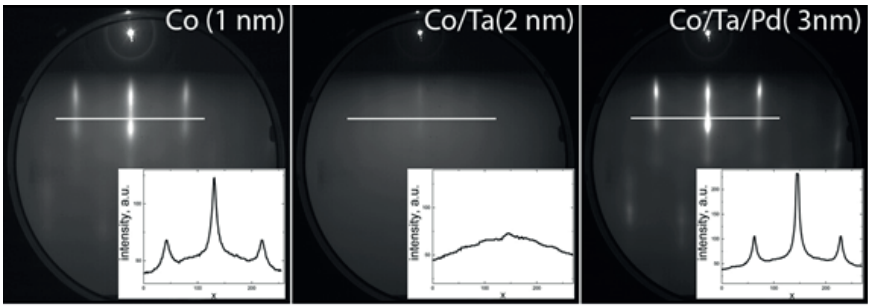

Fig. 1. RHEED images for different layers in Si(111)//Cu(2.1)/Pd(2)/Co(1)/Ta(2)/Pd(3) film

The magnetic properties of Si(111)/Cu/Pd/Co/Ta/Pd films were studied using the magnetic hysteresis loops obtained using VSM in magnetic fields, applied along the in-plane (IP) and out-of-plane (OP) directions. The saturation magnetization normalized to the thickness of the deposited Co layer in Pd/Co/Ta films demonstrates values below the magnetization of bulk single-crystal Co ($M_{s\,Co\,bulk}$ = 1420 G). At a thickness of 0.75 nm of the ferromagnetic layer, M_s is equal about 600 G, and with increasing thickness, Co increases sharply, however, even at a thickness of 4.5 nm, it does not reach the bulk value, as shown on the inset of fig.2(*a*). In this case M_s, determined by the slope of the line graph $(m_s/S) = f(d_{Co})$ is about 1440 G, this is less than epy saturation magnetization of Pd/Co/Pd films (Ms = 1520 G) which was investigated in our previous work [4], where the increase of saturation magnetization is related to the magnetic polarization Pd. It is known that magnetic polarization of the 4*d* Pd boundary layer is observed in Pd/Co/Pd films due to hybridization of 3*d* electrons of Co, which leads to an overall increase in the magnetic saturation moment. In Pd/Co/Ta films, the magnetic moment decreases linearly with decreasing Co thickness; however, the zero moment (the point of intersection of the graph with the abscissa axis) is expected at a nonzero positive value of $d_{Co} \approx 0.4$ nm (Fig. 2, *a*), which indicates the existence of a magnetically disordered 'dead magnetic' layer at the Co/Ta interface. Magnetic polarization at the Pd/Co interfaces shifts the intersection point to negative thicknesses [4] of −0.1 nm, and thus the dead layer thickness can be determined as the difference $d_{DL} \approx 0.4 - (-0.1) \approx 0.5$ nm, which is about 2.5 monolayers of Co(111).

The dependence of the effective magnetic anisotropy on the thickness is shown in Fig. 2, *b*. Epitaxial Pd/Co/Ta films demonstrate the perpendicular magnetic anisotropy at small thicknesses. Compared to epitaxial Pd/Co/Pd films, in which magnetic anisotropy is induced at the interfaces, mainly due to strong crystalline stresses, the energy of perpendicular magnetic anisotropy in Pd/Co/Ta films is significantly lower due to the disordered layer at the Co/Ta interface. Maximum value of effective anisotropy is $K_{eff} \times d_{Co} = 8 \cdot 10^{-5}$ J/m^2 in the range of perpendicular magnetic anisotropy observed at d_{Co} = 1 nm. At the same thickness, there is also a maximum of coercive force $\mu_0 H_c$ = 13 mT. A decrease in the layer thickness leads to a decline of the coercive force, which may be due to a significant influence of dead layer d_{DL} and nonzero roughness of the Pd/Co interface, which can lead to the appearance of sections of a ferromagnetically discontinuous layer. On the other hand, an increase in the thickness of the Co layer to 1.2 nm also leads to a decrease in the coercive force, which is associated with a decrease in the magnetic anisotropy.

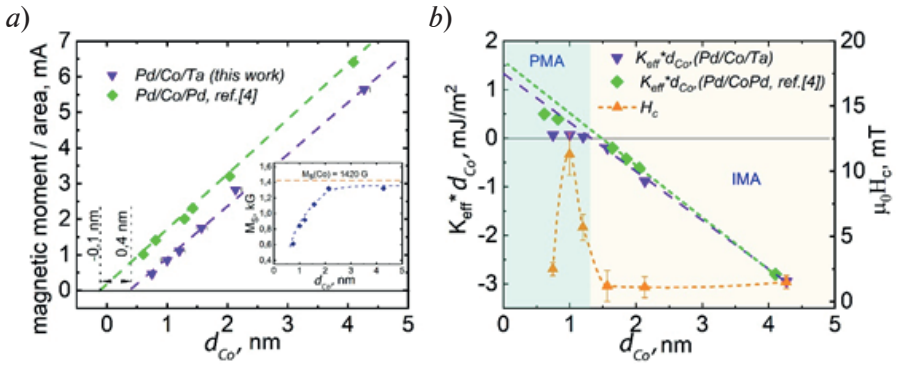

Fig. 2. Magnetic moment per unit of sample area (*a*), saturation magnetization (inset in (*a*)), effective magnetic anisotropy and coercive force (*b*) as a function of d_{Co}

The transition between perpendicular and in-plane anisotropy is observed at a thickness of about 1.3 nm; with a further increase in thickness in-plane magnetic anisotropy is observed at which the coercive force does not exceed the value of $\mu_0 H_c$ = 1–2 mT. Effective magnetic anisotropy may be determined as

$$K_{eff} \cdot d_{\mathrm{Co}} = K_v + \frac{(2)K_s}{d_{\mathrm{Co}}}.$$

The slope of the linear section of curve of the magnetic anisotropy was used to determine the volume contribution to the effective anisotropy K_v = 1 MJ/m^3, and to determine the constant of surface anisotropy K_s = 1.4 mJ/m^2.

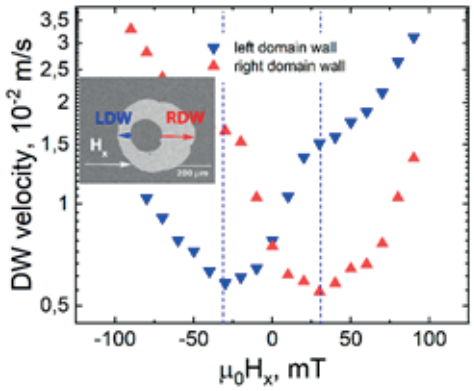

Fig. 3. Dependence of domain wall velocity on in-plane magnetic field H_x. Visualization of magnetic domains was carried out with magnetooptical Kerr microscopy

A simple scheme of the experiment is presented in the inset

The study of the Dzyaloshinskii–Moriya interaction was carried out based on the asymmetry of the propagation of domain walls in the creep mode for the Pd/Co(1)/Ta sample, since it demonstrates the highest perpendicular magnetic anisotropy. The necessary conditions for accurate measurement of the Dzyaloshinskii–Moriya interaction field are the following: stable nucleation of a domain in the same place, the absence of anisotropic macrodefects and roughness, a coercive force of less than 30 mT, and the absence of other domains in the field of view of the selected domain during its propagation. Using by the focused ion beam technique, an artificial defect was formed, which played the role of a stable center of domain nucleation The dynamics of domain wall propagation was studied using a magnetooptical Kerr microscope. On an artificial defect, using a short out-of-plane field (H_z) pulse, with duration of 2 ms, a domain was generated, after which a constant in-plane magnetic field (H_x) was switched on and after that, gave a second pulse of the out-of-plane magnetic field. Under the action of a displacing external in-plane field, the displacement of domain walls moving along the field and against the field occurs unequally (shown in the inset to Fig. 3). The domain wall velocity of movement is recorded from the shift of the left and right domain walls at a known H_z pulse width. The minimum of domain wall velocity is observed at nonzero H_x (Fig. 3). The in-plane displacement field is compensated by the action of the internal non-zero Dzyaloshinskii–Moriya interaction field (HDMI, which is oriented against the direction of the magnetic field), which displaces $H_{\min}$, i.e., the field at which the domain wall velocity is minimal, relative to zero. The shape of the curves at low speeds is quite symmetrical and close to parabolic, suggesting that $\mu_0 H_{\mathrm{DMI}} \approx \mu_0 H_{\min}$ = 30 mT. Slight kinks on the curves indicate an insignificant damping component.

Conclusion

We have studied the structure and magnetic properties of Si(111)/Cu/Pd/Co/Ta/Pd epitaxial films. The study of the layer growth process showed a disordered growth of Ta on the epitaxial Co layer, as well as a tendency to ordering with further deposition of Pd with the preservation of crystallographic symmetry. Ta, when deposited on the Co epitaxial layer, forms a magnetically disordered layer about 0.5 nm thick. The magnetically dead layer leads to a decrease in the perpendicular magnetic anisotropy in comparison with the previously studied symmetric epitaxial structures of the Pd/Co/Pd composition. For the Pd/Co/Ta system, the effective anisotropy components are determined: the volume anisotropy constant K_v = 1 MJ/m^3, and the surface anisotropy constant K_s = 1.4 mJ/m^2. It was expected that the violation of the symmetry of the structure by introducing the Ta layer would lead to an increase H_{DMI}, compared with Pd/Co/Pd films, but this did not happen, since Ta leads to a decrease in anisotropy compared to a symmetrical structure due to strong mixing at the interface. However, breaking of the film symmetry in this case leads to more symmetric velocity curves, which indicates a decrease in the contribution of chiral damping. Thus, despite the disordered growth of Ta and the relatively small $\mu_0 H_{DMI} \approx 30$ mT, it is possible to create DMI-enhanced ordered multilayer superlattices by increasing the number of layers based on the epitaxial films.

Acknowledgments

This research was supported by the grant of the Government of the Russian Federation for state support of scientific research conducted under supervision of leading scientists in Russian institutions of higher education, scientific foundations, and state research centers of the Russian Federation (Project no. 075-15-2021-607).

REFERENCES

1. **Wang L., Liu Ch., Mehmood N., Han G., Wang Ya., Xu X., Feng Ch., Hou Z., Peng Y., Gao X., Yu G.,** ACS Applied Materials & Interfaces 11, 12, (2019) 12098–12104

2. **Davydenko A.V., Kozlov A.G., Ognev A.V., Stebliy M.E., Chebotkevich L.A.,** Applied Surface Science. 384 (2016) 406–412.

3. **Davydenko A.V., Kozlov A.G., Stebliy M.E., Kolesnikov A.G., Sarnavskiy N.I., Iliushin I.G., Golikov A.P.,** Physical Review B 103, (2021) 094435.

4. **Davydenko A.V., Kozlov A.G., Ognev A.V., Stebliy M.E., Samardak A.S., Ermakov K.S., Kolesnikov A.G., Chebotkevich L.A.,** Physical Review B. volume 95, issue 6, 28 (2017) 064430.

5. **Je S.G., Kim D.H., Yoo S.C., Min B.C., Lee K. J., Choe S.B.,** Physical Review B, 88. (2013) 214401.

THE AUTHORS

KUZNETSOVA Mariya A.
kuznetcova.mal@students.dvfu.ru
ORCID: 0000-0002-0070-2817

AYANITOV Oleg E.
aianitov.oe@students.dvfu.ru
ORCID: 0000-0002-8069-7631

SUSLIN German S.
suslin_gs@dvfu.ru
ORCID: 0000-0002-4919-346X

TARASOV Egor V.
tarasov.ev@dvfu.ru
ORCID: 0000-0002-0372-4552

SHISHELOV Aleksandr F.
shishelov.af@students.dvfu.ru
ORCID: 0000-0002-9703-4623

KOZLOV Aleksei G.
kozlov.ag@dvfu.ru
ORCID: 0000-0001-8774-0631

YUSHCHENKO Diana O.
yushchenko.dol@students.dvfu.ru
ORCID: 0000-0003-0410-8126

Received 22.05.2022. Approved after reviewing 13.07.2022. Accepted 25.07.2022.

Conference materials
UDC 538.958 53.096
DOI: https://doi.org/10.18721/JPM.153.110

Investigation of temperature stability of germanium nanowires obtained by electrochemical deposition

D. L. Goroshko [1] ✉, E. A. Chusovitin [1], A. A. Dronov [2], I. M. Gavrilin [2]

[1] Institute of Automation and Control Processes Far Eastern Branch of the RAS, Vladivostok, Russia;
[2] National Research University of Electronic Technology, Moscow, Russia

✉ goroshko@iacp.dvo.ru

Abstract: The effect of vacuum annealing (600 °C, 30 min) on the temperature stability against oxidation in air of germanium nanowires obtained by cathodic deposition from aqueous solutions of germanium oxide was studied by the method of photoluminescence in the visible range and Raman scattering. The stability was checked by laser annealing at temperatures above 1000 °C. It was shown that the evolution of photoluminescence and Raman peaks is associated with the formation of germanium oxide or suboxide upon laser annealing. Preliminary vacuum annealing of the sample significantly suppresses this process. The observed effect is associated with the formation of germanium oxide and the influence of indium atoms on this process.

Keywords: germanium nanowires, germanium oxide, photoluminescence, Raman spectroscopy

Funding: This research was financially supported by the Russian Science Foundation (Project no. 20-19-00720).

Citation: Goroshko D. L., Chusovitin E. A., Dronov A. A., Gavrilin I.M., Investigation of temperature stability of germanium nanowires obtained by electrochemical deposition. St. Petersburg State Polytechnical University Journal. Physics and Mathematics. 15 (3.1) (2022) C. 59–64. DOI: https://doi.org/10.18721/JPM.153.110

Материалы конференции
УДК 538.958 53.096
DOI: https://doi.org/10.18721/JPM.153.110

Исследование температурной стабильности германиевых нанопроволок, полученных электрохимическим осаждением

Д. Л. Горошко [1] ✉, Е. А. Чусовитин [1], А. А. Дронов [2], И. М. Гаврилин [2]

[1] Институт автоматики и процессов управления Дальневосточного отделения РАН, г. Владивосток, Россия
[2] Национальный исследовательский университет «МИЭТ», г. Москва, Россия

✉ goroshko@iacp.dvo.ru

Аннотация. Методом фотолюминесценции в видимом диапазоне и КРС изучено влияние вакуумного отжига (600 °C, 30 мин) на температурную стабильность против окисления на воздухе нанопроволоки германия, полученные методом катодного осаждения из водных растворов оксида германия. Стабильность проверялась путем лазерного отжига при температуре более 1000 °C. Показано, что эволюция пиков фотолюминесценции и КРС связана с формированием оксида или субоксида германия при лазерном отжиге. Предварительный вакуумный отжиг образца существенно подавляет этот процесс. Наблюдаемый эффект связывается с особенностями формирования оксида германия и влиянием на этот процесс атомов индия.

Ключевые слова: германиевые нанопроволоки, оксид германия, фотолюминесценции, комбинационное рассеяние света

Финансирование: Работа выполнена при поддержке Российского научного фонда (проект № 20-19-00720).

Ссылка при цитировании: Горошко Д. Л., Чусовитин Е. А., Дронов А. А., Гаврилин И. М.

Исследование температурной стабильности германиевых нанопроволок, полученных электрохимическим осаждением // Научно-технические ведомости СПбГПУ. Физико-математические науки. 2022. Т. 15. № 3.1. С. 59–64. DOI: https://doi.org/10.18721/JPM.153.110

Introduction

Germanium nanowires (NWs) obtained by cathodic deposition from aqueous solutions of germanium oxide are a promising material for a new elemental base of electronic devices, since, compared to silicon, it has a higher charge carrier mobility, a smaller band gap, and a lower processing temperature [1]. Also of great interest is the use of Ge NWs in lithium-ion batteries [2–4]. In addition, they are an interesting example of nanosized structures in which quantum effects associated with size limitation can be observed [5, 6].

The possibility of electrochemical deposition of Ge NW from aqueous solutions using particles of low-melting metals (Ga, In, etc.) at nearly room temperature has been demonstrated [7, 8]. In this case, liquid metal nanodroplets have been used as an electrode for reduction of Ge-containing ions at the electrode surface, followed by dissolving and crystallizing the melt at the substrate interface. The growth mechanism, which is known as electrochemical liquid–liquid–solid (ec-LLS) crystal growth, is similar to the vapor–liquid–solid method [7].

It was shown in a series of works [9, 10] that successive laser annealing of Ge NWs obtained by this method lead to the recrystallization of samples and the appearance of Ge nanocrystals (NCs) of different sizes from 1.5 to 5 nm, and the behavior of the samples varies greatly depending on the presence or no vacuum annealing. In this paper, we analyze the effect of preliminary vacuum annealing of germanium nanowires obtained by cathodic deposition from aqueous solutions of germanium oxide on the change in their temperature stability against oxidation at high temperature at ambient conditions.

Materials and Methods

Electrochemical deposition of Ge NWs was carried out in a three-electrode cell. Fifty micrometer thickness titanium foil was used as the substrate. Indium nanoparticles were deposited on a Ti foil, as described in previous work [9]. The solution contained 0.05 M of germanium (IV) oxide GeO_2, 0.5 M of potassium sulfate K_2SO_4, and 0.5 M of succinic acid. Deposition was carried out at 0.2 $mA \cdot cm^{-2}$ at a solution temperature of 20 °C. The prepared samples were washed in deionized water and were dried in an argon flow. Some of the obtained samples were annealed at 600 °C in vacuum at a residual pressure below $1 \cdot 10^{-9}$ Torr for 30 min.

Photoluminescence (PL) measurements and backscattered Raman spectra were registered under excitation with focused laser radiation using a NTEGRA Spectra II micro-Raman spectrometer at room temperature and ambient conditions. We used a He-Ne laser (maximal power 50 mW and minimal spot diameter 2 μm) for Raman experiments. Photoluminescence spectra were registered under 405 nm excitation with background subtraction. The laser power was attenuated by means of neutral filters with different optical densities.

Before carrying out experiments on recording Raman and PL spectra, the maximum excitation power was determined, which did not lead to phase transformations in the sample, that would be reflected in changes in the spectra. However, to study the effect of high temperature on the state of the samples, exposure was carried out under a HeNe laser at maximum power for 1 – 60 seconds at ambient conditions. The temperature under the beam at such laser annealing was determined from the ratio of the intensities of the Stokes and anti-Stokes peaks of the optical phonon. Four sets of spectra were taken corresponding to different conditions of the sample. These sample conditions are conventionally presented in Table 1 and will be called accordingly.

Table 1

Sample list

Sample condition	Notation			
	A	B	C	D
Vacuum annealing	–	+	–	+
Laser annealing	–	–	+	+

Results and Discussion

PL was recorded in a wide wavelength range from 0.4 to 2 μm, where the appearance of exciton PL could be expected. The size effect in the samples under considered can lead to appearance of PL in the infrared range (IR), since the Bohr radius of a direct-gap exciton in Ge is 20–30 nm (depending on the conditions and calculation procedure [10], [11]) and can thus exceed the actually achievable size of a germanium nanocrystal or the filament diameter [9]. In this case, the emission of a photon with an energy of 1.3–2.67 eV is expected. Indeed, in a sample with Ge nanocrystals (NCs) 2–6 nm in size formed in a SiO_2 matrix, a weak shoulder with an energy of 1.6–1.8 eV was observed against the background of an intense peak with a position of 2.2–2.4 eV [10]. It should be noted that the intensity of this high-energy peak increased significantly upon annealing but the position did not change; nevertheless, the authors associated the nature of this PL with quantum-confinement effects in Ge NCs. Considering samples with Ge NCs less than 4 nm in size, the authors of [12] attributed the PL in the range of 2.2–2.3 eV to a new crystalline nanostructure in NCs with direct interband transitions; in this case, the absence of a temperature dependence of the position of the PL peak is not commented in any way. The convincing presence of IR PL in Ge nanowires was demonstrated in [13], however, as the authors point out, quantum confinement effects are unlikely to be involved in this, since the NW diameter is 40 nm and exceeds the exciton Bohr radius.

There was no photoluminescence for our samples with NWs in infrared region, but strong PL signal was found in the range of 400–950 nm (Fig. 1). The peak in the region of 450–475 nm in both spectra is associated with a drop in the detector sensitivity at the edge of the range; however, an increase in the intensity in the short-wavelength region below 500 nm is not an artifact of the measurements. It can be seen that in the initial state (without laser annealing, Fig. 1, *a*), a noticeable PL signal with a maximum at 635 nm is manifested only by the sample without vacuum annealing. Laser annealing of this sample for 1 second leads to a 4-fold increase in the PL intensity (Fig. 1, *b*, sample C) and a shift of the maximum to the blue region up to 536 nm. In turn, the PL intensity of the sample in the vacuum-annealed state B (Fig. 1, *a*) and D (Fig. 1, *b*) practically does not change: a slight elevated spectrum is observed in the region of 550–750 nm. A significant increase in the PL signal for sample D is achieved after laser annealing for 60 sec (Fig. 1, *b*); the peak maximum is located at about 600 nm.

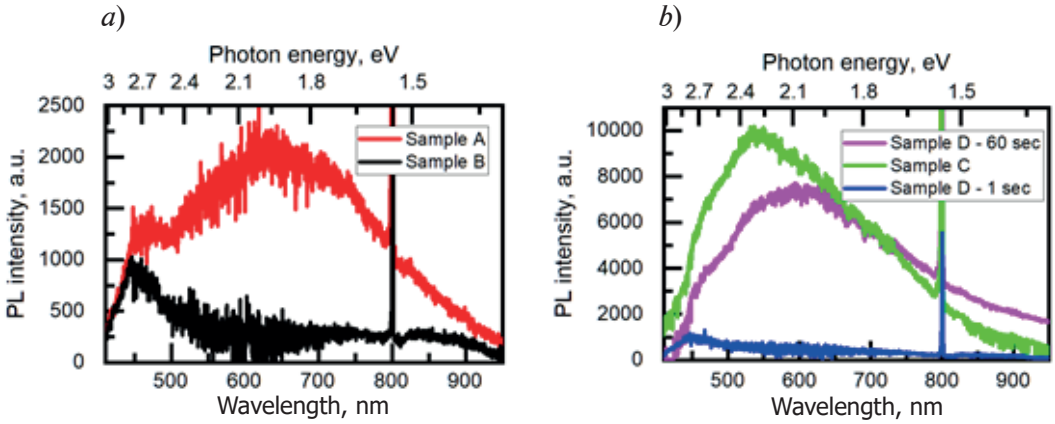

Fig. 1. PL spectra of sample with NWs before (*a*) and after (*b*) vacuum annealing. Different curves in each panel correspond to PL without and with laser annealing of different duration.
The sharp line at 800 nm is a second laser harmonic.

As shown above, the quantum size effect is an unlikely reason for the appearance of PL in a system with Ge NWs. Therefore, there must be other sources of PL observed in the studied samples. First of all, it can be germanium oxide, since germanium is actively oxidized at ambient conditions. The oxidation of germanium as the cause of PL is also indicated by its high intensity in the laser-annealed sample C. An estimate of the temperature in the region of the laser spot during annealing, measured from the ratio of Stokes and anti-Stokes peaks, gives a value of at least 1000 °C.

At present, most authors are inclined to believe that the source of PL in the visible and UV ranges is the Ge/GeO_x or GeO_x interface states. Similar conclusions are reached by studying freestanding Ge/GeO_2 core-shell NCs. Strong PL peaks in the same region are attributed to Ge/GeO_2 interface defect states [14] or GeO_xs [15]. Annealing in air or a hydrogen-containing atmosphere of nanocrystalline germanium obtained by chemical etching also allowed to conclude that the PL from these materials is from GeO_xs [16]. The effect of passivation on the PL from Ge NCs is shown in [17]. The deposition of a thin silicon layer on Ge NCs formed in high vacuum on the SiO_2 surface resulted in the appearance of a weak PL signal with a peak position of 0.85 and 0.82 eV, depending on the NC size. On the other hand, passivation reduced the PL intensity in the visible region due to the prevention of GeO_x formation on the surface.

The change in the state of germanium and its amount in the samples under the laser annealing is well traced in the Raman spectra (Fig. 2). After laser annealing of the sample without vacuum annealing (Fig. 2, *a*), the germanium phonon TO peak shifts from the position of 281 cm^{-1} to 300 cm^{-1}. In turn, the initial position of the TO peak in the vacuum annealed sample was 297.3 cm^{-1}, after laser annealing 300.7 cm^{-1}, and the intensity decreased by a factor of 4. Taking into account the fact that parts of the same sample were used for experiments with and without vacuum annealing, and the measurement conditions for all spectra in Fig. 2 coincided, it can be argued that, after laser annealing of the vacuum annealed sample, a significantly larger amount of germanium contained in NWs was retained in it. The shift of the Raman peaks to the blue region upon annealing is explained by an increase in the size of nanocrystalline grains in NWs. It is noteworthy that, prior to laser annealing, the position of the peak of the vacuum annealed sample is 297.3 cm^{-1}, which indicates recrystallization of NWs during the annealing.

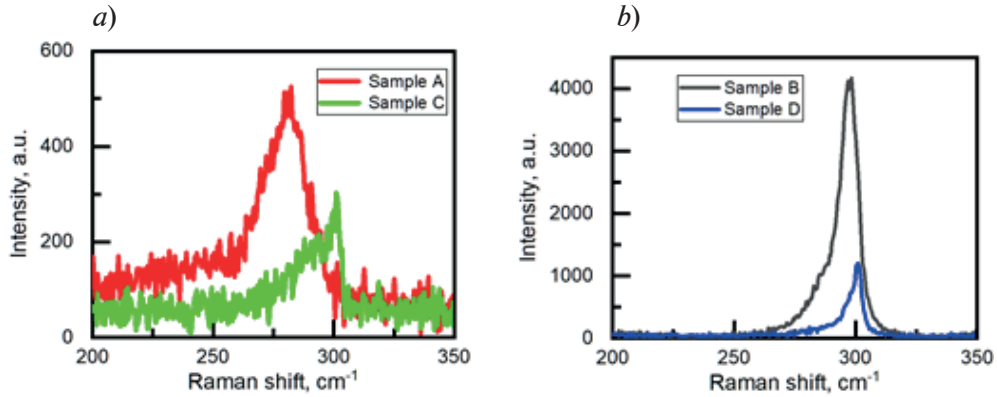

Fig. 2. Raman spectra of the sample with Ge NWs before (*a*) and after (*b*) vacuum annealing. Different curves in each panel correspond to the conditions without (samples A and B) and with (samples C and D) laser annealing.

It should be noted that the need for vacuum annealing in these samples was dictated by the need to get rid of the high concentration of indium used as a catalyst in the formation of NWs. According to our studies using in-situ electron beam annealing in a transmission electron microscope, indium segregates on the surface of the filaments. The results of studies in [18] indicate that the oxidation of germanium occurs at the GeO_2/Ge interface due to the decomposition of GeO_2. The resulting oxygen vacancy plays a key role in Ge oxidation, as oxygen atoms diffuse through these vacancies to interface with germanium with an exchange type of process. In turn, paper [19] presents a theoretical study of the influence of 4 and 3 valence metals on the passivation of vacancies in germanium suboxides in order to find out the reason for the success in obtaining excellent *p*- and *n*- MOSFET mobilities in the GeO_x/Al_2O_3 gate stack [20]. It turned out that the pre-existing oxygen vacancies in the intermediate GeO_2 layer affect the performance of the device. Since indium can exhibit 3 valence electrons in compounds, it can saturate oxygen vacancies in germanium suboxide by suppressing oxygen diffusion to the GeO_2/Ge interface and preventing oxidation. The difference between vacuum and laser annealing of NWs lies in the kinetics of these processes: vacuum annealing at 600 °C is not sufficient for the decomposition of GeO_2 [21], but this temperature is sufficient for active diffusion of indium.

Conclusion

Thus, the observed evolution of the PL spectra depending on the state of the sample is unambiguously related to oxidation of germanium NWs. A strong increase in PL after laser annealing at ambient conditions from a vacuum unannealed sample is explained by the formation of a large amount of oxide from germanium, which is included in NWs. This process correlates with the evolution of the Raman spectra, where the oxidation of NWs is accompanied by a significant decrease in the intensity of the TO phonon peak. After vacuum annealing, NWs become more resistant to oxidation, which manifests itself in the absence of PL in the studied range before laser annealing and its slight increase after a short laser annealing. In turn, the TO Raman peak remains quite intense. However, an increase in the duration promotes the occurrence of diffusion processes in NWs and their oxidation, which results in the appearance of intense PL. The analysis of these phenomena is based on the facts about the features of germanium oxidation, during which suboxides are formed, which, in turn, are the cause of PL in the studied range. Vacuum annealing leads to passivation of these germanium suboxides, resulting in a low PL intensity and resistance of NWs to oxidation at elevated temperatures.

Acknowledgments

This research was financially supported by the Russian Science Foundation (Project no. 20-19-00720).

REFERENCES

1. **Claeys C., Simoen E.,** Germanium-Based Technologies: From Materials to Devices, Elsevier, 2011.

2. **Liu S., Feng J., Bian X., Qian Y., Liu J., Xu H.,** Nanoporous germanium as high-capacity lithium-ion battery anode, Nano Energy. 13 (2015) 651–657.

3. **Tian H., Xin F., Wang X., He W., Han W.,** High capacity group-IV elements (Si, Ge, Sn) based anodes for lithium-ion batteries, Journal of Materiomics. 1 (2015) 153–169.

4. **Gavrilin I.M., Kudryashova Yu.O., Kuz'mina A.A., Kulova T.L., Skundin A.M., Emets V.V., Volkov R.L., Dronov A.A., Borgardt N.I., Gavrilov S.A.,** High-rate and low-temperature performance of germanium nanowires anode for lithium-ion batteries, Journal of Electroanalytical Chemistry. 888 (2021) 115209.

5. **Bruno M., Palummo M., Marini A., Del Sole R., Olevano V., Kholod A.N., Ossicini S.,** Excitons in germanium nanowires: Quantum confinement, orientation, and anisotropy effects within a first-principles approach, Phys. Rev. B. 72 (2005) 153310.

6. **Gu G., Burghard M., Kim G.T., Düsberg G.S., Chiu P.W., Krstic V., Roth S., Han W.Q.,** Growth and electrical transport of germanium nanowires, Journal of Applied Physics. 90 (2001) 5747–5751.

7. **Fahrenkrug E., Maldonado S.,** Electrochemical Liquid–Liquid–Solid (ec-LLS) Crystal Growth: A Low-Temperature Strategy for Covalent Semiconductor Crystal Growth, Acc. Chem. Res. 48 (2015) 1881–1890.

8. **Gavrilin I.M., Gromov D.G., Dronov A.A., Dubkov S.V., Volkov R.L., Trifonov A.Yu., Borgardt N.I., Gavrilov S.A.,** Effect of electrolyte temperature on the cathodic deposition of Ge nanowires on in and Sn particles in aqueous solutions, Semiconductors. 51 (2017) 1067–1071.

9. **Pavlikov A.V., Forsh P.A., Kashkarov P.K., Gavrilov S.A., Dronov A.A., Gavrilin I.M., Volkov R.L., Borgardt N.I., Bokova-Sirosh S.N., Obraztsova E.D.,** Investigation of the Stokes to anti-Stokes ratio for germanium nanowires obtained by electrochemical deposition, Journal of Raman Spectroscopy. 51 (2020) 596–601.

10. **Maeda Y.,** Visible photoluminescence from nanocrystallite Ge embedded in a glassy SiO_2 matrix: Evidence in support of the quantum-confinement mechanism, Phys. Rev. B. 51 (1995) 1658–1670.

11. **Kuo Y.-H., Li Y.-S.,** Variational calculation for the direct-gap exciton in the Ge quantum well systems, Phys. Rev. B. 79 (2009) 245328.

12. **Kanemitsu Y., Uto H., Masumoto Y., Maeda Y.,** On the origin of visible photoluminescence in nanometer-size Ge crystallites, Appl. Phys. Lett. 61 (1992) 2187–2189.

13. **Kawamura Y., Huang K.C.Y., Thombare S.V., Hu S., Gunji M., Ishikawa T.,** Brongersma M.L., Itoh K.M., McIntyre P.C., Direct-gap photoluminescence from germanium nanowires, Phys. Rev. B. 86 (2012) 035306.

14. **Giri P.K., Dhara S.,** Freestanding Core-Shell Nanocrystals with Varying Sizes and Shell Thicknesses: Microstructure and Photoluminescence Studies, Journal of Nanomaterials. 2012 (2012) 1–5.

15. **Kartopu G., Bayliss S.C., Hummel R.E., Ekinci Y.,** Simultaneous micro-Raman and photoluminescence study of spark-processed germanium: Report on the origin of the orange photoluminescence emission band, Journal of Applied Physics. 95 (2004) 3466–3472.

16. **Kartopu G., Bayliss S.C., Karavanskii V.A., Curry R.J., Turan R., Sapelkin A.V.,** On the origin of the 2.2–2.3 eV photoluminescence from chemically etched germanium, Journal of Luminescence. 101 (2003) 275–283.

17. **Aouassa M., Zrir M.A., Jadli I., Hassayoun L.S., Mghaieth R., Maaref H., Favre L., Ronda A., Berbezier I.,** Role of surface passivation on visible and infrared emission of Ge quantum dots formed by dewetting, Bull Mater Sci. 42 (2019) 69.

18. **Wang X., Nishimura T., Yajima T., Toriumi A.,** Thermal oxidation kinetics of germanium, Appl. Phys. Lett. 111 (2017) 052101.

19. **Golias E., Tsetseris L., Chroneos A., Dimoulas A.,** Interaction of metal impurities with native oxygen defects in GeO_2, Microelectronic Engineering. 104 (2013) 37–41.

20. **Zhang R., Huang P.-C., Lin J.-C., Takenaka M., Takagi S.,** Atomic layer-by-layer oxidation of Ge (100) and (111) surfaces by plasma post oxidation of Al_2O_3/Ge structures, Appl. Phys. Lett. 102 (2013) 081603.

21. **Laxman Shinde S., Kar Nanda K.,** Thermal oxidation strategy for the synthesis of phase-controlled GeO_2 and photoluminescence characterization, CrystEngComm. 15 (2013) 1043–1046.

THE AUTHORS

GOROSHKO Dmitry L.
goroshko@iacp.dvo.ru
ORCID: 0000-0002-1250-3372

DRONOV Alexey A.
noiz@mail.ru
ORCID: 0000-0001-6085-2481

CHUSOVITIN Evgeny A.
eliot@list.ru
ORCID: 0000-0002-8162-5533

GAVRILIN Ilya M.
gavrilin.ilya@gmail.com
ORCID: 0000-0002-0278-1598

Received 31.05.2022. Approved after reviewing 07.07.2022. Accepted 08.07.2022.

SIMULATION OF PHYSICAL PROCESSES

Conference materials
UDC 537.9, 544.47, 004.94
DOI: https://doi.org/10.18721/JPM.153.111

Atomic and electronic structure of $YFeO_3$ surface with oxygen vacancies

A. A. Gnidenko [1] ✉, P.G. Chigrin [1]

[1] Institute of Materials of Far Eastern Branch of the RAS, Khabarovsk, Russia

✉ agnidenko@mail.ru

Abstract: The atomic and electronic structure of $YFeO_3$ surfaces at the formation of oxygen vacancies are investigated by the methods of quantum-mechanical calculations. The (100), (001), and (010) surfaces are considered. The dependence of the formation energy of surface oxygen vacancy on its concentration and type of surface is shown. (100) surface oxygen vacancy has the lowest formation energy. During the formation of vacancies on the surface, the 3*d* states of Fe split into bulk, surface, and near-surface states.

Keywords: density functional theory, pseudopotential method, surface effects, yttrium orthoferrite, oxygen vacancies

Citation: Gnidenko A. A., Chigrin P. G. Atomic and electronic structure of $YFeO_3$ surface with oxygen vacancies. St. Petersburg State Polytechnical University Journal. Physics and Mathematics. 15 (3.1) (2022) 65–70. DOI: https://doi.org/10.18721/JPM.153.111

Материалы конференции
УДК 537.9, 544.47, 004.94
DOI: https://doi.org/10.18721/JPM.153.111

Атомная и электронная структура поверхности $YFeO_3$ с кислородными вакансиями

А. А. Гниденко [1] ✉, П. Г. Чигрин [1]

[1] Институт материаловедения Хабаровского научного центра Дальневосточного отделения РАН, г. Хабаровск, Россия

✉ agnidenko@mail.ru

Аннотация. Атомная и электронная структура поверхности $YFeO_3$ при формировании кислородных вакансий исследована при помощи квантово-механических методов моделирования. Рассмотрены поверхности (100), (001) и (010). Продемонстрирована зависимость энергии формирования кислородных вакансий от их концентрации и типа поверхности. С наименьшими энергетическими затратами кислородные вакансии формируются на поверхности (100). При формировании вакансий на поверхности происходит расщепление 3*d*-состояний Fe на объемные, поверхностные и приповерхностные.

Ключевые слова: теория функционала плотности, метод псевдопотенциалов, поверхностные эффекты, ортоферрит иттрия, кислородные вакансии

Ссылка при цитировании: Гниденко А. А., Чигрин П. Г. Атомная и электронная структура поверхности $YFeO_3$ с кислородными вакансиями // Научно-технические ведомости СПбГПУ. Физико-математические науки. 2022. Т. 15. № 3.1. С. 65–70. DOI: https://doi.org/10.18721/ JPM.153.111

Introduction

In the last two decades, complex oxides with a perovskite structure (ABO_3) have become the subject of intensive research over the world [1, 2]. The field of application of these materials is very wide: various types of sensors and detectors, solar cells, photocatalysts and solid oxide fuel cells [3–6]. The functional properties of these compounds are mostly determined by stoichiometry and structural changes within ABO_3 [7]. It was found that defect formation in the crystal lattice of ABO_3 leads to a significant increase in catalytic activity [8], while the oxygen non-stoichiometry of $YFeO_{3-\delta}$ can reach $\delta = 0.25$ [9]. A lot of research has been dedicated to developing perovskite catalysts for redox reactions such as the oxidation of hydrocarbons, soot and carbon monoxide. Thus, perovskite compounds can be used as alternative multifunctional catalysts for neutralizing diesel gases.

The mechanism of carbon oxidation in the presence of catalysts with a perovskite structure has not been comprehensively explored this far. It should be noted that vacancies on the perovskite surface are filled with oxygen from the bulk of the crystal. Thus, the influence of the structural characteristics of perovskite on the mobility, surface/volume reactivity of oxygen, and catalytic activity in carbon oxidation is of great interest for fundamental research. In the present work, yttrium orthoferrite ($YFeO_3$) was considered; the atomic and electronic structure of this perovskite at the formation of oxygen vacancies on the surface was studied using modern computer simulation methods.

Methods and Calculation Parameters

The Quantum Espresso software package [10], based on the density functional theory [11, 12] and the pseudopotential method, was used to perform quantum mechanical calculations. The exchange-correlation contribution to the total energy was described by the generalized gradient approximation. Uniform k-point grids were specified by Monkhorst-Pack procedures and varied depending on the size of the supercell. Cutoff energy of the plane wave basis was about 816 eV. Ultrasoft pseudopotentials for yttrium, iron, and oxygen were taken from the Quantum Espresso pseudopotential database [13] and were tested for a correct description of the properties of the Y and Fe crystal lattices, as well as of the O_2 molecule.

$YFeO_3$ has an orthorhombic primitive cell (*Pnma* space group); according to our calculation, the lattice parameters are $a = 5.65$ Å, $b = 7.64$ Å, $c = 5.29$ Å; deviation from the experimental values is less than 1%. ABO_3 perovskites (where B = Fe) are often antiferromagnets; the equilibrium configuration for $YFeO_3$ corresponds to the G-type antiferromagnetic state, which is consistent with the literature data. Furthermore, Hubbard correction (DFT + U) [14] was applied into the calculations with $U_{eff} = 4$ eV for adequate description of strongly localized $3d$-states of Fe.

Results and Discussion

A primitive orthorhombic cell of $YFeO_3$ was taken to construct the slab models. It contains 4 structural units (20 atoms in total). For simplicity of construction, we considered the facets of the primitive cell, thus we obtained surfaces with indices (001), (010) and (100). To estimate the surface energy of non-stoichiometric slab we calculated a difference between the slab energy before ($E_{unrel.slab}$) and after ($E_{rel.slab}$) atomic relaxation, reduced to a unit of surface area (S):

$$E_{surf} = \frac{E_{unrel.slab} - E_{rel.slab}}{2S}. \quad (1)$$

We considered an asymmetric slab: the lower atomic layers were fixed. Fig. 1 shows the slab where only the middle atomic layers are fixed, before (*a*) and after (*b*) relaxation, as well as the slab with fixed lower atomic layers after relaxation (*c*). Fe atoms in Fig. 1 and 2 are marked in dark grey, Y atoms in light gray, and O atoms in white. Atomic structure analysis showed that the bond lengths in the surface layers after relaxation in both cases coincide with an accuracy of 0.01 Å. The surface energy for the slab with fixed lower layers was determined by a formula similar to (1), but without a factor of 2 in the denominator, since only one (upper) surface is considered. The vacuum gap in our calculations was about 14 Å. The calculated values of surface energies are given in Table 1.

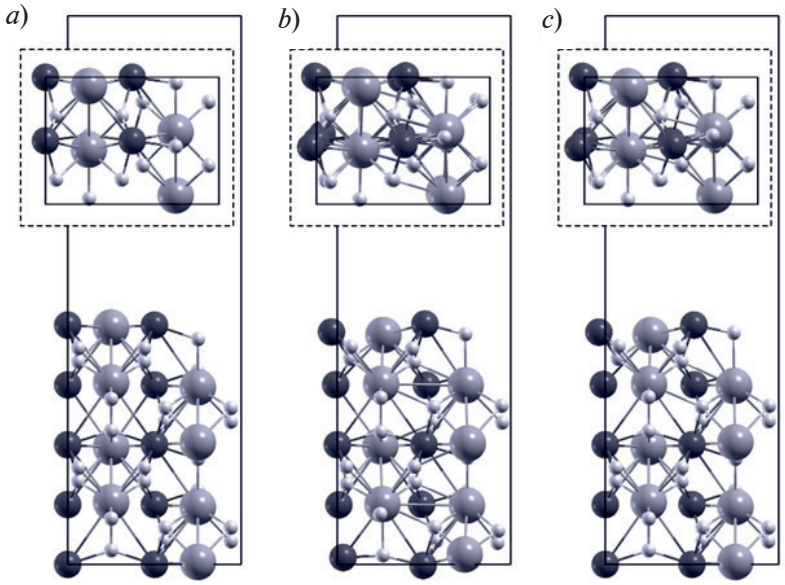

Fig. 1. Slab for the $YFeO_3$ (001) surface in two projections: before relaxation (*a*); after relaxation of the upper and lower atomic layers (*b*); after relaxation of only the upper atomic layers (*c*)

Table 1

Surface energies of $YFeO_3$ (001), (010) and (100)

Surface	Area, m^2	Slab characteristics	Surface energy, J/m^2
(001)	$4.36 \cdot 10^{-19}$	5 layers	0.92
		7 layers	0.91
		5 layers, the lower layers are fixed	0.97
(010)	$3.01 \cdot 10^{-19}$	9 layers (FeO_2)	1.03
		9 layers (YO)	1.31
		9 layers (FeO_2), the lower layers are fixed	1.05
(100)	$4.11 \cdot 10^{-19}$	5 layers	1.06
		5 layers, the lower layers are fixed	1.11

For the (001) surface, the influence of the number of atomic layers on surface energy was estimated. It had been shown that the difference in surface energy between 5- and 7-layer slabs is only 0.01 J/m^2. The fixation of the lower atomic layers leads to an insignificant (within 0.05 J/m^2) increase in the surface energy, which indicates that the approach we have chosen is acceptable. The same results for slabs with fixed lower layers were obtained for $YFeO_3$(100) and $YFeO_3$(010). The number of layers in the (010) slab is 9, because in this direction, the linear size of the unit cell is larger. Additionally, the atomic layers for the direction [010] consist of either Fe and O atoms or Y and O atoms. Our calculations showed that formation of a (FeO_2) surface is more favorable; the energy difference is 0.3 J/m^2. Further, we considered only this type of surface.

In the simplest approximation, taking the chemical potential of oxygen as half the O_2 molecule total energy, the formation energy of a surface vacancy is determined as follows:

$$E_{form} = E_{slab+vac} - E_{slab} + \frac{1}{2}E_{O_2}, \quad (2)$$

where E_{slab} is the energy of the $YFeO_3$ slab, $E_{slab+vac}$ is the energy of the slab with oxygen surface vacancy, E_{O_2} is the energy of an isolated O_2 molecule. The obtained values are shown in Table 2.

For each surface, we considered two cases, which differed from each other by the

Table 2

Energies of oxygen vacancy formation for different types of $YFeO_3$ surfaces

Surface	Area, m^2	E_{form}, eV
(001)	$4.36 \cdot 10^{-19}$	2.40
	$17.45 \cdot 10^{-19}$	1.74
(100)	$4.11 \cdot 10^{-19}$	1.79
	$16.44 \cdot 10^{-19}$	0.81
(010)	$3.01 \cdot 10^{-19}$	3.51
	$12.03 \cdot 10^{-19}$	3.33

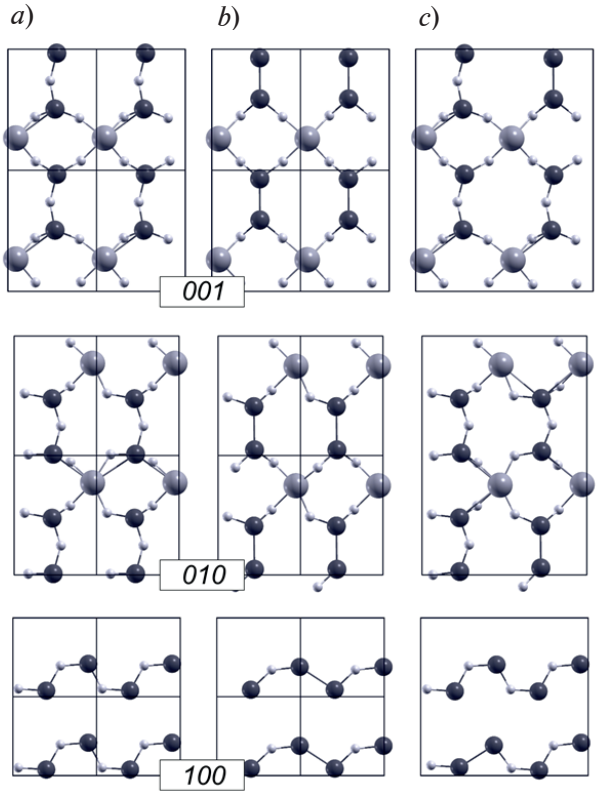

Fig. 2. Atoms of $YFeO_3$ surface layers: without oxygen vacancy (*a*); one vacancy per unit cell cross-section (*b*); one vacancy per cell area increased by 4 times(*c*)

cross-section area. In contrast to the description of bulk oxygen vacancies, we cannot operate in terms of oxygen non-stoichiometry; therefore, below we consider high and low concentrations of surface oxygen vacancies. Fig. 2 shows the atoms forming the surface layer for (001), (100), and (010); the second and third images in each row correspond to high and low vacancy concentrations. To create a vacancy on the surface, we removed the oxygen atom with the highest position in the direction of the slab orientation; for all surfaces, it was an oxygen atom from the Fe-O-Fe bridge. Thus, the formation of an oxygen vacancy leads to the formation of a Fe-Fe bond on the surface (its length varies from 2.62 to 2.82 Å).

It was found that the formation energy of a surface oxygen vacancy decreases with an increase in the cross-section area, i.e., a decrease in the vacancy concentration. Due to the specific arrangement of atoms on the $YFeO_3$(010) surface layer, the formation energies do not differ too much from previously calculated values for bulk oxygen vacancies (3.13–3.79 eV) [15]. However, the vacancy formation energies were significantly lower for the (001) and (100) surfaces; in the case of low concentration on the (100) surface, the lowest value was obtained, amounting to 0.81 eV. For more detailed analysis, we plotted the density of electronic states (DOS) for all considered cases.

The left side of Fig. 3 shows the total and projected densities of electronic states for an ideal $YFeO_3$ cell and a cell with an oxygen vacancy (with high and low concentration). The Fermi level is at zero. The formation of an oxygen vacancy leads to appearance of levels in the band gap, as well as to partial delocalization of 3*d* states of Fe; in the case of high concentrations this is more pronounced. At the vacancy formation on the $YFeO_3$ (010) surface (right panel in Fig. 3), it is noticeable that, in addition to the sharp peak at −8 eV corresponding to 3*d* states of bulk Fe atoms, there are distributed states (in the range from −7 eV to −6 eV) corresponding to surface Fe atoms. In the case of the (001) and (100) surfaces (Fig. 4), there is a partial splitting of the peak corresponding to the bulk states; it becomes the superposition from the states of the bulk and near-surface Fe atoms. This occurs due to formation of the Fe-Fe bond when oxygen is removed from the surface and the surface layers are included in the atomic relaxation process.

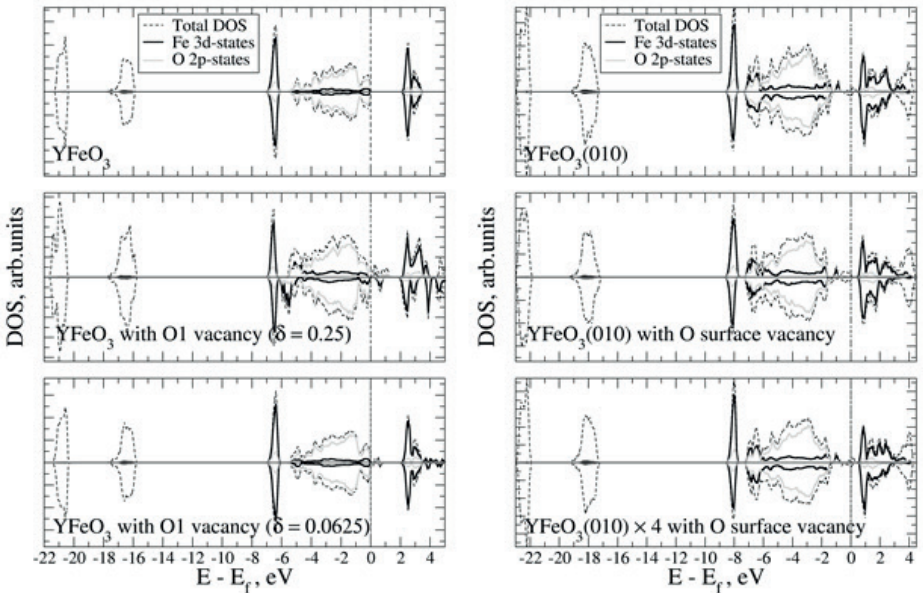

Fig. 3. Densities of electronic states for $YFeO_3$ and $YFeO_3$(010) surface in the absence and presence of oxygen vacancies

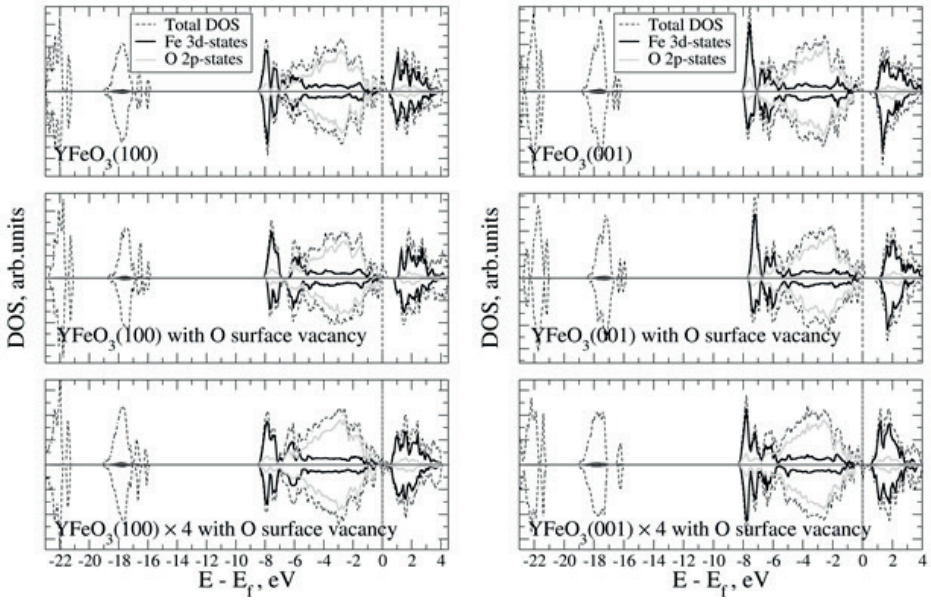

Fig. 4. Densities of electronic states for $YFeO_3$(100) and $YFeO_3$(001) surfaces in the absence and presence of oxygen vacancies

Conclusion

Computer simulation methods have been used to study changes in the atomic and electronic structure upon formation of oxygen vacancies on different surfaces of yttrium orthoferrite. It was found that there is a tendency to a decrease in the formation energy with an increase in the surface area, which corresponds to a decrease in the vacancy concentration. The smallest value of 0.81 eV was obtained for the (100) surface, which is about four times less than the formation energy of a bulk oxygen vacancy. Analysis of the electronic structure showed delocalization of 3*d* states of Fe atoms for the surface formation process; the formation of an oxygen vacancy enhances this effect due to the appearance of Fe-Fe bond.

Acknowledgments

This research was supported by the computational resources provided by the *Akademik V.M. Matrosov* HPC-cluster (Irkutsk) [16].

REFERENCES

1. **Li Ch. H., Ch K., Soh K., Wu P.,** Formability of ABO_3 perovskites, J. Alloys Compd. 372 (2004) 40–48.

2. **Atta N. F., Galal A., El-Ads E. H.,** Perovskite Nanomaterials-Synthesis, Characterization, and Applications, in "Perovskite Materials Synthesis, Characterisation, Properties, and Applications". Edited by Likun Pan Guang Zhu, InTechOpen, 2016, pp. 648.

3. **Shi J., Guo L.,** ABO_3-based photocatalysts for water splitting, Progress in Natural Science: Materials International. 22 (2012) 592–615.

4. **Chroneos A., Vovk R. V., Goulatis I., Goulatis L. I.,** Oxygen transport in perovskite and related oxides: A brief review, J. Alloys Compd. 494 (2010) 190–195.

5. **Cui J., Wang J., Zhang X., Li G., Wu K., Cheng Y., Zhou J.,** Enhanced oxygen reduction reaction through Ca and Co co-doped $YFeO_3$ as cathode for protonic ceramic fuel cells, Journal of Power Sources. 413 (2019) 148–157.

6. **Moure C., Peca O.,** Magnetic features in $REMeO_3$ perovskites and their solid solutions (RE=rare-earth, Me=Mn, Cr), Journal of Magnetism and Magnetic Materials. 337-338 (2013) 1–22.

7. **Pena M., Fierro J.L.G.,** Chemical structures and performances of perovskite oxides, Chem. Rev. 101 (2001) 1981–2017.

8. **Barresi A. A., Mazza D., Ronchetti S., Spinicci R., Vallino M.,** Non-stoichiometry and catalytic activity in ABO_3 perovskites: $LaMnO_3$ and $LaFeO_3$, Studies in Surface Science and Catalysis. 130 (2000) 1223–1228.

9. **Dhal G. Ch., Dey S., Mohan D., Prasad R.,** Solution Combustion Synthesis of Perovskite-type Catalysts for Diesel Engine Exhaust GaS Purification, Materials Today: Proceedings. 4 (2017) 10489–10493.

10. **Giannozzi P., Baroni S., Bonini N., Calandra M., et al.,** QUANTUM ESPRESSO: a modular and open-source software project for quantum simulations of materials, J. Phys.: Condens. Matter. 21 (2009) 395502(19pp).

11. **Hohenberg P., Kohn W.,** Inhomogeneous Electron Gas, Phys. Rev. 136 (1964) B864–B871.

12. **Kohn W., Sham J.L.,** Self-Consistent Equations Including Exchange and Correlation Effects, Phys. Rev. 140 (1965) A1133–A1138.

13. **Corso A. Dal,** Pseudopotentials periodic table: From H to Pu, Comput. Mater. Sci. 95 (2014) 337–350.

14. **Anisimov V. I., Zaanen J., Andersen O. K.,** Band theory and mott insulators: Hubbard U instead of Stoner I. Phys. Rev. B. 44 (1991) 943–954.

15. **Gnidenko A.A., Chigrin P.G., Kirichenko E.A.,** Computer Simulation of Oxygen Vacancy Formation in $YFeO_3$ Perovskite, Solid State Phenomena. 312 (2020) 355–360.

16. Irkutsk Supercomputer Center of SB RAS, URL: http://hpc.icc.ru

THE AUTHORS

GNIDENKO Anton A.
agnidenko@mail.ru
ORCID: 0000-0002-9492-8429

CHIGRIN Pavel G.
pal_chig@mail.ru
ORCID: 0000-0002-1560-489X

Received 21.05.2022. Approved after reviewing 10.06.2022. Accepted 17.06.2022.

Conference materials
UDC 536.9
DOI: https://doi.org/10.18721/JPM.153.112

Method for density-of-states calculation of dipole spin lattices

M. A. Chesnokov [1] ✉ I. N. Nalivaiko [1], V. S Strongin [1]

[1] Far Eastern Federal University, Vladivostok, Russia

✉ chesnokov.ma@students.dvfu.ru

Abstract: The solution to the problem of finding the probability density of all possible states (configurations) in dipole lattices, which also allows obtaining information about the degree of frustration in the system, is considered in the article. As an example, the Cairo lattice of 40 particles (dipoles) was used - a two-dimensional system of artificial spin ice, combining the geometry of square and Kagome lattices. Our method was created by combining the approximate polynomial algorithms of the MC-walk and the Greedy algorithm. We used the Greedy algorithm to obtain the energy data points for each possible spin excess, then partition the space into an equal number of intervals, and MC-walk to accumulate the data points. It was shown that the use of intervals makes it possible to ensure good performance of the method on the most degenerate energy regions but has a problem in finding data points on the least degenerate regions. The distribution of the density of states is constructed.

Keywords: density of states, Cairo lattice, algorithm development, ground state

Funding: The study was financed by Grant for state support of the leading scientific schools of the Russian Federation ((НШ-2559.2022.1.2).

Citation: Chesnokov M. A., Nalivaiko I. N., Strongin V. S. Method for density-of-states calculation of dipole spin lattices. St. Petersburg State Polytechnical University Journal. Physics and Mathematics. 15 (3.1) (2022) 71–75. DOI: https://doi.org/10.18721/JPM.153.112

Материалы конференции
УДК 536.9
DOI: https://doi.org/10.18721/JPM.153.112

Метод расчета плотности состояний для дипольных решеток

М. А. Чесноков [1] ✉, И. Н. Наливайко [1], В. С. Стронгин [1]

[1] Дальневосточный Федеральный Университет, г. Владивосток, Россия

✉ chesnokov.ma@students.dvfu.ru

Аннотация. В статье рассматривается решение проблемы нахождения плотности вероятности всех возможных состояний (конфигураций) в дипольных решетках, также позволяющий получить информацию о степени фрустраций в системе. В качестве примера была использована Каирская решетка – двумерной системе искусственного спинового льда, совмещающей геометрии квадратной и кагоме систем из 40 частиц (диполей). Наш метод создан путем комбинирования приближенных полиномиальных алгоритмов МК-блуждания и Жадного алгоритма. Мы используем Жадный алгоритм для получения энергетических границ для каждого возможного спинового избытка, для последующего разбиения пространства на равное число интервалов, и МК-блуждания для накопления точек данных. Показано, что использование интервалов позволяет обеспечить хорошую работу метода на наиболее вырожденных энергетических участках, но имеет проблему в поиске точек данных на наименее вырожденных участках. Построено распределение плотности состояний.

Ключевые слова: плотность состояний, Каирская решетка, разработка алгоритма, основное состояние

Финансирование: Грант для государственной поддержки ведущих научных школ Российской Федерации (НШ-2559.2022.1.2).

Ссылка при цитировании: Чесноков М. А., Наливайко И. Н., Стронгин В. С. Метод расчета плотности состояний для дипольных решеток // Научно-технические ведомости СПбГПУ. Физико-математические науки. 2022. Т. 15. № 3.1. С. 71–75. DOI: https://doi.org/10.18721/ JPM.153.112

Introduction

Artificial spin ice is a nanomagnetic multiferroic artificial material consisting of nanoparticles of elongated shape. The magnetic moment of a particle consists of many spins, therefore it is called a superspin or macrospin. The behavior of magnetic moment of nanoparticles makes it possible to use the Ising model, since there are only two possible mutually exclusive orientations for it, 'up' or 'down'. Initially, artificial spin ice was understood as a two-dimensional artificial equivalent of spin ice on a pyrochlore lattice. Research on artificial spin ice is of major importance. Thermodynamic properties of systems are investigated. Theoretical work is usually aimed at confirming experimental observations. However, the most fundamental issue is developing algorithms that could allow calculating a complete group of events based on a sample from the state space. Currently, there are no theories and, consequently, technical, software capabilities for accurate calculation of the statistical sum of a large number (>40) of interacting particles of a fully connected model. Therefore, interest in the topic of artificial spin systems is constantly growing.

The method we used for calculating the density of states is independent of geometry and is suitable for studying any dipole lattices.

As an example, the Cairo lattice was used, which is a two-dimensional system of artificial spin ice that combines the geometry of the square and kagome systems [1].

Model and Computational Methods

A system of 40 dipoles was observed, since its dimension is large enough for the obtained data to have statistical value, and at the same time, it is still possible to calculate the exact values by exhaustive search, which is used for comparison.

The greedy algorithm made it possible to 'descend' to low-energy configurations in a relatively small number of operations, but rarely allows to find the ground state or configurations that are energetically close to it [2]. The algorithm can be reversed to find the highest energy in the system.

In the study, we applied this algorithm sequentially for various parameters of the spin excess M to obtain the graph for $E(M)$, which is the basis of the future three-dimensional graph of the density of states. For each M, there are two points that the boundary passes through: $E_{\max}$ and $E_{\min}$ (except $M = N$, where the lines converge). These are the maximum and minimum energies found for a fixed spin excess M respectively.

A random Monte Carlo walk over the system's energy spectrum was used to accumulate a statistically significant number of possible energy values [3]. The algorithm is simple: we generated a random spin configuration, calculated the system's total energy and saved the result. The operation was performed for each of the M possible using the MC averaging steps. The energy of the dipole-dipole interaction of a system of dipoles on the Cairo lattice is calculated using the formula:

$$E_{ij} = \frac{(\vec{m}_i \vec{m}_j)}{\left|\vec{r}_{ij}\right|^3} - 3\frac{(\vec{m}_i \vec{r}_{ij})(\vec{m}_j \vec{r}_{ij})}{\left|\vec{r}_{ij}\right|^5}, \quad (1)$$

where $\vec{m}_i$ is the value of the magnetic moment vector; $\left|\vec{r}_{ij}\right|$ is the vector between the centers of the magnetic moments of the interacting dipoles.

Due to energy degeneracies (states in which several configurations can correspond to the same energy value) some energies are much more common than others, serving to generate the function $g(E)$ corresponding to the upper part of the general three-dimensional density of states.

The step was calculated for dividing the energy space into intervals for each spin excess M using the formula:

$$step = \frac{E_{\max} - E_{\min}}{num}, \quad (2)$$

where *num* is the number of intervals.

Then, for each interval, the degeneracy multiplicity g (describing how many of the previously generated energies are included in each interval) was calculated.

The area under the graph S is equal to the binomial coefficient calculated using formula (3):

$$S = \frac{N!}{M!(N-r)!}. \quad (3)$$

For each spin excess, we multiplied $g(E_i)$ so that the area under the graph is equal to the corresponding binomial coefficient.

Results and Discussion

The energy boundaries were calculated using a greedy algorithm. We generated 100,000 possible energy points for each spin excess M. NVIDIA CUDA parallel computing technology was used to speed up the implementation [4]. For each spin excess M, the energy space was divided into 1,000 intervals with an equal step. This approach made it possible to obtain a fairly correct (with respect to exhaustive search values) distribution of energies and multiplicity of degeneracies using a relatively small amount of data.

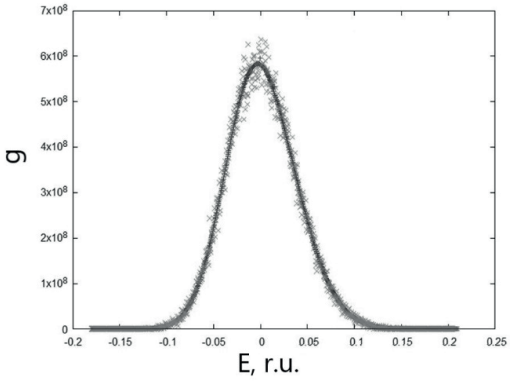

Fig. 1. Function $g(E)$ for spin excess $M = 0$ for exact solution (straight line) and approximate solution (dots).

Fig. 1 shows the $g(E)$ plot for the spin excess $M = 0$, on which the dark straight line is the distribution plot for the exact solution (also divided into intervals, otherwise we would obtain a different dimension), the brighter dots are the approximate data extracted using the algorithm. Evidently, the curves exhibit a similar shape along the entire length with a slight inaccuracy in the peak region, where the largest number of possible energies is located.

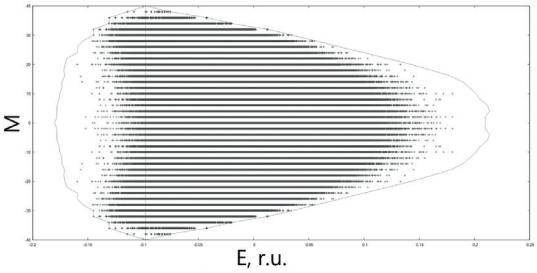

Fig. 2. $M(E)$ for all generated energy points found by the MC method and bounds found by the greedy algorithm.

However, it can be seen from Fig. 2 that the points generated by Monte Carlo do not occupy all the available space (that is also calculated by the approximate greedy algorithm). Because the multiplicities of degeneracy g for the energies located in the middle were much larger, the points along the edges were chosen much less often, or not chosen at all. Fig. 1 shows how strong the growth dynamics was in the middle, relative to the edges. This introduces an additional inaccuracy in the approximate method, requiring to search for solutions.

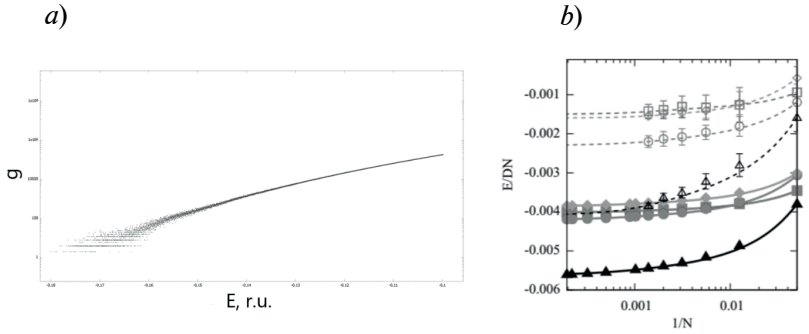

Fig. 3. Function $g(E)$ for the spin excess $M = 0$ (*a*); dependence of the ground state on the number of particles (*b*) [5].

We found from an exhaustive data search that the graph in the low-energy regions close to the ground state can be approximated by a straight line (Fig. 3, *a*) extended to a zone that is well calculated by the Monte Carlo method from the starting point (the ground state or a value close to it).

The first option is to improve the existing greedy algorithm to be able to search for lower energy points close to the ground state for each fixed spin excess M. However, improving of the greedy algorithm is a challenge in itself. A more promising option is to refine the existing method of the ground state energy calculation by scaling. Fig. 3, *b* shows a graph of the change in the minimum energy with a change in the size of the system for the Cairo lattice with different parameters [5].

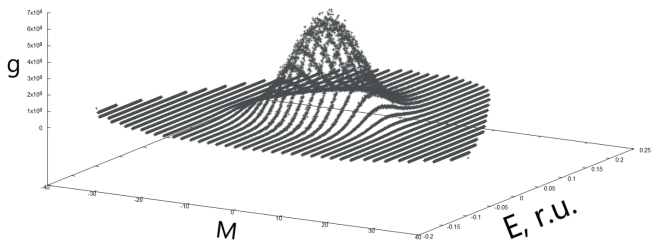

Fig. 4. Density of states (the axis x represents the energy E in arbitrary units; y the spin excess M; z the multiplicity of degeneracy g).

Finally, the binomial coefficients were calculated; the area under each $g(E)$ plot for each spin excess M has been proportionally increased to match the binomial coefficient.

The result is a density of states plot (Fig. 4). We will be able to calculate a fairly accurate DOS after improving the algorithm.

Conclusion

We used 2 approximate methods to construct a polynomial algorithm for finding the density of states for dipole lattices of artificial spin ice. We have found that our approach demonstrates good accuracy for a part of the system (in the center of the energy space) but does not perform well at the edges. We made suggestions about possible ways to solve the problem and improve the algorithm, based on previously obtained data.

REFERENCES

1. **Saccone M. et al.,** Dipolar Cairo lattice: Geometrical frustration and short-range correlations, Physical Review Materials. 3 (10) (2019) 104402.

2. **Bou-Rabee N., Sanz-Serna J. M.,** Geometric integrators and the Hamiltonian Monte Carlo method, Acta Numerica. 27 (2018) 113–206.

3. **Roughgarden T.,** Perfect algorithm. Greedy algorithms and dynamic programming, St. Petersburg: Peter. 2020. 256 p.

4. **Romero J., Bisson M., Fatica M., Bernaschi M.,** High performance implementations of the 2D Ising model on GPUs, Computer Physics Communications. 256 (2020) 107473.

5. **Makarova K. et al.,** Low-energy states, ground states, and variable frustrations of the finite-size dipolar Cairo lattices, Physical Review E. 103 (4) (2021) 042129.

THE AUTHORS

CHESNOKOV Mikhail A.
chesnokov.ma@students.dvfu.ru
ORCID: 0000-0003-1173-8775

STRONGIN Vladislav S.
strongin.vs@dvfu.ru
ORCID: 0000-0002-8420-9893

NALIVAIKO Igor N.
nalivaiko.in@students.dvfu.ru
ORCID: 0000-0003-4433-2990

Received 22.05.2022. Approved after reviewing 25.06.2022. Accepted 04.07.2022.

Conference materials
UDC 538.91, 537.6
DOI: https://doi.org/10.18721/JPM.153.113

Application of hybrid multispin Monte Carlo method to artificial dipole ice on hexagonal and Cairo lattices

K. V. Makarova [1, 2] ✉, A. G. Makarov [1, 2], K. V. Nefedev [1, 2]

[1] Far Eastern Federal University, Vladivostok, Russia;
[2] Institute for Applied Mathematics of the Far Eastern Branch of the RAS, Vladivostok, Russia
✉ makarova.kv@dvfu.ru

Abstract: We apply the hybrid multispin Monte Carlo method to calculate the properties for artificial dipole ice on hexagonal and Cairo lattices. The method is based on combining a random selection of a set of spins (cluster) using the Monte Carlo with complete enumeration of all states of the selected cluster. The method works only for Ising models with a restricted radius of interaction. In addition, the method makes it possible to bring spin systems to the ground state at low temperatures.

Keywords: hybrid Monte-Carlo, dipolar antiferromagnets, spin ice, statistical thermodynamics

Funding: The results of studies related to the development of a theoretical model, samples and physical experiments were obtained within the framework of the state task of the Ministry of Education and Science of Russia (No. 0657-2020-0005). The results of research related to coding were obtained at the expense of the grant of the President of the Russian Federation for state support of the leading scientific schools of the Russian Federation (NSh-2559.2022.1.2). The results of research related to the development of algorithms were obtained within the framework of the state task of the Ministry of Education and Science of Russia (No. 075-00771-22-00).

Citation: Makarova K. V., Makarov A. G., Nefedev K. V. Application of hybrid multispin Monte Carlo method to artificial dipole ice on hexagonal and Cairo lattices. St. Petersburg State Polytechnical University Journal. Physics and Mathematics. 15 (3.1) (2022) 76–81. DOI: https://doi.org/10.18721/JPM.153.113

Материалы конференции
УДК 538.91, 537.6
DOI: https://doi.org/10.18721/JPM.153.113

Применение гибридного мультиспинового Монте-Карло метода для искусственного дипольного льда на гексагональной и Каирской решетках

К. В. Макарова [1, 2] ✉, А. Г. Макаров [1, 2], К. В. Нефедев [1, 2]

[1] Дальневосточный федеральный университет, г. Владивосток, Россия
[2] Институт прикладной математики Дальневосточного отделения РАН, г. Владивосток, Россия
✉ makarova.kv@dvfu.ru

Аннотация. Для расчета характеристик искусственного дипольного льда на гексагональной и Каирской решетках мы применяем гибридный мультиспиновый Монте-Карло метод. Метод основан на сочетании случайного выбора набора спинов (кластера) методом Монте-Карло с полным перебором всех состояний выделенного кластера. Метод работает только для моделей Изинга с ограниченным радиусом взаимодействия. Кроме того, метод позволяет привести спиновые системы к основному состоянию при низкой температуре.

Ключевые слова: гибридный Монте-Карло метод, дипольные антиферромагнетики, спиновой лед, статистическая термодинамика

Финансирование: Результаты исследований, связанных с разработкой теоретической модели, образцов и физических экспериментов, получены в рамках государственного задания Минобрнауки России (№ 0657-2020-0005). Результаты исследований, связанных с программированием, получены за счет гранта Президента Российской Федерации для государственной поддержки ведущих научных школ Российской Федерации (НШ-2559.2022.1.2). Результаты исследований, связанных с разработкой алгоритмов, получены в рамках государственного задания Минобрнауки России (№ 075-00771-22-00).

Ссылка при цитировании: Макарова К.В., Макаров А.Г., Нефедев К.В. Применение гибридного мультиспинового Монте-Карло метода для искусственного дипольного льда на гексагональной и Каирской решетках // Научно-технические ведомости СПбГПУ. Физико-математические науки. 2022. Т. 15. № 3.1. С. 76–81. DOI: https://doi.org/10.18721/ JPM.153.113

Introduction

To calculate the properties of a system of interacting magnetic moments (spins) at a given temperature in thermodynamic equilibrium, it is necessary to determine the partition function, i.e., it is necessary to obtain information about all possible states (configurations). However, in practice, exact calculation of the partition function is possible only in very rare cases. Finding the properties of a full set of events is an important computational problem. Attempts are currently underway to solve this fundamental problem using Monte Carlo algorithms, a combination of Monte Carlo methods and machine learning.

One such method is the Metropolis–Hastings algorithm, which was proposed in 1953 [1]. The Metropolis–Hastings algorithm is one of the most important algorithms that have been developed in the last century [2]. This approach remains to this day one of the most popular not only in statistical mechanics, but also in an extremely wide field of diverse sciences.

Indeed, the Metropolis algorithm has fundamental importance, but the one-spin approach is unfortunately insufficient at low temperatures. This phenomenon is called the 'critical slowing down' [3, 4].

Therefore, efforts are made to develop new approaches. For example, Melko et al. introduced loop flips into the Metropolis algorithm, performing simulations of a spin-ice model at low temperatures [3, 5]. There are combinations of the conventional Metropolis method with single spin rotations and replica exchange method [6, 7], and with the over-relaxation method, with the replica-exchange method [8]. There are Monte Carlo simulations combined with finite-size scaling [9].

In this paper, we applied the hybrid Monte Carlo method of our own design [10, 11], in which, instead of a single spin-flip, we use a complete enumeration of 2^{Nc} states of N_c spins (moments) within a small cluster that interact with a configuration of 'frozen boundary' of N_b spins or moments. The basic idea of our approach is to search for the thermodynamic equilibrium of subsystems of relatively small size at finite temperature at almost adiabatic process. Naturally, equilibrium is achieved significantly faster in small subsystems than in the entire system. If all subsystems with the same local Hamiltonian are physically and statistically equivalent, the statistical thermodynamic characteristics of one subsystem (replica) can be calculated only once to be used to calculate the thermodynamic averages.

Hexagonal Dipolar Spin Ice, Nearest Neighbors Model

'Artificial spin ice' (ASI) is not just an artificial analog of natural spin ice, which is to say, geometrically frustrated magnetic pyrochlores that imitate the ordering of the spins of water protons, but a convenient framework for developing and testing theoretical models of many interacting bodies and new statistical methods, as well as verifying their accuracy.

We use Ising-like point dipoles located on the edges of a two-dimensional hexagonal lattice

with periodic boundary conditions. The magnetic moment of the dipole i is defined as $\vec{m}_i$ and is directed along the edges (see [10, 11] for details). An example of a dipole hexagonal lattice is shown in Fig. 1, *a*.

For the operation of the hybrid Monte Carlo method, we limited the radius of the dipole-dipole interaction to three coordination spheres according to the results [12]. To calculate the energy, it is necessary to determine the neighbors for each dipole. Each cluster dipole has 14 nearest neighbors (see Fig. 1, *b*). Since the boundary conditions are periodic, all elements in the system have the same number of neighbors.

For the method to work correctly, it is necessary to determine the clusters and boundaries of each hexagon. A hexagon is taken as a cluster, and the nearest neighbors of the hexagon dipoles are the boundary that interacts with the cluster and separates it from all other dipoles. The cluster is shown by red arrows in Fig. 1, *a* and consists of six dipoles. The cluster boundary is shown by blue arrows and consists of 24 nearest neighboring dipoles. In total, the cluster and the boundary block contain 30 dipoles, whose states can be easily enumerated by complete enumeration. This block will be subsequently used for sampling.

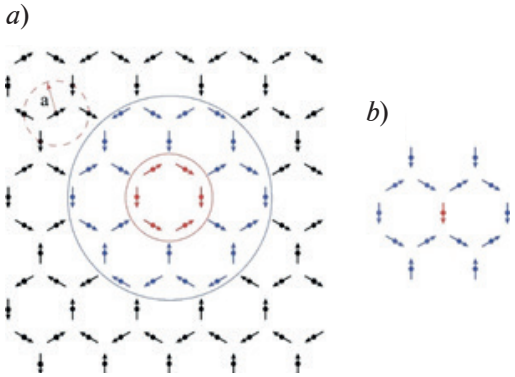

Fig. 1. Example of hexagonal lattice with Ising-like point dipoles (spins): cluster spins are marked in red (small circle) and border spins in blue color (large circle), which are used as subsystems in the hybrid Monte Carlo method (*a*); cluster spin and interacting dipole-dipole neighbors up to the third coordination sphere (*b*)

The energy of the dipole-dipole interaction between dipoles is defined as

$$E = Da^3 \sum_{i<j} \left[\frac{(\vec{m}_i \vec{m}_j)}{\left|\vec{r}_{ij}\right|^3} - 3\frac{(\vec{m}_i \vec{r}_{ij})(\vec{m}_j \vec{r}_{ij})}{\left|\vec{r}_{ij}\right|^5} \right], \quad (1)$$

where $D = \mu_2/a3$ is the dipole coupling constant, $a = \sqrt{3}/2$ is the lattice parameter (Fig. 1, *a*) and $\vec{r}_{ij}$ is the radius vector between dipoles *i* and *j* with magnetic moments $\vec{m}_i$ and $\vec{m}_j$, respectively.

For systems with different numbers *N* of spins, we calculated the specific heat capacity *C*(*T*) per spin depending on temperature

$$C(T) = \frac{1}{N} \frac{\left\langle E^2 \right\rangle - \left\langle E \right\rangle^2}{k_B T^2}, \quad (2)$$

where ⟨E⟩ is the average thermodynamic quantity, k_B is the Boltzmann coefficient, *T* is the temperature.

Hexagonal Dipolar Ice Thermodynamics and Ground State

Using our method, we obtained the specific heat (Fig. 2) for the hexagonal spin ice consisting of different numbers of spins; the data are presented in relative units.

The temperature behavior of the heat capacity has two peaks. An increase in one of the heat capacity peaks with an increase in the size of the system may indicate the presence of a phase transition. In addition, there is no low-temperature peak in the temperature behavior of heat capacity in the model of Ising-like point dipoles on a hexagonal lattice. The low temperature pick

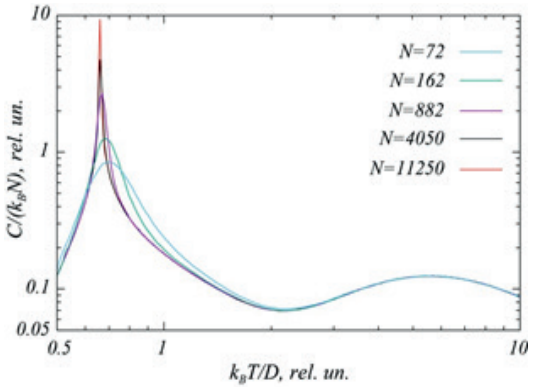

Fig. 2. Temperature behavior of specific heat for different numbers of spins on the hexagonal lattice, calculated by the hybrid Monte Carlo method

was discussed in [13, 14]. The presence of a peak is usually associated with a phase transition to a low-energy phase. The low-temperature transition to long-range order, which is discussed in [15], is absent in the nearest-environment model. Thus, the phase transition to an ordered phase in artificial macrospin ice materials is associated with the long-range nature of dipole interaction, which lifts the macroscopic degeneracy of the ground state.

Developing an algorithm to search for ground state is a fundamental problem. The multispin cluster Monte Carlo method allows to search for configurations of low-energy states. Fig. 2 from [16] shows an example of one of the ground state candidates for the hexagonal lattice of Ising-like dipoles obtained by our method.

Cairo Dipolar Ice, Nearest Neighbors Model

The Cairo lattice with periodic boundary conditions is shown in Fig 3, *a*. The lattice parameters were $a = 472$ nm, $b = 344$ nm, and $c = 376$ nm. The interaction radius and nearest neighbors of one of the dipoles of the cluster are shown in Fig. 3, *b*. To implement the hybrid multispin Monte Carlo method, five dipoles are taken as a cluster, and their nearest neighbors form a boundary (Fig. 3, *c*).

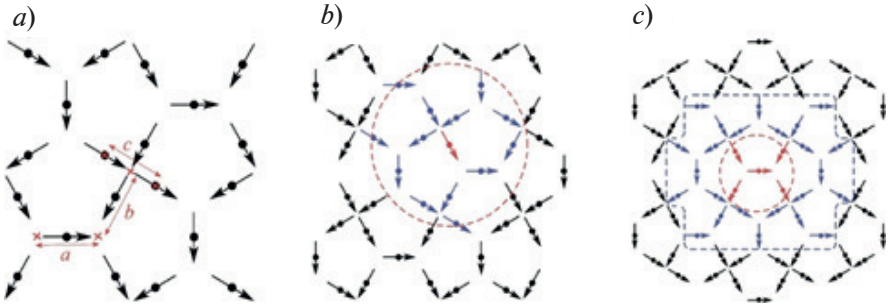

Fig. 3. Example of Cairo lattice with Ising-like point dipoles (spins): relevant parameters *a*, *b*, and *c* (*a*); the cluster spin and interacting dipole–dipole neighbors (*b*); cluster spins are marked in red (small circle) and border spins in blue (large rectangle), which are used as subsystems in the hybrid Monte Carlo method (*c*)

The energy of the dipole-dipole interaction in the Cairo lattice was calculated using Eq. (1).

Thermodynamics Cairo Dipolar Ice and Ground State

Calculating thermodynamic averages allowed calculating the temperature dependence of the specific heat capacity for the pentagonal Cairo lattice as a function of the given number of dipoles. The size of the cluster with the boundary had 29 dipoles. The lattice parameters were $a = 472$ nm, $b = 344$ nm, and $c = 376$ nm

As can be seen from Fig. 4, with an increase in the number of dipoles on Cairo lattice, there is no increase in the height of the heat capacity peak in models with a limited interaction radius.

The absence of size effects in the temperature behavior of the heat capacity is observed. The heat capacity peak height is the same for all studied systems with the number of particles $N = 80$, 500 and 980, in the nearest neighbors model.

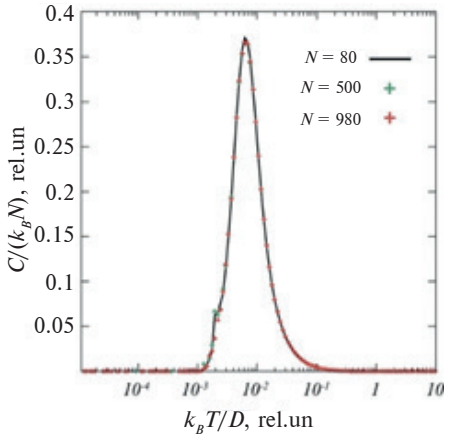

Fig. 4. Temperature behavior of specific heat of Cairo dipolar ice, calculated by hybrid Monte Carlo method

It should be noted that a model and, specifically, the interaction radius should be selected very carefully, since it is known that depending on the value of the interaction radius of Ising dipoles, the same model can lead to existence of several heat capacity peaks. For a limited interaction radius in the model of nearest neighbors, only one heat capacity peak is observed. Moreover, we calculated the ground state of the Cairo lattice of dipoles $N = 80$ dipoles (see [10], Fig. 8).

Conclusion

The hybrid multispin Monte Carlo method allows increasing the size of counting systems and to expand the amount of calculated statistical-thermodynamic parameters while preserving the accuracy and performance at the same level. Furthermore, the method allows to calculate the temperature dependence of thermodynamic quantities such as heat capacity and others, and in some cases solve the fundamental problem of searching for configurations of low-energy states or even ground states at $T \to 0$. It can be easily generalized to spin lattices of arbitrary dimensions, arbitrary Hamiltonian, arbitrary dilution, and external field.

Acknowledgments

The results of studies related to the development of a theoretical model, samples and physical experiments were obtained within the framework of the state task of the Ministry of Education and Science of Russia (No. 0657-2020-0005). The results of research related to coding were obtained at the expense of the grant of the President of the Russian Federation for state support of the leading scientific schools of the Russian Federation (NSh-2559.2022.1.2). The results of research related to the development of algorithms were obtained within the framework of the state task of the Ministry of Education and Science of Russia (No. 075-00771-22-00).

To perform the calculations, we used the computational resources provided by the Shared Facility Center “Data Center of FEB RAS” [17].

REFERENCES

1. **Metropolis N., Rosenbluth A. W., Rosenbluth M. N., Teller A. H., Teller E.,** Equation of state calculations by fast computing machines, The journal of chemical physics 21 (1953) 1087–1092.

2. **Beichl I., Sullivan F.**, The metropolis algorithm, Computing in Science & Engineering 2 (2000) 65–69.

3. **Melko R. G., den Hertog B. C., Gingras M. J. P.,** Long-range order at low temperatures in dipolar spin ice, Phys. Rev. Lett. 87 (2001) 067203.

4. **Bonati C., D'Elia M.,** Topological critical slowing down: variations on a toy model, Physical Review E 98 (2018) 013308.

5. **Melko R. G., Gingras M. J. P.,** Monte Carlo studies of the dipolar spin ice model, Journal of Physics: Condensed Matter 16 (2004) R1277–R1319.

6. **Tanaka K., Hotta C.,** Finite-temperature thermodynamic properties of spin-1 nematics in an applied magnetic field, Phys. Rev. B 102 (2020) 140401.

7. **Schierz P., Zierenberg J., Janke W.,** First-order phase transitions in the real microcanonical ensemble, Phys. Rev. E 94 (2016) 021301.

8. **Mitsumoto K., Kawamura H.,** Replica symmetry breaking in the RKKY skyrmion-crystal system, Phys. Rev. B 104 (2021) 184432.

9. **Lulli M., Parisi G., Pelissetto A.,** Out-of-equilibrium finite-size method for critical behavior analyses, Physical Review E 93 (2016) 032126.

10. **Makarova K., Strongin V., Titovets I., Syrov A., Zinchenko I., Samoylov V., Hofhuis K., Saccone M., Makarov A., Farhan A., et al.,** Lowenergy states, ground states, and variable frustrations of the finite-size dipolar cairo lattices, Physical Review E 103 (2021) 042129.

11. **Makarov A., Makarova K., Shevchenko Y. A., Andriushchenko P., Kapitan V. Y., Soldatov K., Perzhu A., Rybin A., Kapitan D. Y., Vasil'ev E., et al.,** On the numerical calculation of frustrations in the ising model, JETP Letters 110 (2019) 702–706.

12. **Andriushchenko P.,** Influence of cutoff dipole interaction radius and dilution on phase transition in kagome artificial spin ice, Journal of Magnetism and Magnetic Materials 476 (2019) 284–288.

13. **Chern G.-W., Mellado P., Tchernyshyov O.,** Two-stage ordering of spins in dipolar spin ice on the kagome lattice, Physical review letters 106 (2011) 207202.

14. **Möller G., Moessner R.,** Magnetic multipole analysis of kagome and artificial spin-ice dipolar arrays, Physical Review B 80 (2009) 140409.

15. **Skjærvø S. H., Marrows C. H., Stamps R. L., Heyderman L. J.,** Advances in artificial spin ice, Nature Reviews Physics 2 (2020) 13–28.

16. **Makarova K.V., Makarov A.G., Padalko M.A., Strongin V.S., Nefedev K.V.,** Multispin Monte Carlo Method, Far Eastern Mathematical Journal 20 (2020) 212–220.

17. **Sorokin A., Makogonov S., Korolev S.,** The information infrastructure for collective scientific work in the far east of Russia, Scientific and Technical Information Processing 44 (2017) 302–304.

THE AUTHORS

MAKAROVA Kseniia V.
makarova.kv@dvfu.ru
ORCID: 0000-0003-0594-7220

NEFEDEV Konstantin V.
nefedev.kv@dvfu.ru
ORCID: 0000-0001-7330-5137

MAKAROV Aleksandr G.
makarov.ag@dvfu.ru
ORCID: 0000-0002-7778-8364

Received 22.05.2022. Approved after reviewing 14.07.2022. Accepted 26.07.2022.

Conference materials
UDC 536.91
DOI: https://doi.org/10.18721/JPM.153.114

Hybrid Monte Carlo algorithm for studying the Edwards-Anderson model

A. E. Rybin [1, 2] ✉, D. Yu. Kapitan [1, 2], K. V. Nefedev [1, 2],
A. G. Makarov [1, 2], V. Yu. Kapitan [1, 2]

[1] Far Eastern Federal University, Vladivostok, Russia;
[2] Institute of Applied Mathematics of Far Eastern Branch, RAS, Vladivostok, Russia
✉ rybin.ae@dvfu.ru

Abstract: The complexity of the study of spin glasses is related to their frustrations, due to which classical Monte Carlo algorithms experience serious difficulties when trying to calculate such systems. The main object of research in this paper is two-dimensional Edwards-Anderson model on a square lattice. In the paper, we propose an optimized Hybrid Monte Carlo method for calculating the values of thermodynamic averages and ground state energies of the frustrated spin glass model. The validity of the results is confirmed by comparison with numerical simulation with the parallel tempering Monte Carlo method, complete enumeration algorithm and robust machine learning approach-RBM neural network. The proposed algorithm has a number of advantages: possible high parallelization of the algorithm to speed up simulation, calculation accuracy and low resource consumption, which allows to calculate lattices of relatively large size. This algorithm can be applied to calculations of lattices with different geometry and sizes.

Keywords: Edwards-Anderson model, Monte Carlo algorithm, ground state, frustration

Funding: Research on hybrid algorithm and development of the numerical calculation algorithm as a whole was carried out with the financial support of the grant of the President of the Russian Federation for state support of leading scientific schools of the Russian Federation (NSh-2559.2022.1.2). Computer program development and coding of parallel efficient code were carried out within the framework of State Task of the Ministry of Science and Higher Education of the Russian Federation (№ 0657-2020-0005).

Citation: Rybin A. E., Kapitan D. Yu., Nefedev K. V., Makarov A. G., Kapitan V. Yu. Hybrid Monte Carlo algorithm for studying the Edwards-Anderson model. St. Petersburg State Polytechnical University Journal. Physics and Mathematics. 15 (3.1) (2022) 82–86. DOI: https://doi.org/10.18721/JPM.153.114

Материалы конференции
УДК 536.91
DOI: https://doi.org/10.18721/JPM.153.114

Гибридный алгоритм Монте-Карло для изучения модели Эдвардса-Андерсона

А. Е. Рыбин [1, 2] ✉, Д. Ю. Капитан [1, 2], К. В. Нефедев [1, 2],
А. Г. Макаров [1, 2], В. Ю. Капитан [1, 2]

[1] Дальневосточный Федеральный Университет, г. Владивосток, Россия;
[2] Институт прикладной математики Дальневосточного отделения РАН, г. Владивосток, Россия
✉ rybin.ae@dvfu.ru

Аннотация. Сложность исследования спиновых стекол связана с фрустрациями, из-за которых классические алгоритмы Монте-Карло испытывают серьезные трудности

при попытке расчета таких систем. Основным объектом исследования в данной работе является двумерная модель Эдвардса-Андерсона на квадратной решетке. В работе предложен оптимизированный гибридный метод Монте-Карло для расчета значений термодинамических средних и энергий основного состояния модели фрустрированного спинового стекла. Достоверность результатов подтверждается сравнением с численным моделированием с помощью параллельного отжига методом Монте-Карло, алгоритмом полного перебора и надежным алгоритмом машинного обучения - нейронной сети RBM. Предложенный алгоритм обладает рядом преимуществ: возможность параллелизации алгоритма для ускорения моделирования, точность расчетов и низкое потребление ресурсов, что позволяет рассчитывать решетки относительно большого размера. Данный алгоритм может быть применен для расчета решеток с различной геометрией и размерами.

Ключевые слова: модель Эдвардса-Андерсона, алгоритм Монте-Карло, основное состояние, фрустрации

Финансирование: Исследование гибридного алгоритма и разработка алгоритма численного расчета в целом проводились при финансовой поддержке гранта Президента Российской Федерации для государственной поддержки ведущих научных школ Российской Федерации (НШ-2559.2022.1.2). Разработка компьютерной программы и кодирование эффективного параллельного кода проводились в рамках государственного задания Министерства науки и высшего образования Российской Федерации (№ 0657-2020-0005).

Ссылка при цитировании: Рыбин А. Е., Капитан Д. Ю., Нефедев К. В., Макаров А. Г., Капитан В. Ю., Гибридный алгоритм Монте-Карло для изучения модели Эдвардса-Андерсона // Научно-технические ведомости СПбГПУ. Физико-математические науки. 2022. Т. 15. № 3.1. С. 82–86. DOI: https://doi.org/10.18721/ JPM.153.114

Introduction

Nowadays, frustrated spin systems, such as spin glasses and ices, are actively studied in modern condensed matter physics [1–3]. In such models, frustrations arise due to the special lattice topology or the competition of exchange interactions, which leads to the search for new magnetic ground states and unique effects that can arise.

Spin glasses are disordered magnetics, which are characterized by two unique properties that greatly distinguish these systems from others: in such systems there is strong competition between ferromagnetic and antiferromagnetic interactions, i.e., frustrations, and disorder, which is freezing (or solidifying) of atoms in different locations during alloy formation. Many processes occurring in spin glasses cannot be described within the framework of the classical theory of phase transitions and require some new non-standard approaches.

The process of reaching the ground states and studying the thermodynamic properties even in the simplest model, the Ising model, is associated with serious difficulties in theoretical analysis and numerical calculations. This problem is much more complicated than it seems at first sight. Creating an efficient algorithm for finding the ground states is one of the main challenges in the theory of frustrated magnetism.

The classical Monte Carlo algorithm and its many optimizations have their drawbacks. Single-spin sampling methods near critical points drastically lose in efficiency, the so-called ‘critical slowdown’ occurs. In addition, at very low temperatures, only a small fraction of spins makes a flip. The motion of the system in phase space is very slow, so the system requires generation of a very large number of states to move to an equilibrium state. In turn, the use of multicanonical methods has difficulties in calculating the thermodynamics of systems with a relatively large number of spins.

To solve the problem of searching for thermodynamics of frustrated models of many interacting bodies, as well as to search for ground state configurations, a new hybrid multispin method is applied, which is a logical continuation of the Metropolis algorithm.

Edwards-Anderson model

The main object of research in this paper is two-dimensional Edwards-Anderson model on a square lattice (see Fig. 1). Edwards and Anderson proposed in [4] to change the distribution function of the exchange interaction to a more complex one, where the exchange integral J_{ij} is a random function and the average value of J_{ij} is equal to zero. In such systems, half of the spins has ferromagnetic interaction with its nearest neighbors, and the other part is antiferromagnetic one.

The interaction J_{ij} between the spin pair (ij) changes during the transition from one pair to another. The Hamiltonian is then expressed as:

$$H = -\sum_{i,j} J_{i,j} S_i S_j - h\sum_i S_i, \tag{1}$$

S_i, S_j are the spins in lattice, $\langle i,j\rangle$ denotes summation over pairs of interacting spins in a system with the size N, h is the external magnetic field. Edwards and Anderson suggested in [4] that each J_{ij} distributed independently according to the probability distribution $P(J_{ij})$. In this work, we have used the bimodal distribution, i.e., the amount of positive and negative bond values is equal.

The average energy of the spin glass model at temperature T is calculated by Eq. (2) and the average magnetization by Eq. (3).

$$E(T) = \frac{1}{N}\langle H\rangle_T, \tag{2}$$

$$M(T) = \frac{1}{N}\left\langle \sum_i S_i \right\rangle_T. \tag{3}$$

Based on these two main characteristics, we can calculate the various thermodynamic properties, such as magnetic susceptibility (4) and specific heat (5)

$$\chi(T) = \frac{1}{N}\frac{\left\langle |M|^2 \right\rangle - \left\langle |M| \right\rangle^2}{k_B T}, \tag{4}$$

$$C(T) = \frac{1}{N}\frac{\left\langle E^2 \right\rangle - \left\langle E \right\rangle^2}{k_B T^2}. \tag{5}$$

In this study, we investigated models on the square lattice with different number of spins, such as $N = 6\times6$, 10×10, 20×20, 30×30.

Parallel Hybrid Monte-Carlo Algorithm:

Initially, the hybrid algorithm was proposed for field theory studies on a lattice with fermionic degrees of freedom [5]. Subsequently, this algorithm was transferred and adapted for various problems [6, 7]. More recently, we proposed an approach for studying the temperature behavior of the frustration parameter in a geometrically frustrated hexagonal lattice [8]. It is based on combining the canonical and multicanonical sampling of the Gibbs distribution.

However, after comparing the results of the algorithm with the complete enumeration method, it turned out that as the size of the systems increased, the algorithm did not arrive at the ground state. For this reason, the algorithm was optimized and reduced to the form presented below.

- → random *spins* and bonds initialization
- → **for** all *threads* do
  - → choosing random *spin* in the system
    if *cluster* borders are not crossing **then**
    - → copy cluster spin array to private memory
    - → **for** $2*N_c$ steps **do**
      - → **for** every *spin* in the *cluster* **do**
        - → current spin value = ((counter >> $2*Nc$ −1) & 1)
        - → **if** new energy<previous energy **then**
          - → save current configuration as minimal configuration
  - →collect *spin* values in main system array
- → ground state and thermodynamics calculation.

Results and Discussion

To demonstrate the work of the algorithm, we compare its accuracy with different methods [9–11], such as complete enumeration algorithm, ML approach using RBM, see Table 1. Algorithms were tested on a square lattice of the two-dimensional Edwards-Anderson model, with number of spins $N = 6\times6$, 10×10, 20×20, 30×30. As can be seen from the table, proposed hybrid Monte Carlo algorithm demonstrates the same accuracy as the complete enumeration algorithm, but, unlike the latter, it is much less resource-intensive, which allows us to calculate larger systems.

Table 1

Comparison of results obtained by different computational approaches

System size	E_{min}		
	CE	HM	RBM
6 x 6	–1.30	–1.30	–1.30
10 x 10	–	–1.40	–1.40
20 x 20	–	–1.38	–1.38
30 x 30	–	–1.34	–1.34

In contrast to the other algorithms presented in Table 1, the hybrid Monte Carlo algorithm can be used to study other important properties of the system, such as the dependence of the staggered magnetization and the system degeneracy multiplicity on the external magnetic field. It also allows the calculation of basic thermodynamic quantities such as heat capacity and magnetic susceptibility. A comparative graph of the dependence of heat capacity on temperature is shown in Fig. 1. We checked the accuracy of the proposed algorithm by comparing it with the parallel tempering (PT) method, which has proved [12–14] to be excellent for such problems.

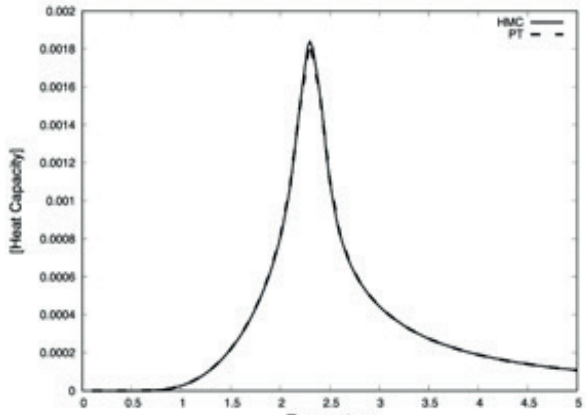

Fig. 1. Dependence of heat capacity on temperature according to Edwards-Anderson with $N = 20\times20$, obtained by Hybrid Monte Carlo (HMC) and Parallel Tempering (PT) algorithms

Based on the values obtained, we can conclude that the optimized hybrid Monte Carlo algorithm is well adapted to searching for the main states of complex lattices, as well as to the calculation of the main thermodynamic characteristics.

Conclusion

In this work, we proposed and implemented an optimization of a hybrid Monte Carlo algorithm. Using this method, various important characteristics on spin glass lattices with different numbers of spins were obtained, such as: energy of ground states, dependence of heat capacity and susceptibility on temperature. The validity of the obtained results was validated using well-proven algorithms. Due to its accuracy and versatility, this algorithm can be used to study systems with a large number of spins and different lattice geometries.

REFERENCES

1. **Belokon V., Kapitan V., Dyachenko O.,** The combination of the random interaction fields' method and the Bethe-Peierls method for studying two-sublattice magnets, Journal of Magnetism and Magnetic Materials. 401 (1) (2016) 651–655.

2. **Kapitan V. Y., Nefedev K. V.,** Labyrinth Domain Structure in the Models with Long-range Interaction, Journal of Nano-& Electronic Physics. 6 (3) (2014) 03005-1-03005-4.

3. **Nefedev K. V., Kapitan V. Y.,** Concentration phase transition and hysteresis phenomena in Co-nanofilms. Computer data processing and simulation, Advanced Materials Research. 718 (1) (2013) 69–73.

4. **Edwards S., Anderson P.,** Theory of spin glasses, Journal of Physics F: Metal Physics. 5 (5) (1975) 965–974.

5. **Duane S., Kennedy A., Pendleton B., Roweth D.,** Hybrid Monte Carlo, Phys. Lett. B. 195 (2) (1987) 216–222.

6. **Efendiev Y., Zachariah M.,** Hybrid Monte Carlo Method for Simulation of Two-Component Aerosol Coagulation and Phase Segregation, Journal of Colloid and Interface Science. 249 (1) (2002) 30–43.

7. **Nagai Y., Okumura M., Kobayashi K.,** Self-learning hybrid Monte-Carlo: A first-principles approach, Phys. Rev. B. 102 (4) (2020) 041124.

8. **Makarov A., Makarova K., Shevchenko Y., Andriushchenko P., Kapitan V., et al.,** On the numerical calculation of frustrations in the ising model, JETP Letters. 110 (10) (2019) 702–706.

9. **Andriushchenko P., Kapitan D., Kapitan V.,** A New Look at the Spin Glass Problem from a Deep Learning Perspective, Entropy. 24 (5) (2022) 697.

10. **Korol A., Kapitan V., Perzhu A., Padalko M.,** Kapitan D., et al., Calculation of the Ground States of Spin Glasses Using a Restricted Boltzmann Machine, JETP Letters. 115 (8) (2022) 466–470.

11. **Padalko M. A., Shevchenko Y. A., Kapitan V. Y., Nefedev K. V.,** Parallel Computing of Edwards-Anderson Model, Algorithms. 15 (1) (2022) 13.

12. **Hartmann A. K.,** Ground-state clusters of two-, three-, and four-dimensional $\pm j$ ising spin glasses, Phys. Rev. E. 63 (1) (2000) 016106.

13. **Bittner E., Nußbaumer A., Janke W.,** Make life simple: Unleash the full power of the parallel tempering algorithm, Physical review letters. 101 (13) (2008) 130603.

14. **Newman M. E., Barkema G. T.,** Monte Carlo methods in statistical physics, Clarendon Press, 1999.

THE AUTHORS

RYBIN Alexey E.
rybin.ae@dvfu.ru
ORCID: 0000-0002-1055-9217

MAKAROV Aleksandr G.
makarov.ag@dvfu.ru
ORCID: 0000-0002-7778-8364

KAPITAN Dmitrii Yu.
kapitan.diu@dvfu.ru
ORCID: 0000-0001-9815-1891

KAPITAN Vitalii Yu.
kapitan.vyu@dvfu.ru
ORCID: 0000-0002-5068-8910

NEFEDEV Konstantin V.
nefedev.kv@dvfu.ru
ORCID: 0000-0001-7330-5137

Received 22.05.2022. Approved after reviewing 18.07.2022. Accepted 19.07.2022.

Conference materials
UDC 536.91
DOI: https://doi.org/10.18721/JPM.153.115

Application of convolutional neural networks to spin models studies

A. V. Perzhu [1], E. V. Vasiliev [1,2], A. O. Korol [1, 2], D. Yu. Kapitan [1, 2]
A. E. Rybin [1, 2], V. Yu. Kapitan [1, 2] ✉

[1] Far Eastern Federal University, Vladivostok, Russia;
[2] Institute of Applied Mathematics FEB RAS, Vladivostok, Russia
✉ kapitan.vyu@dvfu.ru

Abstract: Nowadays, methods and techniques of Deep Learning are being used in various scientific areas. In this paper, the applying of convolutional neural network was considered in frame of problems from statistical physics and computer simulation of magnetic films. In a frame of the first task, CNN was used to determine critical Curie point for Ising model on 2D square lattice. Obtained results were compared with classical Monte-Carlo method and exact solution. Systems of various lattice sizes and the influence of the size effect on the results' accuracy were considered. Also, authors considered the classical two-dimensional Heisenberg model, a spin system with direct short-range exchange, and studied of its competition with the Dzyaloshinskii-Moriya interaction. A neural network was applied to the recognition of Spiral (Sp), Spiral-skyrmion (SpSk) Skyrmion (Sk), Skyrmion-ferromagnetic (SkF) and Ferromagnetic (FM) phases of the Heisenberg spin system with magnetic skyrmions.

Keywords: Convolutional neural network, Metropolis algorithm, Ising model, Heisenberg model, Magnetic Skyrmion

Funding: This work has been supported by the grant of the Russian Science Foundation 21-72-00058 "High-performance intelligent approaches to the study of complex magnetic systems".

Citation: Perzhu A. V., Vasiliev E. V., Korol A. O., Kapitan D. Yu., Rybin A. E., Kapitan V. Yu., Application of convolutional neural networks to spin models studies. St. Petersburg State Polytechnical University Journal. Physics and Mathematics. 15 (3.1) (2022) 87–92. DOI: https://doi.org/10.18721/JPM.153.115

Материалы конференции
УДК 536.91
DOI: https://doi.org/10.18721/JPM.153.115

Применение сверточных нейронных сетей для исследования спиновых моделей

А. В. Пержу [1], Е. В. Васильев [1,2], А. О. Король [1,2]
Д. Ю. Капитан [1,2], А. Е. Рыбин [1,2], В. Ю. Капитан [1,2] ✉

[1] Дальневосточный Федеральный Университет, г. Владвосток, Россия;
[2] Институт прикладной математики ДВО РАН, г. Владивосток, Россия
✉ kapitan.vyu@dvfu.ru

Аннотация. В настоящее время методы глубокого обучения используются в различных научных областях. В данной работе применение сверточной нейронной сети рассмотрено в рамках задач статистической физики и компьютерного моделирования магнитных пленок. В рамках первой задачи CNN использовалась для определения критической точки Кюри для модели Изинга на двумерной квадратной решетке. Полученные

результаты сравнивались с классическим методом Монте-Карло и точным решением. Рассмотрены системы с различными размерами решетки и влияние размерного эффекта на точность результатов. Также авторы рассмотрели классическую двумерную модель Гейзенберга, спиновую систему с прямым короткодействующим обменом, и изучили ее конкуренцию с взаимодействием Дзялошинского-Мория. Нейронная сеть применялась для распознавания Спиральной (Sp), Спирально-скирмионной (SpSk), Скирмионной (Sk), Скирмион-ферромагнитной (SkF) и Ферромагнитной (FM) фаз спиновой системы Гейзенберга с магнитными скирмионами.

Ключевые слова: Сверточная нейронная сеть, алгоритм Метрополиса, модель Изинга, модель Гейзенберга, магнитный скирмион

Финансирование: Работа выполнена при поддержке гранта РНФ № 21-72-00058 “Высокопроизводительные интеллектуальные подходы к изучению сложных магнитных систем”.

Ссылка при цитировании: Пержу А. В., Васильев Е. В., Король А. О., Капитан Д. Ю., Рыбин А. Е., Капитан В. Ю. Применение сверточных нейронных сетей для исследования спиновых моделей // Научно-технические ведомости СПбГПУ. Физико-математические науки. 2022. Т. 15. № 3.1. С. 87–92. DOI: https://doi.org/10.18721/ JPM.153.115

Introduction

In the fundamental scientific works [1, 2], as well as in modern ones [3-6], much attention is paid to lattice structures. The interactions between spins in the lattice sites can lead to collective behavior and macroscopic effects, for example, as widely known as ferromagnetism or antiferromagnetism. Also, recently, structures that have no analogues in natural materials have been actively investigated. This is the reason for the use of supercomputer modelling to study such artificial structures and theoretically predict their properties. Because of supercomputers, it possible to use new classes of algorithms and operate with large and super-large amounts of data to carry out numerical experiments. Numerical methods and computer simulation on a supercomputer are of paramount importance in statistical and mathematical physics, nanophysics, and statistical thermodynamics since supercomputers significantly speed up the solution of various scientific problems [7]. And thanks to the development of machine learning (ML), the software tools for conducting numerical experiments have significantly expanded recently, but scientists are just beginning to reveal the full potential of introducing machine learning methods into their research [8-10].

In our paper, we discussed the applying of CNN in frame of two problems from statistical physics and computer simulation of magnetic films. The first problem is about determination of critical Curie point for Ising model. And the second one is the recognition of different phases of the Heisenberg spin system with magnetic skyrmions.

Research problems and methods

In our work, it was demonstrated that modern machine learning methods can provide new approaches to the study of physical systems within the frame of statistical physics models. For this, the TensorFlow library was used to create a convolutional neural network [11]. In this study, the Metropolis algorithm for Monte Carlo simulation was applied to generate input data for the neural network, and then compared with the results obtained after training the convolutional neural network. We considered two mathematical models of statistical physics: the Ising model with direct exchange and the Heisenberg one with the Dzyaloshinskii-Moriya [12,13] interaction and skyrmions in a system, see more details [7,14]. All values in the work are given in dimensionless values.

A convolutional neural network

We used configurations of spin systems obtained at different simulation parameters for the training and subsequent classification of them in a neural network. To date, the most accurate analysis results are demonstrated by neural networks based on convolutional architecture. We used the TensorFlow library to create a convolutional neural network and to classify our spin systems to different phases.

In our research, we have reduced the problem of determining the phases of spin systems to the problem of image classification - in fact, to the main problem area in which neural networks are used. For recognizing images, CNN accepts them in the RGB format as a three-dimensional matrix. In our case, the convolutional neural network received as input a three-dimensional array representing the components of a spin.

Following this, the convolutional neural network learned, using the training dataset, to highlight the features inherent in one or another spin configuration. Our CNN consists of next layers (main ones), see Figure 1:

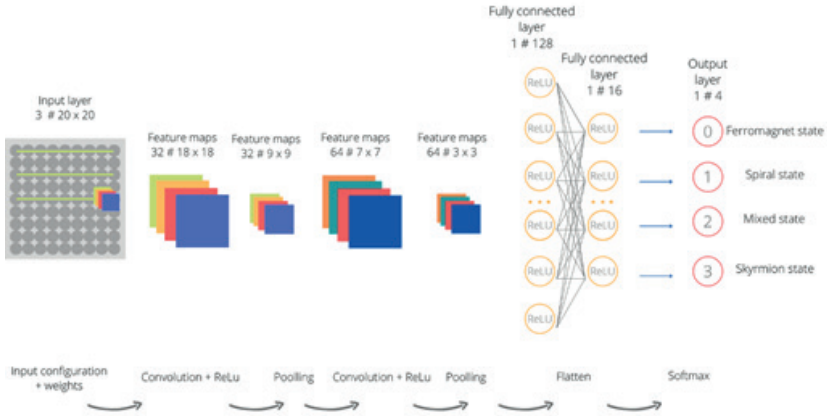

Fig. 1. Architecture of the convolutional neural network

1. Input layer

Input data (configurations of spins), each of the neurons (spins) of which is assigned an initial random weight. The components of a three-dimensional vector were fed to the network input (i.e., the components of Heisenberg spin). The dataset was prepared using Monte Carlo simulation data for training the neural network in state recognition.

2. Convolutional layer with 3×3 filter

When neurons are connected to only a few neurons in the next layer, the layer is said to be convolutional. The convolutional layer acts as a filter that discards the least informative parts of the input data. Each layer has filters (i.e., matrices with weight values). When the filter moves along the matrix of the previous layer, each filter element is multiplied by the value of the neuron, and the values are summed up and written to the feature map.

3. Pooling layer for reducing the dimensions of the data.

4. Fully connected layer

Fully connected layers are used for classification. All layers before the fully connected layer are used to highlight various features that are fed to the input of the classifier. This layer can also be used as the final (output) CNN layer, the result of which is the probability of the input configuration of spins belonging to a certain class.

Results and Discussion

Determination of the second order transition of the Ising model

Different sets of input data of the neural network obtained with different parameters of the Metropolis algorithm for systems of 10×10 and 20×20 Ising spins were used. The obtained data will be used to select the optimal simulation parameters, which will be further used in the study of more complex spin systems. A comparative analysis is carried out with the results of MC modelling and the exact solution of Onsager.

At the first stage, the network was trained on spin configurations obtained during on MC simulation with the following parameters: system size: 10×10, $T = 0.1 \ldots 5.0$ with a step of 0.01, the number of MC steps for preliminary equilibration of the system: 10000, the number of MC steps for calculating thermodynamic averages in the Metropolis algorithm: 10000, the sample size of configurations for training the network: 50 per one step in temperature, the results are shown in Fig. 2. In Fig. 2, the result of applying a convolutional neural network to the calculation of the critical point T_c was presented in comparison with Onsager's exact solution and the result of MC simulation.

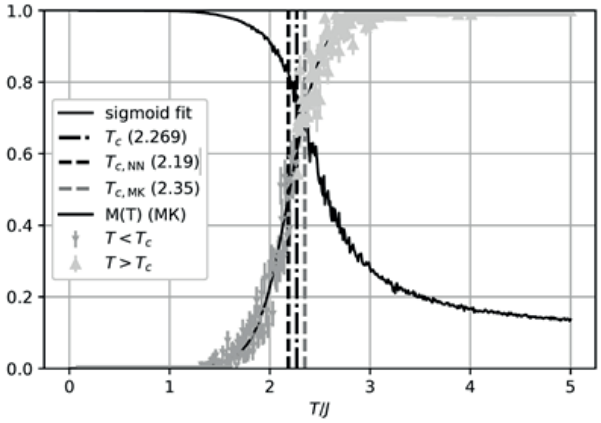

Fig. 2. Results of T_c calculations by various methods

The effect of system size on the accuracy of the obtained results was tested on the system with 20×20 spins. These values were generally similar to the ones given above. It should be noted that an increase of the system size had a positive effect on the results of MC modelling in the calculations of T_c: $T_c = 2.29$, due to a decrease of the influence of the size effect, while the increase in the system size did not significantly affect the results of the neural network operation. The accuracy of the predicted value of the critical temperature, in comparison with the case described above, on average did not change, and in some numerical experiments it even worsened, because network training is based on a probabilistic approach.

The recognition of different phases of the Heisenberg spin system with magnetic skyrmions

Our second way of using the CCN was a data analysis of a study of different phases that appeared depending on the magnitude of the external magnetic field and temperature T at fixed Dzyaloshinskii-Moriya interaction D, see Fig. 3. The diagram in Fig. 3 shows that in the low temperature zone we have ordered phases. Thus, the ground state is the spiral phase, which is observed in the field range $0 - 0.3$; with a further increase in the magnetic field, the spiral phase passes into the skyrmion phase, after which a further transition from one phase to another is observed, up to the temperature range $T > 0.5$, where the system goes into a paramagnetic state. Skyrmions are thermally stable in a fairly wide temperature range, with an external magnetic field H_z from 0.8 to 1.5. The convolutional neural network was used to analyze the data obtained from the Monte Carlo simulations for the recognition of the different phases of the spin system, dependent on the simulation parameters.

One of the conventional methods is to compute the skyrmion number, which is evaluated to keep track of the skyrmion creation process. However, it does not indicate the mixed states of the spin systems very well, depending on the simulation parameters, e.g. a spiral-skyrmion phase, therefore, we use the convolutional neural network in our work.

In a magnetic film, with an increase of the magnetic field strength and temperature, various phases were observed for the flat Heisenberg spin systems: Spiral (S), Labyrinths (L) Spiral-skyrmion (SS) Skyrmion (Sk), Skyrmion-Ferromagnetic (SkF), Ferromagnetic (F), Paramagnetic (P) phases, see Fig. 3. In Skyrmion phase, due to the alignment of the stripes against the magnetic

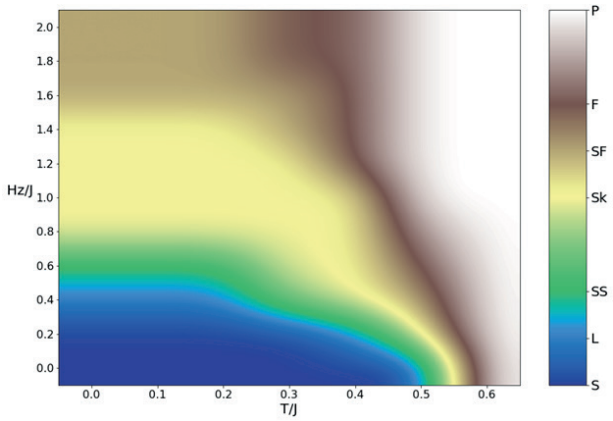

Fig. 3. Phase diagram (T, H_z) at $D = 1.3$

field, stable skyrmions are formed in the system. In these skyrmions, the spins of the nucleus are directed against the magnetic field. In this study, skyrmions of the Bloch type were formed.

Conclusion

The paper considered the application of convolutional neural networks to determine the critical temperature of a second-order phase transition in comparison with performed MC simulations and known solutions. As it was shown above CNN could be successfully used to such problems by reducing them to the problem of classifying spin states at different temperatures. The dependence on the number of Monte Carlo steps and the sample size for the accuracy of training the network and its subsequent application is shown in comparison with the Metropolis algorithm. Systems of various sizes and the influence of the size effect on the accuracy of the results are considered.

The authors also noted the feature of the results obtained using neural networks to determine T_c: if the calculation is performed using the Metropolis algorithm, then always $T_c^{MC} \geq T_c^{exact}$. In turn, in the calculations carried out using convolutional neural networks $T_c^{NN} \geq T_c^{exact}$. The reasons for this behaviour are the subject of future research, during which it is planned to apply neural networks for studying more complex models and lattices.

Also, in the frame of the classical two-dimensional Heisenberg model, a spin system with direct short-range exchange was modelled, and a study of its competition with the Dzyaloshinskii-Moriya interaction was carried out. Due to the direct exchange interaction, the neighbouring spins of the system are collinearly aligned, and, in turn, the Dzyaloshinskii-Moriya interaction contributes to the deviation of the spins from parallel orientation. As a result, competition results between collinear and noncollinear alignments of spins, which leads to the transition of the system of spins from a ferromagnetic to a spiral ground state. In the presence of an external magnetic field, stable topological structures, i.e., magnetic skyrmions, are generated in such systems.

One of the most effective and popular approaches in statistical physics is Monte Carlo simulation, which consists of a stochastic sample over the state space and an estimate of physical quantities. Monte Carlo methods are not only actively used to study various physical systems, but also continue to actively develop and improve due to the development of supercomputers. The ability of modern machine learning algorithms to classify, identify and interpret large data sets and, on their basis, to predict new properties and states of the systems under study provides an additional paradigm to the above approach for processing the exponentially increasing number of analyzed states in statistical physics.

REFERENCES

1. **Sherrington D., Kirkpatrick S.,** Solvable model of a spin-glass, Phys. Rev. Lett. 35, (1975) 1792–1796

2. **Swendsen R. H., Wang J.-S.,** Nonuniversal critical dynamics in Monte Carlo simulations, Phys. Rev. Lett. 58, (1987), 86

3. **Belokon V. I., D'yachenko O. I., Kapitan V. Y.,** On the possible application of the method of random exchange interaction fields for studying the magnetic properties of the rocks, Izvestiya, Physics of the Solid Earth. 51 (5) (2015) 622–629

4. **Belokon V. I., Kapitan V. Y., Dyachenko O. I.,** Concentration of magnetic transitions in dilute magnetic materials, J. of Physics: Conf. Ser., 490 (1) (2014) 012165

5. **Prudnikov P.V., et al.,** Influence of anisotropy on magnetoresistance in magnetic multilayer structures, Journal of Magnetism and Magnetic Materials. 482 (2019) 201–205

6. **Makarov A.G., et al.,** On the numerical calculation of frustrations in the ising model, JETP Letters, 110 (10) (2019) 702–706

7. **Landau D., Binder K.,** A guide to Monte Carlo simulations in statistical physics, Cambridge University press, Cambridge, 2003

8. **Carleo G. et al.,** Machine learning and the physical sciences, Reviews of Modern Physics, 91 (4) (2019), 045002

9. **Carrasquilla J., Melko R. G.,** Machine learning phases of matter, Nature Physics, 13 (5), (2017) 431–434

10. **Kapitan V., et al.,** Numerical simulation of magnetic skyrmions on flat lattices, AIP Adv. 11, (2021) 015041

11. **Abadi M.et al.,** Tensorflow: Large-scale machine learning on heterogeneous distributed systems // arXiv preprint arXiv:1603.04467. 2016.

12. **Dzyaloshinsky I.,** A thermodynamic theory of "weak" ferromagnetism of antiferromagnetics, J. of Physics and Chemistry of Solids, 4 (1958) 241–255

13. **Moriya T.,** Anisotropic superexchange interaction and weak ferromagnetism, Physical Review 120, (1960) 91

14. **Soldatov K. S., Nefedev K. V., Kapitan V. Yu., Andriushchenko P. D.,** J. Phys. Conf. Ser. 741, (2016) 012199

THE AUTHORS

PERZHU Aleksandr V.
perzhu_av@dvfu.ru
ORCID: 0000-0001-9717-3773

KAPITAN Dmitrii Yu.
kapitan.diu@dvfu.ru
ORCID: 0000-0001-9815-1891

VASILIEV Egor V.
vasilev.eva@dvfu.ru
ORCID: 0000-0001-5209-510X

RYBIN Alexey E.
rybin.ae@dvfu.ru
ORCID: 0000-0002-1055-9217

KOROL Alena O.
korol.ao@dvfu.ru
ORCID: 0000-0001-8527-0752

KAPITAN Vitalii Yu.
kapitan.vyu@dvfu.ru
ORCID: 0000-0002-5068-8910

Received 22.05.2022. Approved after reviewing 13.06.2022. Accepted 03.07.2022.

Conference materials
UDC 539.23 539.216.1
DOI: https://doi.org/10.18721/JPM.153.116

Morphology evolution of mesoporous silicon powder formed by Pd-assisted chemical etching at temperatures of 25 – 75 °C

O. V. Volovlikova [1] ✉, G. O. Silakov [1], S. A. Gavrilov [1], E. N. Lazorkina [1]

[1] National Research University of Electronic Technology, Moscow, Russia

✉ 5ilova87@gmail.com

Abstract: In this paper, we report the preparation of porous silicon powder by two-step Pd-assisted chemical etching with metallurgical grade polycrystalline silicon powder by varying the etching time from 30 to 90 minutes and solution temperature from 25 °C to 75 °C with and without thermal stabilization. A rapid temperature increase is observed with a maximum value of 95 – 100 °C in the case of etching without thermal stabilization. A high etching time of 90 minutes and a dissolution temperature above 50 °C have a negative effect on the formation of porous particles, which leads to the complete dissolution of silicon particles. The slow temperature growth for all initial temperatures in the case of the etching with thermal stabilization is observed. We established the positive effect of thermal stabilization in the process of etching on the thickness of the pores walls, reducing the uncontrollably growing rate of silicon etching, as a result, overetching of silicon.

Keywords: porous silicon powder, MACE, crystal size, Raman spectroscopy, thermal stabilization, temperature-time dependencies

Funding: The study was supported by a grant from the Russian Science Foundation (project no. 19-79-00205) in the part related to sample formation, investigations by Quantachrome Nova 3200e device, at the expense of State Task of the Ministry of Science and Higher Education of the Russian Federation 2020-2022 no. FSMR-2020-0018 in the part related to sample characterization using LabRAM HR UV-VIS-NIR.

Citation: Volovlikova O. V., Silakov G. O., Gavrilov S. A., Lazorkina E. N., Morphology evolution of mesoporous silicon powder formed by Pd-assisted chemical etching at temperatures of 25 – 75 °C, St. Petersburg State Polytechnical University Journal. Physics and Mathematics. 15 (3.1) (2022) 93–100. DOI: https://doi.org/10.18721/JPM.153.116

Материалы конференции
УДК 539.23 539.216.1
DOI: https://doi.org/10.18721/JPM.153.116

Эволюция морфологии мезопористого порошка кремния, сформированного Pd-стимулированным химическим травлением при температурах 25-75 °C

О. В. Воловликова [1] ✉, Г. О. Силаков [1], С. А. Гаврилов [1], Е. Н. Лазоркина [1]

[1] Национальный исследовательский университет «МИЭТ», Москва, Россия

✉ 5ilova87@gmail.com

Аннотация. В этой работе мы сообщаем о формировании порошка пористого кремния путем двухстадийного химического травления металлургического порошка поликристаллического кремния с использованием Pd путем изменения времени травления от 30 до 90 минут и температуры раствора от 25 до 75 ° C с термостабилизацией

и без нее. Наблюдается быстрое повышение температуры с максимальным значением 95 – 100°C в случае травления без термостабилизации. Длительное время травления 90 минут и температура растворения выше 50°C оказывают негативное влияние на формирование пористых частиц, что приводит к их полному растворению. Наблюдается медленный рост температуры для всех начальных температур в случае травления с термостабилизацией. Показано положительное влияние термостабилизации в процессе травления на толщину стенок пор, снижающее неконтролируемо растущую скорость травления кремния, и как следствие, перетрав кремния.

Ключевые слова: порошок пористого кремния, MACE, размер кристалла, рамановская спектроскопия, термостабилизация, температурно-временные зависимости

Финансирование: Исследование выполнено за счет гранта Российского научного фонда (проект № 19-79-00205) в части, связанной с формированием образцов, исследованием на приборе Quantachrome Nova 3200e, за счет государственного задания Министерства науки и высшего образования Российской Федерации 2020-2022 № FSMR-2020-0018 в части, связанной с определением характеристик пористого кремния с использованием LabRAM HR UV-VIS-NIR.

Ссылка при цитировании: Воловликова О. В., Силаков Г. О., Гаврилов С. А., Лазоркина Е. Н. Эволюция морфологии мезопористого порошка кремния, сформированного Pd-стимулированным химическим травлением при температурах 25 – 75 °C // Научно-технические ведомости СПбГПУ. Физико-математические науки. 2022. Т. 15. № 3.1. С. 93–100. DOI: https://doi.org/10.18721/ JPM.153.116

Introduction

Increasing energy demand caused by technological advancement results in high consumption of non-renewable natural resources, in particular, natural gas. Depletion of these resources is one of the most significant global issues today. At present, hydrogen fuel cells are one of the most promising resources and energy-saving technologies. Their benefits include low emissions, high efficiency, portability, and silent operation [1]. One possible implementation is generating electricity by means of alcohol oxidation directly in a fuel cell [2, 3]. Recent scientific research results on alternative fuels have highlighted a growing interest in using porous silicon for miniaturized fuel cells and energy generators [4–6]. Potential benefits of using porous silicon for this purpose include several factors; in particular, high specific surface area and surface chemical reactivity, the possibility of modifying the surface morphology of the porous layers at the nano- and micro levels [7, 8]. In this regard, using porous Si powder allows increasing the specific surface area due to an extensive pore network [9] and higher cost-effectiveness thanks to replacing expensive single-crystal wafers with cheaper metallurgical Si powder.

Metal-assisted chemical etching (MACE) is a promising method for porous Si powder fabrication [10, 11] without an external current source. Various metals have been used for studying the MACE of Si powder [7, 12]. It has been shown that Ag [13, 14] and Fe [15] are among the most cost-effective and efficient. The implementation of MACE to Si powders provides the increase of pore diameter range and total porosity. Nonetheless, this results in the additional complexity of technology caused by an increased number of process parameters needing to be monitored. For instance, apart from the reactant concentration, etching duration, type and amount of metal, the formation of pores will also be affected by powder particle size. Furthermore, the etching of metallurgical-grade Si powder is accompanied by a number of difficulties, in particular, flotation, preventing the wetting of Si and hence uniform etching. This concern can be successfully remedied by adding an appropriate surfactant. Another general challenge consists of increasing the solution temperature that leads to a higher etching rate [11]. This causes undesirable effects such as overetching of small particles and underetching of large particles. Additionally, as shown earlier [16], the etching of Si powder with Ag and Fe as a catalyst is accompanied by the formation of silicate sediment. In order to avoid this phenomenon, we proposed using the Pd catalyst [17].

This study aims to adapt the Pd-assisted chemical etching for the metallurgical-grade Si powder so as to control the surface area and porous volume of the porous powder using different process duration and solution temperature; thereby decreasing the flotation and overetching effect using thermal stabilization of the solution during the etching.

Materials and Methods

Porous layers were formed at the surface of metallurgical-grade polycrystalline Si powder (Fig. 1, *a*) by Pd-assisted chemical etching. Mean particle diameter is 0.2 – 5 μm. Si powder was treated in a mixture of 0.5 g/L $PdCl_2$ and 0.65 M HC1 aqueous solutions for 30 min at 25 °C. Constant stirring was used to provide the uniform distribution of Pd particles on the surface of Si powder (Fig. 1, *b*). Etching of Si/Pd powder was carried out in a mixture of 40 % aqueous HF solution, 30 % aqueous H_2O_2 solution, and deionized water in a volume ratio of 25:10:4 25°C, 50°C, and 75°C both with and without thermal stabilization. Etching duration was 30 – 120 minutes. For thermal stabilization, a liquid thermostat was used with water as a heat carrying medium and a Teflon cell provided with a ventilated lid. The solution temperature was controlled using an external *k*-type thermocouple, covered with varnish for HF protection. Finally, the powders were rinsed with a mixture of deionized water and ethanol, centrifuged (MPW-351, Advanced Worldwide Technologies, Russia) and dried in room air for 24 hours.

The surface morphology of porous Si powder was analyzed using a scanning electron microscope (SEM; HeliosNanoLab 650, FEI Company, USA). Raman spectroscopy (LabRAM HR UV-VIS-NIR Raman Microscope, Horiba Scientific, Japan) was used to characterize porous silicon structures. The surface area and pore size of the porous structure formed by etching were measured using N_2 adsorption-desorption isotherms on a Quantachrome Nova 3200e adsorption analyzer (Quantachrome Instruments, USA). Prior to measurements being taken, the porous Si samples were degassed at 300 °C for 3 hours to minimize contamination and water in the pores. Then, nitrogen adsorption and desorption isotherms were measured at 77 K. The specific surface area was calculated using BET (Brunauer-Emmett-Teller) method. The relative pressure interval was from 0.05 to 0.25. The BJH (Barrett-Joyner-Halenda) method was used for the calculation of the mesopore size distribution using the Kelvin model of pore filling [18, 19].

Results and discussions

Figure 1, *c* shows the micrographs of Si powder after 120 min etching in $HF/H_2O_2/H_2O$ at 25 °C.

As a result of the SEM studies carried out, it has been observed that porous silicon powders contain mesopores. Figure 2 shows the nitrogen adsorption/desorption isotherms at 77 K of the Si powder before etching and after etching at 25 °C, 50 °C and 75 °C throughout 30 – 90 minutes. The presence of mesopores is confirmed by a capillary-condensation hysteresis on the isotherms.

The specific surface area of the Si powder determined by the Brunauer-Emmett-Teller (BET) method was found to be 4.7 $m^2 \cdot g^{-1}$ for initial powder, 5.4 – 19.7 $m^2 \cdot g^{-1}$ for samples etched for 25 °C, 6 – 25.9 $m^2 \cdot g^{-1}$ for samples etched for 50 °C, and 4.67 – 13.6 $m^2 \cdot g^{-1}$ for samples etched for 75 °C. The total volume of the Si powder determined by the Barrett-Joyner-Halenda (BJH)

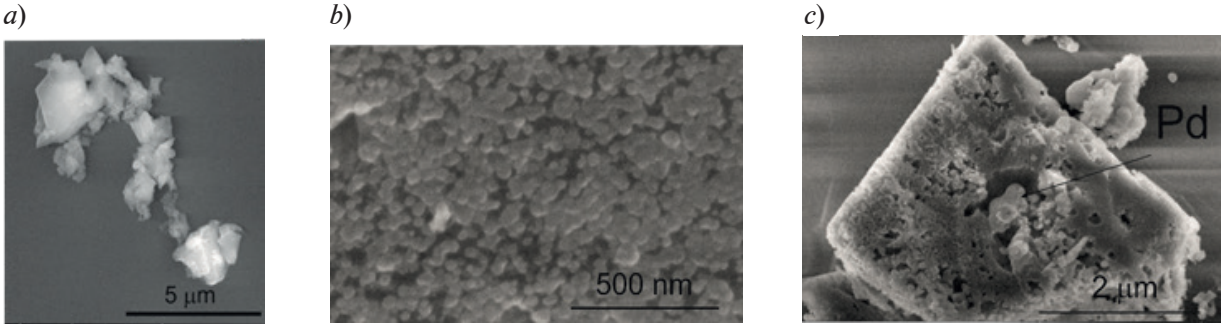

Fig. 1. SEM images of Si powder (*a*), Pd nanoparticles on silicon powder (*b*), porous silicon powder after 120 min etching (*c*)

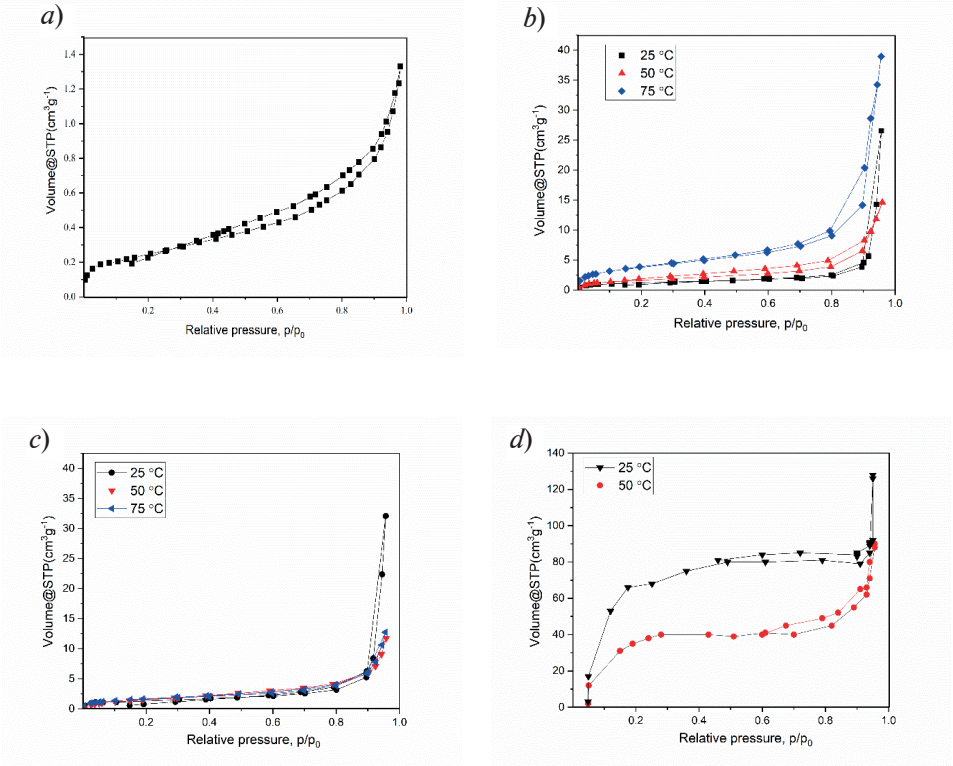

Fig. 2. Isotherms of N_2 adsorption-desorption at 77 K for Si powders before etching (*a*) and after etching for 30 (*b*), 60 (*c*) and 90 min (*d*)

method was found to be 17 cc·g^{-1} for initial powder, 43 – 196 cc·g^{-1} for samples etched for 25 °C, 18 – 45 cc·g^{-1} for samples etched for 50 °C, and 19 – 60 cc·g^{-1} for samples etched for 75 °C. The pore size distribution plots obtained by the BJH method are shown in Fig. 3.

According to the data presented, all samples contain mesopores with diameters in the

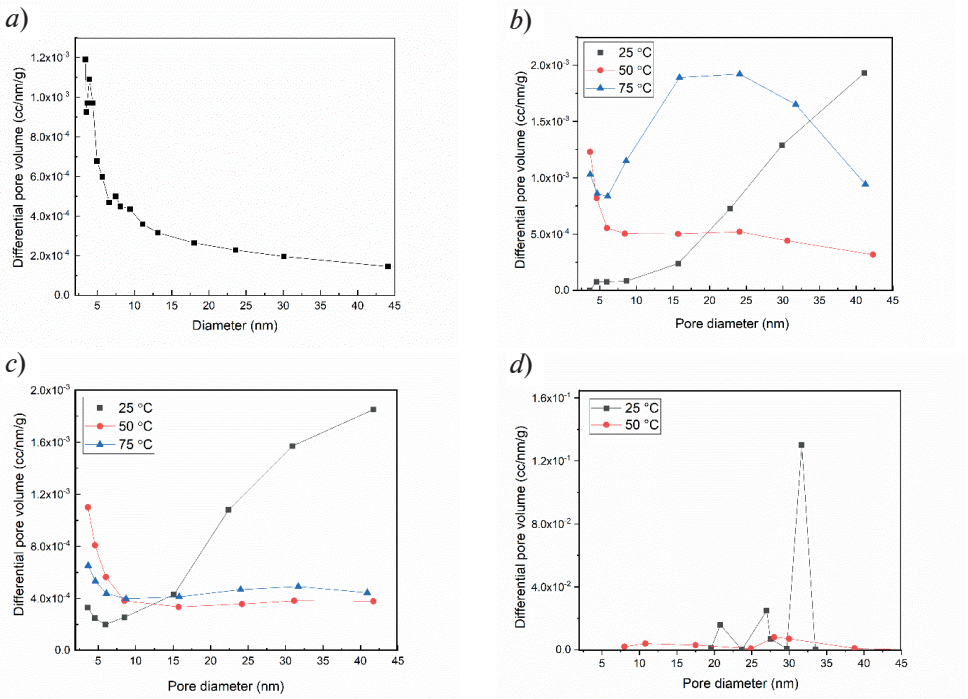

Fig. 3. Pore size distributions for Si powders before etching (*a*), after etching during 30 (*b*), 60 (*c*) and 90 min (*d*)

range of 3 – 42 nm. Etching duration and solution temperature are known to be an essential parameter for the formation of porous materials especially when etching the powder, mainly due to problems such as flotation and possible overetching. The metallurgical-grade Si powders are dominated by pores with a diameter of 4 nm. Moreover, the samples after etching at 25, 50 and 75 °C are dominated by pores with a diameter of 21 – 41.67 nm, 3.65 – 31.1 nm, and 2.41 – 31.7 nm, respectively. The surface area of the porous powder and specific pore volume increase to a certain value with an increase in the solution temperature and etching duration. With further etching, the porous layer dissolves. The size of the pores increased and bond with the nearest pores with an increase in the duration of etching. Subsequently, the quantity of the pores with a big diameter decreases and the quantity of the pores with a small diameter increases.

Raman spectroscopy provides a swift and convenient method for the study of vibrational and structural properties of the porous material. It is also possible to obtain the average size of the crystals (pore walls) from the position of the phonon Raman peak [20, 21]. The shift ($\Delta\omega$) increases with increasing etching time without thermal stabilization. Thus, the maximum shift is 13.6 cm^{-1} for the etching duration of 30 min, 17.1 cm^{-1} for 60 min, and 21.9 cm^{-1} for 90 min at 25 °C. Increasing wavenumber shift indicates that the crystal size decreases, and thus, pore walls become thinner. At the same time, the etching duration of 120 min induces the formation of porous Si powder with $\Delta\omega$ = 9.6 cm^{-1}. Fig. 4 shows the Raman spectra of porous Si powder formed by MACE with 60 min etching duration at 25 °C, 50 °C and 75 °C without thermal stabilization.

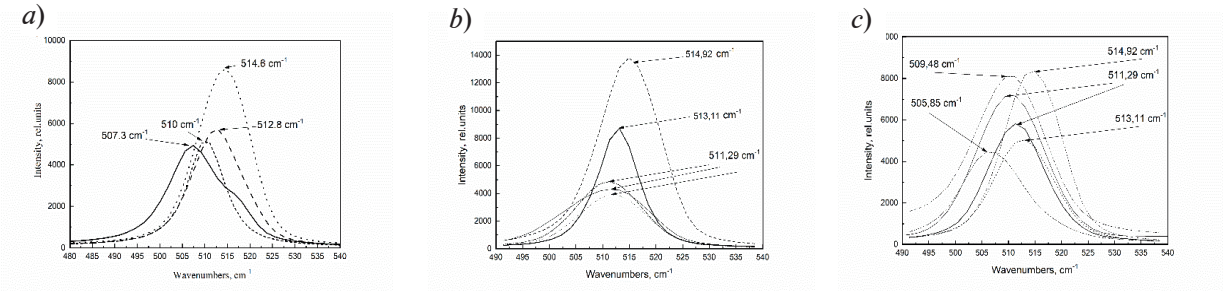

Fig. 4. Raman spectra obtained for Si powder etched in $HF/H_2O_2/H_2O$ with 60 min etching at 25 °C (*a*), 50 °C (*b*), 75 °C (*c*)

The distribution of the size of powder particles is described by several spectra. Thus, the maximum shift $\Delta\omega$ is 17.1 cm^{-1} for 25 °C, 9.61 cm^{-1} for 50 °C and 27.7 cm^{-1} for 75 °C. For pure Si crystal and powder, a peak appears at 520.9 cm^{-1}. We used the equation (1) to calculate the size of the nanoparticles [22]:

$$\Delta\omega(D) = -A \cdot (\alpha/D)^{\gamma}, \quad (1)$$

where $\Delta\omega(D)$ is the Raman shift in nanostructures with diameter D, α is the lattice constant of silicon (0.543 nm) and A = 97.76 cm^{-1}, γ = 1.44 are the fit parameters that describe the phonon confinement in nanometric spheres of diameter D.

Table 1 shows crystal size of porous silicon powder after etching with different temperatures and durations with and without thermal stabilization. It was calculated by data of Raman spectra by Eq. 1.

The crystal size decreases to 2 nm with increasing temperature of etching up to 50 °C and 75 °C without thermal stabilization. Silicon powder completely dissolves, irrespective of the powder/etchant ratio at 75 °C and the etching duration of more than 90 min. According to the results on crystal sizes obtained for the etching with thermal stabilization, crystal size at 25 °C is slightly higher than without thermal stabilization. Crystals 5 – 6 times larger in size were detected at 50 °C. Furthermore, there is no complete dissolution of Si powder at 75 °C.

Table 1

Crystal size of porous Si powder formed by MACE with and without thermal stabilization at different temperatures

Etching duration (t), min	Crystal size (D), nm		
	Without thermal stabilization		
	T = 25 °C	T = 50 °C	T = 75 °C
30	2–7	2	2
60	2–4	2	2
90	2–3	2	full etching
120	2–5	2	full etching
Etching duration (t), min	Crystal size (D), nm		
	With thermal stabilization		
	T = 25 °C	T = 50 °C	T = 75 °C
30	6–10	2–13	2–11
60	2–6	3–10	3–8
90	2–6	2–10	2–8
120	4–13	2–6	2–4

Figure 5 shows plots of solution temperature as a function of etching duration at different initial temperatures. A rapid solution temperature increase is observed with a maximum value of 95 − 100 °C in the case of etching without thermal stabilization. The growth rates of temperature were found to be 16.8 °C/min, 30 °C/min, and 9.6 °C/min for initial temperatures of 25 °C, 50 °C and 75 °C, respectively. Following this, the temperature of the solution decreases monotonously and stabilizes at certain values. Moreover, the increase in temperature up to 90 − 100°C results in an uncontrolled dissolution of the powder and a decrease in the sample weight.

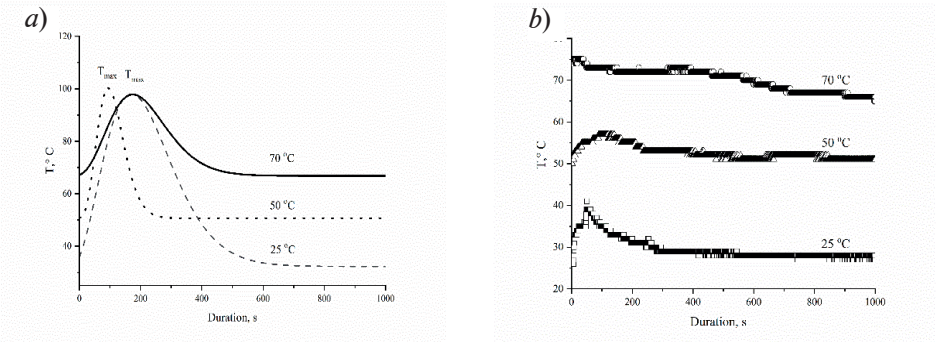

Fig. 5. Temperature-time dependencies for solutions during the Si powder etching process at different initial temperatures without (*a*) and with thermal stabilization (*b*).

Metal-assisted chemical etching, in particular Pd-assisted chemical etching, is an exothermic process. The heating of the solution is always occurrent. The stated temperature of the etching process varies with the surface area of Si particles accessible to the etchant. Therefore, the higher the surface area of Si powder, the higher the etching temperature and consequently, the etching rate. Thermal stabilization (cooling) allows the limitation of the growth rate of temperature (Fig. 5, *b*), and thereby prevents overetching of powder particles. The slow temperature growth for all initial temperatures in the case of the etching with thermal stabilization is observed. The temperature changes were found to be from 25 °C to 41 °C, from 50 °C to 57 °C and from 70 °C to 75 °C for initial temperatures of 25 °C, 50 °C and 75 °C, respectively.

The overetching of the porous layer is not observed due to the absence of solution overheating. It has a positive effect on the surface morphology of the porous powder and material properties. Therefore, the thermal stabilization should be used during the etching of the metallurgical silicon powder in a solution containing HF/H_2O_2.

Conclusions

Thus, it was shown that silicon powder etching in HF/H_2O_2 leads to form porous layer with the specific surface area equaling 5.4 − 19.7 m2·g^{-1} for samples etched for 25 °C, 6 − 25.9 m^2·g^{-1} for samples etched for 50 °C, and 4.67 − 13.6 m^2·g^{-1} for samples etched for 75 °C. The silicon powder etching for 90 and 120 minutes at T = 50 °C and 75 °C without stabilization leads to its complete dissolution. A rapid increase in the solution temperature is observed with a maximum value of 95 °C (100 °C in the case of etching without thermal stabilization). The temperature growth rates were found to be 16.8 °C/min, 30 °C/min, and 9.6 °C/min for initial temperatures of 25° C, 50 °C and 75 °C, respectively. Using thermal stabilization changes the dissolution rate of the powder, which leads to formation of a porous layer with a crystal size 5 − 6 times higher than without thermal stabilization. The temperature changes were found to be from 25 °C to 41 °C, from 50 °C to 57 °C and from 70 °C to 75 °C for initial temperatures of 25 °C, 50 °C and 75 °C, respectively.

REFERENCES

1. **Lazarouk S.K., Dolbik A.V., Jaguiro P.V., Labunov V.A., Borisenko V.E.,** Fast exothermic processes in porous silicon, Semiconductors. 39 (8) (2005) 881−883.

2. **Siwal S.S., Thakur S., Zhang Q.B., Thakur V.K.,** Electrocatalysts for electrooxidation of direct alcohol fuel cell: chemistry and applications, Materials Today Chemistry. 14 (2019).

3. **Shrivastava N.K., Harris T.A.L.,** Direct methanol fuel cells, Encyclopedia of Sustainable Technologies, Elsevier, 2017, 343−357.

4. **Dzhafarov T.D., Yuksel S.,** Alternative Fuel, University of Granada press, 2011, 309.

5. **Gautier G.,** Handbook of Porous Silicon, Canham L. ed., Cham: Springer International Publishing, Switzerland, 2014, 957−964.

6. **Dzhafarov T.D., Aydin Yuksel, S.,** Porous silicon-based direct hydrogen sulphide fuel cells, J. Nanosci. Nanotechnol. 11 (2011) 9012−9015.

7. **Huang Z., Geyer N., Werner P., de Boor J., Gosele U.,** Metal-assisted chemical etching of silicon: a review, Advanced Mater. 23 (2) (2011) 285−308.

8. **Sing N., Sahoo M.K., Kale P.G.,** Effect of MACE parameters on length of porous silicon nanowires (PSiNWs), Journal of Crystal Growth. 496 (2018) 10−14.

9. **Kolasinski K.W., Unger B.A., Ernst A.T., Aindow M.,** Crystallographically Determined Etching and Its Relevance to the Metal-Assisted Catalytic Etching (MACE) of Silicon Powders, Frontiers in Chemistry. 6 (2019) 651.

10. **Volovlikova O.V., Gavrilov S.A., Sysa A.V., Savitskiy A.I., Berezkina A.Yu.,** Ni-Activated Photo-Electrochemical Formation of Por-Si in $HF/H_2O_2/H_2O$ Solution, ElConRus 2017. (2017) 1213−1216.

11. **Pyatilova O.V. et al.,** Effect of ionic Ag+ transfer on localization of metal-assisted etching of silicon surface, Semiconductors. 50 (13) (2016) 1720−1725.

12. **Lee Ch.-L. et al.,** Pore formation in silicon by wet etching using micrometre-sized metal particles as catalysts, J. Mater. Chem. 18 (2008) 1015−1020.

13. **Nakamura T. et al.,** Properties of silver/porous-silicon nanocomposite powders prepared by metal assisted electroless chemical etching, Journal of Applied Physics. 108 (2010) 104315.

14. **Ouertani R., Hamdi A., Amri C., Khalifa M., Ezzaouia H.,** Formation of silicon nanowire packed films from metallurgical-grade silicon powder using a two-step metal-assisted chemical etching method, Nanoscale research letters. 9 (1) (2014) 574.

15. **Loni A. et al.,** Extremely High Surface Area Metallurgical-Grade Porous Silicon Powder Prepared by Metal-Assisted Etching, Electrochem. Solid State Lett. 14 (5) (2011) K25−K27.

16. **Pyatilova O.V., Gavrilov S.A. et all,** Role of Ag+ ion concentration on metal-assisted chemical etching of silicon, Solid State Phenomena. 213 (2014) 103−108.

17. **Volovlikova O.V., Gavrilov S.A., Silakov G.O., Zeleznyakova A.V., Dudin A.A.,** Preparation of hydrophobic porous silicon by metal-stimulated etching in the presence of a Pd Catalyst, Russ. Jour. of Electrochem. 55 (12) (2019) 1452−1462.

18. **Zeng W, Bai H.,** High-performance CO_2 capture on amine-functionalized hierarchically porous silica nanoparticles prepared by a simple template-free method, Adsorption. 22 (2016) 117.

19. **Weidemann S., et al.,** Controlled Pore Formation on Mesoporous Single Crystalline Silicon Nanowires: Threshold and Mechanisms, Journal of Nanomaterials. 16 (1) (2015) 171.

20. **Ossadnik Ch., Veprek S., Gregora I.,** Applicability of Raman scattering for the characterization

of nanocrystalline silicon, Thin Solid Films. 337 (1-2) (1999) 148–151.

21. **Kumar S. et al.,** Effect of power on the growth of nanocrystalline silicon films, Journal of Physics: Condensed Matter. 20 (33) (2008).

22. **Periasamy S. et al.,** Micro-Raman Scattering of Nanoscale Silicon in Amorphous and Porous Silicon, International J. of Res. in Phys. Chem. and Chem. phys. 231 (9) (2017) 1585.

THE AUTHORS

VOLOVLIKOVA Olga V.
5ilova87@gmail.com
ORCID: 0000-0002-4165-1024

SILAKOV Gennady O.
mr.komrad-13@ya.ru
ORCID: 0000-0001-5215-603X

GAVRILOV Sergey A.
pcfme@miee.ru
ORCID: 0000-0002-2967-272X

Lazorkina Elena N.
lena.lazorkina.00@mail.ru
ORCID: 0000-0002-9155-0512

Received 08.05.2022. Approved after reviewing 08.07.2022. Accepted 08.07.2022.

Conference materials
UDC 535.34:004.942
DOI: https://doi.org/10.18721/JPM.153.117

Radiation induced defects of zinc oxide particles with star and flower shapes

A. N. Dudin [1] ✉, V. I. Iurina [1], V. V. Neshchimenko [1], C. Li [2]

[1] Amur State University, Blagoveshchensk, Russia;
[2] Harbin Institute of Technology, Harbin, China
✉ andrew.n.dudin@gmail.com

Abstract: The paper presents the results of modeling a proton beam with energies of 100 keV on zinc oxide particles, with star and flower shapes, in the Geant4 software package. A high ability to accumulate primary defects was demonstrated for star-type particles in comparison with flower-type particles. A comparative analysis of the calculated data on the study of defects as a result of modeling with experimental data is carried out.

Keywords: zinc oxide, flower-shaped particles, star-shaped particles, degradation, radiation resistance, defects, protons, irradiation

Funding: The study was supported by the Ministry of Science and Higher Education of the Russian Federation № 122082600014-6.

Citation: Dudin A. N., Iurina V. I., Neshchimenko V. V., Li C., Radiation induced defects of zinc oxide particles with star and flower shapes. St. Petersburg State Polytechnical University Journal. Physics and Mathematics. 15 (3.1) (2022) 101–106. DOI: https://doi.org/10.18721/JPM.153.117

Материалы конференции
УДК 535.34:004.942
DOI: https://doi.org/10.18721/JPM.153.117

Радиационные дефекты частиц оксида цинка в форме звезды и цветка

А. Н. Дудин [1] ✉, В. Ю. Юрина [1], В. В. Нещименко [1], Ч. Ли [2]

[1] Амурский государственный университет, г. Благовещенск, Россия;
[2] Харбинский технологический университет, г. Харбин, Китай
✉ andrew.n.dudin@gmail.com

Аннотация. Представлены результаты моделирования пучка протонов с энергиями 100 кэВ на частицах оксида цинка в форме звезды и цветка в программном комплексе Geant4. Продемонстрирована высокая способность к накоплению первичных дефектов для частиц звездчатого типа по сравнению с частицами цветочного типа. Проведен сравнительный анализ расчетных данных по исследованию дефектов в результате моделирования с экспериментальными данными.

Ключевые слова: оксид цинка, частицы в форме цветка, частицы в форме звезды, деградация, радиационная стойкость, дефекты, протоны, облучение

Финансирование: Исследование выполнено при поддержке Министерства науки и высшего образования Российской Федерации № 122082600014-6.

Ссылка при цитировании: Дудин А. Н., Юрина В. Ю., Нещименко В. В., Ли Ч. Радиационные дефекты частиц оксида цинка в форме звезды и цветка // Научно-технические ведомости СПбГПУ. Физико-математические науки. 2022. Т. 15. № 3.1. С. 101–106. DOI: https://doi.org/10.18721/ JPM.153.117

Introduction

ZnO is a versatile semiconductor with excellent optical and electrical properties. The presence of a relatively large band gap and binding energy, combined with high optical stability when irradiated with charged particles, makes it promising for use in the space environment as thermal control coatings.

However, with prolonged exposure to sunlight quanta and ionizing study, a number of radiation defects and color centers are formed in zinc oxide grains [1–2]. This leads to degradation of optical properties due to absorption in the ultraviolet and visible regions, as well as to an increase in solar absorption. Therefore, it is important to investigate the effects of morphology on the behavior of the degradation of optical properties and related radiation defects.

Nanostructured particles have a number of differences from bulk materials: an increase in the specific surface of particles, as well as non-stoichiometry and high free surface energy, which provides a driving force for the diffusion of defects; structural distortions caused by size determine the stability of nanostructures; quantum limitation associated with electronic characteristics. The balance of the above properties and the concentration of point defects determine the stability of the optical properties under the action of ionizing radiation.

Studies of the radiation resistance and optical properties of pigments in thermal control coatings based on the direct-gap semiconductor II-IV of the semiconductor group ZnO have shown that the particle morphology plays an important role in the accumulation of radiation defects [3–4]. Therefore, we set ourselves the goal of comparing the resistance of ZnO particles with the 'star' and 'flower' form factors to the effects of low-energy protons, using both a model approach and a direct experimental one.

Materials and Methods

All chemicals used in this experiment were of analytical grade without purification.

Star-type particles were synthesized by the following method [5]: 0.9 mmol of $Zn(CH_3COO)_2 \cdot 2H_2O$ was dissolved in 1 mol of deionized water under magnetic stirring, then 14 mol of NH_4OH (25% aqueous solution) was added, after which 5.5 mmol of KBH_4 was added, continuing mixing. The solution was labeled in a Teflon lined autoclave. The closed autoclave was kept at 140°C for 8 hours. The autoclave was then cooled to room temperature naturally. The white product was collected without centrifugation and washed successively several times with deionized water and ethanol. The solution was dried in air at 60 °C without heat treatment.

To obtain flower type particles, 1 mol of deionized water and 1 mol of ethanol were mixed with 4 mmol of $Zn(CH_3COO)_2 \cdot 2H_2O$, followed by the addition of 25 mmol of NH_4HCO_3 and 0.8 mmol of γ-methacryloxypropyltrimethoxysilane. The solution was poured into a Teflon-coated autoclave, which was kept at 100° C for 6 hours. After cooling, the autoclave was opened, the white product was collected and washed successively several times with deionized water and ethanol. Finally, the thick solution was air dried at 60 °C and then heat treated at 650 °C for 3 hours.

The surface morphologies of the powders were analyzed by using a scanning electron microscope (SEM) Helios NanoLab 600i. The specific surface area of the powder was determined by the Brunauer–Emmet–Teller (BET) method with physical adsorption of nitrogen using an AutoSorb 6iSA technique.

Modeling was carried out in the GEANT4 software package, the star-type target geometry is a set of 13 cylinders 0.25 μm in diameter, crossed with each other, with a total swept diameter of 5 μm. The geometry of the flower-type target was half a sphere with a radius of 3 μm with segments of spheres included in it, forming petals with a thickness of 0.05 μm. The particles under consideration were packed into an ensemble sized 35×35×14 μm for star type particles, 36×36×9 μm for flower type particles.

Irradiation was carried out relative to the normal to the target surface by a monoenergetic proton beam with an energy of 100 keV and a fluence of 5×109 cm^{-2}. The threshold displacement energy for the zinc atom was chosen to be 52 eV, and 57 eV for the oxygen one [6].

When modeling, the processes used in the QGSP_BIG_EMY physics set were taken into

account, including: ionization of the medium, multiple scattering, elastic and inelastic scattering of hadrons, bremsstrahlung, etc.

The Frenkel defect concentration calculated in GEANT4 was determined using the modified Kinchin-Pisa formula [7]:

$$FP \sim \frac{E_{dis}}{2.5E_d}, \quad (1)$$

where E_d is the threshold displacement energy, E_{dis} is the dissipated energy in nuclear collisions.

Samples were tested using the Space Environment Simulator, which was composed of a system of vacuum pumps, chamber 0.06 m^3 in useful volume, a source of electromagnetic solar radiation, electron and proton Van de Graaff accelerators, and an in situ optical reflectance measurement system. The samples were irradiated by protons with an energy of 100 keV fluence 5×10^{15} cm^{-2} with a flux of 5×10^{11} $cm^{-2}s^{-1}$ in vacuum 2.5×10^{-4} Pa, while the initial vacuum was 5× 10×5 Pa.

The comparison was made with synthesized ZnO star and flower particles obtained by the hydrothermal method described above.

Results and Discussion

The SEM micrographs of synthesized particles are presented in Fig. 1. Star-type particles have a hierarchical structure with an average size of about 4 − 7 μm and consist of a radial arrangement of hundreds of nanorods. Flower-type particles with a size of 4 − 8 μm have rounded shapes, consisting of sheets located in an arbitrary direction. The yield of star and flower type particles is about 80%. The resulting nanostructured particles are micron in size, but consist of nanoparticles; accordingly, such particles have a combination of properties at the micro- and nanoscales. The average specific surface area measured by the BET method is 44.3 ± 2.9 m^2g^{-1} for star-type particles and 68.4 ± 6.6 m^2g^{-1} for flower-type particles.

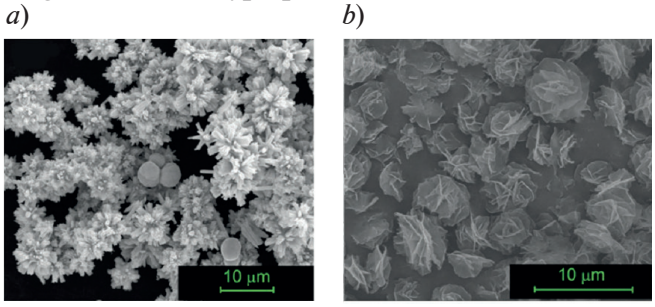

Fig. 1. SEM images of star (*a*) and flower (*b*) ZnO particles

The process of a proton beam with an energy of 100 keV with a fluence of 5×10^9 cm^{-2} passing through particles of the star and flower type is visualized in Fig. 2 and 3, respectively.

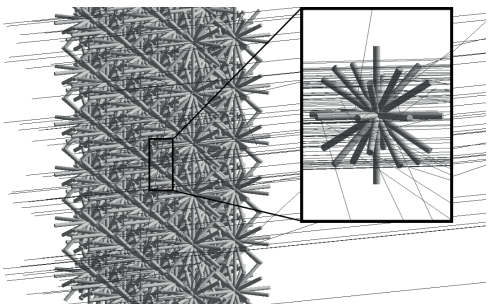

Fig. 2. Simulation in Geant4: zinc oxide particles star shape irradiated by protons

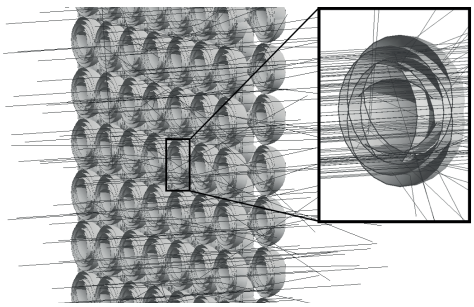

Fig. 3. Simulation in Geant4: zinc oxide particles flower shape irradiated by protons

Numerical calculations of the effect of radiation on a star-type particle give the proton mean free path equal to 1.41 Å The total number of primary knocked-on atoms (PKA) is 4.7×10^6 cm^{-3}. Concentration of formed primary defects (Frenkel pairs) is 1.88×10^{17} cm^{-3}. These parameters

take the following values for a flower-type particle: mean free path of 1.65 Å; PKA of 1.3×10^6 cm^{-3}; concentration of primary defects of 4.82×10^{16} cm^{-3}.

The reflectance spectra of the synthesized particles (Fig. 4) show a close match of the main absorption edge. The diffuse reflection coefficient before ($\rho_{\lambda0}$) and after irradiation ($\rho_{\lambda\phi}$) of flower-type particles is higher than that of star-type particles in the wavelength range from the edge of the main absorption to the near infrared (NIR) region. The difference between the spectra of synthesized particles in the near infrared region of the spectrum is due to free electrons and chemisorbed gases.

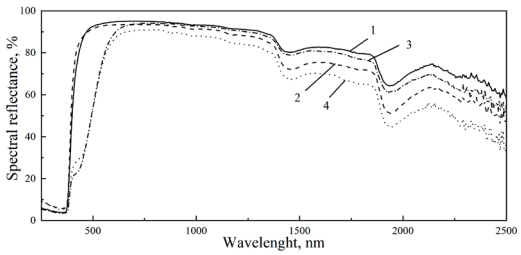

Fig. 4. Reflection spectra of synthesized particles before and after irradiation for flower (*1*, *3*) and star types (*2*, *4*)

The induced absorption spectra (Fig. 5) of the synthesized particles after irradiation with protons ($\Delta\rho_\lambda = \rho_{\lambda0} - \rho_{\lambda\Phi}$) show the main peak in the UV and visible spectral region. The induced absorption bands in the region from 350 to 630 nm of synthesized star and flower particles are similar in intensity and have a maximum value of 60%. As for the near-IR region, there is a decrease in the induced absorption spectrum for flower-type particles, in comparison with star-type particles. The difference in the intensity of the absorption bands in this region reaches 5%.

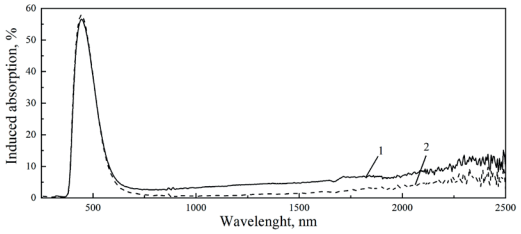

Fig. 5. Induced absorption spectra of synthesized particles for star (*1*) and flower (*2*) types

The ratio of intensities between different types of particles is associated with different concentrations of radiation defects Zn_i, V_{Zn}, O_i and V_O in different charge states, which are absorbed in different parts of the spectrum. The absorption of light quanta in the UV region is due to centers associated with Zn_i, but the absorption in the visible region of the spectrum with V_{Zn}, O_i, V_O and related complexes V_{Zn}-O_i and V_{Zn}-H, which is formed during implantation of hydrogen into the crystal lattice of ZnO. The absorption intensity in the near infrared region of the spectra after irradiation increases due to the Urbach tail.

The basic processes leading to the formation and accumulation of such defects are denoted as follows: Zn_{Zn}^X, O_O^X refer to atoms of zinc and oxygen in the lattice; $Zn_i^{\cdot\cdot}$, $Zn_i^{\cdot}$, V_{Zn}'', V_{Zn}', O_i'', O_i', $V_O^{\cdot\cdot}$, $V_O^{\cdot}$ to interstitial ions and vacancies of oxygen and zinc in different charge states; (H•)*, H• correspond to accelerated and thermalized protons; e′, h• to electron and hole.

The formation and separation of charge carriers by irradiation with accelerated protons may occur during the reactions of the formation of interstitial zinc and oxygen:

$$Zn_{Zn}^X + O_O^X + (H^{\cdot})^* \rightarrow V_{Zn}' + Zn_i^{\cdot\cdot} + O_O^X + H, \quad (2)$$

$$V_{Zn}^{'} + Zn_i^{\bullet\bullet} \rightarrow V_{Zn}^{X} + Zn_i^{\bullet}, \quad (3)$$

$$Zn_{Zn}^{X} + O_O^{X} + (H^{\bullet})^{*} \rightarrow Zn_{Zn}^{X} + V_O^{\bullet\bullet} + O_i^{'} + H, \quad (4)$$

$$V_O^{\bullet\bullet} + O_O^{'} \leftrightarrow V_O^{\bullet} + O_i^{X}. \quad (5)$$

The numerous knocked-out atoms can induce the cascade of atomic collisions. As a result, no equilibrium and inhomogeneous distribution of point defects: in the center vacancies predominate, on the periphery—interstitial atoms. For nanostructured particles at high energies of impinging particles normally only a small part of the projectile energy is deposited onto the nanosystem, in contrast to the case of irradiation of bulk systems when all the energy is eventually dispersed in the sample [8]. The following stage is defect recovery, i.e., the mutual recombination of vacancies and interstitial atoms, resulting in both point defects disappearance. Other processes simultaneously occur, such as vacancies being captured by pores and dislocations of the unoccupied type, the interstitial atoms being absorbed by dislocations, and the association of vacancies with complexes.

The numerous knocked-out atoms can induce the cascade of atomic collisions. As a result, no equilibrium and inhomogeneous distribution of point defects: in the center vacancies predominate, on the periphery—interstitial atoms. For nanostructured particles at high energies of impinging particles normally only a small part of the projectile energy is deposited onto the nanosystem, in contrast to the case of irradiation of bulk systems when all the energy is eventually dispersed in the sample [8]. The following stage is defect recovery, i.e., the mutual recombination of vacancies and interstitial atoms, resulting in both point defects disappearance. Other processes simultaneously occur, such as vacancies being captured by pores and dislocations of the unoccupied type, the interstitial atoms being absorbed by dislocations, and the association of vacancies with complexes.

Thermalized hydrogen and oxygen can diffuse from the lattice to the pigment surface with the subsequent desorption. The remaining defects after this stage are stable to exist for a long time. These defects will further define optical properties of a pigment. These peaks can be attributed to the surface molecules oxygen or hydrogen, or its association with lattice cation vacancies such as (V_{Zn}-H) [8].

Thermalized protons can interact with zinc vacancies or interstitial oxygen:

$$V_{Zn}^{'} + H_i \rightarrow V_{Zn}^{X} + H_i^{'}. \quad (6)$$

The process of release begins with the surface oxygen and subsequently the oxygen in the lattice, which is then accompanied by appearance of anion vacancies and interstitial zinc in differently charged states. The molecular oxygen reaction can occur in the vacuum volume:

$$2O_O + Zn_{Zn} \leftrightarrow Zn_i^{\bullet\bullet} + 2e^{'} + O_2, \quad (7)$$

$$O_O^{X} \leftrightarrow V_O^{\bullet\bullet} + 2e^{'} + \frac{1}{2}O_2, \quad (8)$$

$$O_2 \leftrightarrow 2O_O + V_{Zn}^{''} + 2h^{\bullet}. \quad (9)$$

Conclusion

It has been established that ZnO particles of the flower type have a higher radiation resistance to the action of protons compared to ZnO particles of the star type This is indicated by the calculated values obtained in the simulation, which demonstrate a higher concentration of primary defects for star-type particles, i.e., 1.88×10^{17} cm^3 compared to 4.82×10^{16} cm^{-3} for flower-type particles. The synthesized flower-shaped particles have a higher reflectivity, which indicates a lower concentration of intrinsic pre-radiation defects, which, in turn, can become one of the factors determining a lower concentration of radiation defects compared to star-shaped particles. The induced absorption spectra of synthesized particles demonstrate a high concentration of induced defects for star-type particles, which directly correlates with the data obtained from the simulation. To summarize, we can conclude that ZnO particles of the flower type are more radiation-resistant to the effects of protons compared to ZnO particles of the star type.

REFERENCES

1. **Mikhailov M. M., Dvoretskii M. I.,** Analysis of diffuse reflection and absorption spectra of ZnO in the near-IR region, Sov. Phys. J. 31 (1988) 591–594.

2. **Li C., Lv J., Yao S., Hu J., Liang Z.,** Study of the degradation and recovery of the optical properties of H+-implanted ZnO pigments, Nucl. Instrum. Methods Phys. Res., Sect. B. 295 (2013) 11–15.

3. **Flores N. M., Pal U., Galeazzi R., Sandoval A.,** Effects of morphology, surface area, and defect content on the photocatalytic dye degradation performance of ZnO nanostructures, RSC Advances. 4 (77) (2014) 41099–41110.

4. **Dudin A. N., Neshchimenko V. V., Yurina V. Y.,** Radiation defects induced by proton exposure in hollow zinc-oxide particles, Journal of Surface Investigation: X-Ray, Synchrotron and Neutron Techniques. 14 (4) (2020) 823–829.

5. **Li L., Yang H., Qi G., Ma J., Xie X., Zhao H., Gao F.,** Synthesis and photoluminescence of hollow microspheres constructed with ZnO nanorods by H2 bubble templates, Chemical Physics Letters. 455 (1-3) (2008) 93–97.

6. **Lorenz K., Alves E., Wendler E., Bilani O., Wesch W., Hayes M.,** Damage formation and annealing at low temperatures in ion implanted ZnO, Applied Physics Letters. 87 (19) (2005) 191904–191906.

7. **Leroy C., Rancoita P. G.,** Principles of radiation interaction in matter and detection, 2nd Edition, World Scientific Publishing Co. 2016.

8. **Brauer G., Anwand W., Grambole D., Grenzer J., Skorupa W., Čížek J., Kuriplach J., Procházka I., Ling C.C., So C.K., Schulz D., and Klimm D.,** Identification of Zn-vacancy-hydrogen complexes in ZnO single crystals: A challenge to positron annihilation spectroscopy, Physical Review B. 79 (11) (2009) 115212–115227.

THE AUTHORS

DUDIN Andrey N.
andrew.n.dudin@gmail.com
ORCID: 0000-0002-4791-6353

NESHCHIMENKO Vitaly V.
v1ta1y@mail.ru
ORCID: 0000-0002-5559-4876

IURINA Viktoria I.
viktoriay-09@mail.ru
ORCID: 0000-0003-3611-9495

LI Chundong
lichundong@hit.edu.cn
ORCID: 0000-0003-2546-6395

Received 19.05.2022. Approved after reviewing 19.07.2022. Accepted 20.07.2022.

Conference materials
UDC 538.911; 537.311.33
DOI: https://doi.org/10.18721/JPM.153.118

Structures and electrical conductance at the initial stages of magnesium growth on Si(111)-Pb surface

M. V. Ryzhkova [1] ✉, D. A. Tsukanov [1]

[1] Institute of Automation and Control Processes Far Eastern Branch of the RAS, Vladivostok, Russia
✉ lavric@iacp.dvo.ru

Abstract: In the present work, we have studied the growth of Mg ultrathin films on the Si(111) surface modified by Pb reconstructions using low-energy electron diffraction and the four-point-probe method. The new binary surface reconstructions √7×√7-(Mg, Pb) and √19×√3-(Mg, Pb) have been observed for the first time. The growth of magnesium layers depends both on the structure of Pb-induced surface reconstruction and on the Mg deposition manner. It is assumed that inclusion of magnesium atoms in the √7×√7 surface structure stabilizes the growth of Mg film which is independent of the manner of deposition in this case. We have investigated surface electrical conductance after the formation of magnesium layers at room temperature until about 9 monolayers of Mg coverage. In addition to the magnesium film Mg(0001), the highest electrical conductance among the presented surface structures has been detected for the Si(111)-6×6-(Pb, Mg) surface phase that consists of the maximum number of metal atoms, both lead and magnesium.

Keywords: silicon, electrical conductance, surface structures, metal films, low-energy electron diffraction

Funding: The study was supported by a Russian Science Foundation grant no. 20-02-00497.

Citation: Ryzhkova M. V., Tsukanov D. A., Structures and electrical conductance at the initial stages of magnesium growth on Si(111)-Pb surface. St. Petersburg State Polytechnical University Journal. Physics and Mathematics. 15 (3.1) (2022) 107–112. DOI: https://doi.org/10.18721/JPM.153.118

Материалы конференции
УДК 538.911; 537.311.33
DOI: https://doi.org/10.18721/JPM.153.118

Структуры и электрическая проводимость на начальных стадиях роста Mg на Si(111)-Pb

М. В. Рыжкова [1] ✉, Д. А. Цуканов [1]

[1] Институт автоматики и процессов управления Дальневосточного отделения РАН, г. Владивосток, Россия
✉ lavric@iacp.dvo.ru

Аннотация. В данной работе с помощью дифракции медленных электронов и четырехзондового метода измерения электрической проводимости изучен рост сверхтонких пленок Mg на поверхности Si(111), модифицированной поверхностными фазами свинца. Поверхностные структуры √7×√7-(Mg, Pb) и √19×√3-(Mg, Pb) были получены впервые. Рост слоев магния зависит как от структуры поверхности, модифицированной Pb, так и от способа осаждения Mg. Предполагается, что включение атомов магния в структуру поверхности √7×√7 стабилизирует рост пленки Mg, который в данном случае не зависит от способа осаждения. Мы исследовали электрическую проводимость поверхности после формирования слоев магния при комнатной температуре до покрытия примерно 9 монослоями магния. Помимо пленки магния Mg(0001), наибольшая электрическая проводимость среди представленных поверхностных структур обнаружена для

поверхностной фазы Si(111)-6×6-(Pb, Mg), состоящей из максимального числа атомов металла.

Ключевые слова: Кремний, электрическая проводимость, поверхностные структуры, металлические пленки, дифракция медленных электронов

Финансирование: Исследование выполнено при поддержке РФФИ (грант № 20-02-00497).

Ссылка при цитировании: Рыжкова М. В., Цуканов Д. А. Структуры и электрическая проводимость на начальных стадиях роста Mg на Si(111)-Pb // Научно-технические ведомости СПбГПУ. Физико-математические науки. 2022. Т. 15. № 3.1. С. 107–112. DOI: https://doi.org/10.18721/ JPM.153.118

Introduction

Adsorption of metals on the silicon surface leads to the formation of ultrathin films or other nanostructures and attracts attention from the fundamental point of view as well as of practical interest. In particular, adsorption of magnesium has been intensively studied for the past few years because of the possible application in optoelectronics of the Mg_2Si silicide which is a narrow band gap semiconductor. The growth of Mg-induced superstructures and thin films has been examined previously by several groups [1–5]. It is known that adsorbed magnesium atoms on Si(111)-7×7 surface form a silicide layer at room temperature [1]; specifically, it features the first layer as a silicide formation [1–3], dependence of the growth mode on the flux rate [1, 3] or dependence on the deposition manner [4]. Given high flux rates (at relatively large doses) of magnesium deposition, in the first instance, a Mg_2Si silicide film is formed with the structure of $2/3\sqrt{3}\times2/3\sqrt{3}$ [1–4], followed by the growth of a polycrystalline magnesium film [1–4]. At low flux rate or small Mg doses, silicide islands grow starting from the initial stage of deposition, followed by the growth of a polycrystalline magnesium film [4].

In all cases, a large mass transport of silicon takes place and the resulting surface morphology must be quite complicated. However, when magnesium is deposited onto the 1×1-Pb reconstructed surface, some ordered superstructures, 4×4-(Mg, Pb) or 6×6-(Mg, Pb) [6, 7], are formed, and silicon mass transport is hindered up to 1 monolayer (ML) of adsorbed magnesium coverage. Such conditions have a strong impact on the growth of epitaxial film with an abrupt interface for a reactive system such as the Mg/Si(111) one.

In this work, we have studied the influence of surface reconstructions formed by preliminary Pb deposition on the growth of magnesium films. Moreover, Mg was deposited at room temperature on various surfaces containing both Pb and Mg atoms. The structural ordering of Si(111)-(Mg,Pb) systems was studied by low-energy electron diffraction (LEED) and surface conductance was investigated by four-point-probe (4PP) measurements *in situ*.

Materials and Methods

The experiments were performed in the dual ultrahigh vacuum chamber with a base pressure of 2×10^{-10} Torr. Silicon specimens with (111) surface orientation were used. All samples were *n*-type (P-doped) with the nominal electrical resistivity of 20 – 100 Ohm·cm. The sizes of specimen were 15×5×0.3 mm^3. Mg was deposited from a heated tantalum cell at rate of 0.6 ML/min. A magnesium amount was calibrated by the formation of 4×4-(Pb, Mg) and 6×6-(Pb, Mg) (Fig. 1, *a*, *d*) surface reconstructions, which were formed at 0.4 ML and 1 ML of magnesium coverage, respectively [6, 7]. These phases were created at room temperature so there was no desorption of Mg atoms from the surface. Pb was deposited from heated Ta tube at rate of 0.4 ML/min. Pb was calibrated by formation of 1×1-Pb surface structure containing 1 ML of Pb. Surface structures of the (Pb, Mg)/Si(111) systems were observed by LEED. Surface conductance of the samples was measured by the *in situ* 4PP method where probes are arranged in square cones with the interprobe distance of 0.6 mm. The measured resistance values ($R_{measure}$) were converted into a surface conductance σ according to the formula

$$\sigma(S/\square) = \frac{\ln(2)}{2\pi R_{measure}}.$$

According to this formula, the surface conductance of the bared Si(111)-7×7 sample before the deposition experiments was $7.6 \pm 0.5 \cdot 10^{-5}$ S/□.

Results and Discussion

Figure 1, *a* – *e* shows the LEED patterns observed after Mg adsorption onto the Si(111)-1×1-Pb reconstructed surface at room temperature. It is evident that Mg deposition up to 1 ML coverage leads to a series of consistent transformations of the surface structures. The 4×4 periodicity in (Fig. 1, *a*) was obtained after the adsorption of 0.4 ML of magnesium. After Mg deposition of 0.5 ML, the LEED pattern of so-called 'perforated ribbons' phase [6] is observed (Fig. 1, *b*) while the LEED pattern $6\sqrt{3}\times6\sqrt{3}$ at more than 0.5 ML is seen quite well in the LEED picture together with 4×4 spots (Fig. 1, *c*). With a further increase of the magnesium coverage, a 6×6 (1 ML of Mg) structure is formed (Fig. 1, *d*). At coverage slightly above 1 ML and up to 7 ML the corresponding LEED patterns show a 2×2 periodicity (Fig. 1, *e*). It should be noted that the LEED patterns at this stage of deposition are different depending on the manner of deposition.

At Mg coverage up to 1 ML, it makes no difference whether magnesium is deposited in large or small portions. However, in the case when magnesium is deposited in large doses (each dose is about 2 ML at a time), a 4×4 periodicity appears in the LEED pattern above 2 ML (Fig. 1, *f*) instead of the 2×2 one. After deposition of small Mg doses (each dose is about 0.2 – 0.5 ML at a time), the LEED pattern has shown the 2×2 periodicity. A mixture of 2×2 and 4×4 structures were often observed at average portions of adsorbed Mg. It is suggested in [4] that magnesium grown depends strongly on the deposition manner. It was shown that deposition of large Mg portions of about 4 – 10 ML led to the formation of a silicide film followed by the growth of magnesium islands, while deposition of small Mg portions of about 0.1 ML [4] results in the formation of silicide islands. According to [6], magnesium atoms penetrate under the Pb layer and form stable ties with Si and Pb atoms. During deposition, Pb atoms float on top of the magnesium layer. Therefore, we can assume that Pb atoms form both the 4×4 periodicity and the 2×2 one on the surface of two types of islands formed at large and small portions of deposition, respectively.

Figure 2 illustrates the effect of Mg deposition on the surface conductance of Si(111) samples covered by Pb-induced or binary (Pb, Mg)-induced surface reconstructions. In the case of Mg deposition onto the Si(111)-1×1-Pb surface, some decrease in the surface conductance was

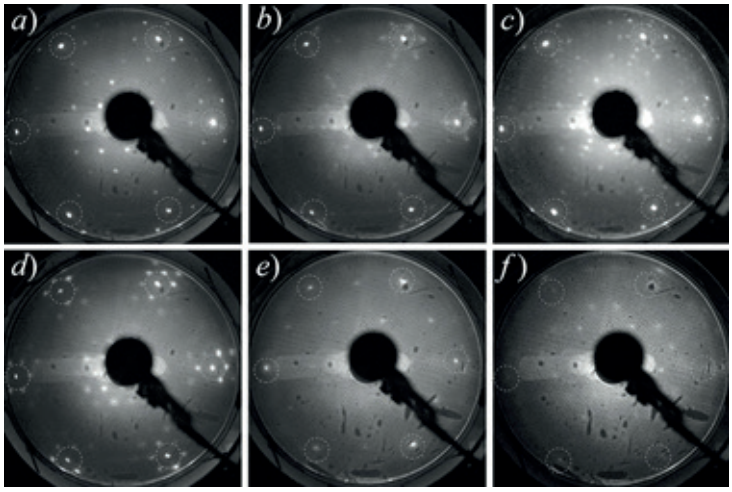

Fig. 1. LEED patterns (40eV) of surface structures formed on Si(111)-1×1-Pb surface at room temperature after Mg deposition. Dashed circles indicate the 1×1 spots;
4×4-(Pb, Mg) with 0.4 ML of Mg (*a*); 'perforated ribbons' with 0.5 ML of Mg (*b*); $6\sqrt{3}$+4×4-(Pb, Mg) structure with 0.5 ML of Mg (*c*); 6×6-(Pb, Mg) with 1 ML of Mg (*d*); 2×2-(Pb, Mg) with 7 ML of Mg at small doses (*e*); 4×4-(Pb, Mg) with 9 ML of Mg at large doses (*f*).

established (Fig. 2). Formation of the $6\sqrt{3}\times6\sqrt{3}$ structure at 0.5 ML of Mg results in the minimum conductance that is extended up to 1 ML magnesium coverage. With a further increase of magnesium coverage (6×6 structure), surface electrical conductance begin to increase. According to [7], the work function increases in the range of 0 – 0.5 ML, which is a fairly natural picture inherent in the deposition of alkali and alkaline earth metals [8, 9], and the resulting band bending leads to a decrease in conductance (see Fig. 2). However, when the 6×6 structure appears, surface electrical conductance increases due the formation of a continuous metal layer. Recently, the presence of metallic states in the Si(111)-6×6-(Mg, Pb) surface phase was confirmed by data of angle-resolved photoemission spectroscopy (ARPES) [6].

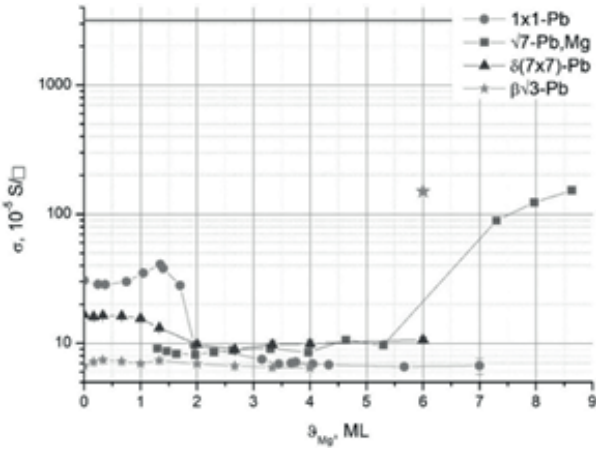

Fig. 2. Surface electrical conductance of surface structures at magnesium deposition.

After the further deposition of magnesium atoms, conductance begins to decrease until 7 ML of Mg depending on the manner of deposition. At large portions of adsorbed Mg (about 2 ML at a time), the corresponding surface electrical conductance was $13.7\cdot10^{-5}$ S/□ whereas at small portions (0.2 – 0.5 ML at a time) surface electrical conductance appeared to be $7\cdot10^{-5}$ S/□.

At the next stage, magnesium was deposited at room temperature onto the Si(111)-$\beta\sqrt{3}\times\sqrt{3}$-Pb reconstructed surface contained the 0.33 ML of Pb [10, 11]. It was observed that $\sqrt{3}\times\sqrt{3}$ superspots in the LEED pattern are fainted gradually while the 1×1 periodicity disappeared only at 6 ML of adsorbed Mg coverage leaving the high background on the screen. Deposition of large portions of Mg leads to appearance of LEED '1×1' spots that are specific to the grown magnesium film with the Mg(0001) orientation (Fig. 3, *a*). This magnesium film demonstrated a relatively high conductivity value (marked by stars in Fig. 2) of $150\cdot10^{-5}$ S/□, which is however lower then the calculated value $3189\cdot10^{-5}$ S/□ for the Mg layer of 1.4 nm (Fig. 2, horizontal line). It was established for the LEED picture that this metal film has a polycrystalline structure (Fig. 3, *a*) because the spots look like arcs meaning a large number of defects on the surface. The ratio of lattice constants was evaluated as Si/Mg = 3.84Å/3.21Å = 1.196, that is, 1/1.196 = 0.84 in reciprocal space. The LEED pattern was used to measure the Si/Mg ratio as 0.86, which is very close to the calculated value (Fig. 3, *a*).

A structure known as a δ(7×7) was observed upon Mg deposition onto the Pb layer preliminarily formed by lead adsorption at room temperature onto the Si(111)-7×7 bared surface. The LEED pattern has shown a gradual uniform decay of diffraction spots following with background after 2.5 ML of deposited Mg. Figure 2 shows the changes in surface conductance (triangles), exhibiting a smooth decrease in conductance after 1 ML of adsorbed Mg reaching the constant value of $1\cdot10^{-4}$ S/□ coverage at about 2 ML of Mg. In that case, electrical conductance is significantly higher than that for the Mg deposited on the $\beta\sqrt{3}$-Pb surface due to the lower

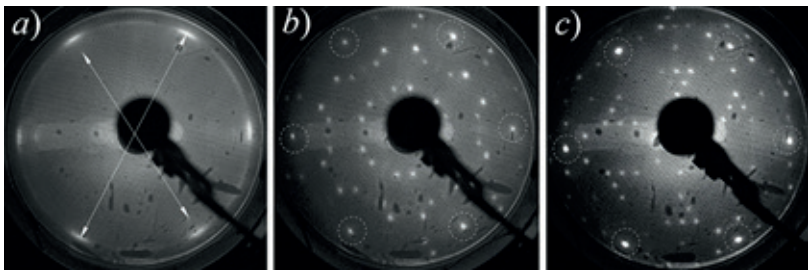

Fig. 3. LEED patterns (40 eV) for magnesium film Mg (0001) of 1.4 nm (*a*); $\sqrt{7}\times\sqrt{7}$-(Pb,Mg) (*b*); $\sqrt{3}\times\sqrt{19}$-(Pb,Mg) (*c*), dashed circles indicate the 1×1 spots.

initial surface electrical conductance of the β√3-Pb sample as compared to the δ(7×7) one (Tab. 1).

Figure 2 shows the changes in the surface electrical conductance during magnesium deposition on the surface phase Si(111)-√7×√7-(Pb, Mg) which already contains both Pb and Mg atoms (squares). The optimal conditions for preparation of this structure are the following: 1 – 1.3 ML of magnesium deposited onto the Si(111)-β√3×√3-Pb surface phase, followed by heating the sample for 30 seconds at 250 °C. The LEED pattern has shown a gradual decay of √7×√7 (Fig. 3, *b*) superspots up to 2.6 ML of adsorbed Mg, then fading of the 1×1 spots intensity is observed and finally the ring appears in the LEED pattern indicating the formation of magnesium film at Mg coverage of 7 ML. This ring is identical to the case of Mg deposition onto the Si(111)-β√3×√3-Pb surface (large Mg portions) (Fig. 3, *c*). It was concluded that formation of the magnesium layer does not depend on the manner of deposition in this case due to a stabilizing role of magnesium in the √7×√7 surface phase. The surface electrical conductance slightly changed until the Mg coverage reached the 5.5 ML and further the conductance began to increase due to the formation of magnesium film.

As indicated in Table 1, an increase in metal coverage in the studied structures results in increase in conductance except for some cases. For example, in the case of √7×√7-(Pb, Mg) structure the conductance value is higher than that for the β√3×√3-Pb one but if the same amount of magnesium is deposited onto the β√3×√3-Pb surface at room temperature conductance is not changed (Fig. 2) due to islanding of adsorbed species. In the case of another structure contained magnesium, Si(111)-√19×√3-(Pb, Mg) (Fig. 3, *c*), obtained by deposition of 0.6 – 0.9 ML of Mg onto the β√3×√3-Pb surface followed by heating the sample for 30 seconds at 350 °C, the electrical conductance is slightly lower than that for the √7×√7-(Pb, Mg) surface phase because the total amount of metal atoms, Mg and Pb, is smaller. The highest electrical conductance among the presented surface structures, except for the magnesium film Mg(0001), was demonstrated for the Si(111)-6×6-(Pb, Mg) surface phase which has a maximum amount of metal atoms, both Pb and Mg, in the structure, 2 ML in total.

Table 1

Surface electrical conductance σ and metal compounds for some surface structures

Structures	σ, 10^{-5} S/□	Θ_{sum}, ML	Θ_{Pb}, ML	Θ_{Mg}, ML
β√3√×3Pb	6.7	0,3	0,3	0
δ(7×7)-Pb	16.6	1	1	0
1×1-Pb	30.7	1	1	0
√3×√19-(Pb, Mg)	6.7	0.9	0.3	0.6
4×4-(Pb, Mg)	28.5	1.4	1	0.4
√7×√7-(Pb, Mg)	9.1	1.3	0.3	1
6×6-(Pb, Mg)	40.8	2	1	1
6√3×6√3-(Pb, Mg)	28.4	1.7	1	0.7
Mg(0001) of 8.6 ML	152.7	8.9	0.3	8.6

Conclusion

Growth of Mg films depends on the deposition manner of magnesium atoms in all cases except for the formation Mg film on the √7×√7-(Pb, Mg). Deposition of the large portions of Mg atoms (about 1-2 ML at once) results in the formation of Mg (0001) polycrystalline film. The small portions (about 0.5 – 1 ML at once) lead to disordered film formation. The corresponding electrical conductance is higher for the magnesium film and lower for the disordered layers. Magnesium growth on the √7-(Pb, Mg) surface does not depend on the

deposition manner. New surface phases containing the Mg and Pb atoms have been obtained, $\sqrt{7}\times\sqrt{7}$-(Pb, Mg) and $\sqrt{19}\times\sqrt{3}$-(Pb,Mg) ones.

REFERENCES

1. **Mamindla R., Niranjan M.K.,** Surface electronic structure, relaxations and thermodynamic energies of (100), (110) and (111) surfaces of Mg_2Si: A first-principles theoretical study, Surface Science 691 (2020) 121506.

2. **Galkin K.N., Kumarb M., Shivaprasad S.M., Galkin N.G.,** The model of the magnesium silicide phase $(2/3\sqrt{3}\times 2/3\sqrt{3})$-R30°on Si(111), Physics Procedia 11 (2011) 47–50.

3. **Gouralnik A.S., Maslov A.M., Ustinov A.Yu., Dotsenko S.A., Shevlyagin A.V., Chernev I.M., Il'yashenko V. M., Kitan S.A., Koblova E.A., Galkin K.N., Galkin N.G., Gerasimenko A.V.,** Formation of Mg_2Si at high temperatures by fast deposition of Mg on Si(111) with wedge-shaped temperature distribution, Applied Surface Science 1 (2018) 282–284.

4. **Lee D., Lee G., Kim S., Hwang Ch., Koo Ja-Yo., Lee H.,** Room-temperature growth of Mg on Si(111): stepwise versus continuous deposition, Journal of Physics: Condensed Matter 19 (2007) 266004.

5. **Fan T., Xie C., Wang Sh., Oganov A.R., Cheng L.,** First-principles study of thermoelectric properties of Mg_2Si–Mg_2Pb semiconductor materials, RSC Advances 8 (2018) 17168.

6. **Tupchaya A.Y., Bondarenko L.V., Yakovlev A.A., Mihalyuk A.N., Gruznev D.V., Denisov N.S., Matetskiy A.V., Aladyshkin A.Yu., Zotov A.V., Saranin A.A.,** 2D system incorporating perforated Mg sheet sandwiched between Pb layer and Si(111), Applied Surface Science 589 (2022) 152951.

7. **Terakawa Sh., Hatta Sh., Okuyama H., Aruga T.,** Mg deposition induced change of structure and electronic properties of Pb/Si(111) surface, In: Annual Meeting of the Japan society of vacuum and surface science, Japan, 23 December, 2020, Report No 2Ba04S.

8. **Ahn J. R., Yoo K., Seo J. T., Byun J. H., Yeom H. W.,** Electronic states of two-dimensional adatom gas and nanocluster array: Na on Si(111)7x7, Physical Review B 72 (2005) 113309.

9. **Min-Ju Y., Ping Z., Xiao-Long D.,** First-principle study of Mg adsorption on Si(111) surfaces, Chinese Physics B 18 (2009) 1.

10. **Owczarek S., Markowski L.,** The role of surfactant in two-components structures formation on Si(111) surface, Surface Science 693 (2020) 121552.

11. **Lifshits V.G., Saranin A.A., Zotov A.V.,** Surface phases on silicon: preparation, structures, and properties, John Wiley and Sons, Chichester, 1994.

THE AUTHORS

RYZHKOVA Maria V.
lavric@iacp.dvo.ru
ORCID: 0000-0001-8990-7140

TSUKANOV Dmitry A.
tsukanov@iacp.dvo.ru
ORCID: 0000-0002-8900-3480

Received 18.05.2022. Approved after reviewing 26.07.2022. Accepted 03.08.2022.

Conference materials
UDC 538.955; 538.975
DOI: https://doi.org/10.18721/JPM.153.119

FORC-investigation of magnetic properties of Ni nanowire arrays synthesized using Al_2O_3 templates with different order of pores

M. I. Sobirov [1], A. Yu. Samardak [1] ✉, S. R. Potapova [1], M. B. Karibov [1],
K. A. Rogachev [1], A. V. Ognev [1], A. S. Samardak [1]

[1] Far Eastern Federal University, Vladivostok, Russia
✉ samardak.aiu@dvfu.ru

Abstract: This paper focuses on the investigation of magnetic properties of Ni nanowire arrays synthesized using Al_2O_3 porous templates with different durations of first anodization. It has been shown that the diameter of the pores in the template is increasing with an increase in the first anodization time up to 2 hours, and the interpore distance becomes more uniform. Using porous templates with short times of anodization results in synthesis of branched Ni nanowires, while templates with longer times allow to achieve cylindrical nanostructures. Magnetic properties of Ni nanowires arrays were studied using the FORC method, which allowed to investigate the distribution of interaction fields and coercive forces in the arrays. It was found that two magnetic phases with different coercive forces and interaction field are observed in the samples with a short duration of first anodization.

Keywords: anodization, aluminum oxide matrices, nanowires, electrochemical deposition, FORC-method

Funding: The study was financially supported by the Russian Science Foundation (Project no. 19-72-20071): sample preparation and FORC measuring. A. S. Samardak is grateful for the support of the Ministry of Science and Higher Education of the Russian Federation (State Assignment no. 0657-2020-0013) for the SEM observation.

Citation: Sobirov M. I., Samardak A. Yu., Potapova S. R., Karibov M. B., Rogachev K. A., Ognev A. V., Samardak A. S., FORC-investigation of magnetic properties of Ni nanowire arrays synthesized using Al_2O_3 templates with different order of pores, St. Petersburg State Polytechnical University Journal. Physics and Mathematics. 15 (3.1) (2022) 113–118. DOI: https://doi.org/10.18721/JPM.153.119

Материалы конференции
УДК 538.955; 538.975
DOI: https://doi.org/10.18721/JPM.153.119

Исследование FORC-методом магнитных свойств массивов Ni нанопроволок, синтезированных с использованием шаблонов Al_2O_3 с разным порядком пор

М. И. Собиров [1], А. Ю. Самардак [1] ✉, С. Р. Потапова [1], М. Б. Карибов [1]
К. А. Рогачев [1], А. В. Огнев [1], А. С. Самардак [1]

[1] Дальневосточный Федеральный Университет, г. Владивосток, Россия
✉ samardak.aiu@dvfu.ru

Аннотация. Данная работа посвящена исследованию магнитных свойств массивов нанопроволок Ni, синтезированных с использованием пористых мембран Al_2O_3 с разной продолжительностью первого анодирования. Показано, что с увеличением времени первого анодирования до 2 часов медианный диаметр пор на верхней поверхности мембраны увеличивается, а расстояние между порами становится более равномерным.

Использование пористых шаблонов с малым временем анодирования приводит к получению разветвленных нанопроволок Ni, а шаблоны с большим временем позволяют получить цилиндрические наноструктуры. Магнитные свойства массивов нанопроволок Ni изучались с использованием FORC метода, который позволил исследовать распределение полей взаимодействия и коэрцитивных сил в массивах. Он показал, что в образцах с малым временем первого анодирования присутствуют две магнитные фазы с разными коэрцитивными силами и полем взаимодействия.

Ключевые слова: анодирование, пористые оксидные матрицы, нанопроволоки, электрохимическое осаждение, FORC-метод

Финансирование: Работа выполнена при финансовой поддержке Российского научного фонда (проект № 19-72-20071): пробоподготовка и измерение FORC. А. С. Самардак выражает благодарность Минобрнауки России за поддержку (Госзадание № 0657-2020-0013) в проведении измерений СЭМ.

Ссылка при цитировании: Собиров М. И., Самардак А. Ю., Потапова С. Р., Карибов М. Б., Рогачев К. А., Огнев А. В., Самардак А. С. Исследование FORC-методом магнитных свойств массивов ni нанопроволок, синтезированных с использованием шаблонов Al_2O_3 с разным порядком пор // Научно-технические ведомости СПбГПУ. Физико-математические науки. 2022. Т. 15. № 3.1. С. 113–118. DOI: https://doi.org/10.18721/ JPM.153.119

Introduction

Many recent studies have focused on the magnetic properties of one-dimensional ferromagnetic nanostructures because of their nontrivial magnetic behavior due to strong uniaxial shape anisotropy [1]. Their potential applications range widely, from biomedicine to nanoelectronics, notably including sources of secondary irradiation in radiotherapy, agents for targeted drug delivery, agents for destroying cancer by hyperthermia and mechanical destruction of tumors, elements of magnetic memory and nanoelectronics, various biosensors and sensors of magnetic fields [2].

Many methods for synthesizing various one-dimensional nanostructures are discussed in the literature [3–5]. Method of electrodeposition into porous alumina matrices, in which the deposited nanostructures replicate the shape of pores in the membrane, is one of the most common and widely used method due to a number of notable advantages. They include, in particular, the possibility to precisely and easily control the geometrical parameters of arrays of synthesized one-dimensional nanostructures by controlling the conditions during two-step anodization of porous Al_2O_3 matrices. This method can be used to obtain arrays of hexagonal ordered high-uniform one-dimensional nanostructures with different diameters, distance between neighbors and the thickness of wall between them [6]. Changing certain parameters can allow to modify the geometry even further, synthesizing one-dimensional nanowires with a shape different than a cylinder.

The goal of this work is to study the effect of the first anodization time on the structure of porous Al_2O_3 matrices and, consequently, on the magnetic properties of Ni nanowire arrays synthesized inside them using the FORC method [7], which allows to estimate the distribution of interaction fields and coercive forces in the investigated samples.

Materials and Methods

To produce porous matrices of aluminum oxide, we used 2×2 cm Al plates with a thickness of 1.7 mm, annealed at 500 °C for 5 hours under vacuum conditions. To obtain a smooth surface, the samples were mechanically polished with abrasive paper and subjected to chemical polishing in HNO_3 (50%) + HF (40%) at T = 100 °C for 60 s. After chemical treatment, samples were electropolished in 1:4 $HClO_4$ + C_2H_5OH solution with the current density of 500 mA/cm, resulting in a mirror-like surface. The non-working side of the plates was coated

with a photoresist to prevent oxide formation, while the working side was left open for contact with an acidic solution. Anodizing was carried out using an Agilent 6030A power supply in 0.3 M solution of oxalic acid ($C_2H_2O_4$) cooled down to 2–3 °C in a soft potentiostatic mode at 40 V. The duration of the first anodization was selected as t = 0, 15 and 120 minutes for different samples, after which the oxide layer was removed with the solution of H_2CrO_4 (1.8%) + H_3PO_4 (6%) at T = 60 °C and magnetic stirring for 15–20 minutes. Second anodization for all samples was carried out for 18 hours. After preparation of porous membranes, a 1 μm thick layer of Cu was deposited by thermal sputtering on the working side to be used as a conductive layer during subsequent electrodeposition and impart additional strength to fragile porous membranes. After Cu deposition, non-oxidized Al was dissolved in 0.08 M CuCl2 + 8% HCl at room temperature until only porous Al_2O_3 membrane left. After that the barrier layer at the bottom of the pores was subjected to dissolution in 1 M H_3PO_4 for 60 minutes to form through pores. Nanowires were electrodeposited using Watts solution containing $NiSO_4$, $NiCl_2$, and H_3BO_3 into prepared matrices in a potentiostatic mode at −1 V for 10 minutes using a Keithley 2460 power supply.

Studies of the surface of porous membranes and the geometry of nanowires were carried out using ThermoScientific $SCIOS_2$ scanning electron microscope (SEM). To study Ni nanowire geometry, they were etched from the oxide matrix using H_2CrO_4 (1.8%) + H_3PO_4 (6%) at T = 60 °C and deposited on a copper plate. The study of the distribution of pore diameters, interpore distances and Fast Fourier Transform (FFT) analysis of SEM pictures were carried out using the Fiji software. Investigation of the magnetic properties of Ni nanowires arrays and FORC-method were performed using LakeShore 7400 vibrating sample magnetometer (VSM) at room temperature.

Results and Discussion

Results of SEM investigation of porous matrices surfaces for all samples are presented in Figure 1. The sample with t = 0 min (Fig. 1, *a*) showed comparably uniform distribution of the pore diameters (D) in the range of 20–50 nm, with the median D = 33 nm (Fig. 1, *g*). FFT image (Fig. 1, *d*) displayed a blurred circle, which corresponds to a somewhat uniform distribution of interpore distances in the matrix. Increasing the time of first anodization t to 15 min results in a drastically changed surface of the porous template (Fig. 1, *b*). Pores with diameters from 25 nm to 125 nm (median D = 50 nm) (Fig. 1, *g*) were placed with no order, resulting in completely vague FFT picture (Fig. 1, *e*). The sample synthesized with t = 120 min (Fig. 1, *c*) revealed that D has increased to 45 nm, with the distribution of diameters 30–60 nm. The FFT image appeared as a thin, non-blurred circle, because of identical interpore distances and close-range order of pores in the membrane. It should be noted that no sample exhibited a long-range order, which would result in non-blurred peaks in hexagonal shape on the FFT picture. Analysis of the SEM pictures of the surface of porous templates demonstrated that the average distance between the pores r_{ip} is about 120 nm for the sample with t = 0 min, r_{ip} = 20–200 nm for the sample with t = 15 min and r_{ip} = 70 nm for the sample with t = 120 min.

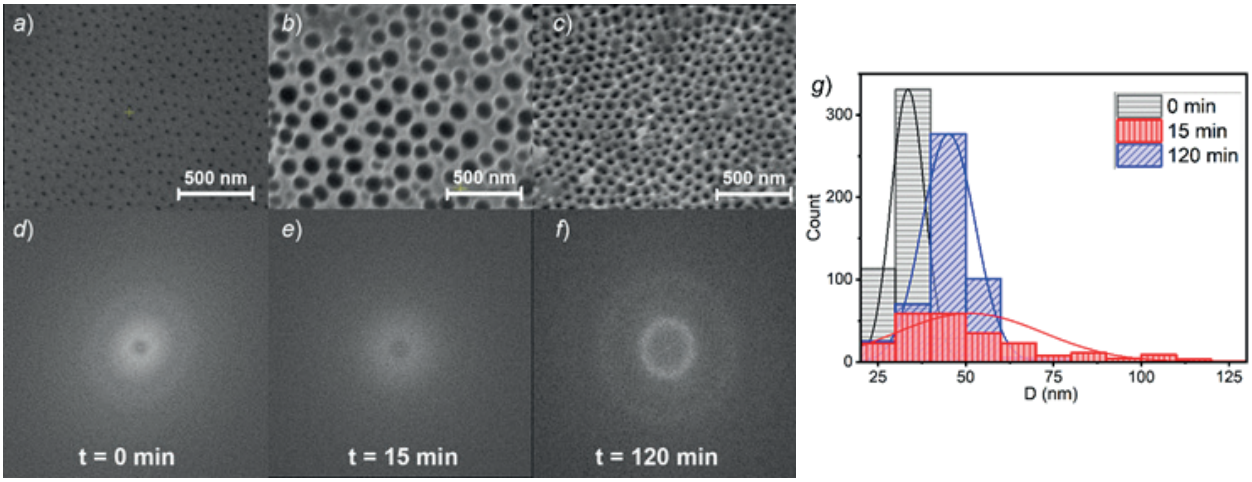

Fig. 1. SEM-images of porous membrane surface, obtained for 0 (*a*), 15 (*b*) and 120 min (*c*) of first anodization; images corresponding to the FFT analysis (*d* – *f*); histogram of distribution of pore diameters for all samples (*g*)

SEM-investigation of Ni nanowires, etched out of porous membrane, revealed that the nanowires appeared branched in samples with $t = 0$ min and $t = 15$ min, due to the branched structure of the pores. The sample with $t = 120$ min showed a cylindrical shape of the nanowires, with no branches. Such geometry of the pores originates in pore creation and merging in the process of oxide growth. Their D followed the diameter of the pores in the template, and the length amounted to 4, 2.5 and 3 μm for 0, 15 and 120 min of the first anodization accordingly.

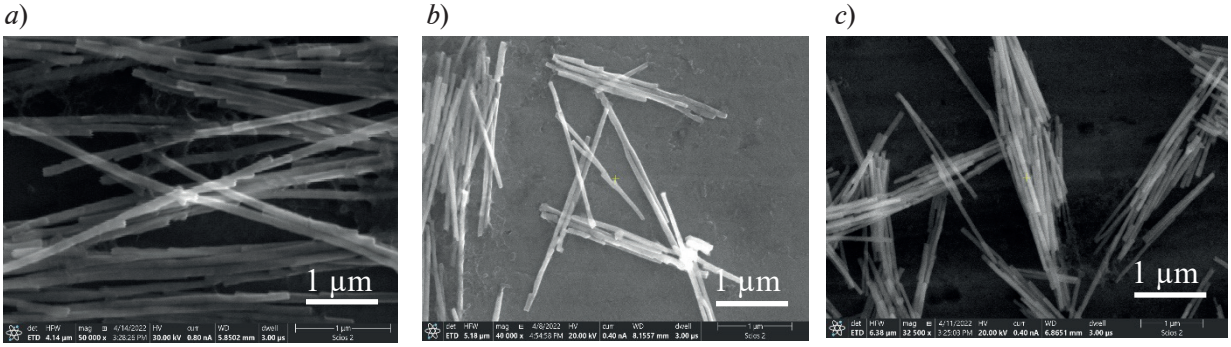

Fig. 2. SEM-images Ni nanowires etched out of porous template with time of first anodization 0 (*a*), 15 (*b*) and 120 (*c*) min on top of the Cu substrate

Magnetic measurements in the direction of external magnetic field H along the long axis of nanowires are presented in Fig. 3 and summarized in Table 1. Measured from the hysteresis loops, the coercive force H_c^{loop} is increasing from $H_c^{loop} = 690$ Oe to $H_c^{loop} = 914$ Oe with first anodization time changing from 0 to 15 min. The sample with $t = 120$ min showed slightly lower coercivity $H_c^{loop} = 914$ Oe than the sample with no first anodization. Such behavior of H_c can be related to the changing D of nanowires, since H_c is very sensitive to that parameter in the single-domain range of diameters (40 − 150 nm). Moreover, nanowires synthesized with the first anodization time below 15 nm are of branched structure (Fig. 2, *a*, *b*), which also can be the reason for increasing Hc, with branches acting as pinning centers.

The ratio of remnant magnetization M_r to saturation magnetization M_s was determined from hysteresis loops (Fig. 3, *a*) as 0.85 for all samples. A ratio so close to 1 corresponds to that in the absence of H, the majority of the nanowires in the array are keeping their magnetization in the way, predetermined by the previously applied H. This behavior can originate from two possible factors: a single-domain micromagnetic state of nanowires and relatively weak interaction fields between them. A single-domain state is common for nanowires with D below 100 nm [8] and resulting in a square hysteresis loop with ratio $M_r/M_s = 1$ for an individual nanowire in the array. On the other hand, strong magnetostatic interaction fields Hu in the array, induced by nanowires with a high value of M_s, often result in the M_r/M_s value tending to zero, changing the critical fields and shifting the hysteresis loop of the single nanowire, due to self-demagnetizing effect. Thus, in our case, it is safe to assume that interwire interactions in investigated samples are limited due to the low M_s of Ni and do not induce any serious changes to magnetic behavior of the array.

To prove this assumption and investigate the H_c distribution in the samples, FORC-method analysis was employed. A set of 70 first-order reversal curves was measured on VSM in the range of the fields from −2000 Oe to +2000 Oe. Using second order derivative of magnetization M

Table 1

Magnetic and structural properties of Ni nanowire arrays

Sample	Time of 1st anodization, min	D, nm	H_c^{loop}, Oe	min H_c^{FORC}, Oe	max H_c^{FORC}, Oe	H_u, Oe
1	0	33	690	594	1013	600
2	15	50	914	712	1382	1200
3	120	45	675	670	1272	980

on starting field of each curve H_r and applied field H, a density of states ρ was achieved from experimental loops, as presented in Fig. 3, $b - d$. The overall similarity of the shape of FORC-diagrams suggests that they have similar magnetization switching processes. Nevertheless, H_c^{FORC} distribution varies differently for samples with different first anodization times. A wide distribution of H_c^{FORC} from 712 Oe to 1382 Oe for the sample with t = 15 min points to their geometrical irregularity, originating from non-uniform pores in the matrix. The range of H_c^{FORC} distribution is comparably lower in the samples with t = 0 and 120 min: H_c^{FORC} = 594–1013 Oe for t = 0 min and H_c^{FORC} = 670–1272 Oe for t = 120 min, due to their comparably more even distribution of D. The FORC-diagram of the sample with t = 0 min is characterized, in contrast to other samples, by an additional ρ distribution peak with a smaller H_c^{FORC} = 280 Oe. This peak could stand for a low-coercive phase, possibly located close to the work surface of the Al_2O_3 template, which has a smaller D of nanowires and thus smaller coercive forces. The interaction fields H_u in the sample with t = 0 min is twice as smaller as in the sample with t = 15 min (H_u = 600 Oe and H_u = 1200 Oe, respectively), possibly due to large distances between nanowires in the first sample and much more closely packed nanowires in the second sample. The sample with t = 120 min is characterized with an average H_u = 980 Oe because of the small distance between the nanowires in the array.

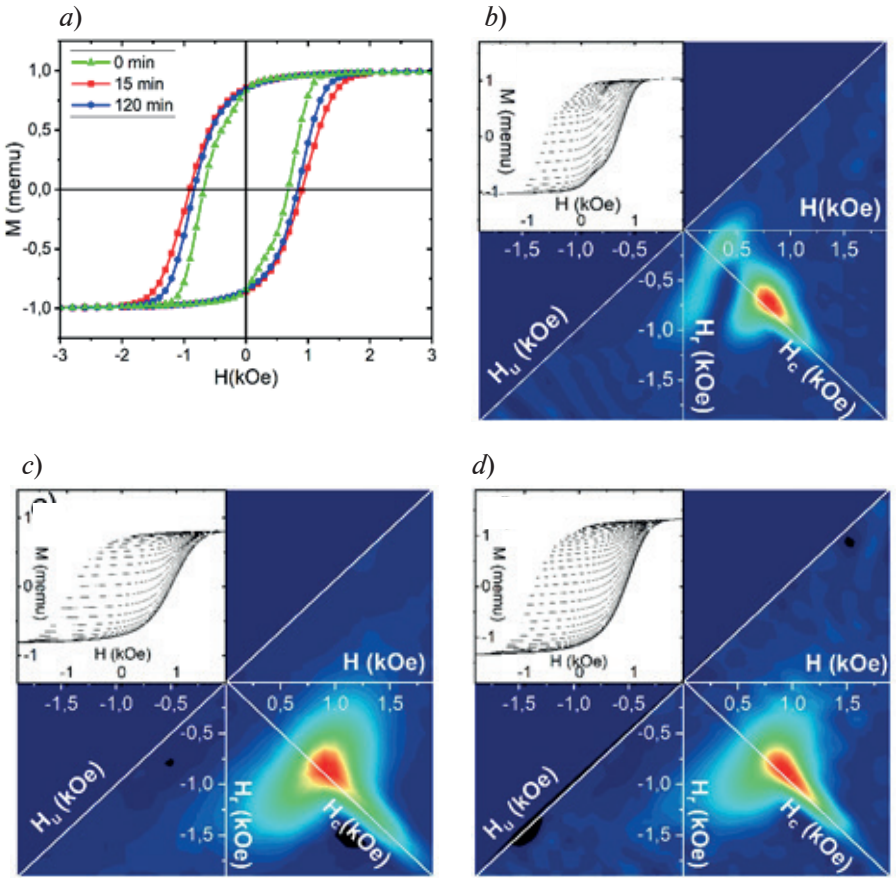

Fig. 3. Hysteresis loops measured in the direction of the external field H along the long axis of nanowires for all samples (*a*). FORC-diagrams in the same orientation of H for samples with t = 0 (*b*), 15 (*c*) and 120 (*d*) min of first anodization.

Conclusion

As a result of the study, magnetic properties of Ni nanowires depending on the time of first anodization of Al_2O_3 membranes were studied. Ni nanowires were obtained by electrochemical deposition into porous matrices, synthesized with the time of first anodization varied from 0 to 120 min. SEM investigation of morphology of the porous templates revealed a heavy dependence of the pore diameters, interpore distance and pore order in the membrane on the time of first

anodization. A morphological study of Ni nanowires showed that samples with $t < 15$ min were characterized by branched structure. A study of magnetic properties demonstrated a possible single-domain micromagnetic structure of the Ni nanowires and low interaction fields in the array. FORC-studies indicated strong dependence of coercive forces on the geometrical parameters of Ni nanowires in the array. It has been shown that the sample with $t = 15$ min possesses a wide distribution of coercive forces due to ununiform diameters of nanowires in the array, while other samples have a more uniform distribution of coercive forces and thus geometrical parameters of the samples. Magnetostatic interactions are also heavily dependent on the distance between pores and show the highest fields for the sample synthesized with a porous matrix anodized for 15 min.

REFERENCES

1. **Samardak A.S., Ognev A.V., Samardak A.Yu., Stebliy E.V., Modin E.B., Chebotkevich L.A., Komogortsev S.V., Stancu A., Panahi-Danaei E., Fardi-Ilkhichy A., Nasirpouri F.,** Variation of magnetic anisotropy and temperature-dependent FORC probing of compositionally tuned Co-Ni alloy nanowires, Journal of Alloys and Compounds. 732 (2018) 683–693.

2. **Moreno J. A., Bran C., Vazquez M., Kosel J.,** Cylindrical Magnetic Nanowires Applications, IEEE Transactions on Magnetics. 57 (4) (2021) 1–17

3. **Nam D. Y., Samardak A. Yu., Jeon Y. S., Kim S. H., Davydenko A. V., Ognev A. V., Samardak A. S., Kim Y. K.,** Magnetization reversal of ferromagnetic nanosprings affected by helical shape. Nanoscale 10 (2018) 20405–20413

4. **Scott J. A., Totonjian D., Martin A. A., Tran T. T., Fang J. H., Toth M., McDonagh A. M., Aharonovich I., Lobo C. J.,** Versatile method for template-free synthesis of single crystalline metal and metal alloy nanowires. Nanoscale 8 (5) (2016) 2804–2810.

5. **Lau Y. M., Chee P. C., Thong J. T. L., Ng V.,** Properties and applications of cobalt-based Material produced by electron-beam-induced deposition. Journal of Vacuum Science & Technology a-Vacuum Surfaces and Films. 20 (4) (2002) 1295–1302.

6. **Ebihara K., Masaichi N.,** Structure and Density of Anodic Oxide Films Formed on Aluminum in Oxalic Acid Solutions. Journal of the Metal Finishing Society of Japan. 34 (11) (1983) 548–553

7. **Mayergoyz I. D.,** Hysteresis Models from the Mathematical and Control-Theory Points of View. Journal of Applied Physics. 57 (8) (1985) 3803–3805.

8. **Ivanov, Y., Chuvilin, A., Vivas, L., Kosel J., Chubykalo-Fesenko O., Vazquez M.,** Single crystalline cylindrical nanowires-toward dense 3D arrays of magnetic vortices. Scientific Reports 6 (2016) 23844.

THE AUTHORS

SOBIROV Mukhammad I.
sobirov.mi@dvfu.ru
ORCID: 0000-0002-8954-8413

ROGACHEV Kirill A.
rogachev.ka@dvfu.ru
ORCID: 0000-0002-8193-3851

SAMARDAK Aleksei Yu.
samardak.aiu@dvfu.ru
ORCID: 0000-0002-0795-374X

OGNEV Alexey V.
ognev.av@dvfu.ru
ORCID: 0000-0002-1619-3666

POTAPOVA Sofia R.
potapova.sr@students.dvfu.ru
ORCID: 0000-0002-4578-5492

SAMARDAK Alexandder S.
samardak.as@dvfu.ru
ORCID: 0000-0001-5917-4361

KARIBOV Muslim B.
karibov.mb@students.dvfu.ru
ORCID: 0000-0003-3264-7821

Received 21.05.2022. Approved after reviewing 05.07.2022. Accepted 20.07.2022.

Conference materials
UDC 539.234
DOI: https://doi.org/10.18721/JPM.153.120

Fabrication of SERS-sensitive nanopipette with silver nanoparticles obtained by vacuum thermal evaporation

A. D. Overchenko [1] ✉, S. V. Dubkov [1], D. V. Novikov [1], V. S. Kolmogorov [2]
L. D. Volkova [3], T. S. Grishin [3], P. A. Edelbekova [3]

[1] National Research University of Electronic Technology, Moscow, Russia;
[2] National University of Science and Technology "MISIS" (MISIS), Moscow, Russia;
[3] Institute of Nanotechnology of Microelectronics RAS, Moscow, Russia
✉ alexsey7840@mail.ru

Abstract: This work is concerned with developing an approach to producing an array of plasmonic Ag nanoparticles on the nanopipette surface. The vacuum thermal evaporation method followed by annealing was used to form the nanoparticle array. The surface morphology of the modified pipettes was investigated by scanning electron microscopy. Based on the SEM images obtained, the most efficient method for particle deposition on the pipette was selected. It was found that two-stage depositions on the horizontally mounted pipette formed an array of silver nanoparticles with a size of about 16 nm. The obtained modified nanopipettes were investigated by Raman spectroscopy. A laser with a wavelength of 532 nm was used to obtain the spectra. Rhodamine in the R6G modification was used as an analytical substance. The enhance factor of the modified pipette was calculated by comparing it with pure glass at the same power values of the laser and concentration of the analytical substance, rhodamine R6G. The developed approach to modifying the surface of nanopipettes allows fabricating SERS pipettes for monitoring various intracellular biomarkers.

Keywords: nanopipette, SERS, Ag-particles, Raman spectroscopy

Funding: The work was supported by the Russian Science Foundation (project № 21-19-00761).

Citation: Overchenko A. D., Dubkov S. V., Novikov D. V., Kolmogorov V. S., Volkova L. D., Grishin T. S., Edelbekova P. A., Fabrication of SERS-sensitive nanopipette with silver nanoparticles obtained by vacuum thermal evaporation, St. Petersburg State Polytechnical University Journal. Physics and Mathematics. 15 (3.1) (2022) 119–124. DOI: https://doi.org/10.18721/JPM.153.120

Материалы конференции
УДК 539.234
DOI: https://doi.org/10.18721/JPM.153.120

Изготовление SERS-чувствительного нанокапилляра с серебряными частицами с помощью метода вакуум термического испарения

А. Д. Оверченко [1] ✉, С. В. Дубков [1], Д. В. Новиков [1], В. С. Колмогоров [2]
Л. С. Волкова [3], Т. С. Гришин [3], П. А. Едельбекова [3]

[1] Национальный исследовательский университет «МИЭТ», г. Москва, Россия;
[2] Национальный Исследовательский Технологический Университет МИСиС, г. Москва, Россия;
[3] Институт нанотехнологий микроэлектроники РАН, г. Москва, Россия
✉ alexsey7840@mail.ru

Аннотация. Данная работа посвящена разработке подхода к формированию массива

плазмонных наночастиц Ag на поверхности нанопипетки. Для формирования массива наночастиц использовался метод вакуум термического испарения с последующим отжигом. Морфология поверхности модифицированных пипеток была исследована с помощью растрового электронной микроскопии. На основе полученных РЭМ изображений была выбрана наиболее эффективная методика осаждения частиц на пипетку. Установлено, что при двух стадийном нанесении на горизонтально закреплённую пипетку формируется массив наночастиц серебра с размером порядка 16 нм. Полученные модифицированные нанопипетки исследовались с помощью рамановской спектроскопии. В ходе получения спектров использовался лазер с длинной волны 532 нм. В качестве аналитического вещества использовался родамин в модификации R6G. Был проведен расчёт коэффициента усиления модифицированной пипетки путём сравнения с чистым стеклом при одинаковых значения мощности лазера и концентрации аналитического вещества родамин R6G. Разработанный подход к модифицированию поверхности нанопипеток возможен для изготовления SERS-пипеток для мониторинга различных внутриклеточных биомаркеров.

Ключевые слова: нанопипетка, SERS, Ag-частицы, рамановская спектроскопия

Финансирование: Исследование выполнено за счет гранта Российского научного фонда (проект № 21-19-00761).

Ссылка при цитировании: Оверченко А. Д., Дубков С. В., Новиков Д. В., Колмогоров В. С., Волкова Л. С., Гришин Т. С., Едельбекова П. А. Изготовление SERS-чувствительного нанокапилляра с серебряными частицами с помощью метода вакуум термического испарения // Научно-технические ведомости СПбГПУ. Физико-математические науки. 2022. Т. 15. № 3.1. С. 119–124. DOI: https://doi.org/10.18721/ JPM.153.120

Introduction

Substance diagnostics is an indispensable part of many fields. It is especially important in the medical industry, where biomarkers are identified to detect various diseases [1]. Detection of biomarkers from a single cell represents an important task today. The low concentration of biomarkers and the dynamic nature of living cells make it challenging to use traditional methods for analysis of intracellular contents of single cells [2, 3]. One example of such methods is atomic force microscopy (AFM). It is difficult to use classical AFM to visualize the dynamics of living biological objects due to the time required to obtain an image of surface morphology. In addition, as the tip always exerts a mechanical load on the sample, it can be damaged, therefore, it is difficult to image soft biomaterials with the AFM [4]. Tip-enhanced Raman spectroscopy (TERS) can be used to obtain the most detailed and accurate information about the studied object. TERS is a well-known method that combines scanning probe microscopy and Raman spectroscopy [5], allowing to carry out effective investigations into the objects of interest [6]. One of the disadvantages of TERS is that it works with only one type of molecule at a time, which limits its deposition [7]. Raman enhancement with TERS is associated with strong fields, which can destroy molecules, leaving only carbon residues [7]. Although the above methods have achieved some success for the study of biochemical processes within cells or the interaction of a cell with its environment, they are still complicated to apply to observation of individual living cells.

Raman spectroscopy has been increasingly used with modified pipettes for analysis of biomaterial because it has a minimal impact on the cell considered during its introduction to the cell due to the nanoscale tip of the pipette (10–100 nm) [8]. The pipette modified with plasmonic metals can be used to regulate the delivery of molecules/ions and perform in situ measurements of the effects of delivered molecules/ions on a living cell via Raman spectroscopy. The main advantage of using nanopipettes is the simplicity and low cost of the manufacturing process, so such pipettes will allow rapid intracellular studies to obtain accurate information about the single cell structure without the need for complex techniques. However, the nanopipette tip

surface has a complicated topology, which makes the formation of plasmonic particles a non-trivial task. Current methods of pipettes modification have a number of limitations. Ho and colleagues [9] developed a modified pipette by holding in a solution of Ag particles synthesized by reduction from $AgNO_3$ with ethanol. During the modification, the authors used a large number of deposition stages, preparation of several solutions and a large amount of time to successfully precipitate the nanoparticles. It was established in [10] that a pipette could be modified with gold for highly sensitive detection of DNA damage in living cells using electrodeposition from $HAuCl_4$ solution was shown. For successful deposition, the pipette was treated with carbon from the inside via butane pyrolysis, which greatly complicates the modification process. The given methods of pipette modification are cheap to use, but they, as well as a number of others, don't have the reproducibility [11,12]. An alternative method of forming arrays of nanoparticles on the pipette surface is the method of vacuum-thermal evaporation followed by annealing. This method has high reproducibility, controllability of the process to control the size of nanoparticles [13, 14]. It is worth noting that the obtained nanoparticle arrays or thin films have a distinct interfacial boundary, which is important for surface plasmon resonance.

This work is dedicated to developing techniques for forming Ag nanoparticles on the nanopipette surface. In the course of the experiments, the morphology of the pipette surface was studied using scanning electron microscopy. The optimal parameters of Raman studies of the modified nanopipette were revealed and the enhance factor was calculated for the obtained SERS (surface enhanced Raman spectroscopy) active structure.

Materials and Methods

We conducted a series of experiments with borosilicate glass pipettes prepared from a CO_2-laser-based glass pipette (P-2000, SutterInstrument Co.). The length of the fabricated pipettes was about 45 mm, the size of the exit hole was about 50–70 nm.

Before the nanoparticles deposition process, the pipettes were washed as usual to remove the impurities. Cleaning was performed in peroxide-ammonia solution (PAS) and deionized water at ~50 °C followed by drying in isopropyl alcohol vapor.

The formation of metallic nanoparticles was performed using vacuum thermal evaporation followed by heat treatment. As the evaporation material for every deposition was used silver with a mass of 3 mg. The working pressure in the chamber was about $3 \cdot 10^{-5}$ Torr. The samples were annealed in vacuum at a pressure of $3 \cdot 10^{-5}$ Torr at 230 °C for 30 minutes.

Two techniques were used to form an array of silver nanoparticles on the pipette: one deposition on the vertically fixed pipette; two consecutive depositions on the two sides of the pipette. A schematic representation of the methods of nanoparticles formation on the pipette is shown in Fig. 1. Depending on the variant of the technique and deposition, the pipette was attached to the substrate holder in different ways and the number of particle deposition processes varied.

A Helios C4 GX scanning electron microscope was used to study the morphology of the obtained arrays of silver nanoparticles. A Raman spectrometer based on an inVia confocal microscope (Renishaw) was used to obtain Raman spectra. A laser with a wavelength of 532 nm and a power of about 100 mW according to the documentation, 44 mW according to the lens exit

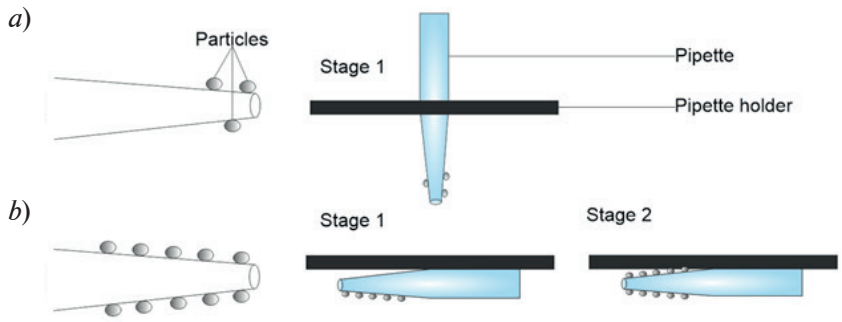

Fig. 1. Illustration of techniques for forming nanoparticles on a pipette: one deposition on a vertically attached sample (*a*); two consecutive depositions on a horizontally attached pipette (*b*)

measurement and a spot size of 2 μm were used. Rhodamine R6G with a concentration of 1 mM was used as the analyte. The analyte was applied by dipping in the appropriate analyte solution for 5 seconds followed by drying for 10 minutes.

Results and Discussion

Analysis of the pipette surface morphology with arrays of silver nanoparticles is shown in Fig. 2. Notably, nanoparticles were not present on the pipette surface when the first technique was used. With the second technique, the average particle size was ~ 16 nm and the distance between them was ~ 14 nm, as shown in Figure 2, *a*.

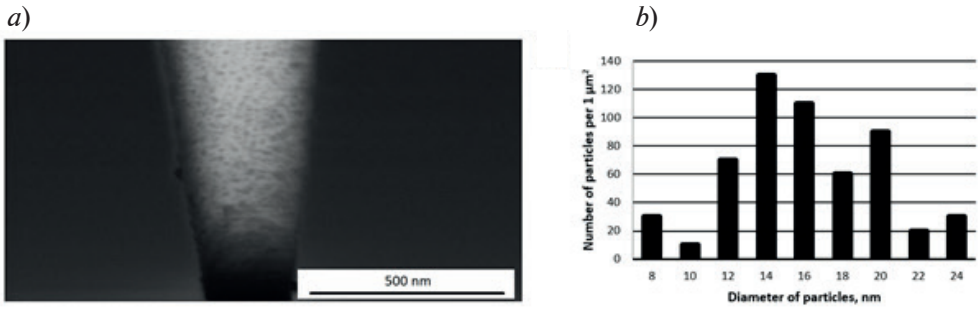

Fig. 2. SEM images of the Ag nanoparticle array for the sample with two horizontal depositions (*a*) and histogram of nanoparticle size distribution per 1 μm^2 (*b*)

Figure 3 shows the results of a Raman spectroscopy study using a pipette with two consecutive depositions at a wavelength of 532 nm, the spot power density was on the order of 0.007 and 0.14 mW/μm^2. Fig. 3 shows that the spectrum obtained at 0.007 mW/μm^2 shows clearly distinguishable peaks corresponding to R6G [15]. When the laser power was increased

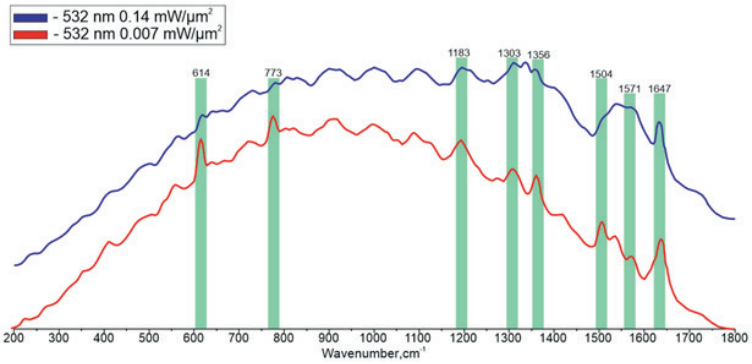

Fig. 3. Raman spectra for a pipette with two consecutive depositions at 532 nm and different laser powers during the study of R6G concentration of 1 mM

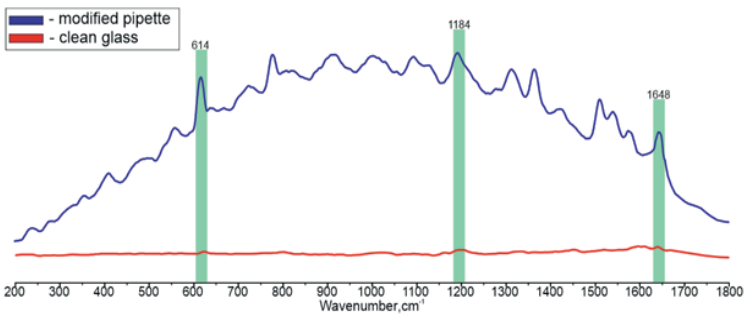

Fig. 4. Raman spectra obtained from pipettes with two consecutive depositions and clean glass at 532 nm of R6G analyte concentration 1 mM

to ~ 0.14 mW/μm^2, individual R6G modes were observed as well as characteristic peaks of amorphous carbon at 1536 cm^{-1} and in the 1500–1600 cm^{-1} region [16]. The presence of characteristic peaks of amorphous carbon is associated with the burning of the analytical substance [17]. Further Raman studies of modified Ag pipettes were performed at ~ 0.007 mW/μm^2.

Figure 4 shows the results of Raman spectroscopy of a pipette with two consecutive depositions and pure glass with the analyte R6G 1 mM at a wavelength of 532 nm with a laser power of 0.007 mW/μm^2. Based on these spectra, the enhance factor of the SERS pipette was calculated [18]. The calculated enhance factor of the modified pipette was ~ 10^3. The lines in (Fig. 4) mark the R6G characteristic peaks, which were used to calculate the enhance factor of the SERS-active pipette.

Conclusion

This paper has outlined an approach to forming the SERS active layer based on the array of silver nanoparticles on the pipette surface by vacuum thermal evaporation method followed by annealing. Morphological study of the modified pipette surface by scanning electron microscopy showed that an array of silver nanoparticles with a size of about 16 nm was formed at two stages of deposition on the horizontally mounted pipette. It was found that the optimal laser power for Raman studies is 0.007 mW/μm, as there are no amorphous carbon peaks at this value. When this laser power is used, the R6G modes are present in the Raman spectrum. The calculated enhance factor of the modified pipette was ~10^3.

REFERENCES

1. **Maruvada P., Wang W., Wagner P.D., Srivastava S.,** Biomarkers in molecular medicine: cancer detection and diagnosis, BioTechniques. 4 (38) (2005) 9–15.

2. **Dittrich P., Jakubowski N.,** Current trends in single cell analysis, Analytical and Bioanalytical Chemistry. 27 (406) (2014) 6957–6961.

3. **Yuan G., Cai L., Elowitz M., Enver T., Fan G., Guo G., Irizarry R., Kharchenko P., Kim J., Orkim S., Quackenbush J., Saadatpour A., Schroeder T., Shvidasani R., Tirosh I.,** Challenges and emerging directions in single-cell analysis, Genome biology 18 (84) (2017) 1–8.

4. **Bandyopadhyay A., Bose S.,** Characterization of biomaterials, Vol. 2, Introduction to Biomaterials: Basic Theory with Engineering Applications, Cambridge University Press, Cambridge, 2013.

5. **Cao Y., Sun M.,** Tip-enhanced Raman spectroscopy, Reviews in Physics. 8 (2022) 100067.

6. **Lin W., Xu X., Quan J., Sun M.,** Propagating surface plasmon polaritons for remote excitation surface-enhanced Raman scattering spectroscopy, Applied Spectroscopy Reviews. 10 (53) (2018) 771–782.

7. **Haldavnekar R., Venkatakrishnan K., Tan B.,** Next generation SERS-atomic scale platform for molecular level detection, Applied Materials Today. 1 (18) (2020) 100529.

8. Bulbul G., Chaves G., Olivier J., Ozel R. E., Pourmand N., Nanopipettes as monitoring probes for the single living cell: state of the art and future directions in molecular biology, Cells 6 (7) (2018) 55.

9. **Ho V. T. T. X., Park H., An S., Kim G., Ly N., Lee S. Y., Choo J., Jung H. S., Joo S. W.,** Coumarin–lipoic acid conjugates on silver nanoparticle-supported nanopipettes for in situ dual-mode monitoring of intracellular Cu (II) and potential chemodynamic therapy applications, Sensors and Actuators B: Chemical. 344 (2021) 130271.

10. **Zhou J., Yang D., Liu G., Li S., Feng W., Yang G., He J., Shan Y.,** Highly sensitive detection of DNA damage in living cells by SERS and electrochemical measurements using a flexible gold nanoelectrode, Analyst. 7 (146) (2021) 2321–2329.

11. **Yang D., Liu G., Li H., Liu A., Guo J., Shan Y., Wang Z., He J.,** The fabrication of a gold nanoelectrode–nanopore nanopipette for dopamine enrichment and multimode detection, Analyst 3 (145) (2020): 1047–1055.

12. **Hong-Na L., Dan Y., Ao-Xue L., Guo-Hui L., Yu-Ping S., Guo-Cheng Y., Jin H.,** Facile fabrication of gold functionalized nanopipette for nanoscale electrochemistry and surface enhanced Raman spectroscopy, Chinese Journal of Analytical Chemistry 8 (47) (2019) 19104–19112.

13. **Gromov, D. G., Dubkov S. V., Savitskiy A. I., Shaman Y. P., Polokhin A. A., Belogorokhov I. A., Trifonov A. Y.,** Optimization of nanostructures based on Au, Ag, AuAg nanoparticles formed by thermal evaporation in vacuum for SERS applications, Applied Surface Science 489 (2019) 701–707.

14. **Dubkov S. V., Savitskiy A. I., Trifonov A. Y., Yeritsyan G. S., Shaman Y. P., Kitsyuk E. P., Tarasov A., Shtyka O., Ciesielski R., Gromov D.G.,** SERS in red spectrum region through array of Ag-Cu composite nanoparticles formed by vacuum-thermal evaporation, Optical Materials. 7 (2020) 100055.

15. **He X. N., Gao Y., Mahjouri-Samani M., Black P. N., Allen J., Mitchell M., Xiong W., Zhou Y. S., Jiang L., Lu Y. F.,** Surface-enhanced Raman spectroscopy using gold-coated horizontally aligned carbon nanotubes, Nanotechnology. 20 (23) (2012) 205702.

16. **Dychalska A., Popielarski P., Frankyw W., Fabisiak K., Paprocki K., Szybowicz M.,** Study of CVD diamond layers with amorphous carbon admixture by Raman scattering spectroscopy, Materials Science-Poland. 4 (33) (2015) 799–805.

17. **Ho M., Lau A.,** Amorphous carbon nanocomposites, Material Science. (2015) 309–328.

18. **Kosuda K. M., Bingham J. M., Wustholz K. L., Van Duyne R. P.,** Nanostructures and surfaceenhanced Raman spectroscopy, Handbook of Nanoscale Optics and Electronics. 309 (2010).

THE AUTHORS

OVERCHENKO Aleksei D.
alexsey7840@mail.ru
ORCID: 0000-0003-1313-2128

VOLKOVA Lidiya D.
Ilidiya.volkova.96@mail.ru
ORCID: 0000-0003-4860-0585

DUBKOV Sergey V.
sv.dubkov@gmail.com
ORCID: 0000-0003-1507-8807

GRISHIN Timofey S.
grishin.t@outlook.com
ORCID: 0000-0001-6261-5316

NOVIKOV Denis V.
tororo@bk.ru
ORCID: 0000-0002-9518-1208

EDELBEKOVA Polina A.
polinaedel51@gmail.com
ORCID: 0000-0002-8422-9798

KOLMOGOROV Vasilii S.
vskolmogorov@gmail.com
ORCID: 0000-0002-7135-8910

Received 21.05.2022. Approved after reviewing 25.07.2022. Accepted 26.07.2022.

Conference materials
UDC 538.9
DOI: https://doi.org/10.18721/JPM.153.121

Facile fabrication of a TiO_2 NW-based glucose sensor by direct ink writing

A. M. Tarasov [1] ✉, S. V. Dubkov [1], D. G. Gromov [1] R. M. Ryazanov [2], L. S. Volkova [3]

[1] National Research University of Electronic Technology, Moscow, Russia;
[2] Scientific-Manufacturing Complex «Technological Centre», Moscow, Russia;
[3] Institute of Nanotechnology of Microelectronics RAS, Moscow, Russia
✉ bloggger4@gmail.com

Abstract: This paper presents the results of facile fabrication of a non-enzymatic glucose sensor by forming a sensing element based on TiO_2 nanofilaments using direct ink writing (DIW). The glucose concentration in the solution was determined by changing the resistance of the TiO_2 layer. Nanowires (NW) were obtained by hydrothermal synthesis in 10 M sodium alkali solution followed by heat treatment. The surface morphology of obtained samples was studied using scanning electron microscopy. The formation of a sensitive layer was carried out on a 3D printer with a specially designed print head from a suspension based on an aqueous solution of polyvinyl alcohol (PVA) followed by heat treatment in air. The suspension was analyzed for viscosity and contact angle. The sensitive layers were formed on a silicon substrate with a SiO_2 surface oxide layer and gold contacts. Layers of TiO_2 NW were formed between the contacts. The sensitivity of the sensor to glucose solutions of various concentrations was studied. As a result of the studies, the studied structures showed sensitivity to a glucose solution in the range from 1 to 100 mmol.

Keywords: TiO_2, nanowires, hydrothermal synthesis, glucose sensor

Funding: This work was financially supported by the grant of President of the Russian Federation (project MK-2201.2021.4).

Citation: Tarasov A. M., Dubkov S. V., Gromov D. G., Ryazanov R. M., Volkova L. S., Facile fabrication of a TiO_2 NW-based glucose sensor by direct ink writing, St. Petersburg State Polytechnical University Journal. Physics and Mathematics. 15 (3.1) (2022) 125–130. DOI: https://doi.org/10.18721/JPM.153.121

Материалы конференции
УДК 538.9
DOI: https://doi.org/10.18721/JPM.153.121

Изготовление сенсора глюкозы на основе нанонитей TiO_2 методом робокастинга

А. М. Тарасов [1] ✉, С. В. Дубков [1], Д. Г. Громов [1] Р. М. Рязанов [2], Л. С. Волкова [3]

[1] Национальный исследовательский университет «МИЭТ», г. Москва, Россия;
[2] Научно-производственный комплекс «Технологический центр», г. Москва, Россия;
[3] Институт нанотехнологий микроэлектроники РАН, г. Москва, Россия
✉ bloggger4@gmail.com

Аннотация. В данной работе приводятся результаты простого изготовления неферментативного сенсора глюкозы путём формирования чувствительного элемента сенсора на основе нанонитей TiO_2 методом робокастинга. Определение концентрации глюкозы в растворе происходило за счёт изменения сопротивления слоя TiO_2. Полученные структуры показали отклик на раствор глюкозы микромолярной концентрации.

Ключевые слова: TiO_2, нанонити, гидротермальный синтез, сенсор глюкозы

Финансирование: Исследование выполнено при финансовой поддержке гранта Президента Российской Федерации (проект МК-2201.2021.4).

Ссылка при цитировании: Тарасов А. М., Дубков С. В., Громов Д. Г., Рязанов Р. М., Волкова Л. С., Изготовление сенсора глюкозы на основе нанонитей TiO_2 методом робокастинга // Научно-технические ведомости СПбГПУ. Физико-математические науки. 2022. Т. 15. № 3.1. С. 125–130. DOI: https://doi.org/10.18721/ JPM.153.121

Introduction

Today, biosensors are attractive objects for research due to their high sensitivity and high detection rate of substances with low concentrations, for example, the level of glucose in human blood. About 85 % of the market for modern glucose sensors is occupied by devices using electrochemical, chemiluminescent and phenylboronic acid-based glucose detection methods [1]. In recent years, FET-based sensors, which determine the concentration by changing the resistance when interacting with an analyte, are considered good candidates for creating glucose sensors. Most often, semiconductor materials (for example, ZnO [2], $BaTiO_3$ [3] or TiO_2 [4]) are used as a sensitive layer in such sensors. A particularly attractive option is using TiO_2 in the form of nanofilaments as a sensitive element of the sensor, due to its high stability and photocatalytic activity, which will allow to construct reusable sensors [5].

The creation of sensitive sensors is associated with difficulties in controlling their properties through using hybrid materials. Traditional methods of microelectronics are quite expensive and require highly qualified personnel. Additive technologies, in particular the method of direct printing from a solution (DIW), can provide an affordable alternative to traditional methods [6]. Additive technologies are introduced today in many areas, such as biomedicine, engineering and sensorics [7].

In this work, we demonstrate the formation of a sensitive layer of a glucose sensor by the DIW method based on TiO_2 NWs obtained by the hydrothermal method. A study of the surface morphology of the obtained TiO_2 nanowires was carried out, an approach to the formation of a sensitive layer was developed, and the sensitivity range of the sensor was identified. As a result, the developed sensor based on TiO_2 made it possible to detect glucose concentrations from 1 to 100 mmol.

Materials and Methods

Titanium dioxide NWs were obtained using the hydrothermal synthesis method. A stainless steel autoclave with a Teflon container was used to prepare 50 ml of 10 M NaOH solution (CAS number: 1310-73-2) and 0.6 mg of commercial TiO_2 powder (CAS number: 13463-67-7). The filling factor was 1/2. Then the autoclave was placed in a muffle furnace and heated to 250 °C. The synthesis time was about 12 hours. After synthesis was completed, the autoclave was cooled together with the oven to room temperature. The resulting nanowires were washed in a 0.1 M HCl solution (CAS number: 7647-01-0) with constant stirring to neutralize alkali residues and Na ions. To remove the acid, the NWs were washed in deionized water with heating to 60 °C and constant stirring. Washing was carried out to normal pH. Then the NWs were dried in air at 100 °C. At the final step, the obtained samples of NWs were heat treated at 700 °C for 4 hours in an air atmosphere. The structure morphology was studied using a Helios Nanolab 650 SEM microscope (20 kV, 10 pA). X-ray phase analysis of TiO_2 nanowires was carried out on a Malverin PanAnalytical Empirean diffractometer.

Ink was prepared for the formation of sensitive elements of the glucose sensor by the DIW method. The ink was based on an aqueous solution of polyvinyl alcohol (PVA). 20 g of PVA was added to 20 ml of deionized water and stirred until complete dissolution. Then, 20 mg of TiO_2 nanofilaments were added to the solution and sonicated for 1 minute using a Skymen JP-010T ultrasonic bath.

The viscosity of the suspension was measured with a VPZh-3 viscometer with a capillary diameter of 0.91 mm. Viscosity was measured at a constant temperature of 30 °C, which was provided by heating the viscometer case using a Lauda Alpha thermostat. The viscometer was filled with a PVA solution using a vacuum pump, then the solution was thermally stabilized for 10 minutes.

The contact angle was measured using an LK-1 goniometer. A drop of suspension with a volume of 0.5 μl was formed on the surface of a silicon wafer. After that, the goniometer focused on the drop and took a picture of the image. The resulting images were processed in the Drop Shape program.

A silicon wafer with SiO_2 on the surface about 300 nm thick was used as a substrate for the glucose sensor. Au-based contacts were formed by vacuum-thermal evaporation of a sample of the corresponding material (about 150 mg). The thickness of the obtained gold contacts was about 100 nm. The dimensions of the contacts were 1×1 mm², the step between the contacts was about 5 mm. The scheme for manufacturing contacts is shown in Figure 1, *a*.

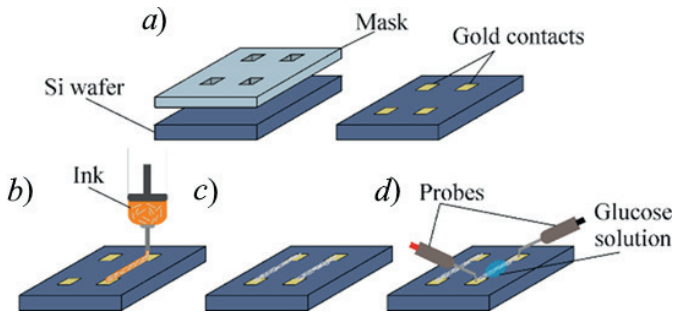

Fig 1. Scheme of sensor fabrication: deposition of gold contacts (*a*), formation of nanowire layer by the DIW method (*b*), polymer burning (*c*), measurement of the current-voltage characteristics of the sensitive layer with a glucose solution on the surface (*d*).

The formation of TiO_2 nanowires layers was carried out on a modified Anet A6 3d printer with a specially designed print head. A glass syringe with prepared ink was installed inside the print head (Fig. 1, *b*). A nozzle with a diameter of 0.4 mm was used for printing. Printing was carried out with a table temperature of 100 °C, and the water evaporated from the polymer in a few seconds. Next, the samples were annealed in air at a temperature of 600 °C for 10 minutes to remove the polymer (Fig. 1, *c*).

Study of the sensory properties of assets obtained by measuring the current-voltage characteristics. A drop of 10 μl of a transparent solution with a concentration of 5, 10, and 100 mM was applied with two gold contacts. Applying voltage to the Agilent e3647a power energy impact sensitive level. The current was measured with a Keithley 6485 picoammeter, and the voltage was measured with a Keithley 2700 multimeter. The measurement circuit is shown in Figure 1,*d*.

Results and Discussion

Figure 2, *a* shows the SEM image of TiO_2 NWs. The histogram of the length distribution of TiO_2 NWs is shown in Figure 2, *b*. Evidently, the length of the nanowires turned out to be fairly uniform. The predominant length of the nanowires was 8 μm.

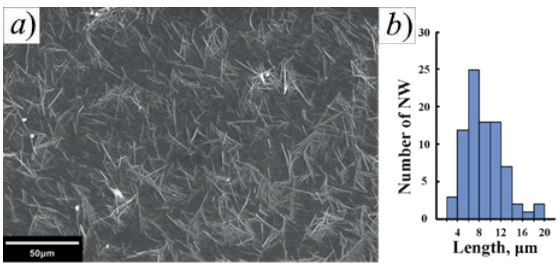

Fig. 2. SEM images of nanowires after 12 hours synthesis at 250 °C (*a*) and histograms of the size distribution of TiO_2 NWs (*b*)

Figure 3 shows X-ray diffraction (XRD) of the synthesized nanowires before and after annealing. The unannealed nanowires do not exhibit the peaks characteristic of anatase and rutile. After synthesis, $Na_2Ti_3O_7$ is formed, which, when washed with hydrochloric acid, passes into $H_2Ti_3O_7$, whose peaks are observed at 24.8° and 48.5° [8]. Annealed nanowires exhibit peaks characteristic of ananthase and rutile.

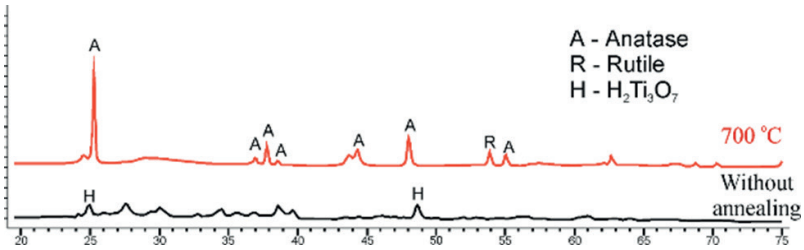

Fig. 3. X-ray diffraction (XRD) of TiO_2 NWs before and after annealing

The measured viscosity of the PVA solution showed a value of 19.44 mm^2/s. The viscosity of water at 30 °C is 0.8 mm^2/s. The addition of PVA to the ink allows the use of aqueous solutions for DIW printing. The edge wetting angle of the PVA solution was 46 °, which is less than that of water. However, the evaporation of water from the solution is faster, so there is no strong spreading of the ink.

Figure 4, *a* shows the SEM image of the formed layers of TiO_2 nanowires. With a nozzle diameter of 0.4 mm, the resulting line thickness is approximately 0.7 mm. This can be attributed to the spreading of ink over the surface of the silicon substrate before the water evaporates. After annealing in air (Fig. 4, *b*), cracking of the layer is observed as a result of polymer boiling.

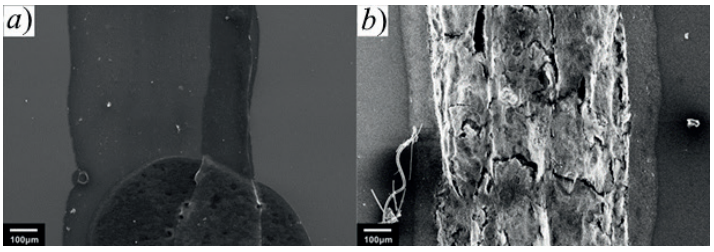

Fig. 4. SEM images of TiO_2 NW layer formed by DIW method before annealing (*a*) and after annealing (*b*)

At a higher magnification (Fig. 5), we can see that the NWs have a predominant direction, which coincides with the direction of movement of the print head. This effect occurs due to the friction that occurs in the nozzle in a viscous medium. For sensing applications, this can be beneficial as it increases the chance of making a contact with nearby nanowires [9].

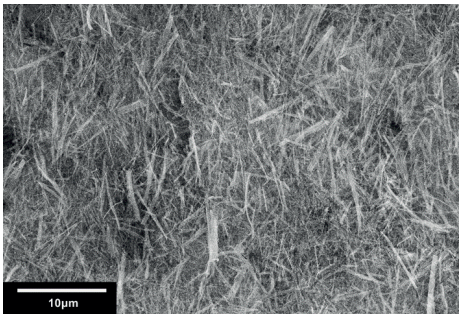

Fig. 5. SEM image of TiO_2 nanowire layer formed by DIW method after annealing

The study of the current-voltage characteristics of sensitive layers at different concentrations of glucose solution showed the results presented in Figure 6. With an increase in the concentration of glucose solution, the conductivity of the structure increases. This effect can be explained by the

doping of the TiO_2 surface with glucose, which plays the role of an electron donor. This increases the conductivity of the sensitive layer [10].

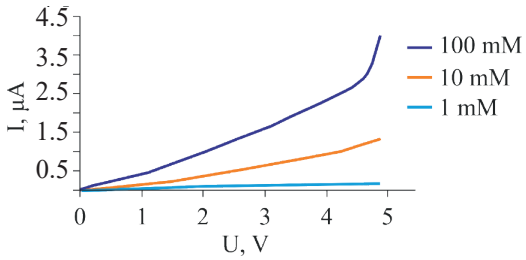

Fig. 6. Volt-ampere characteristic as a function of glucose concentration

Conclusion

In the course of this work, we synthesized TiO_2 nanowires with a length of about 8 μm and a diameter of about 200 nm. An approach using an Anet A6 3D printer was developed to form sensitive sensor layers using the direct ink writing method based on a TiO_2-PVA suspension. The developed suspension based on the TiO_2-polymer has a contact angle of 46° and a viscosity of about 19.44 mm^2/s. A glucose sensor based on TiO_2 nanowires formed by the DIW method made it possible to detect the concentration of a glucose solution from 1 to 100 mM. Additive technology methods make it easy to form functional layers for sensors of arbitrary shape without involving expensive equipment. Using TiO_2 as a sensitive element of the sensor in the future will allow us to study the effect of self-cleaning of the surface of the glucose sensor and create a structure with the option for reuse.

REFERENCES

1. **Yu R., Pan C., Chen J., Zhu, G., Wang, Z. L.,** Enhanced performance of a ZnO nanowire-based self-powered glucose sensor by piezotronic effect, Advanced Functional Materials. 23 (47) (2013) 5868–5874.

2. **Ahmad R., Tripathy N., Park J. H., Hahn Y. B.,** A comprehensive biosensor integrated with a ZnO nanorod FET array for selective detection of glucose, cholesterol and urea, Chemical Communications. 51 (60) (2015) 11968–11971.

3. **Selvarajan S., Alluri N. R., Chandrasekhar A., Kim S. J.,** $BaTiO_3$ nanoparticles as biomaterial film for self-powered glucose sensor application, Sensors and Actuators B: Chemical. 234 (2016) 395–403.

4. **Kim Y., Malliaras G. G., Ober C. K., & Kim E.,** An electrochemical glucose sensor from an organically modified nanocomposite of viologen and TiO_2, Journal of Nanoscience and Nanotechnology. 10 (10) (2010) 6869–6873.

5. **Zhong T., Li H., Zhao T., Guan H., Xing L., Xue X.,** Self-powered/self-cleaned atmosphere monitoring system from combining hydrovoltaic, gas sensing and photocatalytic effects of TiO_2 nanoparticles, Journal of Materials Science & Technology. 76 (2021) 33–40.

6. **Xu Y., Wu X., Guo X., Kong B., Zhang M., Qian X., Mi. S., Sun, W.,** The boom in 3D-printed sensor technology. Sensors. 17 (5) (2017) 1166.

7. **Ngo T. D., Kashani A., Imbalzano G., Nguyen K. T., Hui D.,** Additive manufacturing (3D printing): A review of materials, methods, applications and challenges, Composites Part B: Engineering. 143 (2018) 172–196.

8. **Zhang W., Zhu J., He J., Xu L., Hu L.,** Construction of $NiO/H_2Ti_3O_7$ nanotube composite and its photocatalytic conversion feature for ethyl mercaptan, Applied Physics A. 126 (8) (2020) 1–10.

9. **Malakooti M. H., Julé F., Sodano H. A.,** Printed nanocomposite energy harvesters with controlled alignment of barium titanate nanowires, ACS applied materials & interfaces. 10 (44) (2018) 38359–38367.

10. **Selvarajan S., Alluri N. R., Chandrasekhar A., & Kim, S. J.,** $BaTiO_3$ nanoparticles as biomaterial film for self-powered glucose sensor application, Sensors and Actuators B: Chemical. 234 (2016) 395–403.

THE AUTHORS

TARASOV Andrey M.
bloggger4@gmail.com
ORCID: 0000-0003-3648-8717

DUBKOV Sergey V.
sv.dubkov@gmail.com
ORCID: 0000-0003-1507-8807

GROMOV Dmitry G.
gormadima@gmail.com
ORCID: 0000-0002-4563-9831

RYAZANOV Roman M.
r.m.ryazanov@gmail.com
ORCID: 0000-0002-2464-8712

VOLKOVA Lida S
lidiya.volkova.96@mail.ru
ORCID: 0000-0003-4860-0585

Received 22.05.2022. Approved after reviewing 07.07.2022. Accepted 07.07.2022.

Conference materials
UDC 539.216
DOI: https://doi.org/10.18721/JPM.153.122

Effect of thickness and annealing of the Si(001)2×1-Cu wetting layer on the morphology of layered nanofilms based on Fe, Co, and Cu and their ferromagnetic properties

N. I. Plyusnin[1, 2] ✉, P. A. Usachev[1], V. V. Pavlov [1]

[1] Ioffe Institute, St. Petersburg, Russia;

[2] S. M. Budyonny Communications Academy of the Ministry of Defense of the Russian Federation, St. Petersburg, Russia

✉ plusnin@dvo.ru

Abstract: Layered nanofilms based on Fe, Co, and Cu were grown on Si(001)2×1-Cu wetting layers with thicknesses of 1 and 2 ML and studied using the AES, EELS, and LEED methods in an ultrahigh vacuum chamber. After unloading into air, the samples were studied by AFM and MOKE methods. It was found that an increase in the thickness and annealing of the Si(001)2×1-Cu wetting layer increase the agglomeration of nanofilms and, as a consequence, their magnetization and coercive force. Although, annealing the Cu wetting layer reduces the degree of squareness of the magnetic hysteresis loop.

Keywords: multilayer films, wetting layer, growth, agglomeration, morphology, metals, silicon substrate, hysteresis loop, atomic force microscopy, magneto-optical Kerr effect

Citation: Plyusnin N. I., Usachev P. A., Pavlov V. V., Effect of thickness and annealing of the Si(001)2×1-Cu wetting layer on the morphology of layered nanofilms based on Fe, Co, and Cu and their ferromagnetic properties, St. Petersburg State Polytechnical University Journal. Physics and Mathematics. 15 (3.1) (2022) 131–136. DOI: https://doi.org/10.18721/JPM.153.122

Материалы конференции
УДК 539.216
DOI: https://doi.org/10.18721/JPM.153.122

Влияние толщины и отжига смачивающего слоя Si(001)2×1-Cu на морфологию слоистых нанопленок на основе Fe, Co и Cu и их ферромагнитные свойства

Н.И. Плюснин [1, 2] ✉, П.А. Усачев [1], В.В. Павлов [1]

[1] Физико-технический институт им. А.Ф. Иоффе РАН, Санкт-Петербург, Россия;

[2] Академия связи им. С.М. Буденного МО РФ, Санкт-Петербург, Россия

✉ plusnin@dvo.ru

Аннотация. Слоистые нанопленки на основе Fe, Co и Cu были выращены на смачивающих слоях Si(001)2×1-Cu с толщинами 1 ML и 2 ML и исследованы методами AES, EELS и LEED в сверхвысоковакуумной камере. После выгрузки на воздух образцы были исследованы методами AFM и MOKE. Было обнаружено, что увеличение толщины и отжиг смачивающего слоя Si(001)2×1-Cu увеличивают агломерацию нанопленок и, как следствие, их намагниченность и коэрцитивную силу. Хотя, отжиг смачивающего слоя Cu, уменьшает степень прямоугольности петли магнитного гистерезиса.

Ключевые слова: многослойные пленки, смачивающий слой, рост, агломерация, морфология, металлы, кремниевая подложка, петля гистерезиса, атомно-силовая микроскопия, магнитооптический эффект Керра

Ссылка при цитировании: Плюснин Н. И., Усачев П. А., Павлов В. В. Влияние толщины и отжига смачивающего слоя Si(001)2×1-Cu на морфологию слоистых нанопленок

на основе Fe, Co, и Cu и их ферромагнитные свойства // Научно-технические ведомости СПбГПУ. Физико-математические науки. 2022. Т. 15. № 3.1. С. 131–136. DOI: https://doi.org/10.18721/ JPM.153.122

Introduction

In recent years, considerable attention has been paid to developing spin transistors and spin injectors using spin valves made of multilayer metal nanostructures based on ferromagnetic metals and their alloys [1]. Such nanostructures should have high spin conductivity, degree of polarization, magnetization, and Curie temperature. To increase the spin conductivity, it is suggested to place these nanostructures on top of an intermediate layer of an inert noble metal on a substrate [2]. Additionally, it is proposed to use layered composite nanomaterials from a ferromagnetic metal and a noble metal [3]. Therefore, the study of the influence of intermediate layers of noble metals (Cu) or their wetting layers on the growth, morphology, and magnetic properties of multilayer metal nanostructures on silicon is topical for spintronics.

From a physical point of view, the fundamental interest is a multilayer structure made of dissimilar metals on an alien (silicon) substrate. It is important to understand what phenomena occur during the growth of this structure and how are they related to the growth phenomena of the first wetting layer. In addition, it is important to clarify how the combination of a magnetic transition metal and a noble non-magnetic metal will affect the growth of a multilayer film and its magnetic properties. In this work we try to clarify these questions.

It can be expected that the difference between layers of different nature and degree of reactivity, which wet the substrate to different degrees, can have different effects on the growth of a multilayer film and its morphology. Thus, we can expect a significant morphological dependence on the type of the first metallic film on silicon. On the contrary, the growth of metal on metal may have a weaker morphological dependence on the type of the first metal. However, in general, the film morphology should significantly affect its magnetic properties.

Previously, we studied the growth of ultrathin and atomically smooth layers and films of Cu (1–5 ML) [4], Fe (10–25 ML) [5, 3], and Co (10 ML) [6] on silicon. A technology for their growth was based on a decrease in the temperature of steam in sources during the formation of a wetting layer (see [4–8]). Multilayer nanofilms based on Fe, Co, and Cu were also prepared [3]. However, the morphology of these films, its relation to film production conditions, and the effect on magnetic properties were not studied yet.

Here we present the growth and study of Fe (10–12 ML) and Cu (8 ML)/Fe(16 ML)/Cu (5 ML)/Co(10 mL) multilayer nanofilms on an intermediate two-dimensional layer of Cu (1–2 mL), which plays not only the role of a wetting layer but also that of a buffer layer blocking the formation of compounds or alloys between the overlying and underlying layers. Moreover, two-dimensional layers of noble metals simultaneously play the role of a highly conductive transport layer, which increases the longitudinal conductivity of a two-layer or multilayer nanofilm. The purpose of this study is to determine the effect of the thickness and annealing of a two-dimensional wetting layer on the morphology and magnetic properties of multilayer nanofilms in order to determine the optimal modes for their production as spin injectors.

Experiment

Samples were prepared in a microwave chamber with RIBER analyzers for low energy electron diffraction (LEED) and Auger electron spectroscopy (AES) electron energy loss spectroscopy (EELS). The chamber was equipped with a sample manipulator, a quartz microbalance, as well as molecular beam (ribbon) sources of Fe, Co, and Cu, and other equipment (see [3]).

Metal layers were deposited on silicon at room temperature of the Si(001) substrate and at a low temperature of metal vapors. They were deposited on a Si(001)-2×1-Cu wetting layer (1–2 ML thick) before and after its annealing at 250°C. The thickness of the wetting layer corresponded to the formation of a phase of average composition Cu2Si [5] and was in the range of 1–2 ML.

Phosphorus-doped single-crystal silicon wafers were used as substrates. They had a size of 20×5 mm^2, a thickness of 0.42 mm, orientation (001) and a resistivity of 4.5 Ω·cm. The Si wafers were preliminarily cleaned with organic solvents and then loaded into a degassed ultrahigh vacuum chamber with a base pressure of 5×10^{-10} Torr. After that, the Si wafers were heated at a temperature of 600 °C for several hours. Before the first deposition of metal on a clean Si surface, the temperature of the Si wafers was raised to 1250 °C and then gradually lowered to room temperature, quickly passing the temperature range of about 1000 °C.

The crystallographic quality of the prepared surface of the Si(001)-2×1 silicon substrate was controlled by the presence of sharp and bright 2×1 reflections in the LEED pattern. Surface cleanliness was monitored by the presence of oxygen and carbon peaks in the AES. The temperature of the Si substrate was set by passing a constant electric current through it.

Metal vapors were deposited on the substrate by thermal sublimation of metals from Cu, Co, and Fe films preliminarily deposited onto a Ta tape 5×25 mm^2 in size and 10–20 μm thick. These films were deposited using evaporation from Fe or Co rods placed inside a tungsten coil or from a drop of Cu formed on a V-shaped tungsten wire. All metals had more than 99.98% pure. The metal vapor temperature (T_{Fe} =1250 ºC, T_{Co} = 1130 ºC and T_{Cu} = 900 ºC, $\Delta T < \pm$ 5 ºC) was maintained by passing a direct electric current through tungsten tape or wire heaters. Simultaneously, deposition was carried out on two samples, while the distance from the tape source to the Si substrates was about 2 cm.

Magnetic characteristics of the samples were studied in longitudinal geometry using an experimental setup based on the magneto-optical Kerr effect (MOKE). The light source used in the MOKE studies was a helium-neon laser with the wavelength of 632 nm and whose light intensity was modulated at a frequency of 42 kHz. A PEM-100 photo-elastic modulator from Hinds Instruments was used for modulation, and an SR830 lock-in amplifier from Sanford Research was used for signal detection. The sensitivity to the rotation angle of the polarization plane was about 1 second of arc.

AES and EELS spectra were recorded using low electron energy (300 eV). This made it possible to ensure high sensitivity of the spectra in the film thickness range of 1–10 ML, as well as sensitivity to the state of the interface at a film thickness of 0–3 ML. To obtain LEED images, electron energies were used in the range of 50–100 eV, which ensured a probing depth of about 1 ML. Quantitative analysis of AES was performed with an error of ~20%, taking into account the accuracy of determining the probing depth in the literature. The AFM data were acquired in semi-contact scanning mode on an NT MDT Silver-47 microscope and processed using standard software from NT MDT.

Results and Discussion

The LEED images show that a partial attenuation of the 2×1 reflections occurred after deposition of 1 ML and 2 ML Cu on Si(001)-2×1. However, the 2×1 reflections became brighter after 1st ML annealing, showing the formation of a two-dimensional layer with a 2×1 structure. Complete attenuation of the reflections occurred after the deposition of 3 ML or its annealing, which indicates the growth of a continuous Cu layer with a subcrystalline (cluster) structure.

According to changes in the intensity of Cu, Fe, and Co Auger peaks, after the formation of the Cu (WL) wetting layer, pseudolayered growth of Co (Fe), Cu, Fe, and Cu and Si segregation occurred. The last Si layer was apparently forced out of the substrate during film growth.

The formation stages of surface and bulk plasmonic peaks of Fe and Co losses in EELS also corresponded to pseudolayered growth. However, for Fe and Co on Cu, a slower growth was observed, which indicates film agglomeration and the growth of Fe and Co islands.

The AFM data directly showed film agglomeration in all samples. As can be seen from Fig. 1, the average relief height was in the range of 1–12 nm and, depending on the presence and annealing of the Cu wetting layer, increased by a factor of 1.2–1.5 in the case of an Fe nanofilm and by a factor of 2 in the case of multilayer films. At the same time, the lateral size of grains in the samples and their number decreased.

Since the morphology of the entire multilayer film as a whole is given by the morphology of the first ferromagnetic layer (Co, Fe), it can be concluded that the presence of Cu-WL leads to agglomeration of this first layer. However, as the next layers grow, additional agglomeration occurs and grains of similar sizes are formed (Fig. 1, *c, f*).

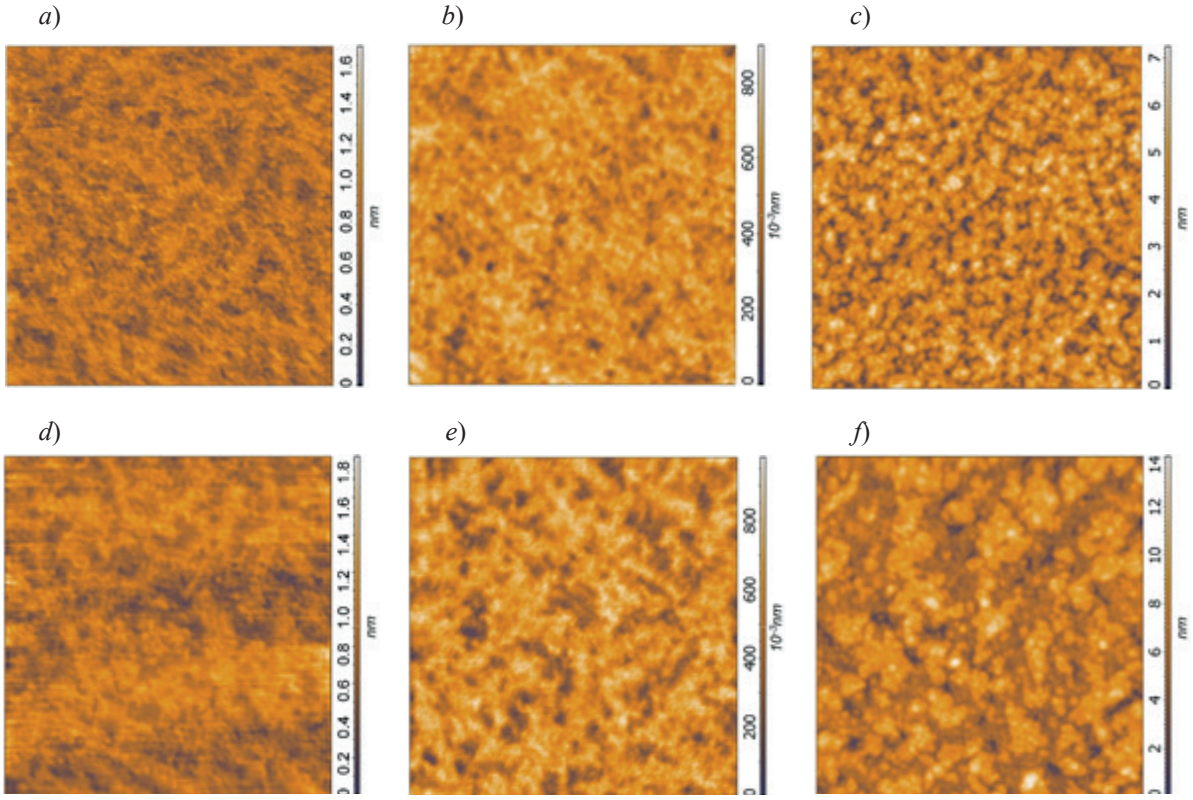

Fig. 1. AFM images (1000×1000 nm²) of Fe (*a, b, d, e*) nanofilms with a thickness of 10–12 ML and Cu/Fe/Cu/Co multilayer (*c, f*) with a total thickness of 39 ML grown on Cu WL, respectively, 1 and 2 ML thick: without pre-annealing (*a, b, c*), subjected to annealing (*d, f*), with Cu WL thickness increasing from 1 ML (*b*) to 2 ML (*e*)

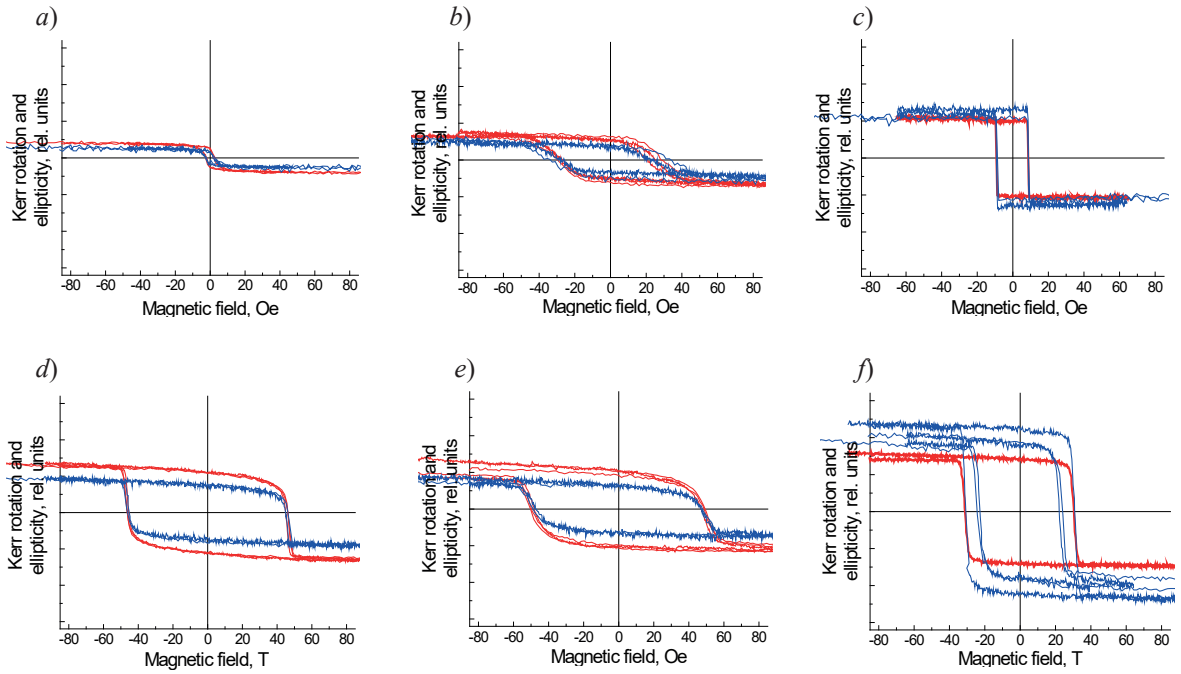

Fig. 2. Longitudinal Kerr rotation (red) and ellipticity (blue) in Fe (*a, b, d, e*) nanofilms with a thickness of 10–12 ML and Cu/Fe/Cu/Co multilayer (*c, f*) with a total thickness of 39 ML grown on a Cu WL respectively, 1 and 2 ML thick: without pre-annealing (*a, b, c*), subjected to annealing (*d, f*), with Cu WL thickness increasing from 1 ML (*b*) to 2 ML (*e*)

When a non-magnetic metal (Cu) is grown on a wetting layer and annealed, the multilayer film composed of Cu/Fe/Cu/Co layers becomes looser and consists of larger islands (Fig. 1, *d, e, f*). In this case, the coercive force and magnetization in the obtained nanofilms become much higher (Fig. 2, *d, e, f*) than without the interlayer and its annealing (Fig. 2, *a, b, c*). At the same time, generally, increased values of the coercive force are observed, which cannot be explained only by a change in the type of metal or morphology. Since, according to the AES data, Si solid solutions are formed in the grown layers, the presence of Si in the Fe and Co layers increases the coercive force.

In general, the observed phenomena have the following explanations. When a metal is deposited on a clean silicon surface, a 2D wetting layer grows, a 3D metastable phase grows, and then a 3D stable bulk metal phase grows [4–5, 8]. At the same time, the 2D-3D transition causes the separation of a small amount of silicon from the substrate and the segregation of silicon atoms (the thickness of the segregated layer is less than the monolayer). At the last stage of growth (when a stable bulk metal phase is formed), the precipitated Si dissolves in the growing metal film. Meanwhile, without an intermediate Cu layer, the formation of silicide and the dissolution of Si suppress the ferromagnetism of the multilayer film.

At the same time, these processes are blocked for wetting with copper, and ferromagnetism becomes more pronounced. Obviously, wetting with copper leads to an increase in the degree of agglomeration of ferromagnetic layers caused by the chemical inertness of copper. In addition, the presence of an intermediate wetting metal layer (Cu) blocks the mixing of the ferromagnetic metal with silicon during its pseudolayer (multi-island) growth. However, during annealing, the Cu layer is partially collected into islands near the substrate steps. This leads to a concentration of multi-island growth on the terraces and the film becomes less continuous.

In both cases, the nanofilm on the Cu wetting layer collects into islands more strongly than when grown on a clean surface of a silicon substrate. As for the growth of intermediate (between ferromagnetic layers) and upper layers of Cu, it proceeds in accordance with the pseudolayer-by-layer growth mechanism, since the Cu layers spread well over the surface of the ferromagnetic metal. In addition, the Cu layers increase the mobility of atoms in the film and help even out the shape of the agglomerates. The subsequent growth of the ferromagnetic metal on Cu also occurs in accordance with the pseudolayer growth mechanism, but is accompanied by an increase in agglomeration. Finally, the last noble metal layer (Cu) spreads over the film again and evens out the shape of the agglomerates.

As can be seen from Figure 2, the larger the diameter and height of the agglomerates, the more pronounced the ferromagnetic properties (magnetization and coercive force) become. This corresponds to the well-known data on the relationship between the sizes of crystals and their magnetic properties (see, for example, [9]). However, as can be seen from Figure 2, *c*, the squareness of the hysteresis loop is obviously more pronounced if there are ferromagnetic grains of the same size, as happens in the case of an unannealed wetting layer. In addition, saving the thickness of the ferromagnetic layers leads to an exchange interaction between the layers and to the formation of the smallest coercive force (coercive force Co) between the two ferromagnetic layers.

Conclusions

· Ultrathin layers of Cu on silicon with a thickness of 1–2 monolayers with and without annealing were prepared, which were used as a wetting and buffer layer for the subsequent growth of ferromagnetic layers of Fe and Co.

· The effect of wetting layer annealing and its thickness on the morphology of layered nanofilms on silicon with ferromagnetic (transition metals Fe and Co) and nonmagnetic (noble metal Cu) layers is shown.

· The degree of agglomeration and grain size in multilayer nanofilms have a decisive influence on the magnetic properties (magnetization and coercive force) of the obtained nanomultilayers.

· Optimum nanofilms for spin valves, in terms of magnetization strength, are nanofilms that are grown with annealing of the Cu wetting layer, and in terms of a more rectangular hysteresis loop and a narrower hysteresis loop, those that are grown without annealing.

REFERENCES

1. **Plusnin N.,** Creation of electrical spin injectors for silicon spintronics: Achievements and prospects. Solid State Phenomena. 245 (2016) 32–41.

2. **Zavaliche F., Wulfhekel W., Xu H., Kirschner J.,** Suppression of silicide formation in Fe films grown on Si (001). Journal of Applied Physics, 88 (9) (2000) 5289–5292.

3. **Plyusnin N. I., Il'yashchenko V. M., Usachev P. A., Pavlov V. V.,** Growth and structural and magnetic properties of multilayer Fe, Co, and Cu nanofilms on silicon. Technical Physics, 60 (10) (2015) 1501–1507.

4. **Plyusnin N. I., Ilyashchenko V. M., Kitan S. A., Tarima N. A.,** Structural-phase transformations at the initial stages of copper condensation on Si(001). Surface. X-ray, synchrotron, and neutron studies (RU). (8) (2011) 29–40.

5. **Plyusnin N. I., Ilyashchenko V. M., Kitan S. A., Krylov S. V.,** Formation, electronic structure, and stability of transition metal film nanophases on silicon. Surface. X-ray, synchrotron and neutron studies (RU), (9) (2009) 86–98.

6. **Plusnin N. I., Il'yashenko V. M., Kitan S. A., Krylov S. V.,** Formation of Co ultrathin films on Si (1 1 1): Growth mechanisms, electronic structure and transport. Applied surface science, 253 (17) (2007) 7225–7229.

7. **Plyusnin N. I., Ilyashchenko V. M., Krylov S. V., Kitan S. A.,** Influence of the power carried by an atomic beam on the formation of the Fe/Si (111) 7x7 interface. Letters to ZhTF (RU), 33 (11) (2007) 79–86.

8. **Plusnin N. I., Il'iashchenko V. M., Krylov S. V.,** Metal thin-film nanophases and their interface with silicon. In Journal of Physics: Conference Series. 100 (5) (2008) 052094.

9. **Qiu Z. Q., Bader S. D.,** Surface magneto-optic Kerr effect (SMOKE). Journal of magnetism and magnetic materials, 200 (1–3) (1999) 664–678.

THE AUTHORS

PLYUSNIN Nikolay I.
plusnin@dvo.ru
ORCID: 0000-0001-9691-9721

PAVLOV Viktor V.
pavlov@mail.ioffe.ru
ORCID: 0000-0001-6139-6123

USACHEV Pavel A.
usachev@mail.ioffe.ru
ORCID: 0000-0002-1386-6466

Received 29.05.2022. Approved after reviewing 29.06.2022. Accepted 29.06.2022.

PHYSICAL ELECTRONICS

Conference materials
UDC 621.382 + 537.312.52 + 535.215.4
DOI: https://doi.org/10.18721/JPM.153.123

Influence of current density, anodization time, and illumination on the thickness of porous silicon in wafers with the built-in *p–n* junction and its photoluminescence

D. T. Yan [1] ✉, N. G. Galkin [2], K. N. Galkin [2], A. V. Nepomnyashchiy [2]

[1] Far Eastern State Transport University, Khabarovsk, Russia;
[2] Institute of Automation and Control Processes FEB RAS, Vladivostok, Russia
✉ dmitry_yan@mail.ru

Abstract: The formation of a porous silicon (por-Si) layer in a thin *p*-type layer epitaxially grown on *n*-type silicon, at two anodizing current densities and different anodizing times is studied and a comparison is made of transverse cleavages, surface morphology, reflection spectra, and photoluminescence spectra. The minimum duration of anodizing (15 and 10 minutes) at current densities of 10 mA/cm^2 and 20 mA/cm^2, at which a single-layer PS structure is formed, is established. With an increase in the anodization time, regardless of the current density, a two-layer structure is formed with an internal tree-like porous silicon layer, whose contribution to photoluminescence is minimal, and the reflection coefficient drops strongly due to irretrievable losses in the porous tree-like layer.

Keywords: silicon, built-in *p—n* junction, current density, anodization time, illumination, porosity

Funding: The study was carried out within the framework of State Assignments of the Ministry of Science and Higher Education of the Russian Federation (no. 0202-2021-0002).

Citation: Yan D. T., Galkin N. G., Galkin K. N., Nepomnyashchiy A. V., Influence of current density, anodization time, and illumination on the thickness of porous silicon in wafers with the built-in *p—n* junction and its photoluminescence, St. Petersburg State Polytechnical University Journal. Physics and Mathematics. 15 (3.1) (2022) 137—142. DOI: https://doi.org/10.18721/JPM.153.123

Материалы конференции
УДК 621.382 + 537.312.52 + 535.215.4
DOI: https://doi.org/10.18721/JPM.153.123

Влияние плотности тока, времени анодирования и освещения на толщину пористого кремния в пластинах со встроенным *p–n* переходом и его фотолюминесценцию

Д. Т. Ян [1] ✉, Н. Г. Галкин [2], К. Н. Галкин [2], А. В. Непомнящий [2]

[1] Дальневосточный государственный университет путей сообщения, г. Хабаровск, Россия;
[2] Институт автоматики и процессов управления ДВО РАН, г. Владивосток, Россия
✉ dmitry_yan@mail.ru

Аннотация. Исследовано формирование слоя пористого кремния (ПК) в тонком слое *p*-типа, эпитаксиально выращенном на кремнии *n*-типа, при двух плотностях тока анодирования и разном времени анодирования, и проведено сравнение поперечных сколов, морфологии поверхности, спектров отражения, и спектры фотолюминесценции. Установлена минимальная продолжительность анодирования (15 и 10 минут) при плотностях тока 10 мА/см^2 и 20 мА/см^2, при которых формируется однослойная структура ПС. С увеличением времени анодирования независимо от плотности тока

формируется двухслойная структура с внутренним древовидным слоем пористого кремния, вклад которого в фотолюминесценцию минимален, а коэффициент отражения сильно падает из-за безвозвратных потерь в пористый древовидный слой.

Ключевые слова: кремний, встроенный *p–n* переход, плотность тока, время анодирования, освещенность

Финансирование: Работа выполнена в рамках системы государственных заданий Минобрнауки России (№ 0202-2021-0002).

Ссылка при цитировании: Ян Д. Т., Галкин Н. Г., Галкин К. Н., Непомнящий А. В. Влияние плотности тока, времени анодирования и освещения на толщину пористого кремния в пластинах со встроенным *p—n* переходом и его фотолюминесценцию // Научно-технические ведомости СПбГПУ. Физико-математические науки. 2022. Т. 15. № 3.1. С. 137—142. DOI: https://doi.org/10.18721/ JPM.153.123

Introduction

For anodizing n-type silicon wafers, regardless of their electrical conductivity, it is necessary to ensure the generation of holes, which are minority carriers. This can be done in two ways [1]: either by applying a critical electric field to induce electrical breakdown, or by illuminating with radiation sufficient to generate holes due to the photoelectric effect [1]. It is known that IR illumination from the reverse side of the substrate provides the generation of electron-hole phases, their separation, and diffusion of holes to the front side of the substrate that is under the action of a negative potential, which in turn leads to formation of macroporous structures during anodization [1, 2]. However, under conditions of illumination from the front side of the silicon substrate [3], depending on the parameters of anodization and the degree of its doping, the formation of a two-layer structure was observed, consisting of a thin nanoporous layer and a thicker macroporous layer. However, complex studies of anodization in silicon with a built-in *p–n* junction, to our knowledge, have not been previously carried out.

Experimental

For anodizing, single-crystal silicon Si(100) wafers of *n*-type conductivity with an epitaxial layer of *p*-type conductivity were used. Layers of porous silicon (por-Si) were formed at two anodizing current densities (10 and 20 mA/cm^2) and etching durations from 10 to 30 minutes, as well as using illumination with a 150 W tungsten lamp during the anodizing process.

A home-made Teflon attachment with a platinum wire cathode was used for anodizing and a copper anode, which was pressed through a layer of conductive silver paste to the reverse side of the silicon sample with the burnt Au-Sb contact. The edges of the front surface of the sample with an area of up to 1 cm^2 were protected with a special varnish. After anodizing, the samples were washed in deionized water and dried in a flow of dry nitrogen.

After mechanical removal of varnish residues and wiping with isopropyl alcohol, a porous silicon layer was studied by optical reflectance and photoluminescent (PL) spectroscopies, as well as by scanning electron microscopy (SEM), including cross-section images for porous structures [4]. During anodization, 8 samples of por-Si were formed with two current densities and different anodization durations.

Results and Discussion

When anodizing with a current density of 10 mA/cm^2 for up to 15 minutes (sample 2-5), the formation of a relatively homogeneous por-Si layer with a low density of punctures is observed. The overall thickness of PS layer is about 0.72 μm (Fig. 1, *a*). It consists of two parts. The lighter part is closer to the surface. Its thickness is about 0.56 μm (Fig. 1, *a*). The darker part with a thickness of 0.16 μm lies under the top layer at the interface with single-crystal silicon. The color of the porous silicon layer is light, which corresponds to a weak absorption of electrons and, accordingly, its low porosity. The darker part of the porous layer should have a higher porosity.

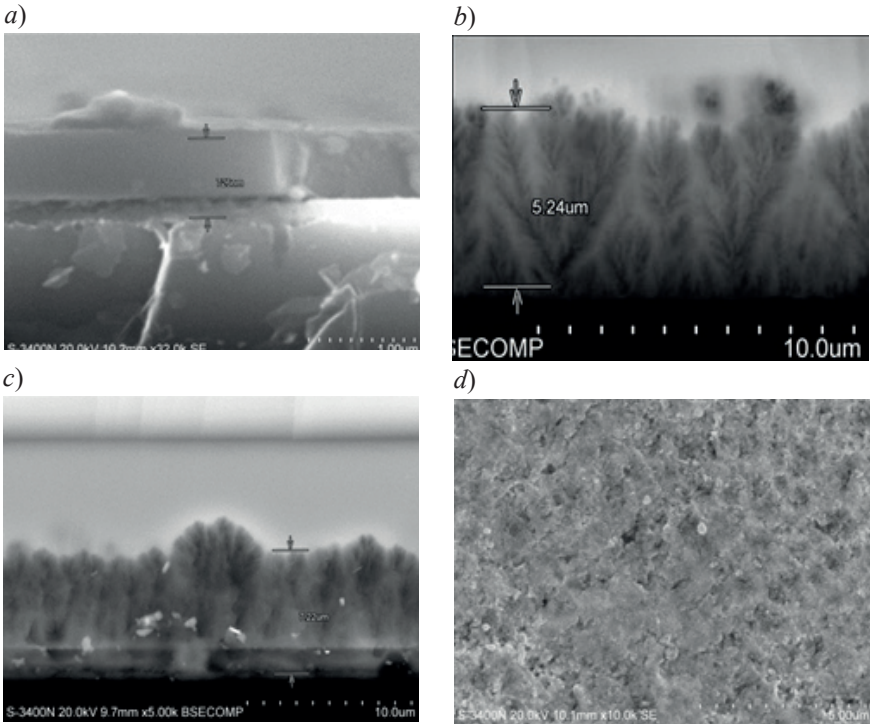

Fig. 1. SEM cross-section images of porous silicon (PS) layers on Si substrate with a *p–n* junction formed at anodizing current density of 10 mA/cm^2 and different anodizing times: 15 minutes for sample 2-5 (*a*); 25 minutes for sample 2-6 (*b*) and 30 minutes for sample 2-2 (*c*). A surface image of PS layer (sample 2-6) after 25 minutes of anodizing is also shown (*d*)

Increasing the anodization time to 25 minutes and then to 30 minutes led to the formation of a por-Si tree-like porous structure inside silicon with an increase in the total por-Si thickness from 5.2 μm to 7.2 μm (Fig. 1, *b, c*). After 25 minutes of anodizing, a certain disturbed layer with a network of small punctures (Fig. 1, *b*) covering the underlying tree-like porous structure is observed on the surface of the porous layer (sample 2-6). Such a disturbed layer is always or often formed over a por-Si layer [5]. After 30 minutes of anodizing (sample 2-2), the thickness of the tree-like porous layer increased (Fig. 1, *c*), but the thickness of the damaged layer also increased to about 2 μm. The upper (disturbed) layer has a darker color, which corresponds to its higher porosity.

The photoluminescence (PL) spectra from the formed samples with porous silicon were studied at room temperature and two laser lines: $\lambda = 405$ nm and $\lambda = 532$ nm.

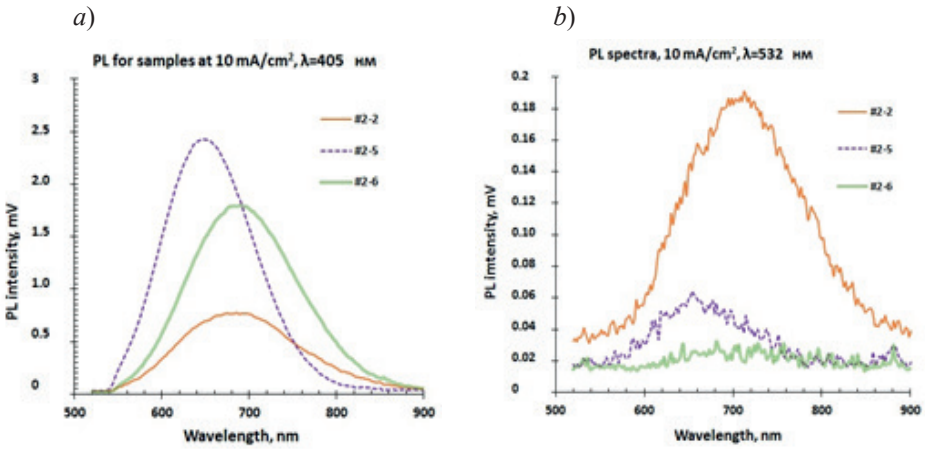

Fig. 2. Photoluminescence (PL) spectra of por-Si layers at different laser wavelengths: 405 nm (*a*) and 532 nm (*b*) for samples formed at anodizing current density of 10 mA/cm^2 and different anodizing times: 15 minutes (sample 2-5), 25 minutes (sample 2-6) and 30 minutes (sample 2-2)

The maximum intensity of the PL spectrum at $\lambda = 405$ nm was observed for the PC layer with an anodizing time of 15 minutes (sample 2-5, Fig. 2, *a*), which indicates high porosity [3] of the internal porous layer (Fig. 1, *a*) and the generation of the PL signal only in this thin internal por-Si layer. With an increase in the anodizing time (samples 2-6 and 2-2), the PL spectra decreased in intensity and red-shifted. With an increase in the laser wavelength ($\lambda = 532$ nm, Fig. 2, *b*) and hence the depth of penetration into the por-Si layer, the intensity of the PL spectra strongly decreased for all samples (Fig. 2, *b*). At the same time, the maximum intensity and red shift of the spectrum was exhibited by a sample with an anodizing time of 30 minutes. This indicates the main contribution to the PL spectrum from the near-surface PS layer for samples 2-6 and 2-5. However, for sample 2-2, the decrease in the PL intensity at $\lambda = 532$ nm is noticeably smaller, and the red shift is larger than for the other two samples (Fig. 2, *b*), which is associated with a larger thickness of the damaged layer and its lower porosity.

Recording the reflectance spectra in the UV-VIS range showed (Fig. 3) that a sharp decrease in reflection is observed over the entire range in layers with a tree-like structure (samples 2-2, 2-6), which indicates an increase in irretrievable light losses in such layers. Noticeable interference features in the reflection spectra (Fig. 3) for samples 2-2 and 2-6 indicate that the por-Si layer remains sufficiently flat. At the same time, the high reflectance for sample 2-5 (15 minutes) corresponds to the preservation of the flat surface of the por-Si layer. Taking into account the noticeable blue shift of the PL spectrum (Fig. 1, *a*) in the sample 2-5, we can suggest the small sizes of Si nanocrystals internal porous layer with a high porosity [3]. The small thickness of porous silicon in sample 2-5 is confirmed by the appearance of peaks from single-crystal silicon, which are observed in the reflection spectrum of this sample at wavelengths of about 270 nm and 360 nm (Fig. 3).

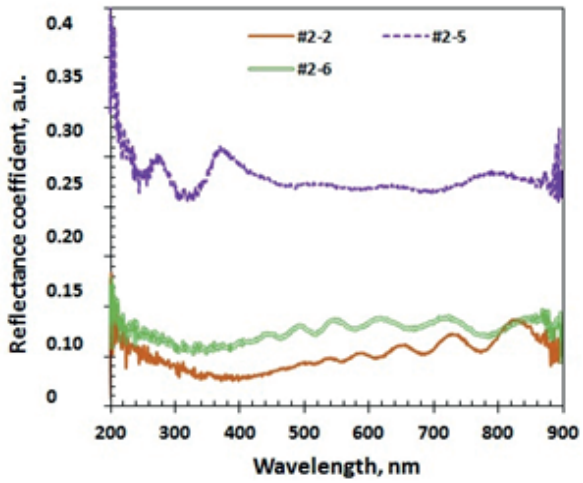

Fig. 3. Reflection spectra of por-Si layers formed at anodizing current density of 10 mA/cm^2 and different anodizing times: 15 minutes (sample 2-5), 25 minutes (sample 2-6) and 30 minutes (sample 2-2)

An increase in the anodization current density to 20 mA/cm^2 led to the formation of a two-layer por-Si structure, which includes a thin homogeneous PS layer (Fig. 4, *a*, sample 2-3) and then a tree-like structure (samples 2-4 and 2-10). The thickness of the entire por-Si layer increased with the etching time (10, 15, 30 min) from 1.67 μm to 16.7 μm.

The position of the maximum in the PL spectra practically did not depend on the anodizing time, and the intensity of the PL peak decreased with increasing anodizing time, which is confirmed by a decrease in the PL intensity upon going from $\lambda = 405$ nm to $\lambda = 532$ nm and PL localization mainly in the upper por-Si layer, but with variable porosity. Porosity turned out to be maximum for the minimum of anodizing time (see samples 2-3 and 2-9 with 10 minutes of anodizing time).

The reflection spectra of the samples of the second series with an anodizing current of 20 mA/cm^2 showed that in the samples with the maximum PL intensity (2-3 and 2-9) with a minimum anodizing time (10 minutes), intense interference peaks are observed (Fig. 6), despite the small thickness of the upper por-Si layer (Fig. 4, *a*). This means that a certain contribution is made by the inner layer with a tree structure and different porosity. The upper flat layer with low porosity is retained in samples 2-4 and 2-10 with a greater thickness of the inner tree-like layer, which determines a greater reflection coefficient. This is confirmed by the presence of peaks from single crystal silicon at wavelengths of 270 nm and 370 nm.

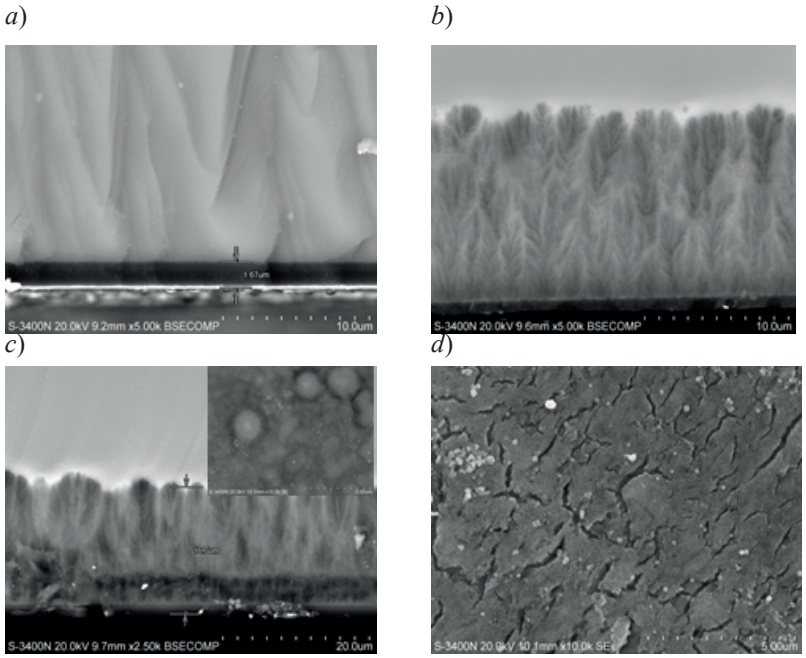

Fig. 4. SEM cross-section images of porous silicon (por-Si) layers on Si substrate with *p–n* junction formed at anodizing current density of 20 mA/cm^2 and different anodizing times: 10 minutes for sample 2-3 (*a*); 15 minutes for sample 2-10 (*b*) and 30 minutes for sample 2-4 (*c*). A surface image of PS layer (sample 2-10) after 15 minutes of anodizing is also shown (*d*). The inset in (*b*) corresponds to the sample surface.

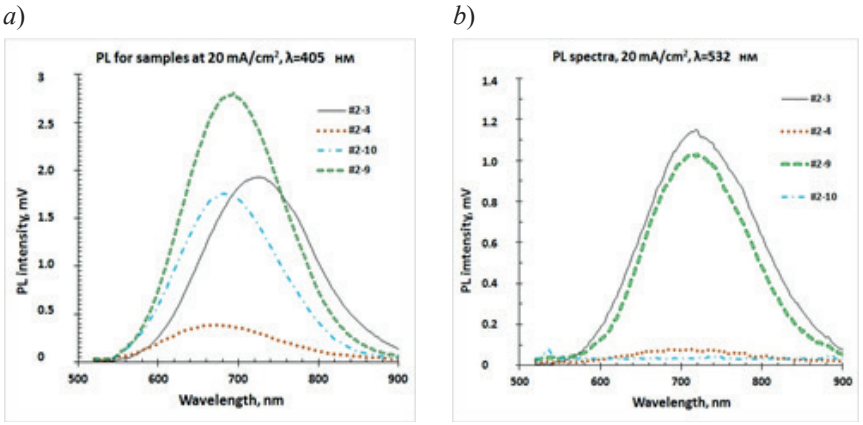

Fig. 5. Photoluminescence (PL) spectra of por-Si layers at different laser wavelengths: (*a*) λ =405 nm and (*b*) λ =532 nm for samples formed at anodizing current density of 20 mA/cm2 and different anodizing times: 10 minutes (samples 2-3 and 2-9), 15 minutes (sample 2-10) and 30 minutes (sample 2-4)

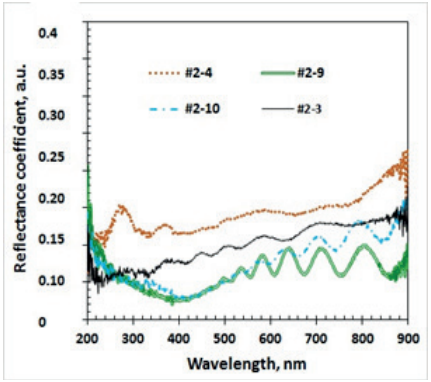

Fig. 6. Reflection spectra of por-Si layers formed at anodizing current density of 20 mA/cm^2 and different anodizing times: 10 minutes (samples 2-3 and 2-9), 15 minutes (sample 2-10) and 30 minutes (sample 2-4)

Conclusion

The effect of anodizing modes (anodizing current and duration) on the formation of porous silicon layers in a Si-*p*/Si-*n* epitaxial structure under conditions of white light illumination has been studied. It has been established that at short anodization times of 10 minutes at 10 mA/cm^2 and 15 minutes at 20 mA/cm^2, an upper porous layer with a noticeable porosity is formed, which ensures strong photoluminescence (PL), which is more pronounced at a laser excitation length of $\lambda = 405$ nm and decreases noticeably at $\lambda = 532$ nm. With an increase in anodizing time (20–30 minutes), a tree-like porous layer is formed inside under the first layer of por-Si, the thickness of which increases with an increase in anodizing time and anodizing current density. The photoluminescence in the double porous structure decreases with an increase in the anodizing time. In this case, the PL intensity from thick tree-like layers is minimal at a laser radiation length $\lambda = 532$ nm. The reflection coefficient in samples with a double porous structure becomes less than 0.1, if the upper layer of the por-Si is highly porous and does not retain the contribution from single-crystal silicon.

REFERENCES

1. **Lehmann V.,** The physics of macropore formation in low doped n-type silicon J. Electrochem. Soc. 140 (1993) 2836–2843.

2. **Kleimann P., Linnros J., Peterson S.,** Formation of wide deep pores in silicon by electrochemical etching, Mater. Sci. & Engineer. B 69 (2000) 29–33.

3. **Levy-Clement C., Logoubi A., Tomkiewicz M.,** Morphology of porous n-type silicon obtained by photoelectrochemical etching: 1. Correlation with material and etching parameters, J. Electrochem. Soc. 141 (1994) 958–967.

4. **Galkin N. G., Yan D.T., Galkin K. N., Nepomnyashchiy A.V.,** Establishment of the relationship between the coefficients of reflection, refraction and porosity index for mesoporous silicon layers with different surface morphology, Chemical Physics and Mesoscopy, 23(4) (2021) 220–230.

5. **Fukuda Y., Zhou W., Furuya K., Suzuki H.,** Photoluminescence Change of As-Prepared and Aged Porous Silicon with NaOH Treatment, Journal of The Electrochemical Society, 146 (7) (1999) 2697–2701.

THE AUTHORS

YAN Dmitriy T.
dmitry_yan@mail.ru
ORCID: 0000-0002-0602-9301

GALKIN Konstantin N.
galkinkn@iacp.dvo.ru
ORCID: 0000-0001-5386-1013

GALKIN Nikolay G.
galkin@iacp.dvo.ru
ORCID: 0000-0003-4127-2988

NEPOMNYASHCHIY Aleksandr V.
santila001@mail.ru
ORCID: 0000-0002-8726-983

Received 04.05.2022. Approved after reviewing 05.07.2022. Accepted 05.07.2022.

Conference materials
UDC 621.382 + 537.312.52 + 535.215.4
DOI: https://doi.org/10.18721/JPM.153.124

Current-voltage characteristics and photoelectric properties of por-Si/Si-*p*/Si-*n* diodes with different porous layer thickness

D. T. Yan [1] ✉, N. G. Galkin [2], K. N. Galkin [2], I. M. Chernev [2]

[1] Far Eastern State Transport University, Khabarovsk, Russia;

[2] Institute of Automation and Control Processes FEB RAS, Vladivostok, Russia

✉ dmitry_yan@mail.ru

Abstract: In this work, the current-voltage and photoelectric spectral characteristics of double heterodiodes por-Si/Si-*p*/Si-*n* and a reference diode with a *p*—*n* junction at room temperature are analyzed and compared with data on the thickness of porous silicon layers and photoluminescence spectra for the synthesized heterostructures. It is shown that photospectral sensitivity in the region of 400—800 nm is exhibited by diodes with a single-layer structure of porous silicon whose thickness does not exceed 2 μm. In this case, the amplitude of the spectral photoresponse decreases with a decrease in the thickness of the porous layer. As for diodes with a two-layer structure of porous silicon (ordinary porous and tree-like porous) and thicknesses from 4.5 μm to 17.4 μm, currents do not flow due to rapid oxidation of such structures. A band energy diagram of a double heterodiode with a layer of porous silicon is proposed based on the experimental data.

Keywords: Silicon, built-in *p*—*n* junction, illumination, porous layer thickness, tree-like porous structure, double heterodiode, current blocking, photoresponse spectra, diode band diagram

Funding: The study was carried out within the framework of State Assignments of the Ministry of Science and Higher Education of the Russian Federation (no. 0202-2021-0002).

Citation: Yan D. T., Galkin N. G., Galkin K. N., Chernev I. M., Current-voltage characteristics and photoelectric properties of por-Si/Si-*p*/Si-*n* diodes with different porous layer thickness, St. Petersburg State Polytechnical University Journal. Physics and Mathematics. 15 (3.1) (2022) 143—148. DOI: https://doi.org/10.18721/JPM.153.124

Материалы конференции
УДК 621.382 + 537.312.52 + 535.215.4
DOI: https://doi.org/10.18721/JPM.153.124

Вольтамперные и фотоэлектрические свойства диодов por-Si/Si-*p*/Si-*n* с разной толщиной пористого слоя

Д. Т. Ян[1] ✉, К. Н. Галкин[2], И. М. Чернев[2], Н. Г. Галкин[2]

[1] Дальневосточный государственный университет путей сообщения, г. Хабаровск, Россия;

[2] Институт автоматики и процессов управления Дальневосточного отделения РАН, г. Владивосток, Россия

✉ dmitry_yan@mail.ru

Аннотация. В данной работе проведен анализ вольтамперных и фотоэлектрических спектральных характеристик двойных гетеродиодов por-Si/Si-*p*/Si-*n* и эталонного диода с *p*—*n* переходом при комнатной температуре и сопоставление с данными о толщине слоев пористого кремнияспектров фотолюминесценции синтезированных гетероструктур. Показано, что фотоспектральной чувствительностью в области 800-400 нм обладают диоды с однослойной структурой пористого кремния и его толщиной не

более 2 мкм. При этом с уменьшением толщины пористого слоя амплитуда спектрального фотоотклика уменьшается. В диодах с двухслойной структурой пористого кремния (обычный пористый и древовидный пористый) и толщиной от 4,5 мкм до 17,4 мкм токи не протекают из-за быстрого окисления такой структуры. На основе экспериментальных данных предложена зонная энергетическая диаграмма двойного гетеродиода со слоем пористого кремния.

Ключевые слова: Кремний, встроенный *p*—*n* переход, освещение, толщина пористого слоя, древовидная пористая структура, двойной гетеродиод, блокировка тока, спектры фотоотклика, зонная диаграмма диода

Финансирование: Работа выполнена в рамках системы государственных заданий Минобрнауки России (№ 0202-2021-0002).

Ссылка при цитировании: Ян Д. Т., Галкин Н. Г., Галкин К. Н., Чернев И. М. Вольтамперные и фотоэлектрические свойства диодов por-Si/Si-p/Si-n с различной толщиной пористого слоя // Научно-технические ведомости СПбГПУ. Физико-математические науки. 2022. Т. 15. № 3.1. С. 143—148. DOI: https://doi.org/10.18721/JPM.153.124

Introduction

Studies dedicated to creating LEDs based on porous silicon (por-Si) heterostructures on single-crystal silicon with a built-in p—n junction are well known [1, 2]. They focus on two issues: increasing the efficiency of electroluminescence and improving the stability of this type of LEDs. It is known that the formed LED structures based on porous silicon lose up to 75% of their integrated electroluminescence intensity for half an hour during operation in ambient conditions [2, 3], which is associated with a decrease in the injection of carriers from por-Si due to rapid oxidation of nanocrystals in an applied electric field even at room temperature. At the same time, the question of the influence of the thickness of the porous silicon layer in a Si wafer with a built-in *p*—*n* junction on the current-voltage and photospectral characteristics of diode structures remained unexplored.

The goal of this study is to establish a correlation between the thickness and microstructure of the porous silicon layer in the double por-Si/S-*p*/Si-*n* mesa-diodes of and their current-voltage and photospectral characteristics.

Experimental

In this work, porous silicon layers were created on *n*-type Si(100) wafers with a resistivity of 0.1 Ω cm with an epitaxial layer of *p*-type silicon (3 μm) with a resistivity of 7—10 Ω·cm by anodizing in a solution of $HF:C_3H_8OH = 1:1$ at two current densities: 10 and 20 mA/cm^2, etching times from 10 to 30 minutes and under illumination with a 150 W tungsten halogen lamp from a distance of 30 cm from the sample. Eight samples were formed at of 10 and 20 mA/cm^2.

A home-made Teflon attachment with a Pt wire cathode was used for anodizing and a copper anode, which was pressed through a layer of conductive silver paste to the reverse side of the silicon sample with the burnt Au-Sb contact. The edges of the front surface of the sample with an area of up to 1 cm^2 were protected with a special varnish. After anodizing, the samples were washed in deionized water and dried in a flow of dry nitrogen.

Results and Discussion

After mechanical removal of varnish residues and wiping with isopropyl alcohol, an Al layer was deposited to the por-Si surface at room temperature in a high vacuum through a square-shaped mask with a square hole in the center (Fig. 1, left). A layer of Au-Sb mixture was deposited on

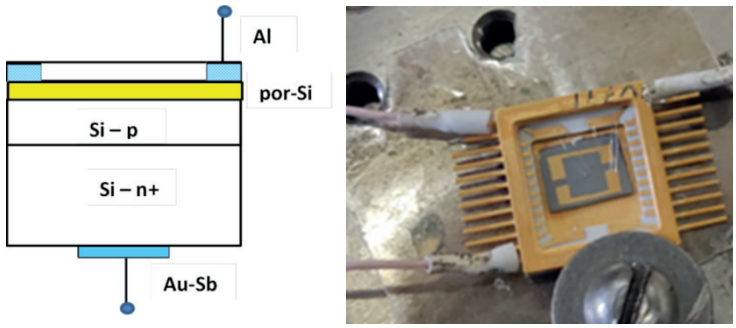

Fig. 1. Scheme of a diode structure (left) based on a layer of por-Si and a built-in *p*–*n* junction in single-crystal silicon. Photo of a diode structure (right) built into the microcircuit package with an aluminum contact (yellow) to a layer of porous silicon

the rear sample surface to form a diode structure. After that, the samples with deposited contacts were subjected to annealing at a temperature of 450°C for 30 minutes. Next, the samples were placed on silver paste in the package of the integrated circuit, and ultrasonic welding of Al wire with a diameter of 20 μm was carried out from Al-plating to the pads of the microcircuit package (Fig. 1, right). The main parameters of the created samples of mesa-diodes are given in Table 1. At room temperature, the current-voltage (*I*–*V*) characteristics were measured in the dark and under illumination with a 150 W tungsten halogen lamp based on a stabilized power source and a microvoltmeter. The spectral characteristics of the photoresponse were studied using a setup based

Table 1

Parameters of double por-Si/Si-*p*/Si-*n* and reference Si-*p*/Si-*n* mesa-diodes

Diode number	Current density, mA/cm^2	Anodizing time, min	Short circuit current density, μA/cm^2	por-Si thickness, μm	Open circuit voltage, V	Fill factor (FF), %	Photo-response maximum, V/W
2-1	10	20	52	0.675	0.1	38	0.2
2-3	20	10	318	1.67	0.069	33.2	0.09
2-5	10	15	300	0.726	0.15	21	0.08
2-7	10	15	351	0.833	0.097	32	0.104
2-8	10	25	124	0.82	0.19	15.2	0.074
PN_ref	–	–	53	–	0.12	29	0.078

on a monochromator with a radiation source, a modulator, and a differential amplification system.

Studies of the current-voltage (*I*–*V*) characteristics of all diodes in the dark and under illumination showed that currents through them are observed only for samples with an anodizing time of 10 to 25 minutes at a current density of 10 mA/cm^2, and a time of no more than 10 minutes at a current density of 20 mA/cm^2. Fig. 2 (left side) shows the *I*–*V* characteristics for a reference diode with a *p*–*n* junction and sample 2-1 (10 mA/cm^2, 20 minutes).

In the dark, the direct branch of the *I*–*V* (sample 2-1, black squares) increases faster than for the reference sample (PN-ref, red circles), but has an order of magnitude greater reverse current. And when illuminated, the characteristics are close, but with minimum short circuit current density (52–53 μ/cm^2) (Fig. 2, right side). With an increase in time from 20 to 30 minutes at a current density of 10 and 20 mA/cm^2, no currents flow through the diodes, both in the dark and in the light. This fact is associated primarily with an increase in the thickness of the porous layer and its tree structure [4], which ensures rapid oxidation of the por-Si layer.

Separately, we compared (Fig. 3, left panel) the *I*–*V* characteristics of diodes formed at two current densities (10 mA/cm^2 and 20 mA/cm^2) and close anodizing times (10 and 15 minutes) in the dark. Sample 2-3 has the maximum forward current density at 1.5 V bias (20 mA/cm^2, 10 minutes). However, sample 2-5 (10 mA/cm^2, 15 minutes) has a lower reverse current, indicating less leakage in the diode structure. Under white light illumination, short circuit current density (J_{sc}), open circuit voltage (V_{oc}), and fill factor (FF) were determined for two diodes (Fig. 3, right

panel and Table 1). Sample 2-5 showed the highest V_{oc}, but a lower fill factor (FF = 2%). As for sample 2-3, the maximum fill factor (FF = 33.2%) was observed at the maximum short circuit current (318 μA/cm²). Comparison of the diode in sample 2-1 with the maximum anodization time (Table 1) and diodes 2-5 and 2-3 (Table 1) showed that an increase in the anodization time leads to a decrease in current through the diodes and a deterioration in their sensitivity to illumination with white light. These facts are related to the additional contribution of the por-Si layers to the photocurrent due to the additional photogeneration of carriers in them upon illumination and separation by the *p*—*n* junction field.

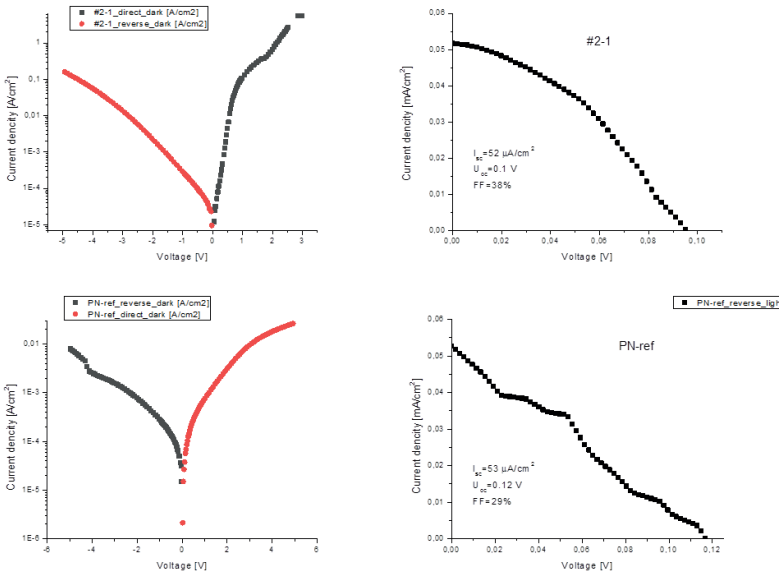

Fig. 2. *I*—*V* characteristics in the dark (left side) and under illumination with a W-lamp (right side) for sample 2-1 (10 mA/cm², 20 min) and a reference sample (PN-ref) with a *p*—*n* junction
The graphs on the right side show the short circuit current (I_{sc}), open circuit voltage (V_{oc}) and fill factor (FF)

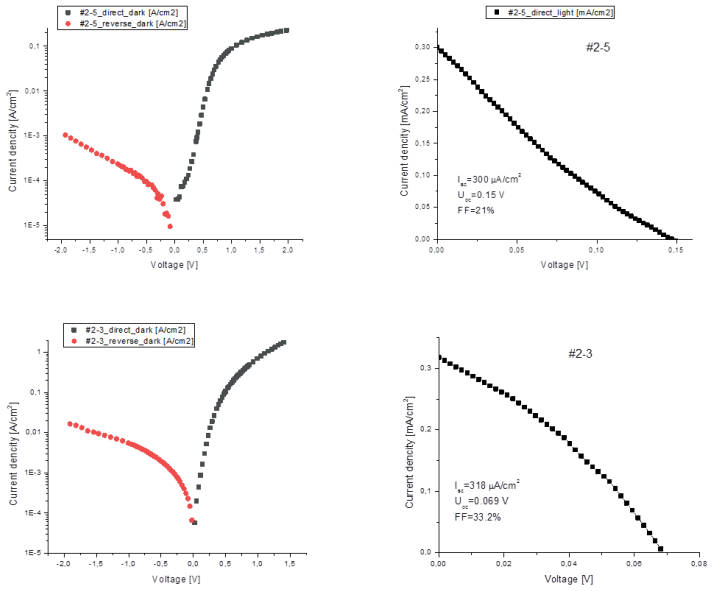

Fig. 3. *I*—*V* characteristics in the dark (left side) and under illumination with a W-lamp (right side) for sample 2-5 (10 mA/cm², 15 min) and sample 2-3 (20 mA/cm², 10 min)
The graphs on the right side show the short circuit current (I_{sc}), open circuit voltage (V_{oc}) and fill factor (FF)

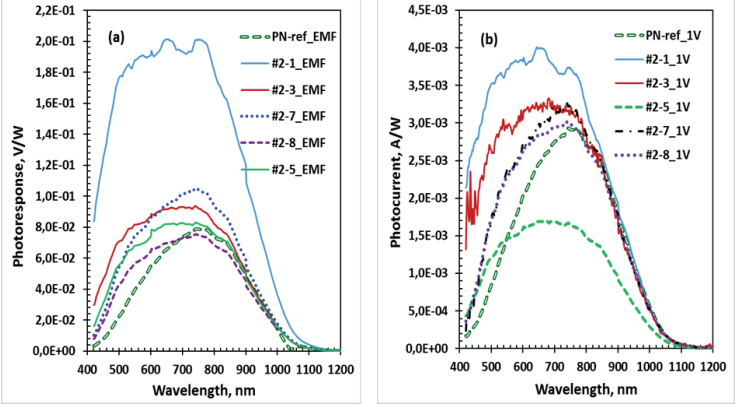

Fig. 4. Spectral dependences of photoresponse (*a*) and photocurrent (*b*) of por-Si *p*–*n* diodes (2-1, 2-3, 2-5, 2-7, 2-8) and reference Si *p*–*n* diode)

Measuring the spectral characteristics of the photoresponse and photocurrent, we found (Fig. 4, *a*, *b*) that sample 2-1 with a minimum por-Si layer thickness of 0,675 μm [4] has the maximum photoresponse and photocurrent. With an increase in the thickness of the por-Si layer from 0.8 μm to 1.09 μm and 2.7 μm, a decrease in the amplitude of the photoresponse (Fig. 4,*a*) and photocurrent (Fig. 4,*b*) is observed. A characteristic difference between the photoresponse spectra of working diodes and a reference diode based on a silicon *p*–*n* junction is an increase in the short-wavelength contribution and a shift in the maximum of the spectra to the short-wavelength region, which is associated with the generation of electron-hole pairs in the wide-gap por-Si layer and their separation by the field of the *p*–*n* junction. A band model of photodiodes is constructed to explain the dependence of the photoresponse on the por-Si layer thickness.

To plot the band diagrams [5] of diode structures based on por-Si layers located over the *p*–*n* junction in single-crystal silicon, it is necessary to take into account its thickness and compare it with the initial thickness of the epitaxial silicon substrate of *n*-type conductivity.

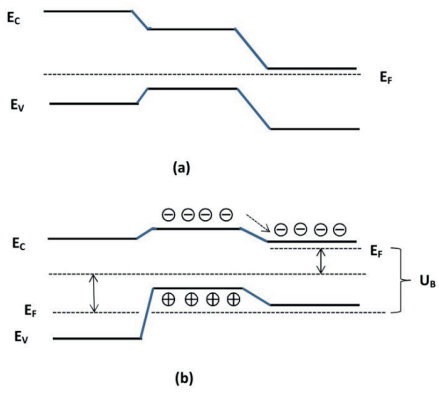

Fig. 5. Energy band diagrams of por-Si/Si-*p*/Si-*n* diodes without bias (*a*) and with bias (U_B) (*b*)

Since anodization began in *p*-type silicon epitaxial layer, the formed por-Si layer should also have *p*-type conductivity. Due to the band gap of 1.7–1.8 eV (from PL data [4]), a heterojunction is formed at the interface with Si-*p* layer. In general, the structure has one *p*-*p* heterojunction and one silicon *p*–*n* junction (Fig. 5,*a*), which blocks the flow of current up to a forward bias of 0.5-0.6 V. In this case, the bias is distributed relative to the Fermi level (Fig. 5,*b*). The wide-gap part provides high-energy photogeneration of carriers and their separation by a Si *p*–*n* junction. This leads to an increase in the contribution to the photoresponse (Fig. 4,*a*) and photocurrent (Fig. 4,*b*) of the por-Si/Si-*p*/Si-*n* diodes at wavelengths from 400 nm to 800 nm compared to the reference photodiode (PN-ref diode). In this case, the maximum photoresponse is observed for sample 2-1 (10 mA/cm^2, 20 minutes) with the maximum por-Si thickness (2 μm), and the minimum for samples with a smaller thickness (2-5 (10mA/cm^2, 15 minutes) and 2-7 (10 mA/cm^2, 15 minutes)). According to [4], there is no direct correlation between the PL signal, which depends on the porosity of the por-Si layer, and the photoresponse, which, on the contrary, is maximum for layers with minimal porosity.

Conclusion

The current-voltage and photoelectric characteristics of diodes based on porous silicon of various thicknesses embedded in a *p*-layer of silicon, which is epitaxially grown on an *n*-type silicon substrate, have been studied. It has been established that *I*–*V* diode characteristics and

photospectral sensitivity are demonstrated by diodes with single-layer porous silicon less than 2 μm thick. In porous Si layers of greater thickness (4–17 μm), a two-layer tree-like structure of porous silicon with different porosity was formed, which was rapidly oxidized, which blocked the flow of current through the diodes. It has been demonstrated that a diode with a porous layer 2 μm thick, low porosity and the absence of photoluminescence has the maximum photosensitivity in the wavelength range of 400–800 nm. Diodes with a noticeable PL signal and a single-layer structure showed a photoresponse close to that of a reference silicon diode. The band energy structure of double heterodiodes is constructed and the photo-emf generation is analyzed.

REFERENCES

1. **Steiner P., Kozlowski F., and Lang W.,** Blue and Green Electroluminescence from a Porous Silicon Device, IEEE Electron Device Letters, 14(7) (1993) 317–319.

2. **Zhang L., Coffer J.L., Gnade B.E., Xu D.X. and Pinizzotto R.F.,** Effects of local ambient atmosphere on the stability of electroluminescent porous silicon diodes, J. Appl. Phys., 77 (1995) 5936–5941.

3. **Gelloz B, and Koshida N.,** Electroluminescence with high and stable quantum efficiency and low threshold voltage from anodically oxidized thin porous silicon diode, Journal of Applied Physics, 88(7) (2000) 4319–4324.

4. **Galkin K.N., Yan D.T., Nepomnyashchiy A.V., Galkin N.G.,** Influence of current density, anodization time and illumination on the thickness of porous silicon in wafers with built-in *p-n* junction and its photoluminescence, ASCO-Nanomat 2022, Proceedings, Dalnauka Publishing, Vladivostok, 2022, –383.

5. **S.M. Sze,** Physics of Semiconductor devices, 2nd Edition, John Wiley and Sons, 1981, p. 868.

THE AUTHORS

YAN Dmitriy T.
dmitry_yan@mail.ru
ORCID: 0000-0002-0602-9301

GALKIN Konstantin N.
galkinkn@iacp.dvo.ru
ORCID: 0000-0001-5386-1013

GALKIN Nikolay G.
galkin@iacp.dvo.ru
ORCID: 0000-0003-4127-2988

Chernev Igor M.
igor_chernev7@mail.ru
ORCID: 0000-0002-8726-9832

Received 09.05.2022. Approved after reviewing 17.06.2022. Accepted 05.07.2022.

Conference materials
UDC 538.91
DOI: https://doi.org/10.18721/JPM.153.125

Effect of thermal annealing on grain size and phase changes in magnetron titanium oxide films

A. S. Chekadanov [1], M. A. Pugachevskii [1], K. Aung Hein [1],
A. P. Kuzmenko [1], A. M. Storozhenko [1] ✉

[1] Southwest State University, Kursk, Russia

✉ storogenko_s@mail.ru

Abstract: Thin TiO_2 films were produced on single-crystal Si-wafers by magnetron sputtering. Subsequently, they were annealed in air at different temperatures. We researched the structure, the phase composition, the morphology, and the dimensional characteristics of the films before and after annealing using X-ray diffraction, energy-dispersive and spectrophotometric analysis, scanning electron microscopy, and small-angle X-ray scattering. The analysis of the influence of annealing parameters on the characteristics of TiO_2 films is carried out. The technique for determining the qualitative and quantitative phase composition of TiO_2 during its polymorphic transformations at high-temperature heating has been developed. It was found that TiO_2 annealing at 400 °C leads to crystallization of the anatase phase, and annealing at 600 °C leads to transformations into the rutile phase. The optical band gap decreases with increasing temperature and with increasing annealing time.

Keywords: titanium dioxide, annealing, phase composition, morphology, polymorphic transformation, SEM, SAXS

Funding: The study was supported by the Russian Foundation for Basic Research (project No. 20-02-00599), Ministry of Education and Science of the Russian Federation (State Assignment 2020 no. 0851-2020-0035), Program of Strategic Academic Leadership Priority-2030 (Agreements no. 075-15-2021-1155 and No. 075-15-2021-1213).

Citation: Chekadanov A. S., Pugachevskii M. A., Aung Hein K., Kuzmenko A. P., Storozhenko A. M., Effect of thermal annealing on grain size and phase changes in magnetron titanium oxide films, St. Petersburg State Polytechnical University Journal. Physics and Mathematics. 15 (3.1) (2022) 149–154. DOI: https://doi.org/10.18721/JPM.153.125

Материалы конференции
УДК 538.91
DOI: https://doi.org/10.18721/JPM.153.125

Влияние термического отжига на размер зерен и фазовые превращения в магнетронных пленках диоксида титана

А. С. Чекаданов [1], М. А. Пугачевский [1], Ч. Аунг Хейн [1],
А. П. Кузьменко [1], А. М. Стороженко [1] ✉

[1] Юго-Западный государственный университет, г. Курск, Россия

✉ storogenko_s@mail.ru

Аннотация. Объектом исследования являются тонкие пленки диоксида титана, полученные методом магнетронного распыления на подложках из монокристаллического кремния. Пленки TiO_2 отжигались на воздухе при различных температурах. Исследовались

структура, фазовый состав, морфология и размерные характеристики пленок до и после отжига. Использовались методы рентгенофазового, энергодисперсионного и спектрофотометрического анализа, сканирующая электронная микроскопия и малоугловое рентгеновское рассеяние. Проведен анализ влияния параметров отжига на характеристики пленок диоксида титана. Разработана методика определения качественного и количественного фазового состава пленок в процессе его полиморфных превращений при высокотемпературном нагреве. Установлено, что отжиг TiO_2 при 400 °C приводит к кристаллизации фазы анатаза, а отжиг при 600 °C — к превращениям в фазу рутила. Оптическая ширина запрещенной зоны уменьшается с повышением температуры и увеличением времени отжига.

Ключевые слова: диоксид титана, отжиг, фазовый состав, морфология, полиморфные превращения, СЭМ, МУРР

Финансирование: Исследование выполнено при поддержке РФФИ (Проект № 20-02-00599), Минобрнауки РФ (Госзадание 2020 № 0851-2020-0035), Программы стратегического академического лидерства «Приоритет-2030» (договоры № 075-15-2021-1155, № 075-15-2021-1213).

Ссылка при цитировании: Чекаданов А.С. и др. Влияние термического отжига на размер зерен и фазовые превращения в магнетронных пленках диоксида титана // Научно-технические ведомости СПбГПУ. Физико-математические науки. 2022. Т. 15. № 3.1. С. 149–154. DOI: https://doi.org/10.18721/JPM.153.125

Introduction

Nanostructured materials are one of the most fast-evolving areas of research. Among all the transition metal oxides, titanium dioxide nanostructures have the largest potential in modern science and technology [1]. TiO_2 can be obtained by oxidation of thin Ti films. TiO_2 has become famous because of its unique photocatalitic properties [2-4]. Active electron-hole pairs can be generated in the electronic structure of TiO_2 due to the absorption of photons with energies above 2.8 eV. When electron-hole pairs emerge on the surface, they participate in redox reactions with the formation of radical complexes. TiO_2 crystal exists in three common polymorphs, i.e., brookite, anatase (A), and rutile (R) [5, 6]. The photocatalytic activity of anatase is estimated to be higher than that of rutile. However, due to the smaller band gap, rutile can absorb a wider range of sunlight up to 450 nm [7, 8].

It is a daunting task to obtain TiO_2 films with suitable characteristics. We applied thermal annealing with trial-and-error adjustment of optimal parameters of the processing mode [9]. On the other hand, it is equally important to determine the qualitative and quantitative phase composition of TiO_2 during its polymorphic transformations at high-temperature heating. Therefore, our goal was to investigate the effect of thermal annealing on the morphology and phase composition of magnetron TiO_2 films under various processing modes.

Materials and Methods

To obtain thin TiO_2 films, we used a magnetron sputtering device, MVU TM Magna T (NIITM, Russia). The films were grown for 30 min on monocrystalline Si substrates in Ar atmosphere at magnetron discharge power of 300 W. Before deposition, the substrates were heated to 120 °C (for 1 min), then we carried out ion beam cleaning at a current of 60 mA (for 2 min). To obtain the Ti oxide, the prepared Ti films were annealed in air at 400 °C, 600 °C and 800 °C for 2, 4 and 6 hours using a Mini Lamp Annealer MILA-5050 heater.

Phase composition of the samples was analyzed by the X-ray crystallography technique. To perform measurements, we used a GBC EMMA powder diffractometer (60 kV/80 mA, 0.005%, radiation power 2.2 kW, goniometer step 0.002). First, we obtained X-ray diffraction patterns from pure Ti films, then from annealed films.

The morphological features and changes in the surface structure of the films were studied using the JEOL JSM-6610LV scanning electron microscope (SEM, 20 kV, up to 100000×). X-Max Silicon Drift Detector (Oxford Instruments) allowed getting the distribution of chemical elements in the samples.

Line-collimation small-angle X-ray scattering was also used in the characterization of the samples (diffractometer SAXSess mc^2, Anton Paar, Austria). This device is designed to find the structural features of objects with sizes from 0.1 to 100 nm. It is equipped with a typical X-ray tube with a Cu anti-cathode and monochromator, which allows obtaining X-rays with a wavelength of 0.154 nm. The measurement time was 30 s. The SAXS data were processed using GIFT software (PCG Software Package).

To study the optical properties of the annealed films, we used an SF-2000 spectrophotometer (OKB Spectr, Russia). Its wavelength range is 190–1100 nm. The obtained reflection spectra were converted to absorption spectra using the Kubelka–Munk equation:

$$\frac{K}{S} = \frac{(1-R_\infty)^2}{2R_\infty}. \quad (1)$$

Here K and S are the absorption and back-scattering coefficients, R_∞ is remission fraction of an infinitely thick layer. The absorption spectra were used to determine the value of band gap.

Results and Discussion

Scanning electron microscopy (SEM) revealed that all our TiO_2 films were polydisperse (scan for 800 °C, 2 hours is shown in Fig. 1,*a*). The grain sizes grow with an increase in annealing time. The minimum grain sizes found on SEM scans are listed in Table 1.

According to SEM results, the thickness of the films varied from 0.95 to 1 μm (Fig. 1, *b*). During the experiment, the samples were placed at an angle of 89° to the horizontal plane.

To gain insights into the integral characteristics of TiO_2 grains, we considered the samples using SAXS. The scattering intensity data (Fig. 2, *a*) were used for plotting the pair distance distribution functions (PDDF) shown in Fig. 2,*b*). The configuration of these functions clearly shows that TiO_2 grains have an irregular shape and different sizes. The Guinier approximation applied at the very beginning of the scattering curves give the minimum dimension of grains, amounting to 20–25 nm.

The phase composition of the annealed films was determined using powder diffractometer. As evident from the obtained spectra, the TiO_2 anatase phase is formed at a temperature of 400 °C, while at 600 °C it transforms into a rutile phase (Fig. 3).

Each peak of the diffractograms was approximated by a Gaussian curve using OriginPro software:

$$y = y_0 + e^{\frac{-(x-x_C)^2}{2w^2}}. \quad (2)$$

a) *b*)

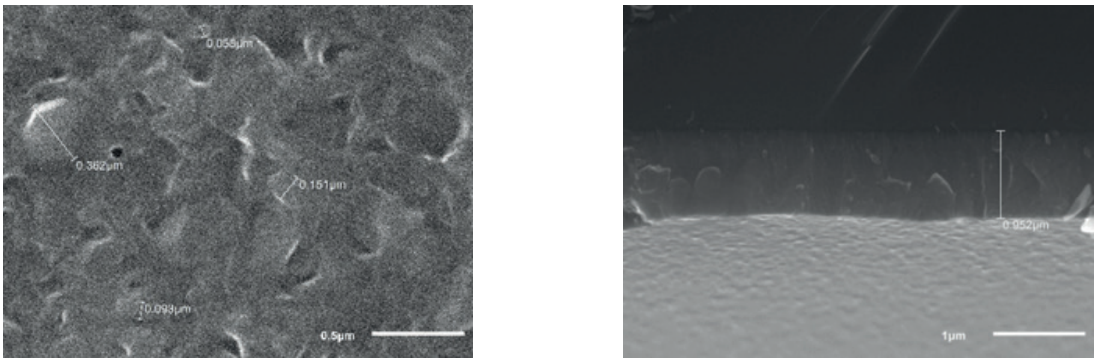

Fig. 1. SEM results: front view (*a*); cross-sectional view (*b*)

Table 1

Minimum grain sizes found in SEM scans

Time	Temperature		
	400 °C	600 °C	800 °C
2 hours	25 nm	25 nm	> 100 nm
4 hours	35 nm	30 nm	
6 hours	40 nm	50 nm	

The concept of the coherent scattering region (CSR) was also used to research TiO_2 films. The CSR size is generally 10–15% smaller than the size of grains identified using electron microscopy, while coherent scattering region corresponds to the inner (ordered) region of grain and does not include severely distorted boundaries [10]. CSR sizes were calculated using the Scherrer equation:

$$D = \frac{k\lambda}{\delta \cos\theta}, \tag{3}$$

where $k = 0.95$ is the dimensionless shape factor; δ is the line broadening at half the maximum intensity; θ is the Bragg angle; $\lambda = 0.154$ nm is the X-ray wavelength. The estimation gives the average size of crystallites is from 3 to 11 nm.

In order to research the influence of the size factor on the width of band gap, we studied the optical absorption spectrums of TiO_2 nanofilms. We obtained the reflection spectrums of the annealed films and then calculated absorption spectrums using Kubelka–Munk equation (1).

According to quantum-mechanical calculations, in the case of intrinsic absorption of semiconductors and dielectric materials, transitions of electrons from valence band to conduction band are determined through the sum of the probabilities α_P for all states of electrons:

$$\alpha_P = \left(2\frac{m_e m_p}{m_e + m_p}\right)^{\frac{3}{2}} \frac{q_e^2}{ncm_e}\left(h\nu - E_g\right)^{\frac{1}{2}}, \tag{4}$$

where m_e and m_p are effective electron and hole masses; q_e is elementary charge; n is refraction coefficient.

For all samples, the band gap E_g was obtained by extrapolating the linear part of the square of absorption spectrum at $(\alpha(h\nu))^2$. The dependence of the band gap values on the annealing time at each temperature appears linear (Fig. 4).

The optical band gap decreases with increasing temperature from 3.10 eV (at 400 °C) to 3.02 eV (at 800 °C). It also decreases with the annealing time growing. SEM and SAXS data prove that the higher the annealing temperature, the larger the crystallite size, which is accompanied by a decrease in the band gap E_g.

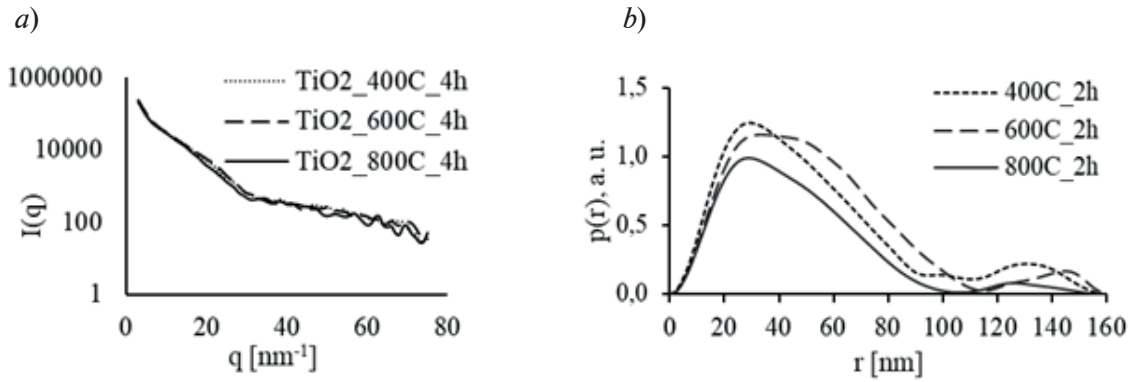

Fig. 2. SAXS results: scattering intensity data (*a*); pair distance distribution functions (*b*)

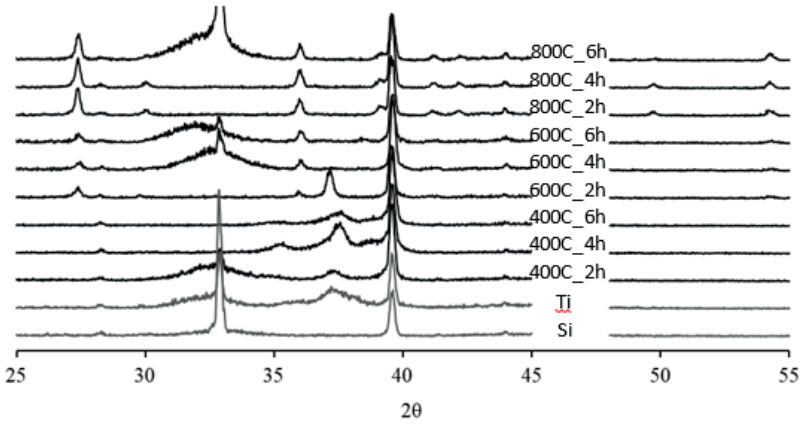

Fig. 3. X-ray diffractograms of TiO_2 films, pure Ti, and pure Si

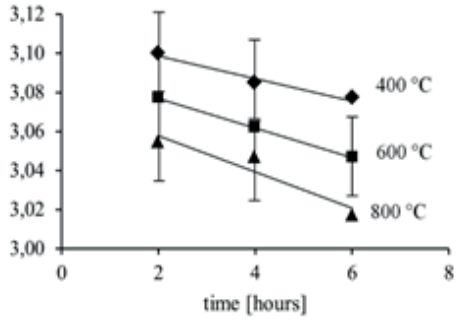

Fig. 4. Dependence of the band gap value on the annealing time

Conclusion

Titanium oxide films were obtained by magnetron Ti sputtering and subsequent annealing in air for 2, 4, and 6 hours at 400 °C, 600 °C and 800 °C. The thickness of the obtained TiO_2 films is ~1 μm. According to SEM and SAXS data, all studied TiO_2 films are polydisperse. The grains have an irregular shape, and their size grows with increasing of temperature and the duration of annealing.

The phase analysis shows that TiO_2 annealing at 400 °C leads to crystallization of the anatase phase, and annealing at 600 °C leads to the transformations into the rutile phase. According to our estimations of coherent scattering region, the average size of crystallites is in the range from 3 to 11 nm. Optical absorption spectra were used to obtain the band gap for each sample. The value of the band gap decreases with increasing annealing time and with increasing temperature. It is 3.10 eV at 400 °C and 3.02 eV at 800 °C. To summarize, it is evident that an increase in the annealing temperature leads to an increase in the crystallite size, which is accompanied by a decrease in the band gap.

REFERENCES

1. **Ali I., Suhail M., Alothman Z.A., Alwarthan A.,** Recent advances in syntheses, properties and applications of TiO_2 nanostructures, RSC Adv. 8 (2018) 30125.

2. **Cerro-Prada E., García-Salgado S., Quijano M.Б., Varela F.,** Controlled synthesis and microstructural properties of sol-gel TiO_2 nanoparticles for photocatalytic cement composites, Nanomaterials 9 (2019) 1.

3. **Guo Q., Zhou Q., Ma Z. , Yang X.**, Fundamentals of TiO_2 photocatalysis: concepts, mechanisms, and challenges, Advanced Materials 31 (2019) 1901997.

4. **Cruz-González N., Calzadilla O., Roque J., Chalé-Lara F., Olarte J.K., Meléndez-Lira M., Zapta-Torres M.,** Study of the effect of TiO_2 layer on the adsorption and photocatalytic activity of

TiO_2-MoS_2 heterostructures under visible-infrared light, International Journal of Photoenergy (2020) 2020.

5. **Henrich V.E.,** The surfaces of metal oxides, Rep. Prog. Phys. 48 (1985) 1481.

6. **Banfield J.F., Bischoff B.L., Anderson M.A.,** TiO_2 accessory minerals: coarsening, and transformation kinetics in pure and doped synthetic nanocrystalline materials, Chem. Geol. 110 (1993) 211.

7. **Na-Phattalung S., Smith M., Kim K., Du M.-H., Wei S.-H., Zhang S., Limpijumnong S.,** First-principles study of native defects in anatase TiO_2, Phys. Rev. B 73 (2006) 125205.

8. **Setvin M., Franchini C., Hao X.,** Direct view at excess electrons in TiO_2 rutile and anatase, Phys. Rev. Letters 113 (2014) 086402.

9. **Pugachevskii M.A., Mamontov V.A., Nikolaeva S.N., Chekadanov A.S., Emelyanov V.M.,** Influence of the size factor on the structure and physical and chemical properties of titanium dioxide nanoparticles, Proc. of the Southwest State Univ. Series: Engineering and Technologies 11 (2021) 104.

10. **Gusev A.I.,** Nanomaterials, nanostructures, and nanotechnologies (in Russian), Fizmatlit, Moscow, 2007.

THE AUTHORS

CHEKADANOV Alexander S.
alexch17@mail.ru
ORCID: 0000-0002-1652-7830

KUZMENKO Alexander P.
apk3527@mail.ru
ORCID: 0000-0001-7089-0692

PUGACHEVSKII Maxim A.
pmaximal@mail.ru
ORCID: 0000-0002-5004-0823

STOROZHENKO Anastasia M.
storogenko_s@mail.ru
ORCID: 0000-0002-4995-7407

AUNG HEIN Kyaw K.
kyawaunghein53@gmail.com
ORCID: 0000-0002-5761-8632

Received 05.05.2022. Approved after reviewing 20.06.2022. Accepted 27.06.2022.

Conference materials
UDC УДК 539.213.2:539.25
DOI: https://doi.org/10.18721/JPM.153.126

Effect of high-speed nonequilibrium on morphological and magnetic properties of melt-spun $Co_{58}Ni_{10}Fe_5Si_{11}B_{16}$ alloy

A. M. Frolov [1] ✉, T. A. Pisarenko [2], G. S. Kraynova [1], N. V. Ilin [1], A. Yu. Ralin [1]

[1] Far Eastern Federal University, Vladivostok, Russia;

[2] Institute of Automation and Control Processes Far Eastern Branch of the RAS, Vladivostok, Russia

✉ froloff5@yandex.ru

Abstract: The work presents a study on the influence of high-speed nonequilibrium of the melt-spinning process on the morphological and magnetic properties of the amorphous $Co_{58}Ni_{10}Fe_5Si_{11}B_{16}$ alloy. It is shown that the amorphous states with a different extent of disordering may be produced by varying the melt-spinning conditions. A correlation has been established between the fractal structure of morphological inhomogeneities and the magnetic properties of the melt-spun alloy: the higher the fractal dimension of the hierarchical mesoscale structure, the more the soft magnetic alloy. The optimal ordering of both the morphological and magnetic structure of the melt-spun Co58Ni10Fe5Si11B16 alloy is achieved at a cooling roller speed of 28 m/s.

Keywords: melt-spun alloy, morphology, mesoscale defects, fractal dimension, magnetism, coercitivity

Funding: The work was supported by State Task of the Ministry of Science and Higher Education of the Russian Federation under Grant no. 0657-2020-0005.

Citation: Frolov A. M., Pisarenko T.A., Kraynova G. S., Ilin N. V., Ralin A. Yu., Effect of high-speed nonequilibrium on morphological and magnetic properties of melt-spun $Co_{58}Ni_{10}Fe_5Si_{11}B_{16}$ alloy, St. Petersburg State Polytechnical University Journal. Physics and Mathematics. 15 (3.1) (2022) 155–161. DOI: https://doi.org/10.18721/JPM.153.126

Материалы конференции
УДК 539.213.2:539.25
DOI: https://doi.org/10.18721/JPM.153.126

Влияние высоко-скоростной неравновесности на структурно-морфологические и магнитные свойства быстрозакаленного сплава $Co_{58}Ni_{10}Fe_5Si_{11}B_{16}$

А. М. Фролов [1] ✉, Т. А. Писаренко [2], Г. С. Крайнова [1], Н. В. Ильин [1], А. Ю. Ралин [1]

[1] Дальневосточный Федеральный Университет, г. Владивосток, Россия;

[2] Институт автоматики и процессов управления Дальневосточного отделения РАН, г. Владивосток, Россия;

✉ froloff5@yandex.ru

Аннотация. В работе представлены результаты исследования морфологии и магнитных свойств сплава $Co_{58}Ni_{10}Fe_5Si_{11}B_{16}$ в зависимости от скоростных режимов получения. Показано, что технология спиннингования при вариации параметров получения позволяет получить аморфные состояния с разной степенью разупорядочения. В ходе работы установлена корреляция фрактальной структуры морфонеоднородностей и магнитных свойств быстрозакаленных сплавов: чем выше фрактальная размерность иерархической мезомасштабной структуры, тем более ярко выражены магнитомягкие свойства. Оптимальное упорядочение как морфологической, так и магнитной структуры сплава $Co_{58}Ni_{10}Fe_5Si_{11}B_{16}$ достигается при скорости роллера 28 м/с.

Ключевые слова: быстрозакаленный сплав, морфология, мезомасштабные дефекты, фрактальная размерность, магнетизм, коэрцитивность

Финансирование: Исследование выполнено при поддержке гранта Минобрнауки РФ № 0657-2020-0005.

Ссылка при цитировании: Фролов А. М., Писаренко Т. А., Крайнова Г. С., Ильин Н. В., Ралин А. Ю. Влияние высоко-скоростной неравновесности на структурно-морфологические и магнитные свойства быстрозакаленного сплава $Co_{58}Ni_{10}Fe_5Si_{11}B_{16}$ // Научно-технические ведомости СПбГПУ. Физико-математические науки. 2022. Т. 15. № 3.1. С. 155–161. DOI: https://doi.org/10.18721/JPM.123.126

Introduction

Amorphous metal alloys (AMA) are of great scientific interest in the study of the physical properties of disordered system. Soft magnetic AMA fabricated by the melt-spinning technique has a high magnetic permeability as a result one may be successfully applied for the manufacture of magnetic heads, magnetic shields, and secondary power supplies [1–4]. These alloys have high strength and corrosion resistance, which is important for operation in aggressive environments.

In order to increase the practical efficiency of such materials in technology, it is necessary to find new ways to control their special properties. For this reason, there has recently been an increased interest in studying the structural state and functional properties of melt-spun alloys, in particular, those made of soft magnetic materials.

The goal of this study is to identify the structural/morphological ordering and magnetic ordering in cobalt-based AMA produced by melt-spinning on a cooling roller at various technological conditions. It is interesting to study the correlations of the surface morphology and physical properties with a change in high-speed nonequilibrium, since, on the one hand, disordered media are characterized by the collective behavior of defects forming a hierarchical system with a fractal structure in the configuration space [5–7], and, on the other hand, it is well known that magnetic properties are structure-sensitive [4, 8, 9].

Materials and Methods

Amorphous $Co_{58}Ni_{10}Fe_5Si_{11}B_{16}$ alloys were fabricated by the melt-spinning technique with a single Cu roller at various linear speeds on the MeltSpinner SC equipment. Several samples of ribbons from this alloy were prepared, parametrized by high-speed production conditions. Technological and geometric parameters of the ribbons are given in Table 1.

Table 1

Parameters of samples

Sample	V, m/s	P_1, mbar	P_2, mbar	t, mm
A	22.0±0.1	50±5	200±5	21.0±4
B	25.1±0.1	50±5	250±5	23.0±1
C	28.3±0.1	50±5	350±5	23.0±1
D	31.4±0.1	50±5	350±5	19.3±0.5
E	37.0±0.1	60±5	400±5	16.0 ±1

Notations. V is the linear speed of the cooling roller, P_1 is the pressure in the chamber, P_2 is the pressure in the crucible, t is the ribbon thickness.

As seen from Table 1, in this series of samples, the cooling roller speed (V) is the most interesting parameter which affects the nonequilibrium of the melt-spinning process. In addition, it should be noted that at low P_1, with an increase of the linear speed of the cooling roller, an increase of P_2 is necessary to maintain the ribbon thickness.

To identify the atomic ordering, we used the X-ray diffraction method by a Bruker D8 Advance diffractometer, Fe-K_α radiation.

Morphology analysis was carried out using amorphous alloy HRTEM images obtained on FEI TITAN 300 TEM. The samples were preliminarily prepared: 3 mm circles were cut from the ribbon bulk, which were then placed in an ionic thinning plant (GATAN PIPS Model 691), where they were thinned until through holes appeared in central part.

Fraunhofer diffraction patterns were obtained by the System for Spectral Analysis of Electron-Optical Imaging software for digital spectral analysis of images, based on the FFT procedure [10]. The spectrum of spatial inhomogeneities (integral frequency characteristic) was calculated as a result of angular convolution of Fraunhofer diffraction pattern. Moreover, HRTEM images were parametrized by fractal dimensions using the fracton technique for analyzing a structural ordering based on the integral frequency characteristic [7].

Hysteresis loops and magnetization curves for the $Co_{58}Ni_{10}Fe_5Si_{11}B_{16}$ alloy were measured on an automated vibromagnetometer.

Results and Discussion

X-ray diffraction analysis showed that the melt-spun $Co_{58}Ni_{10}Fe_5Si_{11}B_{16}$ alloy remains X-ray amorphous at all speed conditions [11], and the profiles of X-ray diffraction patterns practically coincide when superimposed. The diffraction patterns reveal a single diffuse peak at the angle of $2\theta = (57-59)^o$, which corresponds to the short-range order period of (0.203–0.197) nm, while there are no crystalline peaks.

The study of fractograms obtained by antiplanar deformation of the $Co_{58}Ni_{10}Fe_5Si_{11}B_{16}$ ribbons revealed a hierarchical structure in the range from 20 nm to (1–2) μm containing coral-like and cellular structures [11]. To understand the features of structure formation in AMA, it is important to note that the coral-like structure (see Fig. 1) as well as the solidification process, begins from the ribbon contact surface [12]. From the point of view of structure formation of a melt-spun ribbon as a whole, coral branches can be considered as elementary structural units of wave-like heat transfer through the ribbon thickness by means of a density gradient in the mesoscale structure. The hierarchical nature of the coral-like structure implies its quantitative parametrization by fractal dimensions.

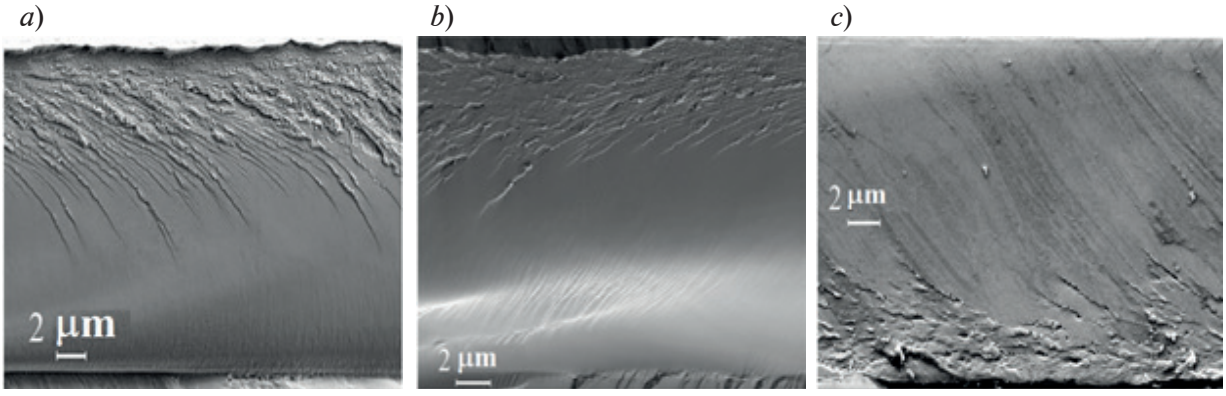

Fig. 1. Electron microscopic images of fractograms for melt-spun $Co_{58}Ni_{10}Fe_5Si_{11}B_{16}$ alloy (characteristic fracture with a coral-like structure): 22 m/s (*a*); 28 m/s (*b*); 38 m/s (*c*)

Fig. 2,*a* shows a fragment of a HRTEM image of the mesoscale structure for the sample *A*. As seen from Fig. 2,*a*, a salt-pepper contrast nanostructure is observed, typical for the amorphous structure observed in TEM images for the as-spun $Co_{58}Ni_{10}Fe_5Si_{11}B_{16}$ ribbon. We applied the fracton technique for analyzing structural ordering [7] to HRTEM images, plotting the dependence D_f(V), see Fig. 3, curve *1*. According to the kinetics of fractal dimensions, two classes of

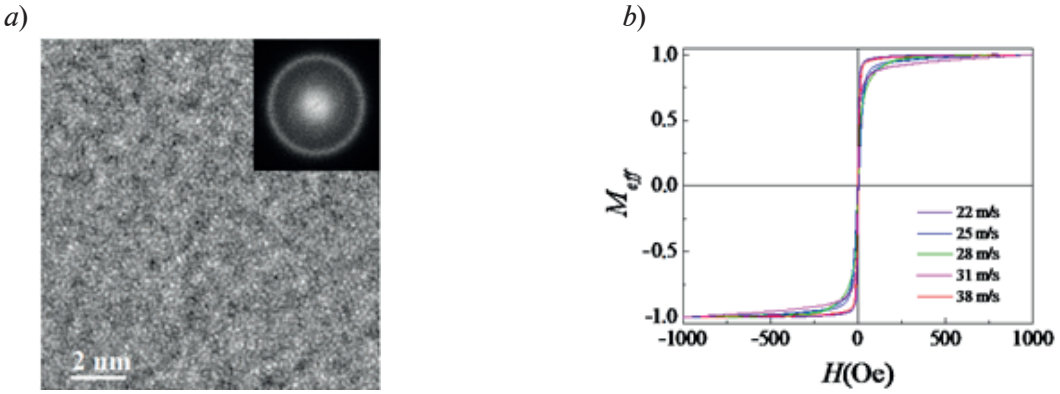

Fig. 2. HRTEM subimage of the $Co_{58}Ni_{10}Fe_5Si_{11}B_{16}$ alloy (Sample A); the inset shows the Fraunhofer diffraction pattern (*a*); hysteresis loops of the melt-spun $Co_{58}Ni_{10}Fe_5Si_{11}B_{16}$ alloy are shown in (*b*)

hierarchical subordination were distinguished by fractal dimensions greater than and less than 2. In the case of $D > 2$, the fractal cluster is the so-called contact cluster that fills the surface, for example, a fractal sponge and fractal foam [5]. Thus, the condition for the formation of a connected spatial cluster is $D > D_T = 2$.

As noted above, structure formation in AMAs affects their functional properties, in our case, magnetic ones. Therefore, it is of interest to analyze the influence of the fractal structure on the magnetic ordering. Hysteresis loops were measured for all $Co_{58}Ni_{10}Fe_5Si_{11}B_{16}$ ribbons produced at different melt-spinning conditions, Fig. 2,*b*. As seen from Fig. 2,*b,* all samples are soft magnetic. In Fig. 3, curve 2 the dependence of the coercive force (H_c) on the high-speed nonequilibrium is present. The shape of the dependence H_c(V) may be interpreted as structural relaxation within the amorphous state, accompanied by a change in the magnetic ordering.

As seen from curve *1* in Fig. 3, a fractal structure is formed in all alloys, which may be interpreted as a fractal percolation σ-cluster near a percolation threshold. However, the condition $D > 2$ is satisfied by only sample *C* (28 m/s), which implies that in this case the deterministic component prevails in the subordination by means of forming a connected spatial percolation cluster, which ensures the minimum coercive force. In cases of $D < 2$, the stochastic component dominates in the subordination; as a result, a frustrated fractal cluster is formed, which weakens largely the magnetic interaction, increasing the coercive force of these alloys.

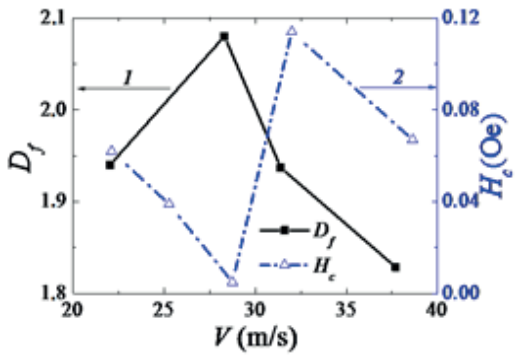

Fig. 3. Dependences of fractal dimension and coercive force for melt-spun $Co_{58}Ni_{10}Fe_5Si_{11}B_{16}$ alloy on cooling roller speed

The H_c decrease in the speed range of 22–28 m/s can be associated with an ordering change of the hierarchical complex structure of mesoscale morphological inhomogeneities due to the appearance of order from chaos (the formation of fractal dissipative structures). Moreover, with an increase of nonequilibrium, the fractal structure becomes more organized.

The amorphous state of the $Co_{58}Ni_{10}Fe_5Si_{11}B_{16}$ alloy, produced at a low speed of 22 m/s, is usually interpreted as microcrystalline, which is characterized by the presence of grain boundaries, which significantly weaken the magnetic interaction. As the cooling roller speed increases to 25 m/s, the alloy structure evolves into a heterogeneous amorphous state, while H_c decreases, identifying an increase of the magnetic interaction. These changes are due to the absence of grain boundaries in the amorphous matrix, on the one hand, and the formation of a more ordered fractal cluster (including magnetic), as a result of emergence of order from chaos, on the other hand. It is possible that the fractal cluster is still frustrated at 25 m/s due to heterogeneity of the amorphous state.

A subsequent increase of the cooling roller speed to 28 m/s results in the so-called nanocrystallization of the melt, when the nanoclusters are dissolved in an amorphous (glassy) matrix, which provides the continuity of the magnetic interaction. Thus, at optimal subordination of the multiscale structure, a minimum of the coercive force is achieved. A high value of $D_f = 2.08$ and a low value of $H_c = 0.008$ Oe indicate that a connected spatial magnetic percolation cluster is formed under these melt-spinning conditions in the amorphous matrix in addition (dualism) to the fractal cluster of morpho-inhomogeneities. In this case, it can be concluded that fractally ordered magnetic nanocrystals dissolve in an amorphous (glassy) matrix [4].

The maximum D_f is due to fractal ordering of the hierarchical complex structure of the morphological inhomogeneities of the alloy. The subsequent decrease in D_f is explained by an increase in high-speed nonequilibrium and, therefore, by a mesoscale structure randomization.

The jump of the H_c dependence from the minimum value to the maximum (Fig. 3, curve *2*) is due to the change in the ordering of the hierarchical mesoscale structure from nanocrystalline ordering, in which nanocrystals are dissolved in an amorphous matrix, where they are fractally ordered, to a homogeneous glassy state, where the magnetic percolation cluster is strongly randomized and, as a result, contains an infinite number of non-intersecting fragments. As the speed increases to 31 m/s, structural randomization destroys the nanocrystalline component, while a magnetic percolation cluster is formed in the atomic scale, which significantly weakens the magnetic interaction, increasing the H_c to a value 0.11 Oe.

The subsequent decrease in H_c with an increase of the roller speed to 38 m/s is associated with the evolution of the coral-like structure due to a reduction in the contact time of the melt with the cooling roller surface. In this case, the coral-like (foamy) structure emerges on the ribbon contact surface (Fig. 1, *c*), since the thermo-hydrodynamic wave does not have time to overcome the ribbon thickness as the ribbon quickly tears away from the cooling roller surface. Thus, the high speed results in strong randomization of the hierarchical mesoscale structure as a whole. The structure randomization is reflected by low D_f (Fig. 3, curve *1*). The short-time contact causes a heat transfer rate (supercooling degree) to decrease at such high-speed conditions, as a result, the solidification process continues after the ribbon separates from the cooling roller surface. In these conditions, magnetic nanocrystals (nanoclusters) are again formed in the glassy matrix, but they are strongly randomized and spatially broken, which follows from the reduction in the fractal dimension. It can be assumed that in the case of sample *C*, a fractal percolation cluster parameterized by $D > 2$ is formed as a result of dynamic chaos, while in other cases, with $D < 2$, the organization of structural ordering decreases as a result of the contribution from orthodox stochastization to the heat transfer process. It is likely that the high-speed conditions in which the solidification process continues outside the roller surface require taking into account the local magnetization inside the magnetic percolation cluster. Then the decrease in the coercive force of the sample *E* can be interpreted as an increase in the magnetization of non-intersecting fragments of the magnetic percolation cluster.

Based on the obtained results, it can be assumed that the hierarchical mesoscale structure of morphological inhomogeneities, characterized by fractal dimension as a randomization measure induced by high-speed nonequilibrium, determines the division of the functional space, in our case, it is the spatial distribution of the magnetic percolation cluster (ignoring magnetization), starting from short-range order scales (atomic scales) to the hierarchical (nano) cluster structure. The spatial division of both the morphological and magnetic structure is fractal (dualism), but not identical, since the obtained fractal characteristics of the hierarchical mesoscale structure of rapidly quenched $Co_{58}Ni_{10}Fe_5Si_{11}B_{16}$ alloy agree with their magnetic parameters only taking into account the difference in the structural-phase composition of the disordered material. Therefore,

the fractally ordered hierarchical mesoscale structure of the ribbons determines only the nature of the magnetic division, disregarding the distribution of the magnetization magnitude. Most likely, high-speed melt-spinning processes are characterized by an increase of the randomization measure, which reduces the fractal dimensionality, on the one hand. On the other hand, an increase in the magnetization of elementary nanoclusters results in an increase in the magnetic interaction of these structures. That is, a magnetic percolation cluster must in addition be characterized by the magnetization magnitude. We can only be certain that the fractally ordered hierarchical mesoscale structure of the rapidly quenched alloy with a fractal dimension $D > 2$ provides an increase in the magnetic interaction. In this case, the $Co_{58}Ni_{10}Fe_5Si_{11}B_{16}$ alloy will have more pronounced soft magnetic properties. Thus, to obtain soft-magnetic materials, it is necessary to form an alloy structure with the maximum fractal dimension, at least in the mesoscale range.

It should be noted that the correlation between the fractal morphological structure and magnetic behaviors has a more complex dependence than that determined in the present study. It is known [8] that a dimension of the magnetic microstructure depends very strongly on the applied magnetization field. For example, the dipole-dipole interaction between nanoparticles of a fractal magnetic cluster will have a significant effect, both in low and in high fields.

Conclusion

In this work, a systematic analysis of the structural and magnetic properties of the melt-spun $Co_{58}Ni_{10}Fe_5Si_{11}B_{16}$ alloy fabricated at different melt-spinning speeds has been carried out. High-speed nonequilibrium (in the speed range $V = 22–38$ m/s) leads to amorphization of the alloy at all melt-spinning speed conditions, however, the structural disorder in these alloys differs largely. It is shown that the amount of order-disorder in an amorphous medium can be characterized by fractal dimension. The maximum fractal dimension is due to the fractal ordering of the hierarchical complex structure of morphological inhomogeneities into a connected spatial percolation cluster, which ensures a minimum coercive force. Thus, study of the functional properties of melt-spun alloys using fractal analysis increases the efficiency of developing technical conditions for the formation of soft magnetic materials.

Acknowledgments

The experimental results were obtained on the equipment of the Center of Collective Usage of the Far Eastern Federal University, registration No. 200556 (Vladivostok).

REFERENCES

1. **Hawelek L., Warsk T., Wlodarczyk P., Polak M., Zackiewicz P., Maziarz W., Wojcik A., Steczkowska-Kempka M., Kolano-Burian A.,** The structure and magnetic properties of rapidly quenched Fe72Ni8Nb4Si2B14 alloy, Materials. 14(1) (2021) 5–9.

2. **Han Y., Ding J., Kong F.L., Inoue A., Zhu S.L., Wang Z., Shalaan E., Al-Marzouki F.,** FeCo-based soft magnetic alloys with high Bs approaching 1.75 T and good bending ductility, Journal of Alloys and Compounds. 691 (2017) 364–368.

3. **Liu C., Inoue A., Kong F.L., Zanaeva E., Bazlov A., Churyumov A., Zhu S.L., Al-Marzouki F., Shull R.D.,** Fe-B-Si-C-Cu amorphous and nanocrystalline alloys with ultrahigh hardness and enhanced soft magnetic properties, Journal of Non-Crystalline Solids. 554 (2021) 120606.

4. **Herzer G.,** Modern soft magnets: Amorphous and nanocrystalline materials, Acta Materialia. 61(3) (2013) 718–734.

5. **Mandelbrot B.B.,** The fractal geometry of nature, Freeman, New York, 1982.

6. **Schroeder M.,** Fractals, chaos, power laws, Freeman, New York, 1991.

7. **Pisarenko T.A., Frolov A.M., Kraynova G.S.,** Evolution of structure-scaling and magnetic properties during thermal loading of melt-spun Fe70Cr15B15(Sn) alloys, Solid State Phenomena. 215 (2014) 190–195.

8. **Komogortsev S.V., Iskhakov R.S., Fel'k V.A.,** Fractal dimension effect on the magnetization curves of exchange-coupled clusters of magnetic nanoparticles, Journal of Experimental and Theoretical Physics. 128(5) (2019) 754–760.

9. **Kotvitckii A.N., Krainova G.S., Frolov A.M., Pechnikov V.S.,** Changes in the magnetic parameters of amorphous alloys as an indicator of structural transformations, Bulletin of the Russian Academy of Sciences: Physics. 77(10) (2013) 1206–1209.

10. **Grudin B.N., Plotnikov V.S.,** Processing and simulating of microscopic images, Dal'nauka, Vladivostok, 2010.

11. **Pustovalov E.V., Modin E.B., Frolov A.M., et.al.,** Effect of the process conditions for the preparation of CoNiFeSiB amorphous alloys on their structure and properties, Journal of Surface Investigation: X-ray, Synchrotron and Neutron Techniques. 13(4) (2019) 600–608.

12. **Pisarenko T.A., Kraynova G.S., Frolov A.M.,** Kinetics of the fractal mesodefect structure of melt-spun Fe70Cr15B15(Sn) alloys during annealing, Solid State Phenomena. 247 (2016) 101–105.

THE AUTHORS

FROLOV Anatoly M.
froloff5@yandex.ru
ORCID: 0000-0003-0162-6278

ILIN Nikita V.
ilin.nva@dvfu.ru
ORCID: 0000-0002-8835-6436

PISARENKO Tatiana T.A.
tata_dvo@iacp.dvo.ru
ORCID: 0000-0002-7977-7474

RALIN Andrey Yu.
ralin.ayu@dvfu.ru
ORCID: 0000-0001-6723-7246

KRAYNOVA Galina G. S.
kraynova.gs@dvfu.ru
ORCID: 0000-0001-9344-3983

Received 12.05.2022. Approved after reviewing 14.06.2022. Accepted 14.06.2022.

Conference materials
UDC 537.622, 537.624
DOI: https://doi.org/10.18721/JPM.153.127

Micromagnetic modeling of the superparamagnetic fraction of Fe_3O_4–$Fe_{3-x}Ti_xO_4$ composites

A. Yu. Ralin [1] ✉, P. V. Kharitonskii [2], N. A. Zolotov [2], K. G. Gareev [2], Yu. A. Anikieva [2]

[1] Far Eastern Federal University, Vladivostok, Russia;

[2] St. Petersburg Electrotechnical University "LETI", St. Petersburg, Russia

✉ ralin.ayu@dvfu.ru

Abstract: Modeling of the hysteresis characteristics of Fe_3O_4–$Fe_{3-x}Ti_xO_4$ composites was performed using the method of magnetic rectangles. Their magnetic properties are well explained within the model of an ensemble of magnetostatically interacting two-phase chemically inhomogeneous particles. It is shown that accounting for the contribution of the superparamagnetic fraction makes it possible to obtain agreement between the theoretical and experimental magnetic characteristics of the samples. The model allows calculating the magnetization reversal fields and magnetizations of the studied composites theoretically and also to show that the main contribution to the remanent magnetization is made by two-phase particles. In addition, a possibility of using this model for samples containing superparamagnetic particles is demonstrated.

Keywords: magnetic granulometry, superparamagnetism, micromagnetic modeling, magnetostatic interaction, two-phase particles

Citation: Ralin A. Yu., Kharitonskii P. V., Zolotov N. A., Gareev K. G., Anikieva Yu. A., Micromagnetic modeling of the superparamagnetic fraction of composites Fe_3O_4–$Fe_{3-x}Ti_xO_4$, St. Petersburg State Polytechnical University Journal. Physics and Mathematics. 15 (3.1) (2022) 162–167. DOI: https://doi.org/10.18721/JPM.153.127

Материалы конференции
УДК 537.622, 537.624
DOI: https://doi.org/10.18721/JPM.153.127

Микромагнитное моделирование суперпарамагнитной фракции в композитах Fe_3O_4–$Fe_{3-x}Ti_xO_4$

А. Ю. Ралин [1] ✉, П. В. Харитонский [2], Н. А. Золотов [2], К. Г. Гареев [2], Ю. А. Аникиева [2]

[1] Дальневосточный Федеральный Университет, г. Владивосток, Россия

[2] Санкт-Петербургский государственный электротехнический университет «ЛЭТИ» имени В. И. Ульянова (Ленина), Санкт-Петербург, Россия

✉ ralin.ayu@dvfu.ru

Аннотация. Методом «магнитных прямоугольников» проведено моделирование гистерезисных характеристик композитов Fe_3O_4–$Fe_{3-x}Ti_xO_4$. Их магнитные свойства хорошо объясняются в рамках модели ансамбля магнитостатически взаимодействующих двухфазных химически неоднородных частиц. Данная модель позволила теоретически рассчитать поля перемагничивания и намагниченности исследуемых композитов, а также показать, что основной вклад в остаточную намагниченность вносят двухфазные частицы. Используемая модель применима для образцов, содержащих суперпарамагнитные частицы.

Ключевые слова: магнитная гранулометрия, суперпарамагнетизм, микромагнитное моделирование, магнитостатическое взаимодействие, двухфазные частицы

Ссылка при цитировании: Ралин А. Ю., Харитонский П. В., Золотов Н. А., Гареев К. Г., Аникиева Ю. А. Микромагнитное моделирование суперпарамагнитной фракции в композитах Fe_3O_4–$Fe_{3-x}Ti_xO_4$ // Научно-технические ведомости СПбГПУ. Физико-математические науки. 2022. Т. 15. № 3.1. С. 162–167. DOI: https://doi.org/10.18721/JPM.153.127

Introduction

Theoretical works dedicated to ensembles of superparamagnetic (SP) particles often use the approximation of non-interacting particles, assuming their chemical homogeneity. Earlier studies [1, 2] considered Fe_3O_4–$Fe_{3-x}Ti_xO_4$ composites, where the presence of a significant fraction of SP particles was found. It was shown that the magnetic properties of the studied samples cannot be explained without accounting for the chemical inhomogeneity of individual particles and the magnetostatic interaction between them, including the SP fraction. Existing micromagnetic modeling methods allow to investigate in detail the magnetic states of individual grains (e.g., [3, 4]). However, significant computational resources are required for considering even small sets of such grains. The approach we adopt allows making a simpler estimate of the magnetic states of individual particles and their ensembles [5, 6].

Materials and Experimental data

Synthesis of composites based on the Fe_mO_n–TiO_2 system was carried out by magnetite precipitation in suspension of TiO_2 powder [1, 2]; 4 g of $FeCl_3 \cdot 6H_2O$ and 2 g of $FeSO_4 \cdot 7H_2O$ (molar ratio 2:1) were dissolved in 100 mL of distilled water. Samples T05L, T10L, and T20L were obtained by dispersing TiO_2 powder (0.5, 1.0, and 2.0 g, respectively) into solution, followed by hydrothermal treatment (240 °C, 50 MPa) for 4 hours. Sample T05H was treated under different conditions (470 °C, 42 MPa). Sample T20R was not subjected to temperature treatment.

According to the experimental data [1, 2], titanomagnetites are formed in very small quantities under the specified conditions. Significant content of hematite is detected, indicating significant oxidation of the samples during processing. The lattice period of 0.8362–0.8367 nm is intermediate between the constants of the lattice of maghemite and magnetite.

Since the particles are grouped into conglomerates, embedding of titanium atoms into the ferrimagnetic does not occur on all sides, but only from a limited number of surfaces. For simplicity, we will assume that titanomagnetite is formed only on one side of the ferrimagnetic particle, i.e., chemically heterogeneous two-phase particles are formed. Since there is little titanomagnetite, the corresponding phase is a thin layer. Besides, if the particle size is smaller than the single-domain size, then two-phase particles that are in a SP state should be present.

Table 1 shows the characteristics of the samples [1, 2]: M_s is the saturation magnetization and M_{rs} is the saturation remanence, H_c is the coercive force and H_{cr} is the remanence coercivity.

For the first four samples, the ratios of M_{rs}/M_s values are in the range of 0.1–0.2 and H_{cr}/H_c in the range of 2–3. For sample T20R, these ratios are approximately 0.01 and 4, respectively. According to magnetic granulometry data, it can be assumed that the first group of samples is dominated by single- and low-domain particles, whereas in sample T20R by SP particles.

Theoretical Modeling

For the modeled samples [1, 2], the presence of three groups of particles was assumed: 1) a fraction of chemically inhomogeneous two-phase particles (magnetite/maghemite–titanomagnetite), 2) a weakly magnetic fraction (mainly hematite), and 3) superparamagnetic particles of the first two fractions. Since the spontaneous magnetization I_{s1} of the first fraction is two orders of magnitude higher than that of the weakly magnetic fraction (I_{s2}), the two-phase particles make the main contribution to the saturation remanent magnetization of M_{rs} samples.

Table 1

Hysteresis characteristics of the samples

Sample	M_s, A·m²/kg	M_{rs}, A·m²/kg	$\mu_0 H_c$, mT	$\mu_0 H_{cr}$, mT	M_{rs}/M_s	H_{cr}/H_c
T05L	26.37	2.95	5.62	14.92	0.11	2.66
T10L	19.53	2.06	4.77	12.61	0.11	2.65
T20L	14.11	1.92	5.97	13.77	0.14	2.31
T05H	23.79	4.15	8.78	18.32	0.18	2.09
T20R	28.95	0.35	0.51	1.90	0.01	3.73

The first fraction is an ensemble of cubic two-phase particles with an infinitely thin boundary between the phases [5]. Each phase is a homogeneously magnetized crystallographically uniaxial ferrimagnetic (magnetite/maghemite and titanomagnetite). The characteristic size of particle a ranged from 20 to 80 nm, and the relative thickness of the second phase $\varepsilon = 0.05–0.20$.

To find the magnetic states and critical fields of remagnetization, the free energy was minimized, including magnetocrystalline, magnetostatic, and Zeeman energies. The magnetostatic energy was calculated by the method of magnetic rectangles [5, 6]. In this case, the two-phase particle can be in four states: the magnetic moments of the phases are parallel to each other along (n_1) or against (n_2) the external magnetic field H or antiparallel to each other (n_3 and n_4). In the absence of an external field, it is possible to determine their relative number in the mth state:

$$n_m\,|_{H=0} = A\exp\left(-E_m/(kT)\right), \tag{1}$$

where A is found from the normalization condition, in which the sum of n_m equals unity.

Then the magnetization of the ensemble of two-phase ferrimagnetic particles is [5]:

$$M(\varepsilon, H) = C_1\left[I_{s\,sm}(1-\varepsilon)(n_1 - n_2 + n_3 - n_4) + I_{s\,wm}\varepsilon(n_1 - n_2 - n_3 + n_4)\right]. \tag{2}$$

Here $C_1 = N\cdot v/V$ is the volume concentration of the first fraction (N and v are the number and average volume of two-phase particles, V is the sample volume), and $I_{s\,sm}$ and $I_{s\,wm}$ are the effective spontaneous magnetizations of the first and second phases, respectively.

If we assume that the random fields of magnetostatic interaction H_i are uniformly distributed in the interval from $-H_{max}$ to $+H_{max}$, the calculation of the magnetization of the fraction of two-phase particles with the same ε in the first approximation is reduced to the case of non-interacting particles with a shift of the critical fields by $-H_{max}$ [5]:

$$\begin{gathered} H_{max} \approx 5C_1 I_{s1} \text{ at } C_1 < 0.07 \text{ and } H_{max} \approx 1.3\sqrt{C_1} I_{s1} \text{ at } C_1 > 0.07\ , \\ I_{s1} = I_{s\,sm}(1-\varepsilon) \pm I_{s\,wm}\varepsilon\ ,\ K_{u1} = K_{u\,sm}(1-\varepsilon) + K_{u\,wm}\varepsilon\ . \end{gathered} \tag{3}$$

Here I_{s1} is the average spontaneous magnetization of a two-phase grain. The plus sign corresponds to the state $n_1 = 1$ (saturation) when the magnetic moments of both phases are oriented along the applied field, and the minus sign indicates the state when the magnetic moments of the phases are directed opposite to each other. $K_{u\,sm}$ and $K_{u\,wm}$ are the crystallographic anisotropy constants of the strongly magnetic (magnetite) and less magnetic (titanomagnetite) phases, respectively, and K_{u1} is the average constant of a two-phase grain (magnetite – $I_s = 484$ kA/m, $K_u = 1.36\cdot10^4$ J/m³; titanomagnetite ($x = 0.1$) – $I_s = 426$ kA/m, $K_u = 2.5\cdot10^4$ J/m³; $T = 290$ K [7]).

During modeling, the saturation remanence was provided by the strongly magnetic two-phase particles and the weakly magnetic fraction. However, it was possible to agree the theoretical values of the saturation magnetization with the experimental data only in the assumption of the presence of a large number of SP particles in the samples. Then for the first four samples

$$M_s = M_{s1} + M_{s2} + M_{s\,sp},\ M_{rs} = M_{rs1} + M_{rs2}. \quad (4)$$

where M_{s1} and M_{rs1}, M_{s2} and M_{rs2}, $M_{s\,sp}$ are the magnetizations of the corresponding three fractions.

Judging by the hysteresis characteristics (Table 1), the fifth sample (T20R) contains mainly superparamagnetic particles. Therefore, the average particle size of this sample varied in the range of 20—30 nm (for spherical magnetite grains, the single-domain size is 29—36 nm). The contribution of all particles to the saturation magnetization was taken into consideration, and only the particles blocked due to the magnetostatic interaction were included in the remanence. In this case, the two-phase particle model was also used for the strongly magnetic fraction.

Magnetostatic interaction results in that a particle with the volume $v > v_b(H_i)$ can contribute to the remanence. Here $v_b(H_i)$ is the volume of a particle whose magnetic moment remains stable when the particle is exposed to the interaction field H_i [8]. In this case, the blocking volume is

$$v_b(H_i) = \begin{cases} v_b / \left(1 + \left|H + H_i\right| / H_0\right)^2, & \left|H + H_i\right| \le H_0; \\ v_b / \left(4\left|H + H_i\right| / H_0\right), & \left|H + H_i\right| > H_0. \end{cases} \quad (5)$$

Here $H_0 \approx H_{cr}$ is the magnetization reversal field, and $v_b \approx 50kT/(I_s H_0)$ is the blocking volume in the zero field [9]. For interacting SP particles, the time-averaged magnetic moment is [8]:

$$m = vI_s \tanh\left[v_b(H_i) I_s \left|H + H_i\right| / kT\right] = vI_{s\,sp}, \quad (6)$$

where $I_{s\,sp}$ is the effective spontaneous magnetization of two-phase SP particles blocked due to magnetostatic interaction, which coincides with $I_s = I_{s1}$ in the saturation field, and when calculating the saturation remanence is about a tenth of the value. Then for the SP sample T20R

$$M_s = M_{s1\,b} + M_{s2\,b} + M_{s\,nb},\ M_{rs} = M_{rs1\,b} + M_{rs2\,b}, \quad (7)$$

where $M_{s1\,b}$ and $M_{rs1\,b}$, $M_{s2\,b}$ and $M_{rs2\,b}$ correspond to the blocked particles and $M_{s\,nb}$ to the unblocked particles. The magnetization reversal fields of the SP particles blocked by the interaction can be estimated as [10]:

$$H_{0\,sp} = H_{0\,sd}\left\{1 - \left[v_b(H_i)/v\right]^{1/2}\right\}, \quad (8)$$

where $H_{0\,sd}$ is the magnetization reversal field of a single-domain particle, and the value of v lies in the range from v_b (without regard to the interaction) to the critical volume of the single-domain. Since most of the particles in the sample T20R are superparamagnetic, then $v \approx v_b$.

Results and Discussion

After calculating the fields H_0 of the strongly magnetic fraction using the uniaxial two-phase particle model and provided that $H_0 = H_{cr1}$, we estimated the coercive force of this group of particles H_{c1}. The value of the coercive force in terms of remanent magnetization for two-phase particles, which in our case are in two possible states n_1 and n_3, is equal to:

$$H_{cr1} = H(n_1, n_3)\cdot(1 - \Delta) + H(n_1)\cdot\Delta,\ \Delta = \left[M(n_1) - M(n_1, n_3)\right] / M(n_1). \quad (9)$$

Here $H(n_1,n_3)$ and $H(n_1)$, $M(n_1, n_3)$ and $M(n_1)$ are the reversal fields and magnetizations of two-phase particles (Eq. (2)) in the states n_1 and n_3 and in the state $n_1 = 1$, respectively. It should be noted that $M(n_1) = M_{s1}$. Let us estimate the coercive force of this fraction of particles as $H_{c1} = (H_{cr1} - H_{max})/3$, where the factor 1/3 accounts for the disordering of magnetic moments' orientations when the external field is removed.

Further on, using the experimental values of H_c and H_{cr} of the sample, we estimate the values of the coercive force and the remanence coercivity for the weakly magnetic fraction with the volume concentration C_2 ($\delta_1 = C_1/(C_1 + C_2)$ and $\delta_2 = C_2/(C_1 + C_2)$ are the relative concentrations):

$$H_{c2} = \left(H_c - H_{c1} \cdot \delta_1\right) / \delta_2,\ H_{cr2} = \left(H_{cr} - H_{cr1} \cdot \delta_1\right) / \delta_2. \quad (10)$$

Saturation remanence of the fraction of two-phase ferrimagnetic particles ($i = 1$) and weakly magnetic fraction ($i = 2$) can be written as follows [11]:

$$M_{rsi} = \frac{C_i I_{rsi}}{(C_i + C_{i\,sp}) I_{si}} \cdot \frac{H_{ci}}{H_{cri}} \cdot M_{si}, \quad (11)$$

where $C_{i\,sp}$ is the concentration of SP particles, I_{rsi} and I_{si} are the effective magnetizations in M_{rs} and M_s states, respectively, and their ratio characterizes the decrease of remanence due to chemical and magnetic inhomogeneities (see Eq. (3)). For the SP sample T20R, the same model of interacting uniaxial two-phase particles was used, taking into consideration Eqs. (6-8).

Table 2 shows the calculated magnetizations for the studied samples. The best agreement with the experiment was obtained with the following parameters. For the first four samples: $a = 60$ nm (greater than the single-domain size of magnetite), $\varepsilon = 0.05–0.20$ (according to the amount of TiO_2 added during synthesis 0.5–2.0 g), $I_{s\,sm} = 400$ kA/m and $I_{s\,wm} = 380$ kA/m, $I_{s2} = 3$ kA/m (corresponding to hematite). For the SP sample T20R: $a = 30$ nm (close to the single-domain size), $\varepsilon = 0.05$, $I_{s\,sm} = 15$ kA/m and $I_{s\,wm} = 13$ kA/m (see Eqs. (3) and (6)), $I_{s2} = 3$ kA/m.

Table 2

Theoretical values of magnetizations, A·m²/kg

Sample	$M_s = M_{s1} + M_{s2} + M_{s\,sp}$		$M_{rs} = M_{rs1} + M_{rs2}$	
T05L	26.37	10.07 + 0.26 + 16.04	2.95	2.89 + 0.06
T10L	19.53	7.26 + 0.24 + 12.03	2.06	2.02 + 0.04
T20L	14.11	6.20 + 0.30 + 7.61	1.92	1.84 + 0.08
T05H	23.79	22.14 + 0.60 + 1.05	4.15	3.79 + 0.36
	$M_s = M_{s1\,b} + M_{s2\,b} + M_{s\,nb}$		$M_{rs} = M_{rs1\,b} + M_{rs2\,b}$	
T20R	28.95	23.74 + 0.51 + 4.70	0.35	0.23 + 0.12

As can be seen from the table, the calculated total values of M_s and M_{rs} of the samples (Table 1) coincide with the experimental values. In all the samples except for the sample T05H obtained at a higher temperature, a large fraction of SP particles is present. In the sample T20R, SP particles clearly dominate, with a significant portion of them blocked due to magnetostatic interaction.

For the first three samples, the theoretical values of the ferrimagnetic volume concentrations of the fractions under consideration are in the following ranges: $C_1 = 0.03–0.05$, $C_2 = 0.16–0.20$, $C_{sp} = 0.27–0.34$. For the sample T05H: $C_1 = 0.11$, $C_2 = 0.40$, $C_{sp} = 0.02$; such values are apparently connected with enlargement of particles and oxidation of magnetite into hematite upon heating. For the SP sample T20R: $C_1 = 0.12$, $C_2 = 0.34$, $C_{sp} = 0.09$; here C_1 and C_2 correspond to the blocked particles of the first two fractions, C_{sp} to the unblocked ones. The second fraction makes a relatively significant contribution to M_{rs} only in the case of the samples T05H and T20R.

Conclusion

The hysteresis characteristics of the simulated composites are well explained within the model of an ensemble of magnetostatically interacting two-phase particles. The superparamagnetic fraction largely determines the magnetic properties of the samples, and its consideration makes it possible to agree their theoretical and experimental characteristics.

Isolation of three fractions of ferrimagnetic particles: strongly magnetic chemically inhomogeneous particles (magnetite/maghemite–titanomagnetite), weakly magnetic particles (hematite, goethite, and other iron hydroxides) and superparamagnetic particles belonging to the first two fractions, served as a basis for theoretical modeling. Assuming a uniform spatial distribution

of ferrimagnetic particles, we used a random magnetostatic interaction field approximation and obtained theoretical estimates of average (effective) spontaneous magnetizations I_{s1} and I_{s2}, remanence coercivities H_{cr1} and H_{cr2}, and coercive forces H_{c1} and H_{c2} of the corresponding particle fractions, which are in good agreement with the experimental data.

The model of two-phase interacting particles allows calculating the magnetization reversal fields and magnetizations of the studied composites theoretically and to show that the main contribution to the remanence is made by chemically inhomogeneous particles. The possibility of using this model for samples containing superparamagnetic particles is demonstrated.

REFERENCES

1. **Kharitonskii P., Kirillova S., Gareev K., et al.,** Magnetic granulometry and Мцssbauer spectroscopy of synthetic Fe_mO_n–TiO_2 composites, IEEE Trans. Magn. 56 (2020) 7200209.

2. **Kharitonskii P. V., Kosterov A. A., Gurylev A. K., et al.,** Magnetic states of two-phase synthesized Fe_mO_n–$Fe_{3-x}Ti_xO_4$ particles: experimental and theoretical analysis, Phys. Solid State. 62 (2020) 1691–1694.

3. **Bisotti M.-A., Cortés-Ortuco D., Pepper R., et al.,** A Finite Difference Atomistic and Micromagnetic Simulation Package, Journal of Open Research Software. 6 (2018) 22.

4. **Conbhuí P., Williams W., Fabian K., et al.,** Micromagnetic Earth Related Robust Interpreted Language Laboratory, Geochemistry, Geophysics, Geosystems. 19 (2018) 1080–1106.

5. **Afremov L. L., Ralin A. Yu., Kharitonskiy P. V.,** Specific features of the magnetization curves of an ensemble of chemically inhomogeneous two-phase grains, Izv. Phys. Solid Earth. 31 (1996) 533–537.

6. **Kharitonskii P. V., Frolov A. M.,** Modeling of magnetostatic interaction in multilayer structures, Izv. vuzov. Fizika, 53 (2010) 197–200.

7. **Akimoto S., Katsura T., Yoshida M.,** Magnetic properties of the Fe3O4–Fe2TiO4 system and their change with oxidation, J. Geomagn. Geoelectr. 9 (1957) 165–178.

8. **Kharitonskii P. V., Gareev K. G., Ionin S. A., et al.,** Microstructure and magnetic state of Fe3O4-SiO2 colloidal particles, J. Magn. 20 (2015) 221–228.

9. **Néel L.,** Théorie du traonage magnétique des ferromagnétiques en grains fins avec application aux terres cuites, Annales de Géophysique. 5 (1949) 99–136.

10. **Morrish A. H.,** The Physical Principles of Magnetism, IEEE Press, New York, 2001.

11. **Kharitonskii P., Bobrov N., Gareev K., et al.,** Magnetic granulometry, frequency-dependent susceptibility and magnetic states of particles of magnetite ore from the Kovdor deposit, JMMM. 553 (2022) 169279.

THE AUTHORS

RALIN Andrey Yu.
ralin.ayu@dvfu.ru
ORCID: 0000-0001-6723-7246

GAREEV Kamil G.
kggareev@yandex.ru
ORCID: 0000-0001-6047-1208

KHARITONSKII Petr V.
peterkh@yandex.ru
ORCID: 0000-0002-0448-7624

ANIKIEVA Yulia A.
y.anikieva111@gmail.com
ORCID: 0000-0001-6151-1021

ZOLOTOV Nikita A.
nikita13300@yandex.ru
ORCID: 0000-0003-4225-8723

Received 14.05.2022. Approved after reviewing 13.06.2022. Accepted 13.06.2022.

Conference materials
UDC 620.197:621.388
DOI: https://doi.org/10.18721/JPM.153.128

Influence of halloysite nanotube incorporation on the properties of PEO-coatings formed on MA8 magnesium alloy

I. M. Imshinetskiy [1] ✉, V. V. Kashepa [1], K. V. Nadaraia [1], D. V. Mashtalyar [1]
S. L. Sinebryukhov [1], S. V. Gnedenkov [1]

[1] Institute of Chemistry FEB RAS, Vladivostok, Russia
✉ igorimshin@gmail.com

Abstract: The properties of the coatings formed on the MA8 magnesium alloy by plasma electrolytic oxidation in electrolytes containing halloysite nanotubes in the concentrations of 0, 10, 20, 30 and 40 g/l were investigated. It has been found that the presence of halloysite nanotubes in the composition of the coatings has a positive impact on protective properties of the coatings and leads to the increase of roughness and heterogeneity. Obtained coatings reduce corrosion current density in comparison with the base PEO layers.

Keywords: plasma electrolytic oxidation, nanoparticles, halloysite nanotubes, protective coatings

Funding: The study was funded by a Russian Science Foundation grant no. 22-23-00937 and Government Assignment of the Ministry of Science and Higher Education of the Russian Federation no. FWFN-2021-0003

Citation: Imshinetskiy I. M., Kashepa V. V., Nadaraia K. V., Mashtalyar D. V., Sinebryukhov S. L., Gnedenkov S. V., Influence of halloysite nanotube incorporation on the properties of PEO-coatings formed on Ma8 magnesium alloy, St. Petersburg State Polytechnical University Journal. Physics and Mathematics. 15 (3.1) (2022) 168–172. DOI: https://doi.org/10.18721/JPM.153.128

Материалы конференции
УДК 620.197:621.388
DOI: https://doi.org/10.18721/JPM.153.128

Влияние внедрения нанотрубок галлуазита на свойства ПЭО-покрытий, сформированных на магниевом сплаве МА8

И. М. Имшинецкий [1] ✉, В. В. Кашепа [1], К. В. Надараиа [1], Д. В. Машталяр [1],
С. Л. Синебрюхов [1], С. В. Гнеденков [1]

[1] Институт химии ДВО РАН, г. Владивосток, Россия
✉ igorimshin@gmail.com

Аннотация. Изучены свойства покрытий, формируемых на магниевом сплаве МА8 методом плазменного электролитического оксидирования в электролитах, содержащих нанотрубки галлуазита в концентрациях 30 ,20 ,10 ,0 и 40 г/л. Установлено, что наличие нанотрубок галлуазита в составе покрытий, приводит к увеличению шероховатости поверхности и положительно влияет на защитные свойства покрытий.

Ключевые слова: плазменное электролитическое оксидирование, наночастицы, нанотрубки галлуазита, защитные покрытия

Финансирование: Грант Российского научного фонда № 22-23-00937; государственное задание Министерства науки и высшего образования Российской Федерации № FWFN-2021-0003.

Ссылка при цитировании: Имшинецкий И. М., Кашепа В. В., Надараиа К. В., Машталяр Д. В., Синебрюхов С. Л., Гнеденков С. В. Влияние внедрения нанотрубок галлуазита на свойства ПЭО-покрытий, сформированных на магниевом сплаве // Научно-технические ведомости СПбГПУ. Физико-математические науки. 2022. Т. 15. № 3.1. С. 168–172. DOI: https://doi.org/10.18721/JPM.153.128

Introduction

Magnesium alloys are lightweight materials with excellent strength and vibration damping capacity that have found application in multiple engineering fields [1]. Interest in magnesium alloys has particularly increased among researchers from the biomedical materials science field since a potential use of Mg as a biodegradable material has been established. However, modern engineering and science face a problem of low corrosion resistance of magnesium alloys. This shortcoming crucially limits their usage as construction materials and alloys for bioresorbable implant fabrication.

One of the most promising methods of protective surface modification for light alloys is plasma electrolytic oxidation (PEO). PEO coatings combine improvement of corrosion resistance of a treated materials along with development of a new functional properties. PEO became widely investigated by the scientific community due to a broad range of adjustable process parameters and a prospect of coatings properties management. Ceramic-like coatings formed by the PEO can be improved through incorporating nanoparticles. PEO coatings with various nanoscale additives demonstrate improved hardness [2–4], corrosion [2, 3] and wear resistance [2, 4–6], biocompatibility [7]. Halloysite nanotubes are naturally formed nanoparticles that can be incorporated into PEO coatings and used as an nanocontainers [8] for loading, storage, and controlled release of active molecules such as drugs, corrosion inhibitors, proteins, etc.

Magnesium alloys with PEO-coating containing halloysite nanotubes are of great scientific interest because of their low density, bioresorbability, and improved corrosion resistance.

In this paper, the formation of protective multifunctional coatings on the MA8 magnesium alloy by the PEO in electrolytes with halloysite nanotubes was investigated. The electrochemical and mechanical properties of the obtained PEO-layers are represented.

Materials and Methods

The MA8 magnesium alloy sheets (Mn 1.30; Ce 0.15; Mg bal. (wt.%)) were used as a substrate. The size of specimens was 20 mm × 15 mm × 2 mm. The base electrolyte contained sodium fluoride (5 g/l) and sodium silicate (20 g/l). In this work, we used the halloysite nanotubes (Halloysite Ural, Russia) with a length of 1–3 μm, an outer diameter of 50–70 nm and inner diameter of 15–30 nm were used. The halloysite nanotubes were dispersed in the base electrolyte in concentrations of 0, 10, 20, 30 and 40 g/l with addition of anionic surfactant (sodium dodecyl sulfate) at concentration of 0.25 g/l. The corresponding coatings were named in reference to the concentration of the halloysite nanotubes in the used electrolytes: H0, H10, H20, H30, and H40, respectively. Samples surface morphology were studied using a Carl Zeiss EVO 40 scanning electron microscope (SEM) (Carl Zeiss, Germany). The thickness of the coatings was measured by eddy-current thickness gauge. The electrochemical tests were carried out using VersaSTAT MC (Princeton Applied Research, USA). The samples were studied in 3.5 wt.% NaCl solution. As a reference electrode was used the saturated calomel electrode (SCE).

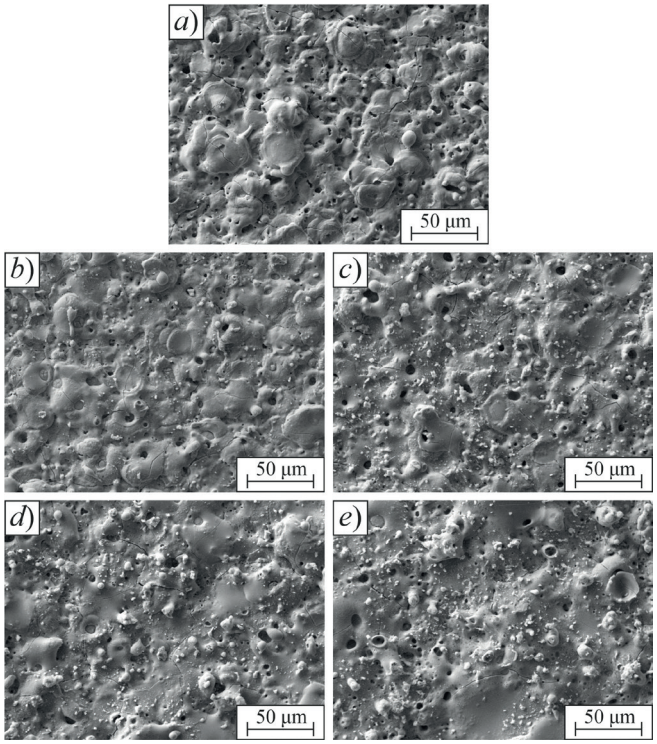

Fig. 1. SEM images of the coatings surface: H0 (*a*), H10 (*b*), H20 (*c*), H30 (*d*), H40 (*e*)

Results and Discussion

The SEM images of surfaces show significant differences in surface morphology of the studied specimens (Fig. 1). Samples obtained in electrolytes with high concentrations of halloysite nanotubes have a more rugged and irregular surface. Heterogeneity of the coatings increased with increasing content of halloysite nanotubes in electrolytes. Thus, clusters and aggregates of nanoparticles are primarily visible on the H20, H30, and H40, which were obtained in electrolytes enriched with nanoparticles.

The same tendency for roughness dependency on nanoparticles content is apparent according to results of optical laser profilometry (Table 1). Agglomerates occurrence rises with halloysite nanotubes content, as well as the surface roughness. The results of the thickness measurements are represented in the Table 1. It is plain to see, that the thickness of the layers is in direct proportion to halloysite nanotubes concentration.

Table 1

Thickness and roughness parameters of the studied samples

Sample name	R_a [μm]	R_z [μm]	Thickness [μm]
H0	1.8 ± 0.4	9.6 ± 2.2	51.4 ± 1.3
H10	2.0 ± 0.3	10.8 ± 2.8	54.8 ± 1.0
H20	2.5 ± 0.6	12.2 ± 2.9	55.0 ± 1.5
H30	3.0 ± 0.7	15.5 ± 2.9	68.6 ± 2.0
H40	3.4 ± 0.7	16.5 ± 3.1	78.8 ± 1.5

Notations: R_a and R_z are the arithmetical mean deviation of the profile, the ten-point height of irregularities, respectively.

The change in corrosion properties of the coatings containing halloysite nanotubes compared to the PEO-coating obtained in the electrolyte without nanoparticles was studied by potentiodynamic polarization test (Fig. 2).

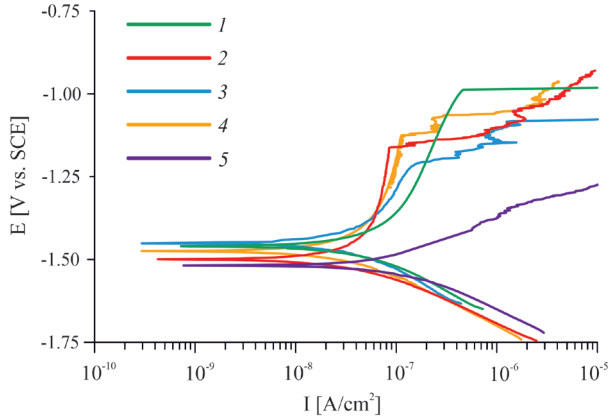

Fig. 2. Polarization curves for the H0 (*1*), H10 (*2*), H20 (*3*), H30 (*4*), H40 (*5*) samples

The corrosion parameters calculated from obtained data are represented in the Table 2. The results of tests demonstrate a decrease of the corrosion current density (I_c) and an increase of the polarization resistance (R_p) up to the concentration of nanoparticles of 20 g/l.

The lowest current density was demonstrated by the sample with coating obtained in the electrolytes containing halloysite nanotubes in concentration of 20 g/l. The corrosion current density for the H20 sample decreased twofold in comparison with the H0 sample (from $1.2 \cdot 10^{-7}$ A/cm^2 for base PEO layer down to $4.9 \cdot 10^{-8}$ A/cm^2 for H20 coating). The H20 samples also exhibited the highest polarization resistance of $1.2 \cdot 10^6$ Ω·cm^2, which is almost two times higher than R_p value for H0 coating. Such results can be explained with nanoparticles incorporation, which leads to partial pores filling with chemically stable halloysite nanotubes. Plasma discharge temperature enables sintering of the halloysite nanotubes on the bottoms of the pores and sealing of incompletely closed channels with sintering products.

Table 2

Corrosion parameters of the obtained coatings

Sample name	R_p [Ω·cm^2]	I_c [A/cm^2]	E_c [V]
H0	6.4×10^5	1.2×10^{-7}	−1.46
H10	8.6×10^5	5.7×10^{-8}	−1.50
H20	1.2×10^6	4.9×10^{-8}	−1.45
H30	1.1×10^6	5.6×10^{-8}	−1.47
H40	2.9×10^5	1.1×10^{-7}	−1.52

A decrease in protective characteristics of coatings obtained in electrolytes with concentrations of halloysite nanotubes above 20 g/l can be observed. The main reason for a such tendency is an increase in heterogeneity of the coatings due to the more intensive nanoparticles incorporation, which led to the porosity increase. As a result, the value of R_p for H40 sample is even lower than for the base PEO coating.

Conclusion

It has been established that PEO-coatings formed on the MA8 magnesium alloy in electrolytes containing halloysite nanotubes have improved electrochemical characteristics in comparison with the surface layers obtained in the electrolyte without nanoparticles. Based on obtained results, it has been concluded that the coatings formed in an electrolyte with a 20 g/l nanoparticle concentration have the highest protective properties in the corrosive medium. The incorporation of nanoparticles led to an increase in the roughness parameters, which are comparably high for all PEO coatings containing halloysite nanotubes. Formed coatings are perspective for biomedical applications due to their suitable roughness parameters and corrosion resistance.

Acknowledgments

The study was carried out within the framework of the Grant of the Russian Science Foundation, project number 22-23-00937. Electrochemical properties were investigated within the framework of Government Assignments from the Ministry of Science and Higher Education of the Russian Federation (project no. FWFN-2021-0003).

REFERENCES

1. **Kulekci M. K.,** Magnesium and its alloys applications in automotive industry, The International Journal of Advanced Manufacturing Technology. 39 (2008) 851–865.

2. **Kaseem M., Fatimah S., Nashrah N., Ko Y. G.,** Recent progress in surface modification of metals coated by plasma electrolytic oxidation: Principle, structure, and performance, Journal of Physics D: Applied Physics. 117 (100735) (2021) 2110–2120.

3. **Asri R.I.M., Harun W.S.W., Samykano M., Lah N.A.C., Ghani S.A.C., Tarlochan F., Raza M.R.,** Corrosion and surface modification on biocompatible metals: A review, Materials Science and Engineering. 77 (2017) 1261–1274.

4. **Mashtalyar D.V., Nadaraia K.V., Imshinetskiy I.M., Sinebryukhov S.L., Gnedenkov S.V.,** New approach to formation of coatings on Mg-Mn-Ce alloy using a combination of plasma treatment and spraying of fluoropolymers, Journal of Magnesium and Alloys. Vol. 10 (4) (2022).

5. **Nadaraia K.V., Suchkov S.N., Imshinetskiy I.M., Mashtalyar D.V., Sinebrykhov S.L., Gnedenkov S.V.,** Some new aspects of the study of dependence of properties of PEO coatings on the parameters of current in potentiodynamic mode, Surface and Coatings Technology. 426 (2021) 127744.

6. **Atapour M., Blawert C., Zheludkevich M.L.,** The wear characteristics of CeO_2 containing nanocomposite coating made by aluminate-based PEO on AM 50 magnesium alloy, Surface & Coatings Technology. 357 (2018) 626–637.

7. **Mashtalyar D.V., Nadaraia K.V., Plekhova N.G., Imshinetskiy I.M., Piatkova M.A., Pleshkova A.I., Kislova S.E., Sinebryukhov S.L., Gnedenkov S.V.,** Antibacterial Ca/P-coatings formed on Mg alloy using plasma electrolytic oxidation and antibiotic impregnation, Materials Letters. 317 (2022) 132099.

8. **Zahidah K.A., Kakooei S., Ismail M. C., Raja P. B.,** Halloysite nanotubes as nanocontainer for smart coating application: A review, Progress in Organic Coatings. 111 (2017) 175–185.

THE AUTHORS

IMSHINETSKIY Igor M.
igorimshin@gmail.com
ORCID: 0000-0002-5055-1834

MASHTALYAR Dmitry V.
madiva@inbox.ru
ORCID: 0000-0001-9645-4936

KASHEPA Viktoriia V.
sobranie72pepper@gmail.com
ORCID: 0000-0002-1610-095X

SINEBRYUKHOV Sergey L.
sls@ich.dvo.ru
ORCID: 0000-0002-0963-0557

NADARAIA Konstantine V.
nadaraiakv@mail.ru
ORCID: 0000-0001-7835-2231

GNEDENKOV Sergey V.
svg21@hotmail.com
ORCID: 0000-0003-1576-8680

Received 20.05.2022. Approved after reviewing 25.06.2022. Accepted 25.06.2022.

Conference materials
UDC 544.63:620.197.3
DOI: https://doi.org/10.18721/JPM.153.129

Composite triazole-containing PEO-coatings for effective corrosion protection of AlMg3 aluminum alloy

Ya. I. Kononenko [1] ✉, A. S. Gnedenkov [1], S. L. Sinebryukhov [1]
V. S. Filonina [1], I. E. Vyaliy [1], S. V. Gnedenkov [1]

[1] Institute of Chemistry, Far Eastern Branch of the RAS, Vladivostok, Russia
✉ kononenko.yai@gmail.com

Abstract: The study considers composite coatings formed on the AlMg3 aluminum alloy, consisting of PEO-coatings impregnated with corrosion inhibitors, 1,2,4-triazole and benzotriazole, in various concentrations. The morphology and composition of the resulting coatings were studied by scanning electron microscopy (SEM) and energy dispersive spectroscopy (EDS). The increase in the protective properties of composite coatings was studied by electrochemical impedance spectroscopy (EIS). SEM-images showed that the coatings have a self-assembled microtubular structure with a tube diameter varying from 300 to 500 nm and average tube height of 9 μm. EIS results showed that samples with composite inhibitor-containing PEO-coatings have better protective properties compared to pure aluminum alloy and base PEO-layer. An increase in the concentration of inhibitors of the triazole group from 0.05 M to 0.1 M during impregnation into a PEO-coating leads to a decrease in the corrosion resistance of the samples with composite coatings.

Keywords: Anti-corrosion composite coating, aluminum alloy, PEO coating, micro-tubular structure, corrosion inhibitor

Funding: Inhibitor-containing bioactive composite coatings on magnesium alloys for implant surgery, no. 20-13-00130; Multifunctional biodegradable coatings of new generation for controlling the resorption of magnesium-based materials: self-healing mechanism, personalized medicine, no. 21-73-10148.

Citation: Kononenko Ya. I., Gnedenkov A. S., Sinebryukhov S. L., Filonina V. S., Vyaliy I. E., Gnedenkov S.V., Composite triazole-containing PEO-coatings for effective corrosion protection of AlMg3 aluminum alloy, St. Petersburg State Polytechnical University Journal. Physics and Mathematics. 15 (3.1) (2022) 173–178. DOI: https://doi.org/10.18721/JPM.153.129

Материалы конференции
УДК 544.63:620.197.3
DOI: https://doi.org/10.18721/JPM.153.129

Композиционные триазолсодержащие ПЭО-покрытия для эффективной защиты от коррозии алюминиевого сплава AlMg3

Я. И. Кононенко [1] ✉, А. С. Гнеденков [1], С. Л. Синебрюхов [1],
В. С. Филонина [1], И. Е. Вялый [1], С. В. Гнеденков [1]

[1] Институт химии Дальневосточного отделения РАН, г. Владивосток, Россия
✉ kononenko.yai@gmail.com

Аннотация. В данной работе на алюминиевом сплаве AlMg3 сформированы композиционные покрытия, состоящие из ПЭО-покрытий, импрегнированных ингибиторами коррозии, 1,2,4- триазолом и бензотриазолом, в различных концентрациях.

Морфология и состав полученных покрытий исследовались методами растровой электронной микроскопии (РЭМ) и энергодисперсионной спектроскопии (ЭДС). Увеличение защитных свойств композиционных покрытий фиксировали методом электрохимической импедансной спектроскопии (ЭИС). РЭМ-изображения показали, что покрытия имеют самоорганизованную микротрубчатую структуру с диаметром трубки варьирующимся от 300 до 500 нм, и высотой трубки, в среднем, составляющей 9 мкм. Результаты ЭИС показали, что образцы с композиционными ингибиторсодержащими ПЭО-покрытиями обладают лучшими антикоррозионными свойствами по сравнению с чистым алюминием сплавом и образцом с базовым ПЭО-покрытием. Увеличение концентрации ингибиторов группы триазолов с 0,05 М до 0,1 М при импрегнировании в ПЭО-покрытие приводит к уменьшению коррозионный стойкости алюминиевого сплава с композиционным покрытием.

Ключевые слова: Антикоррозийное композиционное покрытие, алюминиевый сплав, ПЭО-покрытие, микротрубчатая структура, ингибитор коррозии

Финансирование: Ингибиторсодержащие биоактивные композиционные покрытия на магниевых сплавах для имплантационной хирургии, № 20-13-00130; Многофункциональные биодеградируемые покрытия нового поколения для контроля процессов резорбции материалов на основе магния: механизм самозалечивания, персонализированная медицина, № 21-73-10148.

Ссылка при цитировании: Кононенко Я. И., Гнеденков А. С., Синебрюхов С. Л., Филонина В. С., Вялый И. Е., Гнеденков С. В.Композиционные триазолсодержащие пэо-покрытия для эффективной защиты от коррозии алюминиевого сплава AlMg3 // Научно-технические ведомости СПбГПУ. Физико-математические науки. 2022. Т. 15. № 3.1. С. 173–178. DOI: https://doi.org/10.18721/JPM.153.129

Introduction

Aluminum is a structural material with such important properties as light weight, high strength and ductility, etc. It found application in many industries. However, during operation, aluminum may contact the aggressive environment, which results in corrosion degradation [1, 2].

One of the ways to prevent aluminum corrosion is to produce protective coatings on its surface. Plasma electrolytic oxidation (PEO) is one of the easiest and most optimal methods to protect the surface of valve metals (including aluminum and its alloys) [3–8]. In some cases, the duration of the corrosion protection of PEO-coatings may be insufficient due to high heterogeneity (including porosity) of obtained surface layers. Corrosion inhibitors are widely used for modification of coatings in order to provide autonomous self-healing properties and prolong the provision of protective ability [9–12]. The most studied metallic corrosion inhibitors are phosphates, nitrites, molybdates, tungstates, vanadates, borates, rare earth salts and the organic corrosion inhibitors including different types of triazoles [13]. For example, [14] describes the efficiency of a composite coating applied by a sol-gel method, with benzotriazole. It was established that this corrosion inhibitor, in a protective layer, is capable of starting the process of healing damage of the coating on AA7075 alloy.

This study is focused on forming composite coatings on the AlMg3 alloy introducing inhibitors of the triazole group of various concentrations in the previously formed base PEO-layer with the purpose of improving the protective properties of the material.

Materials and Methods

The experiments were carried out with samples made of the AlMg3 aluminum alloy with the size of 20×30×2 mm. The surface preparation of the samples was realized through wet grinding with SiC paper with a gradual decrease in abrasive grain size from 28–40 to 14–20 μm, followed

by washing in isopropyl alcohol and drying in a desiccator. PEO was carried out in a tartrate-fluoride electrolyte in a galvanostatic mode for 40 s. The current density was equal to 1.79 $A \cdot cm^{-2}$ and the duty cycle was equal to 1. To ensure the best filling of coating microtubes with inhibitor, the formed samples were subjected to vacuum impregnation in aqueous solutions of 1,2,4-triazole and benzotriazole at various concentrations (0.05 M and 0.1 M), with the following exposure to inhibitor solutions for 1 h under constant stirring, and then dried in a desiccator at a temperature of 40 °C for 24 h.

The protective properties of the formed coatings were assessed using the electrochemical techniques, including electrochemical impedance spectroscopy (EIS) and open circuit potential (OCP) measurements. Experiments were carried out in a three-electrode cell with a silver chloride (Ag/AgCl) electrode as a reference electrode and platinum mesh as a counter electrode using the VersaSTAT MC potentiostat/galvanostat electrochemical system (Princeton Applied Research, USA). 3 wt.% NaCl solution was used as an electrolyte. The area of the surface in a contact with solution was 1 cm^2.

A Sigma 300VP (Carl Zeiss, Germany) scanning electron microscope (SEM) with energy dispersive spectroscopy (EDS) was used to analyze the morphology and composition of the surface.

Results and Discussion

As a result of the study the composite inhibitor-containing coatings with high protective properties were obtained on the AlMg3 aluminum alloy. Coatings consisted of a PEO-layer with a microtubular structure (Fig. 1) and inhibitors of the triazole group.

SEM analysis of the sample surface (Fig. 1, *a*) showed that the PEO-coating has a well-ordered porous structure with a pore diameter ranging from 300 to 500 nm. It can be concluded from analyzing the SEM image of the sample cross-section that the coating has a self-organized microtubular structure (Fig. 1, *b*). The tube height averages 9 μm.

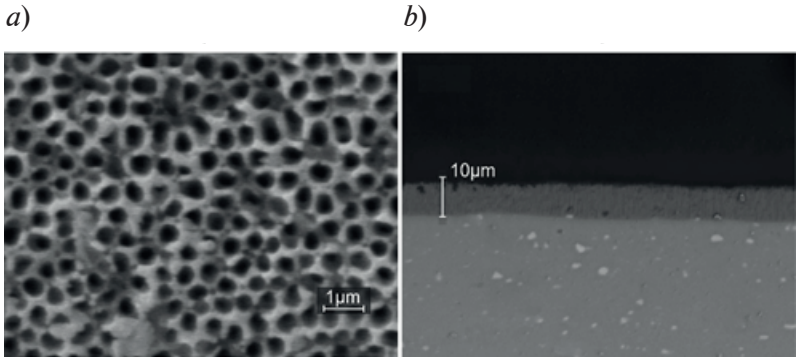

Fig. 1. SEM images of PEO-coating morphology: SEM-image of PEO-coating surface (*a*), SEM-image of a cross-section of PEO-coating (*b*)

Analysis of the results obtained by EDS showed that the main elements of the coating are aluminum (Fig. 2,*a*) and oxygen (Fig. 2, *c*). Magnesium is contained in a smaller amount (Fig. 2, *b*). The presence of Mg in the coating is explained by the composition of the original AlMg3 alloy (that is one of the alloyed elements in this alloy). Such elements as fluorine, carbon, sodium and potassium, which are presented in the composition electrolyte for oxidation of the samples, are absent in the composition of the coating.

Table 1 shows the results of EIS study for an uncoated AlMg3 aluminum alloy (A), the AlMg3 aluminum alloy immersed in 1,2,4-triazole or benzotriazole with a concentration of 0.1 M (B, C), a PEO-coated sample (D), and samples with inhibitor-containing layers (E–H) after the exposure for 1 h in a 3 wt. % NaCl solution. It should be mentioned that Table 1 presents the specific values of the impedance modulus normalized by the area of the sample (i.e., $\Omega \cdot cm^2$).

The obtained results indicate higher protective properties of the AlMg3 1,2,4-tr 0.1 M and AlMg3 b-tr 0.1 M compared to AlMg3 uncoated, which suggests a high efficiency of the inhibitors selected for the AlMg3 alloy (Table 1). As can be seen from the analysis of the impedance modulus measured at the lowest frequency ($|Z|_{f=0.1\ Hz}$, Table 1) after 1 h of exposure, all samples

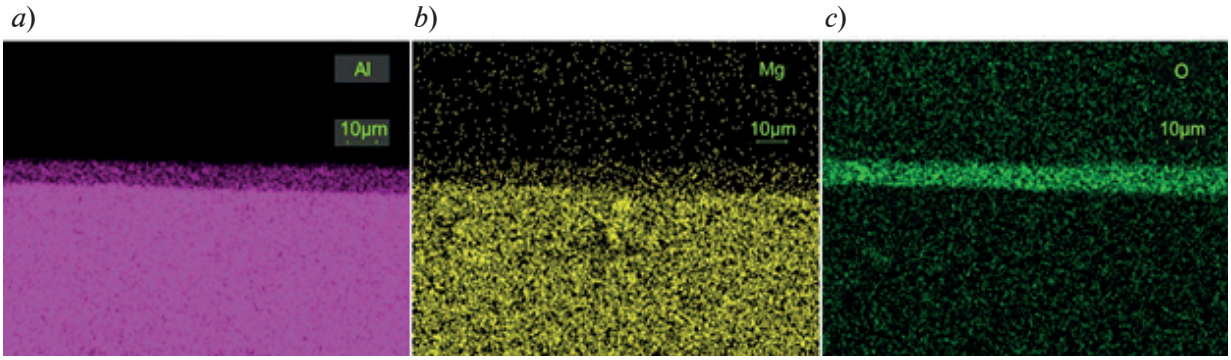

Fig. 2. Image of element distribution in the cross-section of a sample with a PEO-layer, where (*a*) is the distribution of aluminum, (*b*) is magnesium, and (*c*) is oxygen

with composite inhibitor-containing coatings (E—H) have a higher corrosion resistance compared to the uncoated sample (A) and base PEO-layer (D).

The sample with a PEO-layer impregnated with 1,2,4-triazole at a concentration of 0.05 M (E) is characterized by the best protective properties. The value of $|Z|_{f=0.1\ \text{Hz}}$ for this composite coating is more than one order of magnitude higher than one for the sample with base PEO-layer (Table 1). An increase in the concentration of inhibitors to 0.1 M leads to a decrease in the $|Z|_{f=0,1\ \text{Hz}}$, and, as a consequence, a decrease in corrosion resistance, due to the PEO-layer degradation, which is consistent with the data presented in [14]. This result can be related with probable reaction of inhibitor with components of PEO-coating matrix with following formation of the compounds, which have higher solubility as compared to PEO-layer [15]. However all inhibitor-conatining coatings have higher protective properties as compared to base PEO-layer. Therefore, lower values of the $|Z|_{f=0,1\ \text{Hz}}$ for PEO 1,2,4-tr 0.1 M and PEO b-tr 0.1 M as compared to PEO 1,2,4-tr 0.05 M and PEO b-tr 0.05 M can be related with probable lower density of the formed inhibitor layer.

1,2,4-triazole and benzotriazole are used to retard the corrosion rate of Cu, Fe, Zn, Mg and Al materials. The mechanism of the corrosion protection is based on the adsorption on the surface of treated metal or alloy [16—19]. It should be noted that PEO-coating is suitable as a matrix for inhibitor storage due to its complex morphology. As a result of coating degradation during immersion of the sample in an aggressive environment, the inhibitor can be released from the pores of the PEO-layer to the damaged part of the surface and form an additional barrier layer, which will delay the corrosion rate of the material.

Table 1

Coating specification and electrochemical parameters of samples according to the results of EIS test

Sample	Coating type	$\lvert Z\rvert_{f=0.1\ \text{Hz}}$, Ω·cm^2
A	AlMg3 uncoated	$2.56\cdot10^4$
B	AlMg3 1,2,4-tr 0.1 M	$7.23\cdot10^6$
C	AlMg3 b-tr 0.1 M	$6.40\cdot10^6$
D	PEO-coating	$4.65\cdot10^6$
E	PEO 1,2,4-tr 0.05 M	$6.61\cdot10^7$
F	PEO 1,2,4-tr 0.1 M	$6.11\cdot10^6$
G	PEO b-tr 0.05 M	$1.63\cdot10^7$
H	PEO b-tr 0.1 M	$7.72\cdot10^6$

Conclusion

During the study, heterooxide layers with a microtubular structure were obtained on the AlMg3 aluminum alloy. Impregnation of the PEO-coating with corrosion inhibitors contributed to a significant increase in the corrosion resistance of the studied material. The sample impregnated with 1,2,4-triazole at a concentration of 0.05 M is characterized by the best protective properties.

Acknowledgments

The sample preparation, protective coating formation, and electrochemical measurements were supported by a Russian Science Foundation grant no. 21-73-10148 (https://rscf.ru/en/project/21-73-10148/). The study of coating composition was supported by a Russian Science Foundation grant no. 20-13-00130 (https://rscf.ru/en/project/20-13-00130/).

REFERENCES

1. **Gnedenkov A. S., Sinebryukhov S. L., Mashtalyar D. V., Vyaliy I. E., Egorkin V. S., Gnedenkov S. V.,** Corrosion of the Welded Aluminium Alloy in 0.5 M NaCl Solution. Part 1: Specificity of Development, Materials (Basel). 11 (10) (2018) 2053.

2. **Gnedenkov A. S., Sinebryukhov S. L., Mashtalyar D. V., Imshinetskiy I. M., Vyaliy I. E., Gnedenkov S. V.,** Effect of Microstructure on the Corrosion Resistance of TIG Welded 1579 Alloy, Materials. 12 (16) (2019) 2615.

3. **Junyi L., Xiaohu H., Yi R., Lai Mun W., Hongfei L., Shijie W.,** Galvanic corrosion protection of Al-alloy in contact with carbon fibre reinforced polymer through plasma electrolytic oxidation treatment, Scientific Reports. T.12 (2022) №4532.

4. **Gnedenkov A. S., Sinebryukhov S. L., Mashtalyar D. V., Vyaliy I. E., Egorkin V. S., Gnedenkov S. V.,** Corrosion of the Welded Aluminium Alloy in 0.5 M NaCl Solution. Part 2: Coating Protection, Materials. 11 (11) (2018) 2177.

5. **C. Da Silva T., Martin J., Marcos G., Czerwiec T., Henrion G.,** Evidence of in-depth incorporation of carbon nanotubes in alumina layers grown by plasma electrolytic oxidation, Surface and Coatings Technology. (440) (2022) 128489.

6. **Gnedenkov S. V., Khrisanfova O. A., Sinebryukhov S. L., Puz' A. V., Gnedenkov A. S.,** Composite Protective Coatings on Nitinol Surface, Materials and Manufacturing Processes. 8 (23) (2008) 879-883.

7. **Sinebryukhov S. L., Gnedenkov A. S., Khrisanfova O. A., Gnedenkov S. V.,** Influence of plasma electrolytic oxidation on mechanical characteristics of NiTi alloy, Surface Engineering. 8 (25) (2009) 565–569.

8. **Gnedenkov A. S., Lamaka S. V., Sinebryukhov S. L., Mashtalyar D. V., Egorkin V. S., Imshinetskiy I. M., Zheludkevich M. L., Gnedenkov S. V.,** Control of the Mg alloy biodegradation via PEO and polymer-containing coatings, Corrosion Science. (182) (2021) 109254.

9. **Kozlica D. K., Kokalj A., Miloˇsev I.,** Synergistic effect of 2-mercaptobenzimidazole and octylphosphonic acid as corrosion inhibitors for copper and aluminium − An electrochemical, XPS, FTIR and DFT study, Corrosion Science. (182) (2021) 109082.

10. **Yabuki A., Nagayama Y.,** Wahyudhin Fathona I., Porous anodic oxide film with self-healing ability for corrosion protection of aluminum, Electrochimica Acta. (296) (2019) 662–668.

11. **Gnedenkov A. S., Sinebryukhov S. L., Mashtalyar D. V., Gnedenkov S. V.,** Inhibitor-Containing Composite Coatings on Mg Alloys: Corrosion Mechanism and Self-Healing Protection, Solid State Phenomena. (245) (2015) 89–96.

12. **Akhondi M., Jamalizadeh E.,** Fabrication of β-cyclodextrin modified halloysite nanocapsules for controlled release of corrosion inhibitors in self-healing epoxy coatings, Progress in Organic Coatings. (145) (2020) 105676.

13. **Zhang F., Ju P., Pan M., Zhang D., Huang Y., Li G., Li X.,** Self-healing mechanisms in smart protective coatings: A review, Corrosion Science. (144) (2018) 74–88.

14. **Farahani M., Yousefnia H., Seyedraoufi Z. S., Shajari Y.,** The effect of benzotriazole gradual change on the corrosion performance of nanocomposite multilayer self-healing coating based on Titania-Alumina-Benzotriazole on AA7075, Ceramics International. 45 (2019) 16584–16590.

15. **Vaghefinazari B., Wang C., Mercier D., Mei D., Seyeux A., Marcus Ph., Blawert C., Lamaka S. V., Zheludkevich M. L.,** Adverse effect of 2,5PDC corrosion inhibitor on PEO coated magnesium, Corrosion Science. Vol. 192 (2021) 109830.

16. **Zheludkevich M. L., Yasakau K. A., Poznyak S. K., Ferreira M. G. S.,** Triazole and thiazole derivatives as corrosion inhibitors for AA2024 aluminium alloy, Corrosion Science. Vol. 47 (12) (2005) 3368–3383.

17. **Sun M., Yerokhin A., Bychkova M. Ya., Shtansky D. V., Levashov E. A., Matthews A.,** Self-healing plasma electrolytic oxidation coatings doped with benzotriazole loaded halloysite nanotubes on AM50 magnesium alloy, Corrosion Science. Vol. 111 (2016) 753–769.

18. **Williams G., Coleman A. J., Mc Murray H. N.,** Inhibition of Aluminium Alloy AA2024-T3 pitting corrosion by copper complexing compounds, Electrochimica Acta. Vol. 55 (20) (2010) 5947–5958.

19. **Recloux I., Andreatta F., Druart M.-E., Coelho L. B., Cepek C., Cossement D., Fedrizzi L., Olivier M.-G.,** Stability of benzotriazole-based films against AA2024 aluminium alloy corrosion process in neutral chloride electrolyte, Journal of Alloys and Compounds. Vol. 735 (2018) 2512–2522.

THE AUTHORS

KONONENKO Yana I.
kononenko.yai@gmail.com
ORCID: 0000-0002-2299-9009

FILONINA Valeria S.
filonina.vs@gmail.com
ORCID: 0000-0002-9544-3597

GNEDENKOV Andrey S.
asg17@mail.com
ORCID: 0000-0002-9822-7849

VYALIY Igor E.
vyaly@ich.dvo.ru
ORCID: 0000-0003-3806-1709

SINEBRYUKHOV Sergey L.
sls@ich.dvo.ru
ORCID: 0000-0002-0963-0557

GNEDENKOV Sergey V.
svg21@hotmail.com
ORCID: 0000-0003-1576-8680

Received 22.05.2022. Approved after reviewing 19.07.2022. Accepted 20.07.2022.

Conference materials
UDC 548.528
DOI: https://doi.org/10.18721/JPM.153.130

Semipolar GaN layers on nanostructured silicon: technology and properties

V. N. Bessolov [1], E. V. Konenkova [1] ✉, S. N. Rodin [1]

[1] Ioffe Physical Technical Institute of the RAS, St. Petersburg, Russia

✉ lena@triat.ioffe.ru

Abstract: This paper proposes a method for synthesis of hexagonal GaN on Si(100) and Si(113) substrates, where nanostructures with an element size less than 100 nm are formed on the surface. It has been established that the method of gas-phase epitaxy from metalorganic compounds in a hydrogen atmosphere on such substrates makes it possible to form semipolar layers of GaN(10-11) and GaN(11-22) with a minimum half-width of the X-ray diffraction swing curve of about 30 arcmin. It is shown that during the formation of a semipolar AlN layer at the initial stage of epitaxy, a corrugated surface is formed on NP-Si(100) from the semipolar planes AlN(10-11) and AlN(10-1-1) with counter-directional *c* axes. Then, during the growth of the GaN layer, a transition is made from the symmetrical state of the semipolar GaN(10-11) and GaN(10-1-1) planes to an asymmetric state with the orientation of the *c* axis of the GaN(10-11) layer. That transition is apparently determined by the difference in the values of the surface energy of GaN during epitaxy on the corrugated surface.

Keywords: semipolar gallium nitride, nano-patterned Si substrate, surface energy

Funding: The study was supported by a Russian Foundation for Basic Research grant no. 20-08-00096.

Citation: Bessolov V. N., Konenkova E. V., Rodin S. N., Semipolar GaN layers on nanostructured silicon: technology and properties, St. Petersburg State Polytechnical University Journal. Physics and Mathematics. 15 (3.1) (2022) 179–184. DOI: https://doi.org/10.18721/JPM.153.130

Материалы конференции
УДК 548.528
DOI: https://doi.org/10.18721/JPM.153.130

Полуполярные слои GaN на наноструктурированном кремнии: технология и свойства

В. Н. Бессолов [1], Е. В. Коненкова [1] ✉, С. Н. Родин [1]

[1] Физико-технический институт им. А.Ф. Иоффе РАН, Санкт-Петербург, Россия

✉ lena@triat.ioffe.ru

Аннотация. Предложен метод синтеза гексагонального GaN на подложках Si(100) и Si(113), на поверхности которой сформирована наноструктура с размером элементов меньше 100 нм. Установлено, что метод газофазной эпитаксии из металлоорганических соединений в атмосфере водорода на таких подложках позволяет сформировать полуполярные слои GaN(10-11) и GaN(11-22) при минимальной полуширине рентгенодифракционной кривой качания около 30 arcmin. Показано, что в процессе образования слоя полуполярного AlN на начальной стадии эпитаксии на NP-Si(100) формируется гофрированная поверхность из полуполярных плоскостей AlN(10-11) и AlN(10-1-1) с противонаправленными «с»-осями. Затем в процессе роста GaN слоя осуществляется переход из симметричного состояния полуполярных GaN(10-11) и

GaN(10-1-1) плоскостей в асимметричное состояние с ориентацией «c»-оси слоя GaN(10-11), причем переход , по видимому, определяется различием величин поверхностной энергии GaN при эпитаксии на гофрированной поверхности.

Ключевые слова: полуполярный нитрид галлия, наноструктурированная кремниевая подложка, поверхностная энергия

Финансирование: Работа выполнена при поддержке гранта РФФИ 00096-08-20.

Ссылка при цитировании: Бессолов В. Н., Коненкова Е. В., Родин С. Н. Полуполярные слои GaN на наноструктурированном кремнии: технология и свойства // Научно-технические ведомости СПбГПУ. Физико-математические науки. 2022. Т. 15. № 3.1. С. 179–184. DOI: https://doi.org/10.18721/JPM.153.130

Introduction

Gallium nitride is an attractive material for various electronic and optoelectronic applications. An important physical property of III-nitrides with a hexagonal crystal structure is that in the heterostructures of these compounds, layers in the direction along the *c* axis are characterized by the presence of piezoelectric polarization, which leads to an internal electric field, to the spatial separation of electrons and holes in quantum wells and a decrease in their radiative recombination (quantum-dimensional Stark effect) [1]. The Stark effect increases the recombination of charge carriers and negatively affects the injection of carriers [2], which significantly reduces the parameters of optoelectronic and electronic devices.

As a solution to these problems related to polarization, using non-polar and semipolar orientations of GaN has been proposed [3]. Currently, attempts are made to synthesize semipolar gallium and aluminum nitrides on micro [4] and nanostructured Si(100) [5] and Si(113) [6] substrates, in which it is proposed to use an inclined face of Si(111) for synthesis. The known methods for creating semipolar layers of GaN(1011) and GaN(1122) on silicon involve microstructured substrates Si(100) and Si(113), respectively, with a one-sided (111)-face in an array of microchannels [7, 8].

Recently, it has been proposed to use both inclined faces of Si(111) and Si(1-1-1) nanostructures for synthesis on Si(100) and Si(113). (Fig.1, *a*). This work is dedicated to developing a technology of semipolar GaN(10-11) and GaN(11-22) layers on V-shaped and U-shaped nanostructured Si(100) and Si(113) substrates, respectively, with element sizes less than 100 nm.

The nanomask was formed according to the technology described in [9].

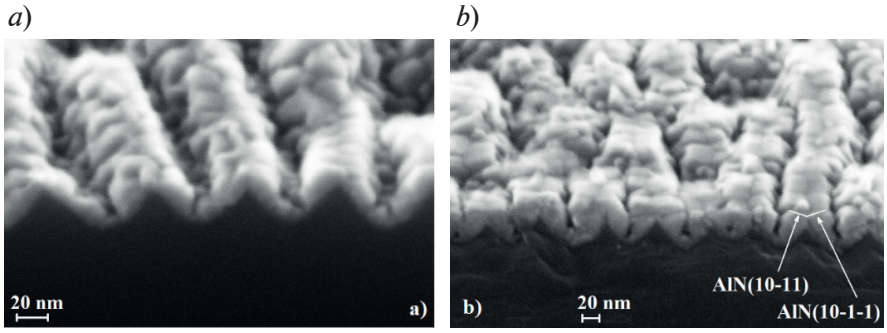

Fig. 1. SEM images of the AlN/NP-Si(100) structure: at the initial stage of growth (*a*), during the formation of a solid layer (*b*)

Materials and Methods

The GaN layers on NP-Si(100) substrates were grown by MOCVD on a modified EpiQuip installation with a horizontal reactor and an induction-heated graphite substrate holder at temperature 1030 °C [5]. Hydrogen was used as the carrier gas, and ammonia, trimethylgallium and trimethylaluminum were employed as precursors. The structures consisted of an AlN layer ~20-40-nm thick and a GaN layer ~1-μm thick. The structural characteristics of the GaN layers were determined by X-ray diffraction, scanning electron microscopy and atomic force microscopy.

A thin AlN layer is formed on the Si(111) and Si(1-1-1) faces at the initial stage of AlN growth on the NP-Si(100) substrate (Fig.1, *a*). A corrugated surface is formed from AlN(10-11) and AlN(10-1-1) layers during further epitaxy (Fig. 1, *b*).

Then the growth of continuous GaN layers on NP-Si(100) occurs in the semipolar direction, as evidenced by the typical nature of the surface morphology (Fig. 2, *a*, *b*) and a minimum half-width of the XRD GaN(10-11) swing curve of about ω_θ = 30 arcmin.

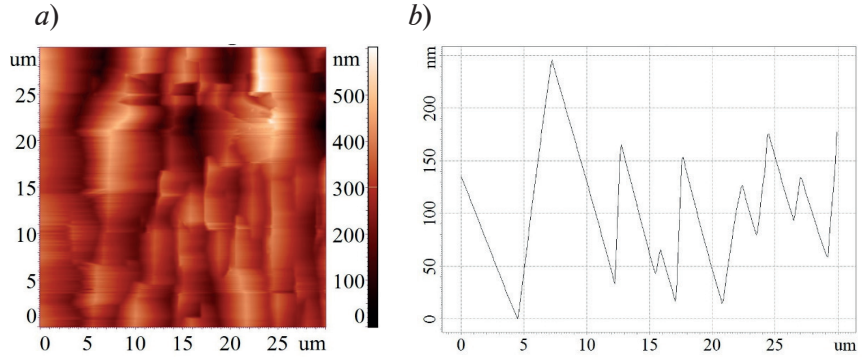

Fig. 2. AFM image and surface profile of the GaN(10-11)/AlN/NP-Si(100) structure

A buffer layer of AlN with a thickness of 20 nm was grown on all structures during epitaxy of AlN and then GaN on NP-Si(113) substrates (Fig. 3, *a*), then either an island layer of GaN(11-22) with dimensions of ~0.05–0.2 μm (Fig. 3, *b*) or a solid layer was grown on the buffer layer thickness ~0.6–1 μm GaN(11-22) (Fig. 4, *a*, *b*). X-ray diffraction analysis showed that the solid layers have a half-width of the X-ray diffraction curve ω_θ ~ 30 arcmin of the semipolar GaN(11-22).

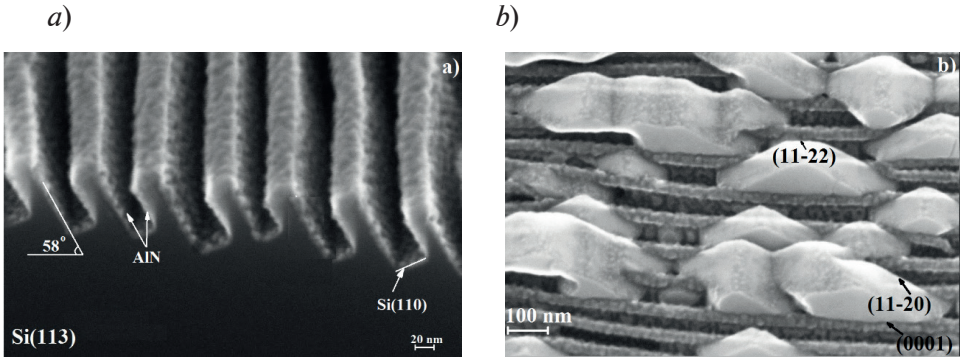

Fig. 3. SEM-images of AlN/ NP-Si(113) structure (a), GaN/AlN/NP-Si(113) for a solid layer formed (*b*)

It can be seen that the AlN layer completely and uniformly covers the NP-Si(113) surface (Fig. 2). The formation of a GaN layer on an NP-Si(113) substrate covered with a buffer AlN layer occurs by an island mechanism on the open faces of Si(111) nanochannels (Fig. 3, *a*). The shape of the crystals of the GaN island layer indicates the presence of (0001), (11-20) and (11-22) faces (Fig. 3, *b*). It can be seen that the island GaN(11-22) layer is given by the direction of the Si(111) plane and tends to form a continuous layer at thicknesses of about 1 mm (Fig. 4).

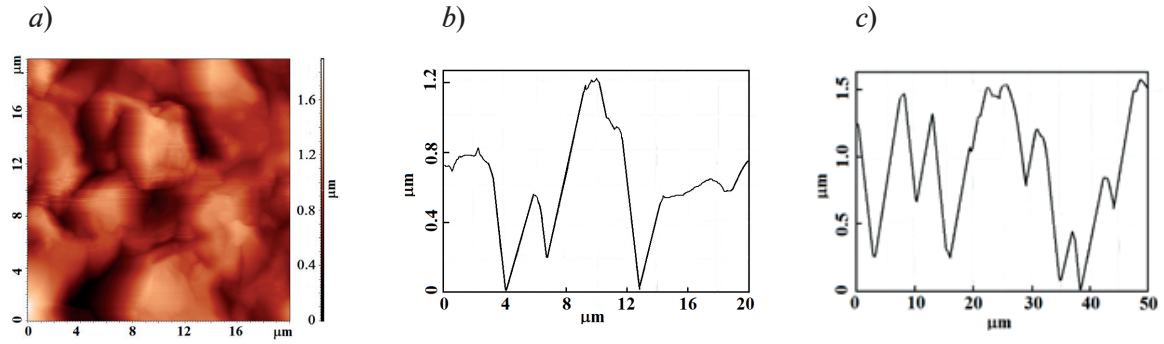

Fig. 4. AFM image (*a*) and surface profiles of the GaN(11-22)/AlN/NP-Si(113) structure in the direction along (*b*) and perpendicular (*c*) to the nanochannel

The surface of the GaN(10-11) and GaN(11-22) layers differs according to atomic force microscopy data (Figs. 2, 4). The surface of the GaN(10-11) layer shows blocks of semipolar gallium nitride elongated along the grooves with a surface inhomogeneity of 150-200 nm (Fig. 2, *b*), and the surface of the GaN(11-22) layer shows rectangular almost square blocks, between which dips of up to 1.3 microns are observed (Fig. 4, *b*). The aspect ratio (the ratio of height to width dimensions) of the blocks is 0,03 for GaN(10-11) and 0,15 for Ga(11-22). (Figs. 2, *b*, 4, *b*).

Results and Discussion

At the initial nucleation stage of the epitaxial AlN layer by MOCVD, AlN(10-11) and AlN(10-1-1) planes form on NP-Si(100) substrates. These planes have different surface energies. The values of surface energies known in the literature are given rather averaged and the influence of surface nanostructuring is not taken into account.

The calculated surface energy of ideal AlN and GaN surfaces with polar and semipolar orientations according to [10] shows that these values are less for polar planes than for semipolar (1-101) and (11-22) planes (Table 1).

Data on the surface energy of ideal GaN surfaces with polar and semipolar orientations in a nitrogen-enriched gas atmosphere show that the energy values also depend on the orientation of the face [11].

It can be seen that the surface energy increases depending on the orientation of the GaN surface in the following order: (0001), (11-22), (1-101), (000-1), (11-2-2) and (1-10-1). The corrugated AlN surface leads to the synthesis of GaN(1-101) and GaN(1-10-1) layers [12], which have different surface energies (Table 2). These differences, as well as differences in the properties of the NP-Si(100) substrate [13], can provide different growth rates of GaN faces in different directions, and lead to the formation of a GaN layer in one direction (Fig. 2, *a*, *b*).

Table 1

Surface energy of ideal AlN and GaN surfaces with polar and semipolar orientations

ev/A^2	(0001)	(000-1)	(1-101)	(11-22)	(11-20)
AlN	0.250	0.255	0.261	0.259	0.170
GaN	0.185	0.228	0.193	0.194	0.141

Table 2

Surface energy of the faces of GaN surfaces in an atmosphere enriched with nitrogen atoms [11]

	(0001)	(000-1)	(1-101)	(1-10-1)	(11-22)	(11-2-2)
eV/A^2	0.204	0.234	0.224	0.257	0.221	0.250

The nucleation of the GaN(11-22) layer occurs on the surface of the AlN/Si(111) face, at higher growth rates than AlN (Fig. 1, *b*). First, an island layer is formed (Fig. 3, *a*, *b*) and after the coalescence stage, a continuous layer with a semipolar GaN(11-22) surface is formed (Fig. 4, *a*, *b*). The different character of the profile of the initial NP-Si(100) and NP-Si(113) leads to different morphology of the GaN(10-11) and GaN(11-22) surfaces. The different morphology of the layers, in our opinion, is associated with the formation of GaN(10-11) at a later stage of growth after the synthesis of the corrugated AlN layer, in contrast to the synthesis of GaN(11-22), which occurs directly on a thin AlN layer on the Si(111) face.

The shape of the insular nucleus (Fig. 2, *b*) shows the presence of the planes *c*-GaN, *m*-GaN and GaN(11-22). The orientation of the nanocrystallites in the array is set by the direction of the plane Si(111) of the nanochannels in NP-Si(113).

The thickness of the layer in the direction of growth [0001] and in the direction of formation of the plane (11-22) is about 100 nm (Fig. 3, *b*), which corresponds to the close values of the surface energy of these planes (Table 1).

The larger size of the nucleus (Fig. 3, *b*) and the larger width of the peaks of the ACM image (Fig. 4,*b*) in the direction along the nanochannels than in the direction perpendicular to them clearly indicates the different diffusion length of Ga-L adatoms during the formation of the insular layer. As is known, $L = (D \cdot t)^{1/2}$, where D is the diffusion coefficient of Ga atoms on the surface, and t is the lifetime of the Ga atom on the surface of the nanostructure. The coefficient D depends on the epitaxy temperature, which has been constant throughout the growth, and we believe that D is the same in both directions and, therefore, the influencing factor t remains. When atoms diffuse along the nanochannels, the adatoms on the surface have a larger value t than in the direction perpendicular to the nanochannels. Perhaps this is due to the presence of nanogrooves in the direction perpendicular to the nanochannels, which lead to a violation of surface diffusion and a decrease in *t;* and, consequently, leads to a shorter period of undulation and a smaller island size in this direction (Fig. 3, *b*).

Conclusion

Thus, it is shown that during the synthesis of GaN(11-22) by MOCVD in a hydrogen atmosphere at the initial stages of growth, the orientation of the layer is set by the direction of the plane of Si(111) nanochannels in NP-Si(113). The detected effect of transition from the symmetric state of semipolar linear AlN(10-11) nanocrystallites with counter-directional *c* axes, which are formed on symmetrical silicon NP-Si(100) nanogrooves of the substrate, to an asymmetric state with a single orientation of the *c* axis GaN(10-11) layer, according to the model, is determined by the difference in surface energy (10-11) and (10-1-1) faces of the GaN layer.

Acknowledgments

The authors are grateful to Quantum Silicon, LLC (Moscow, Russia) for providing NP-Si(100) substrates, as well to A. V. Smirnov for useful discussions, M. Shcheglov for X-ray structural measurements, and A.V. Solomnikova for AFM measurments.

REFERENCES

1. **Romanov A. E., Baker T. J., Nakamura S., Speck J. S.,** Strain-induced polarization in wurtzite III-nitride semipolar layers, Journal of Applied Physics. 100 (2006) 023522.

2. **Fiorentini V., Bernardini F., Della Sala F., Di Carlo A., Lugli P.,** Effects of macroscopic polarization in III-V nitride multiple quantum wells, Physical Review B 60 (1999) 8849.

3. **Zhang Z.-H., Liu W., Ju Z., Tiam Tan S., Ji Y., Kyaw Z., Zhang X., Wang L., Sun X.W., Volkan Demir H.,** InGaN/GaN multiple-quantum-well light-emitting diodes with a grading InN composition suppressing the Auger recombination, Applied Physics Letters. 104 (2014) 243501.

4. **Honda Y., Kameshiro N., Yamaguchi M., Sawaki N..** Growth of (11̄01) GaN on a 7-degree off-oriented (0 0 1) Si substrate by selective MOVPE, Journal of Crystal Growth. 242(1) (2002) 82–86.

5. **Bessolov V., Zubkova A., Konenkova E., Konenkov S., Kukushkin S., Orlova T., Rodin S., Rubets V., Kibalov D., Smirnov V.,** Semipolar GaN(10−11) Epitaxial Layer Prepared on Nano-Patterned SiC/Si(100) Template, Physica Status Solidi B. 256(2) (2019) 1800268.

6. **Yu X., Hou Y., Shen S., Bai J., Gong Y., Zhang Y., Wang T.,** Semi-polar (11−22) GaN grown on patterned (113) Si substrate. Physica Status Solidi C. 13(5−6) (2016) 190−194.

7. **Chen G.-T., Chang S.-P., Chyi J.-I., Chang M.-N.,** Growth and characterization of crack-free semipolar {1-101}InGaN/GaN multiple-quantum well on V-grooved (001)Si substrates, Applied Physics Letters. 92(24) (2008) 241904.

8. **Tanikawa T., Hikosaka T., Honda Y., Yamaguchi M., Sawaki N.,** Growth of semi-polar (11-22) GaN on a (113)Si substrate by selective MOVPE, Physica Status Solidi C. 5(9) (2008) 2966−2968.

9. **Smirnov K., Kibalov D.S.,** Wave-Ordered Structure Induced by Nitrogen Ion Beam on Silicon Surface: A Self-Forming Hard Nanomask and Its Applications, In: Proceedings of the 21st International Conference on Ion-Surface Interactions, Yaroslavl, Russia, 22−26 August 2013; Vol. 1 (2013) p.62−66.

10. **Akiyama T., Seta Y., Nakamura K., Ito T.,** Modified approach for calculating individual energies of polar and semipolar surfaces of group-III nitrides, Physical Review Materials. 3 (2019) 023401.

11. **Kawamura T., Akiyama T., Kitamoto A., Imanishi M., Yoshimura M., Mori Y., Morikawa Y, Kangawa Y., Kakimoto K.,** Absolute surface energies of oxygen-adsorbed GaN surfaces, Journal of Crystal Growth. 549 (2020) 125868.

12. **Wang T.,** Topical Review: Development of overgrown semi-polar GaN for high efficiency green/yellow emission, Semiconductor Science and Technology. 31 (2016) 093003.

13. **Bessolov V., Konenkova E., Rodin S., Kibalov D., Smirnov V.,** Formation of semipolar group-III-nitride layers on textured Si(100) substrates with self-forming nanomask, Semiconductors. 55(4) (2021) 471−474.

THE AUTHORS

BESSOLOV Vasily N.
bes@triat.ioffe.ru
ORCID: 0000-0001-7863-9494

RODIN Sergey N.
s_rodin77@mail.ru
ORCID: 0000-0003-2236-8642

KONENKOVA Elena V.
lena@triat.ioffe.ru
ORCID: 0000-0002-5671-5422

Received 18.05.2022. Approved after reviewing 14.06.2022. Accepted 16.06.2022.

Conference materials
UDC 544
DOI: https://doi.org/10.18721/JPM.153.131

Influence of phenol red in Earle's solution on corrosion properties of coated and uncoated Mg alloy

A. I. Pleshkova [1] ✉, M. A. Piatkova [1], K. V. Nadaraia [1]
A. B. Podgorbunsky [1], S. L. Sinebryukhov [1], S. V. Gnedenkov [1]

[1] Institute of Chemistry FEB RAS, Vladivostok, Russia
✉ othariadna@gmail.com

Abstract: Metallic biomaterials are widely used for clinical purposes due to their excellent mechanical properties and good biocompatibility. Inspired by the functional surface of natural biological systems, many new designs and concepts have recently emerged to create multifunctional surfaces with great potential for biomedical applications. In present study, bioactive coatings were formed on Mg alloy by plasma electrolytic oxidation (PEO). Morphological features and composition of formed layers were studied by SEM and EDS. It was revealed that PEO-coatings have in their composition Ca and P, which can increase biocompatibility. Moreover, obtained coatings demonstrated high corrosion properties: corrosion current density substantially decreased compared to bare alloy.

Keywords: metallic biomaterials, bioactive coatings, plasma electrolytic oxidation

Funding: This work was supported by a Russian Science Foundation grant, RSF 22-23-00915.

Citation: Pleshkova A. I., Piatkova M. A., Nadaraia K. V., Podgorbunsky A. B., Sinebryukhov S. L., Gnedenkov S. V., Influence of phenol red in Earle's solution on corrosion properties of coated and uncoated Mg alloy, St. Petersburg State Polytechnical University Journal. Physics and Mathematics. 15 (3.1) (2022) 185–190. DOI: https://doi.org/10.18721/JPM.153.131

Материалы конференции
УДК 544
DOI: https://doi.org/10.18721/JPM.153.131

Влияние фенолового красного в растворе Эрла на коррозионные свойства сплава магния с покрытием и без покрытия

А. И. Плешкова [1] ✉, М. А. Пяткова [1], К. В. Надараиа [1]
А. Б. Подгорбунский [1], С. Л. Синебрюхов [1], С. В. Гнеденков [1]

[1] Институт химии ДВО РАН, г. Владивосток, Россия
✉ othariadna@gmail.com

Аннотация. Металлические биоматериалы широко используются в клинических целях благодаря их превосходным механическим свойствам и хорошей биосовместимости. В последнее время появилось много новых подходов и концепций для создания многофункциональных поверхностей с большим потенциалом для биомедицинских приложений, которые вдохновлены функциональной поверхностью природных биологических систем. В данной работе биоактивные покрытия были сформированы на сплаве магния МА8 методом плазменного электролитического оксидирования (ПЭО). Установлено, что ПЭО-покрытия имеют в своем составе Ca и P, которые могут повышать биосовместимость. Кроме того, полученные покрытия продемонстрировали

высокие коррозионные свойства: плотность тока коррозии существенно снизилась по сравнению со сплавом без покрытия.

Ключевые слова: металлические биоматериалы, биоактивные покрытия, плазменное электролитическое оксидирование

Финансирование: Работа выполнена при поддержке гранта РНФ 22-23-00915.

Ссылка при цитировании: Плешкова А. И., Пяткова М. А., Надараиа К. В., Подгорбунский А. Б., Синебрюхов С. Л., Гнеденков С. В. Влияние фенолового красного в растворе эрла на коррозионные свойства сплава магния с покрытием и без покрытия // Научно-технические ведомости СПбГПУ. Физико-математические науки. 2022. Т. 15. № 3.1. С. 185–190. DOI: https://doi.org/10.18721/JPM.153.131

Introduction

The current advances in technologies make it possible to create safe implants that are biocompatible with the human body. Developing new materials for implants requires a deep knowledge of the chemical, physical and mechanical properties of natural bone tissue, the qualitative and quantitative characteristics of implant materials. Recently, the possibility of natural regeneration has been actively studied, when the implant material biodegrades and dissolves in body fluids, and the process of healing of damaged tissues occurs with the replacement of the implant with the body's own tissue. This property of bioresorption is exhibited by magnesium and magnesium alloys. Early clinical studies, as well as in vivo and in vitro studies shown that magnesium-based implants are highly biocompatible. It has also been reported that magnesium-based implants can stimulate the bone tissue heals [1].

The unique mechanical properties of Mg alloys also make them desirable for fabrication of load-bearing implants. Magnesium has been tested as non-allergenic and stimulates new bone formation in vivo and in vitro tests [1]. However, the high electrochemical activity of magnesium and low wear resistance of this material can lead to early failure of the implant, which in turn can significantly affect to the patient's healing [2]. As result, magnesium needs additional protection to improve corrosion resistance and reduce wear.

Alloying of metals is a widely used method for improving the functional characteristics of a material, including in the field of protection against corrosion damage. This method of protection is laid down at the stage of creating a certain brand of alloy. The essence of alloying is the addition of certain impurity substances to the composition of metals that improve the mechanical or physico-chemical properties of these compositions.

A suitable alloy composition can improve corrosion resistance, mechanical properties and facilitate the production of magnesium (Mg) based materials. The two main groups of Mg-based alloys are those containing 2–10 wt.% aluminum (Al) with trace additions of zinc (Zn) and manganese (Mn), they show moderate corrosion resistance and improved mechanical properties [3], and those that use a mixture of rare earth elements in combination with another metal such as zinc, yttrium, and a small amount of zirconium, which gives a fine-grained structure and improved mechanical properties [3]. Because these materials are used in the body, non-toxic alloying elements must be selected. However, it is well known that aluminum is harmful to neurons and osteoblasts and also associated with dementia and Alzheimer's disease [4]. The introduction of rare earth metals (Pr, Ce, Y, etc.) can lead to hepatotoxicity. Excess yttrium ions (Y^{+3}) have been shown to alter the expression of several rat genes and adversely affect DNA transcription factors.

One of the possible ways to solve this problem is formation of coating on the surface of a magnesium implant by the plasma electrolytic oxidation (PEO) [5]. Note that this method gives

opportunity creating surface layers of a purposeful structure and composition; thus, the use of PEO makes it possible to form coatings similar in composition to mineral component of human bone tissue [1].

Materials and Methods

Samples. The samples were prepared from rectangular sheets made of MA8 magnesium alloy (Mg–Mn–Ce system, wt.%: 1.30 Mn; 0.15 Ce; Mg to balance), 8×8×1 mm^3 and 30×20×2 mm^3 in size. Before the coatings were produced, all samples were treated with sandpaper, washed with distilled water, and degreased with alcohol.

Coating formation. In accordance with the previously developed principles of directed plasma electrochemical synthesis of coatings on the surface of metals and alloys [6, 7] and conclusions drawn from the analysis of literature data [6,7], plasma electrolytic oxidation was carried out in bipolar mode: in the anode component the voltage 400 V, while in the cathode component, the current decreased from 5 to 3 A at a sweep rate of 0.04 A/s. PEO of the samples was carried out in an electrolyte containing 25 g/l calcium glycerophosphate ($C_3H_7CaO_6P$), 5 g/l sodium fluoride (NaF), and 7 g/l sodium metasilicate (Na_2SiO_3). The duration of the process was 100 s. After the coatings were formed, all samples were washed with distilled water, degreased with alcohol, and dried with warm air.

Coating characterization. To evaluate the morphology and chemical composition of the obtained samples the scanning electron microscopy and energy dispersive spectroscopy were used. EVO 40 scanning electron microscope (SEM, Carl Zeiss, Germany) equipped with INCA X-act instrument (Oxford Instruments, UK) for energy dispersive spectroscopy (EDS) was used for surface characterization [2].

Study of electrochemical properties. The electrochemical parameters of the samples were studied by potentiodynamic polarization using VersaSTAT MC electrochemical system (Princeton Applied Research, USA) in accordance with the technique described in [2].

The measurements were carried out in a three-electrode cell at a temperature of 37 °C in Earle's solution with and without phenol red, which are similar in ionic composition to human blood plasma (Table 1). The concentration of phenol red in Earle's solution was 0.02 g/L. Thus, phenol red is a pH indicator, its often used in medicine and microbiology for determination of metabolic products of bacteria. However, the presence of this substance in solution can directly affect the corrosion of such an electrochemically active material as magnesium/magnesium alloy. In this regard, and due to the fact that solutions with and without phenol red can be used in the course of research on implantation materials, it is of great interest to study the effect of this

Table 1

Ionic concentration (mmol/L) in Earle's solution and human blood plasma

Ion concentration, mmol/L	Human blood plasma	Earle's solution
Na^+	142	143.5
Cl^-	103	123.5
HCO^{3-}	27	26.2
K^+	5.0	5.4
Ca^{2+}	2.5	1.8
Mg^{2+}	1.5	0.8
PO^{-3}_4	1.0	0.9
SO^{-2}_4	0.5	0.8
Glucose, g/L	1.1	1.0

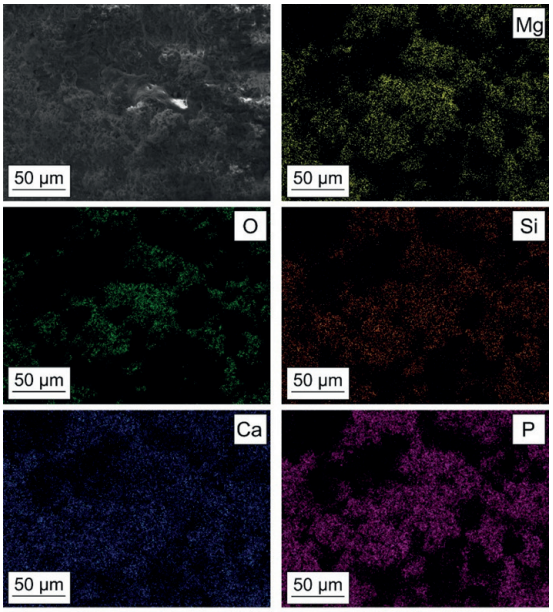

Fig. 1. SEM-image of the PEO-coating and EDS map of the element distribution

substance on the corrosion of Mg alloy, including those with protective PEO-layers.

Results and Discussion

It can be concluded from SEM analysis that the PEO-coating formed has a typical surface morphology with crater-like pores (Fig. 1). This is the result of sharp cooling of the breakdown zone down to the electrolyte temperature after the attenuation of the plasma discharge as well as gas evaporation during the PEO. According to [6], such a developed surface can positively affect cell proliferation and improve bone-to-implant contact.

Analysis of the EDS data indicates the presence of Mg, Si, O, Ca, P in the coating composition (Fig. 1). The presence of Si, Ca, P and O is due to their incorporation from the electrolyte during PEO. Mg is a substrate element. Formed layer is enriched with Ca and P, as result of transfer of these elements in the plasma discharge channel form the electrolyte to the surface of substrate. The presence of Ca and P can significantly increase the biocompatibility of PEO-coatings, because these elements are the main components of bone tissue.

Potentiodynamic polarization data indicate an improvement in the corrosion properties of the samples after coatings formation on their surface. Based on analysis of the potentiodynamic measurements, it can be concluded that the corrosion current density, i_{corr}, decreased after application of PEO-coating on Mg alloy (Table 2).

Table 2

Electrochemical parameters of samples in Earle's solution with and without phenol red

Electro-chemical parameters	Earle's solution without phenol red		Earle's solution with phenol red	
	Bare magnesium alloy	With PEO-coating	Bare magnesium alloy	With PEO-coating
E_{corr} (V vs. SCE)	–1.75	–1.62	–1.82	–1.63
i_{corr} (A/cm^2)	8.6×10^{-6}	6.7×10^{-6}	1.0×10^{-5}	6.9×10^{-6}

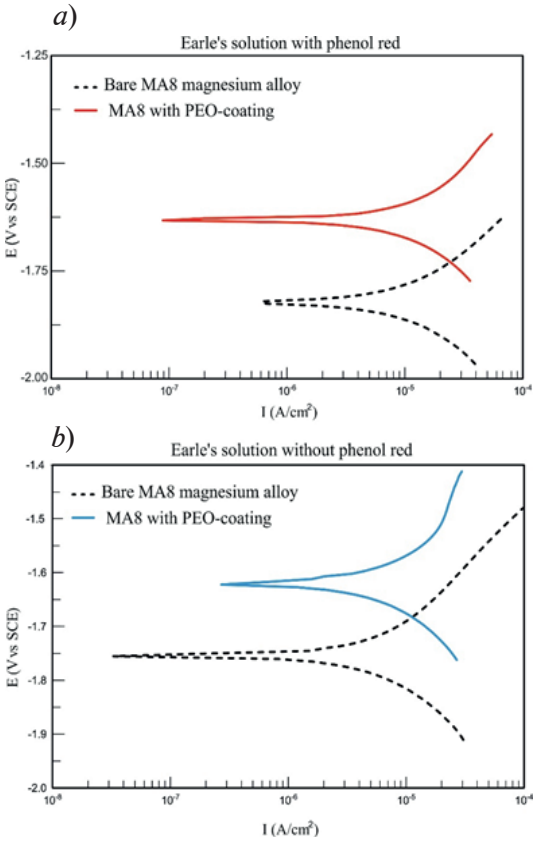

Fig. 2. Polarization curves obtained for MA8 alloy samples with and without PEO-coating in Earle's solution without (*a*) and with (*b*) phenol red

There are no significant differences between the coatings studied in Earle's solution without phenol red and with this compound (Fig. 2, Table 2). This fact is related to the features of the formed coatings. It is known that the PEO-coating consists of an outer porous layer, which mainly determines the mechanical properties, and an inner, practically non-porous sublayer, which is responsible for corrosion resistance [7]. Since the formed sublayer consists of poorly soluble magnesium compounds, in particular, MgF_2 [8], the probability of reactions occurring between it and the substances present in the Earle's solution is extremely low probability. However, for bare Mg alloy, with the addition of phenol red the corrosion current density increased. According to the analysis of the polarization curves, the presence of phenol red leads to a shift in the corrosion potential to more negative values compared to a solution that does not contain this substance (Fig. 2). Accordingly, this leads to an intensification of the magnesium alloy corrosion process. It is known that corrosion of magnesium materials proceeds with alkalization of the medium, which, apparently, leads to reactions between phenol red and evolving hydrogen. In addition, Earle's solution with phenol red has a higher electrical conductivity (14.41 mS/cm) compared to Earle's solution without phenol red (5.67 mS/cm).

Of interest are the details of this interaction, considering the complex composition of Earle's solution, the presence in it of not only phenol red, inorganic compounds, but also organic matter: glucose. The features of the occurring reactions will be the subject of study in our next works.

Conclusion

Coatings containing Ca/P were obtained on MA8 Mg alloy by plasma electrolytic oxidation. Obtained coatings have high corrosion resistance compared to bare alloy. Differences in the results of electrochemical studies showed that the phenol red in Earle's solution affects the course of reactions on the surface of the samples without coatings. However, PEO-coatings demonstrated high protective properties regardless of presence phenol red in Earle's solution, which additionally confirms the high corrosion resistance of the formed surface layers.

REFERENCES

1. **Nassif N., Ghayad I.,** Corrosion Protection and Surface Treatment of Magnesium Alloys Used for Orthopedic Applications, Advances in Materials Science and Engineering, 2013.

2. **Barati Darband G., Aliofkhazraei M., Hamghalam P., Valizade N.,** Plasma Electrolytic Oxidation of Magnesium and Its Alloys: Mechanism, Properties and Applications, Journal of Magnesium and Alloys. 5 (2017) 74–132.

3. **Shinde G. T., Ugle S. S., Bikkad M. D., Ingle S. B.,** Water Aluminium and Alzheimer Disease, International Journal of Pharma and Bio Sciences. 6 (2) (2015) 608–612.

4. **Yang W., Zhang P., Liu J., Xue Y.,** Effect of long-term intake of Y+3 in drinking water on gene expression in brains of rats, Journal of Rare Earths. 24 (3) (2006) 369–373.

5. **Roach P., Eglin D., Rohde K., Perry C. C.,** Modern Biomaterials: A Review - Bulk Properties and Implications of Surface Modifications, Journal of Materials Science: Materials in Medicine. 18 (2007) 1263–1277.

6. **Mashtalyar D.V., Nadaraia K.V., Plekhova N.G., Imshinetskiy I.M., Piatkova M.A., Pleshkova A.I., Kislova S.E., Sinebryukhov S.L., Gnedenkov S.V.,** Antibacterial Ca/P-Coatings Formed on Mg Alloy Using Plasma Electrolytic Oxidation and Antibiotic Impregnation. Materials Letters 317 (2022).

7. **Mashtalyar D.V., Imshinetskiy I.M., Nadaraia K.V., Gnedenkov A.S., Sinebryukhov S.L., Ustinov A.Yu, Samokhin A.V., Gnedenkov S.V.,** Influence of ZrO2/SiO2 Nanomaterial Incorporation on the Properties of PEO Layers on Mg-Mn-Ce Alloy, Journal of Magnesium and Alloys. 10 (2021) 513–526.

8. **Gnedenkov S.V., Khrisanfova O.A., Zavidnaya A.G., Sinebryukhov S.L., Egorkin V.S., Nistratova M.V., Yerokhin A., Matthews A.,** PEO coatings obtained on an Mg–Mn type alloy under unipolar and bipolar modes in silicate-containing electrolytes, Surface & Coatings Technology. 204 (2010) 2316–2322.

THE AUTHORS

PLESHKOVA Arina I.
othariadna@gmail.com
ORCID: 0000-0002-4601-3232

PODGORBUNSKY Anatoly B.
defrag_2008@mail.ru
ORCID: 0000-0002-0764-391X

PIATKOVA Maria A.
piatkova.mariia.al@gmail.com
ORCID: 0000-0002-1208-0947

SINEBRYUKHOV Sergey L.
sls@ich.dvo.ru
ORCID: 0000-0002-0963-0557

NADARAIA Konstantine V.
nadaraiakv@mail.ru
ORCID: 0000-0001-7835-2231

GNEDENKOV Sergey V.
svg21@hotmail.com
ORCID: 0000-0003-1576-8680

Received 21.05.2022. Approved after reviewing 21.07.2022. Accepted 21.07.2022.

Conference materials
UDC 544.722.3
DOI: https://doi.org/10.18721/JPM.153.132

Evaluation of surface free energy of bioactive coatings in titanium and magnesium alloy

S. N. Suchkov [1] ✉, K. V. Nadaraia [1], I. M. Imshinetskiy [1]
D. V. Mashtalyar [1], S. L. Sinebrukhov [1], S. V. Gnedenkov [1]

[1] Institute of Chemistry FEB RAS, Vladivostok, Russia
✉ snsuchkov@yandex.ru

Abstract: Surface free energy (SFE) is a crucial parameter for predicting the cell adhesion and proliferation on implantation materials. In this work, the influence of bioactive calcium-phosphate coatings on the SFE of titanium and magnesium implants was studied. Results shows that the formation of bioactive coatings increase SFE by 139 % for magnesium alloy and 38 % for titanium, which in turn should have a positive effect on the adhesion and proliferation of osteoblasts.

Keywords: titanium, magnesium alloy, plasma electrolytic oxidation, biocompatibility, surface free energy

Funding: The coatings were produced as part of a Russian Science Foundation grant (project no. 21-73-10148). Wettability studies were carried out within the framework of State Assignment of the Ministry of Science and Higher Education of the Russian № FWFN-2021-0003.

Citation: Suchkov S. N., Nadaraia K. V., Imshinetskiy I. M., Mashtalyar D. V., Sinebrukhov S. L., Gnedenkov S. V., Evaluation of surface free energy of bioactive coatings on titanium and magnesium alloy, St. Petersburg State Polytechnical University Journal. Physics and Mathematics. 15 (3.1) (2022) 191–196. DOI: https://doi.org/10.18721/JPM.153.132

Материалы конференции
УДК 544.722.3
DOI: https://doi.org/10.18721/JPM.153.132

Оценка свободной энергии поверхности биоактивных покрытий на титане и магниевом сплаве

С. Н. Сучков [1] ✉, К. В. Надараиа [1], И. М. Имшинецкий [1]
Д. В. Машталяр [1], С. Л. Синебрюхов [1], С. В. Гнеденков [1]

[1] Институт химии ДВО РАН, г. Владивосток, Россия
✉ snsuchkov@yandex.ru

Аннотация. Свободная поверхностная энергия (СПЭ) играет важную роль для прогнозирования адгезии и пролиферации клеток на имплантационных материалах. В данной работе было изучено влияние биоактивных кальций-фосфатных покрытий на свободную поверхностную энергию титановых и магниевых имплантатов. Результаты показывают, что формирование биоактивных покрытий увеличивает СПЭ на 139 % для магниевого сплава и на 38 % для титана, что, в свою очередь, должно оказывать положительное влияние на адгезию и пролиферацию клеток костной ткани.

Ключевые слова: титан, магниевые сплавы, плазменное электролитическое оксидирование, биосовместимость, свободная энергия поверхности

Финансирование: Формирование покрытий проводилось в рамках Гранта Российского научного фонда (проект № 10148-73-21). Изучение смачиваемости проводились в рамках государственного задания Министерства науки и высшего образования Российской Федерации № FWFN-2021-0003.

Ссылка при цитировании: Сучков С. Н., Надараиа К. В., Имшинецкий И. М., Машталяр Д. В., Синебрюхов С. Л., Гнеденков С. В. Оценка свободной энергии поверхности биоактивных покрытий на титане и магниевом сплаве // Научно-технические ведомости СПбГПУ. Физико-математические науки. 2022. Т. 15. № 3.1. С. 191–196. DOI: https://doi.org/10.18721/JPM.153.132

Introduction

Metal implants are the main material for bone surgery [1]. Titanium is widely used for production of dental and orthopedic implants, due to its high strength, corrosion resistance and bioinertness [2]. Magnesium is also of considerable interest as an implantation material, due to its biocompatibility, biodegradability and mechanical properties, which are closer to human bone tissue properties compared to other metals [3]. However, these metals have significant drawbacks, as a result of which the implant surface requires additional processing to improve osseointegration and increase the adhesion of bone tissue cells [3,4].

The coatings formation is one of the modification methods leading to the elimination of the disadvantages of metal surface. Plasma electrolytic oxidation (PEO) is one of the most promising methods of protecting metals from electrochemical dissolution and improving mechanical characteristics [5]; in addition, PEO is used to form bioactive coatings on implants [6,7].

The contact of the implant surface with the living tissue is important for osseointegration. The chemical composition of the implant determines directly the biocompatibility; roughness affects the contact area of the material with the biological environment and cell adhesion. In addition, the bone tissue cell adhesion is associated with wettability, which depends on the surface free energy (SFE) [8]. Many authors note that high-energy surfaces are more desirable for enhancing osteointegration and osteogenesis [9]. Thus, the study of the effect of the modification process on the SFE is important for the further practical application of PEO technology for the treatment of metal implants.

Materials and Methods

Rectangular sheets (35×25×1.5 mm^3) of VT1-0 commercially pure titanium (Ti) and MA8 magnesium alloy (Mg) (1.3–2.2 wt.% of Mn, 0.15–0.35 wt.% of Ce, Mg to balance) were used as the substrates.

PEO of the titanium was carried out in an electrolyte containing 30 g L^{-1} calcium glycerophosphate ($C_3H_7CaO_6P$) and 40 g L^{-1} calcium acetate ($Ca(CH_3COO)_2$) in a monopolar potentiodynamic mode [10], sample is designated as Ti-PEO. PEO of the magnesium alloy was carried out in an electrolyte containing 25 g L^{-1} calcium glycerophosphate ($C_3H_7CaO_6P$), 5 g L^{-1} sodium fluoride (NaF), and 7 g L^{-1} sodium metasilicate (Na_2SiO_3) in a bipolar mode [11], sample is designated as Mg-PEO. The use of different modes of PEO for magnesium alloy and titanium is due to differences in the mechanism of formation of the anode coating on various metals, described in more detail in previous studies [10,11].

The wettability of the investigated samples was studied by the sessile drop method using the drop shape analyzer DSA100 (KRЬSS, Germany). Contact angle (CA) technique is used to estimate wetting properties of the localized area of solid surface. According to this method, the angle between the baseline of the drop and the tangent at the three-phase point was measured. For calculations of CA, the Young-Laplace method was used. Before recording the CA results, the drop stabilized on the surface for 60 s. Deionized water (H_2O) and methylene iodide (CH_2I_2)

were used as test liquids. Before contact angle measurements, metal surfaces were mechanically treated with sanding papers from #150 to #2500 sequentially, washed with distilled water and degreased with alcohol in ultrasonic bath (Bandelin electronic, Germany). The surfaces of PEO coatings were washed with distilled water and dried at 25°C.

Surface free energy (γ_s) was calculated (Eq. 1) as the sum of the dispersed (γ_s^d) and polar (γ_s^p) interactions of a liquid droplet with the solid surface, calculated using a system of equations obtained on the basis of the Owens equation [12]:

$$\begin{cases} \gamma_s^d = \left[C_1 \left(1+\cos\theta_w\right) - C_2 \left(1+\cos\theta_{mi}\right) \right]^2 \\ \gamma_s^p = \left[C_3 \left(1+\cos\theta_w\right) + C_4 \left(1+\cos\theta_{mi}\right) \right]^2, \end{cases} \quad (1)$$

where θ_w, θ_{mi} are the CA for the surface in contact with water and methylene iodide, respectively. The constants C_1–C_4 are determined by the values of the liquid surface tension.

Results and Discussion

Based on the data of X-ray phase analysis and elemental composition [10,11], formed coatings include calcium-phosphate compounds, which can increase the formation rate of hydroxyapatite in body fluids. In addition to calcium phosphate compounds, the coatings consist of titanium dioxide (in the modification of rutile and anatase) for titanium, magnesium oxide and ortho-silicate for magnesium alloy.

Analysis of the wettability of bioactive surface layers on titanium and magnesium alloy indicates a significant decrease in CA in comparison with the metal surface (Table 1). In particular, coatings on Mg alloy exhibit properties close to superhydrophilicity in contact with water. However, the values are approximate, since the drop spreads at a high speed and is absorbed by the material, as a result of which it is difficult to register the real CA.

When wetting Mg-PEO with methylene iodide, the equilibrium CA = 15.7° and is not established immediately but for some time, approximately 30–60 s (Fig. 1). This behavior of liquids on the surface of bioactive coatings on magnesium alloy is a result of high roughness and large porosity, because of which, due to capillary effects, the drop gradually penetrates deep into the texture of the coatings, and spreads over the surface, and the CA, in turn, decreases (Fig. 1).

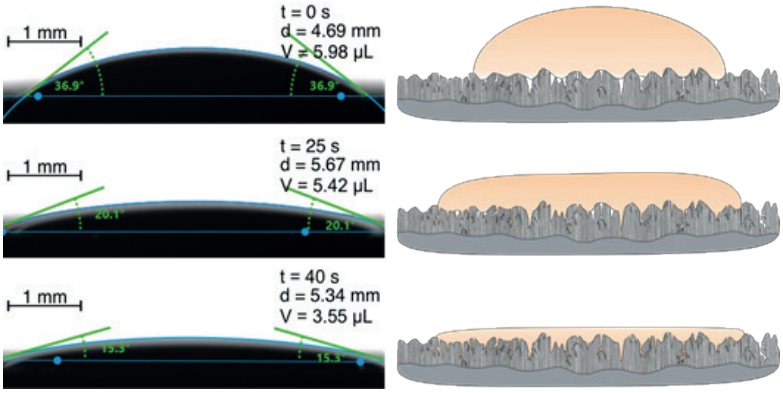

Fig. 1. Optical images (*a*, *c*, *e*) and wetting models (*b*, *d*, *f*) of methylene iodide CA for Mg-PEO surface after 0 s (*a*, *b*), 25 s (*c*, *d*) and 40 s (*e*, *f*) sitting the drop

At the initial stage of wetting (Fig. 1, *a*, *b*), the liquid/solid contact boundary contains both liquid/solid (f_{l-s}) and liquid/vapor (f_{l-v}) sections contained in the pores of the PEO layer. Thus, the wetting satisfies the Cassie-Baxter state (Eq. 2):

$$\cos\left(\theta_C\right) = f_{l-s}\cos\theta_Y - f_{l-v}, \quad (2)$$

where θ_C, θ_Y are Cassie and Young's CA, respectively.

Table 1

Wettability and components of surface free energy for different surfaces

Surface	Contact angle, °		Surface free energy, mJ·m^{-2}		
	H_2O	CH_2I_2	γ_s^p	γ_s^d	γ_s
Mg	82.6 ± 0.6	54.9 ± 1.1	5.23 ± 0.12	28.3 ± 0.3	33.6 ± 0.4
Mg-PEO	5.4 ± 4.3	15.7 ± 0.9	31.35 ± 0.16	48.9 ± 0.2	80.3 ± 0.4
Ti	75.1 ± 0.3	43.7 ± 0.4	5.73 ± 0.14	37.7 ± 0.2	43.5 ± 0.4
Ti-PEO	41.4 ± 1.1	50.0 ± 1.2	26.0 ± 0.8	34.3 ± 0.7	60.2 ± 1.4

Notations: The results are presented as the mean ± standard deviation for 15 measurements.

Next, the contact area increases (Fig. 1, *c*, *d*), as can be seen from the increase in the contact line length (*d*). Accordingly, f_{l-s} increases and f_{l-v} decreases ($f_{l-s} = 1 - f_{l-v}$), which indicates partial filling of the coating pores. Further, there is no increase in the contact line length, and the CA and drop volume (V) decreases, therefore the drop goes deep into the texture of the coating ($f_{l-s} \to 1$) and wetting passes from the Cassie-Baxter state to the Wenzel state (Eq. (3)):

$$\cos(\theta_w) = r\cos\theta_Y, \tag{3}$$

where $f_{l-s} = r$ is the roughness parameter, θ_W is Wenzel's CA.

For Ti-PEO, a stable state is achieved immediately, and the wettability of such a surface improves compared to uncoated metal. Water CA decreases by almost half, and methylene iodide CA increases (Table 1), which is probably a consequence of the presence of titanium oxide on the surface in advantage. A significant difference in the wetting of Mg-PEO and Ti-PEO is due to differences in the morphology of the surface. The size and number of pores of Mg-PEO coatings significantly exceed Ti-PEO [10, 11].

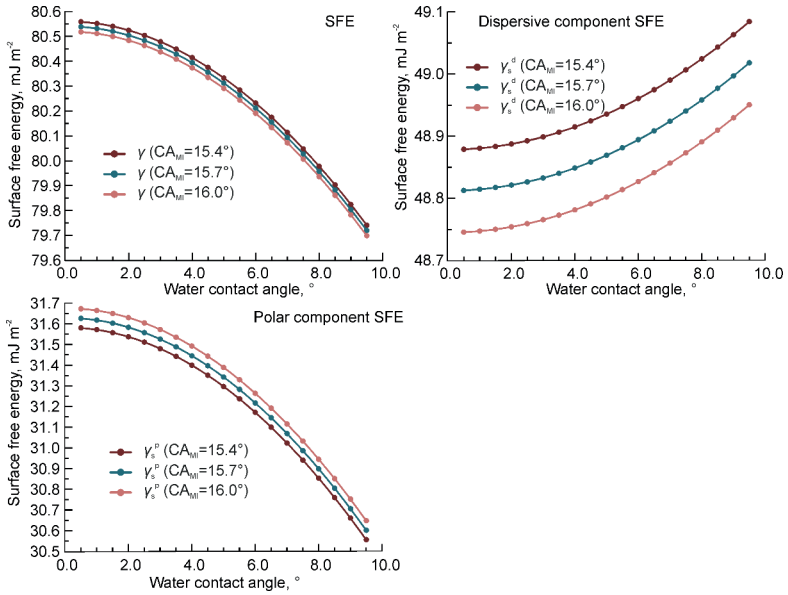

Fig. 2. Theoretical dependences of the SFE (γ, γ^d, γ^p) on the θ_w from 0 to 10° at different values of the θ_{mi}, by the Owens-Wendt equation.

As the CA changes due to formation of PEO coatings on the surface of titanium and magnesium, the value of SFE changes as well. To a large extent, the value of the polar component of the SFE changes for PEO coatings, which is due to a significant difference in the energy of interaction of the liquid with metal and metal oxides.

Since it is difficult to estimate the real water CA with the surface of Mg-PEO due to its high hydrophilicity, determining the value of SFE by the OWRK (Owens-Wendt-Rable-Kaelble) method is also non-trivial. Therefore, the Owens-Wendt equation was graphically presented in the area of the water CA 0–10°, with the value of the methylene iodide contact angle (15.7 ± 0.3)° (Fig. 2).

The results show that at this site the value of the SFE is determined with an accuracy of 1 $mJ \cdot m^{-2}$, which is less than 1 % of the specified value. Also, decomposing the SFE by components, it is clearly seen that the polar component (0.9 $mJ \cdot m^{-2}$) makes the greatest contribution to this difference, and the dispersed component lies within the error (0.2 $mJ \cdot m^{-2}$). According to the data of the graphs, it can be assumed that the SFE of the Mg-PEO surface is 80.3 ± 0.4 $mJ \cdot m^{-2}$.

Conclusion

In general, it is possible to establish the positive effect from treating the metal surface by plasma electrolytic oxidation, since the value of the SFE increases by 139% for magnesium alloy and 38% for titanium. An increase in wettability and, as a consequence, the amount of surface energy is a favorable factor for the biocompatibility and cell adhesion on the surface of the implantation material [8].

REFERENCES

1. **Steinemann S. G.,** Metal implants and surface reactions, Injury. 27 (1996) S/C16-S/C22.
2. **Pałka K., Pokrowiecki R.,** Porous titanium implants: a review, Advanced Engineering Materials. 20 (5) (2018) 1700648.
3. **Roach P., et al.,** Modern biomaterials: a review—bulk properties and implications of surface modifications, Journal of Materials Science: Materials in Medicine. 18 (7) (2007) 1263–1277.
4. **Chouirfa H., et al.,** Review of titanium surface modification techniques and coatings for antibacterial applications, Acta biomaterialia. 83 (2019) 37–54.
5. **Mashtalyar D. V., et al.,** New approach to formation of coatings on Mg-Mn-Ce alloy using a combination of plasma treatment and spraying of fluoropolymers, Journal of Magnesium and Alloys. 10 (4) (2021) 1033–1050.
6. **Cheng Y., et al.,** Microstructure, corrosion and wear performance of plasma electrolytic oxidation coatings formed on Ti–6Al–4V alloy in silicate-hexametaphosphate electrolyte, Surface and Coatings Technology. 217 (2013) 129–139.
7. **Cerchier P., et al.,** Antibacterial effect of PEO coating with silver on AA7075, Materials Science and Engineering: 75 (2017) 554–564.
8. **Schwartz Z., Boyan B. D.,** Underlying mechanisms at the bone–biomaterial interface, Journal of cellular biochemistry. 56 (3) (1994) 340–347.
9. **Ferreirys C. M., et al.,** Surface free energy and interaction of Staphylococcus epidermidis with biomaterials, FEMS microbiology letters. 60 (1) (1989) 89–94.
10. **Mashtalyar D. V., et al.,** Bioactive coatings formed on titanium by plasma electrolytic oxidation: Composition and properties, Materials.13 (18) (2020) 4121.
11. **Mashtalyar D. V., et al.,** Antibacterial Ca/P-coatings formed on Mg alloy using plasma electrolytic oxidation and antibiotic impregnation, Materials Letters. 317 (2022) 132099.
12. **Owens D. K., Wendt R. C.,** Estimation of the surface free energy of polymers, Journal of applied polymer science. 13 (8) (1969) 1741–1747.

THE AUTHORS

SUCHKOV Sergey N.
snsuchkov@yandex.ru
ORCID: 0000-0001-9151-3167

MASHTALYAR Dmitry V.
madiva@inbox.ru
ORCID: 0000-0001-9645-4936

NADARAIA Konstantine V.
nadaraiakv@mail.ru
ORCID: 0000-0001-7835-2231

SINEBRUKHOV Sergey S.L.
sls@ich.dvo.ru
ORCID: 0000-0002-0963-0557

IMSHINETSKIY Igor M.
igorimshin@gmail.com
ORCID: 0000-0002-5055-1834

GNEDENKOV Sergey S.V.
svg21@hotmail.com
ORCID: 0000-0003-1576-8680

Received 21.05.2022. Approved after reviewing 23.06.2022. Accepted 04.07.2022.

Conference materials
UDC 544.6.018.2+546.46
DOI: https://doi.org/10.18721/JPM.153.133

Preparation of layered double hydroxide on PEO-coated MA8 magnesium alloy: electrochemical and corrosion properties

A. D. Nomerovskii [1]✉, A. S. Gnedenkov [1], S. L. Sinebryukhov [1], S. V. Gnedenkov [1]

[1] Institute of Chemistry FEB RAS, Vladivostok, Russia

✉ nomerovskii.ad@outlook.com

Abstract: The coating containing a layered double hydroxide (LDH) was obtained on the MA8 magnesium alloy. The coating morphology, its electrochemical and corrosion behavior were studied. Scanning electron microscopy confirmed the lamellar structure of the LDH. Maps of the element distribution on the surface (the aluminum content on the surface is 3.2 wt.%) and the diffraction pattern of the sample (the presence of a hydrotalcite phase) also confirmed the presence of LDH. The electrochemical and corrosion behavior of the base PEO-coating, an LDH-containing coating, and the LDH-containing coating after impregnation with sodium oleate was compared. According to the experimental data analysis the positive role of LDH in the protection of the magnesium alloy was established. Treatment of the LDH-containing coating with a 0.1 M solution of sodium oleate makes it possible to increase the impedance modulus measured at the frequency of 0.1 Hz by order of magnitude compared to the inhibitor free protective layer. The obtained LDHs have a positive effect on the stability of the protective properties in aggressive medium, which was shown by the decrease in corrosion current density for the investigated sample.

Keywords: magnesium alloys, layered double hydroxide, electrochemistry, corrosion, inhibition, plasma electrolytic oxidation

Funding: The study was supported by Russian Science Foundation grants RNF 21-73-10148, RNF 20-13-00130.

Citation: Nomerovskii A. D., Gnedenkov A. S., Sinebryukhov S. L., Gnedenkov S. V. Preparation of a layered double hydroxide on the PEO-coated MA8 magnesium alloy: electrochemical and corrosion properties. St. Petersburg State Polytechnical University Journal. Physics and Mathematics. 15 (3.1) (2022) 197–203. DOI: https://doi.org/10.18721/JPM.153.133

Материалы конференции
УДК 544.6.018.2+546.46
DOI: https://doi.org/10.18721/JPM.153.133

Получение слоистого двойного гидроксида на ПЭО-покрытии, сформированном на сплаве магния МА8: электрохимические и коррозионные свойства

А. Д. Номеровский [1]✉, А. С. Гнеденков [1], С. Л. Синебрюхов [1], С. В. Гнеденков [1]

[1] Институт химии ДВО РАН, г. Владивосток, Россия

✉ nomerovskii.ad@outlook.com

Аннотация. На магниевом сплаве МА8 было получено покрытие, содержащее слоистые двойные гидроксиды (СДГ) в своей структуре. Изучена морфология полученного покрытия, его электрохимическое и коррозионное поведение. Ламеллярная структура СДГ подтверждена анализом данных, полученных с помощью сканирующей

электронной микроскопии. Наличие СДГ также подтверждено картами распределения элементов на поверхности (содержание алюминия на поверхности 3.2 масс.%) и дифрактограммой образца (присутствие фазы гидротальката). Было проведено сравнение электрохимического и коррозионного поведения базового ПЭО-покрытия, покрытия, содержащего СДГ, и покрытия, содержащего СДГ, после импрегнирования олеатом натрия. Согласно полученным экспериментальным данным, установлена положительное влияние СДГ на защитные свойства покрытия. Обработка 0.1 М раствором олеата натрия покрытия, содержащего СДГ, позволяет увеличить модуль импеданса, измеренного на частоте 0.1 Гц, на порядок по сравнению с покрытием без ингибитора. Полученные СДГ положительно влияют на устойчивость сплава с ПЭО-покрытием в агрессивной среде что следует из уменьшения плотности тока коррозии для исследуемого образца.

Ключевые слова: магниевые сплавы, слоистый двойной гидроксид, электрохимия, коррозия, ингибирование, плазменно-электролитическое оксидирование

Финансирование: Исследование выполнено при поддержке грантов РНФ 10148-73-21, РНФ 00130-13-20.

Ссылка при цитировании: Номеровский А. Д., Гнеденков А. С., Синебрюхов С. Л., Гнеденков С. В. Получение слоистого двойного гидроксида на ПЭО-покрытии, сформированном на сплаве магния МА8: электрохимические и коррозионные свойства // Научно-технические ведомости СПбГПУ. Физико-математические науки. 2022. Т. 15. № 3.1. С. 197–203. DOI: https://doi.org/10.18721/JPM.153.133

Introduction

Magnesium and its alloys are light materials with a density of about 1.8 g/cm^3, which is lower than that of aluminum (about 2.7 g/cm^3), titanium (about 4.5 g/cm^3) and steel (about 7.8 g/cm^3). Magnesium alloys have attracted considerable interest from researchers due to their good specific strength, lightness, high damping capacity, and good recyclability [1, 2].

Magnesium alloys do not have a protective oxide layer on their surface, unlike stainless steel, aluminum and titanium alloys. Therefore, Mg alloys are subject to strong corrosion in the marine atmosphere and other environment [2–5]. One of the well-known methods for applying ceramic-like coatings to metals and their alloys is plasma electrolytic oxidation (PEO), which is used to protect valve metals such as Al, Mg, Ti, Ta, Nb, and others [6–10]. This method is based on polarization of the material in electrolyte solutions at voltages that cause the flow of microdischarges on the surface of treated materials [11].

Currently, technologies aimed at obtaining the smart coatings are widespread [12]. To date, there is a need to develop eco-friendly self-healing coatings [13]. This type of coating has the property of self-healing in case of damage, which is based on the gradual release of corrosion inhibitors that prevent the material against degradation. In the aerospace industry the intensive aluminum corrosion was prevented using Cr(VI) salts, but this inhibitor has a negative (toxic) effect to environment. Alternative protection options were developed using coatings based on Zr/Ti, rare earth elements, including those based on LDH [12, 14–16].

However, for magnesium, a smaller number of possible protection methods (in comparison to Al) can be observed [3, 15], since Mg is a rather active metal. Previously, the coating impregnation with 8-hydroxyquinoline [18] was proposed as an additional protection for magnesium with a PEO-layer. This treatment made it possible to significantly improve the corrosion resistance of the base PEO-coating.

In [14, 19], it was proposed to use LDH as a paint pigment for steel, with the preliminary incorporation of 2-mercaptobenzothiazole, which makes it possible to inhibit corrosion processes. LDH [17, 18] is the ionic solids with the general formula $[(M^{2+})_{1-x}(M^{3+})_x(OH)_2]^{x+}[(A^{n-})_{x/n}\cdot mH_2O]$.

LDH has a hydrotalcite-like structure (the structure of brucite-like layers, that consist of mixed metal hydroxides, in which these metals are in an octahedral molecular geometry, and the interlayer space is filled with charge-compensating anions and water molecules [22, 23]. Due to the peculiarities of this structure, inhibitor molecules can be incorporated in the intercalated layers [14, 24–26] and subsequently be released to suppress corrosion [25].

In this paper, we propose the way of preparation and use of LDHs as nanocontainers for the protection of the PEO-coated MA8 magnesium alloy. Sodium oleate was chosen as a corrosion inhibitor [27].

Materials and Methods

Samples with the size of 20×20×2 mm^3 made of MA8 magnesium alloy were used in this work as a substrate. The specimens were preliminarily processed on a grinding machine using an emery paper with a grit of P320, then washed with isopropyl alcohol and air-dried.

The following coatings were formed on MA8 magnesium alloy: base PEO-coating (MA8-PEO), PEO-coating containing LDH (MA8-PEO-LDH), and PEO-coating containing LDH and treated with an inhibitor (MA8-PEO-LDH-oleat).

PEO treatment was carried out in an electrolyte containing 15 g/L $Na_2SiO_3 \cdot 5H_2O$ and 5 g/L NaF in the bipolar mode. The duration of the process was 600 s. During the entire oxidation process, the potential of the cathode phase was maintained equal to -30 V, and the potential of the anode phase increased linearly from 30 to 300 V. The pulse duration was 30 ms with a pause for each phase.

To obtain LDH the treatment of the PEO-coating [24, 25] was carried out in a solution containing 50 g/L EDTA-Na, 40 g/L NaOH, 5 g/L Al (aluminum granules were preliminarily dissolved in sodium hydroxide). The samples were immersed in the solution and soaked for 48 h at 60 °C (hot solution treatment).

Treatment with the inhibitor was performed in a solution containing 0.1 M sodium oleate for 24 h.

An AUW120D analytical balance (Shimadzu, Japan) was used for sample weighting. To control the coating thickness, a VT-201 eddy current thickness gauge (KID, Russia) was used. SEM images and element distribution maps were obtained using an EVO 40 electron microscope (Carl Zeiss, Germany). X-ray phase analysis (XRD) was performed on a D8 Advance diffractometer (Bruker, USA). Electrochemical measurements were carried out using a VersaSTAT MC electrochemical station (Princeton Applied Research, USA) in a 3.5 % NaCl solution in a three-electrode cell with an Ag/AgCl electrode as a reference electrode and Pt mesh as a counter one. The impedance spectra and polarization curves were processed using the ZView® and CView® programs, respectively (Scribner, USA).

Results and Discussion

The thickness of the resulting coatings for all samples was 15 ± 2 μm. The weight gain for the MA8-PEO-LDH sample was equal to 0.8 mg compared to MA8-PEO, and for the sample impregnated with the inhibitor, the weight gain was equal to 0.4 mg compared to MA8-PEO-LDH. For samples with PEO-coating containing LDH, a change in the color of the coating was noted. The original PEO-coating was white, PEO-coating with inhibitor free LDH was yellow. The color of the MA8-PEO-LDH coating did not change when treated with an inhibitor.

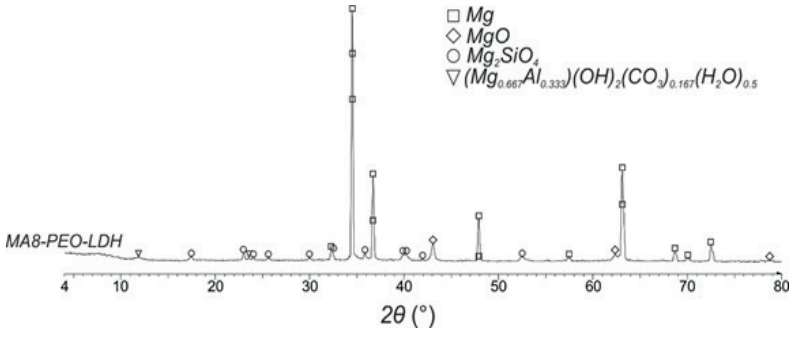

Fig. 1. XRD patterns of MA8, MA8-PEO, MA8-PEO-LDH samples

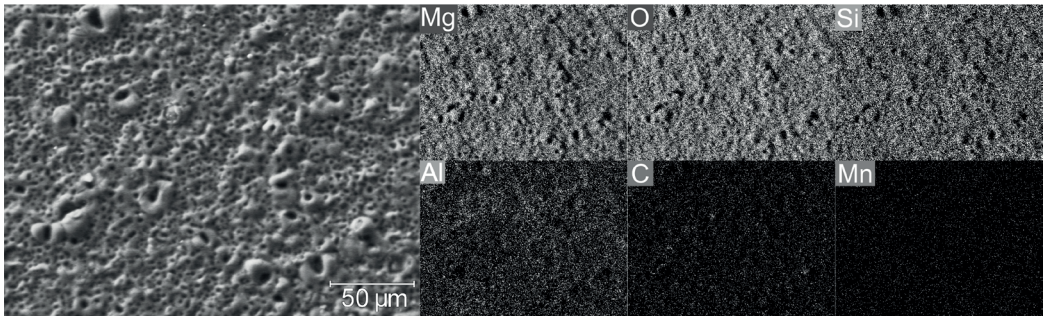

Fig. 2. SEM image and EDX maps of the MA8-PEO-LDH

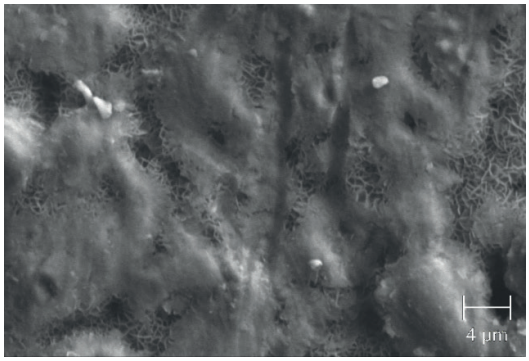

Fig. 3. SEM image of the MA8-PEO-LDH

The XRD patterns (Fig. 1) and EDX maps of the distribution of elements (Fig. 2) indicate the formation of the layered double hydroxide (Mg-Al-LDH) phase $(Mg_{0.667}Al_{0.333})(OH)_2(CO_3)_{0.167}(H_2O)_{0.5}$. The main phases of the base PEO-coating such as (Mg, MgO (periclase), Mg_2SiO_4 (forsterite)) are presented in the MA8-PEO-LDH sample. The element composition of the sample is as follows (wt.%): O, 46.0; Mg, 26.6; C, 15.1; Si, 7.8; Al, 3.2; Na, 1.3.

The surface morphology of MA8-PEO-LDH is shown in the SEM image (Fig. 2). This protective layer has a structure, which is typical for PEO-coating. According to the EDX maps, one can note the homogeneity of the distribution of Mg, Si, O in the PEO-coating. Aluminum is also homogeneously distributed over the sample surface (3.2 wt.%). This means that the process of formation of the LDH was successful. The high-resolution SEM image (Fig. 3) of the LDH-containing PEO-coating shows areas with a lamellar structure, which corresponds to LDH, that is in accordance with [3, 12, 20, 25]. It should also be noted that not whole PEO-coating was covered with LDH crystallites, since PEO-coating structure was detected among the LDH. Fig. 3 shows that LDH formation was mainly occurred in porous part of the PEO-layer.

Table 1

Electrochemical characteristics of the samples in 3.5% NaCl

Sample	β_a, mV	β_c, mV	E_c, mV, vs Ag/AgCl	I_c, mA/cm^2	R_p, Ω·cm^2	$\lvert Z\rvert_{f=0.1Hz}$, Ω·cm^2
MA8	43.3	169.9	–1512.2	16.67	$8.7\cdot10^2$	$6.7\cdot10^2$
MA8-PEO	97.2	251.6	–1411.2	0.41	$7.4\cdot10^4$	$8.4\cdot10^3$
MA8-PEO-LDH	135.3	543.7	–1422.2	0.35	$1.4\cdot10^5$	$1.7\cdot10^4$
MA8-PEO-LDH-oleat	44.9	267.6	–1391.8	0.26	$1.7\cdot10^5$	$2.1\cdot10^5$

Notations: β_a, β_c, E_c, I_c, R_p, $|Z|_{f=0.1Hz}$ are the anodic and cathodic slope of Tafel curves, corrosion potential, corrosion current density, polarization resistance and impedance modulus at 0.1 Hz, respectively.

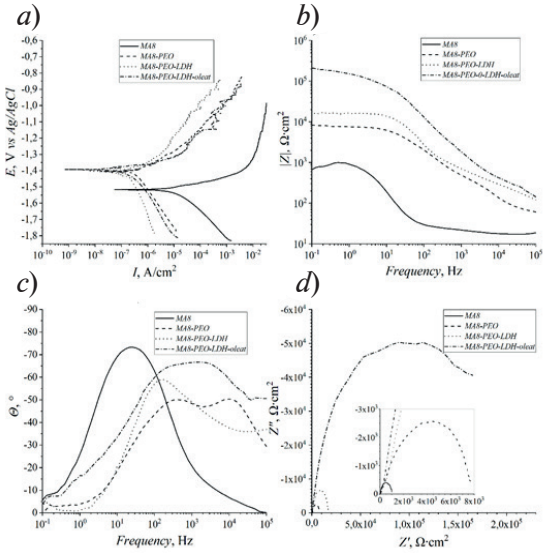

Fig. 4. Potentiodynamic curves (*a*); impedance spectra of MA8 samples with and without coatings; Bode plots (dependence of impedance modulus $|Z|$ (*b*) and phase angle θ (*c*) on frequency); Nyquist plots (*d*) (dependence of the imaginary part of the impedance Z'' on the real part of the impedance Z')

The analysis of the potentiodynamic polarization curves (Fig. 4, *a*) shows a shift in the corrosion potential to the positive direction for coated MA8 samples. The curves for MA8 with different types of protective coatings lies in the same region. A decrease in the corrosion current density indicates a positive effect of LDH formation on the surface of PEO-layer. The results of electrochemical impedance spectroscopy (Fig. 4, *b*, *c*, *d*) show high protective properties of the LDH-containing coatings. The analysis of the Bode plot clearly shows the positive effect of the presence of LDH in the structure of the protective coating, an increase in impedance modulus is noted over the entire frequency range. Treatment with sodium oleate also increases the impedance values as compared to the specimen with inhibitor free LDH-containing coating. The electrochemical characteristics of MA8 alloy sample with and without protective coatings are presented in Table 1.

Conclusion

The Mg-Al-LDH was formed on the PEO-coating containing MgO and Mg_2SiO_4 using hot solution treatment. The obtained LDHs have a positive effect on the stability of the coating obtained by the PEO method in the corrosive environment. The impedance modulus measured at the lowest frequency (0.1 Hz) resistance was increased as compared to one for sample without coating. The corrosion current density decreased after forming a 'smart coating' on MA8 Mg alloy. Inhibitor treatment also improves the corrosion resistance of the protective coating. This work allows us to suggest the effective way of self-healing coating formation on the surface of PEO-treated magnesium alloy.

Acknowledgments

Electrochemical measurements and coating formation were supported by the Grant of Russian Science Foundation, Russia (project no. 21-73-10148, https://rscf.ru/en/project/21-73-10148/). The study of material`s structure and composition were supported by the Grant of Russian Science Foundation, Russia (project no. 20-13-00130, https://rscf.ru/en/project/20-13-00130/).

REFERENCES

1. **Nazeer F., Long J., Yang Z., Li C.,** Superplastic deformation behavior of Mg alloys: A-review, Journal of Magnesium and Alloys. 10 (1) (2022) 97–109.

2. **Xu W., Birbilis N., Sha G., Wang Y., Daniels J.E., Xiao Y., Ferry M.,** A high-specific-strength and corrosion-resistant magnesium alloy, Nature Materials. 14 (12) (2015) 1229–1235.

3. **Guo L., Wu W., Zhou Y., Zhang F., Zeng R., Zeng J.,** Layered double hydroxide coatings on magnesium alloys: A review, Journal of Materials Science & Technology. 34 (9) (2018) 1455–1466.

4. **Gnedenkov A.S., Lamaka S. V., Sinebryukhov S.L., Mashtalyar D. V., Egorkin V.S., Imshinetskiy I.M., Zavidnaya A.G., Zheludkevich M.L., Gnedenkov S.V., Electrochemical** behaviour of the MA8 Mg alloy in minimum essential medium, Corrosion Science. 168 (2020) 108552.

5. **Gnedenkov A.S., Sinebryukhov S.L., Filonina V.S., Egorkin V.S., Ustinov A.Y., Sergienko V.I., Gnedenkov S.V.,** The detailed corrosion performance of bioresorbable Mg-0.8Ca alloy in physiological solutions, Journal of Magnesium and Alloys. 10 (5) (2022) 1326–1350.

6. **Kozlov I.A., Vinogradov S.S., Tarasova K.G., Kulyushina N.V., Manchenko V.A.,** Plasma electrolytic oxidation of magnesium alloys (review), Aviation materials and technologies. 54 (1) (2019) 23–36.

7. **Mamayev A.I., Ramazanova Zh.M., Savelyev Yu.A., Butyagin P.I.,** Coating method for valve metals and their alloys. Pat. 2077612 Russian Federation, MPK6 C 25 D 11/02.; applicant and patentee Mamayev Anatoliy Ivanovich. № 93044630/02; appl. 14.09.93; publ. 20.04.97. 6 p.

8. **Gnedenkov A.S., Sinebryukhov S.L., Mashtalyar D. V., Vyaliy I.E., Egorkin V.S., Gnedenkov S.V.,** Corrosion of the welded aluminium alloy in 0.5 M NaCl solution. Part 1: Specificity of development, Materials. 11 (10) (2018) 2053.

9. **Gnedenkov A.S., Sinebryukhov S.L., Mashtalyar D. V., Vyaliy I.E., Egorkin V.S., Gnedenkov S.V.,** Corrosion of the Welded Aluminium Alloy in 0.5 M NaCl Solution. Part 2: Coating Protection, Materials. 11 (11) (2018) 2177.

10. **Gnedenkov A.S., Lamaka S. V., Sinebryukhov S.L., Mashtalyar D. V., Egorkin V.S., Imshinetskiy I.M., Zheludkevich M.L., Gnedenkov S.V.,** Control of the Mg alloy biodegradation via PEO and polymer-containing coatings, Corrosion Science. 182 (2021) 109254.

11. **Yarovaya T.P., Nedozorov P.M.,** Method for obtaining wear-resistant coatings on aluminum alloys. Pat. 2764535 Russian Federation, MPK6 C 25 D 11/06.; applicant and patentee FBIS ICh FEB RAS. № 2021106412; appl. 11.03.2021; publ. 18.01.2022, Byul. № 2. 9 p.

12. **Bouali A.C., Serdechnova M., Blawert C., Tedim J., Ferreira M.G.S., Zheludkevich M.L.,** Layered double hydroxides (LDHs) as functional materials for the corrosion protection of aluminum alloys: A review, Applied Materials Today. 21 (2020) 100857.

13. **Reisch M.S.,** Confronting the looming hexavalent chromium ban, Chemical & Engineering News. 95 (9) (2017) 28–29.

14. **Tabish M., Zhao J., Wang J., Anjum M.J., Qiang Y., Yang Q., Mushtaq M.A., Yasin G.,** Improving the corrosion protection ability of epoxy coating using CaAl LDH intercalated with 2-mercaptobenzothiazole as a pigment on steel substrate, Progress in Organic Coatings. 165 (2022) 106765.

15. **Rodriguez J., Bollen E., Nguyen T.D., Portier A., Paint Y., Olivier M.G.,** Incorporation of layered double hydroxides modified with benzotriazole into an epoxy resin for the corrosion protection of Zn-Mg coated steel, Progress in Organic Coatings. 149 (2020) 105894.

16. **Huang M., Lu G., Pu J., Qiang Y.,** Superhydrophobic and smart MgAl-LDH anti-corrosion coating on AZ31 Mg surface, Journal of Industrial and Engineering Chemistry. 103 (2021) 154–164.

17. **Song S., Yan H., Cai M., Huang Y., Fan X., Cui X., Zhu M.,** Superhydrophobic composite coating for reliable corrosion protection of Mg alloy, Materials & Design. 215 (2022) 110433.

18. **Gnedenkov A.S., Filonina V.S., Sinebryukhov S.L., Sergiyenko V.I., Gnedenkov S.V.,** Hybrid polymer-containing coatings impregnated with a corrosion inhibitor for the protection of bioresorbable magnesium implants, Vestnik DVO RAN. 5 (2021) 56–64.

19. **Dong Y., Wang F., Zhou Q.,** Protective behaviors of 2-mercaptobenzothiazole intercalated Zn–Al-layered double hydroxide coating, Journal of Coatings Technology and Research. 11 (5) (2014) 793–803.

20. **Kuang Y., Zhao L., Zhang S., Zhang F., Dong M., Xu S.,** Morphologies, Preparations and Applications of Layered Double Hydroxide Micro-/Nanostructures, Materials. 3 (12) (2010) 5220–5235.

21. **Evans D.G.,** Structural aspects of layered double hydroxides Berlin/Heidelberg: Springer-Verlag, 2005.

22. **Nestroynaya O.V., Ryltsova I.G., Yapryntsev M.N., Lebedeva O.Ye.,** Influence of the method of synthesis of layered double hydroxides on their phase composition and magnetism, Neorganicheskiye materialy. 56 (7) (2020) 788–795.

23. **Poznyak S.K., Tedim J., Rodrigues L.M., Salak A.N., Zheludkevich M.L., Dick L.F.P., Ferreira M.G.S.,** Novel inorganic host layered double hydroxides intercalated with guest organic inhibitors for anticorrosion applications, ACS Applied Materials and Interfaces. 1 (10) (2009) 2353–2362.

24. **Chen J., Fang L., Wu F., Xie J., Hu J., Jiang B., Luo H.,** Corrosion resistance of a self-healing rose-like MgAl-LDH coating intercalated with aspartic acid on AZ31 Mg alloy, Progress in Organic Coatings. 136 (2019) 105234.

25. **Tedim J., Poznyak S.K., Kuznetsova A., Raps D., Hack T., Zheludkevich M.L.,** Ferreira M.G.S., Enhancement of active corrosion protection via combination of inhibitor-loaded nanocontainers, ACS Applied Materials and Interfaces. 2 (5) (2010) 1528–1535.

26. **Guo X., Zhang F., Evans D.G., Duan X.,** Layered double hydroxide films: synthesis, properties and applications, Chemical Communications. 46 (29) (2010) 5197.

27. **Ogorodnikova V.A., Kuznetsov Yu.I., Andreyeva N.P., Chirkunov A.A.,** Adsorption of sodium oleate from alkaline solutions on oxidized magnesium, Corrosion: materials, protection. 5 (2018) 27–31.

28. **Li C.Y., Gao L., Fan X.L., Zeng R.C., Chen D.C., Zhi K.Q.,** In vitro degradation and cytocompatibility of a low temperature in-situ grown self-healing Mg-Al LDH coating on MAO-coated magnesium alloy AZ31, Bioactive Materials. 5 (2) (2020) 364–376.

29. **Paulhiac J.L.,** Clause O., Surface coprecipitation of cobalt(II), nickel(II), or zinc(II) with aluminum(III) ions during impregnation of .gamma.-alumina at neutral pH, Journal of the American Chemical Society. 115 (24) (1993) 11602–11603.

30. **Liu J., Li Y., Huang X., Li G., Li Z.,** Layered Double Hydroxide Nano- and Microstructures Grown Directly on Metal Substrates and Their Calcined Products for Application as Li-Ion Battery Electrodes, Advanced Functional Materials. 18 (9) (2008) 1448–1458.

THE AUTHORS

NOMEROVSKII Aleksei D.
nomerovskii.ad@outlook.com
ORCID: 0000-0002-3118-5971

SINEBRYUKHOV Sergey L.
sls@ich.dvo.ru
ORCID: 0000-0002-0963-0557

GNEDENKOV Andrey S.
asg17@mail.com
ORCID: 0000-0002-9822-7849

GNEDENKOV Sergey V.
svg21@hotmail.com
ORCID: 0000-0003-1576-8680

Received 21.05.2022. Approved after reviewing 07.07.2022. Accepted 09.07.2022.

Conference materials
UDC 667.6
DOI: https://doi.org/10.18721/JPM.153.134

Anti-icing composite fluoropolymer coatings on titanium

E. A. Belov [1]✉, K. V. Nadaraia [1], D. V. Mashtalyar [1],
S. L. Sinebryukhov [1], S. V. Gnedenkov [1]

[1] Institute of Chemistry FED RAS, Vladivostok, Russia
✉ belov_eal@mail.ru

Abstract. Developing anti-icing coatings is an important topic for many scientists. In this work, we describe composite coatings prepared by a combination of plasma electrolytic oxidation and deposition of polytetrafluoroethylene from suspension. The composite layers obtained had high strength and adhesion to metal, which made it possible to use them in extreme environmental conditions. The change in the adhesion strength of ice to the coating surface was considered with various methods for forming composite layers on the surface of the metal and compared with the base PEO layer. The wettability of the resulting coatings as well as the relationship between the contact angle and the ice adhesion strength were evaluated.

Keywords: titanium, anti-icing coatings, protective coatings, composite coatings, plasma electrolytic oxidation, F4-d, superdispersed polytetrafluoroethylene

Funding: Formation of composite coatings and adhesion tests of ice to the surface were carried out within the framework of the RFBR grant (project no. 19-29-13020 mk). Studies of the wetting of the obtained coatings were carried out under Government Assignments of the Ministry of Science and Higher Education of the Russian Federation no. FWFN-2021-0003.

Citation: Belov E. A., Nadaraia K. V., Mashtalar D. V., Sinebryukhov S. L., Gnedenkov S. V., Anti-icing composite fluoropolymer coatings on titanium, St. Petersburg State Polytechnical University Journal. Physics and Mathematics. 15 (3.1) (2022) 204–209. DOI: https://doi.org/10.18721/JPM.153.134

Материалы конференции
УДК 667.6
DOI: https://doi.org/10.18721/JPM.153.134

Противообледительные композиционные фторполимерные покрытия на титане

Е. А. Белов [1]✉, К. В. Надараиа [1], Д. В. Машталяр [1],
С. Л. Синебрюхов [1], С. В. Гнеденков [1]

[1] Институт химии ДВО РАН, Владивосток, Российская Федерация
✉ belov_eal@mail.com

Аннотация. Разработка способов снижения образования льда на различных конструкциях представляет большой научный и практический интерес. В данной работе рассмотрено использование композиционных покрытий, полученных комбинацией методов плазменно-электролитного оксидирования и осаждения политетрафторэтилена из суспензий. Полученные композитные слои обладают высокой прочностью и адгезией к металлу, что позволяло использовать их в экстремальных условиях. В работе рассмотрено изменение прочности сцепления льда с поверхностью покрытий при различных способах формирования композиционных слоев на поверхности металла

и проведено сравнение с базовым ПЭО-слоем. Оценена смачиваемость полученных покрытий водой, а также взаимосвязь между контактным углом и прочностью сцепления льда с покрытием.

Ключевые слова: титан, антиобледенительные покрытия, защитные покрытия, композиционные покрытия, плазменное электролитное оксидирование, ультрадисперсный политетрафторэтилен

Финансирование: Формирование композиционных покрытий и исследование прочности адгезии льда с поверхностью выполнены в рамках гранта РФФИ (проект № 13020-29-19 мк). Изучение взаимосвязи смачиваемости полученных покрытий с их морфологией и составом проводились в рамках государственного задания Министерства науки и высшего образования Российской Федерации, Россия (проект № FWFN-2021-0003).

Ссылка при цитировании: Белов Е. А., Надараиа К. В., Машталяр Д. В., Синебрюхов С. Л., Гнеденков С. В. Противообледительные композиционные фторполимерные покрытия на титане // Научно-технические ведомости СПбГПУ. Физико-математические науки. 2022. Т. 15. № 3.1. С. 204–209. DOI: https://doi.org/10.18721/JPM.153.134

Introduction

Ice accretion is one of the main problems that arise during operation of various equipment in the coastal regions of the Far North and in winter [1–3]. It leads to many problems that can cause the loss and destruction of equipment. Increased mass of the structure is one of the main problems for ships and aircraft, consequently increasing the consumption of fuel, and potentially leading to complete breakdown of equipment due to large quantities of ice. Furthermore, as water penetrates into cracks and surface defects, they expand, grow and violate the integrity of the structure, which can also cause breakdowns and even destruction under operating conditions.

The body of research on preventing the formation of ice on the surface of metal structures has accumulated as interest grew towards oil fields located in the Arctic Ocean. The conditions under which mining is carried out contribute to ice formation on the surface of structures. To protect ships, aircraft and mining structures, various anti-icing coatings were developed.

Most studies aimed at obtaining anti-icing coatings are associated with the formation of hydrophobic layers on the surface with high contact angles and low contact angle hysteresis [2–7]. This is ensured by the formation of a developed surface structure with the formation of micro- and nanoscale irregularities, which make it possible to achieve a superhydrophobic surface. However, at low ambient temperatures, with constant contact with a supercooled drops of water in the air, an ice can form at developed surface. That leads to damage to the structure and loss of the original superhydrophobic and anti-icing properties. At the same time, attempts to remove this ice from the surface can lead to further damage to a layer up to its detachment from the substrate.

To prevent this destructive process, it is necessary to change the principles underlying the formation of protective surfaces. Since one of the main problems observed when using protective coatings is the surface structure developing that ice can very easily adhere to, producing a flat and smooth surface which reduces the level of ice contact with the material. Fabricating smooth coatings is a more technologically simple method of forming anti-icing coatings, which also produces surfaces with high anti-corrosion properties through isolating the substrate from the environment with a strong surface layer. Nevertheless, for a better level of surface anti-icing, the protective layer had to be made of a material with strong hydrophobic properties, such as polytetrafluoroethylene [8, 9].

In this work, a protective composite coating was formed on the commercially pure titanium VT1-0 using polytetrafluoroethylene [8, 9]. To form composite layers, two types of fluoropolymer suspensions were used: commercial suspension F4-d and isopropanol suspension of superdispersed polytetrafluoroethylene (SPTFE). Changes in the adhesion strength of ice to the surface depending on the processing method and processing conditions were considered.

Materials and Methods

Commercially pure titanium VT1-0 (98.6% Ti, 1.4 % impurities) was used as the substrate material for manufacturing the samples. The dimensions of the samples were 50×50×1 mm^3. Before coating, the samples were subjected to mechanical processing with sandpaper with a decrease in abrasive grain size to 30 μm. The samples were then washed with deionized water and alcohol using an ultrasonic bath for 5 min.

The coating was formed by plasma electrolytic oxidation in a phosphate electrolyte containing 25 g/l sodium phosphate (Na_3PO_4). The process was carried out in two stages using a potentiodynamic mode. In the first stage, the potentiodynamic voltage changed from 80 to 300 V, at a rate of 1.83 V/s. In the second one, the voltage was decreased from 300 to 240 V, at a rate of 0.1 V/s. During the process, the electrolyte temperature was maintained at a level of about 16 °C using a ChillerSmart H150-3000 cooling unit (LabTech Group, UK). After that, the samples were washed and dried in an oven at a temperature of 105 °C.

The composite coating was formed by immersion in an industrial aqueous suspension F-4d at an angle of 15° to the horizon and holding for 60 s, followed by slow withdrawal at a rate of 60 mm/min and air drying. Then the samples were subjected to heat treatment at 365 °C for 20 min. Heat treatment was carried out after each application of the fluoropolymer to obtain a smooth uniform surface of composite coating.

The second method consisted in vertical immersion of the samples with base PEO-coating in an alcohol suspension with SPTFE concentration 15% for 10 s, after which they were removed and dried in air. Samples with deposited polymer were etched for heat treatment in an oven at 315 °C for 15 min.

Samples with composite coatings formed with both polymers were processed from 1 to 3 times.

Samples subjected to plasma electrolytic oxidation will be referred to as the Basic PEO layer. Samples with composite coatings receive the designation SS with the designations of one- (1*X*), two- (2*X*) and three-fold (3*X*) application of fluoropolymer materials and an indication of the source of the material for application: commercial suspension (F-4d), and suspension of superdispersed polytetrafluoroethylene (SPTFE).

To determine the ice adhesion to the surface the shear test was carried out. An ice column of deionized water 30 mm in diameter and 7 ml in volume was formed on the surface of the sample at a temperature of −10 °C. After that, the sample with the formed column was fixed in on a rigid frame and, under constant cooling, an increasing load was exerted on the column with a rod with a diameter of 5 mm at 1 mm from the sample surface using an AG-Xplus Universal Testing Machine (Shimadzu, Japan). At the moment of ice shear, the obtained load values were recorded and compared with those obtained for the base PEO-layer.

The wettability of the coatings was studied by the sessile drop method using a DSA-100 (Krьss, Germany). The sessile drop method measures the optical contact angle (CA) and is used to evaluate the wetting properties of a localized region of a solid surface. Distilled water was used as the test liquid. To take into account the gravitational distortions of the contour of a drop under its own weight, the Young−Laplace method was used in this work when calculating the contact angle.

Results and Discussion

The base PEO-coating formed on titanium has high hydrophilic properties, which are due to their composition (titanium dioxide) and a developed surface, on which the pores and micron size defects, due to which a capillary effect occurs, are presented. Due to this, during icing, the base PEO-layer is easily covered with a thick layer of ice. At the same time, during the formation of ice, the volume of water, that has penetrated into the pores and defects, expands, causing the formation of larger cracks, ruptures and undermining the PEO-layer. During shear, the cracked parts of the PEO-coating will finally break (Fig. 1), removing not only the ice column, but also part of the protective coating. This is the reason for such a high adhesion strength of ice to the surface, which can be observed in Table 1.

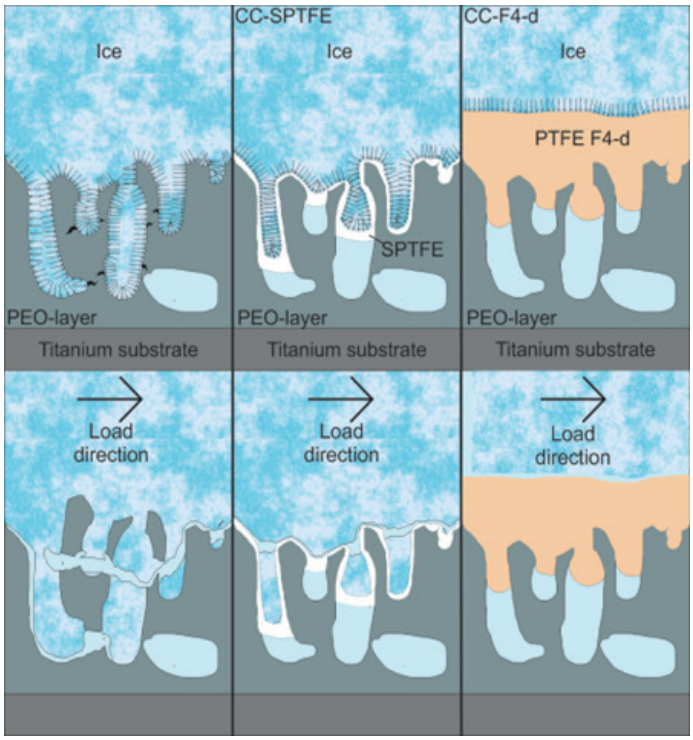

Fig. 1. Schematic representation of ice adhesion to various types of coatings

Comparing the adhesion strength of the ice to the base PEO-layer and composite coatings of the two types, we can trace noticeable changes even after a single application. Thus, for composite coatings obtained using SPTFE, the ice adhesion strength to the coating decreased by more than 4 times compared the sample with base PEO-coating. This was due to the change in the level of interaction between water and the surface. Due to the hydrophobicity of PTFE, fewer spots are available for the ice formation, which reduces the ice adhesion to the coating. However, the adhesion strength is still high due to presence of open pores and defects in the coating, forming cavities and irregularities to which the ice can still adhere (Fig. 1). The processing of composite coatings with SPTFE affects the change in the adhesion force of ice to the surface. Triple application of polytetrafluoroethylene on the base PEO-coating reduces the ice adhesion strength to the surface by 6 times. This is due to penetration of PTFE into the pores and defects of the coating. This decrease is the result of obtaining smooth surface with small amount of defects compared to the PEO-coating or composite coatings obtained with single and double treatment with SPFTE (Table 1).

Table 1

Strength of ice adhesion to the surface of samples for different processing methods

Coating	Ice adhesion strength (kPa)
Base PEO-layer	653
CC-1X–F-4d	27
CC-2X–F-4d	17
CC-3X–F-4d	5
CC-1X–SPTFE	157
CC-2X–SPTFE	111
CC-3X–SPTFE	107

Table 2

Changes in contact angle depending on processing

Processing type	Contact angle (°)
Base PEO-layer	72.2
CC-1X–F-4d	115.7
CC-2X–F-4d	114.6
CC-3X–F-4d	111.3
CC-1X–SPTFE	98.2
CC-2X–SPTFE	141.2
CC-3X–SPTFE	137.1

At the same time, composite coatings formed using the commercial suspension F-4d have an even lower ice adhesion strength between to the surface. This is caused by the formation of a more uniform and smoother fluoropolymer film on the surface, which closes pores and defects, and evens out most of the irregularities on the coating surface providing fewer contact points. This reduces the ice adhesion strength to the coating by more than 20 times. Further observation and evaluation of the adhesion strength of the coating to the surface showed that a single application does not provide the most uniform distribution of the polymer over the surface. There are still some defects that the ice can catch on. Further processing of the composite coating makes it possible to obtain a more uniform distribution of the polymer over the coating, which reduces the adhesion force of ice to the surface by more than two orders of magnitude in comparison with base PEO-layer.

The wettability of the obtained coatings is an important indicator of ice adhesion probability since they are in close contact with water. Depending on wettability, the composite coatings have a certain chance to prevent ice growth. However, as can be seen from the values in Table 2, the ice adhesion in the event of ice formation also depends on which contact angle provides the coating.

Analyzing the wettability of the PEO-layer, we established that the coating possesses hydrophilic properties (Table 2). Because of this, water actively interacts with the coating and penetrates into the pores of the layer. In the process of water freezing and ice is formed, the ice is locked and fixed on the surface due to a large number of pores and defects, which leads to the high of ice adhesion.

However, it should be noted that there is no direct correlation between the wettability of the composite coatings and the ice adhesion to their surface (Table 2). Thus, the wettability of composite coatings obtained using the F-4d suspension is higher than that of the layers formed using the SPTFE suspension (Table 2). However, the latter's adhesion to the surface is much higher (Table 1). This is explained by the difference in the structure of the composite layer. Therefore, F-4d can be used to form a smooth and thick polymer film on the surface, which exhibits low hydrophobic properties. Hydrophobicity also decreases with increasing multiplicity of treatment due to increasing surface continuity. At the same time, SPTFE envelops the already existing PEO-layer surface relief, retaining most of the protrusions and irregularities that crystallizing ice can catch on during formation, which provide high wetting angles of the coating, but the presence of a fluoropolymer on the surface reduces the adhesion force of ice to the treated surface.

Thus, it can be concluded that a more important parameter in the formation of anti-icing coatings is to obtain a smooth surface with a minimum number of defects, and not to achieve high hydrophobicity or superhydrophobicity of the surface. However, low wettability as such is still an important factor in the case of a decrease in the ice adhesion to the surface of the material.

Conclusion

In the course of the work, composite coatings were obtained on commercially pure titanium VT1-0 using a 15 % alcohol suspension of SPTFE, and commercial suspension F-4d. Studies have been carried out on ice adhesion to the surface of coatings, which showed a strong decrease (by 6 times) in the ice adhesion strength to the surface for the surface layers obtained using SPTFE, and by two orders of magnitude for composite structures formed with using the commercial suspension, compared to the base PEO-layer. The wettability of the obtained surfaces was also

studied to identify the main causes affecting the ice adhesion to the surface. The resulting smooth films have the lowest strength of ice adhesion to the surface due to the small interaction between the ice and the surface, as well as the absence of any large number of surface irregularities that crystallizing ice can catch onto.

REFERENCES

1. **Barabadi A., Garmabaki A.H.S., Zaki R.,** An icing risk index for Arctic Offshore, Cold Regions Science and Technology. 124 (2016) 77–78.

2 **Wu Q., Xu H., Pei B., Wei Y.,** Conceptual design and preliminary experiment of icing risk management and protection system , Chinese Journal of Aeronautics. 35 (2021) 101–115.

3 **Hildebrandt S., Sun Q.**, Evaluation of operational strategies on wind turbine power production during short icing events. Journal of Wind Engineering and Industrial Aerodynamics. 219 (2021) 104795.

4 **Sultana K.R., Dehghani S.R., Pope K., Muzychka Y.S.,** A review of numerical modelling techniques for marine icing applications. Cold Regions Science and Technology. 145 (2018) 40–51.

5 **Koshio K., Waku T., Hagiwara Y.,** Ice-phobic glass-substrate surfaces coated with polypeptides inspired by antifreeze protein. Des surfaces de substrats de verre glaciophobes recouvertes de polypeptides inspirйes des protйines antigel. International Journal of Refrigeration. 114 (2020) 201–209.

6 **Zhang Z., Ma L., Liu Y., Ren J.**, **Hu H.,** An experimental study of rain erosion effects on a hydro-/ice-phobic coating pertinent to Unmanned-Arial-System (UAS) inflight icing mitigation. Cold Regions Science and Technology. 181 (2021) 103196.

7 **Mashtalyar D.V., Nadaraia K.V., Belov E.A., Imshinetskiy I.M., Kiryukhin D.P., Sinebryukhov S.L., Buznik V.M., Gnedenkov S.V.,** Synthesis of polymeric system based on polyethylene oxide and tetrafluoroethylene telomers to obtain films with switchable wettability. Journal of Molecular Liquids. 350 (2022) 118225.

8 **Mashtalyar D.V., Nadaraia K.V., Imshinetskiy I.M., Belov E.A., Filonina V.S., Suchkov S.N., Sinebryukhov S.L., Gnedenkov S.V.,** Composite coatings formed on Ti by PEO and fluoropolymer treatment . Applied Surface Science. 536 (2021) 14976.

9 **Mashtalyar D.V., Imshinetskiy I.M., Nadaraia K.V., Gnedenkov A.S., Sinebryukhov S.L., Ustinov A.Yu., Samokhin A.V., Gnedenkov S.V.,** Influence of ZrO_2/SiO_2 nanomaterial incorporation on the properties of PEO layers on Mg-Mn-Ce alloy. Journal of Magnesium and Alloys. 10 (2022) 513–526

THE AUTHORS

BELOV Evgeny A.
Belov_eal@mail.ru
ORCID: 0000-0001-9734-1482

NADARAIA Konstantine V.
nadaraiakv@mail.ru
ORCID: 0000-0001-7835-2231

MASHTATYAR Dmitry V.
madiva@inbox.ru
ORCID: 0000-0001-9645-4936

SINEBRUKHOV Sergey L.
sls@ich.dvo.ru
ORCID: 0000-0002-0963-0557

GNEDENKOV Sergey V.
svg21@hotmail.com
ORCID: 0000-0003-1576-8680

Received 25.05.2022. Approved after reviewing 01.07.2022. Accepted 01.07.2022.

Conference materials
UDC 667.637.2, 667.613, 620.199
DOI: https://doi.org/10.18721/JPM.153.135

Influence of SPTFE on corrosion behavior of composite coatings during salt-spray test

N. V. Izotov [1] ✉, V. S. Egorkin [1], U. V. Kharchenko [1]
I. E. Vyaliy [1], A. N. Minaev [1], S. L. Sinebryukhov [1], S.V. Gnedenkov [1]

[1] Institute of Chemistry, FEB RAS, Vladivostok, Russia
✉ nikolaj.izotov@mail.ru

Abstract: Plasma electrolytic oxidation has been used to create a sublayer on aluminum alloy to form a composite coating to improve the corrosion properties of the processed material. The evolution of protective characteristics of the resulting coatings were examined by potentiodynamic polarization during the exposure in a salt spray chamber. The absence of pittings after a 10-day test for the entire series of composite coatings on aluminum alloy confirms the high level of barrier properties of the coated samples.

Keywords: plasma electrolytic oxidation (PEO), composite coating (CC), potentiodynamic polarization, salt spray testing

Funding: The study was carried out with the financial support of the Russian Foundation for Basic Research, grant. no. 19-29-13020.

Citation: Izotov N. V., Egorkin V. S., Kharchenko U. V., Vyaliy I. E., Minaev A. N., Sinebryukhov S. L., Gnedenkov S. V. Influence of SPTFE on the corrosion behavior of composite coatings during salt-spray test, St. Petersburg State Polytechnical University Journal. Physics and Mathematics. 15 (3.1) (2022) 210–214. DOI: https://doi.org/10.18721/JPM.153.135

Материалы конференции
УДК 667.637.2, 667.613, 620.199
DOI: https://doi.org/10.18721/JPM.153.135

Влияние УПТФЭ на коррозионное поведение композиционных покрытий при испытаниях в солевом тумане

Н. В. Изотов [1] ✉, В. С. Егоркин [1], У. В. Харченко [1]
И. Е. Вялый [1], А. Н. Минаев [1], С. Л. Синебрюхов [1], С. В. Гнеденков [1]

[1] Институт химии ДВО РАН, г. Владивосток, Россия
✉ nikolaj.izotov@mail.ru

Аннотация. Плазменное электролитическое оксидирование использовали для создания подслоя на сплаве алюминия для формирования композиционного покрытия для улучшения коррозионных свойств обрабатываемого материала. Изменение защитных характеристик сформированных покрытий оценивали методом потенциодинамической поляризации в ходе проведения испытаний в камере соляного тумана. Отсутствие точечной коррозии после 10-дневного испытания для всей серии композиционных покрытий на сплаве алюминия подтверждает высокий уровень защиты, обеспечиваемый образцами с покрытиями.

Ключевые слова: плазменно-электролитическое оксидирование (ПЭО), композитное покрытие (КП), потенциодинамическая поляризация, испытания в камере соляного тумана

Финансирование: Исследование выполнено при финансовой поддержке РФФИ, проект № 19-29-13020.

Ссылка при цитировании: Изотов Н. В., Егоркин В. С., Харченко У. В., Вялый И. Е., Минаев А. Н., Синебрюхов С. Л., Гнеденков С. В. Влияние УПТФЭ на коррозионное поведение композиционных покрытий при испытаниях в солевом тумане // Научно-технические ведомости СПбГПУ. Физико-математические науки. 2022. Т. 15. № 3.1. С. 210–214. DOI: https://doi.org/10.18721/JPM.153.135

Introduction

In order to provide protection against long-term corrosion, aluminum parts are coated by various protection methods: anodizing, painting, and others. Another modern method of corrosion protection is plasma electrolytic oxidation (PEO) [1,2]. However, such oxide layers possess a porous structure. Pores could be the pathway for corrosive media to the substrate. In order to overcome this drawback, a composite coating comprising a combination of paint applied to a PEO-coating could be formed. Additionally, the paint itself could be modified by different fillers aimed at providing new functional characteristics. Examples include biofouling coatings, which advance mainly in two directions: hydrophobic fouling-release and biocide-free coatings based on siloxanes and fluoropolymers that reduce the attachment of organisms, and antifouling systems, in particular, new environmentally friendly biocides with reduced toxicity and regulated leaching rates. To modify the paint, we have used the unique fluoropolymer material, superdispersed polytetrafluoroethylene (SPTFE) [3,4,5], which is a micropackage of nanofilms. Such coatings should possess high level of corrosion protection. Salt spray testing is an accelerated corrosion test that produces a corrosive attack to coated samples in order to evaluate the suitability of the coating. This paper reports on the evolution of electrochemical properties of a composite coating formed by spray coating of the PEO layer with the paint modified by SPTFE during salt spray testing.

Materials and Methods

Rectangular plates of the $AlMg_3$ aluminum alloy with size of the 50 mm×50 mm×2 mm were used for the experiments. all samples were subsequently ground with SiC sand papers from 120 to 1200 grit, washed with distilled water, air dried and degreased with alcohol.

Plasma electrolytic oxidation (PEO) is an electrochemical surface treatment process for generating oxide coatings on valve metals. Process of PEO was carried out in the electrolyte, containing 20 g/L $Na_2SiO_3 \cdot 5H_2O$, 10 g/L $Na_2B_4O_7 \cdot 10H_2O$, 2 g/L NaF, and 2 g/L KOH, dissolved in deionized water. All samples were processed in two stages in bipolar mode, with periodic alternation of cathodic and anodic pulses. At the first stage, the voltage in the anodic period increased from 30 to 540 V with a sweep rate of 3.4 V/s, and then the voltage value was fixed at 540 V for 750 s. In the cathodic period, the current was held at 6.5 A for 900 s. The duty cycle was equal to 1. The presented electrolyte composition and mode parameters allowed us to obtain thick surface layers with a developed surface [1].

On the formed PEO coating, 5 types of paints were applied by spraying. Jotun SeaForce 30 was chosen for modification. SPTFE was added to this paint in different concentrations from 0 to 20 wt.%. As a result, 5 composite coatings were obtained for further study.

Morphology of surface was investigated by a field emission scanning electron microscope (SEM) Sigma 300 VP (Carl Zeiss, Germany).

The electrochemical properties of the coatings were investigated using the VersaSTAT MC electrochemical system (Princeton Applied Research, USA). The measurements were carried out in a three-electrode cell at room temperature in a 3% NaCl solution. A platinum-coated niobium mesh was used as a counter electrode, and a calomel electrode was used as a reference electrode. The working area of the sample was 1 cm^2. To establish the corrosion potential E_C the samples were kept in a solution for 30 min. Potentiodynamic measurements were carried out with a sweep rate of 1 mV/s.

Salt spray tests [5, 6, 7] were carried out in a salt spray chamber according to GOST 30630.2.5-2013. 5% solution NaCl was sprayed for 15 min every 45 min. The temperature in the S120 salt spray chamber (Ascott Analytical Equipment Ltd, UK) was maintained at 27 ± 2 °C. The duration of the test was 10 days with an intermediate analysis after 4 days of exposure. Coatings were rinsed by deionized water and dried at room temperature for 120 min.

Results and Discussion

The morphology of the PEO coating and composite coatings is shown in Fig. 1.

Analysis of the surface morphology of the coatings (Fig. 1), the following can be noted: PEO coating has porous and convoluted morphology, which ensure stable adhesion with paint, sprayed paint without the addition of SPTFE and with 5% SPTFE has the same morphology, subsequent increase in the concentration of SPTFE leads to appearance of a large number of depressions, which, when the concentration of SPTFE is brought to 15%, begin to combine.

The formed PEO coating has a thickness of 45±5 μm (Fig. 2). The application of a paint on a PEO coating resulted in an increase in the coating thickness to 120±12 μm. Fig. 2 shows that paint fills the pores of the formed PEO coating.

The electrochemical characteristics of the studied samples were evaluated by potentiodynamic polarization. The polarization curves taken for the samples under study are presented in Fig. 3.

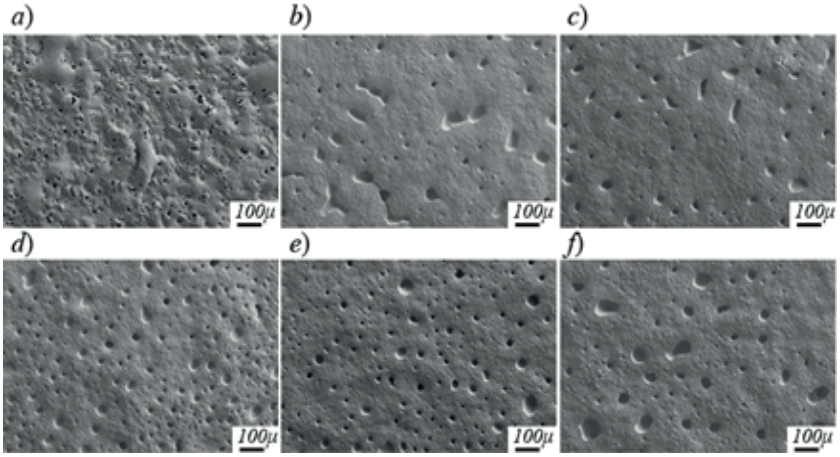

Fig. 1. Morphology of the studied coatings: PEO-coating (*a*), CC without SPTFE (*b*), CC with 5% SPTFE (*c*), CC with 10% SPTFE (*d*), CC with 15% SPTFE (*e*), CC with 20% SPTFE (*f*)

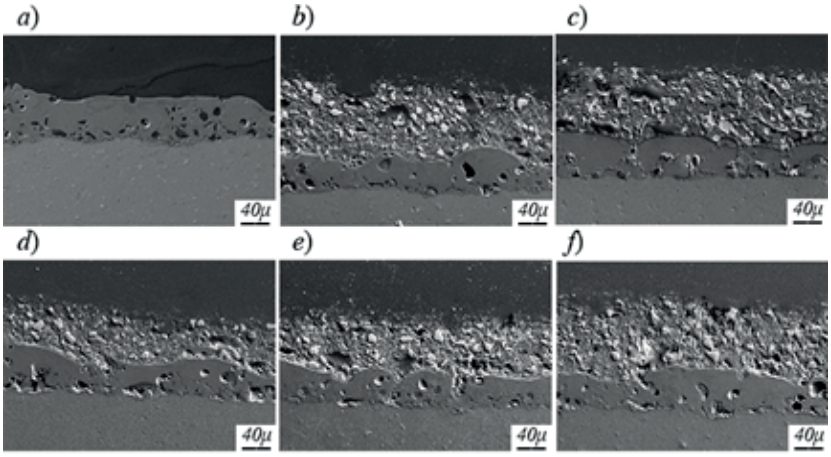

Fig. 2. Morphology of the studied coatings (sections): PEO-coating (*a*), CC without SPTFE (*b*), CC with 5% SPTFE (*c*), CC with 10% SPTFE (*d*), CC with 15% SPTFE (*e*), CC with 20% SPTFE(*f*)

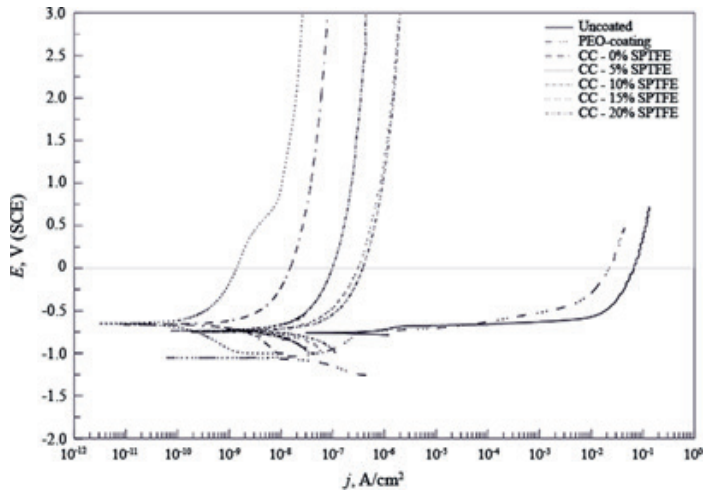

Fig. 3. Potentiodynamic polarization curves for the studied samples taken in 3% NaCl

Analysis of the data in Fig. 3 showed that all protective coatings have a lower corrosion current density compared to pure aluminum $AlMg_3$ ($3.47 \cdot 10^{-7}$). Composite coatings also showed increased barrier properties compared to PEO coatings ($4.80 \cdot 10^{-8}$). The lovest value of corrosion current density was demonstrated by the CC with the addition of 5% SPTFE to the paint ($1.88 \cdot 10^{-10}$). Relative to this CC, in both directions there is an increase in y by an order of magnitude without SPTFE in the coating ($1.56 \cdot 10^{-9}$) and with 10% SPTFE in the coating ($2.79 \cdot 10^{-9}$). A further increase in the concentration of SPTFE leads to another increase in the corrosion current density by one order of magnitude ($1.19 \cdot 10^{-8}$ for 15%, $1.95 \cdot 10^{-8}$ for 20%).

The appearance of the samples during testing changed as the aluminum alloy became covered with a corrosive film, the PEO coating became darker (initially light gray) due to water uptake but without visible corrosion damage, and the composite coatings remained unchanged.

Fig. 4 shows the bar graph with a change in the corrosion current density depending on the exposure time in the salt spray chamber.

It follows from analysis of the obtained electrochemical parameters that the sample with a composite coating with 5% SPTFE has the best characteristics. Fig. 4 shows that the corrosion current density did not change significantly over 10 days for this sample. The same changes are observed in the sample with a composite coating without SPTFE, but this coating initially has an order of magnitude higher corrosion current density (see Fig. 3). The remaining composite coatings have, on average, an increase in the corrosion current density by one order of magnitude (for a concentration of 10% SPTFE, it is slightly less, for a concentration of 20% SPTFE, more than one order of magnitude). We can assume from analyzing Fig. 4 that the barrier properties of the paint, with and without the addition of SPTFE, decrease with increasing exposure time in the salt spray chamber. However, due to the unchanged morphology with the addition of 5% SPTFE, it could be assumed that this coating will have better characteristics among the presented coatings and will be capable of withstanding approximately 30 days of exposure.

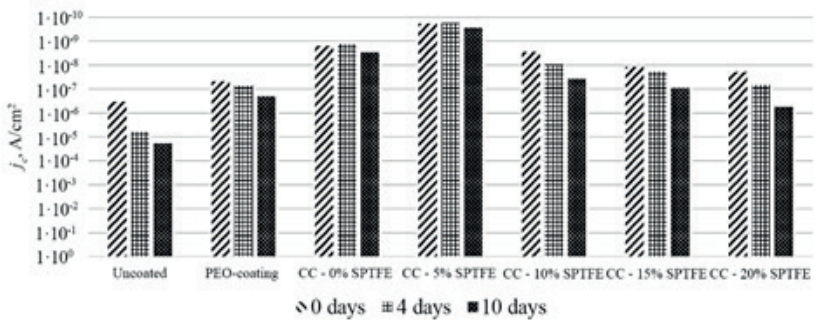

Fig. 4. Corrosion current density vs. exposure time in the salt spray chamber

Conclusion

As a result of the performed study, it was found that adding 5% of SPTFE to paint leads to a significant increase of the protective properties. Thus, the value of corrosion current density for this sample is more than three, two, and one order of magnitude lower compared to the uncoated sample, PEO-coating, and unmodified CC, accordingly. Despite the fact that appearance of the CCs remained unchanged, application of potentiodynamic polarization allowed to unveil the difference in the dynamics of changes in the electrochemical parameters of coatings during exposure. These data are explained by the fact that adding a small concentration (5% SPTFE) does not lead to a change in the morphology of the coating. According to the results of microscopic study, the number of pores increases with increased concentration, at the same time the values of corrosion current increase. We can thus conclude that an increase in concentration leads to a change in the structure (appearance of defects and pores) through which the saline solution penetrates more easily into the substrate.

REFERENCES

1. **Egorkin V.S., Mashtalyar D.V., Gnedenkov A.S., Filonina V.S., Vyaliy I.E., Nadaraia K.V., Imshinetskiy I.M., Belov E.A., Izotov N.V., Sinebryukhov S.L., Gnedenkov S.V.,** Icephobic performance of combined fluorine-containing composite layers on Al-Mg-Mn-Si alloy surface, Polymers. 13(21) (2021).

2. **Friedemann A.E.R., Thiel K., Haßlinger U., Ritter M., Gesing Th M., Plagemann P., I**nvestigations into the structure of PEO-layers for understanding of layer formation, Appl Surf Sci, 443 (2018).

3. **Gnedenkov S.V., Sinebryukhov S.L., Egorkin V.S., Vyalyi I.E., Mashtalyar D.V., Nadaraia K.V., Ryabov D.K., Buznik V.M.,** Formation and properties of composite coatings on aluminum alloys, Russian journal of inorganic chemistry. 62 (1) (2017).

4. **Egorkin V.S., Vyaliy I.E., Sinebryukhov S.L., Gnedenkov S.V., Sviridov N.S., Minaev A.N.,** Formation and electrochemical properties of the hydrophobic composite coatings on aluminum alloy, Defect and Diffusion Forum. (386) (2018).

5. **Ren Hui Zhang, Juan Zhao, Jun Liangc,** A novel multifunctional PTFE/PEO composite coating prepared by one-step method, Surface and Coatings Technology. 299 (2016).

6. **Saeedikhani M., Javidi M., Yazdani A.,** Anodizing of 2024-T3 aluminum alloy in sulfuric-boric-phosphoric acids and its corrosion behavior, Trans. Nonferrous Met. Soc. China, 23 (2013).

7. **Finke A., Escobar J., Munoz J., Petita M.,** Prediction of salt spray test results of micro arc oxidation coatings on AA2024 alloys by combination of accelerated electrochemical test and artificial neural network, Surface and Coatings Technology, 421 (127370) (2021).

THE AUTHORS

EGORKIN Vladimir S.
egorkin@ich.dvo.ru
ORCID: 0000-0001-5489-6832

MINAEV Alexander N.
minaev.an@dvfu.ru
ORCID: 0000-0002-8072-306X

IZOTOV Nikolai V.
nikolaj.izotov@mail.ru
ORCID: 0000-0001-9504-1523

SINEBRYUKHOV Sergey L.
sls@ich.dvo.ru
ORCID: 0000-0002-0963-0557

KHARCHENKO Ulyana V.
ulyana-kchar@mail.ru
ORCID: 0000-0001-5166-5609

GNEDENKOV Sergei V.
svg21@hotmail.com
ORCID: 0000-0003-1576-8680

VYALIY Igor E.
igorvyal@gmail.com
ORCID: 0000-0003-3806-1709

Received 21.05.2022. Approved after reviewing 19.07.2022. Accepted 21.07.2022.

Conference materials
UDC 544.63
DOI: https://doi.org/10.18721/JPM.153.136

Composition and morphology of calcium phosphate coatings formed on resorbable substrates based on pure Mg and Mg-HAp composite

M. V. Sidorova [1] ✉, A. B. Podgorbunsky [1], M. S. Gerasimenko [1]
S. L. Sinebryukhov [1], S. V. Gnedenkov [1]

[1] Institute of Chemistry, FEB RAS, Vladivostok, Russia
✉ sidorova-01-02@rambler.ru

Abstract: We considered coatings obtained on a magnesium based substrate with a different content of a bioactive component, nanosized hydroxyapatite (HAp). The properties of coatings formed by plasma electrolytic oxidation (PEO) in electrolytes containing calcium compounds were compared. Coatings obtained in the electrolyte with HAp demonstrated higher strength characteristics compared to coatings obtained in the glycerophosphate electrolyte. It can be explained by the hardness of the components included in the coating (Mg_2SiO_4) as well as by the presence of hydroxyapatite nanoparticles. Oxidation of composite samples in an electrolyte with HAp leads to a decrease in the corrosion current density by 2 orders of magnitude compared to this parameter for uncoated samples.

Keywords: bioresorbable composite, magnesium, hydroxyapatite, PEO, adhesion

Funding: The study was funded by grant no. 22-23-00915.

Citation: Sidorova M. V., Podgorbunsky A. B., Gerasimenko M. S., Sinebryukhov S. L., Gnedenkov S. V., Composition and morphology of calcium phosphate coatings formed on pure mg and Mg-HAp composite resorbable substrates, St. Petersburg State Polytechnical University Journal. Physics and Mathematics. 15 (3.1) (2022) 215–221. DOI: https://doi.org/10.18721/JPM.153.136

Материалы конференции
УДК 544.63
DOI: https://doi.org/10.18721/JPM.153.136

Состав и морфология кальций-фосфатных покрытий, сформированных на резорбируемых подложках на основе чистого Mg и композита Mg-HAp

М. В. Сидорова [1] ✉, А. Б. Подгорбунский [1], М. С. Герасименко [1]
С. Л. Синебрюхов [1], С. В. Гнеденков [1]

[1] Институт химии ДВО РАН, г. Владивосток, Россия
✉ sidorova-01-02@rambler.ru

Аннотация. В данной работе были исследованы ПЭО-покрытия для нужд имплантационной хирургии, полученные на магнии с различным содержанием биоактивного компонента – наноразмерного порошка гидроксиапатита кальция. Было проведено сравнение свойств покрытий, сформированных методом ПЭО в электролитах, содержащих соединения кальция. Покрытия, сформированные в электролите с гидроксиапатитом, демонстрируют более высокие прочностные характеристики и антикоррозионные свойства, по сравнению с покрытиями, полученными в электролите с глицерофосфатом.

Ключевые слова: биорезорбируемый композит, магний, гидроксиапатит, ПЭО, адгезия

Финансирование: Исследование выполнено при поддержке гранта № 22-23-00915.

Ссылка при цитировании: Сидорова М. В., Подгорбунский А. Б., Герасименко М. С., Синебрюхов С. Л., Гнеденков С. В. Состав и морфология кальций-фосфатных покрытий, сформированных на резорбируемых подложках на основе чистого mg и композита Mg-ГА // Научно-технические ведомости СПбГПУ. Физико-математические науки. 2022. Т. 15. № 3.1. С. 215–221. DOI: https://doi.org/10.18721/JPM.153.136

Introduction

Over the recent decades, implant surgery has made a great leap both in the methodological approach and in the variety of materials used [1]. Stents, orthopedic implants, including plates, prostheses, screws, etc., as well as bone substitute materials, can radically differ in the requirements for strength characteristics and surface properties [2–4]. An important role in the orthopedics of cortical bones is played by the implant resorption, which, in the case of restoring the functionality of the bone, excludes secondary surgical intervention to remove it, thereby improving the quality of life and health of the patient [4–6]. Biodegradable magnesium and its alloys evincing huge potential to be used as a new class of implant materials [7, 8] due to outstanding features of biodegradation [9], antibacterial [10], osteogenesis inductivity and some other biofunctional properties [11]. Among plenty techniques aimed to reducing the corrosivity of magnesium and its alloys the plasma electrolytic oxidation (PEO) is a powerful method for application an oxide coating on the metal substrate [12], which significantly reduces the tendency of the metal to corrode and wear out. Mg-PEO-coatings can ensure a stable composition, excellent adherence to the substrate and controllable surface roughness [13]. Wherein poor bioactivity due to moderation the adsorption and reproduction of osteoblast, remaining a disadvantage [14]. Calcium phosphorus compounds (specifically, hydroxyapatite – HAp) presence can activate bioactivity of implants [15] and enhance the healing process of wound in body fluid environment. A number of approaches have been used with combined PEO technology or as a preliminary step to fabricate calcium phosphate protective coatings on the implant surface [16]. It is well known that coating morphology and properties of PEO-coating is greatly dependent on the electrolyte and polarization mode. Incorporating nanoparticles into PEO-coatings is recognized as a promising and effective method for pores filling and introducing some functional properties to PEO-coatings. In present work, a versatile approach is proposed to form a PEO-CaP composite coating on Mg-HAp composite substrate using in-situ suspending synthesized HAp nanoparticles into the basic sodium silicate electrolyte as well as an electrolyte with calcium-phosphate salts (glycerophosphate) at the stage of forming a PEO-coating. The influence of hydroxyapatite nanoparticles concentration and processing parameters on the dynamics of the growth of the coating, its morphology and composition were evaluated and studied with SEM and EDS, respectively. Evaluating the corrosion performance of the coatings was held by electrochemical impedance spectroscopy (EIS).

Materials and Methods

Magnesium powder (Mg, purity ≥99.9%, size ≤40 μm, Merck) and pre-synthesized hydroxyapatite were used as the basis for biodegradable substrate design. Hydroxyapatite nanoparticles (HAp, size ≤80 nm) were obtained by preparing an aqueous solution of $(NH_4)_2HPO_4$ (Merck) and $Ca(OH)_2$ (Merck) through gradual pouring until a suspension was formed. Aging of the suspension were followed by microwave radiation. Resulting precipitate was centrifuged, washed and then dried at 343 K overnight. The final powder was subjected to sequential screening through sieves with a mesh size of 100–75–20 μm (Cisa, Italy). Magnesium and obtained hydroxyapatite powders were mixed in ratios of 97:3 and 93:7 (wt.), dispersed in solvent (ethanol), followed by

evaporation of the solvent followed by continuous stirring. The resulting mixture as well as source magnesium powder were proceed using spark plasma sintering on an SPS-515S unit (Dr. Sinter-LABTM, Japan) at a temperature of 823 K under a constant pressure of 25 MPa at a heating rate of 373 K/min. Sintering was carried out in a graphite mold in vacuum (10−5 atm), the samples were held at the maximum temperature for 5 min and then cooled for 45 min to room temperature.

The formation of calcium-phosphate PEO-coating on magnesium samples was carried out by the PEO in various electrolytes using bipolar modes as described in our previous works [17, 18]. The composition of the electrolyte containing calcium glycerophosphate, $C_3H_7CaO_6P$ (25 g/l), NaF (5 g/l) and Na_2SiO_3 (8 g/l) described in [18]. Electrolyte containing HAp nanoparticles (20 g/l) also included sodium fluoride (5 g/l) and silicate (20 g/l) as well as sodium dodecylsulfate (used as a stabilizer) in the amount of 0.5 g/l.

The phase composition of the surface layers was determined on a Rigaku X-ray diffractometer (XRD) (SmartLab, Japan), using CuK_α-radiation. Bragg-Brentano geometry focusing was used in the 2θ angle range from 10° to 80°. Adhesive properties were studied on three samples with the same type of coating using Revetest Scratch Tester (CSM Instruments, Switzerland). The experiments were carried out at a track length of 5 mm with a gradual increase of the applied load from 1 to 30 N (Mg−7−H sample up to 60 N) using a Rockwell diamond indenter. The load, at which abrasion of the coating to the substrate occurs were determined, average value and error were calculated, the measurement error was up to 3%. The electrochemical tests were carried out using VersaSTAT MC (Princeton Applied Research, USA). EIS and potentiodynamic polarization were performed at room temperature using three-electrode K0235 Flat Cell (PAR, USA) in 0.9 wt.% NaCl solution. The platinized niobium grid was used as a counter electrode, the saturated calomel electrode (SCE) was used as a reference electrode. The area of contact of the sample with electrolyte was equal to 1 cm^2. The cross sections of the coated specimens were prepared using EpoxySet epoxy resin (NA) by cold pouring into a mold with a diameter of 30 mm, then polished using a Tegramin-25 polishing machine. The morphology of the cross sections as well as sample's surface were studied by SEM measurements (Carl Zeiss EVO 40 Series and Hitachi S5500). Element mapping by means of SEM-EDS measurements were performed by Carl Zeiss EVO 40 Series using the AZtec 3.0 SP2 program (Oxford Instruments, USA).

Results and Discussion

The properties of coatings formed by the PEO in electrolytes containing osteoinductive components: calcium glycerophosphate and hydroxyapatite were studied in the work (Table 1).

Using X-ray phase analysis, it was found that the coatings formed in the electrolyte with glycerophosphate contain Mg, MgO, $Ca_5(PO_4)_3F$, $Mg_3(PO_4)_2$, and those formed in the electrolyte with hydroxyapatite contain Mg, MgO, Mg_2SiO_4.

It has been established that the thickness of the oxide PEO-layers increases with a growth of calcium hydroxyapatite content in the composition of the substrate (Table 1). The adhesive properties of the coatings are represented by the parameter L_{C3}, which is the load at which the coating is abraded to the metal (Fig. 1). With almost the same thicknesses of the Mg−3−G and Mg−3−H-coatings, the L_{C3}

Table 1

Designation of the samples

Ca content in the substrate (wt.%)	Sample/coating thickness*, μm		
	Bare	+PEO obtained in the electrolyte	
		with glycerophosphate	with HAp
0	Mg–0	Mg–0–G / 73 ± 5	Mg–0–H / 47 ± 8
3	Mg–3	Mg–3–G / 110 ± 8	Mg–3–H / 110 ± 7
7	Mg–7	Mg–7–G / 130 ± 10	Mg–7–H / 186 ± 12

Note. The asterisk corresponds to eddy current measurements.

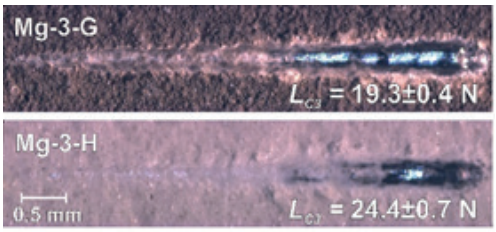

Fig. 1. Appearance of scratches on the coatings at a load of 30 N

values differ significantly and amount to 19.3 N and 24.4 N, respectively. Composition of the substrate has a great influence on the adhesion properties of coatings. In the absence of calcium phosphate compounds in the substrate composition, the adhesive properties of the Mg–0–G and Mg–0–H PEO-layers are nearly identical, despite a significant (almost 2 times) difference in thickness. The Mg–7–G-coating with the maximum content of calcium hydroxyapatite in the substrate reaches a thickness of 130 μm, while the thickness of the PEO-layer obtained in the electrolyte with HAp nanoparticles is even greater and reaches 186 μm (Mg–7–H-sample). It should be taken into account that the data obtained by the eddy current measurements are somewhat overestimated, but the analysis of SEM-images of cross sections confirms the indicated trend (see below). This effect can be associated with the electrophoretic deposition of Hap-particles during the formation of the oxide layer, which provides a significant thickness of the coating, not excluding, at the same time, the variation of the thickness. Comparing the thickness of the PEO-layers and the L_{C3} load, it can be concluded that coatings formed in the electrolyte with hydroxyapatite have higher adhesive characteristics. It can be explained with the hardness of the components including in the coating as well as HAp nanoparticles. On the Mohs scale, fluorapatite ($Ca_5(PO_4)_3F$), contained in the sample Mg–3–G has a hardness of 5, while the forsterite (Mg_2SiO_4) detected in Mg–3–H sample has a hardness value of 7.

During the formation of PEO-coatings on composites obtained by the spark plasma sintering, there are differences in the behavior of the current and voltage curves vs treatment time compared to traditional curves for wrought magnesium alloy [18]. There is an initial voltage rise with a steepness of ~1 V s^{-1}, and the slope is much smaller, while it is "smeared" over the processing time (Fig. 2). That process occurs when a barrier film forms on the surface during conventional anodizing stage and, according to the absence of a drop in the current density curves, the anodizing process continues throughout the treatment. Depending on the surface area and concentration of non-metallic additives, modes were selected as increased current density from 0.59 A/cm^2 to 0.97 A/cm^2 (Mg–0 → Mg–7).

The difference in the strength characteristics of the studied coatings is also probably associated with different surface morphology of the layers. The coatings formed in the electrolyte with hydroxyapatite have a more uniform dense structure, while the coating obtained in glycerophosphate electrolyte is characterized by a more "fungous" structure (Fig. 3).

Table 2

Corrosion properties of the uncoated/coated samples

Sample	E (V vs SCE)	I_c (A·cm^{-2})	R_p (Ω·cm^2)	$\|Z\|$ (Ω·cm^2)
Mg–0	–1.61	$1.06\cdot10^{-5}$	$1.61\cdot10^{2}$	$1.77\cdot10^{3}$
Mg–3	–1.55	$1.21\cdot10^{-5}$	$4.21\cdot10^{2}$	$3.90\cdot10^{2}$
Mg–7	–1.57	$2.88\cdot10^{-5}$	$5.67\cdot10^{2}$	$8.48\cdot10^{2}$
Mg–0–G	–1.58	$1.25\cdot10^{-6}$	$1.07\cdot10^{4}$	$1.26\cdot10^{4}$
Mg–3–G	–1.59	$9.80\cdot10^{-7}$	$2.29\cdot10^{4}$	$2.96\cdot10^{4}$
Mg–7–G	–1.57	$1.33\cdot10^{-6}$	$1.46\cdot10^{4}$	$1.33\cdot10^{4}$
Mg–0–H	–1.54	$7.37\cdot10^{-7}$	$7.06\cdot10^{4}$	$4.71\cdot10^{4}$
Mg–3–H	–1.66	$1.27\cdot10^{-7}$	$4.05\cdot10^{5}$	$3.32\cdot10^{5}$
Mg–7–H	–1.69	$6.30\cdot10^{-7}$	$1.52\cdot10^{5}$	$1.07\cdot10^{5}$

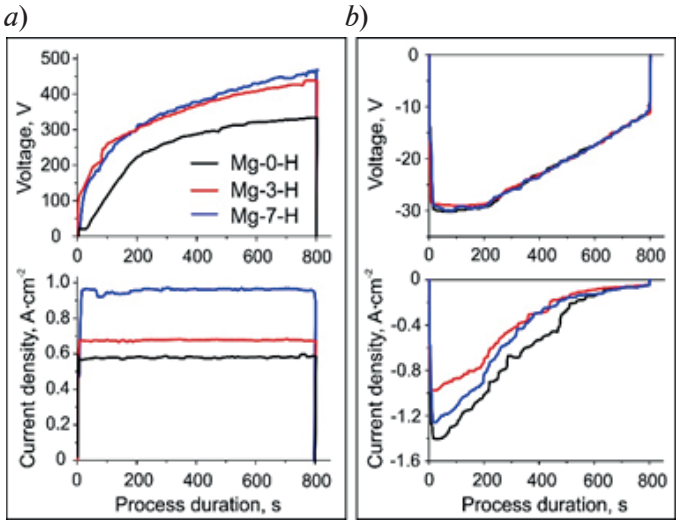

Fig. 2. Evolution of current and voltage with time for bipolar PEO-process in electrolyte with HAp; anodic (*a*) and cathodic (*b*) phases are presented separately

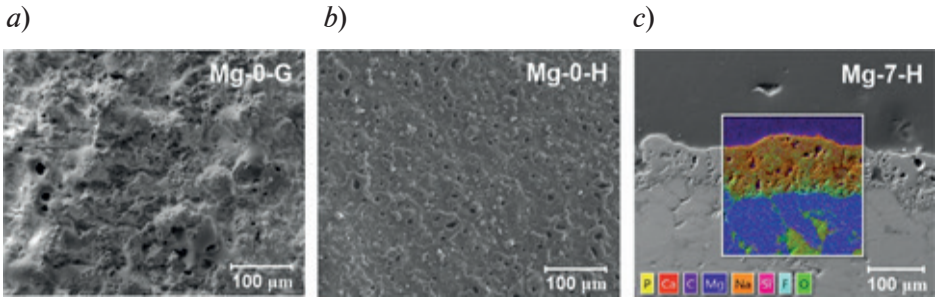

Fig. 3. SEM images of the surface of Mg-HAp composites coated with PEO, obtained in various electrolytes (*a*, *b*) and cross-section of Mg–7–H-sample (*c*)

Evaluation of the results of electrochemical studies showed that the spectra for the samples Mg–0–G, Mg–7–G on the Bode plot (impedance modulus vs frequency) exhibit the same $|Z|$ at low frequencies, while the Mg–3–G-sample shows a greater value of the impedance modulus (Fig. 4). The same trend can be traced in the values of the corrosion current density and polarization resistance (Table 2). Both PEO-coatings formed on the substrate containing 3 wt.% hydroxyapatite in two used electrolytes, demonstrated greater corrosion resistance. But the coatings obtained in an electrolyte with hydroxyapatite on the Mg–3-substrate, have a higher anticorrosion characteristic, compared to the coatings formed in the electrolyte with calcium glycerophosphate.

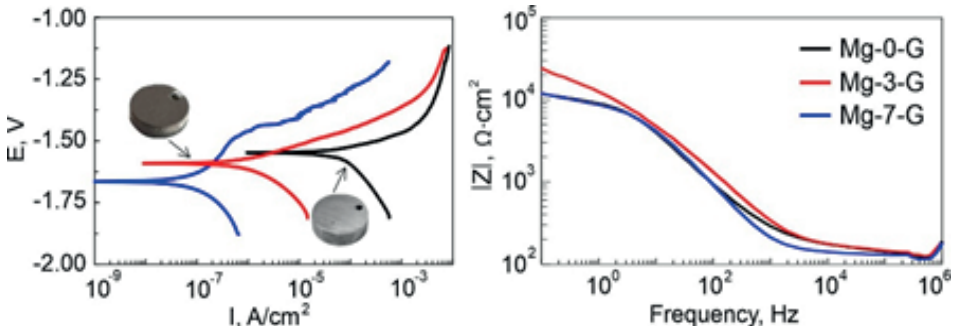

Fig. 4. Polarization curves and Bode plot for the studied samples

Conclusion

Coatings formed by the PEO on a composite material containing magnesium and hydroxyapatite obtained by spark plasma sintering have been studied. The phase composition of the PEO-layers is established, which explains their mechanical properties. It has been established that the strength of the PEO-layer obtained in an electrolyte with hydroxyapatite (Mg–3–H) is 20% higher than the strength of coatings formed in an electrolyte with glycerophosphate (Mg–3–G). This mechanism is mainly due to the formation of the silicon-containing forsterite phase with high hardness. Coatings formed in an electrolyte with glycerophosphate allows to reduce the corrosion current density by 1 order of magnitude compared to untreated samples (from $1.1 \cdot 10^{-5}$ to $1.3 \cdot 10^{-6}$ A·cm^{-2}). Protective layers obtained in an electrolyte with hydroxyapatite nanoparticles further reduce corrosion currents by 2 orders of magnitude: up to $6.30 \cdot 10^{-7}$ A·cm^{-2}. Oxidation of composite samples in electrolyte with hydroxyapatite leads to increase in polarization resistance and impedance modulus by 3 orders of magnitude against uncoated samples. In addition, it has been demonstrated that the uncoated composites sintered with HAp demonstrate better protective properties than magnesium samples.

Acknowledgements

The authors are grateful to O.O. Shichalin from the Far Eastern Federal University (FEFU, Vladivostok, Russia) for sintering composites by SPS-method.

REFERENCES

1. **Hoare D., Bussooa A., Neale S., Mirzai N., Mercer J.,** The future of cardiovascular stents: bioresorbable and integrated biosensor technology, Advanced Science. 6 (20) (2019) 1900856.

2. **Dhandapani R., Krishnanc D., Zenniferc A., Kannanc V. et al.,** Additive manufacturing of biodegradable porous orthopaedic screw, Bioactive Material. 5 (3) (2020) 458–467.

3. **Onuma Y. and Serruys P.W.,** Bioresorbable Scaffold, Circulation. 123 (7) (2011) 779–797.

4. **Bohner M.,** Bone substitute materials, Encyclopedia of Biomedical Engineering. (2018) 513–529.

5. **Garimella A., Awale G., Parai R., Ghosh S.B., Bandyopadhyay-Ghosh S.,** An integrated approach to develop engineered metal composite bone scaffold with controlled degradation, Materials Technology. 34 (14) (2019) 858–866.

6. **Yang Y., He Ch., E D., Yang W., Qi F., Xie D. et al.,** Mg bone implant: Features, developments and perspectives, Materials and Design. 185 (2020) 108259.

7. **Chakraborty Banerjee P., Al-Saadi S., Choudhary L., Harandi S.E., Singh R.,** Magnesium Implants: Prospects and Challenges, Materials. 12 (1) (2019) 136.

8. **Sezer N., Evis Z., Koз M.,** Additive manufacturing of biodegradable magnesium implants and scaffolds: Review of the recent advances and research trends, Journal of Magnesium and Alloy. 9 (2) (2021) 392–415.

9. **Wittea F., Fischer J., Nellesen J., Crostack H.-A., Kaesec V., Pisch A. et al.,** In vitro and in vivo corrosion measurements of magnesium alloys, Biomaterials, 27 (7) (2006) 1013–1018.

10. **Robinson D.A., Griffith R.W., Shechtman D., Evans R.B.,** Conzemius M.G., In vitro antibacterial properties of magnesium metal against Escherichia coli, Pseudomonas aeruginosa and Staphylococcus aureus, Acta Biomaterialia, 6 (5) (2010) 1869–1877.

11. **Wu N. and Veillette A.,** Magnesium in a signalling role, Nature, 475 (7357) (2011) 462–463.

12. **Barati Darband G., Aliofkhazraei M., Hamghalam P., Valizade N.,** Plasma electrolytic oxidation of magnesium and its alloys: Mechanism, properties and applications, Journal of Magnesium and Alloy. 5 (1) (2017) 74–132.

13. **Martin J., Nominé A.V., Stef J., Nominй A., Zou J.X., Henrion G., Grosdidier T.,** The influence of metallurgical state of substrate on the efficiency of plasma electrolytic oxidation (PEO) process on magnesium alloy, Material and Design, 178 (2019) 107859.

14. **Kaesel V., Tai P.-T., Bach F.-W., Haferkamp H., Witte F., Windhagen H.,** Approach to Control the Corrosion of Magnesium by Alloying, in Magnesium: Proceedings of the 6th International Conference Magnesium Alloys and Their Applications, Weinheim, FRG: Wiley-VCH Verlag GmbH & Co. KGaA. (2005) 534–539.

15. **Ma R. and Guo D.,** Evaluating the bioactivity of a hydroxyapatite-incorporated polyetheretherketone biocomposite, Journal of Orthopaedic Surgery and Research, 14 (1) (2019) 32.

16. **Gnedenkov S.V., Sharkeev Yu. P., Sinebryukhov S.L., Khrisanfova O.A., Legostaeva E.V. et al.,** Functional coatings formed on the titanium and magnesium alloys as implant materials by plasma electrolytic oxidation technology: Fundamental principles and synthesis conditions, Corrosion Reviews, 34 (1–2) (2016) 65–83.

17. **Mashtalyar D.V., Sinebryukhov S.L., Imshinetskiy I.M., Gnedenkov A.S. et al.,** Hard wearproof PEO-coatings formed on Mg alloy using TiN nanoparticles, Appl. Surf. Sci., 503 (2020) 144062.

18. **Gnedenkov S.V., Sinebryukhov S.L., Egorkin V.S., Mashtalyar D.V. et al.,** Magnesium fabricated using additive technology: Specificity of corrosion and protection, Journal of Alloys and Compounds 808 (2019) 151629.

THE AUTHORS

SIDOROVA Marina V.
sidorova-01-02@rambler.ru
ORCID: 0000-0003-3606-4682

SINEBRYUKHOV Sergey L.
sls@ich.dvo.ru
ORCID: 0000-0002-0963-0557

PODGORBUNSKY Anatoly B.
pab@ich.dvo.ru
ORCID: 0000-0002-0764-391X

GNEDENKOV Sergeiy V.
svg21@hotmail.com
ORCID: 0000-0003-1576-8680

GERASIMENKO Maria S.
gerasimenko.ms00@mail.ru
ORCID: 0000-0002-0764-391X

Received 21.05.2022. Approved after reviewing 20.06.2022. Accepted 22.06.2022.

Conference materials
UDC 538.9
DOI: https://doi.org/10.18721/JPM.153.137

Investigation of changes in the composition of anodic TiO_2 nanotubes at different stages of formation by AES and TOF SIMS methods

D. A. Dronova [1] ✉, S. A. Gavrilov [1], A. A. Dronov [1]

[1] National Research University of Electronic Technology, Moscow, Russia

✉ demetpatakai@gmail.com

Abstract: The article presents comprehensive studies of the chemical composition and morphology of nanotubular anodic TiO_2 layers at the first stages of the porous structure nucleation, by scanning electron microscopy (SEM), Auger spectroscopy (AES), time-of-flight secondary ion mass spectrometry (TOF.SIMS). Our goal was to show the profile distribution of chemical elements and reaction products at each of the initial stages of the anodic oxide growth in the ethylene glycol-based electrolyte containing fluoride, which will help expand the understanding of pore formation mechanism.

Keywords: TiO_2, nanotubes, anodization, AES, TOF.SIMS

Funding: The study was financially supported by a Russian Foundation for Basic Research grant no. 19-33-90287 and State Assignment FSMR-2020-0018.

Citation: Dronova D. A., Gavrilov S. A., Dronov A. A., Investigation of changes in the composition of anodic TiO_2 nanotubes at different stages of formation by AES and TOF SIMS methods, St. Petersburg State Polytechnical University Journal. Physics and Mathematics. 15 (3.1) (2022) 222–226. DOI: https://doi.org/10.18721/JPM.153.137

Материалы конференции
УДК 538.9
DOI: https://doi.org/10.18721/JPM.153.137

Исследование изменения состава анодных нанотрубок TiO_2 на разных стадиях формирования методами AES и TOF SIMS

Д. А. Дронова [1] ✉, С. А. Гаврилов [1], А. А. Дронов [1]

[1] Национальный исследовательский университет «МИЭТ», г. Москва, Россия

✉ demetpatakai@gmail.com

Аннотация. В статье обсуждаются комплексные исследования химического состава и морфологии нанотрубчатых анодных слоев TiO_2 на первых этапах зарождения пористой структуры методами сканирующей электронной микроскопии (СЭМ), Оже-спектроскопии (ОЭС), времяпролетной вторично-ионной масс-спектрометрии (ВИМС). Цель такого комплексного исследования — показать профильное распределение химических элементов и продуктов реакции на каждой из начальных стадий формирования анодного оксида во фторсодержащих электролитах на основе этиленгликоля, что позволит расширить представления о механизме порообразования в оксиде титана.

Ключевые слова: TiO_2, нанотрубки, анодирование, ОЭС, ВИМС

Финансирование: Исследование выполнено при поддержке гранта РФФИ № 19-33-90287 и Госзадания № ФСМР-2020-0018.

Ссылка при цитировании: Дронова Д. А., Гаврилов С. А., Дронов А. А. Исследование изменения состава анодных нанотрубок TiO_2 на разных стадиях формирования методами AES и TOF SIMS // Научно-технические ведомости СПбГПУ. Физико-математические науки. 2022. Т. 15. № 3.1. С. 222–226. DOI: https://doi.org/10.18721/JPM.153.137

Introduction

Nanostructured titanium oxide currently represents a major research interest due to its possible application in the storage of energy sources [1], photocatalysis [2], and solar cells [3].

One of the promising nanostructured modifications of titanium oxide is nanotubular anodic titanium oxide (TiO_2 NTs). The anodic formation process makes it possible to create not only a highly ordered TiO_2 NTs array on a titanium substrate, which facilitates the formation of electronic structures based on them but also allows very precise control of geometric parameters during growth, in contrast to classical powder nanomaterials based on TiO_2 [4]. Despite the extensive studies of the structure-properties based on TiO_2 NTs, the nucleation and growth mechanism of pores is still not fully clear.

In this article, the distributions of chemical elements and ionic fragments of nanotube titanium oxide during the formation stages were demonstrated by Auger spectroscopy and time-of-flight secondary ion mass spectrometry methods.

Materials and Methods

TiO_2 NTs were formed on titanium foil (0.89 mm thick, 99.7% metal basis, Alfa Aesar). The substrate was pretreatment in acetone in an ultrasonic bath for 15 min. Prior to anodization, substrates were chemically polished in HNO_3:HF solution during 120 s, then washed in deionized water (18.2 MΩ) and dried in an air stream. The electrochemical growth of titanium oxide was carried out in a potentiostatic mode (60 V) and a temperature of 20 °C. A platinum grid was used as a counter electrode. Anodizing was performed in 98 vol.% ethylene glycol with the addition of 0.3 vol.% NH_4F and 2 vol.% H_2O. After anodizing, the samples were washed in ethyl alcohol and dried in an air stream. Subsequently, ready samples were not subjected to heat treatment and remained in the amorphous state.

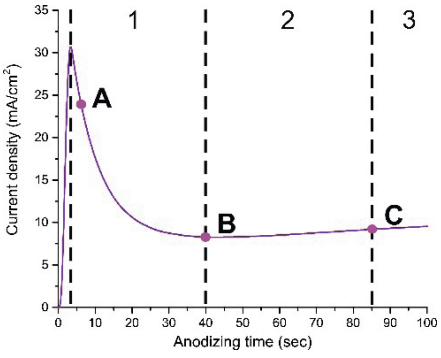

Fig. 1. Chronoamperometry curve for growth of nanotube TiO_2 layer

Fig. 1 shows a typical chronoamperometric curve of the nanotubes layer growth process with highlighted formation stages (1, 2, 3) and critical current density points A, B, C. These critical points were chosen to analyze the chemical composition of the samples by the depth.

At the beginning of the anodizing process (i.e., when a potential is applied) in stage 1, the current sharply decreases to a critical value due to the formation of an initial oxide layer with high resistance. The current rises as the pores develop to a local maximum (stage 2). Finally, the current reaches a constant value in stage 3, when the equilibrium state of the formation of TiO_2 is reached, which is achieved by the equality of the oxide formation rate at the metal/oxide interface and the dissolution rate at the oxide/electrolyte interface [5].

Research methods for titanium oxide

Morphological characterization of anodized samples was employed by scanning electron microscopy (FEI Quanta 3D FEG). No charging effects were observed; therefore, no additional coatings on the samples were required. The accelerating voltage used for imaging was 3 kV and the working distance was 4 mm.

The AES system used for investigations was Physical Electronics PHI-670xi Scanning Auger Nanoprobe. The argon ion gun operated at 2 kV with ion current 0.35 A was used for sample surface sputtering during depth profiling. The etching rate was controlled by a 1 × 1.5 mm^2 ion beam raster. Depth profiling over an area was performed at the primary electron beam energy of 10 keV and a current of 20 nA. A profile research of the composition of the TiO_2 oxide layer was carried out on an area 75–100μm in diameter by a primary electron beam.

Time of flight secondary ion mass spectrometry investigations was performed on TOF.SIMS-5 instrument (IonTOF GmbH, Germany). For depth profiles acquired in this study, 500V Cs^+ with 40 nA current was used to create a 300 μm by 300 μm area, and the middle 100 μm by 100 μm area was analyzed using a pulsed 0.6 pA Bi_3^{++} primary ion beam at 30 kV accelerating voltage with 14 ns pulse width and 112 ns buncher delay.

Results and Discussion

Point A

As can be seen from the SEM image (Fig. 2, *a*), during the first 6 seconds of anodizing, a textured dense titanium oxide layer of about ~23–26 nm thickness is formed on the surface of the titanium foil.

Two types of carbon, one of which is hydrocarbon contamination (C_{surf}) and the other corresponds to the carbide state of carbon in the oxide film volume (C_{vol}), can be seen in the depth distribution graph obtained by Auger-electron spectroscopy (Fig. 2, *b*). A more detailed description of the features of the analysis and the rationale for the choice of the analyzed peaks of chemical elements are presented in our previous work [6]. Surface contamination disappears almost completely at about a depth of 10 nm, while the signal of carbide begins to drop noticeably only at a depth of about 20 nm. The carbide form of the carbon Auger peak can be associated with chemical bonds of titanium with organic fragments, i.e. the Ti-C bond [7].

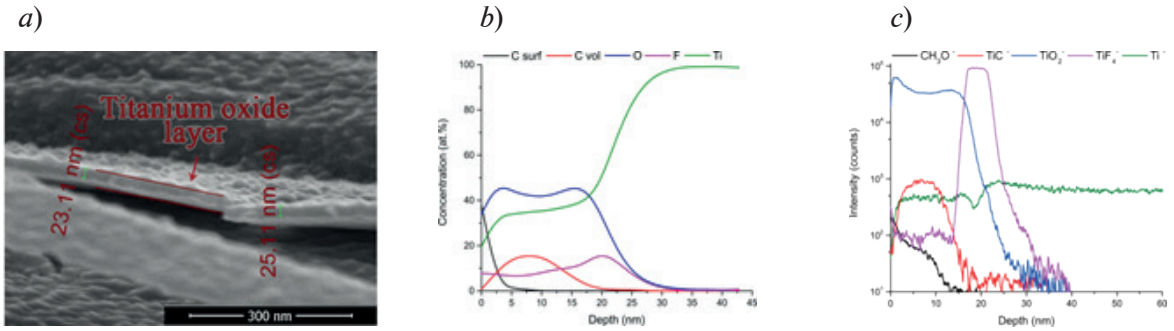

Fig. 2 Cross-sectional SEM images for an array of TiO_2 detached from Ti foil (*a*), AES profile analysis (*b*) and TOF.SIMS profile (*c*) at point A

The presence of fluorine atoms in the structure is associated with the use of fluoride electrolytes, the anions of which are incorporated into the film during growth. In addition, as was shown in [8], F^- ions have a higher migration rate through the titanium oxide film as compared to oxygen ions O^{2-}. This speed difference results in the formation of a fluorine-rich layer at the interface between the oxide and the titanium substrate.

Secondary ion time-of-flight mass spectrometry (TOF.SIMS) was used to establish the chemical bonds of fluorine and carbon with other elements in the oxide. The possible chemical bonds and their variations of fluorine and carbon in the TiO_2 oxide layer can be determined by analyzing the depth distribution of ionic fragments.

From the results of TOF.SIMS profile analysis (Fig. 2, *c*) we can see that on the surface of the oxide (about 5 nm) there is an increased intensity of organic contamination, represented by the ionic fragment CH_3O^-, which gradually decreases and is probably associated with the residual reaction products from the electrolyte.

The ionic fragment of TiF_4^- repeats the shape of the distribution from fluorine in the AES method. The intensity of the TiF_4^- fragment is at the upper limit of sensitivity of the device (10^5).

The shape of the distribution of the TiC^- ion fragment also repeats the shape of the distribution of C_{vol} by AES.

From the depth distribution profile of TiO_2, it can be said that the oxide layer formed during the first 6 seconds of anodizing was about 25 nm, which agrees with the SEM image and the AES profile analysis. It is known that hydrocarbon contamination as well as matrix modification during ion sputtering changes the yield of secondary ions. This effect can influence the decrease of signal intensity from TiF_4^- and TiC^- ion fragments after removal of hydrocarbon-contaminated layer by ion sputtering.

Point B

At point B, the pores continue to grow (Fig. 3, *a*). At the previous anodization point, C_{vol} was practically not observed in the fluorine-enriched area. At point B, the C_{vol} concentration decreases from 10 to 5 at.% in the fluorine-enriched layer volume (Fig. 3, *b*). It should be noted that the highest carbon concentration is within the first 20–100 nm and is probably the thickness of the initial layer, which forms a porous crust over the nanotube array, which correlates with the results of SEM image. This is also confirmed by the results of the TOF.SIMS profile analysis (Fig. 3, *c*).

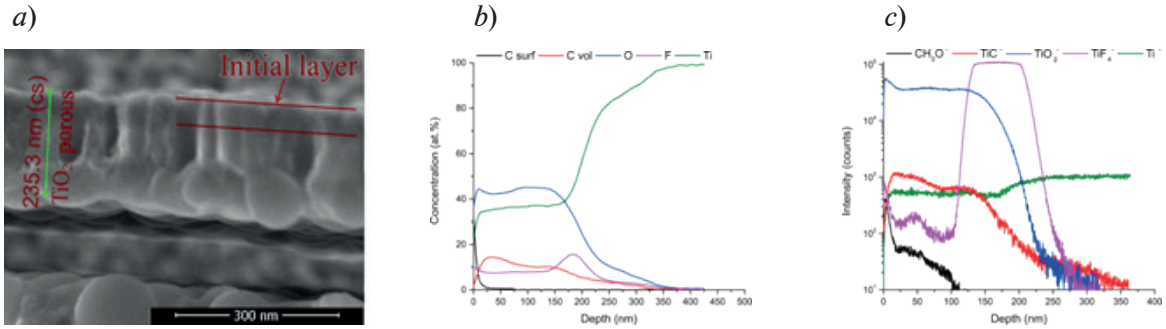

Fig. 3 Cross-sectional SEM images for an array of TiO_2 detached from Ti foil (*a*), AES profile analysis (*b*) and SIMS profile (*c*) at point B

Point C

At point C, the pores become titanium oxide nanotubes (Fig. 4, *a*). According to the AES analysis at point C (85 s of anodization) (Fig. 4, *b*), the distribution of C_{vol} and F in the titanium oxide volume is uniform and is about 15 at.%. In previous work [6], we showed that a single TiO_2 nanotube has a three-layer structure, where C_{vol} is only in the inner layer of the tube, and fluorine is only contained on the outer part of the nanotube. The analysis of the TOF.SIMS depth profile (Fig. 4, *c*) shows that the CH_3O^- ion fragments have a stable intensity from 100 to 500 nm, which indicates the presence of reaction products from the electrolyte in the tube array. The AES data confirm this, but due to the low sensitivity the hydrocarbon signal does not exceed 1–0.5 at.%. The distribution of the profile of the remaining ionic fragments confirms the results of the AES depth analysis.

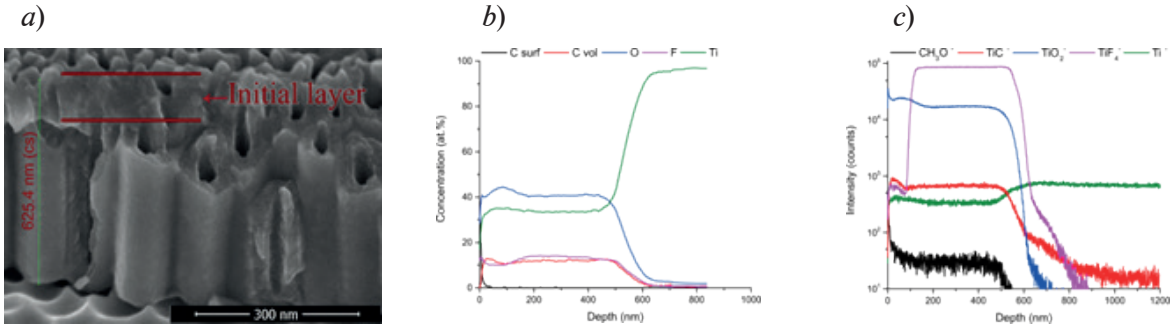

Fig. 4 Cross-sectional SEM images for an array of TiO_2 (*a*), AES profile analysis (*b*) and SIMS profile (*c*) at point C

Conclusions

It can be concluded that a compact initial layer of titanium oxide is formed on the titanium surface at the first stage of anodizing. Then, fluorine and oxygen ions diffuse through it, under the influence of an electric field, to form a fluorine-enriched layer at the oxide/metal interface. Over time, the surface of the initiating oxide layer becomes more textured and the thickness increases. The fluorine-enriched layer also becomes thicker and eventually forms a porous/tubular structure underneath the compact oxide layer.

REFERENCES

1. **Gao Z.-D., Zhu X., Li Y.-H., Zhou X., Song Y.-Y., Schmuki P.,** Carbon cladded TiO_2 nanotubes: fabrication and use in 3D-RuO2 based supercapacitors, Chemical Communications. 51 (2015) 7614–7617.

2. **Costa L.L., Prado A.G.S.,** TiO_2 nanotubes as recyclable catalyst for efficient photocatalytic degradation of indigo carmine dye, Journal of Photochemistry and Photobiology A: Chemistry. 201 (2009) 45–49.

3. **Nah Y.-C., Paramasivam I., Schmuki P.,** Doped TiO_2 and TiO_2 Nanotubes: Synthesis and Applications, ChemPhysChem. 11 (2010) 2698–2713.

4. **Lee K., Mazare A., Schmuki P.,** One-Dimensional Titanium Dioxide Nanomaterials: Nanotubes, Chemical Reviews. 114 (2014) 9385–9454.

5. **Regonini D., Bowen C.R., Jaroenworaluck A., Stevens R.,** A review of growth mechanism, structure and crystallinity of anodized TiO2 nanotubes, Materials Science and Engineering: R: Reports. 74 (2013) 377–406.

6. **Dronov A., Gavrilin I., Kirilenko E., Dronova D., Gavrilov S.,** Investigation of anodic TiO2 nanotube composition with high spatial resolution AES and ToF SIMS, Applied Surface Science. 434 (2018) 148–154.

7. **Song Y., Roy P., Paramasivam I., Schmuki P.,** Voltage Induced Payload Release and Wettability Control on TiO Angewandte Chemie International Edition. 49 (2010) 351–354.

8. **Habazaki H., Fushimi K., Shimizu K., Skeldon P., Thompson G.E.,** Fast migration of fluoride ions in growing anodic titanium oxide, Electrochemistry Communications. 9 (2007) 1222–1227.

THE AUTHORS

DRONOVA Daria A.
demetpatakai@gmail.com
ORCID: 0000-0002-9730-1138

DRONOV Alexey A.
noiz@mail.ru
ORCID: 0000-0001-6085-2481

GAVRILOV Sergei A.
pcfme@miee.ru
ORCID: 0000-0002-2967-272X

Received 21.05.2022. Approved after reviewing 29.06.2022. Accepted 30.06.2022.

Conference materials
UDC 620.193:544.653
DOI: https://doi.org/10.18721/JPM.153.138

In vitro corrosion behavior of bioresorbable Mg-Ca alloy with hydroxyapatite-containing protective coating

V. S. Filonina [1] ✉, A. S. Gnedenkov [1], S. L. Sinebryukhov [1]
A. N. Minaev [1], S. V. Gnedenkov [1]

[1] Institute of Chemistry FEB RAS, Vladivostok, Russia
✉ filonina.vs@gmail.com

Abstract: The paper presents the results of the study of corrosion performance of HAp-containing coating obtained on the Mg-0.8Ca bioresorbable magnesium alloy using plasma electrolytic oxidation (PEO). Electrochemical measurements were carried out in minimal essential medium (MEM) using electrochemical impedance spectroscopy (EIS), potentiodynamic polarization (PDP) and monitoring of open circuit potential (OCP) techniques. It was established that the PEO treatment of Mg-0.8Ca leads to a significant increase in corrosion resistance of the material. Formation of heterooxide layer on magnesium alloy contributes to a decrease in corrosion current density (IC) more than three times. The impedance modulus measured at low frequency ($|Z|_{f=0.1\ \mathrm{Hz}}$) for a coated material increased by two times compared to an uncoated one.

Keywords: Magnesium, magnesium alloys, corrosion protection, plasma electrolytic oxidation (PEO), hydroxyapatite

Funding: The study was supported by the Russian Science Foundation as part of the project "Multifunctional biodegradable coatings of new generation for controlling the resorption of magnesium-based materials: self-healing mechanism, personalized medicine" (no. 21-73-10148).

Citation: Filonina V. S., Gnedenkov A. S., Sinebryukhov S. L., Minaev A. N., Gnedenkov S. V., In vitro corrosion behavior of bioresorbable Mg-Ca alloy with hydroxyapatite-containing protective coating, St. Petersburg State Polytechnical University Journal. Physics and Mathematics. 15 (3.1) (2022) 227–231. DOI: https://doi.org/10.18721/JPM.153.138

Материалы конференции
УДК 620.193:544.653
DOI: https://doi.org/10.18721/JPM.153.138

Коррозионное поведение биорезорбируемого Mg-Ca сплава с гидроксиапатитсодержащим защитным покрытием *in vitro*

В. С. Филонина [1] ✉, А. С. Гнеденков [1], С. Л. Синебрюхов [1]
А. Н. Минаев [1], С. В. Гнеденков [1]

[1] Институт химии ДВО РАН, г. Владивосток, Россия
✉ filonina.vs@gmail.com

Аннотация. В работе представлены результаты исследования уровня защиты от коррозии гидроксиапатитсодержащих покрытий, полученных на поверхности биорезорбируемого магниевого сплава Mg-0,8Ca методом плазменного электролитического оксидирования (ПЭО). Электрохимические измерения проводились в среде для культивирования клеток млекопитающих minimal essential medium (MEM) с использованием методов электрохимической импедансной спектроскопии (EIS), потенциодинамической

поляризации (PDP), а также мониторинга электродного потенциала (OCP). Установлено, что обработка поверхности сплава Mg-0,8Ca методом ПЭО способствует значительному повышению коррозионной стойкости материала. Формирование гетерооксидного слоя на поверхности магниевого сплава способствует снижению значений плотности тока коррозии (IC) более, чем в 3 раза. Повышение значений модуля импеданса, измеренного на низкой частоте ($|Z|_{f=0,1}$), для материала с покрытием составило 2 раза по сравнению с материалом без защитного слоя.

Ключевые слова: Магний, магниевые сплавы, коррозионная защита, плазменное электролитическое оксидирование (ПЭО), гидроксиапатит

Финансирование: Исследование выполнено в рамках проекта «Многофункциональные биодеградируемые покрытия нового поколения для контроля процессов резорбции материалов на основе магния: механизм самозалечивания, персонализированная медицина» (№ 21-73-10148).

Ссылка при цитировании: Филонина В. С., Гнеденков А. С., Синебрюхов С. Л., Минаев А. Н., Гнеденков С. В. Коррозионное поведение биорезорбируемого Mg-Ca сплава с гидроксиапатитсодержащим защитным покрытием in vitro // Научно-технические ведомости СПбГПУ. Физико-математические науки. 2022. Т. 15. № 3.1. С. 227–231. DOI: https://doi.org/10.18721/JPM.153.138

Introduction

Features of magnesium degradation process determines its great prospects in application as an implant material. Unfortunately, rapid and heterogeneous degradation as well as an alkalization of a surrounding area obstruct the expansion of magnesium scope [1–7]. Improving the corrosion resistance of bioresorbable magnesium-based materials will make it possible to control the degradation process of the material in the human body in order to ensure matching the rates of implant resorption and osteogenesis [8]. The most common way to improve both corrosion resistance and bioactivity of magnesium is to form protective coatings, containing Ca, P, Mg and their compounds, including hydroxyapatite (inorganic components of a bone) [9, 10]. According to [11], magnesium has a positive effect on the activity of osteoblasts and osteoclasts, and therefore on bone growth. In turn, the release of calcium ions and phosphates from surface layer compounds forms a saturated ionic solution at the interface. In this case, there is an ion exchange between the implant material and the patient's bone. Some of these ions can deposit on the bone matrix, forming new bone tissue. One of the easiest and technological ways to improve the corrosion resistance of valve metals (including Mg) is plasma electrolytic oxidation (PEO) [12, 13]. The PEO processing allows to create on magnesium surface protective layers of various morphology and composition, including hydroxyapatite-containing ones [14–18].

Materials and Methods

The experiments were carried out on Mg-0.8Ca alloy samples (0.8 wt.% Ca, balance Mg) with a size of 15×30×1 mm. Samples were ground with Si-C abrasive paper with gradual reduction of a grain size to 14–20 μm (P1000) with following rinsing in isopropyl alcohol and drying in air. Plasma electrolytic oxidation (PEO) coating was formed in a combined bipolar mode with the current density below 0.75 $A \cdot cm^{-2}$. Duty cycle was equal to 1, total oxidation time reached 120 s. The composition of the formed coating was studied via XRD using a SmartLab diffractometer (Rigaku, Japan). The measurements were carried out in the range $2\theta = 4°–90°$ with a step of 0.01°. To evaluate the corrosion resistance of formed samples, electrochemical measurements (including potentiodynamic polarization (PDP), electrochemical impedance spectroscopy (EIS) and monitoring of open circuit potential (OCP) change) were realized. Experiments were carried out using a Versa STAT MC electrochemical system (Princeton Applied Research, USA) and the electrolyte was minimal essential medium (MEM) solution (a synthetic mammalian cell culture medium).

Table 1

Equivalent electrical circuit parameters, obtained during the fitting the impedance spectra for PEO-coated sample exposed to MEM for 42 h

Immersion time, h	CPE_1		R_1, Ω·cm²	CPE_2		R_2, Ω·cm²
	Q_1, Sm·cm^{-2}·s^n	n_1		Q_2, Sm·cm^{-2}·s^n	n_2	
1	$1.00\cdot10^{-5}$	0.69	678	$1.90\cdot10^{-6}$	0.86	16641
11	$1.19\cdot10^{-5}$	0.57	1100	$9.05\cdot10^{-6}$	0.86	45776
21	$9.89\cdot10^{-6}$	0.54	1760	$1.08\cdot10^{-5}$	0.85	76060
31	$7.32\cdot10^{-6}$	0.54	2156	$1.28\cdot10^{-5}$	0.82	89374
42	$3.61\cdot10^{-6}$	0.59	3307	$1.53\cdot10^{-5}$	0.76	87448

Results and Discussion

As a result of the PEO process, ceramic-like coating with high heterogeneity of the surface relief were obtained on the surface of a Mg-0.8Ca bioresorbable magnesium alloy. XRD analysis showed that the main component of the PEO-coating was hydroxyapatite. The other component of protective layer was periclase. According to data obtained by potentiodynamic polarization (PDP) and electrochemical impedance spectroscopy (EIS) methods, the formation of a PEO-layer provides the material an advanced corrosion resistance. The corrosion current density (I_C) for a coated sample (I_C = $2.8\cdot10^{-6}$ A·cm^{-2}) is more than 3 times lower than the one for an uncoated Mg-0.8Ca (I_C = $9.5\cdot10^{-6}$ A·cm^{-2}) (Fig. 1). The results of the analysis of electrochemical impedance spectroscopy data also make it possible to confirm the higher corrosion resistance of the sample with a PEO-coating, compared to the bare alloy. The values of the impedance modulus measured at a low frequency ($|Z|_{f=0.1\ Hz}$) after 1 h exposure to the MEM for a sample with a PEO-layer are more than 2 times higher ($|Z|_{f=0.1\ Hz}$ = $1.7\cdot10^4$ Ω·cm²) than the value for uncoated Mg-0.8Ca ($|Z|_{f=0.1\ Hz}$ = $8.1\cdot10^3$ Ω·cm²) (Fig. 2). For the coated sample the increase in the diameter of the half-cycle on the complex plane of Nyquist plot due to increase both the values of resistance of outer (porous, R_1) and inner (nonporous, R_2) layers of the PEO-coating (Figs. 2,*d*, 3, Table 1) is observed during the whole immersion time (42 h). This is due to the formation of a Ca-P film composed of corrosion products of the sample (including PEO-layer and substrate material) and components of the MEM, which leads to sealing the pores of the PEO-layer. For comparison, uncoated material is characterized by an increase in these parameters only during the first 30 h of exposure, then protective properties of the surface layer decrease noticeably, which is associated with the intensification of the corrosion process, leading to the destruction of the Ca-P compounds film [4].

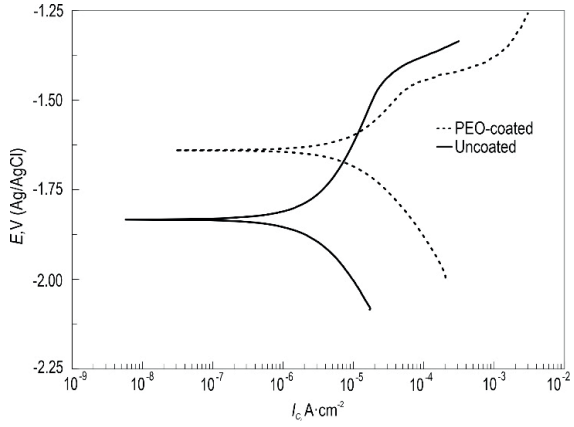

Fig. 1. Polarization curves obtained as a result of electrochemical tests (PDP measurements) in MEM

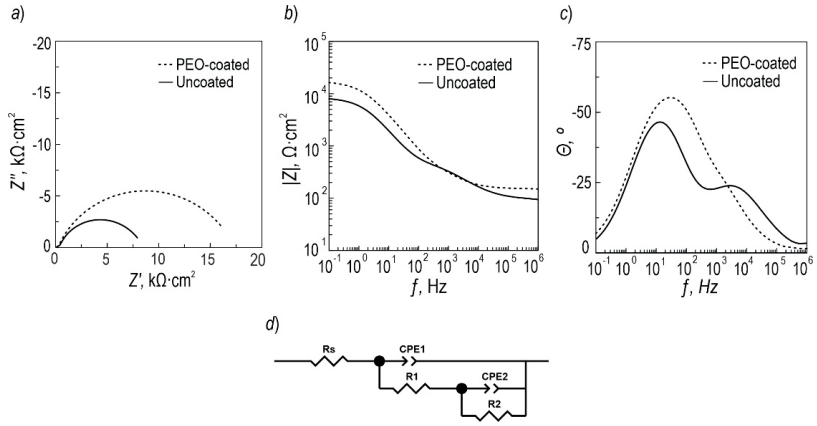

Fig. 2. Impedance spectra presented as Nyquist (*a*) and Bode (*b*, *c*) plots after 1 h of exposure of the samples to the MEM and an equivalent electrical circuit (EEC) used for fitting the impedance spectra (*d*)

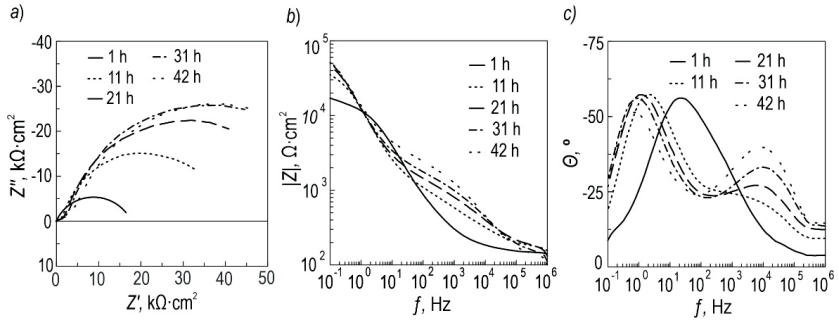

Fig. 3. Impedance spectra presented as Nyquist (*a*) and Bode (*b*, *c*) plots during 42 h of exposure of the PEO-coated sample to MEM

Conclusion

The way to improve the corrosion resistance of bioresorbable Mg-0.8Ca magnesium alloy was obtained during the presented study. Formation of the hydroxyapatite-containing oxide layers leads both to a significant decrease in the values of I_C and increase in $|Z|_{f=0.1\ Hz}$. Based on the analysis of the obtained data, the prospects for use of calcium-phosphate PEO-coatings on a bioresorbable magnesium alloy for the needs of implant surgery were established.

Acknowledgments

This work was supported by the Grant of Russian Science Foundation (project no. 21-73-10148, https://rscf.ru/en/project/21-73-10148/).

REFERENCES

1. **Gnedenkov A. S., Lamaka S. V., Sinebryukhov S. L., Mashtalyar D. V., Egorkin V. S., Imshinetskiy I. M., Zavidnaya A. G., Zheludkevich M. L., Gnedenkov S. V.,** Electrochemical behaviour of the MA8 Mg alloy in minimum essential medium Corrosion Science, (168) (2020) 2–15.

2. **Li H., Zheng Y., Qin L.,** Progress of biodegradable metals, Progress in Natural Science: Materials International 24 (2014) 414–422.

3. **Gnedenkov A. S., Sinebryukhov S. L., Mashtalyar D. V., Gnedenkov S. V.,** Inhibitor-containing composite coatings on Mg alloys: Corrosion mechanism and self-healing protection, Solid State Phenomena (245) (2016) 89–96.

4. **Gnedenkov A. S., Sinebryukhov S. L., Filonina V. S., Egorkin V. S., Ustinov A. Yu., Sergienko V. I., Gnedenkov S. V.,** The detailed corrosion performance of bioresorbable Mg-0.8Ca alloy in physiological solutions, Journal of Magnesium and Alloys (10) (2022) 1326–1350.

5. **Yazdimamaghani M., Razavi M., Vashaee D., Moharamzadeh K., Boccaccini A. R., Tayebi L.,** Porous magnesium-based scaffolds for tissue engineering, Materials Science and Engineering C (71) (2017) 1253–1266.

6. **Zheng Y. F., Gu X. N., Witte F.,** Biodegradable metals, Materials Science and Engineering: R: Reports (77) (2014) 1–34.

7. **Ratna Sunil B., Sampath Kumar T. S., Chakkingal U., Nandakumar V., Doble M., Devi Prasad V., Raghunath M.,** In vitro and in vivo studies of biodegradable fine grained AZ31 magnesium alloy produced by equal channel angular pressing, Materials Science and Engineering: C (59) (2016), 356–367.

8. **Song M. S., Zeng R. C., Ding Y. F., Li R. W., Easton M., Cole I., Birbilis N., Chen X. B.,** Recent advances in biodegradation controls over Mg alloys for bone fracture management: A review Journal of Materials Science & Technology 4 (35) (2019) 535–544.

9. **Mohamed A., El-Aziz A. M., Breitinger H. G.,** Study of the degradation behavior and the biocompatibility of Mg–0.8Ca alloy for orthopedic implant applications, Journal of Magnesium and 2 (7) (2019) 249–257.

10. **Rahman M., Li Y., Wen C.,** HA coating on Mg alloys for biomedical applications: A review, Journal of Magnesium and Alloys 3 (8) (2020) 929–943.

11. **Sammons R.,** Biological responses to hydroxyapatite, Hydroxyapatite (HAp) for Biomedical Applications (2015).

12. **Gnedenkov A. S., Sinebryukhov S. L., Mashtalyar D. V., Vyaliy I. E., Egorkin V. S., Gnedenkov S. V.,** Corrosion of the welded aluminium alloy in 0.5 M NaCl solution. Part 2: Coating protection, Materials 11 (11) (2018) 2177–2199

13. **Gnedenkov A. S., Sinebryukhov S. L., Mashtalyar D. V., Vyaliy I. E., Egorkin V. S., Gnedenkov S. V.,** Corrosion of the welded aluminium alloy in 0.5 M NaCl solution. Part 1: Specificity of development, Materials 11 (10) (2018) 2053.

14. **Santos-Coquillat A., Esteban-Lucia M., Martinez-Campos E., Mohedano M., Arrabal R., Blawert C., Zheludkevich M. L., Matykina E.,** PEO coatings design for Mg-Ca alloy for cardiovascular stent and bone regeneration applications, Materials Science and Engineering: C (105) (2019) 1–19.

15. **Stojadinović S.,** Plasma electrolytic oxidation of metals Journal of the Serbian Chemical Society 78 (5) (2013) 713–716.

16. **Paital S. R., Dahotre N. B.,** Calcium phosphate coatings for bio-implant applications: Materials, performance factors, and methodologies, Materials Science and Engineering R Reports 66 (1) (2009) 1–70.

17. **Kirkland N. T., Birbilis N., Staiger M. P.,** Assessing the corrosion of biodegradable magnesium implants: A critical review of current methodologies and their limitations, Acta Biomaterialia 8 (3) (2011) 925–36.

18. **Gnedenkov A. S., Lamaka S. V., Sinebryukhov S. L., Mashtalyar D. V., Egorkin V. S., Imshinetskiy I. M., Zheludkevich M. L., Gnedenkov S. V.,** Control of the Mg alloy biodegradation via PEO and polymer-containing coatings, Corrosion Science (182), (2021), 109254.

THE AUTHORS

FILONINA Valeriia S.
filonina.vs@gmail.com
ORCID: 0000-0002-9544-3597

MINAEV Alexander N.
minaev.an@dvfu.ru
ORCID: 0000-0002-8072-306X

GNEDENKOV Andrey S.
asg17@mail.com
ORCID: 0000-0002-9822-7849

GNEDENKOV Sergey V.
svg21@hotmail.com
ORCID: 0000-0003-1576-8680

SINEBRYUKHOV Sergey L.
sls@ich.dvo.ru
ORCID: 0000-0002-0963-0557

Received 22.05.2022. Approved after reviewing 25.07.2022. Accepted 02.08.2022.

Conference materials
UDC 544.6
DOI: https://doi.org/10.18721/JPM.153.139

Effect of thermal annealing on the composition of Ge-Co nanostructure obtained by electrochemical deposition

I. K. Martynova [1] ✉, I. M. Gavrilin [1]

[1] National Research University of Electronic Technology, Moscow, Russia

✉ Irisha-windsurfer@yandex.ru

Abstract: Cobalt-based catalysts are one of the possible candidates for catalysts that accelerate the decomposition of water to produce energy. In this work, the one-dimension Ge-Co nanostructures have been prepared by electrochemical deposition in a three-electrode cell. The samples have been annealed in atmosphere at various temperature (300 °C, 450 °C, 600 °C). Effect of thermal annealing on the composition of Ge-Co nanostructure has been studied. The morphology of the obtained Ge-Co nanostructures has been investigated using scanning electron microscopy The method of X-ray diffraction analysis has been used to investigate composition changes of Ge-Co. Diffractograms show the presence of Co_2GeO_4 catalyst at an annealing temperature of 600 °C. The sample with this annealing temperature shows the best properties as oxygen evolution catalyst.

Keywords: Ge-Co nanostructures, oxygen evolution catalyst, Ge nanowires, electrochemical deposition

Funding: The work was supported by the Grant of the President of the Russian Federation no. MK 5839.2021.1.3 and by the State assignment 2020-2022 no. FSMR-2020-0018.

Citation: Martynova I. K., Gavrilin I. M., Effect of thermal annealing on the composition of Ge-Co nanostructure obtained by electrochemical deposition. St. Petersburg State Polytechnical University Journal. Physics and Mathematics. 15 (3.1) (2022) 232–236. DOI: https://doi.org/10.18721/JPM.153.139

Материалы конференции
УДК 544.6
DOI: https://doi.org/10.18721/JPM.153.139

Влияние термического отжига на фазовый состав наноструктуры Ge-Co, полученной методом электрохимического осаждения

И. К. Мартынова [1] ✉, И. М. Гаврилин [1]

[1] Национальный исследовательский университет «МИЭТ», г. Москва, Россия

✉ Irisha-windsurfer@yandex.ru

Аннотация. В работе получены наноструктуры Ge-Co с помощью электрохимического осаждения. Исследовано влияние температурного отжига (300 °C, 450 °C, 600 °C) на фазовый состав этой структуры методом рентгеновского дифракционного анализа. Выявлено присутствие катализатора Co_2GeO_4 при температуре отжига в 600 °C. Образец при таком отжиге также показал наилучшие каталитические свойства.

Ключевые слова: наноструктуры Ge-Co, катализатор, нанонити Ge, электрохимическое осаждение

Финансирование: Исследование выполнено при поддержке гранта Президента Российской Федерации № МК 5839.2021.1.3 и Госзадания 2020-2022 № ФСМР-2020-0018.

Ссылка при цитировании: Мартынова И. К., Гаврилин И. М. Влияние термического отжига на фазовый состав наноструктуры Ge-Co, полученной методом электрохимического осаждения // Научно-технические ведомости СПбГПУ. Физико-математические науки. 2022. Т. 15. № 3.1. С. 232–236. DOI: https://doi.org/10.18721/JPM.153.139

Introduction

At present, due to the development of the global energy industry, there is a need to use clean and cheap fuel, including to reduce carbon dioxide emissions.

One of the ways to obtain ecological fuel is the electrolysis of water to produce hydrogen [1]. However, this process has a disadvantage, which is the slow reaction rate on conventional electrodes. To eliminate it, it is necessary to investigate various substances that accelerate electrochemical reactions, which are called catalysts. In this case, catalysts are needed for two processes on two electrodes: the hydrogen evolution reaction and the oxygen evolution reaction (OER). Oxygen evolution reaction (OER) is a limiting reaction in the process of generating molecular oxygen through chemical reaction, such as electrolysis of water into oxygen and hydrogen, and electrocatalytic oxygen evolution from oxides and oxoacids [2].

One of the promising areas of research on effective and stable oxygen evolution catalysts (OECs) are cobalt-based catalysts because of its OER activity and thermal stability [3]. There are many known methods for the synthesis of a cobalt-based catalysts, such as a method of selective reduction-oxidation from metal nitrates for getting cobalt catalyst doping Ag [4] or synthesis by chemical reduction followed by a process of thermal oxidation, which allows to obtain a compound of cobalt with rare-earth materials: ruthenium and iridium in powder form [5]. There are also such methods for obtaining cobalt-based catalysts as the sol-gel method [6] and vacuum-diffusion method [7] and electrochemical deposition [8]. The electrochemical deposition method is characterized by the absence of a high vacuum system, its speed and the ability to vary the parameters of the process to obtain various materials.

In this work, we report about formation OEC based on the one-dimension nanostructure Ge-Co by electrochemical deposition and investigate effect of thermal annealing on the composition of this structure.

Materials and Methods

In the syntesis of Ge-Co nanostucture the 50 μm-thickness titanium foil (batch VT 1–00) has been used as a substrate. These titanium samples have been previously cleaned in a mixture of H_2O_2:NH_4OH:H_2O (1:1:4) at 80 °C for 15 min, and then they have been washed in hot and cold deionized water for 5 min and dried. Then the samples surface has been activated in a mixture of HF:HNO_3:H_2O (1:2:6), washed in deionized water and dried again.

After that an array of spherical indium nanoparticles has been deposited by vacuum-thermal evaporation at the residual pressure of 1×10^{-5} Torr of material weighed portion of 35 mg from a Mo evaporator, placed at 40 cm from the substrate. After depositing the metals, the samples have been annealed in vacuum at 150 °C for 10 min.

Ge-Co structures have been formed on the substrates by electrochemical deposition in a three-electrode cell. A platinum plate has been used as an counter electrode, and a standard silver chloride electrode has been used as a reference one.

The solution contained 0.05 M of germanium (IV) oxide GeO_2, 0.5 M of potassium sulfate Na_2SO_4 and 0.1 M of tartaric acid with the addition of 0.05 g $CoCl_2$. The solution pH has been brought to 6.5 by adding NH_4OH. The solution temperature has been controlled using a LAUDA Alpha thermostat (LAUDA, Germany).

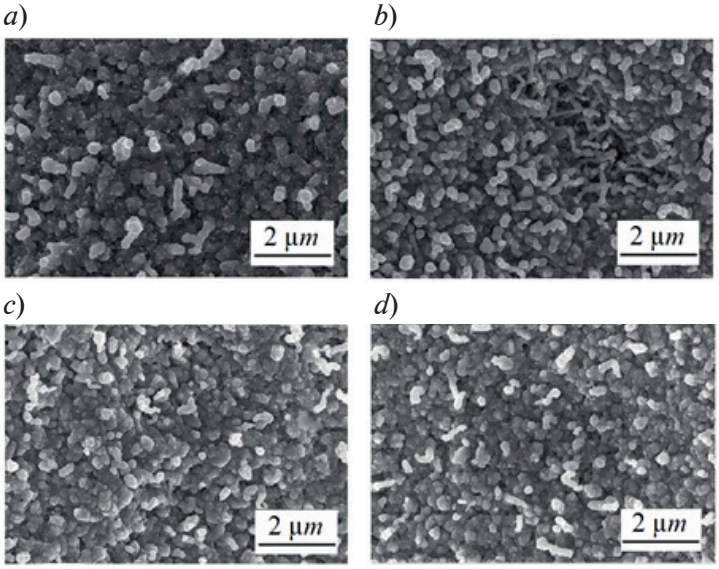

Fig. 1. SEM images of Ge-Co nanowires: sample without annealing (*a*), annealing 300 °C (*b*), annealing 450 °C (*c*), annealing 600 °C (*d*)

Deposition has been performed at constant voltage of −1.3 V for 1 min at the solution temperature of 85 °C. The voltage has been set using Autolab PGSTAT302N potentiostat/galvanostat (Metrohm, Netherlands).

After deposition, the samples have been annealed in atmosphere at various temperature (300 °C, 450 °C, 600 °C).

The method of X-ray diffraction analysis (XRD) has been used to deteminate the crystalline phases (germanium, cobalt, their oxides, etc.) after the formation of the Ge-Co compound and to investigate the effect of annealing at different temperatures on the composition of Ge-Co.

X-ray diffraction patterns (diffractograms) of synthesized samples have been obtained using the RADIAN DR-02 device with a copper X-ray tube and a nickel filter.

CV measurements have been performed by sweeping the potential from a value of 0.1 to 1.2 V (vs Ag/AgCl) using Autolab PGSTAT302N and a three-electrode system.

Results and Discussion

The images of the morphology of the Ge-Co structures both with annealing and without it obtained by scanning electron microscopy are shown in Fig.1.

According to the SEM images, a structural transformation of nanowires is observed in the annealing process. In the image of the sample without annealing (Fig. 1,*a*), some nanowires formations with a thickness of 250 nm can be seen, but the nanowires structures are not predominant. At 300 °C more nanowires appear, the thickness of which varies from 150 to 200 nm (Fig. 1,*b*). Annealing at 450 °C and 600 °C has a similar effect on the morphology of Ge-Co nanowires (Fig. 1, *c*, *d*). Nanowires become less visible, the thickness of nanowires decreases to about 100 nm. However after annealing at 600 °C it can be noticed more nanowires than that after annealing at 400 °C.

The results of X-ray diffraction after annealing germanium nanostructures with cobalt Ge-Co at various temperature are shown in Fig. 2. The sample without annealing has peaks of two phases: crystalline germanium and titanium substrate.

At annealing temperatures of 300 °C and 450 °C, there is an increase in the intensity of germanium peaks, especially the first peak (27.3°) [9]. With an increase in the annealing temperature, a slight shift of the germanium peaks to the right to the reference values is also noticeable.

However, at an annealing temperature of 600 °C, the diffractogram shows a presence of germanium-cobalt compounds in the nanostructure, particularly cobalt germanate Co_2GeO_4 at $2\theta = 30-40°$ [4], which has not been observed at lower annealing temperatures. A well-marked phase of titanium oxide and a certain amount of the compound Ti_5Ge_3 are also visible.

The first peak of germanium becomes indistinguishable due to the presence of titanium oxide, which leads to the overlap of two peaks and its sharp increase.

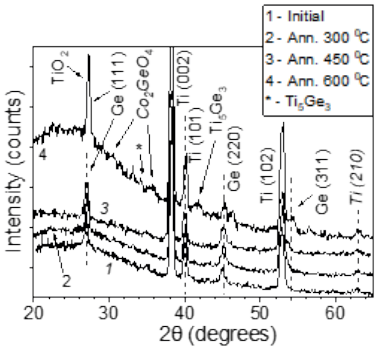

Fig. 2. X-ray diffractograms of Ge-Co samples after annealing at different temperatures

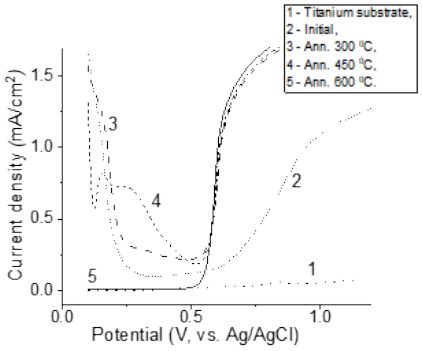

Fig. 3. CV curve of initial/annealing Ge-Co samples and titanium substrate

Additionally obtained Ge-Co samples after annealing and without it have been also tested for the OER activity in a solution of 1 M NaOH. Graphics of current density-voltage curve (CV curve) based on the results of the sample study are shown in Fig. 3. This figure also shows the CV curve of a pure titanium substrate obtained for comparison.

According to the graph of the titanium substrate, it can be seen that the current density almost does not change in the voltage range, which means that there are practically no electrochemical processes.

The current density for Ge-Co samples (except for the sample after annealing at 600°C) at a potential of 0.2 V to 0.5 V indicates reactions caused with the oxidation of germanium and cobalt. At a potential of 0.5 V, the current density increases due to the beginning of oxygen release. For a sample without annealing, the current density increases more slowly compared to annealing samples, which indicates its lower OER activity.

At the same time, with an annealing at 600 °C, reactions caused only with the release of oxygen are observed on the sample (the current density begins to increase only at a potential of 0.5 V) due to the presence of a cobalt germanate. It can be concluded that the annealing temperature at 600 °C is the most optimal temperature for the formation of an oxygen evolution catalyst based on Ge-Co nanostructure.

Conclusion

In the present work nanostructures Ge-Co have been prepared by electrodeposition from the aqueous solution. The effect of thermal annealing on the composition of Ge-Co has been investigated. According to the results of X-ray diffraction, with an increase in the annealing temperature, the crystal phase of germanium decreases and germanium compounds with cobalt are formed. On an annealing temperature at 600 °C, a compound cobalt germanate Co_2GeO_4 is found that could be a good oxygen evolution catalyst.

Acknowledgments

The "Educational and Methodical Center of Lithography and Microscopy", M.V. Lomonosov Moscow State University Research Facilities Sharing Centre was used.

REFERENCES

1. **Chen X. L., Li C. N., Gratzel M. T., Kostecki R. M.,** Nanomaterials for renewable energy production and storage, Chemical Society Reviews. 41 (23) (2012) 7909–7937.

2. **She Z.W., Kibsgaard J. K., Dickens C. F., Chorkendorff I. K., J.K.,** Combining theory and experiment in electrocatalysis: Insights into materials design, Science. 355 (6321) (2017) 1 12.

3. **Zhe X. Y., Wenchao L. S., Xiaohui W. Z., Bing W. X.,** Novel Cobalt Germanium Hydroxide for Electrochemical Water Oxidation, ACS Applied Materials & Interfaces. 10 (36) (2018) 30357–30366.

4. **Dong R. T., Du H. X., Sun Y. T, Huang K. W.,** Selective reduction-oxidation strategy to the conductivity-enhancing Ag-decorated Co-based 2D hydroxides as efficient electrocatalyst in oxygen evolution reaction, ACS Sustainable Chemistry & Engineering. 6 (10) (2018) 13420–13426.

5. **Xue Z. H, Su H., Yu Q. Y., Wang H. H.,** Janus Co/CoP nanoparticles as efficient Mott-Schottky electrocatalysts for overall water splitting in wide PH range, Advanced Energy Materials. 7 (12) (2017) 16023–16034.

6. **Su C., Wang W., Chen Y., Yang G.,** SrCo(0.9)Ti(0.10O(3-δ) as a new electrocatalyst for the oxygen evolution reaction in alkaline electrolyte with stable performance, ACS applied materials & interfaces. 7 (32) (2015) 17663–17670.

7. **Corona-Guinto J.L., Cardeco-García L., Martнnez-Casillas D.C., Sandoval-Pineda J.M.,** Performance of a PEM electrolyzer using RuIrCoOx electrocatalysts for the oxygen evolution electrode, International Journal of Hydrogen Energy. 38 (2013) 12667–12673.

8. **Huang B., Wang Y., Zhan S., Ye J.,** One-step electrochemical deposition of Schiff base cobalt complex as effective water oxidation catalyst, Applied Surface Science. 396 (2017) 121–128.

9. Crystallography Open Database URL: http://www.crystallography.net/cod/. Accessed May 13, 2022.

THE AUTHORS

MARTYNOVA Irina K.
Irisha-windsurfer@yandex.ru
ORCID: 0000-0002-6128-5244

GAVRILIN Ilya M.
gavrilin.ilya@gmail.com
ORCID: 0000-0002-0278-1598

Received 22.05.2022. Approved after reviewing 04.07.2022. Accepted 04.07.2022.

Conference materials
UDC 544.6
DOI: https://doi.org/10.18721/JPM.153.140

Laser-induced periodic surface structures formation and reversible crystallization in amorphous $Ge_2Sb_2Te_5$ thin films as a result of femtosecond irradiation

A. V. Kolchin [1] ✉, S. V. Zabotnov [1], D. V. Shuleiko [1], D. E. Presnov [1, 2, 3], M. E. Fedyanina [4], E. V. Kuzmin [5], P. K. Kashkarov [1]

[1] Lomonosov Moscow State University, Faculty of Physics, Moscow, Russia
[2] Lomonosov Moscow State University, Skobeltsyn Institute of Nuclear Physics, Moscow, Russia
[3] Lomonosov Moscow State University, Quantum Technology Center, Moscow, Russia
[4] National Research University of Electronic Technology, Institute of Advanced Materials and Technologies, Zelenograd, Russia
[5] Lebedev Physical Institute of the Russian Academy of Science, Moscow, Russia
✉ avkolchin@physics.msu.ru

Abstract. Femtosecond laser structuring opens for chalcogenide semiconductor $Ge_2Sb_2Te_5$ new perspectives in photonics applications due to wide change of its structural and optical properties in such processing. We studied laser-induced modification of amorphous $Ge_2Sb_2Te_5$ thin films on silicon substrates. The investigations show that periodic relief formation is accompanied by phase transitions to the fcc crystalline phase and back. Furthermore, the irradiated $Ge_2Sb_2Te_5$ samples demonstrate optical transparency in the near infrared region. The examined structures are interesting for further studies as a base of new memory devices which may possess optical anisotropy and be integrated into fiber optics applications.

Keywords: $Ge_2Sb_2Te_5$, femtosecond laser processing, laser-induced periodic surface structures, reversible phase transitions

Funding: This study was funded by the Russian Foundation for Basic Research (project no. 20-32-90111).

Citation: Kolchin A. V., Zabotnov S. V., Shuleiko D. V., Presnov D. E., Fedyanina M. E., Kuzmin E. V., Kashkarov P. K., Laser-induced periodic surface structures formation and rewersible crystallization in amorphous $Ge_2Sb_2Te_5$ thin films as a result of femtosecond irradiation, St. Petersburg State Polytechnical University Journal. Physics and Mathematics. 15 (3.1) (2022) 237–242. DOI: https://doi.org/10.18721/JPM.153.140

Материалы конференции
УДК 544.6
DOI: https://doi.org/10.18721/JPM.153.140

Лазерно-индуцированное формирование поверхностных периодических структур и обратимая кристаллизация в аморфных тонких пленках $Ge_2Sb_2Te_5$ как результат фемтосекундного облучения

А. В. Колчин [1] ✉, С. В. Заботнов [1], Д. В. Шулейко [1], Д. Е. Преснов [1, 2, 3], М. Е. Федянина [4], Е. В. Кузьмин [5], П. К. Кашкаров [1]

[1] Московский государственный университет имени М.В. Ломоносова, Физический факультет, Москва, Россия
[2] Московский государственный университет имени М.В. Ломоносова, Научно-исследовательский институт ядерной физики имени Д.В. Скобельцына, Москва, Россия

[3] Московский государственный университет имени М.В. Ломоносова,
Центр квантовых технологий, Москва, Россия
[4] Национальный исследовательский университет «Московский институт электронной техники»,
Институт перспективных материалов и технологий, Зеленоград, Россия
[5] Физический институт имени П.Н. Лебедева РАН, Москва, Россия
✉ avkolchin@physics.msu.ru

Аннотация. Фемтосекундное лазерное структурирование открывает для халькогенидного полупроводника $Ge_2Sb_2Te_5$ новые перспективы использования в приложениях фотоники благодаря широкому изменению его структурных и оптических свойств при такой обработке. Нами исследована лазерно-индуцированная модификация тонких аморфных пленок $Ge_2Sb_2Te_5$ на кремниевых подложках. Исследования показывают, что периодическое формирование рельефа сопровождается фазовыми переходами в ГЦК-кристаллическую фазу и обратно. Кроме того, облученные образцы $Ge_2Sb_2Te_5$ демонстрируют оптическую прозрачность в ближней инфракрасной области. Рассмотренные структуры представляют интерес для дальнейших исследований в качестве основы новых запоминающих устройств, которые могут обладать оптической анизотропией и быть интегрированы в волоконно-оптические приложения.

Ключевые слова: $Ge_2Sb_2Te_5$, фемтосекундная лазерная обработка, лазерно-индуцированные поверхностные периодические структуры, обратимые фазовые переходы

Финансирование: Работа выполнена в рамках гранта Российского фонда фундаментальных исследований № 20-32-90111.

Ссылка при цитировании: Колчин А. В., Заботнов С. В., Шулейко Д. В., Преснов Д. Е., Федянина М. Е., Кузьмин Е. В., Кашкаров П. К. Лазерно-индуцированное формирование поверхностных периодических структур и обратимая кристаллизация в аморфных тонких пленках $Ge_2Sb_2Te_5$ как результат фемтосекундного облучения // Научно-технические ведомости СПбГПУ. Физико-математические науки. 2022. Т. 15. № 3.1. С. 237–242. DOI: https://doi.org/10.18721/JPM.153.140

Introduction

The laser-induced periodic surface structures (LIPSS or “ripples”) based on $Ge_2Sb_2Te_5$ (GST225) promise large perspectives in the development of novel memory technologies and reconfigurable nanophotonic devices [1]. Usually, LIPSS have the period which is comparable to the wavelength of acted radiation and is significantly less than the laser spot diameter. Optical anisotropy in the visible and near-infrared ranges may emerge in such structures [2]. This is a promising way to encode information, especially in the case of GST225 processing via femtosecond laser irradiation when rewritable phase transitions to the crystalline phase are possible [3]. The significant difference between the optical properties of amorphous and crystalline phases of this material [4] makes a considerable contribution to optical anisotropy. Therefore, currently of great interest is the simultaneous LIPSS formation and phase transitions in amorphous GST225 thin films induced by femtosecond laser irradiation, including reversible phase transitions.

Thus, in this work we have irradiated thin GST225 films by femtosecond laser pulses to simultaneously fabricate LIPSS on the surface and achieve crystallization of GST225 and then investigated structural and optical properties of the modified samples.

Materials and Methods

Initial thin amorphous GST225 films with the thicknesses of 130 nm were deposited on dielectric substrates by magnetron sputtering of a crystalline target (ACI Alloys). Subsequent irradiation was provided by femtosecond laser system Avesta (wavelength $\lambda = 1250$ nm, pulse duration $\tau = 135$ fs, repetition rate $\upsilon = 10$ Hz). The laser fluence F varied from 0.05 to 0.15 J/cm^2. The

focused laser spot diameter was $D = 120 \pm 10$ μm. The samples were irradiated at normal incidence while moving continuously in one direction along the laser polarization at various speeds. As a result, single scanlines with the number of overlapping laser spots N_s from 3 to 750 were formed on the sample surface. Additionally, based on the results obtained for the single scanlines, a square 3x3 mm^2 area was fabricated in a raster mode for the pulse number $N_s = 150$ and step between scanlines $\Gamma = 100$ μm, for optical properties investigation.

The structural properties of initial and modified samples were studied by scanning electron microscopy (SEM; Carl Zeiss Supra 40) and Raman spectroscopy (Horiba Jobin Yvon HR800) at 488 nm excitation, as well as energy-dispersive X-ray (EDX) spectroscopy (Tescan Vega 3). Optical properties were defined via ellipsometry data analysis in the range 300–2000 nm (Horiba Uvisel 2). The type of phase transitions observed in the modified film was analyzed via the two-temperature model (TTM) calculations [5].

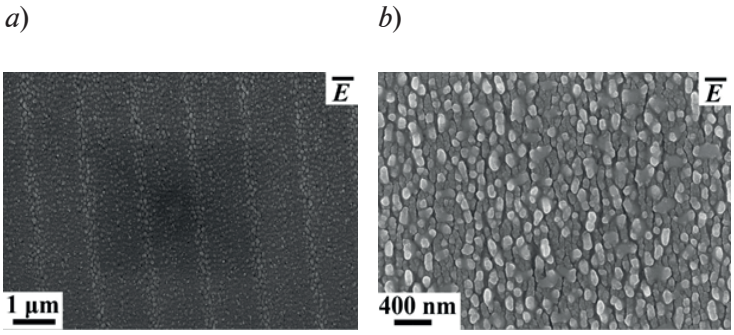

Fig. 1. SEM images of GST225 thin film, irradiated by the N_s=150 (*a*) and N_s=750 (*b*) laser pulses

Results and Discussion

According to SEM data the LIPSS formation on the samples irradiated with $F = 0.10 \pm 0.02$ J/cm^2 occurs at N_s=150 and higher values. Observed ripples period Λ varied from 1150 to 1350 nm, which is close to the wavelength of modifying laser pulses λ (Fig. 1,*a*). In all cases the gratings are directed orthogonally to the laser polarization. Such characteristics of the surface relief commonly indicate its formation mechanism as a result of interference between surface plasmon-polaritons and incident laser radiation [6]. In case of semiconductors such as GST225, the surface electromagnetic waves can be excited due to the transition of the near-surface layer to metal-like state, which means the dielectric permittivity of the irradiated material changes the sign from the positive to the negative one due to the intensive photoinduced generation of free charge carriers.

With the further increase of the $N_s \geq 300$ another LIPSS type was observed on the irradiated surface, in a form of ordered elongated clusters with the period $\Lambda = 130 \pm 30$ nm (Fig. 1,*b*). The orientation of obtained clusters is also perpendicular to the laser polarization. The clusters possess the longitudinal size in the range of 50–200 nm and the transversal size about 50 nm. The formation of such LIPPS is most likely explained by the thermo-capillar effects at the times which exceed pulse duration [7].

Raman spectroscopy indicated that surface modification of amorphous GST225 thin films induced by femtosecond laser pulses is accompanied by reversible phase transitions (Fig. 2). The Raman spectra of non-irradiated GST225 areas (N_s=0) shows the wide broadband at the range of 110–200 cm^{-1} due to the short-range crystallographic order of the amorphous phase (Fig. 2,*a*) [8]. The band consists of several lines near 125, 140, 158, 190 and 270 cm^{-1} which correspond to the A_1 $GeTe_{4-n}Ge_n$ (n = 1,2) corner-sharing tetrahedra, Sb_2Te_3 pyramids, A_{1g} hexagonal $GeTe_{4-n}Ge_n$ (n = 1,2), A_1 $GeTe_{4-n}Ge_n$ (n = 1,2) edge-sharing tetrahedra and F_2 $GeTe_4$ mode vibrations [8].

After femtosecond laser irradiation, the Raman spectra demonstrate the next transformations. The intensity of narrow peak near 125 cm^{-1}, which corresponds to $Ge_nTe_{4-n}Ge_n$ (n=1,2), increases with the growth of N_s from 3 to 15 (Fig. 2, *a*, *c*) while the line at 158 cm^{-1} decreases in intensity (Fig. 2,*d*). Such behavior may indicate transition to the face-centered cubic (fcc) crystalline phase [8]. The TTM calculations for the $F = 0.1$ J/cm^2 confirm this hypothesis (Fig. 3,*a*). According to the calculations the temperature of electron gas achieves ~$1.4 \cdot 10^4$ K during single

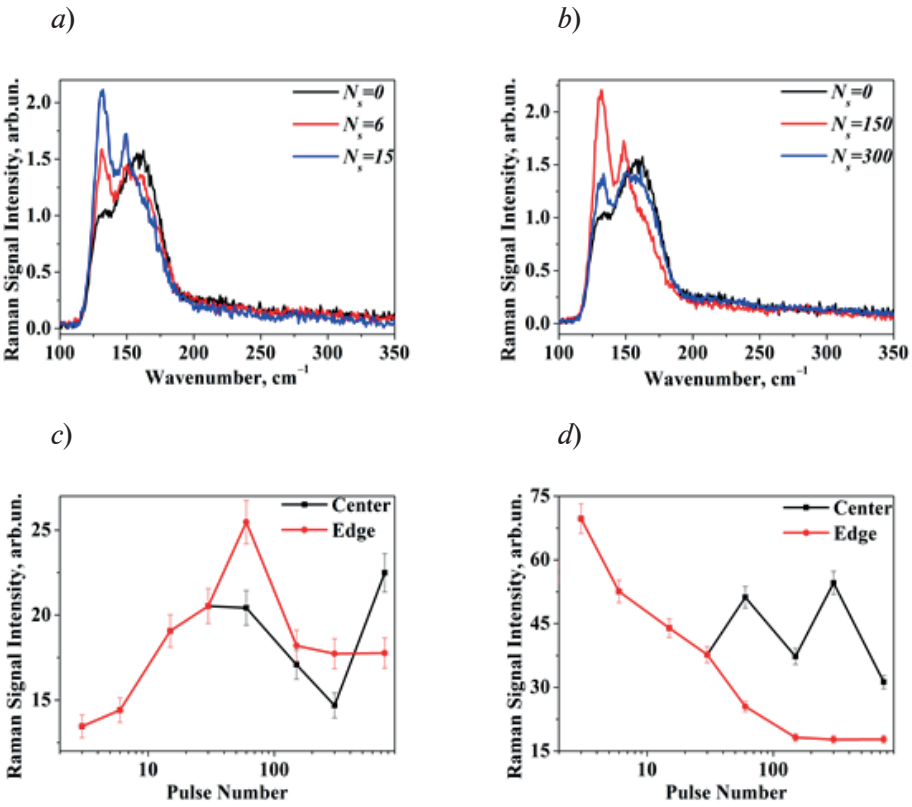

Fig. 2. Raman spectra of non-irradiated GST225 thin film (N_s=0) and samples for N_s=6 and N_s=15 (*a*). Raman spectra of non-irradiated GST225 thin film (N_s=0) and samples for N_s=150 and N_s=750 (*b*). Dependencies of integrated intensities of 125 cm^{-1} (*c*) and 158 cm^{-1} (*d*) line for center and edge of the scanlines on N_s

pulse treatment. The lattice temperature then increases due to the electron-phonon relaxation, and 2 ps after the laser pulse end exceeds the temperature of transition to fcc crystalline phase, which is 410 K. The peak temperature the GST225 lattice achieves during such heating is 480 K.

Additionally, at the values of $N_s > 75$, the 125 cm^{-1} Raman line decreases in intensity compared to the scan line edge (Fig. 2, *b*, *c*). Consequently, in the scan line center the Raman spectra become similar to non-irradiated GST225 thin films for $N_s \approx 300$ and higher. Such behavior can indicate re-amorphization of GST225. Such reversible phase transition is possible due to metastability of fcc crystalline GST225 [9] or rapid quenching of the melted material [10]. The cooling velocity more 10^{10} K/s and heat removal to the surface substrate contribute to the second mechanism of re-amorphization. It should be noted that the stoichiometry of GST225 film is not changed by femtosecond laser irradiation, which is confirmed by EDX spectroscopy data (Table 1).

Table 1

Concentration of Ge, Sb and Te atoms in initial amorphous GST225 thin film (N_s=0), as well as irradiated for the N_s=3, N_s=150 and N_s=750, defined by EDX spectroscopy

N_s	Atomic concentration, %		
	Ge	Sb	Te
0	18.9±1.5	25±3	56±3
3	17.1±1.0	25±1	58±5
150	19.5±1.2	26±2	55±2
750	18.9±0.7	27±1	54±3

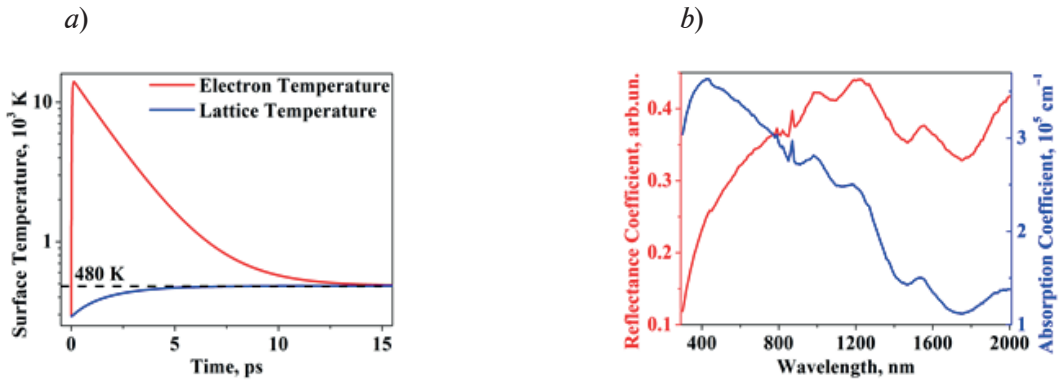

Fig. 3. Simulated surface temperature of GST225 during pulse treatment (*a*); reflectance and absorption spectra of irradiated GST225 sample, defined by ellipsometry data (*b*)

The reflectance and absorption spectra of irradiated GST225 sample are presented in Fig. 3,*b*. The reflectance coefficient grows from the 0.1 to 0.35 with the wavelength increase from 300 to 800 nm. Additionally, it demonstrates oscillations in the range of 800–2000 nm. Such behavior can be caused by the interference in GST225 thin film. On the other hand, the absorption coefficient decreases from $3.5 \cdot 10^5$ cm^{-1} to 10^5 cm^{-1} with the wavelength increase from 400 to 1800 nm. Thus, the studied GST225 films are transparent in the near-infrared range after femtosecond laser treatment and look promising for further studies and the development of new memory devices which may be compatible with the fiber optics applications, among other things.

Conclusion

We observed that surface modification of amorphous GST225 thin films induced by femtosecond laser pulses is accompanied by phase transitions to the fcc crystalline phase and back which is confirmed by Raman analysis and TTM simulations. Additionally, LIPSS with the period close to the laser wavelength were formed on GST225 surface at such treatment and the irradiated films are transparent in the near-infrared range. Therefore, the examined structures are interesting for further studies as a base of new memory devices which may possess optical anisotropy and be integrated into fiber optics applications.

Acknowledgments

The initial amorphous GST225 thin films fabrication, as well as ellipsometry measurements of the modified samples were provided at the MEMS and Electronic Components Core facilities centers, National Research University of Electronic Technology. SEM analysis was performed in the Educational and Methodical Center of Lithography and Microscopy, Lomonosov Moscow State University. Authors are grateful to L.A. Golovan, P.I. Lazarenko and S.A. Kozyukhin for fruitful discussions.

REFERENCES

1. **Smayev M.P., Lazarenko P.I., Budagovsky I.A., Yakubov A.O., Borisov V.N., Vorobyov Y.V., Kunkel T.S., Kozyukhin S.A.,** Direct single-pass writing of two-phase binary diffraction gratings in a $Ge_2Sb_2Te_5$ thin film by femtosecond laser pulses, Optics and Laser Technology. 153 (2022) 108212.

2. **Drevinskas R., Beresna M., Gecevičius M., Khenkin M., Kazanskii A.G., Matulaitiene I., Niaura G., Konkov. O.I., Terukov E.I., Svirko Y.P., Kazansky P.G.,** Giant birefringence and dichroism induced by ultrafast laser pulses in hydrogenated amorphous silicon, Appl. Phys. Lett. 106 (2015) 171106.

3. **Trofimov P.I., Bessonova I.G., Lazarenko P.I., Kirilenko D.A., Bert N.A., Kozyukhin S.A., Sinev I.S,** Rewritable and tunable laser-induced optical gratings in phase-change material films, ACS Appl. Mater. Interfaces. 13(27) (2021) 32031–32036.

4. **Xu Z., Chen C., Wang Z., Wu K., Chong H., Ye. H.,** Optical constants acquisition and phase change properties of $Ge_2Sb_2Te_5$ thin films based on spectroscopy, RSC Adv. 8 (37) (2018) 21040.

5. **Rethfeld B., Ivanov D.S., Garcia M.E., Anisimov S.I.,** Modelling ultrafast laser ablation, J. Phys. D.: Appl. Phys. 50 (2017) 193001.

6. **Bonse J., Rosenfeld A., Krüger J.,** On the role of surface plasmon polaritons in the formation of laser-induced periodic surface structures upon irradiation of silicon by femtosecond-laser pulses, J. Appl. Phys. 106 (2009) 104910.

7. **Rudenko A., Mauclair C., Garrelie F., Stoian R., Colombier J.P.,** Amplification and regulation of periodic nanostructures in multipulse ultrashort laser-induced surface evolution by electromagnetic-hydrodynamic simulations, Phys. Rev. B 99 (2019) 235412.

8. **Nemec P., Nazabal V., Moreac A., Gutwirth J., Benes L., Frumar M.,** Amorphous and crystallized GeSbTe thin films deposited by pulsed laser: Local structure using Raman scattering spectroscopy, Materials Chemistry and Physics 136 (2012) 935.

9. **Yamada N., Ohno E., Nishiuchi K., Akahira N., Takao M.,** Rapid-phase transitions of GeTe-Sb_2Te_3 pseudobinary amorphous thin films for an optical disk memory, J. Appl. Phys. 69 (1991) 2849.

10. **Huang H., Zuo F., Zhai F., Wang Y., Lai T., Wu Y., Gan F.,** Fast phase transition process of film induced by picosecond laser pulses with identical fluences, J. Appl. Phys. 106 (2009) 063501.

THE AUTHORS

KOLCHIN Aleksandr V.
avkolchin@physics.msu.ru
ORCID: 0000-0003-3033-9083

FEDYANINA Maria E.
mfh.miet@gmail.com
ORCID: 0000-0001-9779-2574

ZABOTNOV Stanislav V.
zabotnov@physics.msu.ru
ORCID: 0000-0002-2528-4869

KUZMIN Evgenii V.
e.kuzmin@lebedev.ru
ORCID: 0000-0002-6322-6838

SHULEIKO Dmitrii V.
shuleyko.dmitriy@physics.msu.ru
ORCID: 0000-0003-3555-6693

KASHKAROV Pavel K.
kashkarov@physics.msu.ru

PRESNOV Denis E.
denis.presnov@phys.msu.ru
ORCID: 0000-0002-9213-0165

Received 22.05.2022. Approved after reviewing 25.07.2022. Accepted 25.07.2022.

Conference materials
UDC 543.421/.424
DOI: https://doi.org/10.18721/JPM.153.141

Development of a technique for studying trimethylamine oxide solutions using planar SERS structures

D. V. Novikov [1] ✉, E. V. Latipov [2], S. V. Dubkov [1], A. I. Savitskiy [3], H. V. Bandarenka [4]
Af. A. Bestavashvili [5], P. Yu. Kopylov [5], D. G. Gromov [1]

[1] National Research University of Electronic Technology, Moscow, Russia;
[2] Institute of Nanotechnology of Microelectronics RAS, Moscow, Russia;
[3] 5Scientific-Manufacturing Complex «Technological Centre», Moscow, Russia;
[4] Belorussian State University of informatics and radioelectronic, Minsk, Belarus;
[5] World-Class Research Center "Digital Biodesign and Personalized Healthcare",
I. M. Sechenov First Moscow State Medical University, Moscow, Russia
✉ tororo@bk.ru

Abstract: This work is devoted to revealing the parameters of preparing SERS substrates for studying a low concentration trimethylamine oxide (TMAO) solution by Raman spectroscopy. A study was made of the effect of treatment with a 3,5% HCl solution, deionized water, and isopropanol vapor of planar surface enhance Raman spectroscopy (SERS) structures on the resulting Raman spectra of TMAO. We used a SERS substrate representing a multilayer structure: a mirror silver layer, a thin dielectric SiO_2 insulating layer, and an array of plasmonic Ag nanoparticles about 25 nm in size. The influence of the duration of the substrate soaking in the analyte solution on the quality of the Raman spectra was established. Raman studies of SERS substrates with TMAO were carried out using 532 and 785 nm lasers.

Keywords: nanoparticles, silver, trimethylamine oxide, SERS

Funding: This work was supported by State Assignment for 2020—2022 no. FSMR-2020-0018.

Citation: Novikov D. V., Latipov E. V., Dubkov S. V., Savitskiy A.I., Bandarenka H. V., Bestavashvili Af. A., Kopylov P. Yu., Gromov D. G., Development of a technique for studying trimethylamine oxide solutions using planar SERS structures. St. Petersburg State Polytechnical University Journal. Physics and Mathematics. 15 (3.1) (2022) 243—247. DOI: https://doi.org/10.18721/JPM.153.141

Материалы конференции
УДК 543.421/.424
DOI: https://doi.org/10.18721/JPM.153.141

Разработка методики исследования растворов триметиламин оксида с использованием планарных ГКР-структур

Д. В. Новиков [1] ✉, Е. В. Латипов [2], С. В. Дубков [1], А. И. Савицкий [3],
А. В. Бондаренко [4], А. А. Бестaвашвили [5], Ф. Ю. Копылов [5], Д. Г. Громов [1]

[1] Национальный исследовательский университет «МИЭТ», г. Москва, Россия;
[2] Институт нанотехнологий микроэлектроники РАН, г. Москва, Россия;
[3] Научно-производственный комплекс «Технологический центр», г. Москва, Россия;
[4] Белорусский государственный университет информатики и радиоэлектроники, г. Минск, Беларусь;
[5] Институт персонализированной кардиологии Центра «Цифровой биодизайн и персонализированное здравоохранение», Первый Московский Медицинский университет им.И.М.Сеченова, г. Москва, Россия
✉ tororo@bk.ru

Аннотация. Данная работа посвящена выявлению параметров подготовки ГКР-подложек для исследования раствора триметиламин оксида (ТМАО) малой концентрации методом Рамановской спектроскопии. Было проведено исследование влияния обработки 3,5% (масс.) раствором HCl , деионизованной водой и парами изопропанола планарных структур гигантского комбинационного рассеяния (ГКР) на получаемые спектры ТМАО. В работе использовалась ГКР-подложка, представляющая многослойную структуру: зеркальный серебряный слой, тонкий диэлектрический слой-изолятора SiO_2, массив плазмонных наночастиц Ag размером порядка 25 нм. Установлено влияние длительности вымачивания подложки в растворе аналита на качество рамановских спектров. Рамановские исследования ГКР-подложек с ТМАО производились с использованием лазеров 532 и 785 нм.

Ключевые слова: наночастицы, серебро, триметиламин оксид, гигантское комбинационное рассеяния

Финансирование: Работа выполнена в рамках государственного задания 2022-2020 гг. соглашение FSMR-2020-0018.

Ссылка при цитировании: Новиков Д. В., Латипов Е. В., Дубков С. В., Савицкий А. И., Бондаренко А. В., Бестaвашвили А. А., Копылов Ф. Ю., Громов Д. Г. Разработка методики исследования растворов триметиламин оксида с использованием планарных ГКР-структур // Научно-технические ведомости СПбГПУ. Физико-математические науки. 2022. Т. 15. № 3.1. С. 243–247. DOI: https://doi.org/10.18721/JPM.153.141

Introduction

Today, the medical industry needs faster, more sensitive, and more accurate methods for analyzing biological samples. Effective methods have already been found to detect and determine the concentration for most components of human blood (cells, large proteins, inorganic salts) [1]. However, there are biomarkers that require long and painstaking analysis for their detection. One such substance is trimethylamine oxide. The risk of atherosclerosis, thrombosis and even stroke increase if the concentration of TMAO exceeds 2,25 μM [2]. TMAO detection is possible using the High Performance Liquid Chromatography (HPLC) method [3]. HPLC has disadvantages that prevent the effective use of this method everywhere - a significant amount of human blood, complex equipment, high price, complicated sample preparation, analysis duration (more than 2 days) [3].

Surface enhanced Raman spectroscopy is an alternative method for diagnosing and detecting biomarkers [4]. This method is highly sensitive due to SERS-substrates based on nanoparticles of plasmonic metals (Au, Cu, Ag) [4]. The resulting spectrum makes it possible to judge the concentration of one or another component of the sample in the case of a study of a complex composition. However, high sensitivity may require compliance with a number of conditions: tight contact between the surface of the nanoparticle and the molecules under study; using a laser of a suitable wavelength; substrate pretreatment. Thus, there is an increased interest in determining these parameters for a quick and inexpensive study of TMAO in human blood.

In this work, we used planar SERS substrates based on a metal–dielectric mirror and an array of Ag nanoparticles. TMAO at a concentration of 10 mM used as the analyte. A weakly concentrated solution of hydrochloric acid and vapors of boiling isopropanol were used to treat the substrates. Lasers of two different wavelengths were used to study TMAO.

Materials and Methods

The SERS substrate was created in accordance with the method presented in earlier works [5]. Si(100) substrate with 300 nm SiO_2 thickness was used as the basis for the SERS structure. The adhesive layer Cr 50 nm deposited by magnetron sputtering. Then, a 100 nm Ag reflective layer formed on the substrate by vacuum thermal evaporation. After that, the reflective layer coated

with 20 nm SiO_2 as an insulator by the method of electron beam evaporation. The final step was the formation of an monolayer of uniformly distributed silver nanoparticles (NP) with average diameter 25 nm by annealing a 5 nm thin dispersed Ag film in vacuum at a temperature of 230 °C for 10 minutes. The size and distribution of nanoparticles were controlled by a Helios NanoLab 660 FEI scanning electron microscope. The formed monolayer of nanoparticles repeats the result obtained in previous work [5].

Before applying the analyte, some of the finished substrates were not processed. The second part was soaked in 3.5% (mass.) solution of hydrochloric acid (HCl) and washed in a slow flow of deionized water. The use of an identical technique by the authors in [6] showed that the treatment of Ag NPs in a weak solution of hydrochloric acid makes it possible to restore the intensity of the SERS signal for structures with different storage periods in air to the initial values. Thus, it can be assumed that the sulfide-oxide layer removed during the treatment from the surface of the nanoparticles is so small, so the treatment does not significantly affect the surface morphology. The third part treated with hot vapors of isopropyl alcohol 98.5%.

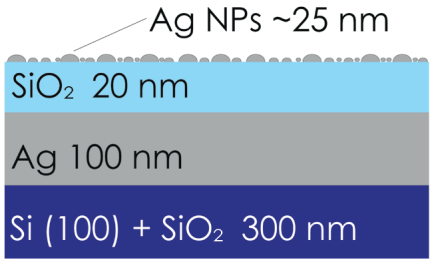

Fig. 1. SERS-substrate scheme

In this work TMAO with a concentration of 10 mM solutions used as analyte. The analyte was applied in two ways: by soaking the finished SERS structure in an analyte solution and by a drop from a dispenser. The substrates were soaked in the analyte solution for 5, 30, and 60 minutes. The substrates with the applied analyte dispenser dried in a fume hood at room temperature. Part of the samples with drops was covered with a cover slip for distribution and preservation in liquid form until the moment of examination.

The study was carried out on an inVia confocal microscope from Renishaw with the following parameters: wavelengths of 532 and 785 nm; laser power 5 mW; light spot diameter 4 μm; spectrum accumulation time 60 s.

Results and Discussion

Considering the effect of soaking on untreated substrates (see Fig. 1) in the solution, we found that the most rational approach is to expose the sample for 30 minutes (Fig. 2). Increasing the exposure time to 60 minutes (in 2 times) increases the intensity of the SERS spectrum by only 18%. It should be noting that the soaking of the samples made it possible to distribute the analyte much more uniformly than when applied by a drop.

The study of the pretreatment effect showed that the use of dilute hydrochloric acid makes it possible to increase the efficiency of SERS substrates due to the removal of oxide and sulfide layers from silver nanoparticles that appear as a result of annealing and in a natural way, respectively (Fig. 3). Processing for 30 seconds and subsequent washing in a weak stream of deionized water for 10 seconds showed the following results: reduction of noise level; an increase in the intensity of characteristic TMAO peaks; reduction of the thermal decomposition [7]. The use of an isopropanol led to a drop in the quality of the spectrum to the level of noise.

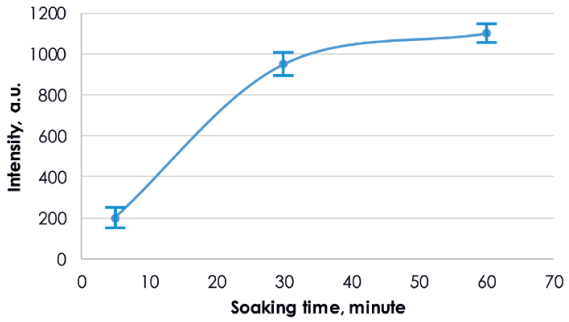

Fig. 2. Dependence of the SERS intensity of the 760^{-1} cm TMAO peak on the soaking time, wavelength 532 nm

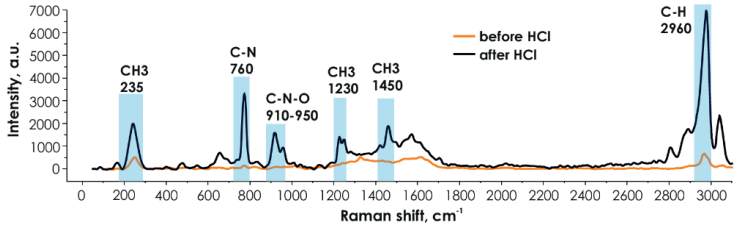

Fig. 3. Raman spectra of TMAO without and with preliminary treatment of the SERS-substrate in 3,5% HCl solution for 30 s, wavelength 532 nm

The study of the influence of the treatment time on the intensity of the SERS spectrum showed that the optimal time for holding the substrate in the acid solution is from 15 to 30 seconds (Fig. 4). A further increase in the treatment time of the substrate leads to a rapid decrease in the intensity.

Fig. 5 demonstrates the influence of the laser wavelength on the efficiency of recording the Raman spectrum of TMAO. The TMAO spectra are of a high quality at 532 and 785 nm. The wavelength of 532 nm provides better visibility of more peaks, due to the greater plasmonic activity of Ag NPs in the blue-green region of the spectrum. The 785 nm wavelength provides better visibility of C-N and C-N-O bond peaks and reduces the thermal degradation of the analyte.

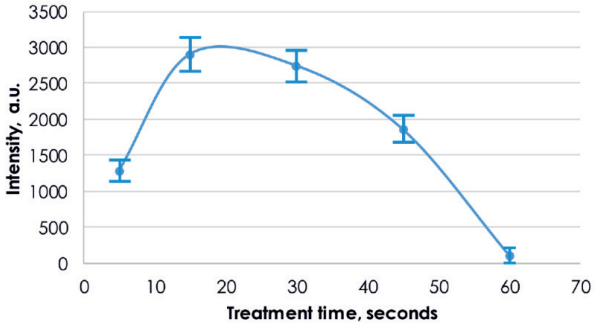

Fig. 4. Dependence of the intensity of the 760 cm^{-1} peak on the treatment time, wavelength 532 nm

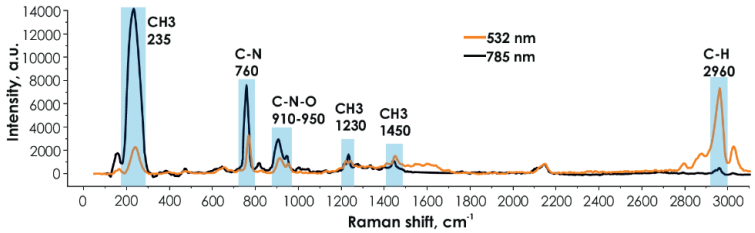

Fig. 5. TMAO spectra at different laser wavelengths, treatment time in acid solution ~30 s

Conclusion

In the course of the work, it was possible to establish the importance of a pre-treatment, soaking time and the laser used on the effectiveness of the study of TMAO. It was founding that the greatest effect in the study of TMAO using SERS-substrate based on Ag NPs will be provided that the following parameters are observed: treatment of the substrate in a 3,5% HCl solution for 15 to 30 seconds, followed by washing in a weak stream of deionized water; soaking time in TMAO solution for at least 30 minutes; using a 532 nm laser to search for C-H bonds of TMAO; using a 785 nm laser to search for C-N and C-N-O bonds of TMAO.

Acknowledgments

This work was supported by the State assignment 2020-2022 № FSMR-2020-0018.

REFERENCES

1. Encyclopedia Britannica. URL: https://www.britannica.com/science/blood-analysis. Accessed May 20, 2022.

2. **Gatarek P., Kaluzna-Czaplinska J.,** Trimethylamine N-oxide (TMAO) in human health, EXCLI JOURNAL. 20 (2021) 301–319.

3. **Leonardo P., Saleh A., Federico S., Alisdair R.,** Ultra-high-performance liquid chromatography high-resolution mass spectrometry variants for metabolomics research, Nature Methods. 18 (2021) 733–746.

4. **Cialla D., Мдrz A., Böhme R., Theil F., Weber K., Schmitt M., Popp J.,** Surface-enhanced Raman spectroscopy (SERS): progress and trends, Analytical and Bioanalytical Chemistry. 403 (2012) 27–54.

5. **Dubkov S.V., Savitskiy A.I., Trifonov A.Yu., Yeritsyan G.S., Shaman Yu.P., Kitsyuk E.P.,** Tarasov A., Shtyka O., Ciesielski R., Gromov D.G., SERS in red spectrum region through array of Ag-Cu composite nanoparticles formed by vacuum-thermal evaporation, Optical Materials: X. 7 (2020) 100055.

6. **Girel K.V., Panarin A.Y., Bandarenka H.V., Isic G., Bondarenko V.P., Terekhov S.N.,** Plasmonic silvered nanostructures on macroporous silicon decorated with graphene oxide for SERS-spectroscopy, Nanotechnology. 29 (2018) 395708.

7. **Munroe K.L., Magers D.H., Hammer N.I.,** Raman Spectroscopic Signatures of Noncovalent Interactions Between Trimethylamine N-oxide (TMAO) and Water, The Journal of Physical Chemistry B. 23 (115) (2011) 7699–7707.

THE AUTHORS

NOVIKOV Denis V.
tororo@bk.ru
ORCID: 0000-0002-9518-1208

BANDARENKA Hanna V.
h.bandarenka@gmail.com
ORCID: 0000-0003-4254-8261

LATIPOV Egor V.
la_019@mail.ru
ORCID: 0000-0002-6809-1952

BESTAVASHVILI Afina A.
afinabestavashvili@gmail.com
ORCID: 0000-0001-7551-1268

DUBKOV Sergey V.
sv.dubkov@gmail.com
ORCID: 0000-0003-1507-8807

KOPYLOV Philip Yu.
kopylov_f_yu@staff.sechenov.ru
ORCID: 0000-0001-5124-6383

SAVITSKIY Andrey I.
andr.savitskiy@gmail.com
ORCID: 0000-0002-8137-4340

GROMOV Dmitry G.
gromadima@gmail.com
ORCID: 0000-0002-4563-9831

Received 22.05.2022. Approved after reviewing 08.07.2022. Accepted 08.07.2022.

Conference materials
UDC 539.232+620.178.16
DOI: https://doi.org/10.18721/JPM.153.142

Evolution of tribological properties of the composite coatings on AMG3 aluminum alloy during the atmospheric exposure

I. E. Vyaliy [1] ✉, V. S. Egorkin [1], N. V. Izotov [1], U. V. Kharchenko [1],
A. N. Minaev [2], S. L. Sinebryukhov [1], S. V. Gnedenkov [1]

[1] Institute of Chemistry FEB RAS, Vladivostok, Russia
[2] Far Eastern Federal University, Vladivostok, Russia
✉ vyaly@ich.dvo.ru

Abstract: The paper presents the results of an evaluation of the tribological characteristics of samples with composite coatings during 12 months of atmospheric corrosion. Composite coatings were obtained by treating oxide layer formed by plasma electrolytic oxidation (PEO) with fluoropolymers: superdispersed polytetrafluoroethylene (SPTFE) or polyvinylidene fluoride (PVDF), as well as a suspension of SPTFE in PVDF. It was found that the composite coatings formed in suspension with a ratio of PVDF to SPTFE 1:5 demonstrate the best tribological performance among the studied samples and characterizes by initial coefficient of friction 0.006–0.010. It is shown that samples with composite coatings have 1–1.5 orders of magnitude lower wear rate ($9.7\cdot10^{-5}$–$4.4\cdot10^{-4}$ mm^3/(N·m)), in comparison with the PEO-treated sample ($3.9\cdot10^{-3}$ mm^3/(N·m)).

Keywords: aluminum, protective coating, plasma electrolytic oxidation, composite coating, tribology

Funding: This study was funded by RFBR, grant number 19–29–13020.

Citation: Vyaliy I. E., Egorkin V. S., Izotov N. V., Kharchenko U. V., Minaev A. N., Sinebryukhov S. L., Gnedenkov S. V., Evolution of tribological properties of the composite coatings on AMG3 aluminum alloy during the atmospheric exposure, St. Petersburg State Polytechnical University Journal. Physics and Mathematics. 15 (3.1) (2022) 248–252. DOI: https://doi.org/10.18721/JPM.153.142

Материалы конференции
УДК 539.232+620.178.16
DOI: https://doi.org/10.18721/JPM.153.142

Эволюция трибологических свойств композиционных покрытий на алюминиевом сплаве АМГ3 в процессе натурных испытаний

И. Е. Вялый [1] ✉, В. С. Егоркин [1], Н. В. Изотов [1], У. В. Харченко [1],
А. Н. Минаев [2], С. Л. Синебрюхов [1], С. В. Гнеденков [1]

[1] Институт химии ДВО РАН, г. Владивосток, Россия
[2] Дальневосточный Федеральный Университет, г. Владивосток, Россия
✉ vyaly@ich.dvo.ru

Аннотация. В работе представлены результаты оценки изменения трибологических характеристик образцов с композиционными покрытиями в течение 12 месяцев атмосферной коррозии. Композиционные покрытия формировали обработкой

оксидных слоев, получаемых методом плазменного электролитического оксидирования (ПЭО), фторполимерами: ультрадисперсным политетрафторэтиленом (УПТФЭ) или поливинилиденфторидом (ПВДФ), а также суспензией УПТФЭ в ПВДФ. Выявлено, что композиционные покрытия, формируемые в суспензии с соотношением ПВДФ и УПТФЭ 1:5 демонстрируют наилучшие трибологические показатели среди исследованных образцов, обладая начальным значением коэффициента трения равным 0,006–0,010 Установлено, что образцы с композиционными покрытиями характеризуются меньшей на 1–1,5 порядка величины ($9{,}7\cdot10^{-5}$ – $4{,}4\cdot10^{-4}$ мм^3/(Н·м)) скоростью износа в сравнении с ПЭО-покрытием ($3{,}9\cdot10^{-3}$ мм^3/(Н·м)).

Ключевые слова: алюминий, защитное покрытие, плазменное электролитическое оксидирование, композиционное покрытие, трибология

Финансирование: Исследование выполнено при поддержке гранта РФФИ № 19-29-13020.

Ссылка при цитировании: Вялый И. Е., Егоркин В. С., Изотов Н. В., Харченко У. В., Минаев А. Н., Синебрюхов С. Л., Гнеденков С. В. Эволюция трибологических свойств композиционных покрытий на алюминиевом сплаве АМГ3 в процессе натурных испытаний // Научно-технические ведомости СПбГПУ. Физико-математические науки. 2022. Т. 15. № 3.1. С. 248–252. DOI: https://doi.org/10.18721/JPM.153.142

Introduction

The formation of wearproof protective surface layers on aluminum and its alloys is an important scientific and practical task. One of the possible ways to solve this problem is the creation of the composite polymer-containing coatings [1]. Plasma electrolytic oxidation (PEO) could be a suitable method to form the oxide matrix for such composite layers. The presence of CF_2 groups provides polytetrafluoroethylene with nonpolarity and both low surface energy and a low coefficient of friction [2, 3]. The performed research established the high level of protection provided by such coatings to aluminum alloy [4, 5]. For the layers formed using PVDF:SPTFE suspensions additional increase in barrier properties is provided by the multimodal surface relief formed by the SPTFE microparticles. This type of morphological structure is responsible for the appearance of a three-phase coating/air/electrolyte interface. This results in a low part of the surface (less than 3%) being in direct contact with corrosive medium [6]. However, it is necessary to verify the obtained parameters under appropriate exploitation conditions due to the fact that properties of the polymeric layers could be affected by the UV light. The paper presents the results of an evaluation of changes in the tribological characteristics of samples with composite coatings during 12 months of atmospheric corrosion. Composite coatings were formed by treating oxide layers obtained by plasma electrolytic oxidation (PEO) with fluoropolymers: superdispersed polytetrafluoroethylene (SPTFE) or polyvinylidene fluoride (PVDF), as well as a suspension of SPTFE in PVDF.

Materials and Methods

AMg3 aluminum alloy rectangular sheets with dimensions 50×50×2 mm^3 were used as samples to form the coatings.

For the formation of PEO-layers a two-stage bipolar mode was used. At the first stage the voltage during the anode period increased from 30 to 540 V at a rate of 3.4 V/s, and then during the second stage the voltage was maintained at 540 V for 750 s. In the cathodic period the current density was hold at 0.12 A/cm^2 for 900 s. The electrolyte contained 20 g/L $Na_2SiO_3\cdot5H_2O$, 10 g/L $Na_2B_4O_7\cdot10H_2O$, 2 g/L NaF and 2 g/L KOH. The presented electrolyte composition and mode polarization parameters allowed us to obtain thick surface layers with a developed surface.

In order to form composite coating on the sample with the PEO-layer by dip-coating method, the 15% suspension of SPTFE in isopropyl alcohol) was used (SPTFE sample). The samples were then

heat treated at 315 °C for 15 min to provide the best pores filling with a fluoropolymer material. The PVDF-layer was formed by immersing the sample in a 6% solution of polyvinylidenefluoride (PVDF sample) in N-methyl-2-pyrrolidone followed by drying at 70 °C for 2 h. To form PVDF/SPTFE-coating, SPTFE particles were added to the PVDF solution at a ratio 1:5 (PVDF:SPTFE 1:5 sample). Then the samples were dip-coated and dried at 65 °C for 3 h.

Thickness of the formed PEO and composite coatings was measured using a VT-201 eddy current thickness gauge (KID, Russia).

The atmospheric corrosion testing of the samples during one year exposure was carried out at the Marine Corrosion Test Station of the Institute of Chemistry of FEB RAS, located on Russkiy Island, Rynda Bay (Sea of Japan). This water area has a salinity of seawater close to the average oceanic (34 ‰) and classifies according to ISO 9223:2012 as category C3, i.e., a marine environment with medium atmospheric corrosivity. The samples were exposed at an angle of 45 to the horizon on racks located about 20 m away from the coastline. The samples were withdrawn from the test site after 3, 6 and 12 months of exposure.

Tribological tests were carried out using Tribometer (CSM Instruments, Switzerland) operated via InstrumX software. Tests were performed according to the "ball–disk" test scheme: Ø10 mm corundum ball at load of 10 N and a linear rotation speed of 50 mm/s was used as a counterbody. After tribological tests, the wear tracks were examined using the MetekSurtronic 25 profilometer and the wear rate was calculated using InstrumX software (CSM Instruments, Switzerland).

Results and Discussion

Fig. 1 shows the dependences of the coefficient of friction (COF) on the number of cycles for SPTFE-coated samples tested after atmospheric exposure. The data for uncoated aluminum alloy and PEO-coating are provided for comparison. For the AMg3 aluminum alloy, there is a sharp rise in the COF from 0.11–0.14 to 0.55–0.56, which was stable during the entire test at 100 cycles. The sample with 69±6 μm thickness PEO-coating showed a slightly smoother rise in COF from 0.15–0.16 to 0.84 with a gradual decrease to 0.80 over 42,000 cycles at the moment of abrasion of the coating to the substrate, which is accompanied by a sharp drop in COF, tending to the level of the uncoated sample.

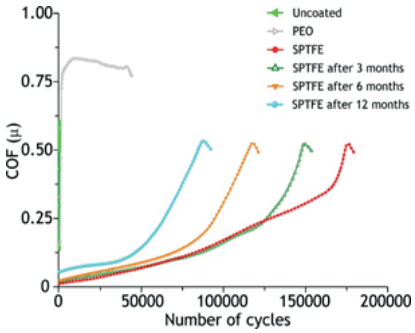

Fig. 1. Dependencies of the coefficient of friction on the number of cycles for uncoated samples, samples with PEO-coating and with SPTFE-coating during atmospheric corrosion

For samples with 70±4 μm thickness PEO-coatings with SPTFE (Fig. 1), with 79±3 μm thickness PEO-coatings with PVDF-film and with 82±5 μm thickness with PVDF:SPTFE 1:5-layer (Fig. 2), there is a significant decrease in the coefficient of friction, in comparison with the sample with PEO-coating only. As both graphs show, in comparison with the PEO-layer, the composite coatings reduce the COF by 16–17 times. For samples with composite coatings before corrosion testing, the coefficient of friction was equal to 0.009 for SPTFE-layers, 0.019 for PVDF-layers and 0.006 for PVDF:SPTFE 1:5-coatings. As a result of exposure for 3–12 months the increase in the coefficient of friction is observed from 0.015 to 0.060 for SPTFE, from 0.03 to 0.04 for PVDF and from 0.007 to 0.010 for PVDF:SPTFE 1:5 samples.

The shape of the curves indicates that despite the tendency of tribological characteristics to decrease, the wear mechanism itself has not changed: it was uniform abrasion. However, after

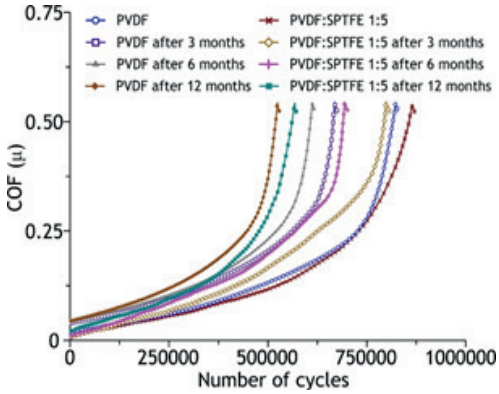

Fig. 2. Dependencies of the coefficient of friction on the number of cycles for PVDF and PVDF:SPTFE 1:5 samples during atmospheric corrosion test

12 months exposure to atmosphere, the smallest increase in the initial coefficient of friction from 0.01 to 0.02 was recorded only for the PVDF:SPTFE 1:5 sample (Fig. 2).

The results presented in Table 1 allow us to conclude that samples with composite coatings have 1 to 1.5 orders of magnitude lower wear rate ($9.7 \cdot 10^{-5} - 4.4 \cdot 10^{-4}$ mm^3/(N·m)), in comparison with PEO-treated ($3.9 \cdot 10^{-3}$ mm^3/(N·m)) and uncoated aluminum alloy samples ($5.8 \cdot 10^{-3}$ mm^3/(N·m)).

The SPTFE sample showed the highest wear ($4.4 \cdot 10^{-4}$ mm^3/(N·m)) among the samples with polymer layers, due to the peculiarities of its preparation and smaller thickness, in comparison with PVDF and PVDF:SPTFE 1:5 samples ($2.2 \cdot 10^{-4}$ mm^3/(N·m) and $1.1 \cdot 10^{-4}$ mm^3/(N·m)), respectively.

Table 1

Number of cycles and wear rate for the samples under study after the atmospheric corrosion test for 0, 3, 6, 12 months

Samples	Number of cycles ($\times 10^3$)*				Wear rate, mm^3/(N·m)			
	0	3	6	12	0	3	6	12
Uncoated	0.1	–			$5.8 \cdot 10^{-3}$	–		
PEO	42	–			$3.9 \cdot 10^{-3}$	–		
SPTFE	174	149	117	86	$4.2 \cdot 10^{-4}$	$4.2 \cdot 10^{-4}$	$4.3 \cdot 10^{-4}$	$4.4 \cdot 10^{-4}$
PVDF	823	669	614	525	$1.2 \cdot 10^{-4}$	$1.8 \cdot 10^{-4}$	$1.9 \cdot 10^{-4}$	$2.2 \cdot 10^{-4}$
PVDF:SPTFE 1:5	864	802	694	565	$9.7 \cdot 10^{-5}$	$9.7 \cdot 10^{-5}$	$9.9 \cdot 10^{-5}$	$1.1 \cdot 10^{-4}$

Note. The number of cycles was fixed until the coating was abraded to the substrate.

Conclusion

Evolution of tribological properties of the composite coatings on AMg3 aluminum alloy during one year of atmospheric corrosion tests. The least increase of the rate wear is observed for the SPTFE sample (from $4.2 \cdot 10^{-4}$ to $4.4 \cdot 10^{-4}$ mm^3/(N·m), which is associated with its lower thickness compared to PVDF and PVDF:SPTFE 1:5 samples. For the last two CCs, having similar thickness, the rate wear increased from $1.2 \cdot 10^{-4}$ to $2.2 \cdot 10^{-4}$ mm^3/(N·m) and from $9.7 \cdot 10^{-5}$ to $1.1 \cdot 10^{-4}$ mm^3/(N·m), respectively. Such a decrease in characteristics may be associated with some degradation of the polymer layer (due to exposure to solar radiation, temperature changes, penetration of a corrosive medium into coating microdefects). At the same time, it should be noted that the coating formed using SPTFE microparticles not only demonstrated the highest wearproof, but also the here smallest decrease.

REFERENCES

1. **Egorkin V. S., Vyaliy I. E., Sviridov N. S., Minaev A. N., Sinebryukhov S. L., Gnedenkov S. V.,** Formation and electrochemical properties of the hydrophobic composite coatings on aluminum alloy, Defect and Diffusion Forum 386 (2018) 315–320.

2. **McKeen L.W.,** The effect of UV light and weather on plastics and elastomers, 3rd ed.; William Andrew: Norwich, NY, USA, (2013) 400.

3. **Yu Y., Chen L., Weng D., Wang, J., Chen C., Mahmood A.,** A promising self-assembly PTFE coating for effective large-scale deicing, Prog. Org. Coat. 147 (2020) 105732.

4. **Gnedenkov S. V., Sinebryukhov S. L., Egorkin V. S., Vyalyi I. E., Mashtalyar D. V., Nadaraia K. V., Ryabov D. K., Buznik V. M.,** Formation and properties of composite coatings on aluminum alloys, Russ. J. Inorg. Chem. 62 (2017) 1–11.

5. **Egorkin V. S., Mashtalyar D. V., Gnedenkov A. S., Filonina V. S., Vyaliy I. E., Nadaraia K. V., Imshinetskiy I. M., Belov E. A., Izotov N. V., Sinebryukhov S. L., Gnedenkov S. V.,** Icephobic performance of combined fluorine-containing composite layers on Al-Mg-Mn-Si alloy surface, Polymers 13 (2021) 3827.

6. **Gnedenkov S. V., Sinebryukhov S. L., Egorkin V. S., Mashtalyar D. V., Alpysbaeva D. A., Boinovich L. B.,** Wetting and electrochemical properties of hydrophobic and superhydrophobic coatings on titanium, Colloids Surf., A. 383 (2011) 61–66.

THE AUTHORS

VYALIY Igor E.
vyaly@ich.dvo.ru
ORCID: 0000-0003-3806-1709

MINAEV Aleksander N.
aminaev@mail.ru
ORCID: 0000-0002-8072-306X

EGORKIN Vladimir S.
egorkin@ich.dvo.ru
ORCID: 0000-0001-5489-6832

SINEBRYUKHOV Sergey L.
sls@ich.dvo.ru
ORCID: 0000-0002-0963-0557

IZOTOV Nikolai V.
nikolaj.izotov@mail.ru
ORCID: 0000-0001-9504-1523

GNEDENKOV Sergey V.
svg21@hotmail.com
ORCID: 0000-0003-1576-8680

KHARCHENKO Ulyana V.
ulyana-kchar@mail.ru
ORCID: 0000-0001-5166-5609

Received 23.05.2022. Approved after reviewing 07.06.2022. Accepted 09.06.2022.

Conference materials
UDC 539.232+620.193.75
DOI: https://doi.org/10.18721/JPM.153.143

Changes in barrier properties of protective composite coatings on aluminum alloy during climatic testing

I. E. Vyaliy [1] ✉, V. S. Egorkin [1], N. V. Izotov [1], U. V. Kharchenko [1],
A. N. Minaev [2], S. L. Sinebryukhov [1], S.V. Gnedenkov [1]

[1] Institute of Chemistry FEB RAS, Vladivostok, Russia
[2] Far Eastern Federal University, Vladivostok, Russia
✉ vyaly@ich.dvo.ru

Abstract: The paper reveals the changes in corrosion properties of the samples with composite coating subjected to atmospheric corrosion test for 6 months. Composite coating (CC) was formed by treatment of oxide layer obtained by plasma electrolytic oxidation (PEO) with suspension of superdispersed polytetrafluoroethylene microparticles (SPTFE) in polyvinylidenefluoride (PVDF). The corrosion current density was compared for the composite coatings, PEO-coated and untreated samples. It is shown that corrosion current density for the sample with CC tested for 6 months ($2.9 \cdot 10^{-11}$ A·cm^{-2}) is more than 3 orders of magnitude lower in comparison with the sample with PEO-layer ($3.5 \cdot 10^{-8}$ A·cm^{-2}) and almost 6 orders of magnitude less than for uncoated aluminium alloy ($1.7 \cdot 10^{-5}$ A·cm^{-2}).

Keywords: aluminum, protective coating, plasma electrolytic oxidation, composite coating, electrochemistry

Funding: This study was funded by RFBR, grant number 19-29-13020.

Citation: Vyaliy I. E., Egorkin V. S., Izotov N. V., Kharchenko U. V., Minaev A. N., Sinebryukhov S. L., Gnedenkov S. V., Changes in barrier properties of protective composite coatings on aluminum alloy during climatic testing, St. Petersburg State Polytechnical University Journal. Physics and Mathematics. 15 (3.1) (2022) 253–258. DOI: https://doi.org/10.18721/JPM.153.143

Материалы конференции
УДК 539.232+620.193.75
DOI: https://doi.org/10.18721/JPM.153.143

Изменение барьерных свойств защитных композиционных покрытий на алюминиевом сплаве при климатических испытаниях

И. Е. Вялый [1] ✉, В. С. Егоркин [1], Н. В. Изотов [1], У. В. Харченко [1],
А. Н. Минаев [2], С. Л. Синебрюхов [1], С. В. Гнеденков [1]

[1] Институт химии ДВО РАН, г. Владивосток, Россия
[2] Дальневосточный Федеральный Университет, г. Владивосток, Россия
✉ vyaly@ich.dvo.ru

Аннотация. В работе представлены данные, характеризующие динамику изменения коррозионных свойств образцов с композиционным покрытием, подвергнутых атмосферной коррозии в течение 6 мес. Композиционное покрытие (КП) формировали обработкой оксидного слоя, полученного плазменно-электролитическим оксидированием (ПЭО), суспензией микрочастиц ультрадисперсного политетрафторэтилена (УПТФЭ)

в поливинилиденфториде (ПВДФ). Проведено сопоставление полученных значений тока коррозии после 3 и 6 месяцев испытаний с соответствующими значениями для необработанного образца и образца с ПЭО-покрытием. Установлено, что барьерные свойства образца с КП более чем на 3 порядка выше по сравнению с образцом с ПЭО-слоем и почти на 6 порядков выше, чем у сплава без покрытия.

Ключевые слова: алюминий, защитное покрытие, плазменное электролитическое оксидирование, композиционное покрытие, электрохимия

Финансирование: Исследование выполнено при поддержке гранта РФФИ № 19-29-13020.

Ссылка при цитировании: Вялый И. Е., Егоркин В. С., Изотов Н. В., Харченко У. В., Минаев А. Н., Синебрюхов С. Л., Гнеденков С. В. Изменение барьерных свойств защитных композиционных покрытий на алюминиевом сплаве при климатических испытаниях // Научно-технические ведомости СПбГПУ. Физико-математические науки. 2022. Т. 15. № 3.1. С. 253–258. DOI: https://doi.org/10.18721/JPM.153.143

Introduction

Protection of aluminum and its alloys, which are prone to corrosion in halide-containing media, is an important scientific and sought after practical task [1]. The performed studies established a high level of protection provided by a composite coating (CC), where heterogeneous oxide layer is used as a matrix for the polymer layer on AMg3 aluminum alloy [2, 3]. However, the conditions of exploitation and electrochemical express-testing may vary significantly [4]. Therefore, it is necessary to verify the obtained parameters under appropriate exploitation conditions. For this purpose, as the most suitable for testing and evaluating the influence of these factors on the anti-corrosion properties of composite coatings the estimation of protective properties assessed via electrochemical study of samples subjected to atmospheric corrosion test for 3 and 6 months was performed.

Materials and Methods

Plasma electrolytic oxidation of AMg3 aluminum alloy samples with size of 30 × 30 × 2 $(mm)^3$ was carried out in bipolar mode for 15 minutes. The voltage during the anodic period was increased from 30 to 540 V at a rate of 3.4 V/s. During the cathodic period current density was maintained at 0.12 $A \cdot cm^{-2}$. The duty cycle was equal to 1. The silicate electrolyte (20 g/L $Na_2SiO_3 \cdot 5H_2O$, 10 g/L $Na_2B_4O_7 \cdot 10H_2O$, 2 g/L NaF and 2 g/L KOH) and polarization mode led to formation of the layer with a complex morphology [1].

To form CC, superdispersed polythetrafluoroetylene (SPTFE) particles were added to the 6% polyvinylidenefluoride (PVDF) solution in N-methyl-2-pyrrolidone [1]. Then the samples were dip-coated and dried at 65 °C for 3 h.

To study the dynamics of changes in electrochemical properties during the atmospheric corrosion, the samples were installed at the Marine Corrosion Test Station of the Institute of Chemistry of FEB RAS, located on Russkiy Island, Rynda Bay [5]. This water area has a salinity of seawater close to the average oceanic (34‰) and classifies according to ISO 9223:2012 as category C3, i.e. a marine environment with medium atmospheric corrosivity. Samples with size of 30×30×2 $(mm)^3$ were exposed at an angle of 45 to the horizon on racks located about 20 m away from the coastline. The witness samples were taken after 3 and 6 months of field testing.

The morphology of the composite coatings was investigated by scanning electron microscopy (SEM) using Carl Zeiss EVO 40 microscope with an acceleration voltage of 20 kV.

Electrochemical properties were investigated using ModuLab XM ECS (Solartron analytical, Farnborough, UK). Measurements were carried out in a three-electrode cell in a 3 wt.% NaCl. Platinum mesh was used as a counter electrode, and saturated calomel electrode was used as a reference electrode. The exposed area of samples was equal to 1 cm^2. The samples were kept

in a solution for 60 minutes prior to electrochemical tests to achieve a steady state. To record the impedance spectrum, a sinusoidal signal with an amplitude of 10 mV (rms) was used. The experiments were carried out in the frequency range from 0.1 MHz to 0.01 Hz at a logarithmic sweep of 10 points per decade. The potentiodynamic polarization measurements were carried out at a scan rate of 1 mV·s^{-1} in the range from E_c –0.25 V to E_c +2 V, where E_c is the corrosion potential. The values of polarization resistance R_p were determined in separate experiments from the linear potential current density plot in range of $E_c \pm 20$ mV as the $R_p = \Delta E/\Delta j$.

Results and Discussion

Analysis of the SEM-images in Fig. 1 indicates that PEO-layer formed in the established oxidation mode and electrolyte, have a complex morphology. Application of PVDF solution with SPTFE microparticles atop the PEO-layer leads to a shielding of microdefects and pores and covers surface with uniformly distributed particles. PVDF solution embeds microparticles and provides adhesion to the PEO-coating.

Moreover, the microparticles form large agglomerates, which probably better cover the porous part of the PEO-layer and increase its anti-corrosion parameters [1].

SEM image of the CC surface after 6 months of the atmospheric exposure is presented in Fig. 2. Composite coating has high strength and resistance to temperature changes, as well as resistance to ultraviolet radiation and atmospheric precipitation. The SPTFE particles sealed the pores and defects, preventing pitting corrosion. At the same time, there are no defects in the PEO-coating, which, during 6 months of atmospheric corrosion, remained completely covered with a PVDF/SPTFE-layer.

In the investigated range of potentials, the potentiodynamic curve for an uncoated aluminum alloy is the typical for this material. After the cathodic part of the curve (Fig. 3), a breakdown of the natural oxide-hydroxide film occurs with a corresponding sharp increase in the current density during the development of the corrosion process. The potentiodynamic curves obtained for the coated samples are located in the zone of significantly lower currents compared to the curve for the uncoated alloy and demonstrate a significant inhibition of the corrosion process.

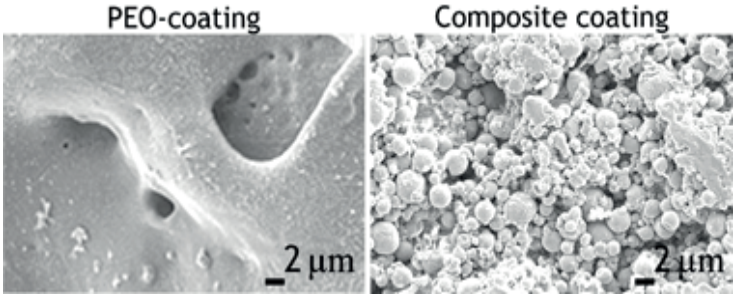

Fig. 1. SEM-images of the PEO and composite coatings formed on the AMg3 aluminum alloy

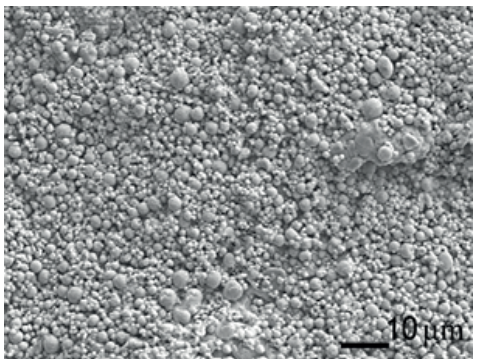

Fig. 2. SEM-image of the composite coating after 6 months of the atmospheric corrosion test

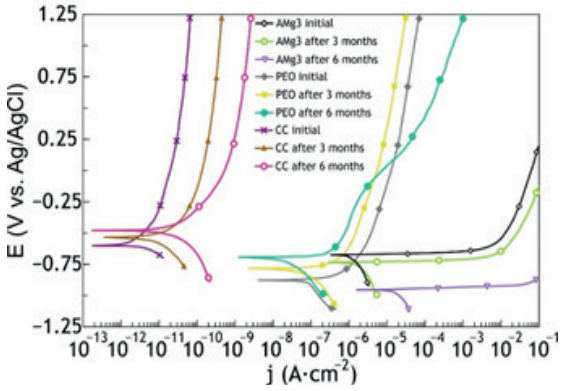

Fig. 3. Evolution of the electrochemical properties for uncoated, PEO-coated and composite polymer contained AMg3 aluminum alloy during atmospheric exposure

Electrochemical studies of the samples found that the formed protective layers significantly reduce the corrosion current density.

Thus, for a sample with a composite coating, the corrosion current density is equal to $7.5 \cdot 10^{-12}$ A·cm^{-2}, which is more than 4 and 5 orders of magnitude lower than this parameter for the PEO-coated ($I_c = 8.4 \cdot 10^{-8}$ A·cm^{-2}) and for the uncoated AMg3 aluminum alloy ($I_c = 1.1 \cdot 10^{-6}$ A·cm^{-2}), respectively.

The composite coating has the highest barrier properties among the studied layers due to its multimodal textured surface (Fig. 1). According to the results of [6], the area of direct contact of such coatings with an aggressive medium, calculated using the Cassie-Baxter equation, is no more than 3% of the total area of the sample immersed in a chloride-containing media. The stable state of the entrapped air in the irregularities of the multimodal surface, which prevents the formation of a wetting film between the liquid and the developed surface of the coating, provides high anti-corrosion properties [6]. Therefore, a sample with a composite coating, having a multilevel relief formed by agglomerates of SPTFE microparticles, has a higher value of polarization resistance ($R_p = 3.9 \cdot 10^{10}$ Ω·cm^2) compared to samples without a coating ($R_p = 1.9 \cdot 10^5$ Ω·cm^2) and with a PEO-coating ($R_p = 2.4 \cdot 10^4$ Ω·cm^2).

The results of electrochemical studies of samples after atmospheric corrosion are presented in Table 1 and Fig. 3. For sample with PEO-coating, the corrosion current density during 6 months exposition is reduced by 2.5 times due to the sealing of its pores with corrosion products. Similarly, the polarization resistance increases for it (in 3 times). Also, the corrosion current density for the sample with CC tested for 6 months ($I_c = 2.9 \cdot 10^{-11}$ A·cm^{-2}) is 3 orders of magnitude lower in comparison with the sample with PEO-layer ($I_c = 3.5 \cdot 10^{-8}$ A·cm^{-2}) and almost 6 orders of

Table 1

Electrochemical parameters calculated for the samples without coating, with PEO-layer and composite coating before and after atmospheric corrosion test for 0, 3 and 6 months

Samples	β_a, mV	β_c, mV	E_c, V vs. SCE	I_c, A·cm^{-2}	R_p, Ω·cm^2
AMg3	17.5	154.8	−0.67	$1.1 \cdot 10^{-6}$	$2.4 \cdot 10^4$
AMg3 after 3 months	7.6	207.9	−0.73	$1.6 \cdot 10^{-6}$	$2.5 \cdot 10^3$
AMg3 after 6 months	11.2	179.3	−0.95	$1.7 \cdot 10^{-5}$	$3.8 \cdot 10^2$
PEO	39.0	429.5	−0.87	$8.4 \cdot 10^{-8}$	$1.9 \cdot 10^5$
PEO after 3 months	86.3	334.3	−0.79	$6.9 \cdot 10^{-8}$	$4.3 \cdot 10^5$
PEO after 6 months	78.3	422.1	−0.69	$3.5 \cdot 10^{-8}$	$5.7 \cdot 10^5$
CC	488.8	243.2	−0.59	$7.5 \cdot 10^{-12}$	$3.9 \cdot 10^{10}$
CC after 3 months	279.3	416.4	−0.53	$1.5 \cdot 10^{-11}$	$4.9 \cdot 10^9$
CC after 6 months	305.0	302.3	−0.48	$2.9 \cdot 10^{-11}$	$2.3 \cdot 10^9$

magnitude less than for uncoated AMg3 aluminum alloy (I_c = 1.7·10^{-5} A·cm^{-2}). The polarization resistance for this sample over the same period showed the value 2.3·10^9 Ω·cm^2, which is more than 3 orders of magnitude higher than one for sample with a PEO-layer (R_p = 5.7·10^5 Ω·cm^2) and almost 7 orders of magnitude greater than for uncoated AMg3 aluminum alloy (R_p = 3.8·10^2 Ω·cm^2).

Comparison of the corrosion current values obtained as a result of field tests (Table 1) with the literature data showed that after six months of exposure, both PEO (I_c = 3.5·10^{-8} A·cm^{-2}) and composite coating (I_c = 2.9·10^{-11} A·cm^{-2}) have higher barrier properties compared to other PEO coatings (I_c = 3.9·10^{-8} A·cm^{-2}) [5], (I_c = 1.5–4.5·10^{-6} A·cm^{-2}) [7], as well as composite coatings (I_c = 7.6·10^{-10} A·cm^{-2}) [7]. The initial values of corrosion current density for Alodine 1200s and PreCoat A32 chromium (VI) containing conversion coatings (I_c = 8.0-9.5 10^{-7} A·cm^{-2}) in the work [8] an order of magnitude higher compared to the values registered for the PEO-layer (I_c = 8.4·10^{-8} A·cm^{-2}) and 5 orders of magnitude higher than for the composite coating (I_c = 7.5·10^{-12} A·cm^{-2}). Even after 6 months of exposure the CC shows higher level of barrier properties (I_c = 2.9·10^{-11} A·cm^{-2}) in comparison with PTFE-containing IFKhANAL-3 conversion coating (I_c = 1.0–2.0·10^{-6} A·cm^{-2}) [9]. It can also be noted that the corrosion current density for the presented composite coating is one order of magnitude lower than estimated for the superhydrophobic coating formed by treatment of laser-processed aluminum alloy with fluorosilane (I_c = 10^{-10}–10^{-11} A·cm^{-2}) presented in [10].

Conclusion

It has been established that composite coating provides reliable protection even after a long-term exposure, the difference in currents is half an order of magnitude. This result is ensured by the high stability of both the polymeric materials and the PEO-coating used as the matrix. The increase in protective parameters for the PEO-coating is explained by the sealing of its pores with corrosion products.

Acknowledgments

Far Eastern Center for Electron Microscopy, Federal State Institution of Science A.V. Zhirmunsky National Scientific Center of Marine Biology of the Far Eastern Branch of the Russian Academy of Sciences (Vladivostok, Russia) for assistance in the study of coating morphology.

REFERENCES

1. **Egorkin V. S., Mashtalyar D. V., Gnedenkov A. S., Filonina V. S., Vyaliy I. E., Nadaraia K. V., Imshinetskiy I. M., Belov E. A., Izotov N. V., Sinebryukhov S. L., Gnedenkov S. V.,** Icephobic performance of combined fluorine-containing composite layers on al-mg-mn–si alloy surface, Polymers 13 (2021) 3827.

2. **Gnedenkov S. V., Sinebryukhov S. L., Egorkin V. S., Vyalyi I. E., Mashtalyar D. V., Nadaraia K. V., Ryabov D. K., Buznik V. M.,** Formation and properties of composite coatings on aluminum alloys, Russ. J. Inorg. Chem. 62 (2017) 1–11.

3. **Egorkin V. S., Vyaliy I. E., Sviridov N. S., Minaev A. N., Sinebryukhov S. L., Gnedenkov S. V.,** Formation and electrochemical properties of the hydrophobic composite coatings on aluminum alloy, Defect and Diffusion Forum 386 (2018) 315–320.

4. **Egorkin V. S., Vyaliy I. E., Gnedenkov A. S., Izotov N. V., Tolkanov D. K., Runov A. K., Minaev A. N., Sinebryukhov S. L., Gnedenkov S. V.,** Influence of formation conditions on corrosion behavior of PEO-coatings during salt-spray test, Solid State Phenomena 312 (2020) 319–324.

5. **Egorkin V. S., Medvedev I. M., Sinebryukhov S. L., Vyaliy I. E., Gnedenkov A. S., Nadaraia K. V., Izotov N. V., Mashtalyar D. V., Gnedenkov S. V.,** Atmospheric and marine corrosion of PEO and composite coatings obtained on Al-Cu-Mg aluminum alloy, Materials. 13(12) (2020) 2739.

6. **Gnedenkov S. V., Sinebryukhov S. L., Egorkin V. S., Mashtalyar D. V., Alpysbaeva D. A., Boinovich L. B.,** Wetting and electrochemical properties of hydrophobic and superhydrophobic coatings on titanium, Colloids Surf. A. 383 (2011) 61–66.

7. **Cerchier P., Pezzato L., Gennari C., Moschin E., Moro I., Dabala M.,** PEO coating containing copper: A promising anticorrosive and antifouling coating for seawater application of AA 7075, Surf. Coat. Technol. 393 (2020) 125774.

8. **Proença C. S., Pereira A. M., Pigliaru L., Rohr T., Correia J., Cabral A. M.,** Alternative chemical conversion pre-treatment for aeronautical aluminium alloy: characterisation and anticorrosion performance, CEAS Space J. (2022).

9. **Kuzenkov Y. A., Anufriev N. G., Oleinik S. V. Ty Fan Ba, Filichev N. L., Karpov V. A.,** Corrosion protection of aluminum alloys AMg3 and D16 with chromate-free conversion coatings in a tropical marine climate. Prot. Met. Phys. Chem. Surf. 56. (2020) 1315–1320.

10. **Sataeva N. E., Boinovich L. B., Emelyanenko K. A., Domantovsky A. G., Emelyanenko A. M.,** Laser-assisted processing of aluminum alloy for the fabrication of superhydrophobic coatings withstanding multiple degradation factors, Surf. Coat. Technol. 397 (2020) 125993.

THE AUTHORS

VYALIY Igor E.
vyaly@ich.dvo.ru
ORCID: 0000-0003-3806-1709

MINAEV Aleksander N.
aminaev@mail.ru
ORCID: 0000-0002-8072-306X

EGORKIN Vladimir S.
egorkin@ich.dvo.ru
ORCID: 0000-0001-5489-6832

SINEBRYUKHOV Sergey L.
sls@ich.dvo.ru
ORCID: 0000-0002-0963-0557

IZOTOV Nikolai V.
nikolaj.izotov@mail.ru
ORCID: 0000-0001-9504-1523

GNEDENKOV Sergey V.
svg21@hotmail.com
ORCID: 0000-0003-1576-8680

KHARCHENKO Ulyana V.
ulyana-kchar@mail.ru
ORCID: 0000-0001-5166-5609

Received 23.05.2022. Approved after reviewing 24.07.2022. Accepted 24.07.2022.

Journal

ST. PETERSBURG STATE POLYTECHNICAL UNIVERSITY JOURNAL: PHYSICS AND MATHEMATICS

Vol. 15, No. 3.1, 2022

Founder and publisher: Peter the Great St. Petersburg Polytechnic University

The journal is registered with the Federal Service for Supervision of Communications, Information Technology and Mass Media (Roskomnadzor).
Certificate ПИ ФС77-51457 issued 19.10.2012.

Phone 8 (812) 294-22-85

Website https://physmath.spbstu.ru/

E-mail: physics@spbstu.ru

Typesetting by *N.A. Bushmanova*, *A.S. Kolgatina*

Published 30.09.2022. Format 60x84/8. Digital print.

Printer's sheets Print circulation 1000. Order ID .